

DTIC QUALITY INSPECTED 2

LOW-VELOCITY IMPACT ON COMPOSITE
SANDWICH PLATES

DISSERTATION

Eric J. Herup
Major, USAF

AFIT/DS/ENY/96-11

DISTRIBUTION STATEMENT A

Approved for public release;
Distribution Unlimited

DEPARTMENT OF THE AIR FORCE
AIR UNIVERSITY
AIR FORCE INSTITUTE OF TECHNOLOGY

Wright-Patterson Air Force Base, Ohio

19970501 169

AFIT/DS/ENY/96-11

LOW-VELOCITY IMPACT ON COMPOSITE
SANDWICH PLATES

DISSERTATION

Eric J. Herup
Major, USAF

AFIT/DS/ENY/96-11

Approved for public release; distribution unlimited

The views expressed in this dissertation are those of the author and do not reflect the official policy or position of the Department of Defense or the U.S. Government.

AFIT/DS/ENY/96-11

LOW-VELOCITY IMPACT ON COMPOSITE SANDWICH PLATES

DISSERTATION

Presented to the Faculty of the Graduate School of Engineering
of the Air Force Institute of Technology

Air University

In Partial Fulfillment of the
Requirements for the Degree of
Doctor of Philosophy

Eric J. Herup

Major, USAF

July 1996

Approved for public release; distribution unlimited

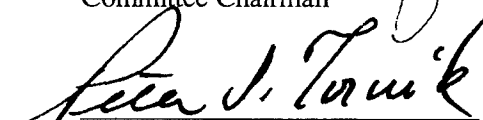
LOW-VELOCITY IMPACT ON COMPOSITE SANDWICH PLATES


Eric J. Herup


Major, USAF

Approved:


 29 July '96
ANTHONY N. PALAZOTTO
Committee Chairman

 29 July 96
PETER J. TORVIK
Committee Member

 29 July 96
DAVID L. COULLIETTE
Committee Member

 29 Jul 96
DENNIS C. DIETZ
Dean's Representative

Accepted:

 2 Aug 1996
Robert A. Calico
Dean, School of Engineering

Acknowledgments

The greatest of my debts, which are many, I will humbly attempt to acknowledge here. First and last, I owe my very being to my Maker, Defender, Redeemer, and Friend, the Lord Jesus Christ. If Christ is a crutch, with the sweet psalmist of Israel (David, Psalm 51) I gladly acknowledge my moral and spiritual disability (sin) and need of the same. Thanks be to God for His unspeakable gift.

Of course, there are many earthly debts I must also confess. Dr. Anthony N. Palazotto, my research advisor, provided insight, guidance, and often, motivation for the effort. I am sure that I am not even aware of all I owe to him. I thank my other committee members, Dr Peter J. Torvik, and Lieutenant Colonel David L. Coulliette for their enthusiastic technical guidance. I owe a special thanks to the sponsor of this research, Mr. William Baron of WL/FIB, who provided specimens, testing facilities, and support throughout the experimental phase. My thanks also to Dr. L. N. B. Gummadi, who provided insights, references, and important dialogue throughout the analytical effort.

For much of the AFIT program I have followed in the footsteps of Major James Greer. From “administrivia,” to focus for major exam preparation, to UNIX tips, my indebtedness has been so apparent to me that many times I have told him that if I graduate it will be his fault. If you ever read this Jim, it’s your fault. Thanks Bro.

My dear wife, Naomi, has endured the AFIT program twice now, (M.S. and PhD.) and her ear has graciously received much more of this effort than her natural interests would have. He who finds a wife, finds a good thing, and receives favor from the Lord (Proverbs 18:22). Our children, Rachel, Paul, Joshua, and Caleb have had a part as well in providing much needed breaks for “Play time with Papa” and the reality check to let me see again what is really important. Ultimately, just a few things (Micah 6:8) deserve the attention that many things demand.

Eric J. Herup

Table of Contents

ACKNOWLEDGMENTS	iii
TABLE OF CONTENTS.....	iv
LIST OF FIGURES	ix
LIST OF TABLES.....	xv
ABSTRACT	xvii
1. INTRODUCTION	1-1
1.1 MOTIVATION	1-1
1.2 OBJECTIVE	1-3
1.3 APPROACH.....	1-3
<i>1.3.1 Experimental investigation.</i>	<i>1-3</i>
<i>1.3.2 Analytical development.</i>	<i>1-4</i>
1.4 NOVELTY	1-6
1.5 OVERVIEW	1-6
1.6 SPONSORSHIP	1-7
2. BACKGROUND.....	2-1
2.1 SANDWICH PLATE	2-1
2.2 FAILURE CRITERIA.....	2-2
<i>2.2.1 Fiber failure criteria.</i>	<i>2-3</i>
<i>2.2.2 Matrix failure criteria.</i>	<i>2-3</i>
<i>2.2.3 Delamination failure criteria.</i>	<i>2-4</i>
2.3 PROGRESSIVE DAMAGE.....	2-4
<i>2.3.1 Monolithic laminate (facesheet) damage.</i>	<i>2-5</i>
<i>2.3.2 Core properties/damage.</i>	<i>2-7</i>
2.4 THREE-DIMENSIONAL EQUILIBRIUM CONSIDERATIONS	2-8
2.5 FINITE ELEMENT SOLUTION	2-8
2.6 CONTACT PROBLEM.....	2-8
2.7 NON-CONSERVATIVE FORCES	2-9
3. INSTRUMENTED IMPACTOR SYSTEM CHARACTERIZATION	3-1

	page
3.1 ENERGY CALCULATIONS	3-1
3.2 POSSIBLE ERROR SOURCES	3-4
3.3 MEASURED FORCE IN LOAD CELL	3-9
3.4 ONE- AND TWO-DEGREE OF FREEDOM MODELS	3-9
3.5 THREE-DEGREE OF FREEDOM MODEL	3-11
3.5.1 <i>Equations of motion (three-degree of freedom model).</i>	3-11
3.5.2 <i>Exact solution (three-degree of freedom model).</i>	3-12
3.5.3 <i>Empirically derived parameters.</i>	3-16
3.5.4 <i>Contact force history, comparison to previous test data.</i>	3-17
3.5.5 <i>Source of high frequency oscillations.</i>	3-19
3.5.6 <i>Absorbed energy implications.</i>	3-20
3.6 TUP TIP MASS	3-22
3.7 CONCLUSIONS	3-24
4. EXPERIMENTAL INVESTIGATION	4-1
4.1 OBJECTIVES	4-1
4.2 APPROACH	4-3
4.3 PARAMETERS	4-5
4.4 STATIC INDENTATION TEST SYSTEM	4-7
4.4.1 <i>Calibration.</i>	4-8
4.4.2 <i>Data reduction.</i>	4-9
4.5 DYNAMIC IMPACT TEST SYSTEMS	4-10
4.5.1 <i>Drop weight test system.</i>	4-11
4.5.2 <i>Pendulum test system.</i>	4-12
4.5.3 <i>Impact test calculations.</i>	4-13
4.6 DAMAGE ANALYSIS	4-16
4.6.1 <i>C-scan.</i>	4-16
4.6.2 <i>Photomicroscopy.</i>	4-16
4.7 RESULTS	4-17
4.7.1 <i>Absorbed energy.</i>	4-17
4.7.2 <i>Force history.</i>	4-29
4.7.3 <i>Global and local stiffness.</i>	4-36
4.7.4 <i>Transverse strain.</i>	4-42
4.7.5 <i>Dynamic and static compared.</i>	4-45
4.8 CONCLUSIONS	4-57
5. ELASTICITY SOLUTION	5-1

	page
5.1 OBJECTIVES.....	5-2
5.1.1 Analytical solution for undamaged plate.....	5-2
5.1.2 Failure criteria checkout.....	5-2
5.1.3 Benchmark for FEA.....	5-2
5.2 CYLINDRICAL BENDING SOLUTION.....	5-3
5.2.1 Material properties.....	5-8
5.2.2 Sinusoidal load, same material and geometry as test specimens.....	5-8
5.2.3 Extension for indentation problem.....	5-9
5.2.4 Cylindrical bending solution to Hertzian loaded sandwich plate.....	5-10
5.2.5 Failure criteria checkout.....	5-22
5.3 THREE-DIMENSIONAL SOLUTION TO HERTZIAN LOADED PLATE.....	5-51
5.4 CONCLUSIONS.....	5-53
6. THEORY AND APPROACH.....	6-1
6.1 SANDWICH PLATE.....	6-1
6.1.1 Geometry and coordinate systems.....	6-1
6.1.2 Plate assumptions.....	6-2
6.2 KINEMATICS.....	6-2
6.2.1 Plate midplane displacements without delamination.....	6-2
6.2.2 Plate midplane displacements with delamination.....	6-5
6.3 STRAIN-DISPLACEMENT RELATIONS.....	6-11
6.3.1 Full nonlinear strain displacement relations.....	6-11
6.3.2 Von Karman-type nonlinear strain displacement relations.....	6-12
6.4 CONSTITUTIVE RELATIONS.....	6-14
6.4.1 Before damage.....	6-14
6.4.2 Matrix damage.....	6-15
6.4.3 Fiber failure.....	6-16
6.4.4 Core properties/damage.....	6-16
6.4.5 Core/facesheet adhesive bondline damage.....	6-18
6.4.6 Interface (delamination) damage.....	6-18
6.5 IMPACT DYNAMICS.....	6-19
6.6 THREE-DIMENSIONAL EQUILIBRIUM EQUATIONS.....	6-19
6.6.1 Transverse stresses.....	6-19
6.6.2 Inconsistency of in-plane stresses.....	6-33
6.7 FINITE ELEMENT SOLUTION.....	6-35
6.7.1 General ideas.....	6-35

	page
6.7.2 Higher order element development	6-38
6.7.3 Higher order element testing.....	6-43
6.7.4 Generalized Newton-Raphson method.....	6-59
6.8 FAILURE CRITERIA	6-61
6.8.1 Matrix cracking and core damage.....	6-62
6.8.2 Delamination.....	6-62
6.9 CONTACT PROBLEM.....	6-63
6.10 ADAPTIVE MESH	6-70
6.11 CORE PROPERTIES	6-71
6.12 DAMAGE PROGRESSION	6-72
6.12.1 Matrix cracking.....	6-72
6.12.2 Core damage.....	6-72
6.12.3 Delamination.....	6-74
6.13 LOCAL MODEL SOLUTION ALGORITHM	6-74
6.14 GLOBAL MODEL SOLUTION ALGORITHM.....	6-76
6.15 LOCAL/GLOBAL INTERACTION	6-77
6.16 SUMMARY	6-77
7. COMPARISON TO ELASTICITY THEORY	7-1
7.1 GENERAL IDEAS	7-1
7.2 THREE-DIMENSIONAL SOLUTION	7-2
7.3 TWO-DIMENSIONAL (CYLINDRICAL BENDING) SOLUTION	7-7
7.4 CONCLUSIONS.....	7-11
8. COMPARISON TO EXPERIMENT.....	8-1
8.1 GENERAL IDEAS	8-1
8.2 MESH REFINEMENT	8-2
8.3 CORE STRESS VERSES STRAIN	8-7
8.4 TEST CASES	8-8
8.4.1 Case 1, no damage.....	8-8
8.4.2 Case 2, core damage only.....	8-9
8.4.3 Case 3, facesheet and core damage.....	8-9
8.5 METRICS FOR SUCCESS OF THE ANALYSIS	8-10
8.5.1 Contact radius.....	8-10
8.5.2 Load verses displacement curve.....	8-10
8.5.3 Delamination pattern.....	8-10

	page
8.6 TEST RESULTS	8-11
8.6.1 Case 1, no damage.	8-11
8.6.2 Case 2, core damage only.....	8-13
8.6.3 Case 3, facesheet and core damage.	8-16
8.7 SUMMARY	8-23
9. SUMMARY AND CONCLUSIONS	9-1
APPENDIX A: MATHCAD ELASTICITY SOLUTIONS	A-1
APPENDIX B: FORTRAN ELASTICITY SOLUTIONS WITH HERTZIAN CONTACT	B-1
BIBLIOGRAPHY	BIB-1
VITA	V-1

List of Figures

Figure 3-1	Typical force and energy histories for an event without damage [5].	3-3
Figure 3-2	Simulation of force and energy histories of figure 3-1.	3-5
Figure 3-3	Schematics of one- and two-degree-of-freedom models [13].	3-10
Figure 3-4	Schematic of three-degree of freedom model.	3-11
Figure 3-5	Plate indentation and contact stiffness.	3-12
Figure 3-6	Schematic of the one-degree of freedom systems used to estimate plate effective mass.	3-16
Figure 3-7	Comparison of experiment and three-degree of freedom model.	3-18
Figure 3-8	Three-degree of freedom model contact force error with and without the tup mass ratio correction.	3-19
Figure 3-9	Instrumented impactor model calculated and corrected energy histories.	3-21
Figure 3-10	Impulse response of instrumented impactor showing effect of tup tip mass.	3-22
Figure 3-11	Load histories showing effect of tup tip mass	3-23
Figure 4-1	Impact test matrix.	4-7
Figure 4-2	Schematic of static indentation test system. (The direction of the applied displacement is shown by δ).	4-8
Figure 4-3	Typical "static" loading sequence. (100 data points were recorded per second).	4-10
Figure 4-4	Schematic of Dynatup drop weight impact test system.	4-11
Figure 4-5	Schematic of pendulum impact test system.	4-13
Figure 4-6	4-ply Velocities of impact (V_{in}) and rebound (V_{out}) versus impact energy. Pendulum data only.	4-20
Figure 4-7	8-ply Velocities of impact (V_{in}) and rebound (V_{out}) versus impact energy. Pendulum and drop weight data.	4-21
Figure 4-8	32-ply Velocities of impact (V_{in}) and rebound (V_{out}) versus impact energy. Pendulum data only.	4-22
Figure 4-9	48-ply Velocities of impact (V_{in}) and rebound (V_{out}) versus impact energy. Pendulum data only.	4-23
Figure 4-10	Rebound velocity calculation difference versus rebound velocity. Pendulum data only.	4-24
Figure 4-11	4-ply Absorbed energy versus impact energy showing threshold near 0.3 J. Pendulum data only.	4-25
Figure 4-12	8-ply Absorbed energy versus impact energy showing threshold near 0.45 J. Pendulum and drop weight data.	4-25
Figure 4-13	16-ply Absorbed energy versus impact energy showing threshold near 1.0 J. Drop weight data only.	4-26
Figure 4-14	32-ply Absorbed energy versus impact energy showing threshold near 5.1 J. Pendulum data only.	4-26
Figure 4-15	48-ply Absorbed energy versus impact energy showing threshold near 8.5 J. Pendulum data only.	4-27

	page
Figure 4-16	Absorbed energy/impact energy verses facesheet plies showing decreasing absorbed energy ratio (hence decreasing relative damage) from a given impact energy as the facesheet thickness is increased..... 4-29
Figure 4-17	4-ply Force histories offset by impact energy showing possible damage initiation near 400 N in the 0.094 J event while first major load drop does not occur until near 550 N in the > 0.3 J events. Note the 0.11 J and 0.22 J events do not evidence damage even though the lower energy 0.094 J event does. Pendulum data only..... 4-30
Figure 4-18	8-ply Force histories offset by impact energy showing possible damage initiation near 1000 N in the 0.47 J event while first major load drop does not occur until near 1100 N in the > 0.4 J events. Pendulum (< 1 J) and drop weight (> 1 J) data..... 4-30
Figure 4-19	16-ply Force histories offset by impact energy showing damage initiation near 2700 N in the impact energy > 1.3 J events. Drop weight data..... 4-31
Figure 4-20	32-ply Force histories offset by impact energy showing damage initiation near 8000 N in the impact energy > 5.2 J events. Pendulum data..... 4-31
Figure 4-21	48-ply Force histories offset by impact energy showing damage initiation near 14000 N in the impact energy > 10.0 J events. Pendulum data..... 4-32
Figure 4-22	Peak transverse stress for unit (1 N) transverse force assuming Hertzian contact law..... 4-37
Figure 4-23	16-ply Static force verses displacement showing "global" and "local" response including the effects of damage..... 4-39
Figure 4-24	Contact radius and peak stress (assuming Hertzian contact) as a function of applied load on a 16-ply specimen showing an inverse relationship between applied force and peak stress..... 4-41
Figure 4-25	Transverse strain verses displacement for static indentation showing strain jumps presumed to be indicative of multiple cell core failure..... 4-43
Figure 4-26	Load and absorbed energy associated with first major load drop. This shows that thicker facesheets take a greater load before the first major load drop and that they dissipate more energy in the damage associated with that load drop..... 4-45
Figure 4-27	C-scans for static and dynamic events found to exhibit the first major load drop (magnified 150%)..... 4-46
Figure 4-28	4-ply Static and dynamic force verses displacement showing the effects of damage..... 4-49
Figure 4-29	8-ply Static and dynamic force verses displacement showing the effects of damage..... 4-50
Figure 4-30	16-ply Static and dynamic force verses displacement showing the effects of damage..... 4-51
Figure 4-31	32-ply Static and dynamic force verses displacement showing the effects of damage..... 4-52
Figure 4-32	48-ply Static and dynamic force verses displacement showing the effects of damage..... 4-52
Figure 4-33	8-ply Static and dynamic force verses displacement showing the dynamic equilibrium effects of damage progression..... 4-53
Figure 4-34	16-ply Static and dynamic force verses displacement showing the dynamic equilibrium effects of damage progression..... 4-54
Figure 4-35	Comparison of load at the first major load drop for static and dynamic tests showing that specimens fail at lower load under static than dynamic tests..... 4-55
Figure 4-36	Comparison of energy absorbed in the first major load drop for static and dynamic tests showing that specimens absorb less energy with static than dynamic tests..... 4-56
Figure 5-1	Cylindrical bending plate notation..... 5-4

	page
Figure 5-2	Geometry for sinusoidally loaded sandwich plate in cylindrical bending. 5-9
Figure 5-3	Hertzian load approximation by truncated Fourier series for the 1.59 mm contact radius case showing that minimal improvement is obtained by increasing the number of terms above 150. 5-10
Figure 5-4	Normalized transverse direct stress under the center of a Hertzian load showing how thicker facesheets serve to reduce the compressive stress seen by the core, thus delaying core failure. Contact half-width was 1.59 mm and normalization is by the peak applied stress. 5-12
Figure 5-5	Transverse direct stress under the center of a Hertzian load scaled to match the peak stress and contact radius for the first major load drop seen in the experiments. For comparison, uniaxial core strength is also plotted indicating that the core achieves a stress higher than its uniaxial compression strength before failure. 5-13
Figure 5-6	Apparent core strength as calculated by equation 5-16. 5-15
Figure 5-7	In-plane direct stress under the center of a Hertzian load normalized by peak applied (transverse) stress showing the reduction in in-plane stress brought about by thicker facesheets. Contact half-width was 1.59 mm and normalization is by the peak applied stress. 5-17
Figure 5-8	Transverse direct stress under the center of a Hertzian load scaled to show values for the first major load drop seen in the experiments. For comparison, ultimate tensile and compressive strengths of the facesheets are also plotted indicating that the facesheets achieve a stress higher than ultimate strength before the first major load drop. 5-18
Figure 5-9	Normalized transverse shear stress in the midplane of the top facesheet showing how thicker facesheets serve to reduce the peak transverse shear stress and move its location away from the center of the plate. Contact half-width was 1.59 mm and normalization is by the peak applied stress. 5-19
Figure 5-10	Transverse shear stress at the location of the peaks found in figure 5-8, normalized by peak applied (transverse) stress, showing the reduction in transverse shear stress brought about by thicker facesheets. Contact half-width was 1.59 mm and normalization is by the peak applied stress. 5-20
Figure 5-11	Transverse shear stress at the location of the peaks found in figure 5-8, scaled to show values for the first major load drop seen in the experiments. For comparison, ultimate shear strengths of the 0 and 90 degree plies of the facesheets are also plotted indicating that for most facesheet thicknesses a maximum stress criteria would indicate matrix cracking before the first major load drop. 5-21
Figure 5-12	Cylindrical bending and three-dimensional plate geometries. 5-22
Figure 5-13	Cylindrical bending fiber failure metric for applied load that produced first major load drop in the three-dimensional indentation tests of the 4-ply specimens. This shows that the in-plane stress predicted by the cylindrical bending assumption is very high compared to the actual three-dimensional experiment which saw no fiber failure. Positive z is up and load is applied to the positive z side of the plate in the negative z direction. 5-25
Figure 5-14	Cylindrical bending fiber failure metric at the plate center for applied load that produced first major load drop in the three-dimensional indentation tests. Hashin criterion. 5-26
Figure 5-15	4-ply specimen cylindrical bending matrix failure metric in the top facesheet near the plate center for applied load that produced first major load drop in the three-dimensional indentation tests. 5-29

	page
Figure 5-16 8-ply specimen cylindrical bending matrix failure metric in the top facesheet near the plate center for applied load that produced first major load drop in the three-dimensional indentation tests.	5-30
Figure 5-17 16-ply specimen cylindrical bending matrix failure metric in the top facesheet near the plate center for applied load that produced first major load drop in the three-dimensional indentation tests.	5-31
Figure 5-18 32-ply specimen cylindrical bending matrix failure metric in the top facesheet near the plate center for applied load that produced first major load drop in the three-dimensional indentation tests.	5-32
Figure 5-19 48-ply specimen cylindrical bending matrix failure metric in the top facesheet near the plate center for applied load that produced first major load drop in the three-dimensional indentation tests.	5-33
Figure 5-20 Part A of 0° cross section of 4-ply specimen after 1.4 J impact (25X). From [5] figure 3.9. Label D identifies a matrix crack and label I identifies a failed core cell wall.	5-34
Figure 5-21 Part B of 0° cross section of 4-ply specimen after 1.4 J impact (25X). From [5] figure 3.10. Label B identifies matrix cracks with a delamination. Label A identifies nearly vertical matrix cracks The arrow shows the approximate x-location of the point of impact and labels F and G identify failed core cell walls adjacent to the point of impact.	5-35
Figure 5-22 Part C of 0° cross section of 4-ply specimen after 1.4 J impact (25X). From [5] figure 3.11. Label E identifies matrix cracks and label H identifies a failed core cell wall.	5-35
Figure 5-23 Part A of 0° cross section of 8-ply specimen after 2.7 J impact (25X). From [5] figure 3.47. Label G identifies matrix cracks and labels E and D identify failed core cell walls.	5-36
Figure 5-24 Part B of 0° cross section of 8-ply specimen after 2.7 J impact (25X). From [5] figures 3.47 and 3.48. The arrow shows the approximate x-location of the point of impact. Label H identifies matrix cracks and label F identifies a failed core cell wall under the point of impact.	5-37
Figure 5-25 Part C of 0° cross section of 8-ply specimen after 2.7 J impact (25X). From [5] figure 3.48. Labels C, B, and A identify major delaminations.	5-37
Figure 5-26 Part A of 0° cross section of 16-ply specimen after 4.1 J impact (25X). From [5] figure 3.90.	5-38
Figure 5-27 Part B of 0° cross section of 16-ply specimen after 4.1 J impact (25X). From [5] figures 3.90 and 3.91. The arrow identifies the approximate location of the impact point.	5-39
Figure 5-28 Part C of 0° cross section of 16-ply specimen after 4.1 J impact (25X). From [5] figure 3.91.	5-40
Figure 5-29 Part A of 0° cross section of 32-ply specimen after 5.0 J impact (25X). From [5] figure 3.119. Label B identifies matrix cracks and labels D and E identify failed core cell walls.	5-42
Figure 5-30 Part B of 0° cross section of 32-ply specimen after 5.0 J impact (25X). From [5] figure 3.120. The arrow identifies the approximate location of the impact point.	5-43
Figure 5-31 Part C of 0° cross section of 32-ply specimen after 5.0 J impact (25X). From [5] figure 3.120.	5-44
Figure 5-32 Part A of 0° cross section of 48-ply specimen after 9.7 J impact (25X). From [5] figure 3.161. The arrow identifies the approximate location of the impact point.	5-44

	page
Figure 5-33	Part B of 0° cross section of 48-ply specimen after 9.7 J impact (25X). From [5] figure 3.162. 5-47
Figure 5-34	Core failure metric at the center of the specimen for the applied load that produced first major load drop. This shows that the strengths of figure 5-5 effectively normalize the metric to unity at the top of the core when the first major load drop occurs. 5-50
Figure 5-35	Core failure metric at the top of the core for the applied load that produced first major load drop. This shows that the strengths of figure 5-5 effectively normalize the metric to unity at the center of the specimen when the first major load drop occurs. 5-52
Figure 5-36	Truncated Fourier sine series representations of Hertzian contact with 1.59 mm contact radius showing poor representation of loading with the number of terms for which a three-dimensional solution was available. The maximum number of terms for a sandwich was 11 (4-ply). 5-52
Figure 5-37	Truncated Fourier sine series representations of Hertzian contact with 12.7 mm contact radius showing marginal representation of loading with the number of terms for which a three-dimensional solution was available. 5-52
Figure 6-1	Sandwich plate geometry and coordinate systems. 6-2
Figure 6-2	Plate displacement vector components. 6-5
Figure 6-3	X-direction displacement jump across a delamination. 6-6
Figure 6-4	Transverse shear as calculated by elasticity theory, constitutive relations, and equilibrium equations for sinusoidally loaded plate in cylindrical bending. Dimensions, material properties, and scaling from Pagano [236]. 6-20
Figure 6-5	Four-node plate element geometry and coordinate systems. 6-36
Figure 6-6	Pascal's triangle showing interpolation polynomials for 3 rd and 5 th order shape functions. Note, polynomials are complete to 3 rd and 5 th order, respectively. 6-39
Figure 6-7	Four-node plate elements with 7, 11, and 14 degrees of freedom per node. 6-43
Figure 6-8	Geometry and boundary conditions for 7, 11, and 14 DOF per node element tests. 6-44
Figure 6-9	Comparison of current and elasticity solutions for 4-ply sandwich plate. 6-46
Figure 6-10	Comparison of current and elasticity solutions for 8-ply sandwich plate. 6-48
Figure 6-11	Comparison of current and elasticity solutions for 16-ply sandwich plate. 6-49
Figure 6-12	Comparison of current and elasticity solutions for 32-ply sandwich plate. 6-50
Figure 6-13	Comparison of current and elasticity solutions for 48-ply sandwich plate. 6-51
Figure 6-14	Comparison of current and elasticity solutions for 4-ply monolithic plate. 6-54
Figure 6-15	Comparison of current and elasticity solutions for 8-ply monolithic plate. 6-55
Figure 6-16	Comparison of current and elasticity solutions for 16-ply monolithic plate. 6-56
Figure 6-17	Comparison of current and elasticity solutions for 32-ply monolithic plate. 6-57
Figure 6-18	Comparison of current and elasticity solutions for 48-ply monolithic plate. 6-58
Figure 6-19	Boundary conditions common to each square quarter plate 6-61
Figure 6-20	Contact problem geometry and coordinate system 6-64
Figure 6-21	Finite element displacements for initial small load. 6-65
Figure 6-22	After first step of FEM/3D-equations of motion. 6-66

	page
Figure 6-23	Tup surface as a constraint on the plate top surface displacement 6-67
Figure 6-24	Typical convergence of tup surface radius and contact radius with contact iteration 6-69
Figure 6-25	Schematic of core failure 6-73
Figure 6-26	Local-global solution algorithm flowchart. 6-75
Figure 6-27	Global solution algorithm flowchart 6-77
Figure 7-1	Comparison of top facesheet in-plane direct stress, σ_x , at the center of the plate for the large contact radius, three-dimensional case (12.7 cm square sandwich plate, 16-ply facesheets, 1.0 N load, 12.7 mm contact radius). 7-3
Figure 7-2	Comparison of top facesheet transverse direct stress, σ_z , at the center of the plate for the large contact radius, three-dimensional case (12.7 cm square sandwich plate, 16-ply facesheets, 1.0 N load, 12.7 mm contact radius). 7-5
Figure 7-3	Comparison of top facesheet transverse shear stress, τ_{xz} , at the location of the peak for the large contact radius, three-dimensional case (12.7 cm square sandwich plate, 16-ply facesheets, 1.0 N load, 12.7 mm contact radius). 7-6
Figure 7-4	Comparison of top facesheet in-plane direct stress, σ_x , at the center of the plate for the small contact radius, two-dimensional case (cylindrical bending, 12.7 cm wide sandwich plate strip, 16-ply facesheets, 4.65 N/m load, 1.0 mm contact radius). 7-8
Figure 7-5	Comparison of top facesheet transverse direct stress, σ_z , at the center of the plate for the small contact radius, two-dimensional case (cylindrical bending, 12.7 cm wide sandwich plate strip, 16-ply facesheets, 4.65 N/m load, 1.0 mm contact radius). 7-9
Figure 7-6	Comparison of top facesheet transverse shear stress, τ_{xz} , at the location of the peak for the small contact radius, two-dimensional case (cylindrical bending, 12.7 cm wide sandwich plate strip, 16-ply facesheets, 4.65 N/m load, 1.0 mm contact radius). 7-10
Figure 8-1	5x5 grid for contact radius = 1.0 mm. Maximum aspect ratio = 73. 8-3
Figure 8-2	9x9 grid for contact radius = 1.0 mm. Maximum aspect ratio = 115. 8-4
Figure 8-3	13x13 grid for contact radius = 1.0 mm. Maximum aspect ratio = 141. 8-4
Figure 8-4	Plate center displacement verses grid size (4- and 48-ply sandwich plate, 1.0 N load, contact radius = 1.0 mm), showing that above 9 elements per side, the solution does not significantly change. 8-5
Figure 8-5	Top facesheet midplane transverse shear along the y axis (4-ply sandwich plate, 1.0 N load, contact radius = 1.0 mm) 8-6
Figure 8-6	Top facesheet midplane transverse shear along the y axis (48-ply sandwich plate, 1.0 N load, contact radius = 1.0 mm) 8-7
Figure 8-7	Core stress verses strain curves. 8-8
Figure 8-8	Contact radius predicted by local finite element model without considering damage (16-ply). 8-11
Figure 8-9	Load verses displacement predicted by local finite element model without damage (16-ply). 8-13
Figure 8-10	Contact radius predicted by local finite element model with only core damage considered (16-ply). 8-14
Figure 8-11	Load verses displacement predicted by local finite element model with and without considering core damage (16-ply). 8-15

		page
Figure 8-12	Contact radius predicted by local finite element model with facesheet and core damage considered (16-ply).	8-16
Figure 8-13	Load verses displacement predicted by local finite element model with and without considering facesheet and core damage (16-ply).	8-18
Figure 8-14	Illustration of the progress of core damage under a constant applied force.	8-20
Figure 8-15	Delamination patterns predicted by local finite element model for 2250 N load (16-ply).	8-22

List of Tables

page

Table 5-1	Material properties.....	5-8
Table 5-2	Cylindrical bending matrix failure metric figures with their experimental counterparts.	5-34

Abstract

The response of composite sandwich plates to low-velocity impact is the subject of this research. The objective of the research is to analytically model the response of composite sandwich plates to low-velocity impact. A displacement based, plane stress, finite element code is modified for this purpose. Major new algorithms include 5th order Hermitian interpolation, three-dimensional equilibrium integration for transverse stress calculations, sandwich core modeling as an elastic-plastic foundation, loading by simulated contact with a spherical indenter, adaptive mesh, damage prediction, damage progression via stiffness reduction, and local-global analysis for displacement. An experimental effort is also included in which composite sandwich plates with graphite-epoxy facesheets and Nomex honeycomb core are subjected to low velocity impact (instrumented impactor) and static indentation. Comparison of static and dynamic results indicates limitations for the quasi-static assumptions typically made. Dynamic simulation of the impact event is provided by a one-dimensional, three-degree of freedom model. Classical three-dimensional and cylindrical bending elasticity solutions attributed to Pagano are modified for Hertzian contact and sandwich structures, providing an exact solution against which the finite element analysis is benchmarked. The two-dimensional (plane stress) finite element analysis, when combined with the three-dimensional equations of stress equilibrium predicts the three-dimensional state of stress in an undamaged composite sandwich under contact-type loading. The three-dimensional stresses obtained from the equilibrium equations and the in-plane finite element stresses compare favorably with the elasticity solution. When compared to the experimental data, the finite element analysis shows the ability to model some of the important features of static indentation of composite sandwich structures. In particular, the slope of the load displacement curve (stiffness), including contact, before damage is well represented. Core failure load is predicted by the analysis within ten percent of the experimental value. Delamination patterns predicted by the analysis are similar in shape to the delaminations observed by C-scans from the experiments, but are smaller for the same load.

LOW-VELOCITY IMPACT ON COMPOSITE SANDWICH PLATES

1. Introduction

1.1 Motivation

Sandwich structures have long been recognized as one of the most efficient constructions for resisting bending loads. These hybrid constructions consist of two relatively dense and stiff outer facesheets that are bonded to either side of a low-density core. The facesheets usually carry axial loads and the core sustains shear and compressive stresses normal to the panel while preventing wrinkling or buckling of the facesheets under axial compressive loading [1]. The core usually contributes little in-plane and flexural stiffness to the sandwich structure, but it can have significant transverse stiffness and adequate shear stiffness. The existence of the core places the facesheets away from the plate bending neutral axis, enhancing the bending resistance of the facesheets. The result is a thicker plate or shell with a higher bending stiffness-to-weight ratio than the facesheets alone. Considering that corrugated cardboard is a sandwich structure, sandwich constructions are perhaps the most common means employed to enhance the bending stiffness to weight ratio of a material.

The need for stiff, lightweight structures in aerospace vehicle components then, has motivated the design and analysis of sandwich plates and shells using composite materials. The aerospace industry, with its many bending stiffness dominated structures and its need for low weight, has employed sandwich constructions using aluminum honeycomb cores extensively. The most common currently fielded sandwich constructions suffer from two major maintenance problems: corrosion damage to the core from trapped moisture, and low-velocity impact damage. The core corrosion problem can be greatly reduced by using a non-corrosive core such as Nomex honeycomb. Low-velocity impact damage to such structures is the subject of the present research.

A principal drawback of laminated composite panels in general and composite sandwiches in particular is their susceptibility to low-velocity impact damage such as that brought about by dropped tools and runway/taxiway debris. In particular, significant loss of compressive strength has been found to occur without any visible sign of damage [2-4]. This situation is a major

concern for both manufacturers and end-users who need to locate damages and define criteria for acceptance and/or repair of structural members. There remains considerable room for improvement of composite sandwich low-velocity impact damage resistance (ability to resist low-velocity impact without structural damage) and low-velocity impact damage tolerance (ability to resist design loads after damage from low-velocity impact). Increasing either the low-velocity impact damage resistance of a structure or its low-velocity impact damage tolerance requires understanding of its response to low-velocity impact loads. The response of laminated composite sandwich plates to low-velocity impact loads is also considered in the present research.

Predicting the response of laminated composite plates to mechanical loads is complicated due to effects such as: through-the-thickness property variation, geometric and material nonlinearity, transverse shear, and multiple and coupled damage modes. The addition of a low-density core in sandwich constructions further complicates the analysis. Closed-form methods are limited to linear solutions (with many simplifying assumptions) for specific geometries, lay-ups, and boundary conditions. Experimental testing can yield response data for a particular plate and load, but it is not generally practicable, in terms of time and monetary expense, to experimentally characterize the effects of a wide range of variables. Such characterization is required to direct an optimization of any design. The characterization is also needed for modification and repair design since any structural variation must be evaluated in terms of its contribution to low-velocity impact damage resistance and low-velocity impact damage tolerance of the structure.

In contrast to experimental testing, numerical techniques like the finite element method (FEM) can be applied to plates and shells of different shapes, sizes, compositions, loadings and supports without the expense and lead time required for testing. The accuracy and practicality of FEM are dependent on the governing theories, model complexity, mesh refinement, user's skill (in the representation of the geometric structures, material properties, boundary conditions and loads), and a given computer's memory capacity, speed, and precision. The failure modes commonly observed in low-velocity impact to composite sandwich plates (fiber failure, matrix cracking, delamination, core crushing [5]) are driven by three-dimensional stress states. This implies that any model representing low-velocity impact to composite sandwich plates should be capable of accurately predicting three-dimensional stresses. The obvious approach is to employ a three-dimensional FEM, but the detail required in such a model very quickly overwhelms the

computational capacity available to the analyst. A two-dimensional FEM that can accurately represent low-velocity impact to composite sandwich structures can dramatically reduce the computational expense.

A simple hypothetical example will illustrate this. Suppose an analysis of a typical simply supported, center loaded, 20 cm x 20 cm, 64-ply (0.127 mm ply thickness) laminated plate is required. What computational capacity would one need to model such a structure? Three-dimensional stresses will determine failure. A three-dimensional model seems appropriate. A reasonable approach is to use a stack of 24 degree-of-freedom, eight noded (3 displacements per node) three-dimensional brick elements. Maintaining a maximum aspect ratio of seven, the maximum in-plane element dimension is a tiny 0.89 mm. The minimum number of elements for the model is $115 \times 115 \times 64 = 846,400$. The model has over 2.5 million degrees-of-freedom. If plate elements are used instead, a symmetric $11 \times 11 = 121$ element grid of shear deformable, 56 degree-of-freedom, four noded (see Chapter 4 for description of this element) plate finite elements will probably prove sufficient. The number of elements in each in-plane direction is reduced by an order of magnitude because two-dimensional elements do not suffer the aspect ratio problems associated with the small ply thickness. After boundary conditions are applied, this model has less than 1800 degrees-of-freedom. For this scenario, the number of degrees-of-freedom required by the three-dimensional model is at least 1400 times that of the two-dimensional model. If the plate was a sandwich construction, the difference is even more dramatic. This is admittedly a contrived problem. The analyst could choose to accept poorly shaped elements (in the regions of small stress gradients) without significant loss of accuracy. This example nevertheless illustrates the advantage of a plate solution of a laminated composite. Considering the nonlinearities associated with contact, geometry, and material properties, a full three-dimensional solution is, in many cases, prohibitively expensive. Therefore, an accurate method to account for low-velocity impact induced damage of a composite sandwich plate without resorting to a three-dimensional FEM should prove to be a significant contribution.

1.2 Objective

The object of this research is to provide understanding of and ultimately predict the initiation and progression of damage to a composite sandwich plate due to low velocity impact. This

prediction will be based on a two-dimensional finite element model will. The finite element program developed for this research is capable of modeling composite sandwich plates while extracting quasi three-dimensional stress values by employing the differential equations of equilibrium for a deformable continuous body [221]. Geometric nonlinearity and transverse shear effects are modeled. Contact between the plate and the impactor is also modeled. Appropriate damage initiation and progression criteria are identified and the code reduces the stiffness of the damaged elements to model the effects of matrix cracking, delamination, fiber failure, and core crushing damage progression.

1.3 Approach

This research involved both experimental and analytical efforts.

1.3.1 Experimental investigation.

To provide a basic understanding of the physical processes involved in low-velocity impact to composite sandwich plates and to validate the analytical developments of this study, an experimental investigation was performed. Several plates of a particular material and geometric configuration were impacted by a free-falling (drop weight) or free swinging (pendulum) hemispherical-nosed mass (the tup). Contact force was monitored throughout the impact event through the use of an instrumented impactor. In addition, plates of each configuration were subjected to static indentation simulating one or more of the same impact loads. After impact or static loading, each specimen was carefully analyzed to determine the damage modes present and the extent of damage by each mode. A range of impact energies provided a characterization of the damage as a function of impact energy. Comparison of the static and impact damages over a range of facesheet thicknesses provided insight into the range of applicability of quasi-static assumptions commonly made in thin monolithic laminate analyses to sandwich constructions in general and thick facesheet structures in particular. This information fills voids in the published data [5] (particularly at low impact energies), indicates when dynamic analyses are required, and validates the finite element program.

1.3.2 Analytical development.

Transverse impact damage progression in a composite sandwich panel is a three-dimensional phenomenon. This can be seen by a superficial examination of the failure modes exhibited in typical damages while considering the stresses that can give rise to them. Fiber failure is driven most strongly by in-plane direct stress in the fiber direction. Matrix cracking is driven most strongly by transverse shear stress and in-plane direct stress normal to the fibers. Delamination is driven by transverse shear stress and transverse direct stress. Core crushing is driven by transverse direct stress. A two-dimensional (plane stress) model of the plate in which transverse shear strain is compatible at the lamina interfaces has the significant limitations that transverse direct stress is assumed to be zero (plane stress) and transverse shear stress is not necessarily compatible at the lamina interfaces (due to constitutive differences from ply to ply). These limitations must be overcome if a plane stress model is to be used for predicting damage progression in a composite sandwich panel. It is here that the three-dimensional differential equations of equilibrium of a deformable continuous body are employed.

The approach for this effort involves a local/global method. The local model represents a single facesheet and its supporting core by plate finite elements (the facesheet) with an elastic foundation (the core). The global model represents the entire sandwich structure by plate finite elements in which the facesheets and the core contribute to the stiffness of each element. In both cases the plate elements incorporate cubic kinematics and in the local model a post-processing algorithm integrates three-dimensional equilibrium equations producing a quasi three-dimensional stress tensor. Contact between the plate and the tup is assumed to produce a Hertzian pressure distribution under the tup. In the local model, the transverse strains (obtained from the three-dimensional stresses) are integrated to establish the contact surface between the plate and the impactor. The contact radius is a product of the local model and is obtained through an iterative algorithm in which the three-dimensional shape of the top surface of the plate under the load is made to conform to the known shape of the tup. In this way, an iterative scheme produces a stress field satisfying compatibility (via the plate finite element model), the contact problem, and the approximately satisfying the three-dimensional differential equations of equilibrium for the plate.

Once this contact radius is known from the local model, it establishes the distribution of load on the global model since the total force is known for the given load increment and the form of

the distribution of the force is assumed to be Hertzian. The sandwich plate (global) FEM is then run to obtain the midplane displacement of the sandwich. This is required because the local model includes no sandwich plate midplane displacement and it is desired to compare displacement with the experimental data. In particular, the top surface displacement is taken to be the sum of the top surface displacement in the local model (for which sandwich midplane displacement was zero) and the midplane displacement from the global model.

The six components of stress within the top facesheet resulting from this procedure are used with failure criteria to update the constitutive relationship in the local finite element model. When the transverse load of the plate reaches sufficient magnitude, the failure criteria indicate localized failure of the composite sandwich structure via fiber failure, matrix cracking, and delamination. The displacement from the local finite element model establishes an average core stress by an empirical elastic-plastic relationship between core strain and core stress derived from the core manufacturer's uniaxial compression test data [128]. This core stress provides the foundation pressure distribution that supports the facesheet. The displacement from the local finite element model divided by the core thickness is taken to be the average core strain. The failure of the core is predicted by a simple maximum strain criteria in which the core is assumed to fail (core crushing/crippling) when the strain reaches the magnitude of the failure strain in a uniaxial compression test [128]. In this way, appropriate failure criteria estimate both the modes and extent of the failure at any given load increment. As the individual plies or interfaces fail, a stiffness reduction routine simulates the varying material response, smearing the effect of the damage over the damaged element(s). As the core fails, the foundation stiffness for a given element is reduced to simulate the fact that a crushed/crippled core does not provide transverse support to the facesheet.

Thus, the analytical code developed for this dissertation simulates many of the important features of composite sandwich plate impact.

1.4 Novelty

With regard to empirical data for low-velocity impact to composite sandwich plates, this research extends, bridges gaps in, and most importantly provides an interpretative framework for

the existing database. The current work also provides a cost effective analytical tool for modeling the low-velocity impact event in composite sandwich plates. The novelty of this research lies in six principal areas. The first three relate to the experimental investigation: (1) the effects of instrumented impactor dynamics on impact test results; (2) a correlation of instrumented impactor load data to damage progression in composite sandwich plates; and (3) the time-dependence of the low-velocity impact response of composite sandwich plates and its implications for quasi-steady analyses and tests. The last three areas are the means by which the following are accounted for in a low-velocity impact to composite sandwich plate analysis: (1) through-the-thickness stresses; (2) local deformations in the contact zone; (3) core, intra-ply, and inter-ply damage progression.

1.5 Overview

Chapter 2 presents the background for the current work and reviews some of the literature contributing to the understanding of the physical processes involved in the initiation and progression of damage in laminated composites in general and sandwich structures in particular. Some of the literature relevant to: modeling sandwich plates, failure theories, progressive damage, three-dimensional equilibrium considerations, finite element solution, contact, impact dynamics, and instrumented impactor testing are also briefly reviewed.

Chapter 3 presents the characterization and improvements to the experimental test systems used in the experimental investigation portion of the current work. Corrections to the data reduction algorithms to account for tup dynamics are also developed.

Chapter 4 presents the experimental investigation portion of the current work. Static indentation and impact test data for composite panels with graphite-epoxy cross-ply face sheets and Nomex honeycomb core are presented and interpreted. The two primary variables of interest in these tests were facesheet thickness (number of cross plies) and impact energy. General trends are identified and discussed. Implications of these data relevant to modeling of the structures and damage processes involved are addressed.

Chapter 5 extends the elasticity theory of Pagano [236-237] to sandwich strips and plates with contact-type loads simulated by a Hertzian pressure distribution. This provides exact (elastic) solutions with which to benchmark the finite element code.

Chapter 6 briefly reviews finite element theory as it applies to the current work and presents the theory developed for the several new algorithms in the analytical code.

The results of some geometrically and materially linear analyses are given in Chapter 7. Comparisons to the elasticity solution of Chapter 5 are presented for the cases of a plate in cylindrical bending with a known small contact half-width and a square plate simply supported on its perimeter and loaded in the center with a known large contact radius.

Nonlinearities are introduced in Chapter 8. Geometric nonlinearity, nonlinear contact, and nonlinear material properties (damage) are included. Comparisons to the experimental results of Chapter 4 are made.

A summary and some conclusions are given in Chapter 9.

Mathcad templates for the three-degree of freedom model of sandwich plate impact and for generating the elasticity solution for Hertzian contact loaded sandwich plates are given in Appendix A. *Mathematica* source code used in the development of the SANDI (Sandwich indentation) program, instructions for use, and a sample input form which doubles as an abbreviated users manual are found in Appendix B.

1.6 Sponsorship

This work is sponsored by William Baron (WL/FIBA) of the Air Force Flight Dynamics Directorate of Wright Laboratories.

2. Background

Due to the importance of composite structures and their susceptibility to low-velocity impact damage, low-velocity impact to monolithic laminated composite structures has been the subject of intensive study for a number of years. The quantity of existent published material specifically addressing low-velocity impact to composite sandwich plates is, by comparison, small. Nevertheless, since an article need not specifically address low-velocity impact to composite sandwich plates to be of interest to that research, a very substantial database (well over 700 articles) of material relating to the research topic has been collected by the writer. The fact that this database by no means exhausts the literature base is evident from the fact that one area of the research, finite element method in contact-impact problems, is represented in the literature by at least 469 articles published between 1980 and 1993 [14]. It is therefore necessary to limit the scope of this review to those articles which: 1) have provided direction to this research; 2) support a particular claim of this dissertation; or 3) are representative of other theories or approaches which should be considered.

2.1 Sandwich Plate

Low-velocity impact to composite sandwich plates can be addressed from two perspectives, "damage resistance," and "damage tolerance." Damage resistance considers the amount of damage a material or structure sustains from a particular event, i.e. the relationship between the type and "magnitude" of the event and the resulting damage. The "particular event" is either low-velocity impact by a hard blunt object, or static indentation. Damage tolerance considers the ability of the material or structure to sustain design loads after damage. For composite sandwich structures, the "design loads" are generally taken to be uniaxial compression because the types of damage normally present after impact can substantially reduce the residual uniaxial compression strength.

Damage resistance, and not damage tolerance, is the focus of this research. In the following sections, relevant work in the area of low-velocity impact damage resistance of composite sandwich plates is briefly reviewed, but the much more extensive body of literature on low-velocity impact damage resistance of monolithic laminated composite structures is also reviewed

where it provided guidance for this research. The review papers of Cantwell and Morton [16] and Abrate [13] are excellent starting points for review of the low-velocity impact resistance of monolithic laminates as are the "Previous Work" chapter of Tsang's Ph.D. thesis [15] and the review paper of Noor et al [240] for composite sandwich structures.

2.2 Failure Criteria

There are three fundamentally different types of damage that result from low-velocity impact to composite sandwich plates: 1) intraply damage within the facesheet lamina (e.g. fiber breakage, matrix cracking); 2) interply damage (delamination) in the facesheet laminates; and 3) compressive (e.g. buckling, crippling, or crushing) damage to the core. In a typical impact analysis, a mathematical model representing the equations of motion of the of the structure is "loaded" by force and displacement boundary conditions. The output of the model is the predicted response of the structure including displacements and internal loads (stresses). Often in such models, an underlying assumption is that the strain energy stored in the structure is monotonic with applied load. Real materials do not behave this way. Instead, with increasing load there is often range of load over which the strain energy drops due to the propagation of internal material flaws. Failure criteria are used to predict the onset of this flaw propagation process. Typical failure criteria define a metric based on stress, strain, or internal energy which is supposed to have a critical value (often unity) which can be identified with the onset of material failure. Scores of failure theories are documented in survey papers in the literature [17-20] and several have been applied to composites [17-55]. The relative merits of most of these theories are summarized in Nahas [17].

The four failure theories used most in composite design are maximum strain, maximum stress, Azzi-Tsai, and Tsai-Wu. Of these, maximum strain and maximum stress determine the failure mode and have the benefits of ease of use and applicability to the core failure as well as facesheet failure. Azzi-Tsai, and Tsai-Wu do not, by themselves determine the failure mode. With the assumption that matrix cracking occurs well before fiber and fiber-matrix bond failure in low-velocity impact and the recognition that these theories can not predict delamination or core failure, these theories can be assumed to "determine" the failure mode. That is, violation of these criteria in low-velocity impact problems can be assumed to indicate matrix cracking. In this research, maximum strain, maximum stress, a generalized, three-dimensional form of Azzi-Tsai by Hashin

[21, 32, 242] which is capable of predicting delamination, and a three-dimensional quadratic form similar to Tsai-Wu by Lee [66] were considered. In the following criteria, σ_i ($i=1,2,3$) refers to the direct stress in the fiber, lateral, and transverse directions and τ_{ij} ($i,j=1,2,3; i \neq j$) refers to the shear stress on the "i" plane in the "j" direction. The strengths of the lamina in uniaxial tension and compression parallel to the fibers are X_t and X_c , perpendicular to the fibers they are Y_t and Y_c , and the shear strengths are corresponding to τ_{ij} are S_{ij} .

2.2.1 Fiber failure criteria.

The first failure criteria to be addressed is for fiber failure. Two different stress-based criteria were used to predict fiber failure. The following inequalities define stress states in which fiber failure was assumed to exist.

<p>maximum stress:</p> <p>case $\sigma_1 > 0$,</p> $\left(\frac{\sigma_1}{X_t}\right)^2 \geq 1$ <p>case $\sigma_1 < 0$,</p> $\left(\frac{\sigma_1}{X_c}\right)^2 \geq 1$	<p>Hashin [242]:</p> <p>case $\sigma_1 > 0$,</p> $\left(\frac{\sigma_1}{X_t}\right)^2 + \left(\frac{\tau_{12}}{S_{12}}\right)^2 + \left(\frac{\tau_{13}}{S_{13}}\right)^2 \geq 1$ <p>case $\sigma_1 < 0$,</p> $\left(\frac{\sigma_1}{X_c}\right)^2 \geq 1$
--	--

(2-1)

The first case in each of the inequalities in equation 2-1 represents a tensile fiber failure mode while the second case represents a compressive (fiber buckling) mode. The difference between these two criteria is that Hashin considers the contribution of shear to fiber tensile failure while maximum stress considers only the fiber direct stress.

2.2.2 Matrix failure criteria.

Three different matrix cracking failure criteria were used to predict damage to the facesheets. These are, maximum tensile stress, Lee [66], and Hashin [242]. The maximum matrix tensile stress is based on the direct in-plane stress seen by the matrix, while the Lee criterion considers only in-plane and transverse shear. In contrast, the Hashin criterion considers direct in-plane and transverse stress seen by the matrix as well as in-plane and transverse shear. The criteria are given in equations (2-2).

<p>maximum stress:</p> <p>case $\sigma_2 > 0$,</p> $\left(\frac{\sigma_2}{Y_t}\right)^2 \geq 1$ <p>case $\sigma_2 < 0$,</p> $\left(\frac{\sigma_2}{Y_c}\right)^2 \geq 1$	<p>Lee [66]:</p> $\left(\frac{\tau_{12}}{S_{12}}\right)^2 + \left(\frac{\tau_{23}}{S_{23}}\right)^2 \geq 1$	<p>Hashin [242]:</p> <p>case $(\sigma_2 + \sigma_3) > 0$,</p> $\left(\frac{\sigma_2 + \sigma_3}{Y_t}\right)^2 + \frac{\tau_{23}^2 - \sigma_2 \sigma_3}{S_{23}^2} + \frac{\tau_{12}^2}{S_{12}^2} + \frac{\tau_{13}^2}{S_{13}^2} \geq 1$ <p>case $(\sigma_2 + \sigma_3) < 0$,</p> $\left(\frac{\sigma_2 + \sigma_3}{Y_c}\right)^2 \left\{ \left(\frac{Y_c}{2S_{23}}\right)^2 - 1 \right\} + \left(\frac{\sigma_2 + \sigma_3}{2S_{23}}\right)^2 + \frac{\tau_{23}^2 - \sigma_2 \sigma_3}{S_{23}^2} + \frac{\tau_{12}^2}{S_{12}^2} + \frac{\tau_{13}^2}{S_{13}^2} \geq 1 \quad (2-2)$
--	---	---

2.2.3 Delamination failure criteria.

The last stress-based failure criteria to be addressed is for delamination. Three different stress-based criteria were used to predict delamination. The following inequalities define stress states in which delamination was assumed to exist.

<p>maximum stress:</p> <p>case $\sigma_3 > 0$,</p> $\left(\frac{\sigma_3}{Y_t}\right)^2 \geq 1$ <p>case $\sigma_3 < 0$,</p> <p>no failure</p>	<p>Lee [66]:</p> $\left(\frac{\tau_{13}}{S_{13}}\right)^2 + \left(\frac{\tau_{23}}{S_{23}}\right)^2 \geq 1$	<p>Hashin [242]:</p> <p>case $\sigma_3 > 0$,</p> $\left(\frac{\sigma_3}{Y_t}\right)^2 + \frac{\tau_{13}^2 + \tau_{23}^2}{S_{13}^2} \geq 1 \quad (2-3)$ <p>case $\sigma_3 < 0$,</p> $\frac{\tau_{13}^2 + \tau_{23}^2}{S_{13}^2} \geq 1$
---	---	--

2.3 Progressive Damage

Progressive damage of composite structures has been investigated extensively both experimentally and analytically [6, 8, 10, 17, 21, 24, 28, 32, 34, 36, 37, 39-41, 43, 51, 52, 56-112]. Experimental investigations have demonstrated the complex and coupled nature of the processes involved. The analysis of progressive damage with arbitrary lay-ups and loading requires both a laminate stress analysis model that can account for general states of stress and a failure model that can account for general modes of damage. After pointwise stresses in each

layer of the composite are known from laminate analysis, failure of the composite is predicted either by employing a phenomenological failure criterion at the macromechanical (lamina) level or by relating the lamina stresses to the stresses in each constituent of the composite and employing a failure criterion at the micromechanical level. Micromechanical criteria were not considered for this research.

2.3.1 Monolithic laminate (facesheet) damage.

Talreja [75] classified the effects of transverse cracking on the constitutive response of composite laminates including the constraints provided by plies neighboring the cracking plies. For orthotropic laminates, his method required four material constants obtained from test data for damaged and undamaged specimens for which crack density is known. His method showed better agreement with experimental data than the ply discount method.

Hwang and Sun [21] developed a three-dimensional finite element model for damage prediction in laminated composite materials. They used the Tsai-Wu failure criterion to predict failure. They set the stiffness properties related to the predicted mode of failure to zero in each damaged element. For example, when fiber failure occurred in an element, the material stiffness coefficients Q_{11} , Q_{12} , Q_{13} , Q_{55} , and Q_{66} were set equal to zero in that element. When only matrix failure was predicted, the coefficients Q_{12} , Q_{22} , Q_{23} , Q_{44} , and Q_{66} were set equal to zero. The entire stiffness matrix was set to zero if fiber and matrix failure modes occurred. Good agreement with experimental results was obtained for angle-ply and cross-ply tension specimens.

Allix and Ladeveze [61] modeled fiber fracture, matrix cracking, and fiber-matrix debonding at the lamina level, with damage in the form of microcracks being coupled with plastic behavior of the matrix. Strain energy based damage evolution laws were developed employing two experimentally determined material constants. Delamination at edges of laminates was also analyzed by modeling the three-dimensional stress state in these regions. The entire procedure was implemented into a nonlinear finite element code. No direct-comparisons with experimental results were given.

Pandey and Reddy [113] and Reddy and Reddy [19] each developed a two-dimensional nonlinear finite element code for laminate analysis and performed progressive failure analysis using several different lamina failure criteria. They found that the various failure criteria predicted

quite different failure loads, with the disparity in predictions greater for nonlinear analysis than for linear analysis.

Micromechanics based matrix damage models of various sorts were developed by Averill [58], Bakuckas et al [114], Joshi and Goode [115], among others.

Wang [116] and the references there cited present the theory for application of fracture mechanics (stress singularity) principles to the investigation of delamination problems in composite materials. Without exception, the assumed geometry and loading are much simpler than that inherent in low-velocity impact.

Comninou [117], Comninou & Schmueser [118], Comninou & Dundurs [119], and Gautesen & Dundurs [120-122] taken together provide an approach which incorporates contact zones at the crack tips (zones with normal tractions only in which the cracks slide but do not separate near the tip, avoiding the overlapping problem inherent in a perfect-bond/traction-free discontinuity at the tip seen by England [123] and Malyshev & Salganik [124]). The work was two-dimensional (plane strain) and extension to three-dimensions as this research requires is not obvious.

Corigliano [7] takes interface models several steps further. He makes particular reference to composite delamination, discusses the difficulties of using them in numerical analyses, proposes a numerical integration scheme for the interface constitutive laws, and presents an algorithm for structural analysis in the presence of softening interfaces. It works like this: a nonlinear constitutive law is integrated *elastically* (via FEA) in a predictor phase, checked for *consistency*, and run through a plastic-damage corrector phase to obtain displacement discontinuities from tractions. These displacement discontinuities are the new degrees-of-freedom in the delaminated element proposed (but not developed) by the present research.

Another method to account for progressive damage is the displacement step function method. Here the discontinuity is accounted for by Heaviside step functions in the kinematic expressions. Chattopadhyay and Gu [6] used a new plate theory including Heaviside step functions in the kinematics to investigate delamination buckling and growth within composite laminates. In that paper, in-plane displacements are assumed to be forth-order polynomials in z .

Those authors apply their method to one-dimensional (beam) delamination problems using strain energy release rate as the crack growth indicator. The kinematics in this paper inspired the new delamination-capable finite element proposed in the present research.

Ladeveze [56] presents a damage mechanics delamination model. A bridge between damage mechanics and fracture mechanics is outlined in this paper and a strain energy-based damage evolution law is employed. The interface is considered a thin resin rich zone having the following characteristics: orthotropic behavior, unilateral damage normal to the in-plane direction (there is no damage under mode I compression), stiffness variation indicates damage, interface behavior is elastic-damage. The ideas in this paper are the basis for the delamination propagation modeling within the new delamination-capable finite element proposed in the present research. Other damage mechanics based analytical investigations of delamination progression in laminated composites are documented [6, 28, 59, 60, 125] among others.

Chang and Kutlu [125] considered a plane strain model of a pressure loaded cylindrical shell with a delaminated strip along its length. A nonlinear finite element code and a two mode (modes I and II) strain energy release rate criterion for crack extension were used. Mode II was found to dominate.

Hu [60] used offset node beam elements in a dynamic model to predict delamination growth.

2.3.2 Core properties/damage.

2.3.2.1 Experimental investigations.

Experimental investigations of nomex honeycomb core properties/damage are documented in the following references [5, 126-131]

2.3.2.2 Analytical investigations.

Analytical investigations nomex honeycomb core properties/damage are documented [69, 101, 130, 133]. Hussein et al [133] treated the core as a semi-infinite medium in which the displacement is an exponentially decaying function of distance from the facesheet. Damage to the core was not considered. Oplinger and Slepetz [130] modeled the core as an elastic foundation.

Damage to the core was not considered. Tsang [131] treated the core as a homogeneous isotropic plate attached to two homogeneous transversely isotropic plates. Each of the previous treatments did not consider damage to the core. On the other hand, Minguet [69] assumed the undamaged core to behave as a linear orthotropic solid without shear/extension coupling. After damage, the core stiffness was reduced by employing a change of variable technique to enforce $\sigma_{zz} = 0$ at the interface.

2.4 Three-Dimensional Equilibrium Considerations

The displacement-based shear-deformable FEM in which stresses are obtained from strains (via constitutive relations) and strains are calculated from displacement derivatives often produce good results for in-plane stresses, but neglect transverse direct stress σ_z and produce poor estimates of transverse shear stresses σ_{zx} and σ_{yz} . In order to improve the prediction of the transverse stress components many researchers (beginning perhaps with Pryor and Barker [134] but including [41, 135-171]) have abandoned the constitutive relations for calculating σ_{zx} and σ_{yz} in favor of satisfying the three-dimensional equilibrium equations with the FEA in-plane stresses as a means of estimating both transverse direct stress σ_z and transverse shear stresses σ_{zx} and σ_{yz} . The stresses thus obtained are an improvement over those obtained from the constitutive equations alone [172]. This is the approach used for the present work.

2.5 Finite Element Solution

The references available for finite element analyses are much too numerous to consult them all, let alone cite them here. The principal references used for this research are Cook et al [173], Palazotto & Dennis [172], Dennis [174], Siler [153], and Tsai & Palazotto [175]. In addition, many other reference books, papers, and dissertations have provided insights and guidance for this research.

2.6 Contact Problem

The majority of the analytical work on low-velocity impact of composite laminates to date has used some variation of a Hertzian contact law to load the laminate. The references here cited are the exceptions, in which the mixed boundary value problem (displacements under the impactor and traction free surfaces elsewhere) is considered. Some references are [32, 34, 47, 52,

67, 153, 176-191]. Jung [32] deals with an axisymmetric problem, and presents an elegant algorithm in which the load is incremented in steps sized to bring the contact degrees of freedom into contact one at a time. He also considers friction, but finds premature matrix failure to result. Keer et al [177] considers both normal and tangential contact loads between spheres for which global slip is an issue. They conclude that a Amontons-Coulomb frictional law in the contact region produces good results for the transverse shear stresses. The review articles of Jaeger [241], and Zhong and Mackerle [14] provide a good starting point for a review of the mechanics of impact contact.

2.7 *Non-Conservative Forces*

For thin laminates and large contact radii (related to large impactor radii) such that the ratio of contact radius to laminate thickness is $\gg 1$, through the thickness shear stress is commonly neglected [178, 193, 194] (and two references called out in [178]). This implies that the surface traction is also zero. This criteria is not met by the sandwich plates within the present study.

Most low-velocity impact papers tacitly assume this surface traction can be neglected, among these are all those assuming Hertzian-like or pressure type contact laws: e.g. Lie [195], Kan et al [196], Ramkumar & Chen [197], Takeda & Sierakowski [198], Sun [186], Thangjitham et al [199], Tan & Sun [187], Yang & Sun [200], Jackson & Poe [201], Koller [202, 203], Oplinger & Slepetz [130], Wu & Springer [46, 204], Choi & Chang [205], Siler [153], Thomsen [188], Sun [206], Greszczuk [207], Bucinell & Nuismer [208], Sankar & Sun [209]; as well as the following that use a rigid-elastic or elastic-elastic model: Liu [51, 182], Liu & Chang [34], Wu & Yen [189], Whitcomb [210]. To the author's knowledge, none of these papers address the assumption directly. Warnings about neglecting surface traction (but no help in quantifying when it is important) can be found in: Liu [67]. Frictionless contact is justified by comparison with experiment for $[0_n, 90_m, 0_n]$ beams (n and m in the range 2-8) in Liu & Kutlu [52]. Nothing relating transverse (normal) impact energy to contact surface tangential traction was found in the literature search performed in support of this research. No one seems to be concerned about it except Liu [67] and his warning was in the context of fiber-matrix bonding on the micromechanical level.

For the present research, the contact radius (and hence the distribution of the applied force) was a function of the finite element displacements. This implied that the force on a given element was a function of the displacement of the element and therefore potentially non-conservative. The argument made to justify proceeding with a solution for a conservative system follows. First, it must be observed that the method used to obtain the transverse displacements away from the finite element midplane was explicitly dependent on the finite element solution; there was no coupling between the three-dimensional stresses and the two-dimensional finite element solution. Thus it need only be demonstrated that a conservative two-dimensional finite element solution procedure was appropriate. The pressure distribution on a given element depended on the displacement, but the integral of that pressure over all of the loaded elements (i.e. the applied force) was independent of the displacement (conservative). The area over which the force acted was small compared to the dimensions of the plate, so by Saint-Venant's principle, the distributed pressure was statically equivalent to a point load (which would be conservative). In practice, the finite element solution was very minutely effected by the small changes in contact radius made during the contact iteration, instead, it was the transverse stresses (obtained by post-processing after the finite element solution was obtained) which were strongly dependent on the contact radius. Thus, the finite element solution responded as if the loading were conservative. Since the transverse stresses were determined explicitly by the finite element solution, they too were unaffected by the potentially non-conservative nature of the loading.

3. Instrumented Impactor System Characterization

Experimental studies of the impact force history resulting from low-velocity impact on composite plates [e.g. 5, 217, 218] have revealed that the impact force is not a smooth function of time. Load drops on the impact force vs. time plot are often taken to be indicative of strain energy release due to damage propagation within the plate. When an instrumented impactor system is used for impacts at energy levels low enough to avoid significant damage to the plate, regular localized load peaks and valleys have still been observed. The impact force histories of such an elastic event are reminiscent of the superposition of a half sine wave with a sine wave having an order of magnitude greater frequency and lower amplitude than the half sine wave (figure 3-1). Excitation of some plate or plate-lumped-mass normal mode has been speculated as the source of the secondary oscillations. Yet higher frequency tertiary oscillations are also observed most prominently following an abrupt change in load. In order to resolve the sources of these oscillations and establish an understanding of the results of an instrumented impactor test (thereby enhancing confidence in the results and boldness in their interpretation) a significant effort was made to characterize the instrumented impactor test system.

3.1 Energy Calculations

In instrumented impactor tests, impact energy and specimen absorbed energy are often used to characterize the event. Impact energy is the kinetic energy of the impactor (tup) at the instant that it strikes the specimen. Impact energy is usually controlled by varying the mass of the tup, m_{tup} , and the height from which it is dropped (or swung in the case of a pendulum impactor). Thus the potential energy of the tup before release is an upper bound for its kinetic energy at the time of impact. Energy losses during the acceleration of the tup (sliding friction at the guide rails, air resistance, etc.) are typically accounted for by measuring the velocity of the tup just prior to impact, $V_{tup}(0)$. Impact energy is then calculated by the relation,

$$\text{Impact energy} = \frac{m_{tup}}{2} V_{tup}(0)^2 \quad (3-1)$$

The impact event transfers energy between the initially moving tup and the initially stationary specimen. Specimen absorbed energy (usually called “absorbed energy”) is that net portion of the impact energy at any given time, which has been transferred to the specimen. It includes the strain energy of the specimen, the kinetic energy of the specimen, the total strain energy released from the specimen up to that time through damage progression, and frictional losses in the contact area and at the boundaries of the plate. Frictional losses at guide rails and air resistance during the impact event are usually assumed small, but they are actually implicitly included in the absorbed energy. The absorbed energy is calculated by the kinetic energy loss of the tup in which the tup velocity, $V_{tup}(t)$, is integrated from the contact force, $F(t)$, by the relation

$$V_{tup}(t) = V_{tup}(0) - \frac{1}{m_{tup}} \int_0^t F(\tau) d\tau \quad (3-2)$$

and the kinetic energy loss of the tup, called the “absorbed energy” or often just “energy” and labeled $E(t)$, is then

$$E(t) = \frac{m_{tup}}{2} (V_{tup}(0)^2 - V_{tup}(t)^2) \quad (3-3)$$

Thus, absorbed energy is a calculated, not directly measured, quantity. Its accuracy depends on the accuracy of the measured velocity $V_{tup}(0)$, the measured contact force $F(t)$, the measured mass m_{tup} , and the neglected frictional losses during the impact event. Figure 3-1 is a typical load and absorbed energy history from a low-velocity impact event in which the specimen was a composite sandwich plate and the force was measured using an instrumented impactor (in this case drop weight). After the event of figure 3-1, no damage was detected in the specimen.

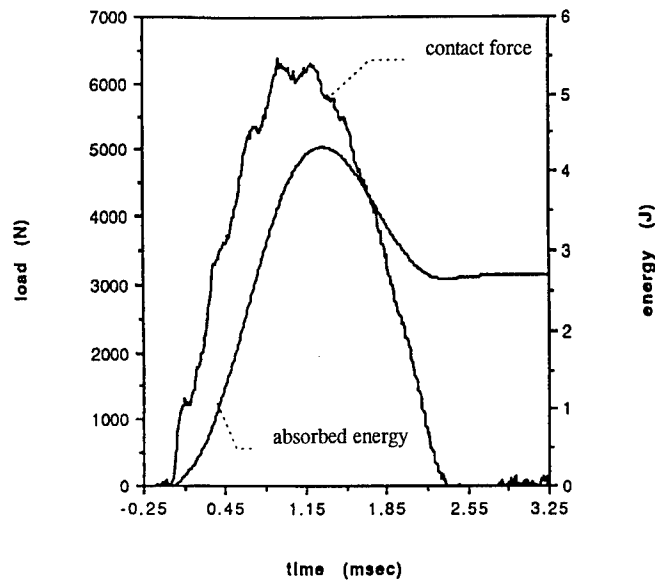


Figure 3-1 Typical force and energy histories for an event without damage [5].

In figure 3-1 it can be observed that the absorbed energy for an impact event which produced no damage detectable by C-scan, in the sandwich plate indicates that a significant amount of energy is not returned to the tup (absorbed energy does not return to zero when force does). This residual energy (absorbed energy at the end of the impact event) poses a problem to those interpreting the results. If the panel were damaged, one could attribute this residual to energy released in the process of damage production. For the undamaged plate, some energy will be dissipated by damping (perhaps over many cycles if the plate "rings" after being hit) but intuition might lead one to expect such energy to be small compared with the impact energy for a near-elastic collision. Other losses such as vibration modes in the impactor, air resistance, and frictional losses at the plate boundaries and in the contact region are also expected to be small. As shown in the figure 3-1, the calculated residual energy can be a large portion (more than 60 percent) of the impact energy (the maximum on the energy plot) for low-velocity impact to composite sandwich plates. That is, if the absorbed energy in the plate is correct, the undetectable damage and other losses absorbed the majority of the impact energy. The author considers it more likely that an error has been introduced in the calculation of absorbed energy (the kinetic energy lost by the tup). A subsequent test of a thin steel plate at very low impact energy (elastic) in which the calculated residual energy was actually greater than the impact energy (not physically possible) supported this conjecture.

3.2 Possible Error Sources

The possible sources of error in the calculated energy are: 1) inaccurate tup mass, 2) inaccurate initial velocity measurement as described in [214], or 3) inaccurate force measurement. Any of these sources is capable of producing apparent residual energy in the plate. To illustrate this fact as well as quantify the magnitude of the error that is required in any of these parameters to produce the apparent absorption of impact energy shown in figure 3-1, a simple model proves valuable. Consider the time dependent force in figure 3-1 to be the superposition of two sine waves. Letting time zero be defined as the time that the force starts to increase from zero, the first sine wave has a period of twice the time at which the force returns to zero (2.3 msec in figure 3-1) and an amplitude roughly equal to the peak contact force. Since this sine wave defines the primary features of the event, call it the primary sine wave. The second sine wave defines the wiggles seen on the contact force in figure 3-1. These oscillations are of smaller amplitude and higher frequency than the primary sine wave, so call the second sine wave the secondary sine wave. A good representation of the force is provided by the function

$$F(t) = F_1 \sin\left(\frac{\pi}{t_f} t\right) + F_2 \sin\left(\frac{n\pi}{t_f} t\right) \quad (3-4)$$

in which F_1 and F_2 are chosen to match the primary and secondary amplitudes of the force while t_f is the event time and n is the number of secondary half-cycles observed within the event time. For the test in figure 3-1, the chosen parameters are

$$\begin{aligned} F_1 &= 6377 \text{ newton} \\ F_2 &= 250 \text{ newton} \\ t_f &= 0.0023 \text{ sec} \\ n &= 15 \end{aligned} \quad (3-5)$$

while the measured parameters for the impact event are given in [5] to be

$$\begin{aligned} m_{tup} &= 3.62 \text{ kg} \\ V_{tup}(0) &= 1.6 \text{ m / sec} \end{aligned} \quad (3-6)$$

The integration of equation 3-1 with the substitutions of equations 3-4 through 3-6 combined with the application of equation 3-3 produces the simulation for the event shown in figure 3-2. The apparent residual energy at $t_f = 2.3$ msec is

$$E(t_f) = 2.93 \text{ J} \quad (3-7)$$

Comparison with figure 3-1 shows good agreement.

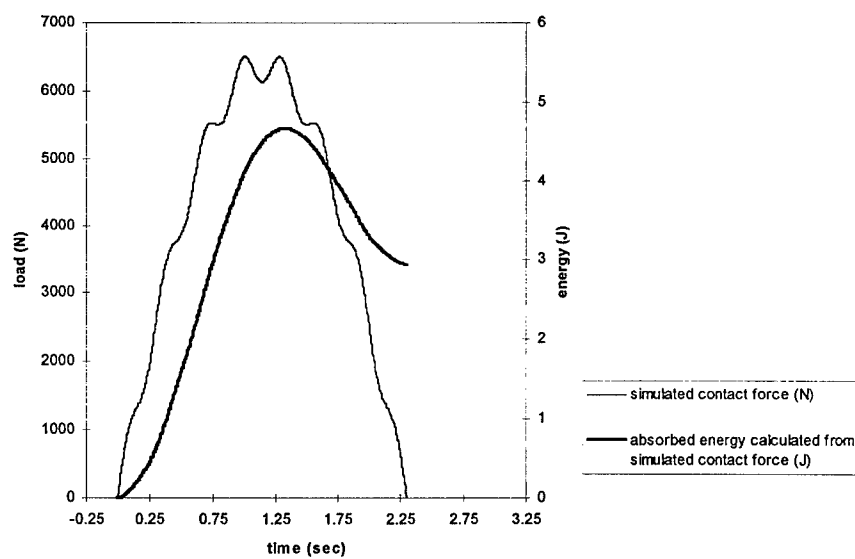


Figure 3-2 Simulation of force and energy histories of figure 3-1.

The force model of equation 3-4 used to generate figure 3-2 can now be used to evaluate the influence of the three parameters suspected of responsibility for the apparent residual energy, namely; m_{tup} , $V_{tup}(0)$, and F_1 . Frictional losses during the impact event will not be considered. Though it is possible that multiple errors contribute to the residual energy, we consider only one at a time. With regard to each parameter, the questions of interest are: if an error in this parameter is responsible for the residual energy, how big and in what direction is the error? and; is such an error likely?

- 1) Assume the only error is in m_{tup} .

Let the measured tup mass be m_{tup} as labeled in equation 3-6 and the unknown true tup mass be m_{true} . The other parameters in equations 3-5 and 3-6 are, for the moment, assumed correct. It is

evident that the calculations of equations 3-1 through 3-3 were in error and the true impact energy, velocity, and absorbed energy were

$$\begin{aligned}\text{True impact energy} &= \frac{m_{true}}{2} V_{tup}(0)^2 \\ V_{true}(t) &= V_{tup}(0) - \frac{1}{m_{true}} \int_0^t F(\tau) d\tau \\ E_{true}(t) &= \frac{m_{true}}{2} (V_{tup}(0)^2 - V_{true}(t)^2)\end{aligned}\tag{3-8}$$

Further assume that the event was without losses so that true absorbed energy returned to zero at the end of the impact event, i.e.

$$E_{true}(t_f) = 0\tag{3-9}$$

Substituting equations 3-8 into equation 3-9 and manipulating we find

$$\int_0^{t_f} F(\tau) d\tau = 2m_{true}V_{tup}(0)\tag{3-10}$$

The left hand side of equation 3-10 can be evaluated by integrating equation 3-4.

$$\int_0^{t_f} F(\tau) d\tau = \int_0^{t_f} \left[F_1 \sin\left(\frac{\pi\tau}{t_f}\right) + F_2 \sin\left(\frac{n\pi\tau}{t_f}\right) \right] d\tau = \frac{2t_f}{\pi} \left(F_1 + \frac{F_2}{n} \right)\tag{3-11}$$

Equating the right hand sides of equations 3-10 and 3-11 and solving for m_{true} .

$$m_{true} = \frac{t_f}{\pi V_{tup}(0)} \left(F_1 + \frac{F_2}{n} \right) = 2.93 \text{ kg}\tag{3-12}$$

Thus, for an error in measured tup mass to be responsible for the residual energy, the error was,

$$\text{Tup mass error} = \frac{m_{tup} - m_{true}}{m_{true}} = 24\%\tag{3-13}$$

That large an error does not seem likely to the author for two reasons; 1) because 24% is very gross and the measurement is very simple, and 2) the error is just as likely to be a low measurement in mass as a high one but none of the instrumented impactor data the author has seen

show the characteristic of a low m_{tup} measurement (negative residual energy, i.e. $E(t_f) < 0$). It is concluded that tup mass measurement error is not the cause of the apparent residual energy.

2) Assume the only error is in $V_{tup}(0)$.

Let the measured initial velocity be $V_{tup}(0)$ and the unknown true initial velocity be $V_{true}(0)$. The other parameters in equations 3-5 and 3-6 are, for the moment, assumed correct. As for the m_{tup} error calculations, it is evident that the calculations of equations 3-1 through 3-3 were in error and the true impact energy, velocity, and absorbed energy were

$$\text{True impact energy} = \frac{m_{tup}}{2} V_{true}(0)^2$$

$$V_{true}(t) = V_{true}(0) - \frac{1}{m_{tup}} \int_0^t F(\tau) d\tau \quad (3-14)$$

$$E_{true}(t) = \frac{m_{tup}}{2} (V_{true}(0)^2 - V_{true}(t)^2)$$

Again we assume that the event was without losses so that true absorbed energy returned to zero at the end of the impact event so that equation 3-9 still holds. Analogous to equation 3-10 we find

$$\int_0^{t_f} F(\tau) d\tau = 2m_{tup} V_{true}(0) \quad (3-15)$$

Equating the right hand sides of equations 3-15 and 3-11 and solving for $V_{true}(0)$ we obtain,

$$V_{true}(0) = \frac{t_f}{\pi m_{tup}} \left(F_1 + \frac{F_2}{n} \right) = 1.29 \text{ m/sec} \quad (3-16)$$

Thus for an error in initial velocity to be responsible for the residual energy, that error had to be

$$\text{Initial velocity error} = \frac{V_{tup}(0) - V_{true}(0)}{V_{true}(0)} = 24\% \quad (3-17)$$

Error is expected because of the measurement must be taken while the tup is still accelerating in "free fall" and can not be taken immediately at the time of impact [214]. The potential for error in the initial velocity is more pronounced for lower velocity tests due to the simple fact that a given

error is a greater percentage of a small velocity than of a large one. The expected error, however, is in the other direction (measured < actual). The measured value will not include the acceleration that takes place after the velocity measurement and before impact, and should therefore be low, not high. It is concluded that initial velocity measurement error is not the cause of the apparent residual energy.

3) Assume the only error is in contact force measurement, F_1 .

Let the measured amplitude of the primary sine wave of the contact force be F_1 and the unknown true amplitude be F_{1true} . The other parameters in equations 3-5 and 3-6 are, for the moment, assumed correct. Equation 3-1 is then correct while equations 3-2 and 3-3 were in error and the true velocity, and absorbed energy were

$$V_{true}(t) = V_{tup}(0) - \frac{1}{m_{tup}} \int_0^t F_{true}(\tau) d\tau \quad (3-18)$$

$$E_{true}(t) = \frac{m_{tup}}{2} (V_{tup}(0)^2 - V_{true}(t)^2)$$

in which,

$$\int_0^t F_{true}(\tau) d\tau = \int_0^t \left[F_{1true} \sin\left(\frac{\pi\tau}{t_f}\right) + F_2 \sin\left(\frac{n\pi\tau}{t_f}\right) \right] d\tau \quad (3-19)$$

so that,

$$\int_0^{t_f} F_{true}(\tau) d\tau = \int_0^{t_f} \left[F_{1true} \sin\left(\frac{\pi\tau}{t_f}\right) + F_2 \sin\left(\frac{n\pi\tau}{t_f}\right) \right] d\tau = \frac{2t_f}{\pi} \left(F_{1true} + \frac{F_2}{n} \right) \quad (3-20)$$

Again we assume that the event was without losses so that true absorbed energy returned to zero at the end of the impact event so that equation 3-9 still holds. Analogous to equation 3-10 we find

$$\int_0^{t_f} F_{true}(\tau) d\tau = 2m_{tup} V_{tup}(0) \quad (3-21)$$

Equating the right hand sides of equations 3-20 and 3-21 and solving for F_{1true} we obtain,

$$F_{true} = \left[2m_{tup}V_{tup}(0) - \frac{2t_f F_2}{n\pi} \right] \frac{\pi}{2t_f} = 7894 \text{ N} \quad (3-22)$$

Thus for an error in contact force amplitude to be responsible for the residual energy, that error had to be

$$\text{Contact force amplitude error} = \frac{F_1 - F_{true}}{F_{true}} = -19\% \quad (3-23)$$

Error is expected because the measured force is the force acting on a load cell within the impactor and not actually the force acting between the tup and the specimen.

Of the three parameters initially suspected of responsibility for the apparent residual energy (namely; m_{tup} , $V_{tup}(0)$, and F_1), m_{tup} and $V_{tup}(0)$ can be eliminated as sole sources of the residual energy. This leaves force measurements as the principle, if not lone, suspect. The remainder of this chapter deals with an attempt to account for, and correct, force measurement error in instrumented impactor tests.

3.3 Measured Force in Load Cell

A bit of background information which proved most useful is that the force data taken for these experiments using the instrumented impactor system came from a load cell inside the tup. In the drop weight configuration, most of the tup mass is above the load cell, but there is a small portion of the tup mass below the load cell (the hemispherical impactor) which is usually neglected. For static loads, there are no inertial forces, so the mass below the load cell has no effect on the measured force. This is not the case for dynamic loading. Several simplified dynamic models of the test system were considered in an effort to understand how the measured force in the load cell differed from the actual force applied to the plate and correct for this error.

3.4 One- and Two-Degree of Freedom Models

A single degree of freedom system (figure 3-3a) was used by Caprino et al [211] to analyze results from a drop-weight impact test of small glass cloth-polyester panels (80 x 80 x 3.5 mm) with a 4.90 kg impactor. The spring constant, k , corresponds to the static rigidity of the panel at the impact point. Very good agreement with experimental results was reported for this series of tests. It should be noted that the mass of the plate is negligible compared to that of the impactor

and that contact times are relatively long, so that the dynamics of the plate can be neglected. Rotem [212] used the same model to study the impact of a simply supported composite beam by a mass. The response of beams to the impact of a mass using one and two degree of freedom models was compared to that predicted using continuous beam models by Chou and Flis [213]. It was shown that the simple models are accurate when the mass of the beam is small compared to that of the impactor.

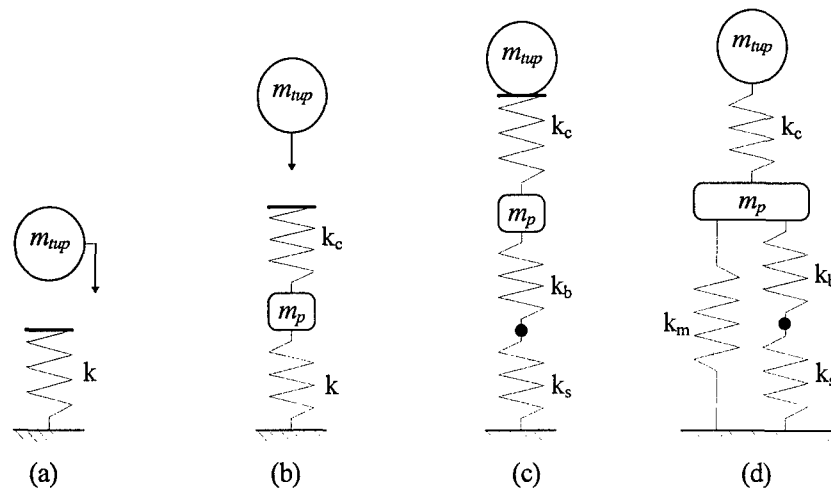


Figure 3-3 Schematics of one- and two-degree-of-freedom models [13].

Sjoblom et al [214] suggested the use of a two-degree-of-freedom model (figure 3-3b), where k is the rigidity of the plate and k_c is a highly nonlinear spring representing the contact rigidity. No discussion of how to derive k and k_c is included. In the spring-mass model of Lal [215] (figure 3-3c), three different springs are used to represent the flexural (k_b), shear (k_s), and contact (k_c) stiffnesses. Deflections larger than the plate thickness are considered, so that membrane effects are included using the large deflection theory of plates. Lal [216] also considered the effect of material degradation during impact by modeling the variation of rigidity during a static test.

Shivakumar et al [40] presented a spring-mass model for analyzing the impact of a circular plate by a sphere. The model consists of four springs representing bending (k_b), shear (k_s), membrane (k_m), and contact (k_c) rigidities (figure 3-3d).

The most notable deficiency the author sees in these models is that they all assume the tup to be rigid. Any strain energy in the tup is neglected.

3.5 Three-Degree of Freedom Model

Simple models allow us to understand the main features of impact and are useful in reducing experimental data. An approach consists of representing the structure by an assemblage of springs and masses so that a discrete system with few degrees of freedom is analyzed instead of a continuum. The above mentioned one-degree of freedom and two-degree of freedom spring-mass models have been used to analyze the results of drop-weight impact tests of panels [13]. In these models, the impactor is assumed to be rigid and is modeled as a single mass. The instrumented impactor, used in this research, has an internal load cell which has a finite stiffness and a split mass in which the majority of the mass is above the load cell, but some portion of the mass (the tup tip mass) is below the load cell. Thus, the force measured by the load cell is different from the contact force. This difference is usually neglected. It is hereby proposed that for cases in which the impactor mass is small (less than $\sim 50 \times$ the tup tip mass) the difference should not be neglected and can be accounted for with a few parameters for the system and the plate.

3.5.1 Equations of motion (three-degree of freedom model).

To model the instrumented impactor, two unequal masses connected by a stiff spring were used in this study, bringing the total degrees of freedom to three. The spring-mass model used in this study includes separate masses for tup main mass (m_1), tup lower mass (m_2), and plate effective mass (m_3). Three springs model the stiffnesses of the load cell (k_1), contact stiffness (k_2), and plate stiffness (k_3). These are connected in series as in figure 3-4.

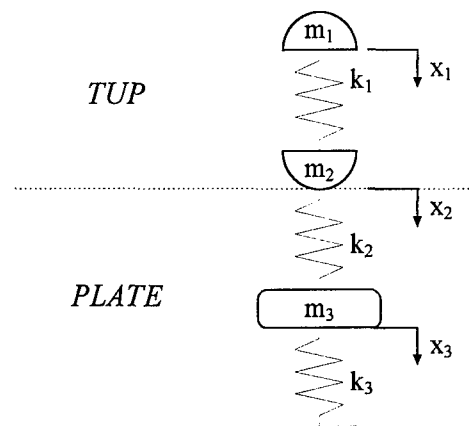


Figure 3-4 Schematic of three-degree of freedom model.

Thus two stiffnesses are associated with the plate as in the previous two-degree of freedom models, while a new stiffness (k_1) is associated with the load cell. Clearly, the real impactor is not rigid as the one- and two-degree of freedom models assume. Force is measured using strain gages in the load cell, implying that the load cell stiffness is not infinite. This new stiffness, k_1 , is the ratio of load cell force to displacement of the tup tip (m_2) relative to the impactor main mass (m_1). It represents the internal strain within the impactor. The new degree of freedom allows relative motion between the two masses that form the tup.

To illustrate the difference between contact stiffness and plate stiffness consider figure 3-5. In that figure, the plate top and bottom surfaces are represented by solid lines while the plate midplane is represented by a broken line. The total motion of the tup from initial impact is shown as x_2 . This motion is the sum of the midplane motion of the plate (x_3) and the indentation of the plate ($x_2 - x_3$). The contact stiffness (k_2) is the force generated between the tup and the plate by a unit plate indentation ($x_2 - x_3$), whereas the plate stiffness (k_3) is the force generated between the plate and its supports by a unit plate midplane deflection (x_3). It should be noted that for dynamic problems, these forces differ by the plate's inertia.

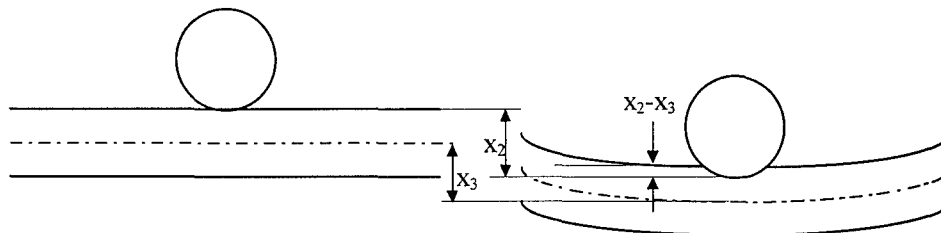


Figure 3-5 Plate indentation and contact stiffness.

3.5.2 Exact solution (three-degree of freedom model).

From free-body diagrams of each mass in figure 3-4 and the application of Newton's second law, the equations of motion for the three-degree of freedom system with linear springs are easily obtained as:

$$\mathbf{M}\ddot{\mathbf{X}} + \mathbf{K}\mathbf{X} = 0 \quad (3-24)$$

In which the displacements x_1 , x_2 , and x_3 , are functions of time and

$$\mathbf{X}(t) = \begin{Bmatrix} x_1(t) \\ x_2(t) \\ x_3(t) \end{Bmatrix}, \quad \mathbf{M} = \begin{bmatrix} m_1 & & \\ & m_2 & \\ & & m_3 \end{bmatrix}, \quad \text{and} \quad \mathbf{K} = \begin{bmatrix} k_1 & -k_1 & \\ -k_1 & k_1 + k_2 & -k_2 \\ & -k_2 & k_2 + k_3 \end{bmatrix} \quad (3-25)$$

With the assumption of simple harmonic motion of angular frequency ω , phase angle φ , and displacement amplitudes A_i ($i=1,2,3$),

$$\mathbf{X} = \begin{Bmatrix} A_1 \\ A_2 \\ A_3 \end{Bmatrix} \sin(\omega t + \varphi), \quad \text{so that} \quad \ddot{\mathbf{X}} = -\omega^2 \begin{Bmatrix} A_1 \\ A_2 \\ A_3 \end{Bmatrix} \sin(\omega t + \varphi) \quad (3-26)$$

and the equation of motion becomes

$$(\mathbf{K} - \mathbf{M}\omega^2) \begin{Bmatrix} A_1 \\ A_2 \\ A_3 \end{Bmatrix} \sin(\omega t + \varphi) = 0 \quad (3-27)$$

a generalized eigenvalue problem.

In solving the eigenvalue problem, the eigenvalues may be represented by λ_i and the corresponding eigenvectors by ξ_i . The general solution can be expressed as the sum:

$$\mathbf{X} = \sum_{i=1}^3 B_i \xi_i \sin(\sqrt{\lambda_i} t + \varphi_i) \quad (3-28)$$

in which six constants B_i and φ_i ($i = 1,2,3$) have been introduced and which can be expressed as

$$\mathbf{X} = [\xi] \begin{Bmatrix} B_1 \sin(\sqrt{\lambda_1} t + \varphi_1) \\ B_2 \sin(\sqrt{\lambda_2} t + \varphi_2) \\ B_3 \sin(\sqrt{\lambda_3} t + \varphi_3) \end{Bmatrix} \quad (3-29)$$

in which $[\xi]$ is a matrix formed by arranging the eigenvectors in columns and we now have six constants to be determined by the initial conditions. The initial conditions are

$$\mathbf{X}(0) = \begin{Bmatrix} 0 \\ 0 \\ 0 \end{Bmatrix}, \quad \text{and} \quad \dot{\mathbf{X}}(0) = \begin{Bmatrix} V_{tup}(0) \\ V_{tup}(0) \\ 0 \end{Bmatrix} \quad (3-30)$$

where $V_{imp}(0)$ is the impact velocity.

The first three initial conditions give rise to

$$\varphi = \begin{Bmatrix} 0 \\ 0 \\ 0 \end{Bmatrix} \quad (3-31)$$

and with these the second three of equations 3-30 can be expressed as

$$[\xi] \begin{Bmatrix} B_1 \sqrt{\lambda_1} \\ B_2 \sqrt{\lambda_2} \\ B_3 \sqrt{\lambda_3} \end{Bmatrix} = \begin{Bmatrix} V_{imp}(0) \\ V_{imp}(0) \\ 0 \end{Bmatrix} \quad (3-32)$$

from which the other three constants can be determined as

$$\begin{Bmatrix} B_1 \\ B_2 \\ B_3 \end{Bmatrix} = \left[[\xi] \begin{bmatrix} \sqrt{\lambda_1} & & \\ & \sqrt{\lambda_2} & \\ & & \sqrt{\lambda_3} \end{bmatrix} \right]^{-1} \begin{Bmatrix} V_{imp}(0) \\ V_{imp}(0) \\ 0 \end{Bmatrix} \quad (3-33)$$

Hence, the solution in terms of displacement and velocity is

$$X(t) = [\xi] \begin{Bmatrix} B_1 \sin(\sqrt{\lambda_1} t) \\ B_2 \sin(\sqrt{\lambda_2} t) \\ B_3 \sin(\sqrt{\lambda_3} t) \end{Bmatrix} = [\xi] \begin{bmatrix} \sin(\sqrt{\lambda_1} t) & & \\ & \sin(\sqrt{\lambda_2} t) & \\ & & \sin(\sqrt{\lambda_3} t) \end{bmatrix} \left[[\xi] \begin{bmatrix} \sqrt{\lambda_1} & & \\ & \sqrt{\lambda_2} & \\ & & \sqrt{\lambda_3} \end{bmatrix} \right]^{-1} \begin{Bmatrix} V_{imp}(0) \\ V_{imp}(0) \\ 0 \end{Bmatrix} \quad (3-34)$$

and

$$\dot{X}(t) = [\xi] \begin{bmatrix} \sqrt{\lambda_1} \sin(\sqrt{\lambda_1} t) & & \\ & \sqrt{\lambda_2} \sin(\sqrt{\lambda_2} t) & \\ & & \sqrt{\lambda_3} \sin(\sqrt{\lambda_3} t) \end{bmatrix} \left[[\xi] \begin{bmatrix} \sqrt{\lambda_1} & & \\ & \sqrt{\lambda_2} & \\ & & \sqrt{\lambda_3} \end{bmatrix} \right]^{-1} \begin{Bmatrix} V_{imp}(0) \\ V_{imp}(0) \\ 0 \end{Bmatrix} \quad (3-35)$$

With the displacements known in terms of the eigenvectors and eigenvalues by equation 3-34, the forces developed by the springs shown in figure 3-4 are simply proportional to the relative displacements of the masses and can be expressed as

$$F(t) = \begin{Bmatrix} (x_1(t) - x_2(t))k_1 \\ (x_2(t) - x_3(t))k_2 \\ x_3(t)k_3 \end{Bmatrix} \quad (3-36)$$

The most important result of this model is that a correction for force is now available. The first component of force in equation 3-36 corresponds to the load cell force actually measured in instrumented impactor tests, $F_{loadcell}(t)$. The force which must be integrated in equation 3-2 to obtain the correct tup velocity and plate energy (equation 3-3) is the contact force, $F_{contact}(t)$, which corresponds to the second component of force in equation 3-36. That is,

$$F_1(t) = F_{loadcell}(t), \quad \text{and}, \quad F_2(t) = F_{contact}(t) \quad (3-37)$$

The ratio is the appropriate time-dependent correction for force. Thus, the force of interest, $F_2(t)$, is now known as a function of the force measured, $F_1(t)$, by the relation

$$F_2(t) = F_1(t) \frac{k_2 (x_2(t) - x_3(t))}{k_1 (x_1(t) - x_2(t))} \quad (3-38)$$

In equation 3-38, x_i are known in terms of the initial conditions, eigenvectors, and eigenvalues, via equation 3-34. It is desirable to have a correction factor rather than a time-dependent correction. A correction factor may provide a time-averaged correction, but the time-dependent portion of the error will not be corrected. To obtain a correction factor, we choose to correct for the lowest frequency mode (λ_1, ξ^1). The lowest frequency mode corresponds to the "primary sine wave" in the simulated contact force history of figure 3-2, which is given as the first term on the right hand side of equation 3-4. This can be considered a first-order correction because it corrects the largest component of the force. Retaining only the first eigenvalue and first eigenvector, equation 3-34 reduces to

$$\mathbf{X}(t) \approx \begin{Bmatrix} \xi_1^1 \\ \xi_2^1 \\ \xi_3^1 \end{Bmatrix} \frac{V_{tup}(0) \sin(\sqrt{\lambda_1} t)}{\xi_1^1 \sqrt{\lambda_1}} \quad (3-39)$$

so that the time dependence of equation 3-38 cancels out to produce

$$F_{contact}(t) \approx F_{loadcell}(t) \frac{k_2 \left(\xi_2^1 - \xi_3^1 \right)}{k_1 \left(\xi_1^1 - \xi_2^1 \right)} \quad (3-40)$$

Equation 3-40 can be used as a first order correction to the contact force. The measured load cell force is simply scaled by the factor shown to obtain an estimate of the contact force. Use of equation 3-40 requires that the eigenvalue problem defined by equations 3-25 and 3-27 be solved. This solution requires knowledge of the specimen and the impact test system masses and stiffnesses used in equations 3-25.

3.5.3 Empirically derived parameters.

There are still seven parameters in the model to be specified. These are the three masses, the three stiffnesses, and the impact velocity. It is these seven parameters which uniquely define a particular impact event. Of the seven, m_1 , m_2 , k_1 , k_3 , are readily measured, k_2 (contact stiffness) is measurable with more difficulty, and $V_{tup}(0)$ is assumed to be known. This leaves one less-easy-to-pin-down quantity, m_3 (effective plate mass). Effective plate mass will depend on the actual mass of the plate as well as the plate stiffness and the boundary conditions of the test. Turning to test data for help here, m_3 can be determined by recognizing that the secondary oscillations in the force history of an undamaged or a typical non-damaging impact event (e.g. figure 3-1) have a known frequency. Assuming that the secondary oscillations are the result of the plate vibrations and not impactor vibrations and that the mass of the plate is much less than the mass of the impactor, we isolate the plate from the rest of the system shown in figure 3-4 as shown in the left schematic of figure 3-6. The right schematic in figure 3-6 represents a separate test in which the free vibration frequency of the specimen (not in contact with the tup) has been measured by a strain gage.

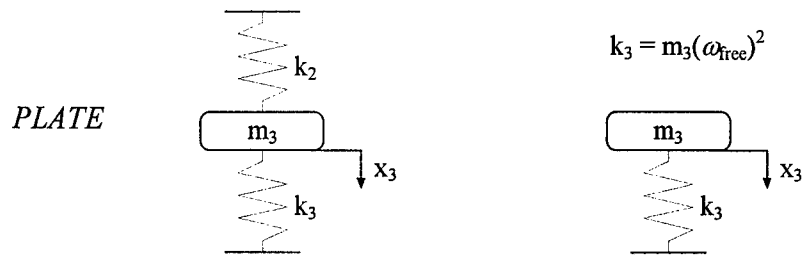


Figure 3-6 Schematic of the one-degree of freedom systems used to estimate plate effective mass.

In the systems shown in figure 3-6, the free vibration frequency ω_{free} is related to m_3 and the plate stiffness k_3 as shown. The secondary the vibration frequency $\omega_{\text{secondary}}$ is related to m_3 and the effective plate stiffness k_{Eff} by:

$$\omega_{\text{secondary}} = \sqrt{\frac{k_{\text{Eff}}}{m_3}} \quad (3-41)$$

where:

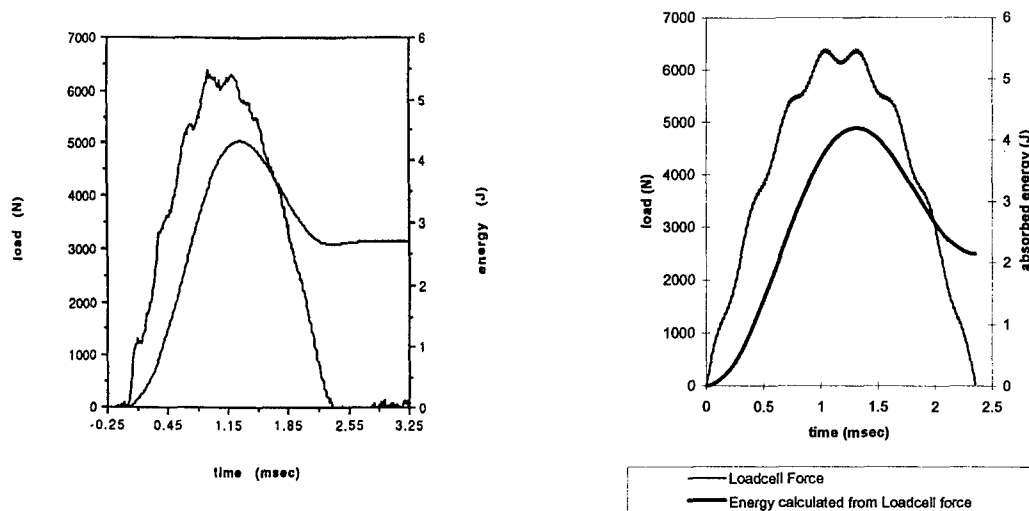
$$k_{\text{Eff}} = k_2 + k_3 \quad (3-42)$$

From this then, an estimate of m_3 is available from the test data. This also leads to a simple way to estimate the contact stiffness, k_2 . The plate effective stiffness k_{Eff} must be such that the model predicts the correct (empirical) event time. In the three-degree of freedom model, the event time is the time at which the force returns to zero or half of the period of the first vibratory mode of the plate-lumped mass system. Since k_3 is known from m_3 and ω_{free} , k_2 is thereby determined. Having thus measured or inferred all seven parameters, the three-degree of freedom model can now be applied to an elastic (at least no apparent damage) impact event to show the salient features of the dynamics which have now been modeled.

3.5.4 Contact force history, comparison to previous test data.

The three-degree of freedom model was applied to the impact event of figure 3-1 observed by Harrington [5]. The model was able to resolve several important features of the impact force history. That is, with appropriate parameters, the following output quantities matched (to some degree) the instrumented impactor data (figure 3-6).

1. time scale of the event
2. peak load seen
3. frequency of secondary oscillations
4. magnitude of secondary oscillations
5. calculated energy history



Instrumented impactor

Three-degree of freedom model

Figure 3-7 Comparison of experiment and three-degree of freedom model.

Additional insights into the test system were now available since the forces on each spring were known exactly. For all cases modeled, the load cell force was always below the contact force. This indicates a correction should be applied to the instrumented impactor test results because the contact force is the actual load the plate responds to while the load cell force is the only force quantity measured by the system. For the parameters chosen, a simple empirically-derived correction by the tup mass ratio defined as

$$F_{contact}(t) \approx F_{loadcell}(t)(\text{tup mass ratio}) \quad (3-43)$$

in which,

$$\text{tup mass ratio} = \frac{m_1 + m_2}{m_1} \quad (3-44)$$

does the same as the more involved calculation of equation 3-40 since it brings the primary component of the impact force (the half sine wave) to the correct values. It should be noted that while the correction of equation 3-40 has physical and mathematical justification, tup mass ratio is purely empirical and its range of validity has not been tested. The value of the correction of equation 3-43, where it can be shown to be valid, is that unlike the correction of equation 3-40, it has no stiffness dependence and hence should be applicable even when there is damage in the plate. The secondary component (secondary oscillations reminiscent of a smaller amplitude

modulated sine wave added to the primary component) is not corrected by either of these means, though it can be corrected by equation 3-38 for impact events without damage.

The three-degree of freedom model is next used to highlight the error inherent in assuming that the load cell force, which is measured, is the same as the contact force, which is not measured. We define the error as

$$\text{force error} = F_{\text{contact}} - F \quad (3-45)$$

in which F_{contact} is the exact contact force known for the three-degree of freedom model and F represents the load cell force, F_1 , or corrected force $F_1(\text{tup mass ratio})$. The time-dependent nature of the error is illustrated in figure 3-8 where the uncorrected force error is plotted with the corrected force error. For the chosen parameters, which model the test data of figure 3-1, tup mass ratio and the correction factor given by equation 3-40 are very close (less than 0.1 percent difference). It is evident that the tup mass ratio correction greatly reduced the force error. In this case, the tup mass ratio was 1.17.

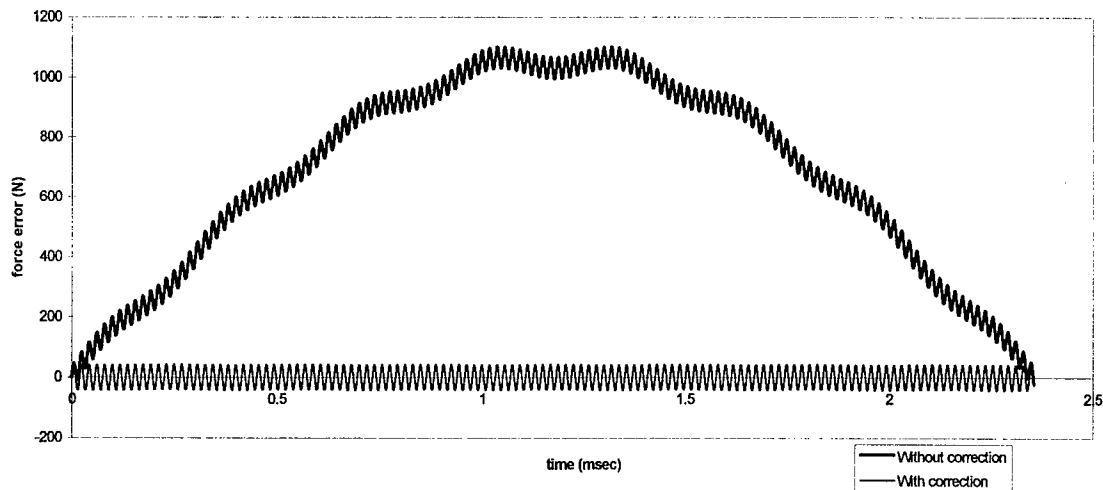


Figure 3-8 Three-degree of freedom model contact force error with and without the tup mass ratio correction.

3.5.5 Source of high frequency oscillations.

In the three-degree of freedom solution, the load cell force has a relatively small tertiary oscillatory component (notice the high frequency oscillations in the error in figure 3-8), while the contact force (the force actually seen by the plate) has only the half sine wave and a secondary oscillatory component. Removing m_2 entirely confirmed that the secondary oscillatory component

on the plate response force is attributable to the plate dynamics while the tertiary oscillatory component on the load cell force is attributable to the dynamics of the tup. In some cases (such as for low range load cells in which k_1 is significantly less than the example cited here) the plate dynamics frequency could be similar to the tup dynamics frequency and this may lead the researcher to incorrectly attribute all of the oscillations observed to plate dynamics when in fact a significant portion could be tup dynamics in the instrumented impactor data. It is apparent that tup dynamics have the potential to produce both steady-state (correctable) and time-varying (non-correctable) errors in instrumented impactor force data.

3.5.6 Absorbed energy implications.

Perhaps the most important result of the three-degree of freedom model is the insight into the energy calculations for instrumented impactor systems. Purely elastic impact should be expected to return virtually all of the impact energy to the tup. Though this is the expected result, the calculated plate energy could never return to zero because the load on which it was based was lower than the actual contact load. That is, the force assumed to be doing work on the tup was too low, so the work done by the force was too small, so the energy returned to the tup was too small. This is illustrated in figure 3-9 which includes the calculated absorbed energy (calculated from the load cell force, not the contact force) and the exact absorbed energy for the three-degree of freedom model. The exact solution is available for the three-degree of freedom model by using the contact force rather than the load cell force in equation 3-2. If presented with the calculated values, one might conclude that there was damage in this event when actually it was perfectly elastic. This underscores the fact that one must use caution in interpreting instrumented impactor results. If the load cell is calibrated statically (so that during calibration the load cell force and contact force are the same) and used for a dynamic test, then the calculated impact forces and energies will be incorrect. A dynamic calibration should be used. Fortunately, a first-order dynamic calibration is a simple scaling of the load cell output as described above. Corrected force data improves the calculated absorbed energy values greatly as seen in figure 3-9. In that figure, exact energy is calculated using the known contact force while the corrected energy is calculated using the load cell force scaled by the tup mass ratio.

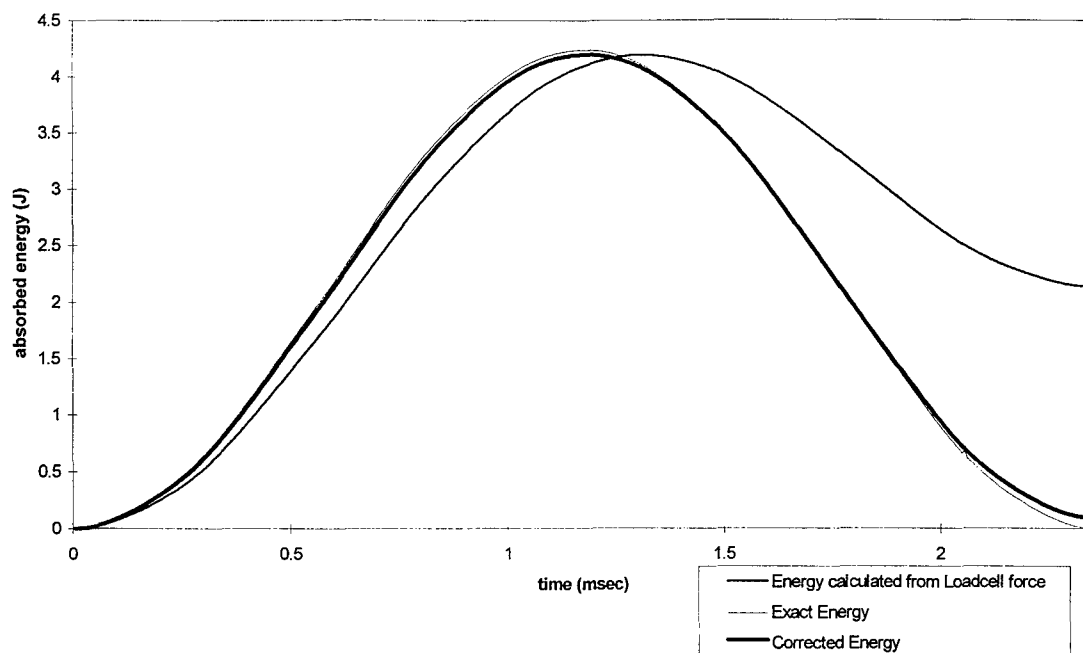


Figure 3-9 Instrumented impactor model calculated and corrected energy histories.

The consequences of an error in instrumented impactor force measurement are particularly significant if the calculated absorbed energy from this data is believed to be the actual absorbed energy. The force error always increases the calculated absorbed energy at the end of the event. It is apparent that tup dynamics have the potential to introduce significant errors to instrumented impactor data and should be understood and controlled to the greatest extent possible. The present correction does a good job of correcting the time-averaged errors in both force and energy.

3.6 Tup Tip Mass

The tup mass ratio (equation 3-44) points to a better approach to getting higher fidelity force and energy data from instrumented impactor tests. When the tup tip mass, m_2 , is very small compared to the main tup mass, m_1 , the tup mass ratio approaches unity. This condition indicates that the correction to remove the effects of tup dynamics becomes much less significant. In the limit, no correction is required at all and the model is reduced to two degrees of freedom. Clearly, the tup tip mass should be as low as it is practical to make it. This idea is illustrated graphically in figure 3-9 in which the response of an instrumented impactor load cell (load range 0-15 kN) was subjected to an axial impulse load from a hammer strike. With the manufacturer-supplied 151.4 gm tup tip a large portion of the impact energy was evidently transferred to the first axial vibration mode of the tup and slowly dissipated by light damping. Thus the tup “rings” as seen in the lowest curve. Though it was not measured, one must conclude that a significant portion of the impact energy was not returned to the hammer which lost contact with the tup after the first half-cycle. In contrast, the center curve shows the impulse response with the tup tip removed. The much higher fidelity impulse response indicates that very little energy is absorbed by tup vibrations. The upper most curve in figure 3-10 shows the response with a much lighter tup tip fabricated for the current work. It is evident that the new tup tip approximates the response of no tup tip. In practice the tup mass ratio correction was not needed when the reduced-mass tup tip was used.

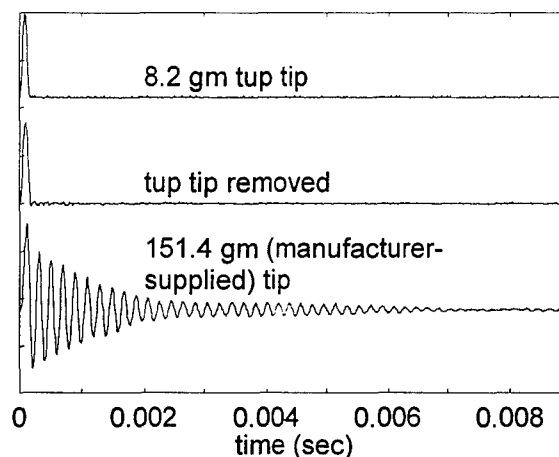


Figure 3-10 Impulse response of instrumented impactor showing effect of tup tip mass.

The effect of the reduced-mass tup tip on the fidelity of the force history in an actual composite sandwich plate impact event is illustrated in figure 3-11. In that figure the large amplitude

oscillations present in the 151.4 gm tup tip data are not actually loads seen by the plate, but are load cell loads induced by the dynamics of the tup. The two different 8.2 gm tests (#1 and #2) are shown to indicate the variation of response from one event to another.

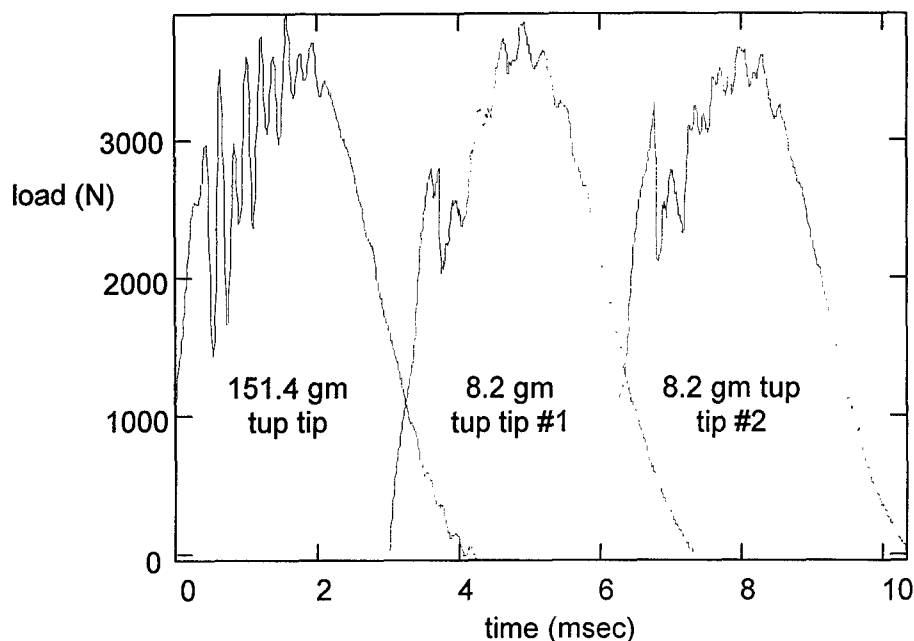


Figure 3-11 Load histories showing effect of tup tip mass

Reducing the tup tip mass from the manufacturer-supplied 151.4 gm tip to the new 8.2 gm tip has been shown to significantly enhance the fidelity of the load histories available from instrumented impactor tests. The improvement is most valuable for more flexible (low range) load cells and manifests itself most strongly following a load drop like those often seen in composite impact tests. The lesson here is that the force oscillations following a load drop in an instrumented impactor test can be the result of instrumentation dynamic response and should not be blindly attributed to the dynamics of the specimen. For the load cell used in this work (15kN) a relatively low frequency, relatively high energy axial vibration mode existed when the manufacturer-supplied tup tip was used. This mode contributed significant error to the observed load history. Reducing the tup tip mass presumably increased the frequency of the error but reduced its magnitude to the point that it could not be observed in the impulse response of the system. Without this improvement the tup tip dynamics can effectively mask the high frequency response of the plate (figure 3-11). With this minor system improvement there is hope of being able to correlate load history with damage. Without it, the noise overwhelms the signal and it appears very unlikely that such a correlation can

be made. It should be emphasized that for a given load cell it is the tup mass ratio, and not the tup tip mass per se, that dictates the strength of the tup dynamics (force noise). With the 15 kN load cell and the main mass, m_1 , used in this work, the 151.4 gm tup tip provided a tup mass ratio of 1.043 while the 8.2 gm tup tip reduced the ratio to 1.002. The stiffness of the load cell must also be considered. Higher stiffness is better from the point of view of temporal resolution, but a tradeoff is made here in that the higher the stiffness, the poorer the load resolution due to the fact that the force is measured by internal strain gages and strain is inversely proportional to stiffness. When load resolution requirements dictate a low stiffness load cell be used, minimizing the tup mass ratio is shown to significantly improve the temporal fidelity of the load data produced by an instrumented impactor test system.

3.7 Conclusions

The three-degree of freedom model was able to resolve several important features of the impact force history and provide insight into the low-velocity impact event.

A simple empirically-derived force correction can significantly improve the energy histories obtained from instrumented impactor tests.

Minimizing the tup mass ratio is shown to significantly improve the temporal fidelity of the load data produced by an instrumented impactor test system.

4. Experimental Investigation

To guide and validate the analytical developments of this study, an experimental investigation of low-velocity impact to laminated composite sandwich plates was performed. Square, flat, sandwich panels of uniform in-plane size and core thickness and varying facesheet thickness were subjected to a transverse load applied at their center by a steel spherical indenter (tip). Both quasi-static indentation and dynamic impact were considered and compared. Contact force was monitored throughout the event through the use of an instrumented impactor.

4.1 Objectives

4.1.1 Understand damage initiation and progress.

The experimental parameter space was designed to reveal the course of events which transpire when a composite sandwich plate is subjected to low-velocity impact. Loads applied, measurements taken, calculations made, and both non-destructive and destructive inspections after impact were all tailored to maximize the insights available into these events. These insights, in turn, can be used in an attempt to identify general trends and, ultimately, guide subsequent research aimed at controlling and reducing the degradation of residual properties of impacted composite sandwich structures.

4.1.2 Provide benchmark data for analysis.

In order to tie the analysis of Chapter 6 into the actual physics of the problem, empirical data was required. In particular, load versus impactor displacement and damage versus impact energy data for various facesheet thicknesses provide a means to determine the range of validity of the analytical method, and suggest which assumptions and simplifications to the theory should be relaxed in order to extend that range. For example, the difference between the empirical and the analytical results can indicate that a more detailed analysis considering dynamics and/or full three-dimensional displacement and/or crack tip singularity effects is required.

4.1.3 Relate damage to load history.

Instrumented impactor tests are attractive because of the simplicity of the procedure and the relative swiftness with which a large number of impact events can be performed. The principal measurement in instrumented impactor tests is load as a function of time. This load history is used

to integrate the two equations of motion to infer the displacement and absorbed energy of the plate. To measure damage within the plate, more time- and labor-intensive procedures such as C-scan, radiography, and photomicrography are generally employed. It is desirable to reduce or eliminate these procedures if the needed information available by them can be obtained by other means.

Damage within the plate changes the plate stiffness and hence its response to load. In this way damage can be expected to show up as an equilibrium change which may be observable in the load history. One objective of the experimental portion of the current work was to correlate the observed load history to the internal damage. This correlation has the potential to greatly reduce the cost of testing these structures and/or increase the number of impact events (hence increase the resolution or parameter envelope) any given test program can provide to the existing database.

4.1.4 Investigate relationships between absorbed energy, damage, and plate geometry.

Separate from the roles of providing benchmark data for the analysis and general improvements to the methodology of impact testing of composite sandwich structures, the current experimental effort had the objective of contributing to the existing database directly. As a matter of fact, it is this role that originally justified the expense of fabricating the test articles. An example of the contribution the database provides might be an answer to the following: "Bending stiffness required of a given structure can be obtained with thin facesheets and thick core or thick facesheets and thin core. Weight considerations drive toward the former. Impact damage resistance presumably drives toward the latter. For a given anticipated impact event, how thin can one make the facesheets without measurable damage?"

4.1.5 Validate quasi-static assumption.

An important simplification very common to low-velocity impact testing and modeling is that the damage depends not upon the impact energy per se, but upon the peak load reached in the process of transferring that energy. If this is the case, static tests and static analyses can be expected to adequately simulate the impact event. The objective here was to validate this simplification and (within the context of the parameters varied) define the boundaries of the usefulness of quasi-static assumptions.

4.1.6 Investigate applicability of plate theory.

The analytical effort of the current work is based on a two-dimensional plate finite element model. Such a model has inherent limitations for impact analyses in that it is based on a plane stress assumption which is manifestly erroneous in the neighborhood of the applied transverse load. Although this error may be partially alleviated through the post-processing, if a portion of the parameter space shows that the structural response is fundamentally and globally three-dimensional, then plate theory can not be expected to provide useful results. The question here might be posed as, "Are these specimens acting globally like plates with a local three-dimensionality, or are they acting like three-dimensional blobs of material bearing no resemblance to plates?"

4.2 Approach

4.2.1 Multiple facesheet lay-ups.

One of the very obvious decisions required of a designer of a composite sandwich plate structure is how thick to make the facesheets. As mentioned above, bending stiffness will be a principal consideration here. Damage resistance will be another important and potentially constraining consideration. For this reason, a range of facesheet thicknesses were tested, providing impact resistance data as a function of facesheet thickness. In an effort to limit the number of parameters being varied, the core thickness was held constant for all tests. The fact that facesheet thickness varied while core thickness was held constant necessarily meant that bending stiffness varied with facesheet thickness. If a particular bending stiffness is required, these data alone can not suggest the appropriate facesheet thickness. To provide this kind of information to a designer, an experimental effort to characterize damage as a function of facesheet thickness and bending stiffness (independently) would be needed. For such an experimental program, impact resistance data would be required for a range of bending stiffnesses, each of which would require a range of facesheet thicknesses (varying core thickness to keep bending stiffness constant). Unless a standard low-velocity impactor shape and stiffness were agreed upon, the experimental program might be called upon to vary these as well. All of this must then be done for a range of impact energies. Clearly, the investment in such a test program would be great. In contrast, the approach anticipated by this research uses the experimental work to validate and qualify an analytical code which can then be exercised to fill in the needed parameter space. In this way, the experimental parameter space need only be broad enough to provide confidence that the analytical code can be trusted for the parameter

values of interest. Nevertheless, in reporting the current experimental work, general trends of plate response as a function of facesheet thickness are observed and discussed.

4.2.2 Static and dynamic testing.

Although load histories for the “static” and dynamic events are on time scales several orders of magnitude different, load verses displacement (equilibrium) curves for the two types of events can be compared directly. Differences between these curves provide insight into the dynamics of the impact event and the errors likely to be present in static analyses or simulations. Both static and dynamic tests were performed in an effort to mark off that portion of the parameter space in which time-dependence of the process of damage should not be ignored. The principal tool used to make this judgment is the load verses displacement curve. If the process were indeed quasi-static, one would expect the load verses displacement curve to be independent of the speed at which the load was applied. Where inertial stiffening is significant, the dynamic equilibrium curve should have a greater slope than the static. Where dynamic effects are not important to the damage process, such characteristics as peak load before damage, the magnitude of the load drop associated with a particular damage, stiffness after damage, and energy absorbed by the damage process should all be independent of the loading rate. Thus, static and dynamic test data are compared and implications for analyses based upon quasi-static assumptions are discussed.

4.2.3 Instrumented impactor.

A load cell mounted within the impactor/indenter provided load histories for all of the events. As discussed in Chapter 3, a reduced-mass tup tip effectively removed tup dynamics from the measurements providing excellent temporal fidelity in the load history (and hence velocity, energy, and displacement histories).

4.2.4 Post-impact C-scan and photomicrographs.

After the load was removed, damage present in the specimens was observed through the use of ultrasonic time-of-flight C-scans. Focused pressure waves were directed transverse to the top facesheet and echoes were timed and recorded as the focal point was traversed over the surface of the specimen. The first reflection (from the plate surface) was used to set the observation window (in time) so that the time of any subsequent returns was indicative of their depth relative to the first surface. By this process, delaminations are observed as returns and are recorded on a two-

dimensional color map indicating, for each point, the depth of the delamination nearest the top surface of the specimen. On the C-scans, the color at any point represents the time of the first observed reflection after the reflection from the top surface. This reflection corresponds to the shallowest (i.e. nearest the top surface) delamination present at the given point. Thus, only the uppermost delamination was recorded at any given point. If, for example, at some point within the specimen there were three delaminations located at ply interfaces 1, 3, and 5 (numbering interfaces sequentially from the top of the plate), then the C-scan would show a color at that point representing the depth of interface 1. The existence of the other two delaminations would not be observable at that point in the C-scan. Neither fiber failure, matrix cracking, nor core crushing were observable by C-scans. To see these modes of damage, several specimens were sliced through their thickness in several equally spaced planes perpendicular to the fiber direction. The exposed surfaces were stabilized with an epoxy potting compound, polished, and viewed under visible reflected light at various magnifications. This process allowed the viewer to record (photographically and by sketch) the damage present in any of the slice planes. The majority of the cross-section data used in this research was observed by Harrington in reference [5].

4.2.5 Observed damage forms.

Damage observed was in the forms of matrix cracks, delaminations, and crushed core walls. The delaminations observed in the slices were correlated to those observed in the C-scans and interpolation between slices allowing a three-dimensional map of the delamination pattern to be produced. Similarly, but without the aid of the C-scans, matrix cracking, and core crushing were also mapped. It should be noted that only matrix cracks in the zero degree plies could be observed in these slices due to the fact that the ninety degree fibers were in the plane of the slice.

4.3 Parameters

As mentioned, a primary purpose of the experimental portion of this research was to provide validation data for the analytical work. Toward this end, a particular material and geometry set was identified which provides the needed data while not overcomplicating the analysis. The panels consist of AS4/3501-6 graphite-epoxy face sheets secondarily bonded to 1.27 cm thick HRH-10-1/8-9.0 Nomex honeycomb core using two layers of FM300-2 film adhesive. The face sheets had the following stacking sequences: $[0/90]_8$, $[0/90]_{2S}$, $[0/90]_{4S}$, $[0/90]_{8S}$, and $[0/90]_{12S}$. In the following, sandwich structures made from these facesheets are referred to as 4-, 8-, 16-, 32-, and 48-ply,

respectively. Each of the panels from which the individual specimens were cut were C-scanned to ensure no significant flaws were present before impact. The specimen size was 17.8 cm by 17.8 cm and they were restrained in a steel fixture simulating simple supports [5] having dimensions of 12.7cm by 12.7 cm. The same restraint fixture was used for both static and dynamic tests. All tests were performed at room temperature. The impactor/indenter radius was 1.27 cm and constant for all tests. For pendulum tests the tup mass was 3.48 kg while that for drop weight tests was 3.49 kg. Tup tip mass for the drop weight tests was 8.2 gm while that for the pendulum tests was 12.3 gm. Drop height (or pendulum swing) was varied to provide impact energies between 0.06 and 25 joules. For each facesheet thickness the impact energies were chosen to span the damage initiation energy (threshold) and extend for at least a factor of two above it. The entire impact test matrix is given in figure 4-1.

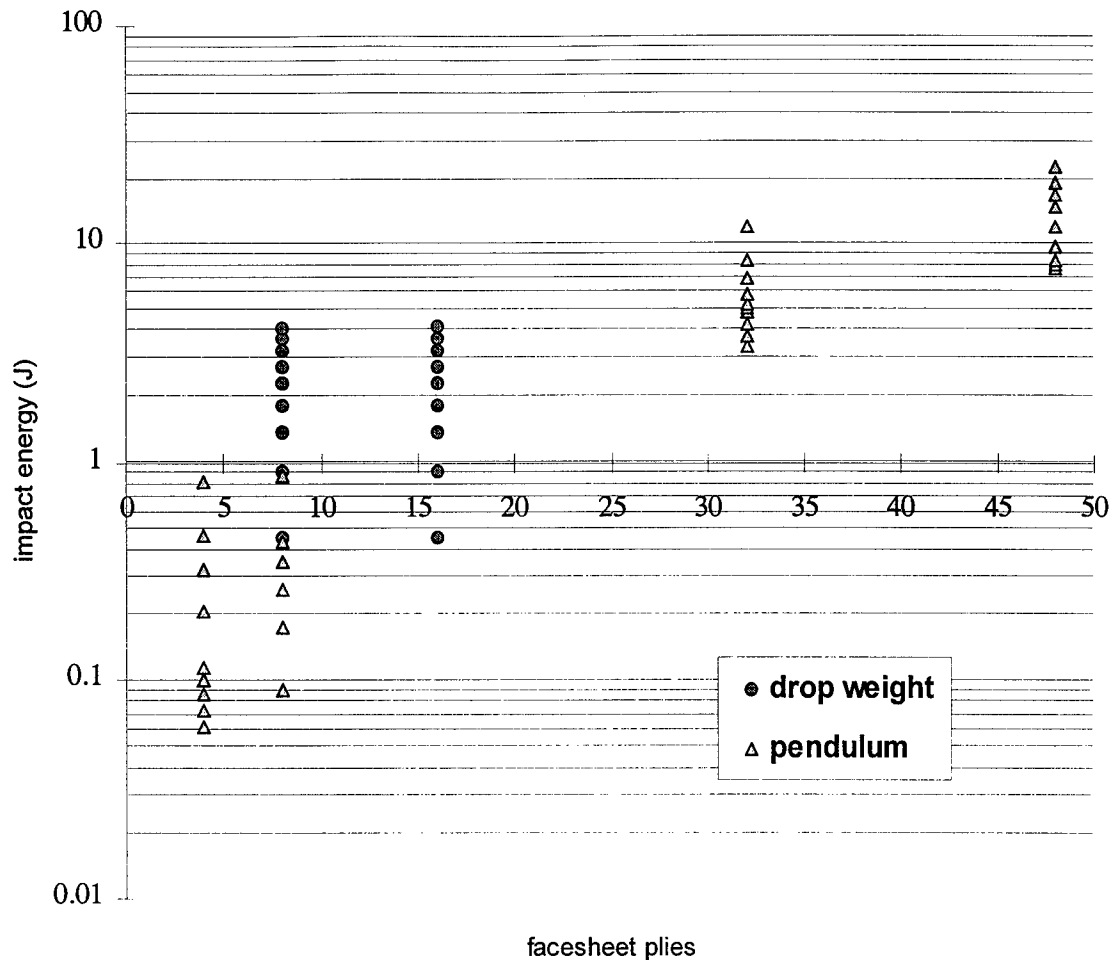


Figure 4-1 Impact test matrix.

4.4 Static Indentation Test System

The test system used to slowly (i.e., “statically”) load the test specimens transverse to the midplane was a United Calibration screw-type load frame. Control was provided by a dedicated PC. The data were collected using a Nicolet digital data acquisition system triggered manually just prior to the beginning of the test. A United Calibration 2000 lbf (8896 N) load cell was used to measure load for the 4-, 8-, 16-, and 32-ply specimens and a United Calibration 20000 lbf (88960 N) load cell was used for the 48-ply specimens. Crosshead displacement was known from the constant crosshead velocity and a constant sampling rate. The crosshead was assumed to be rigid compared to the plate so that crosshead displacement and top surface displacement under the point of load were assumed identical. A displacement transducer (LVDT) was used to measure the displacement

of the lower surface of the plate. The static test system is shown schematically in figure 4-2. The principal features are: 1) a stiff crosshead driven down by precisely controlled screws; 2) a stiff load cell mounted under the crosshead which measures the force between the crosshead and the specimen; 3) a 12.7 mm radius hardened steel ball bearing between the load cell and the specimen (this bearing served the same purpose as the tup tip in the dynamic tests); 4) a stiff restraint fixture to hold the specimen; 5) an LVDT mounted under the specimen; 6) a control system; 7) signal conditioners; and 8) a digital data acquisition system.

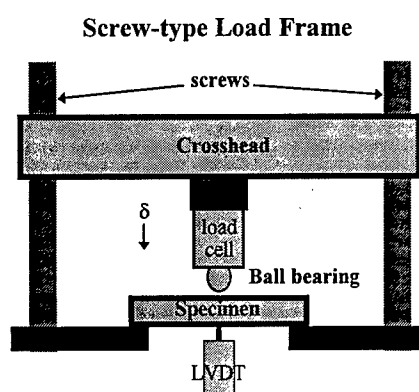


Figure 4-2 Schematic of static indentation test system. (The direction of the applied displacement is shown by δ).

4.4.1 Calibration.

The load cells were factory calibrated for the data acquisition system built into the dedicated PC that also controlled the test system. A separate data acquisition system was used for these tests due to the fact that the built-in system could not be easily modified to read the LVDT output. This meant that the load cells had to be calibrated for the new data acquisition system. The calibration was performed by noting the load output on the built in system before the test and the maximum value reached during the test. Using these two values and the measured voltage change gave the appropriate scaling from volts to force units. The crosshead velocity was calibrated in the factory and confirmed to be correct with a ruler and a stop watch. The range of the LVDT used for this work was 25 mm while the maximum displacement of the tup was 3.5 mm. Since the bottom surface displacement measured by the LVDT was always less than the tup displacement, only a relatively small portion of the LVDT range was used, resulting in a rather noisy signal. To smooth the signal, a low-pass (100 Hz) filter was used. The LVDT was then calibrated by driving it with the crosshead at a constant velocity and fitting a straight line to the resulting voltage verses

displacement curve. In this way, LVDT voltage was related to known LVDT displacement (a linear function of time due to the constant velocity).

4.4.2 Data reduction.

The data recorded for each test consisted of voltages representing force and bottom surface displacement and time. The data acquisition system provided two ASCII text files for each test. The first contained load cell voltage and time while the second contained LVDT voltage and time. Data were recorded at uniform time intervals (10 msec) and the crosshead velocity was known, so crosshead position (top surface displacement) was calculated from the time integral of velocity. A Mathcad template served as a data reduction program, reading these files and generating a third file containing all of the values of interest with the appropriate units. These included top and bottom surface displacements (where the load was applied), load, average transverse strain, indentation depth, and time. Average transverse strain under the loading point was calculated from top and bottom surface displacements and the known thickness of the particular plate.

In each test data set, five distinct time intervals were present. These are represented in figure 4-3. The first interval represented the time before the crosshead began to move. During this time, a nominal 10 N pre-load was present which served to remove the majority of the slack from the system. At the beginning of the second interval, the crosshead began to move at a predefined rate, usually 5.08 mm/min. The acceleration from rest to this velocity was ignored. The third interval began when the crosshead was manually stopped. The command to stop the crosshead was given via the PC that controlled the test system and was issued when the load reached the predetermined stopping value or immediately after the first major load drop. It is the latter case for the example shown in figure 4-3. Since this control was manual and the load was fluctuating during the test, it was generally not possible to precisely control the stopping load. The fourth interval followed when a manual input directed the crosshead to begin returning (unloading). This motion was also at a constant velocity, usually 12.7 mm/min. Each of the above intervals was readily detectable in the load data by an abrupt change in slope of the load versus time curve. The Mathcad data reduction template presented the user with detailed views of the data in the areas of transition from one interval to the next and the user manually chose the four points that broke the data into the five intervals as shown in figure 4-3. The beginning of the fifth interval was the end of the unloading sequence (when the crosshead lost contact with the plate) and was less easily discerned due to the

fact that the slope of the load verses time curve approached zero asymptotically as the slack in the system was allowed to accumulate. The end of the unloading was taken to occur when the locally averaged (smoothed) load dipped below the initial 10 N preload. With practice, all transition points could be chosen consistently by this method. Intervals 2, 3, and 4 captured the entire event and intervals 1 and 5 were cropped from the data by the Mathcad template.

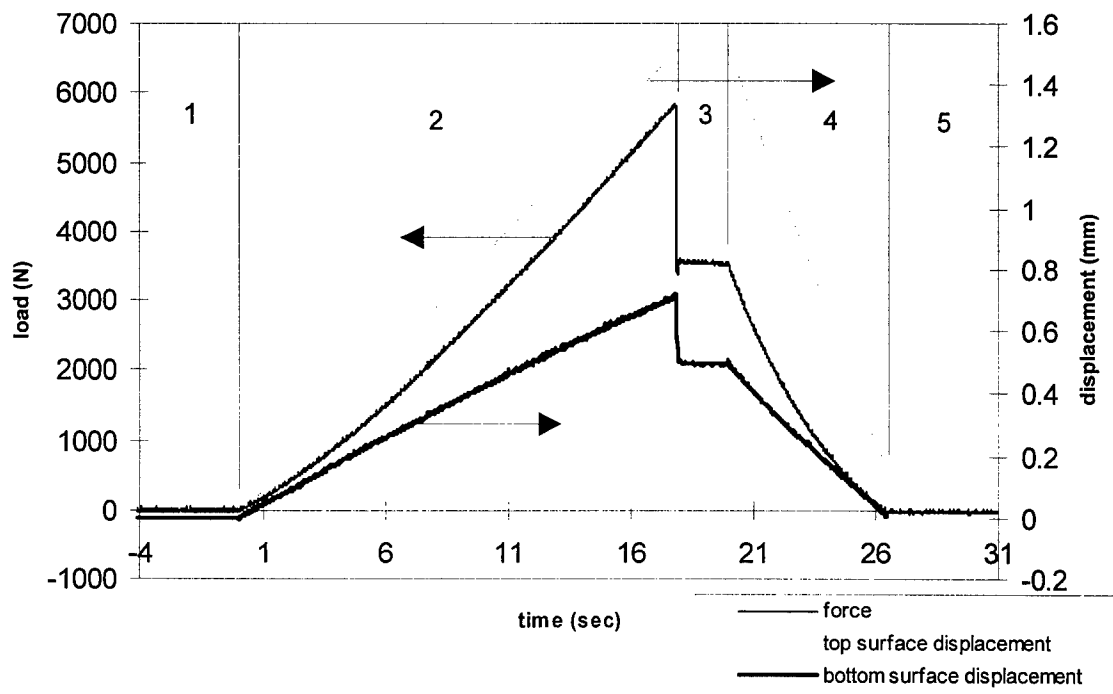


Figure 4-3 Typical "static" loading sequence. (100 data points were recorded per second).

4.5 Dynamic Impact Test Systems

Force and energy histories are part of the reduced data generally available from instrumented impactor impact test systems. To facilitate comparisons with static test data as well as static analysis data, force verses tup displacement plots were also generated. For the analytical investigation, the degree to which the predicted contact force verses tup displacement matches that of the experiments (including load drops) was a principal measure of success. If the analytical investigation predicts both the peak value and the magnitude of the first significant load drop and then follows the experimental load verses tup displacement any further, it is judged to be a success. Clearly, contact force verses tup displacement data are required from the experiments, yet neither contact force nor

tup displacement were measured directly. An instrumented tup measured a force close to, but not the same as, the contact force (Chapter 3), and integration of the tup equations of motion produced the tup displacement.

In the early portion of the testing, a drop weight impact testing system made by Dynatup was used to impact 8- and 16-ply sandwich specimens. The minimum energy for which data could be obtained with this system was ~ 0.5 J. This minimum was found to be unacceptable because the initiation of damage in the 8-ply specimens occurred at less than this value. In order to obtain data for lower energies, the remainder of the test matrix was filled using the same load cell, but mounting it in a pendulum impact test system. The minimum energy at which the pendulum system could be used (without reducing tup mass) was found to be less than 0.05 J and this was low enough to resolve the initiation of damage in the 8-ply as well as the 4-ply specimens.

4.5.1 Drop weight test system.

The Dynatup drop weight test system used for all of the 16-ply and part of the 8-ply portion of the test matrix is shown schematically in figure 4-4. Its principal features are: 1) a stiff, guided, near-free-falling mass; 2) a stiff load cell mounted under the falling mass which measures the force between the mass and the specimen; 3) a spherical 12.7 mm radius hardened steel tup tip between the load cell and the specimen; 4) a light gate to measure tup velocity just prior to impact; 5) a stiff restraint fixture to hold the specimen; 6) a control system including brakes to prevent multiple hits; and 7) a digital data acquisition system.

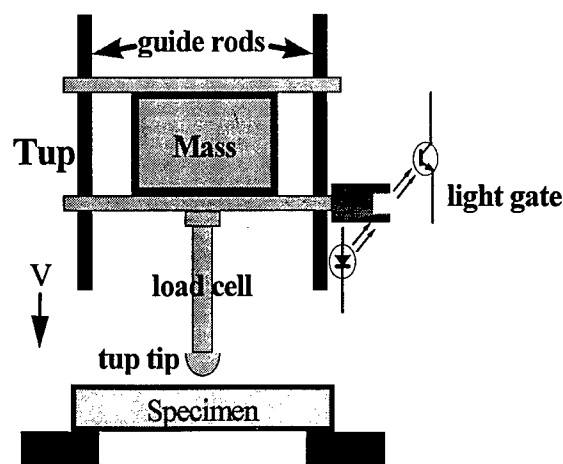


Figure 4-4 Schematic of Dynatup drop weight impact test system.

4.5.2 Pendulum test system.

The pendulum impact test system had several advantages over the drop weight test system. Not only could it reliably take data at an order of magnitude smaller impact energy for the same tup mass, but also it had the singular advantage of measuring both impact velocity and rebound velocity. Thus absorbed energy was effectively measured, providing a check for the integrations of the tup equation of motion. In addition, the fact that these velocity measurements were taken at the bottom of the pendulum swing (when the tup acceleration is near zero) provided a greater degree of consistency in the impact velocity measurements than was available from the drop weight system. The handicap that the drop weight system had in this regard was that the acceleration of the tup at the time that impact velocity was measured was not zero, in fact the acceleration was constant during the whole drop. Thus any small variability in the location of the velocity measurement light gate with respect to the specimen had a significantly greater effect on the drop weight impact velocity calculation than it would have had on the pendulum impact velocity calculation. In short, the pendulum was a more forgiving system.

The pendulum impact test system was used for all of the 4-, 32-, and 48-ply tests and the low-energy part of the 8-ply tests. The system is shown schematically in figure 4-5. Its principal features are: 1) four 3.6 m kevlar strings positioned so as to provide a 3.37 m effective pendulum arm with a stable planar swing and a consistent impact point; 2) a stiff suspended mass; 3) a stiff load cell mounted on the swinging mass which measures the force between the mass and the specimen; 4) a spherical 12.7 mm radius hardened steel tup tip between the load cell and the specimen; 5) a light gate to measure tup velocity just prior to and just after impact; 6) a stiff restraint fixture to hold the specimen; and 7) a digital data acquisition system. Control of the pendulum was significantly less automated than the drop weight system. For example, to control the energy of impact the user must calculate the appropriate "swing length" via the relation,

$$\text{swing length} = \sqrt{\text{drop height} \times (2 \times \text{string vertical length} - \text{drop height})} \quad (4-1)$$

and then manually (and deftly, so as not to induce any off-axis motion) release the tup after pulling it back that distance from the specimen. The user must then physically catch the tup after the event to prevent a second hit.

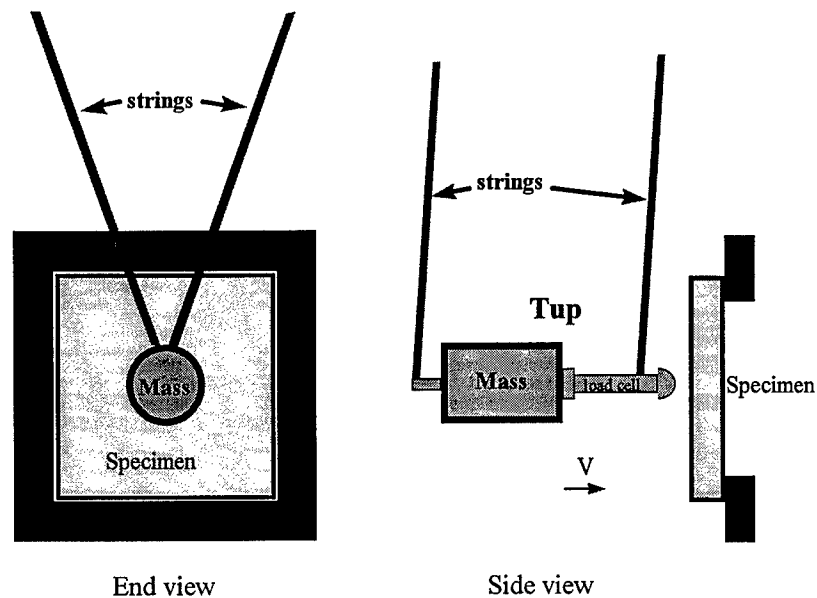


Figure 4-5 Schematic of pendulum impact test system.

4.5.3 Impact test calculations.

Other differences aside, the calculations required for the pendulum and drop weight data were nearly identical. The fact that the pendulum is horizontal and the drop weight system was vertical did not influence the calculations. In the first place, the deflections were small, so the change in tup potential energy while in contact with the plate was neglected. In the second place, the acceleration due to gravity was assumed to be small compared to the acceleration produced by the impact force. Both of these higher order effects would have had a much greater influence on the drop weight calculations than on the pendulum. The important calculations for the dynamic impact tests are outlined below.

4.5.3.1 *Velocity.* Newton's second law for the tup is integrated to calculate velocity as a function of time. Initial velocity, $V(0)$, is a measured quantity. Time zero is the instant that the tup first makes contact with the specimen and is taken to be that time when the force increases from nominal zero. This calculation is important because the net loss in tup kinetic energy is taken to be the energy absorbed by the specimen and is used as a measure for damage. The tup velocity, $V_{tup}(t)$, is integrated from the contact force, $F(t)$, by the relation

$$V_{tup}(t) = V_{tup}(0) - \frac{1}{m_{tup}} \int_0^t F(\tau) d\tau \quad (4-2)$$

The trapezoidal rule was used to carry out the time integration in equations 4-2 and 4-3. Since the time interval between data points was a constant 10 msec, 100 force registers were read per second.

4.5.3.2 Displacement. Determining displacement as a function of time requires an additional time integration. Initial displacement, $\delta(0)$, is zero. This calculation is important because load versus displacement is used to compare static and dynamic test data in order to judge the applicability of the quasi-static assumption. The tup displacement, $\delta(t)$, is integrated from the tup velocity, $V_{tup}(t)$, by the relation

$$\delta(t) = \int_0^t V_{tup}(\tau) d\tau + \delta(0) \quad (4-3)$$

4.5.3.3 Energy. Three energies are important to this work. The first, impact energy, is a principal measure of the severity of the impact event. The second, tup kinetic energy, is a measure of the system energy not residing in the plate. Here it should be noted that the tup is assumed to be effectively rigid so that tup strain energy is ignored. The limitations and liabilities of this assumption were discussed in Chapter 3. The third and last important energy is the arithmetic difference between the first two and is called the absorbed energy. Absorbed energy is similar to the strain energy of the specimen but it also includes system losses. The losses are both those within the plate (e.g. strain energy release, viscous damping) and those outside the plate (e.g. friction, dissipated tup strain energy, etc.).

There are at least three alternative methods of calculating impact energy: 1) from the potential energy of the tup before release; 2) from the kinetic energy of the tup just prior to impact; and 3) from the maximum of the absorbed energy history (the energy calculated to be in the plate when the tup is stopped). Of the three, the last has by far the most opportunity for error since nearly every measurement made and two time integrations on the force history contribute to it. The potential energy before release is the method used to attempt to obtain a particular impact energy, but it has a great deal of potential human error in it. The author considers the kinetic energy of the tup just prior to impact to be the most reliable and objective measure for the impact energy.

$$\text{Impact energy: } E_{\text{impact}} = T(0) = \frac{1}{2} m_{\text{tup}} V(0)^2 \quad (4-4)$$

Unlike impact energy, only one way is used to calculate the tup kinetic energy and absorbed energy histories.

$$\text{Tup kinetic energy: } T(t) = \frac{1}{2} m_{\text{tup}} V(t)^2 \quad (4-5)$$

$$\text{Absorbed energy: } E_{\text{absorbed}}(t) = T(0) - T(t) - U(t) \quad (4-6)$$

For the pendulum tests, tup velocity (hence kinetic energy) is measured both before and after impact. This provides a check for absorbed energy history calculation since the difference between the tup kinetic energy before and after the impact event is the energy absorbed (or dissipated, or otherwise lost by the tup). Note, tup potential energy, $U(t)$, is assumed to be constant during the impact event (small displacement) and is therefore eliminated.

4.6 Damage Analysis

4.6.1 C-scan.

The primary tool used for both pre-impact and post-impact non-destructive inspection of the test articles was pulse echo ultrasonic time-of-flight C-scan. It was established by Harrington [5] that for low-velocity impact to the specimens used in the current work damage, when present, is confined to the upper facesheet and the core. Therefore, after impact only the upper facesheet was scanned for the present work. The specimens were first immersed a bath of water which acted as an acoustic coupling agent. An ultrasonic probe with a 7.6 cm focal length was used for all scans. This probe produced pressure pulses which the water coupled to the specimen surface. Two significant reflections were then observed in a known virgin portion of the specimen. The experienced technician operating the C-scan system identified these two reflections as those from the top surface of the plate and from the lower surface of the adhesive layer that bonded the top facesheet to the core. The time difference between these reflections was converted to a relative distance from the probe by the C-scan system software. The difference between the distances of the reflective surfaces confirmed that the two surfaces producing the significant reflections were separated by the facesheet thickness, consistent with the technicians identification of the sources. A time window was set to pick up any reflection from a surface between these two surfaces. Where no delaminations existed, no such surfaces existed (at least not perpendicular to the probe) and the reflection from the lower surface of the adhesive layer provided a background return. The adhesive layer was not uniform in thickness due to the filleting of the adhesive into the interface between individual cell walls and the facesheet. This unevenness can be seen in the C-scans from which one can make out the general pattern of the honeycomb. By this process delaminations patterns were observed and are recorded on a two-dimensional color map. Only the first subsurface return was recorded so that if more than one delamination were present at any given point, only the depth of the delamination nearest the probe was indicated for that point by color.

4.6.2 Photomicroscopy.

The C-scans could not resolve multiple delaminations through the thickness. In addition, other damage types were not observed by the C-scans. In particular, fiber failure, matrix cracking, and core crushing were not seen by C-scans. To overcome these limitations, several specimens were

sliced through their thickness in equally spaced planes perpendicular to the fiber direction. After being stabilized with an epoxy potting compound, the exposed surfaces were polished, and viewed under visible reflected light at various magnifications. This process allowed the viewer to record (photographically and by sketch) the damage present in any of the slice planes. The particular damages seen by this method include delaminations, matrix cracking, and core crushing. While the C-scans provided a vertical view of the damage pattern, the sectioning of the specimens provided the only in-plane view. Melding the two views and interpolating between slice planes provided a near-three-dimensional representation of the damage.

4.7 Results

As indicated by the impact test matrix given in figure 4-1, two parameters were varied for the dynamic portion of this research. These are, facesheet thickness (or number of plies) and impact energy. For each event, a number of measures can provide insight into the physics. The measures found most prominently in the literature are force history, absorbed energy history, and C-scans. In addition to these, other measures were found to be quite useful in the present research. These include absorbed energy at the end of the event, photomicrographs, and most significantly load-displacement curves. In discussing the results of a test matrix varying facesheet thickness and impact energy, one could choose to take one facesheet thickness at a time and show the effect of different energies on each measure, or one energy at a time and discuss the effect of facesheet thickness on each measure. In contrast to these admittedly logical presentation orders, the organization of the following was chosen because it enhances the communication of the key ideas gleaned from these data while minimizing the repetition of words. For this presentation, the measures (not the experimental parameters) provide the top level discussion points and the effects of first facesheet thickness and then impact energy are discussed in relation to each measure.

4.7.1 Absorbed energy.

In the case of drop weight tests post-impact (rebound) velocity was not measured. Absorbed energy was calculated from tup velocity which was calculated from force history and initial velocity via equation 4-2. For pendulum tests the measured post-impact velocity allowed direct calculation of

absorbed energy at the end of the impact event by substituting equations 4-3 and 4-4 into equation 4-5.

The difference between the kinetic energy of the tup at the beginning of the impact event and that at the end of the impact event is here called the absorbed energy. Many processes could be responsible for this loss of energy. Some possible energy loss mechanisms are friction at the boundaries of the plate and within the contact area; high frequency vibration modes of the tup, specimen, and supports; velocity measurement errors; and strain energy release associated with the accumulation of damage within the specimen. Friction is not believed to be a significant contributor because the in-plane displacements at the boundaries and under the tup are very small. Vibratory modes of the tup are a greater concern as outlined in Chapter 3, but with the reduced tup tip mass they should also be small compared to the impact energy. Dynamics of the specimen have not been rigorously evaluated for their contribution to absorbed energy, but the analyst would expect that the energy absorbed by higher frequency vibration modes of the specimen would increase with impact energy and specimen mass (i.e. facesheet thickness). Vibration of the supports was minimized by making them both massive and stiff compared to the tup and specimen. Velocity measurement errors could be either random noise or a linear error in velocity which would produce a quadratic error in energy. If the pre-impact and post-impact velocity measurements were such that the post-impact measurement were consistently low, then the ratio of absorbed energy to impact energy for an elastic event would be a nonzero constant for all impact energies and facesheet thicknesses. In addition, post-impact velocity calculated from the tup equation of motion should be consistently different from that measured by the light gate.

For the pendulum tests, a flag was attached to the tup and two light gates were located in the path of the flag such that as the pendulum approached the specimen the leading edge of the flag blocked first gate 1 and then gate 2 just prior to impact. On rebound the gates were cleared by the leading edge in opposite order. Velocity was measured by recording two time intervals,

$$\begin{aligned}\Delta t_1 &= \text{time gate 2 blocked} - \text{time gate 1 blocked} \\ \Delta t_2 &= \text{time gate 1 cleared} - \text{time gate 2 cleared}\end{aligned}\tag{4-7}$$

The light gates were set 2.54 cm apart, so the velocity (m/sec) was calculated by

$$\begin{aligned}
 \text{impact velocity:} & \quad \frac{0.0254 \text{ m}}{\Delta t_1} \\
 \text{rebound velocity:} & \quad \frac{0.0254 \text{ m}}{\Delta t_2}
 \end{aligned}
 \tag{4-8}$$

Error in the velocity measurement could have resulted from inaccurate relative placement of the light gates, chronometer error, or differences between the gates in terms of the time it takes the photocells in the light gates to turn on and the time it takes them to turn off. That is, the leading edge progressively blocks the light from the light source in gate 1 over some finite time. During that time the gate 1 photocell voltage is dropping. At some point the voltage is low enough that the electronics start the clock for Δt_1 . Later the leading edge progressively blocks the light from the light source in gate 2. If the two gates do not have identical light sources, photocells, and electronics, a different amount of blockage might trigger gate 2 than gate 1 and the tup may have moved more or less than 2.54 cm past the point where it was when the clock for Δt_1 started when the gate 2 electronics stop the clock for Δt_1 . The only calibration of the light gates that was done specifically for this research was to verify the physical spacing between the gates. Discounting the possibility of chronometer error as remote due to modern quartz technology, the effect of any of the other errors just discussed would be of the same form. The distance that the tup traveled in the measured time interval would be other than 2.54 cm. The error (difference between actual velocity and the measured velocity) would be linear with velocity.

Equations 4-4 through 4-6 demonstrate the importance of velocity measurement to the energy calculations. There were two different methods of obtaining rebound velocity used in this research. In order to show the difference between the two, impact velocity (V_{in}) as well as rebound velocity (V_{out}) as obtained by these two methods are shown in figures 4-6 through 4-9 for 4-, 8-, 32-, and 48-ply specimens. Since only the drop weight impactor tests were performed on the 16-ply specimens, no light gate rebound velocity data were available for 16-ply specimens. In figures 4-6 through 4-9, the two ways of obtaining rebound velocity were 1) measurement by the light gate (labeled "from light gate") and 2) calculation from force history and initial velocity via equation 4-2 (labeled "from load history").

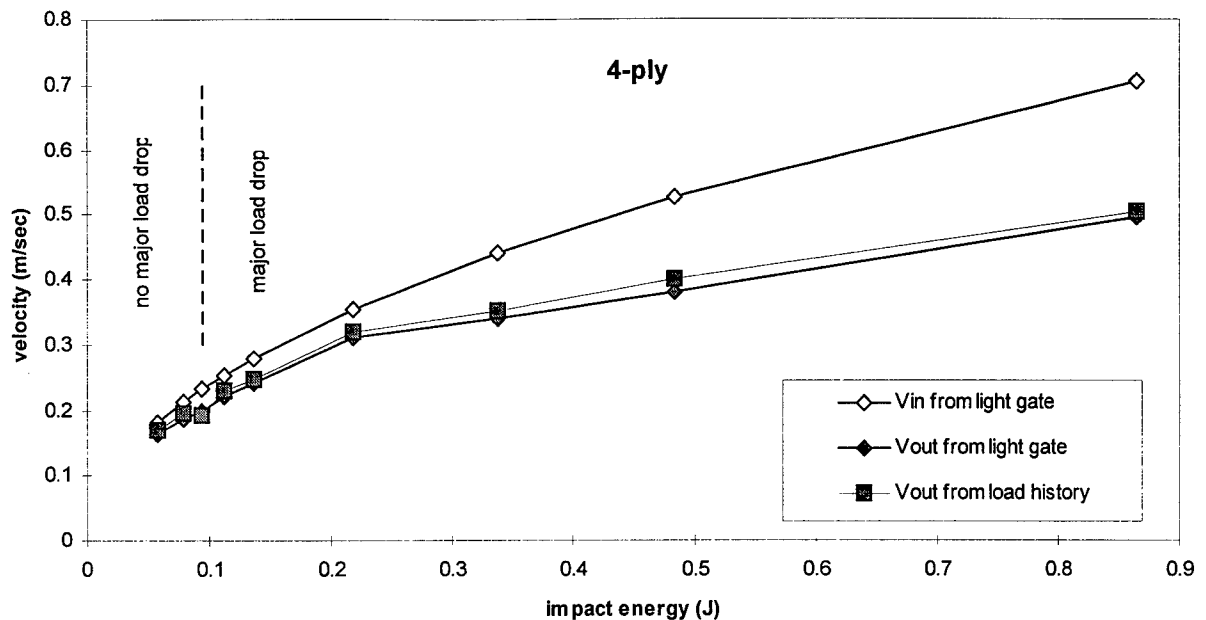


Figure 4-6 4-ply Velocities of impact (V_{in}) and rebound (V_{out}) versus impact energy. Pendulum data only.

Figure 4-6 shows that for the 4-ply tests the rebound velocity calculated by the integration of the force history is close to, but consistently greater than, the velocity measured by the light gate. If the light gate is correct, the force is too low (equation 4-2) leading to an error in rebound velocity (too high), and the absorbed energy calculated from the load history will be too low. If the force is correct, then the rebound velocity from the light gate is too low and the absorbed energy calculated from the light gate rebound velocity will be too low. This line of reasoning provides the key to discerning which of the velocity calculations is the most trustworthy. Of the two methods, the one that produces the highest absorbed energy must be the better method.

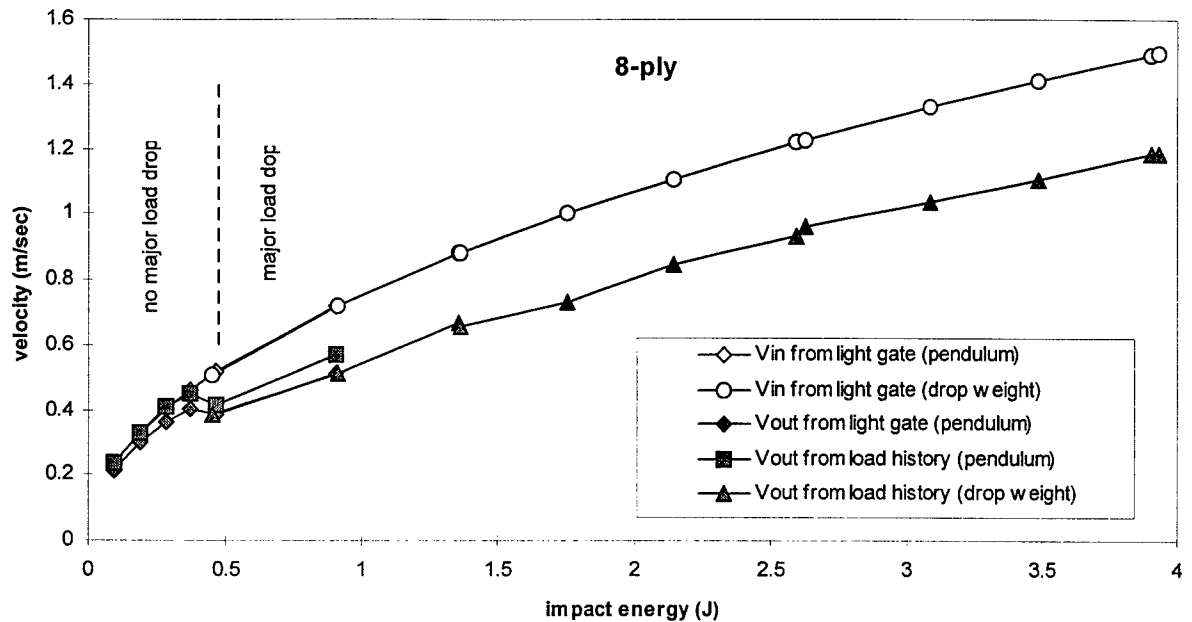


Figure 4-7 8-ply Velocities of impact (V_{in}) and rebound (V_{out}) versus impact energy. Pendulum and drop weight data.

Figure 4-7 shows that for the 8-ply tests the trend of load history calculating greater rebound velocity identified in the 4-ply data continues, but the difference between the rebound velocity calculated by the integration of the force history and that measured by the light gate is more significant than it was for the 4-ply tests. Significantly, at the low energies where no major load drop was observed, the rebound velocities calculated by integration of the force histories are nearly the same as the impact velocity, indicating that nearly all the impact energy is returned to the tup. The fact that the rebound velocity calculated by the force history does not exceed the impact velocity provides some confidence that the force could be correct.

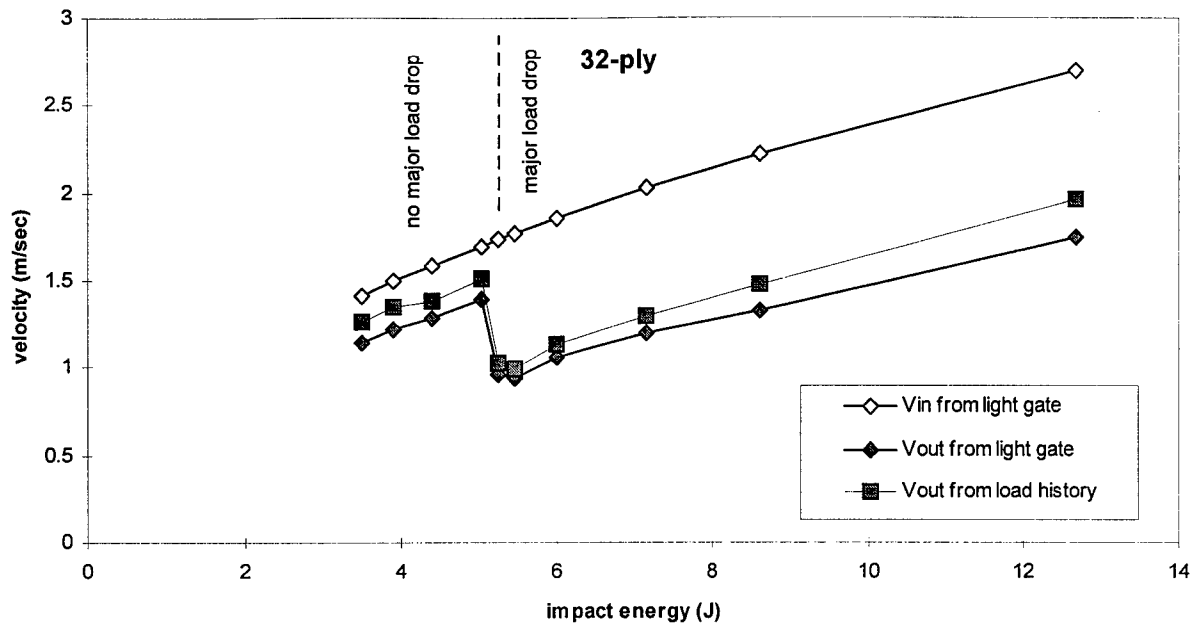


Figure 4-8 32-ply Velocities of impact (V_{in}) and rebound (V_{out}) versus impact energy. Pendulum data only.

The rebound velocities calculated from the force histories for the 32-ply data shown in figure 4-8 show the same trend as those of the thinner facesheets. An important difference between this figure and figures 4-6 and 4-7 is that no matter which way rebound velocity was calculated, it was significantly less than the impact velocity even at impact energies for which no major load drop was observed. This suggests that the thicker facesheet specimens have an energy absorbing process (damage mechanism) that takes place at energies lower than that required to produce a major load drop.

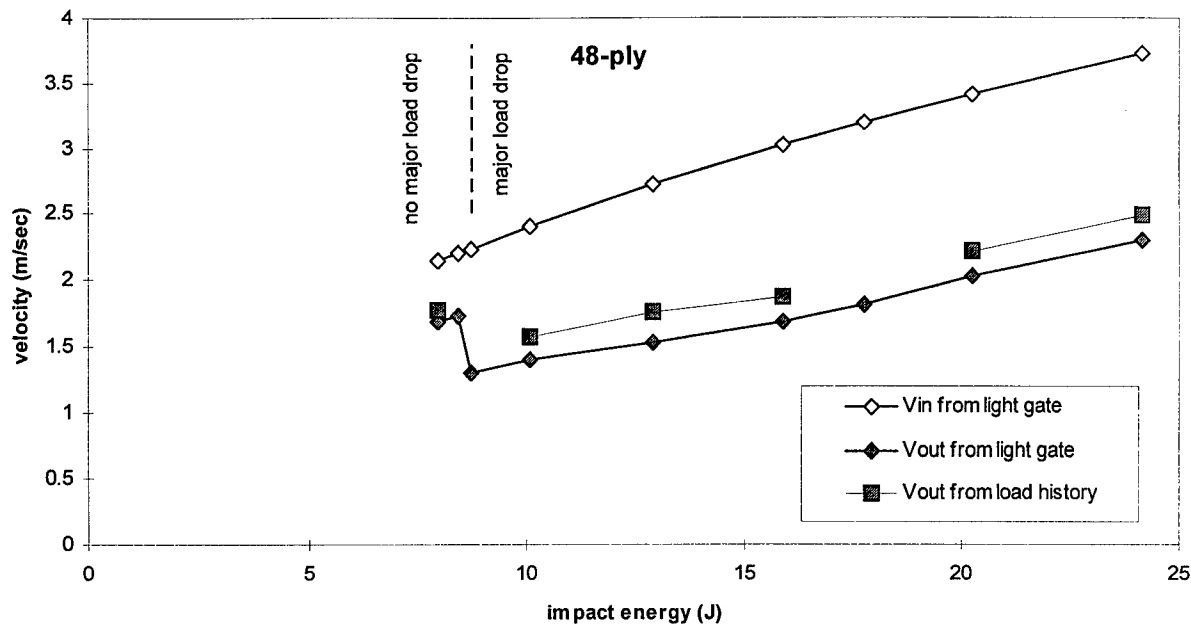


Figure 4-9 48-ply Velocities of impact (V_{in}) and rebound (V_{out}) versus impact energy. Pendulum data only.

For the 48-ply data shown in figure 4-9, three load histories were lost due to failure of the oscilloscope which was recording the data to trigger. As a result, V_{out} could not be obtained from the load histories for those tests. Breaks in the line connecting the square markers in figure 4-9 identify the missing data. The rebound velocities calculated from the force histories for the 48-ply data shown in figure 4-9 show the same trends as those of the 32-ply specimens. Like the 32-ply specimens, no matter which way rebound velocity was calculated, it was significantly less than the impact velocity even at impact energies for which no major load drop was observed. This supports the conjecture made above that the thicker facesheet specimens have an energy absorbing process (damage mechanism) that takes place at energies lower than that required to produce a major load drop.

It has been suggested that velocity measurement errors could be either random noise or a linear error in velocity. To investigate this, the difference between the two rebound velocity calculations was plotted against rebound velocity and is shown in figure 4-10. In such a plot, a linear error in velocity would show up because all of the data would collapse to a straight line regardless of the facesheet thickness, while a random error in velocity would show up as scatter.

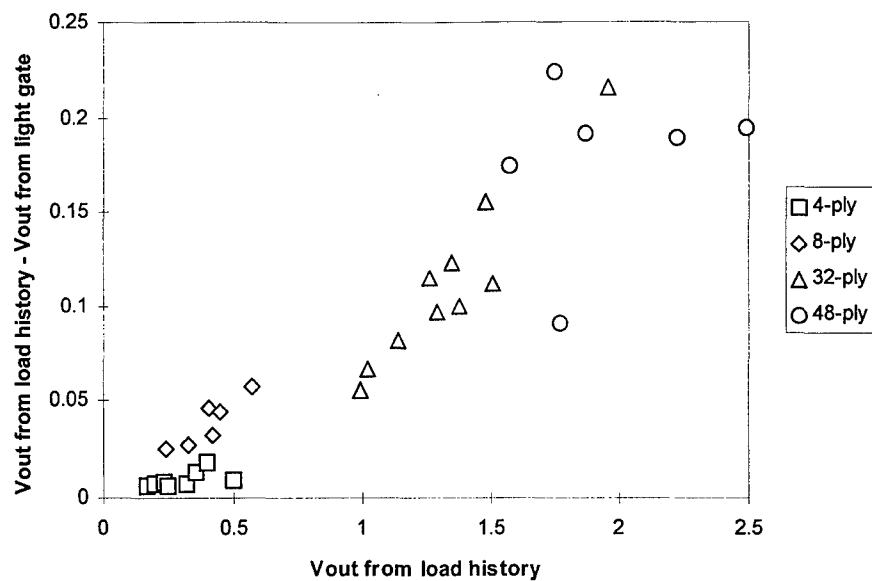


Figure 4-10 Rebound velocity calculation difference versus rebound velocity. Pendulum data only.

While there is a definite increasing trend in the difference between these velocity calculations with increasing rebound velocity, figure 4-10 does not collapse all of the data to a straight line. If the light gate was in error as discussed above, these data should be much closer to linear.

In figures 4-11 through 4-15 absorbed energy has been nondimensionalized by impact energy and plotted versus impact energy.

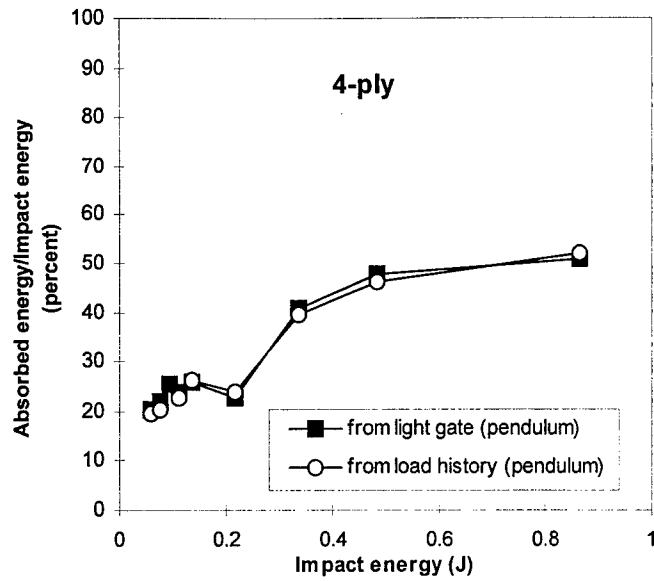


Figure 4-11 4-ply Absorbed energy versus impact energy showing threshold near 0.3 J. Pendulum data only.

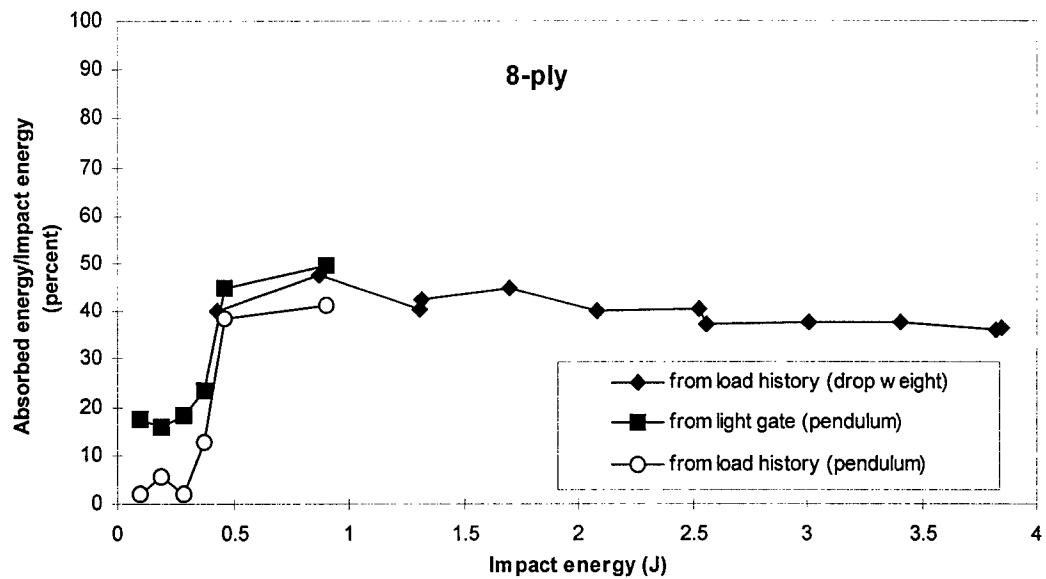


Figure 4-12 8-ply Absorbed energy versus impact energy showing threshold near 0.45 J. Pendulum and drop weight data.

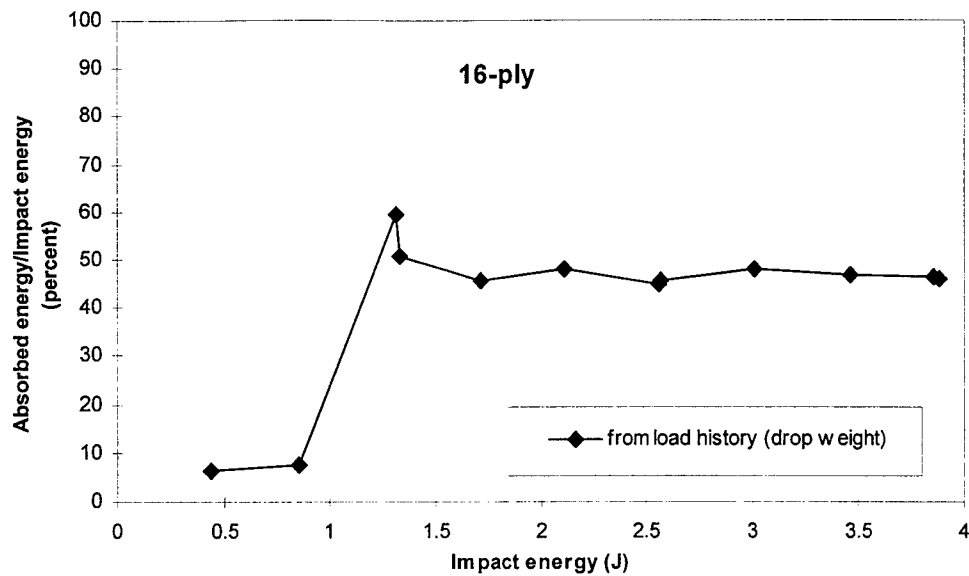


Figure 4-13 16-ply Absorbed energy versus impact energy showing threshold near 1.0 J. Drop weight data only.

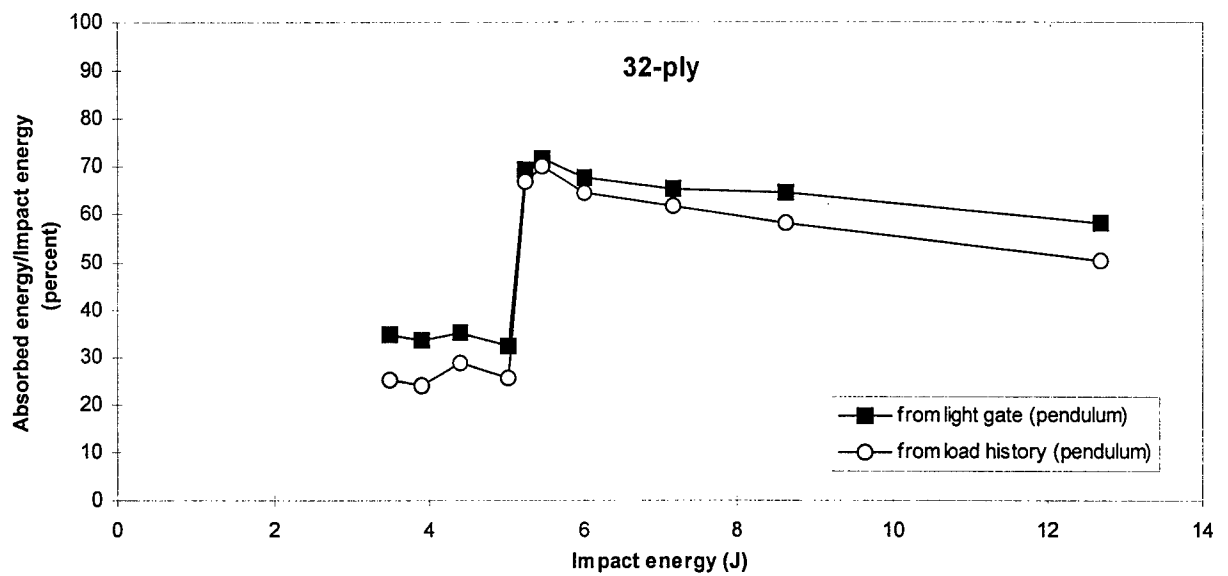


Figure 4-14 32-ply Absorbed energy versus impact energy showing threshold near 5.1 J. Pendulum data only.

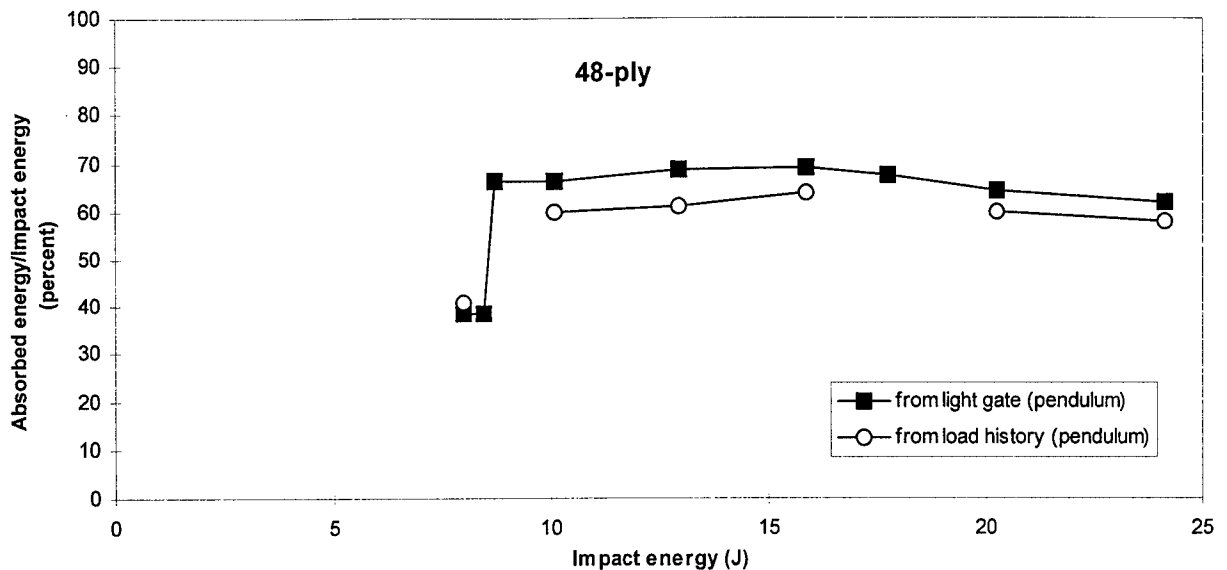


Figure 4-15 48-ply Absorbed energy versus impact energy showing threshold near 8.5 J. Pendulum data only.

Several important trends are observable in figures 4-11 through 4-15. First, the absorbed energy based on the light gate velocity measurement is almost universally greater than that based on the load history. As discussed, this indicates that the light gate velocity measurement (and energies based on it) are more likely to be correct than the load history velocity calculation (and energies based upon it). Secondly, for all of the pendulum data (figures 4-11, 4-12, 4-14, and 4-15) at least 15 percent of the impact energy was not returned to the tup. This was the case even for impact energies low enough to produce no detectable damage. Thirdly, in each figure a threshold impact energy is evident below which the absorbed energy has one relationship to impact energy and above which a significantly larger portion of the impact energy is absorbed. This threshold impact energy corresponds precisely with the damage initiation impact energy determined by post-impact inspections of the specimens. Absorbed energy appears to be a reliable indicator of damage. This is to be expected since the strain energy release associated with damage progression is an energy loss to the system. What is interesting is how sharply the threshold can be seen as each plot approximates a step function. The fourth important trend is that, after the damage initiates, the absorbed energy increases linearly with impact energy. This trend can be seen in figures 4-11 through 4-15 by observing that for impact energies above the threshold impact energy the absorbed energy/impact energy ratio is independent of impact energy. This constant ratio implies that

doubling the impact energy will simply double the absorbed energy. Since the absorbed energy is related to the damage in the specimen, an empirically derived relationship between impact energy and damage may be possible. This relationship is conveyed in the rest of this chapter by various statements concerning the damages discussed and the impact energies at which they initiated. A fifth trend is that the absorbed energy/impact energy ratio for damaged specimens seems to increase with facesheet thickness. That is, as facesheet thickness increases the energy absorbed in the process of damage also increases. An interpretation of this may be, damage is delayed (i.e. threshold impact energy is increased) by increasing facesheet thickness but at the cost of making the damage more severe when threshold is breached.

It is also of interest to consider what effect increasing facesheet thickness has on the damage brought about by a given impact energy. Though the test matrix (figure 4-1) was not designed to show this, it did include similar impact energies for different facesheet thicknesses, so the effect of increasing facesheet thickness while holding impact energy constant could be observed from this data. In order to present the data in a concise form, a suitable scalar measure of damage proved helpful. The damage measure chosen was the absorbed energy/impact energy ratio, since it so clearly identified the damage threshold in figures 4-11 through 4-15. Figure 4-16 shows how the absorbed energy/impact energy ratio changes with facesheet thickness for several impact energies. The most important and obvious trend shown by figure 4-16 is that increasing the facesheet thickness reduces the absorbed energy/impact energy ratio associated with a given impact energy. That is, thicker facesheets absorb a smaller portion of the impact energy. This stands to reason, since the threshold impact energy increases with facesheet thickness. The lesson here is that sandwich plates with thicker facesheets are more damage resistant than those with thinner facesheets. No inferences with regard to damage tolerance should be made from these data.

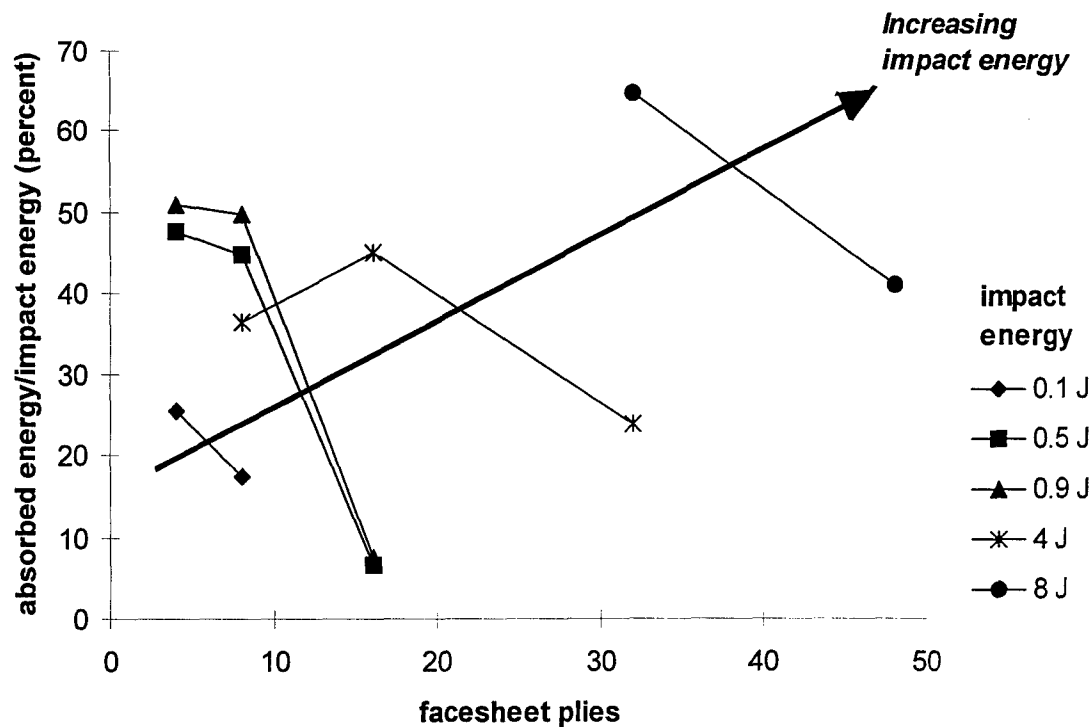


Figure 4-16 Absorbed energy/impact energy versus facesheet plies showing decreasing absorbed energy ratio (hence decreasing relative damage) from a given impact energy as the facesheet thickness is increased.

4.7.2 Force history.

Force histories for several impact energies near the threshold impact energy for each facesheet thickness are shown in figures 4-17 through 4-21. In each of those figures the facesheet thickness is held constant and the impact energy is varied. To keep the data from each event distinct, as well as to give the reader a graphic feeling for how the events change with impact energy, each event history is offset to the right (i.e. the time of the beginning of the event is shifted) by,

$$t_{i,j} = t_{i,j} + Timescale \times E_{impact_j} \quad (4-9)$$

in which, j delineates a particular impact event, i a particular data point, t is time (sec), and $Timescale$ (sec/J) is a scaling chosen distinctly for each plot to spread the ordinates of the data out in an appealing fashion. This shifting of the data ordinates makes it possible to observe the relative magnitudes of the impact energies for each event simply by visually observing the ordinate shift.

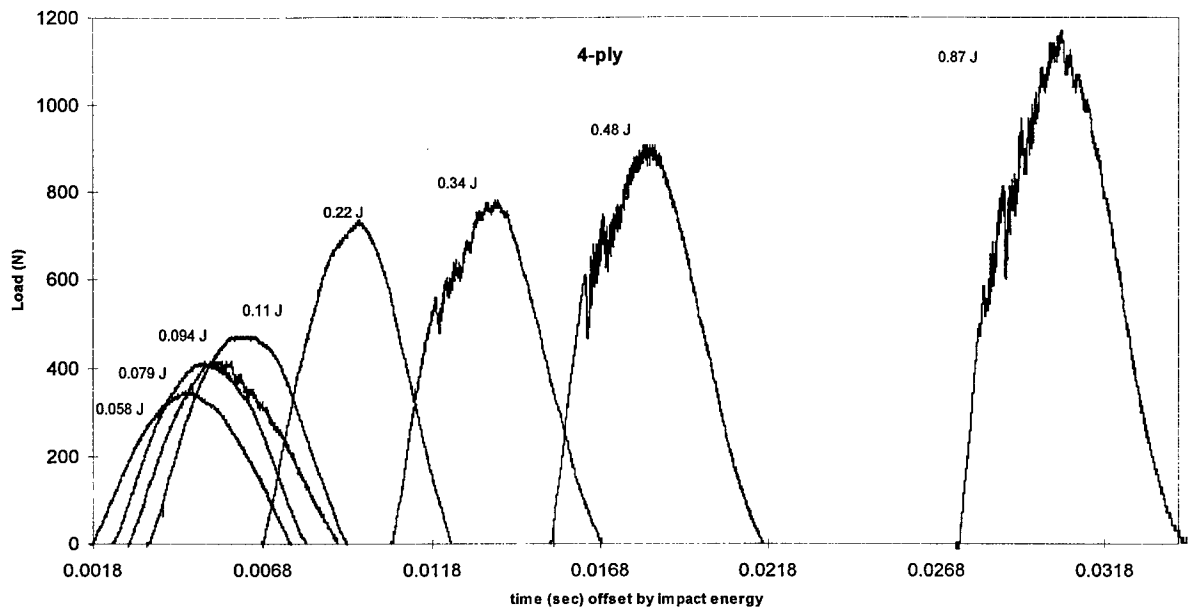


Figure 4-17 4-ply Force histories offset by impact energy showing possible damage initiation near 400 N in the 0.094 J event while first major load drop does not occur until near 550 N in the > 0.3 J events. Note the 0.11 J and 0.22 J events do not evidence damage even though the lower energy 0.094 J event does. Pendulum data only.

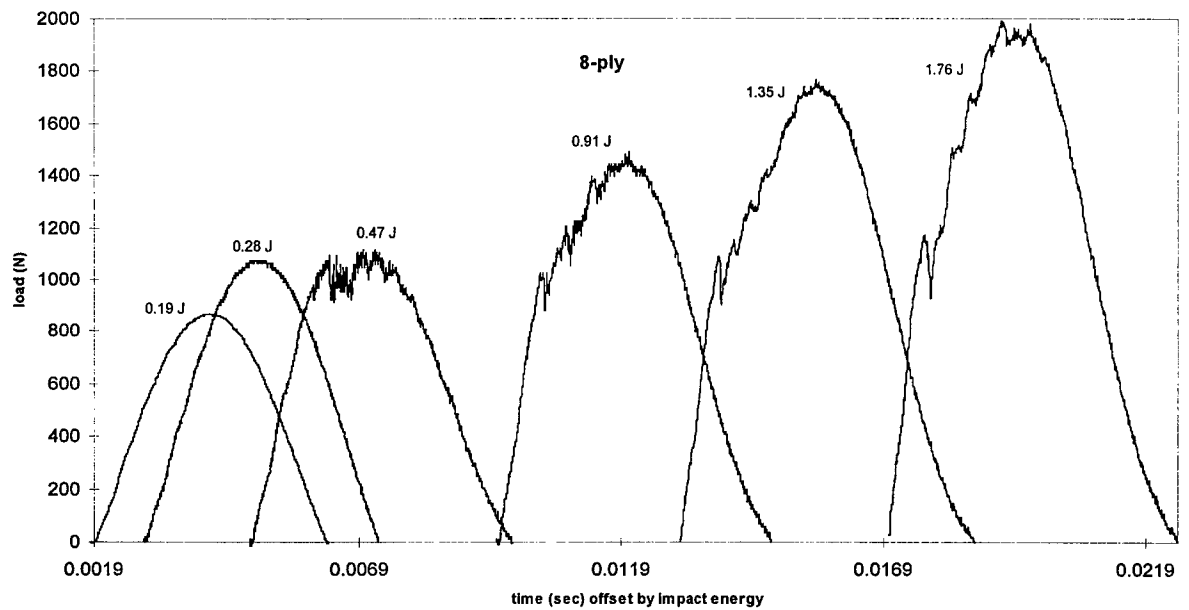


Figure 4-18 8-ply Force histories offset by impact energy showing possible damage initiation near 1000 N in the 0.47 J event while first major load drop does not occur until near 1100 N in the > 0.4 J events. Pendulum (<1 J) and drop weight (> 1 J) data.

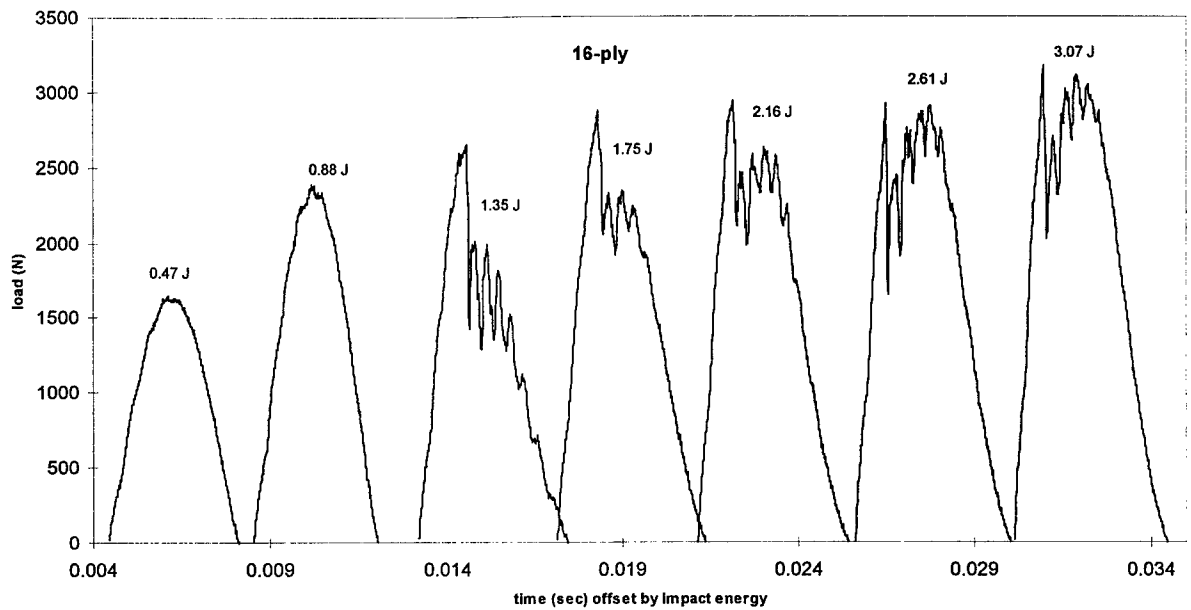


Figure 4-19 16-ply Force histories offset by impact energy showing damage initiation near 2700 N in the impact energy > 1.3 J events. Drop weight data.

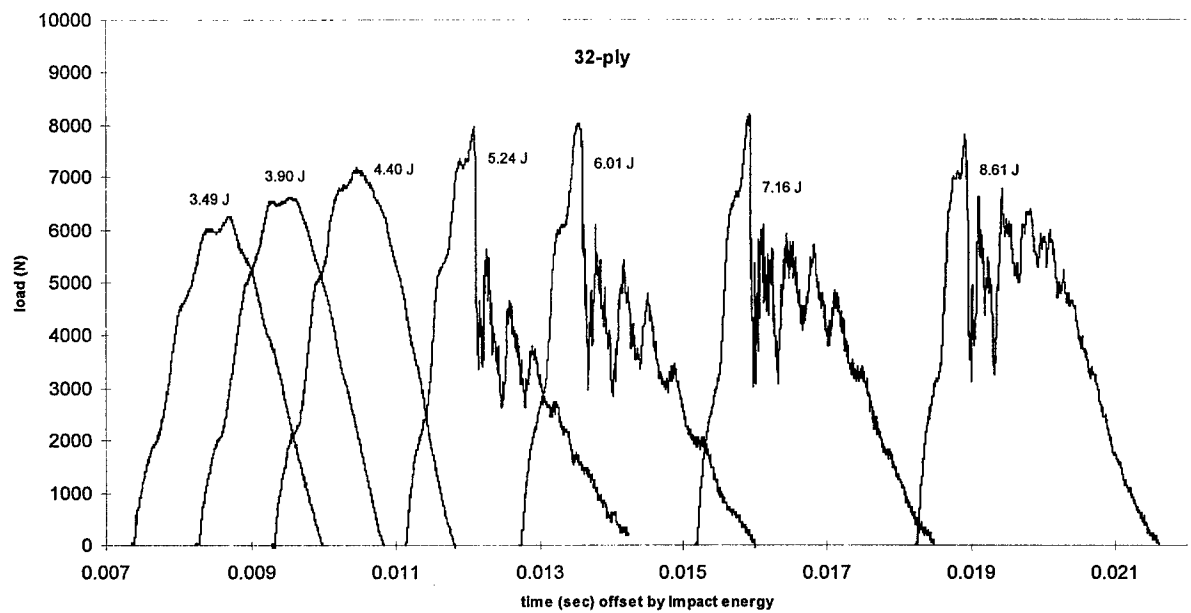


Figure 4-20 32-ply Force histories offset by impact energy showing damage initiation near 8000 N in the impact energy > 5.2 J events. Pendulum data.

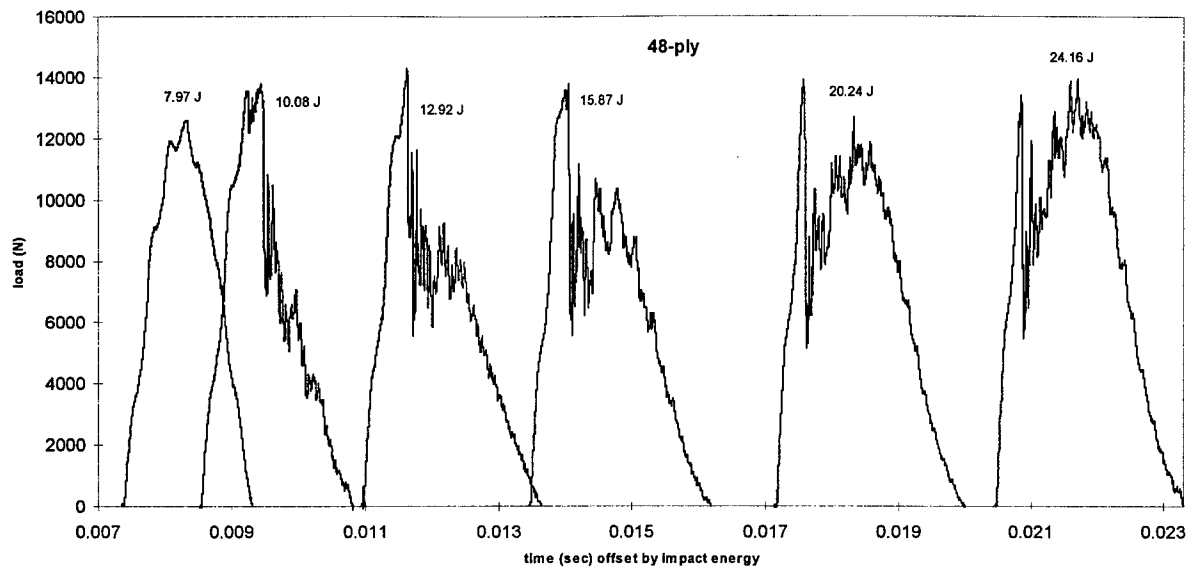


Figure 4-21 48-ply Force histories offset by impact energy showing damage initiation near 14000 N in the impact energy > 10.0 J events. Pendulum data.

Some general trends which can be seen in these data are:

1. At impact energies below the threshold impact energy, the loading and unloading is relatively smooth and not unlike a half sine wave with a superposed smaller-amplitude higher-frequency secondary sine wave.

The secondary sine wave feature is most clearly identifiable in the thicker specimens, but is present in all cases. The three degree of freedom model in Chapter 3 predicts such a feature. In that model, it is the dynamics of the plate with the “attached” tup mass that produces the secondary sine wave. A significant difference between the three-degree of freedom model and this result is that in the experiment the oscillations die away during the unloading while in the model they do not. An explanation of this is suggested by considering a few of the known weaknesses of the three degree of freedom model. The model includes no damping and employs a linear contact spring. Damping alone could explain the difference, but the fact that the oscillations do not appear to be strongly damped until after the peak load is reached indicates that something more is going on. In the model, the linear contact spring provides a force proportional to the relative motion of the plate mass to the tup tip mass. Linearity implies that if the plate moves away from the tup tip a fictitious tensile force will be

produced. This tensile force obviously can not exist in the experiment since the tup is free to lose contact with the plate. Though the tup may never actually lose contact with the plate in the experiment, the relative displacement of the plate and tup can fluctuate. Perhaps during the loading portion of the event the contact is firm (i.e. the relative displacement of the plate and tup is large and negative) because the plate mass is constrained to follow the tup displacement and the contact stiffness is large and constant (linear). During unloading, the contact is softer because the relative displacement of the plate and tup is smaller because the plate mass is no longer constrained to follow the tup displacement. This softer contact stiffness smoothes out the force history during unloading.

2. Increasing the facesheet thickness increases the prominence of the secondary sine wave.

This fact supports the conjecture that the secondary sine wave may be attributable to specimen-tup dynamics. The specimen mass, and therefore the maximum specimen kinetic energy increases with facesheet thickness. Thus the prominence of the dynamics is expected increase with facesheet thickness.

3. For any given facesheet thickness, as impact energy increases, eventually a point is reached where the load history is no longer smooth, instead, a major load drop occurs and is followed by multiple cycles of loading and partial unloading.

It is of interest to identify the damage or damages that give rise to the major load drop. The damage that is responsible is a major energy absorbing process. Clearly, the principal reason for this and all structural research is to influence decisions made in the design of structural members. Whether the design criteria drives toward increasing energy absorption (as in vehicle structures designed to protect the occupants during a crash) or decreasing energy absorption (damage resistance) the damage associated with the major load drop is of interest. Force history alone can not reveal the damage that produces this load drop, but the current work does eventually identify the damage associated with the major load drop.

4. For any given facesheet thickness, the load at which the major load drop occurs is independent of impact energy.

This is the fact often observed in the literature which motivates the idea that damage from low-velocity impact is controlled by the maximum load reached and not by the energy of the impact. From this, the assumption that quasi-static analyses and static indentation tests can be used to model and simulate impact tests was born. The range of validity of this assumption is of concern in this work and will be investigated by comparing load displacement curves and C-scans from statically and dynamically loaded specimens.

5. Increasing the facesheet thickness increases the load at which the major load drop occurs.

This idea is intuitive, a thick facesheet is more damage resistant than a thin one. If there is a design requirement that a certain impact event be sustainable without damage, that requirement apparently translates to a particular minimum facesheet thickness. This line of thinking, of course, assumes that no other means are available to increase damage resistance. It may prove better to change something else such as ply orientations, material properties, core design, or move to a textile facesheet, but these are beyond the scope of the current work.

6. Increasing the facesheet thickness increases the magnitude of the major load drop.

This idea agrees with the absorbed energy data which found that the thicker facesheet specimens absorbed a greater proportion of the impact energy when they did receive damage.

7. The average initial loading rate (slope of the load history at the beginning of the event) and final unloading rate (slope of the load history at the end of the event) are of the same magnitude for those events not showing a major load drop, while the final unloading rate drops off for those events showing a major load drop.

The major load drop has been attributed to damage. The damage can be considered a loss of stiffness. The reduction in the final unloading rate (without noticeable reduction unloading rate immediately after the damage) may indicate that the damage present induces a nonlinearity in the stiffness. The effect of the nonlinearity is to locally soften the structure for small displacements (or loads) but for large displacements (or loads) the global stiffness of the structure dominates and the structure stiffens. This effect will be considered more directly in the discussion of the load versus displacement curves.

8. The major load drop is followed by a response that appears to have a superposed secondary sine wave of nearly the same frequency as was seen before damage but with much greater amplitude.

The major load drop appears to the undamaged portion of the plate to be a negative step function in load. It is to be expected that such an abrupt change in load will excite a broad range of natural frequencies of the plate (or plate with a lumped mass, the tup). The most prominent of these frequencies is the same as that seen before damage, indicating that the global stiffness of the specimen has not changed significantly. This point argues for a localized damage.

4.7.3 *Global and local stiffness.*

A measure of the stiffness of a centrally loaded plate is the ratio of applied load to resulting center displacement. When the load is confined to a small portion of the plate surface, the stiffness will depend upon the vertical location at which center displacement is measured. This is due to the three-dimensional nature of the displacement in the vicinity of the applied load. Two different stiffnesses then can be defined. Away from the point of application of the load (global) and immediately under the load (local). For a sandwich construction in which the transverse core stiffness is significantly less than the transverse stiffness of the facesheets, the difference between global and local stiffness will be more significant than it is in a monolithic laminate.

A composite sandwich structure differs from a monolithic laminate in that the sandwich is composed of two distinct monolithic laminates (the facesheets) that are separated by a relatively flexible core. Before damage, the primary coupling between the transverse displacement of the top and bottom facesheets of a sandwich is provided by the transverse direct stiffness of the core which may be an order of magnitude smaller than that of the facesheets. When the core fails in compression, little or no transverse direct stiffness of the core remains in the damaged area to keep the facesheets from moving toward one another. Instead, the vertical load is resisted by bending of the top facesheet and is transferred to the undamaged core by shear.

Low-velocity impact often involves small contact areas (typically in the range of 1.0 to 4.0 mm for the current research). Small contact areas will lead to high transverse applied stresses. For example, a unit force distributed over a very small contact area will produce a high applied transverse direct stress whereas the same force applied over a much larger contact area will produce a much smaller applied transverse direct stress. This idea is expressed graphically for Hertzian contact in figure 4-22. Composite sandwich structures can be particularly susceptible to damage from high transverse stresses due to the fact that the transverse compressive strength of the core may be an order of magnitude less than that of the facesheets. Near the applied load then, one should expect the plate response, and particularly damage to be dominated by the applied stress. Saint-Venant's principle indicates that far from the applied load the effect of these high stresses will not be apparent. We can therefore conclude that for low-velocity impact two regions can be considered. A local region in the vicinity of the contact region dominated by the applied stress profile, and a global region away from it which responds to the applied force. Local stiffness is here

defined as the slope of the curve representing transverse force verses top surface displacement, where the top surface displacement is taken to be that at the center of the application of the force (i.e. the center of the specimen). This definition is flawed by the fact that displacement at the center of the plate actually has both local and global displacements superposed. The definition proves useful nevertheless. It is important to recognize that local stiffness will depend not only upon the properties of the specimen, but also on the radius of the impactor (since this affects the distribution of the load). For all of the current research the impactor radius was 12.7 mm (spherical). Impactor radius should not be confused with contact radius. For a given impactor radius the load is applied, the contact radius changes. In this way, the applied stress is a function of both the applied force and the plate response to that force since plate response dictates the contact radius. Local displacements are dependent on the applied stress (not just force) while global displacements depend only on the applied force (not the applied stress, i.e. they are independent of contact radius for a given applied force).

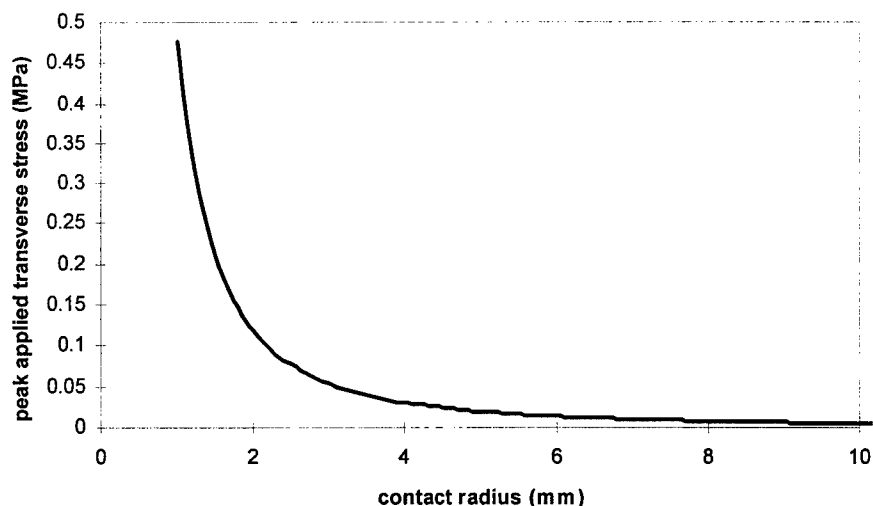


Figure 4-22 Peak transverse stress for unit (1 N) transverse force assuming Hertzian contact law.

The local response of a composite sandwich structure will be greatly affected by the presence of low-velocity impact induced damage. Damage in the forms of matrix cracking, delaminations, and core failure all serve to soften the response of the plate to transverse loading. Core damage will have a significant effect because it fundamentally changes the way the transverse load is transferred within the plate. Local stiffness will therefore be strongly influenced (reduced) by the presence of low-velocity impact induced damage while global stiffness is expected to be little affected. Unless a

significant portion of the facesheet lost membrane stiffness, global stiffness would not change drastically. Local stiffness is typically the only stiffness available from instrumented impactor tests because the calculated displacement (equation 4-3) is that of the tup (i.e. right under the load). In order to provide insight into the process of damage within a composite sandwich plate, some measure of global stiffness is desirable. A true measure of global stiffness must be made outside the region near the contact because the displacement used in the true global stiffness must be unaffected by the localized high stresses. In the current work, a less than true measure of global stiffness (the ratio of load to bottom surface displacement) was adopted which was able to show some of the global characteristics of the plate response.

In addition to the impact tests of figure 4-1, three specimens of each facesheet thickness were subjected to static indentation. Figure 4-23 shows a representative sample of the static indentation test data. In these tests displacement of both the top surface and the bottom surface of the plate at the point of application of the load were measured (section 4.4). The addition of the bottom surface displacement measurement provided a measure of the global plate stiffness as well as insight into the damage mechanisms which affected the response of the plate. For the purposes of the following discussion, global stiffness is defined as the slope of the load versus bottom surface displacement curve, where the bottom surface displacement is taken to be that at the center of the plate. Like the definition of local stiffness, this definition is flawed by the fact that the displacement of the bottom surface actually includes components of both the global plate bending and the local displacement. That is, the displacement of the bottom surface at the center of the plate is not sufficiently removed from the point of application of the load to be considered truly global. The influence of local effects on the "global stiffness" can be seen in figure 4-23. The leftmost loading/unloading curve in that figure shows the applied load versus bottom surface displacement. The slope of this curve is the "global stiffness" as defined here. The curve is concave up, indicating that for small loads the stiffness is lower than for large loads. This stiffening effect can be explained by considering the three-degree of freedom model of the impact (or in this case indentation, since the load was applied "statically") event as shown in figure 3-4. In that figure, static indentation as performed in the test represented in figure 4-23 consists of an applied x_2 displacement. The stiffness, k_{Eff} , resisting such a displacement by generating a response force is the combined stiffness of k_2 and k_3 , in which k_2 is the contact stiffness and k_3 is the plate bending stiffness. These combine as,

$$k_{\text{Eff}} = \frac{1}{\frac{1}{k_2} + \frac{1}{k_3}} \quad (4-10)$$

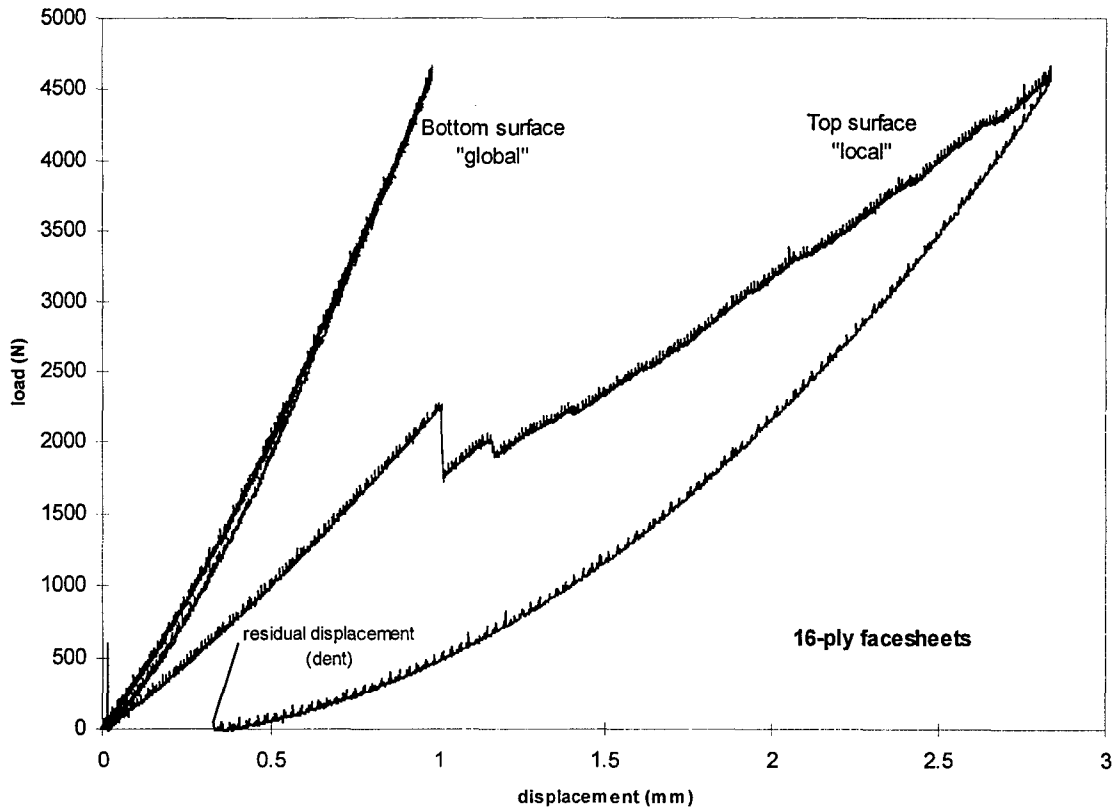


Figure 4-23 16-ply Static force verses displacement showing “global” and “local” response including the effects of damage.

Equation 4-10 provides the key to the explanation of the concave-up nature of both loading curves in figure 4-23. While bending stiffness k_3 is essentially constant, k_2 is highly nonlinear [214]. As the displacement increases, k_2 becomes large compared to k_3 so that k_{Eff} increases. In the limit of large k_2 , k_{Eff} is equal to k_3 . Thus, the initially soft plate stiffens as the contact develops, accounting for the concave-up nature of the loading curves. While this effect is expected in the local response, the fact that the “global” response shows this effect indicates that the bottom surface loading curve does not provide a true global stiffness, except, perhaps, in the limit of large displacements. One can view the bottom surface loading as follows. Initially, the bottom surface displaces both from a local “bulging” due to the high peak applied transverse stress associated with the initially small contact radius (figure 4-22) and from a global bending of the entire plate due to applied transverse force.

The bottom surface displacement is the sum of the global displacement and the local displacement characterized as “bulging” due to the high peak stress. As the displacement and applied force increase, the contact radius increases, reducing the peak stress. While the global displacement increases linearly with increasing applied force, the local displacement increases more slowly or may actually decrease.

To show the inverse relationship between applied force and peak stress, a small set of tests was conducted in which contact radius was measured by placing a piece of carbon paper and a piece of parchment (carbon toward the parchment) between the indenter and the specimen. The specimens were then loaded “statically” to a given load and then unloaded. The specimens used for these tests were the same material as the 16-ply specimens cut to half of the in-plane dimensions of those of the impact tests, so they were placed on a rigid support rather than in the 12.7 cm simple support fixture. The imprint of the carbon on the parchment provided a record of the contact footprint (hence contact radius) for the given load. Peak applied stress was then calculated for Hertzian contact by,

$$\text{peak stress} = \frac{3 \times \text{applied force}}{2\pi \times (\text{contact radius})^2} \quad (4-11)$$

Only one facesheet thickness was used, and the boundary conditions were different than the impact and static indentation tests, but the inverse relationship between applied force and peak stress can be seen in figure 4-24.

Before damage (the drop in load visible at 1 mm displacement in the top surface load curve of figure 4-23), both the top surface and the bottom surface displacement curves show a nonlinear displacement stiffening effect. While one might be tempted to interpret this as membrane stiffening, it is clearly not that. The displacements shown (less than 3 mm) are for a plate nearly 17 mm thick, so membrane effects are almost certainly negligible. The nonlinearity of the top surface stiffness is expected because the contact problem is nonlinear. As the load increases, the area of the top surface in contact with the indenter increases and the load is continuously redistributed over this growing area. The peak pressure under the indenter is thus decreasing with increasing load so that three-

dimensional effects become less important. The compliance of the initial contact problem is gradually depleted as the contact area develops.

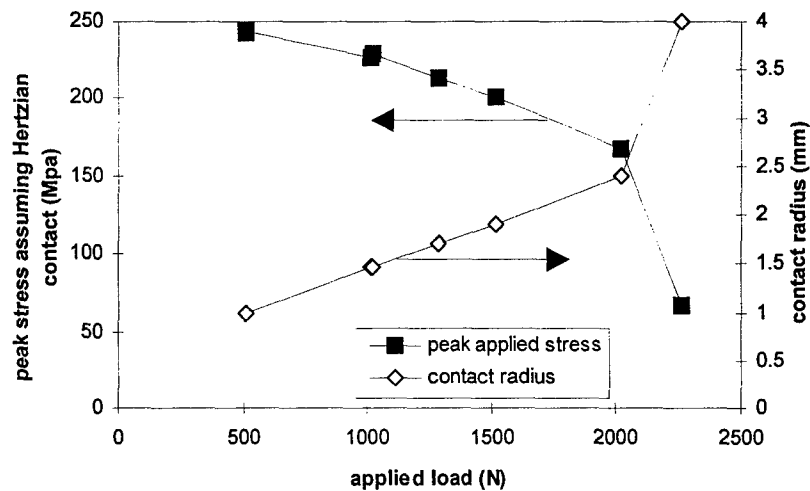


Figure 4-24 Contact radius and peak stress (assuming Hertzian contact) as a function of applied load on a 16-ply specimen showing an inverse relationship between applied force and peak stress.

Several other points should be made from figure 4-23. As expected, the global stiffness (the slope of the load versus bottom surface displacement curve) is greater than the local stiffness (the slope of the load versus top surface displacement curve). The major load drop seen at 1.0 mm top surface displacement is seen to be the result of a process that permanently changes the equilibrium curve of the top surface while the bottom surface “unloads” and subsequently reloads along the same equilibrium curve. In fact, the unloading and reloading data for bottom surface at the first major load drop (2200 N in figure 4-23) lie on top of each other and are indistinguishable from the undamaged (prior to the load drop) portion of the loading curve. This indicated that the effect of the damage, while locally significant, has little effect on the global stiffness of the structure. An analyst seeking to model this event with a global-local model might justify ignoring damage in the global model. This approach was taken for the analytical portion of the present research (Chapter 6).

The unloading portions of the load versus displacement curves in figure 4-23 tell a tale as well. The load versus bottom surface displacement curve shows loading and unloading to be nearly along the same path, while the load versus top surface displacement curve shows a very significant difference between the loading and unloading slopes. Indeed, were it not for the abrupt load drops, the top surface curve would resemble an elastic, work hardening equilibrium curve for a metal in

uniaxial tension. This analogy suggests that what is going on in the post-load-drop portion of the curve is not simply a new elastic equilibrium brought about by damage which took place suddenly (at the load drop) but is a near-continuous progression of damage under continuing displacement. Significantly, note that the final loading and initial unloading slopes are the same for the bottom surface while they differ greatly for the top surface. This suggests a "plastic" behavior which may be the progressive crushing of the core and/or the growth of delaminations and matrix cracks.

Finally, the residual displacement shown in figure 4-23 represents a very visible depression left in the top surface of the specimen after the load was removed.

4.7.4 Transverse strain

The average (through the thickness) transverse strain immediately under the indenter gives additional insight into the damage processes. Knowing the displacement of both surfaces δ_{Top} and δ_{Bottom} , as well as the original sandwich thickness, average transverse strain is defined as

$$\text{average transverse strain} = \frac{\delta_{Top} - \delta_{Bottom}}{\text{thickness}} \quad (4-12)$$

This quantity is plotted against top displacement for specimens of each facesheet thickness in figure 4-25.

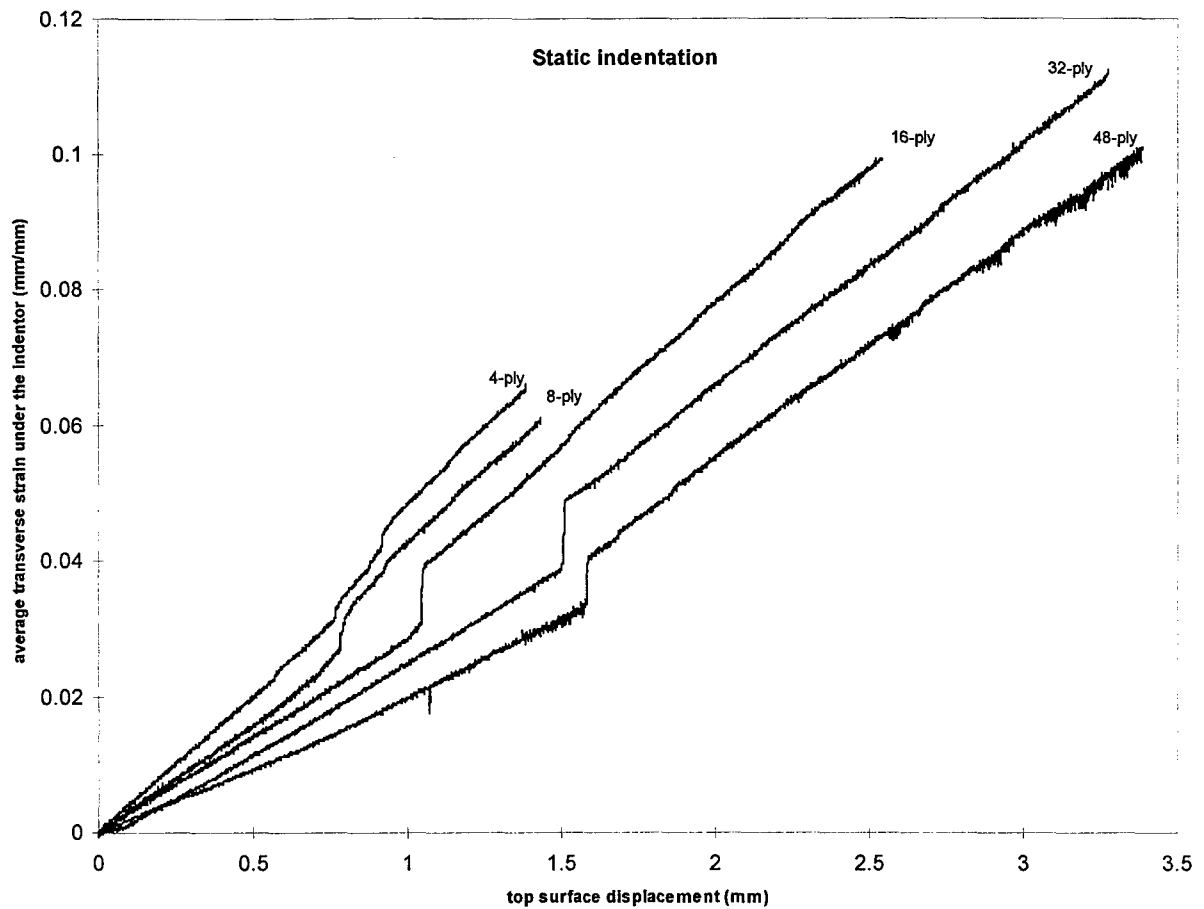


Figure 4-25 Transverse strain versus displacement for static indentation showing strain jumps presumed to be indicative of multiple cell core failure.

The value of the transverse strain measure outlined above is that it highlights the points in the loading sequence when the top surface and the bottom surface moved toward each other abruptly. That is, the top surface moved down slowly with the crosshead and the bottom surface followed except for certain times when it moved rapidly back up. In figure 4-23, this can be seen by recognizing that displacement control was used so that the load drop seen in the top surface data is not accompanied by a change in top surface displacement while the bottom surface curve shows unloading (back down the same equilibrium path) is accompanied by a reduction in displacement. That is, the top surface stays still while the bottom surface moves back up. These rapid movements of the bottom surface generally coincided with load drops. A drop in load for a given top surface displacement indicates strain energy release, or damage progression. The question is, what form or forms of damage are producing these load drops? Undamaged core between the facesheets resists

transverse strain. By Hooks law, an abrupt increase in transverse strain indicates either an abrupt increase in transverse stress or and abrupt decrease in transverse stiffness. Since the load, and hence the transverse stress, is dropping (or at least not increasing) these jumps in transverse strain must indicate a drop in transverse stiffness. Of the two possible contributors to this stiffness drop, facesheet and core, core has by far the greater potential for causing such a large strain jump. If the top facesheet failed by delamination or matrix cracking without core failure, the transverse facesheet strain jumps implied by the observed average transverse strain jumps are unreasonably high (e.g. ~8 percent for the 16 ply case). Therefore, the observed average transverse strain jumps are assumed to indicate abrupt core failure. If the core had no attached facesheets and were under compression from the indenter directly, only that portion in contact with the indenter would fail. The facesheet distributes the transverse stress over an area of core that is larger than the contact area through shear. The facesheet effectively spreads the transverse load out over the core. The thicker the facesheet, the greater the core area over which the transverse stress is spread. Thus sandwiches with thicker facesheets should be expected to take a higher load before the core fails. In addition, when they fail, a larger portion of the core should be expected to fail so that the strain energy released should be expected to be greater.

To check out these ideas, we make the switch now from static indentation data to low-velocity impact test data, in which absorbed energy was calculated from impact and rebound velocities. We assume for the moment that net absorbed energy at the end of the impact event is directly related to strain energy released by damage progression. Given this assumption, both of the intuitive ideas of the previous paragraph are supported by the impact data as shown in figure 4-26. In that figure, the peak load and absorbed energy for the lowest impact energy event showing a major load drop is plotted against the number of plies in the facesheets.

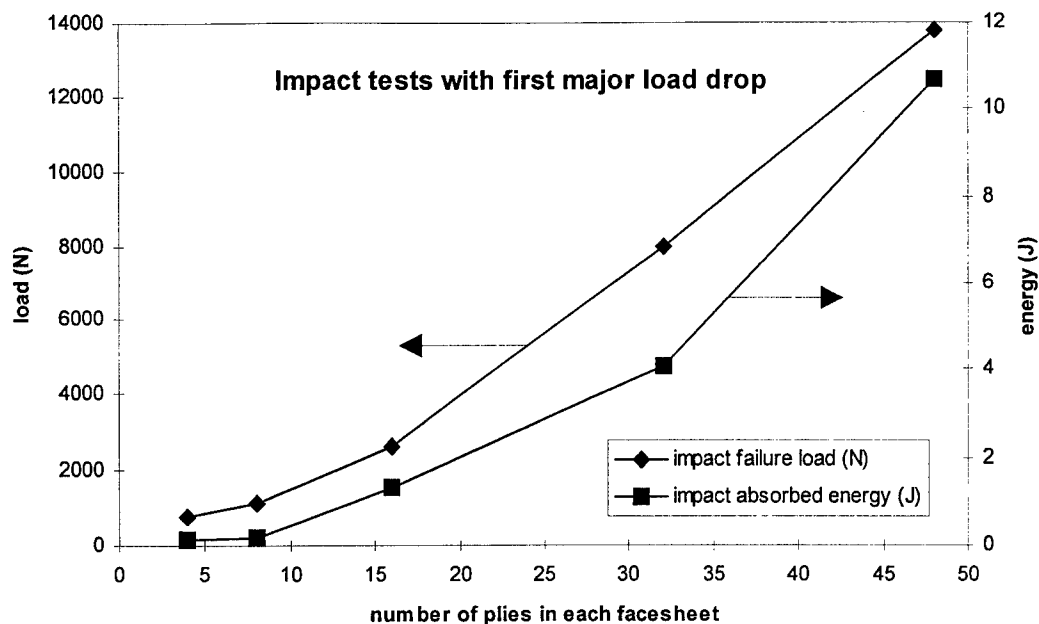


Figure 4-26 Load and absorbed energy associated with first major load drop. This shows that thicker facesheets take a greater load before the first major load drop and that they dissipate more energy in the damage associated with that load drop.

4.7.5 Dynamic and static compared.

A major question addressed by this research is the range of validity of the assumption that low-velocity impact to composite sandwich plates is a quasi-static process. This question bears directly on the applicability of the analytical portion of the research, which is a static finite element based code. Chapter 3 addressed the problem from an analytical point of view, but only for undamaged plates. In that chapter it was shown that certain characteristics of the loading history can be attributed to simple vibratory modes of the testing system. In this portion of the experimental effort, a first look at the importance of these dynamics on the processes of damage initiation and progression is available. Three metrics will be used to compare static and dynamic data, C-scan, load verses tup displacement curve, and absorbed energy.

4.7.5.1 C-scan. After impact or static indentation, all specimens were ultrasonically inspected for damage using the time-of-flight C-scan technique. The images thus produced show delamination patterns and can be used to qualitatively compare damages from different events. Figure 4-27 shows a direct comparison of C-scans for static and impact events. The events were chosen for that comparison based upon a similarity in the load histories. In particular, the impact

events were performed first and the lowest energy event that showed a major load drop was chosen. These events are the same as those of figure 4-26 and their load histories are identified as 0.34 J, 0.47 J, 1.35 J, 5.24 J, and 10.08 J respectively in figures 4-17 through 4-21. The static events were created specifically for this comparison based on a similar criteria, that is, the crosshead displacement was slowly increased until the first major drop in load was observed and then the crosshead displacement was slowly decreased. The comparison static and dynamic impact damages shown in figure 4-27 then, is not based on equivalent peak loads. The conventional wisdom that, "equivalent peak loads produce equivalent damage," was not validated by this research. This idea will be discussed when the load verses displacement curves are compared. The equivalence found in this research is based on load drops rather than peak loads, so the static and dynamic data associated with the first major load drop are compared in figure 4-27.

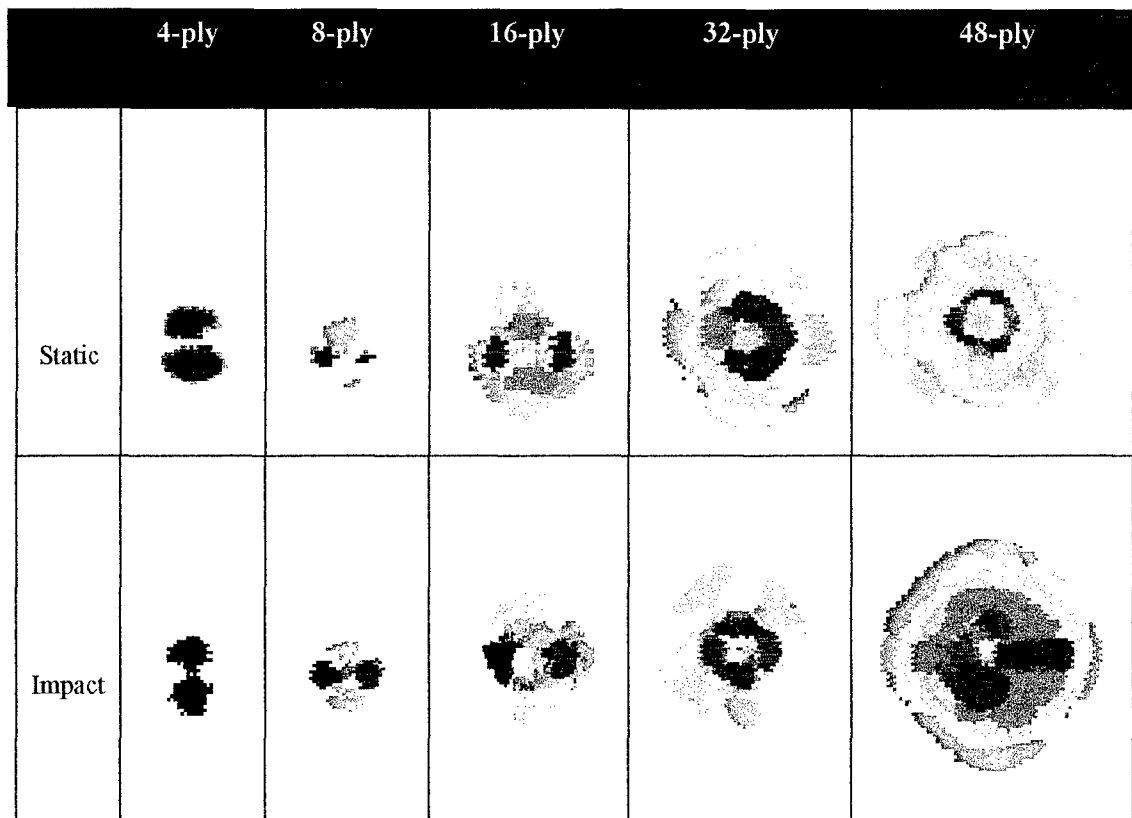


Figure 4-27 C-scans for static and dynamic events found to exhibit the first major load drop (magnified 150%).

The colors in the C-scans of figure 4-27 indicate the depths (distance from the top surface) of the delaminations present in the specimens after impact. The scales relating color to delamination

depth are different for each scan, so colors should not be compared between scans. The colors are shown to give the overall perspective that delaminations are occurring at different depths and that the delaminations become larger in the deeper interfaces. The colors also allow a better view of the in-plane shapes of the delaminations. The C-scans in figure 4-27 show some similarity between the damage associated with the first major load drop in a static test and the damage associated with the first major load drop in a dynamic test. This similarity can be seen in figure 4-27 by comparing the overall sizes and shapes of the delaminations. The similarity is present for all facesheet thicknesses tested. In particular, the overall size of the deepest and shallowest delaminations, the number of interfaces (different colors) found to have delaminations, and the general shape of the delamination pattern all compare well between static and dynamic data.

If a comparison were made of C-scans of statically and dynamically loaded plates with similar peak loads, a very different story would be obtained. The essence of the difference is that the dynamically loaded plates reached a higher peak load before failure. Thus, dynamic events reaching the same peak loads as the static events of figure 4-27, show no delaminations in the C-scans. Alternatively, however, static events reaching the same peak loads as the dynamic events of figure 4-27, show delaminations similar to those of figure 4-27. Peak load, then, is not an appropriate equivalence between the static indentation and dynamic impact events for composite sandwich plates since two specimens loaded to the same peak load (one impact, the other static) may or may not show similar damages. This indicates that quasi-static analysis and testing in which peak load is compared with the peak load from a dynamic event, may indicate failure at a lower peak load than an actual impact event would find.

Comparison of the C-scans in figure 4-27 might lead one to conclude that there are both similarities and differences between the static and dynamic delamination fields. A word of caution is appropriate here. At best, the general shapes (hour glass and crossed hour glasses) and gross size of the delamination patterns of the 4- and 8-ply data are repeatable. There is also a good deal of randomness in the patterns observed. This randomness can be seen in figure 4-27 when one considers the fact that all loads, material properties, and boundary conditions possessed bilateral symmetry while the delamination patterns deviate from this symmetry somewhat. Less can be said for the thicker facesheet specimens. For the thicker facesheet specimens, the gross size may be repeatable and the general feature of delaminations becoming wider as the depth increases is

characteristic of all of the data, but to try to compare color by color and shape by shape is asking too much of these data. The purpose of figure 4-27 is to show overall similarity of delamination patterns and sizes for static indentation and dynamic impact loaded composite sandwich plates. Meaningful comparisons stop there.

4.7.1.1 Load-displacement curves. In C-scans, a time integrated result of the damage processes is in view. No information about the equilibrium states leading to damage or the effect of the damage on those states is available from C-scans. Thus, C-scans can give a perspective of what happened but can tell very little about how it happened. In contrast to this, a load verses displacement curve is essentially a record of the equilibrium states before, during, and after damage. No information about the physical effect of the damage processes is available from a load verses displacement curve. In an attempt to make a definitive statement about quasi-static assumptions in low-velocity impact to composite sandwich plates, load verses displacement curves provide a direct comparison of equilibrium states between the static and dynamic processes.

Figures 4-28 through 4-32 show load verses displacement curves under static loading as well as several impact loadings with and without damage. By these figures the reader is intended to observe both the similarities and differences between static indentation and dynamic impact for the several facesheet thicknesses tested. The load histories for the impact events in figures 4-28 through 4-32 were previously given in figures 4-17 through 4-21. In all but the 4-ply case (figure 4-28), the static displacement was increased until the first major load drop, then it was decreased. For the 4-ply case, the first "major" load drop was a more subjective judgment (load drops occurred at 270 N, 330 N and 530 N as well as the easily seen drop at 690 N) so data for the full range of static displacement is shown in figure 4-28.

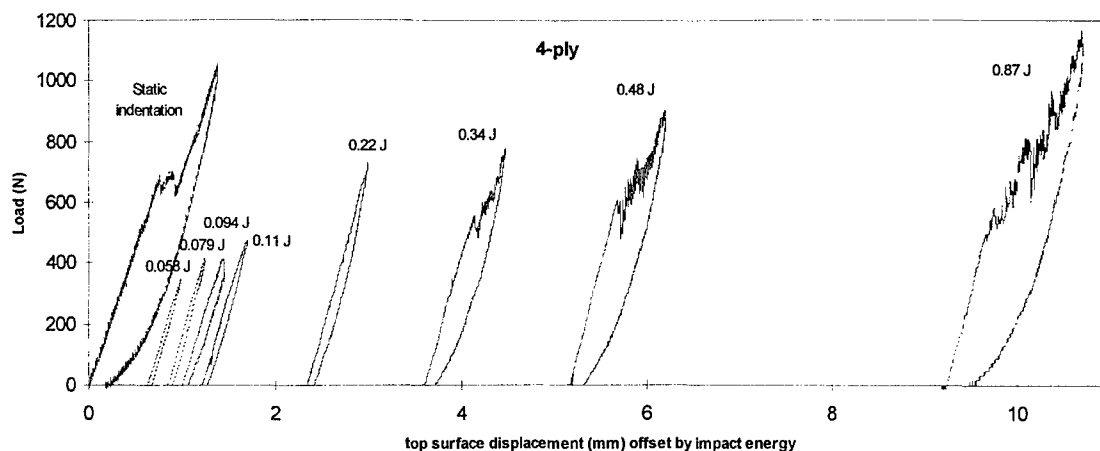


Figure 4-28 4-ply Static and dynamic force verses displacement showing the effects of damage.

The first major load drop was difficult to distinguish in the 4-ply impact data. Damage is apparent in the 0.34 J event and in the 0.094 J event (see figure 4-17) but not in the 0.11 J and 0.22 J events. It is thought that for this very thin facesheet the contact pressure is transferred almost directly to the core. That is, the facesheets have very little bending stiffness and hence do a poor job of spreading out the contact stress. As a result, a very small area of the core sees all of the transverse load. This small portion of the core may be a single cell or just part of a cell. The loaded portion of the core begins to fail very early but since it is so small the strain energy released by the failure is also small. Thus the almost imperceptible load drop at 325 N in the static case may in fact be the first core failure. Another drop at 510 N in the static case is more readily discerned and may represent the failure of adjoining cell walls. The next few drops near 700 N in the static case are easy to see and are more like those seen on the thicker facesheet specimens, perhaps indicating that the contact is fully established and core failure and facesheet delamination are happening en mass. If this explanation is correct, then turning to the dynamic data, the anomaly of damage in the 0.34 J event and in the 0.094 J event but not in the 0.11 J and 0.22 J events could be simply the result of minor differences of the impact point with respect to the honeycomb cells. Suppose the 0.094 J event had the impact point directly over a cell wall while the 0.11 J and 0.22 J events had the impact point near the center of a cell. In this case, the 0.094 J case might be expected to fail at a lower load because a fewer cell walls were available to react the load. For impact energies above 0.3 J, the 4-ply data are consistent in showing a first major load drop near 600 N.

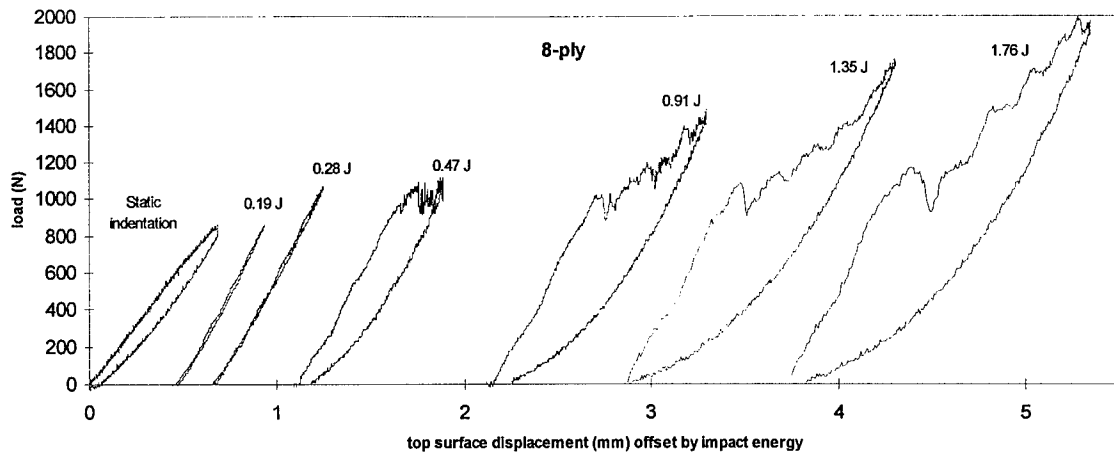


Figure 4-29 8-ply Static and dynamic force verses displacement showing the effects of damage.

The 8-ply data in figure 4-29 show loading and unloading for the 0.19 J and 0.28 J events to be almost perfectly following the same path. This fact is thought to indicate that no damage is taking place and that the energy absorbed by the dynamics of the system is small. Interestingly, the 0.28 J event reaches a load which is equal to the load for the first major load drop in the higher energy events and is more than 15 percent greater than that which caused the first major load drop in the static indentation data. In figure 4-29 it can be seen that the static test shows the first major load drop near 830 N while the impact tests show it near 1100 N. The tendency for the static loading to bring about the first major load drop at a lower applied load than the dynamic loading was consistent among all facesheets tested. The slopes of the curves here represent the local stiffness of the plate. In the dynamic tests, the applied force can be thought of as having two components. The first is the product of the static stiffness and the displacement, and the second is the product of the plate effective mass and acceleration (Newton's second law). For the purposes of the following discussion, the second term will be referred to as the "inertial stiffening force." In the 8-ply data the inertial stiffening effect is more pronounced than in the 4-ply data as can be seen by the "waviness" of the slope in the impact curves before the first load drop. This is believed to be an effect brought about by the increased inertia related to the larger mass of the thicker specimens.

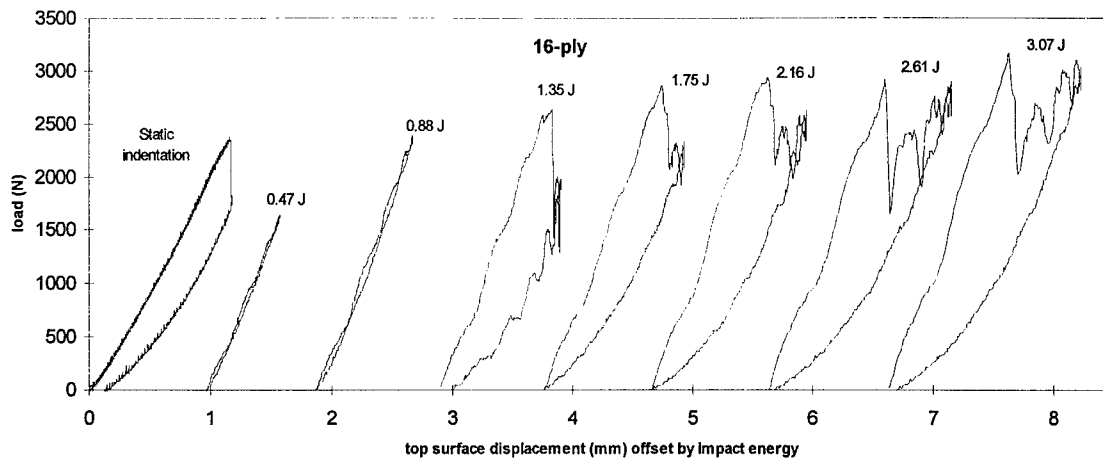


Figure 4-30 16-ply Static and dynamic force verses displacement showing the effects of damage.

Similar to the 8-ply data, the 16-ply data in figure 4-30 show loading and unloading for the 0.47 J and 0.88 J events to be nearly following the same path. Much more dramatic than the 8-ply data, however, is the magnitude of the first major load drop. Since the magnitude of the load drop reflects the strain energy released, these data indicate that much more energy is absorbed by the damage causing first failure in the 16-ply specimens than in the 8- and 4-ply specimens. In these data it can be seen that the static test shows the first major load drop near 2300 N while the impact tests show it near 2800 N. Also, the magnitude of the load drop is roughly 600 N for the static test while it ranges from 800 N to 1100 N for the impact tests. In the 16-ply data the inertial stiffening effect is even more pronounced than in the 8-ply data as can be seen by the greater initial slope of the load verses displacement curve for the impact events. This is believed to be an effect brought about by the increased mass of the specimen.

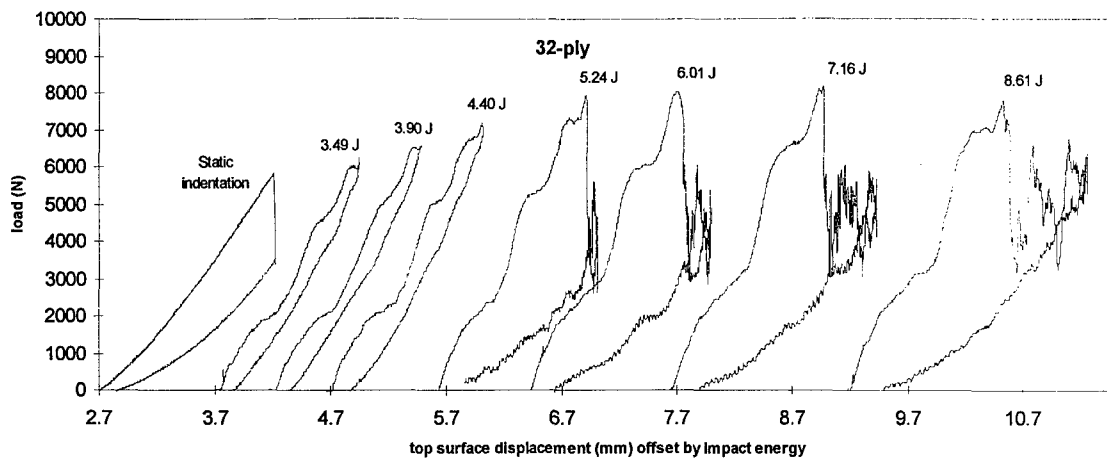


Figure 4-31 32-ply Static and dynamic force verses displacement showing the effects of damage.

Unlike the 8- and 16-ply data, the 32-ply data in figure 4-31 show loading and unloading for events not exhibiting a major load drop (3.49 J, 3.90 J and 4.40 J) do not follow the same path. There are evidently more energy losses in these tests than in the thinner facesheet tests. The dramatic load drop of the 16-ply data continues in the thicker 32-ply data. The static test shows the first major load drop near 5800 N while the impact tests show it near 8000 N. Also, the magnitude of the load drop is roughly a factor of 2.0 lower for the static test than it was for the impact tests. The inertial stiffening effect continues to become yet more pronounced than in the thinner facesheets.

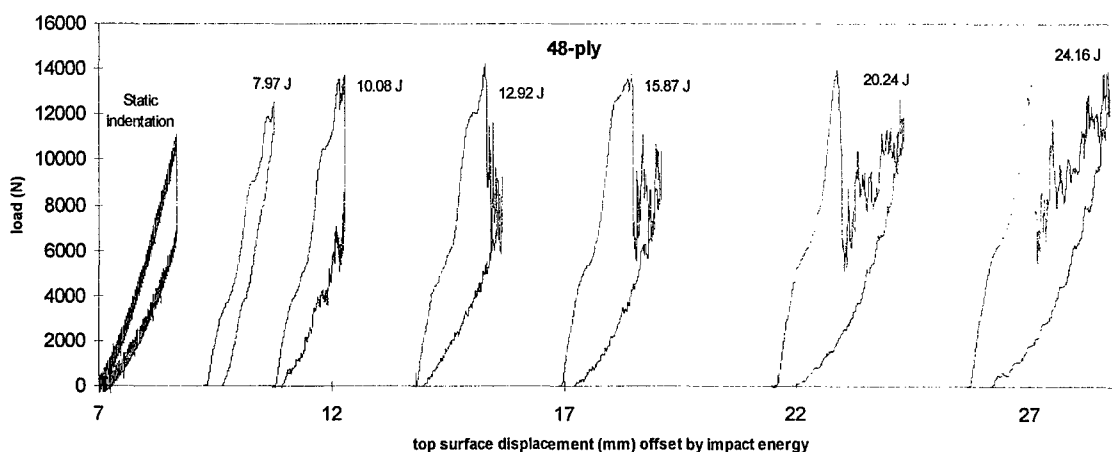


Figure 4-32 48-ply Static and dynamic force verses displacement showing the effects of damage.

All the trends observed in the 32-ply data continue in the 48-ply data. The static test shows the first major load drop near 10500 N while the impact tests show it greater than 13000 N. The magnitude of the load drop is roughly a factor of 1.5 lower for the static test than it is for the impact tests.

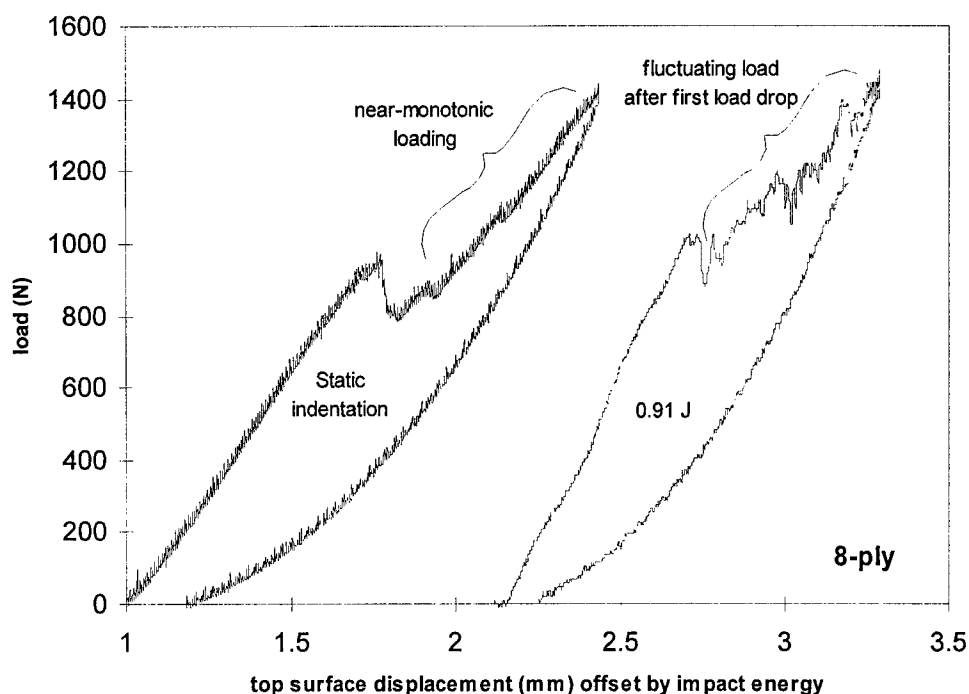


Figure 4-33 8-ply Static and dynamic force verses displacement showing the dynamic equilibrium effects of damage progression.

Figures 4-33 and 4-34 are included to show that after the initial load drop the static and dynamic events behave quite differently. The large load fluctuations present in the dynamic case and absent from the static case can be seen in the load histories (figures 4-18 and 4-19). The load histories show that the fluctuations are not pure noise, they have identifiable frequency components. The lowest of these frequencies is presumed to be associated with the first vibratory mode of the plate-lumped mass system. The effect these force oscillations have on the damage progression is unknown. The load drops can be thought of as an inverse step function. Such a function would excite the vibratory modes of the system. The load fluctuations following the first major load drop are thought to be the dynamic response of the specimen to the inverse step function loading that is produced by the dramatic load drop. Since dynamics are eliminated from the static case, the fluctuations are not present in the static loading curves. The smaller load drops and constant-load

motions visible in the static data are believed to be indications of core damage progression. Core failure is present in the dynamic tests as well, but it is mixed in with the dynamic fluctuations.

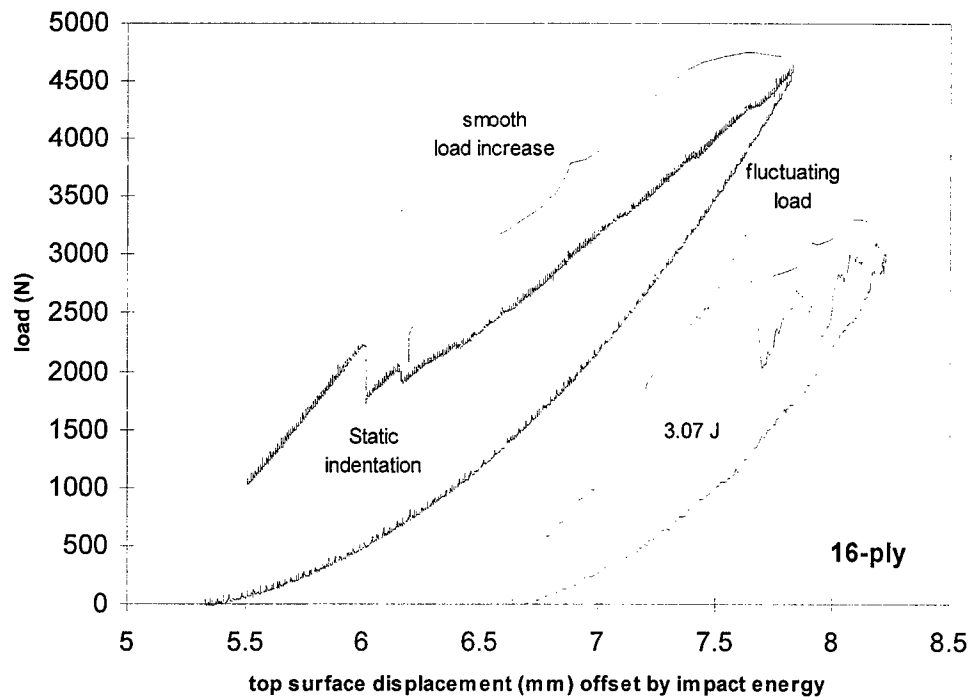


Figure 4-34 16-ply Static and dynamic force verses displacement showing the dynamic equilibrium effects of damage progression.

A general statement about the influence of facesheet thickness on the dynamics of the impact event can now be made. The load verses displacement curves of the static and dynamic tests compare better for thin facesheets than for thick ones. Thus, increasing the facesheet thickness makes the dynamics of impact more important. This is expected because the additional mass of the thicker facesheets increases the inertia of the specimens.

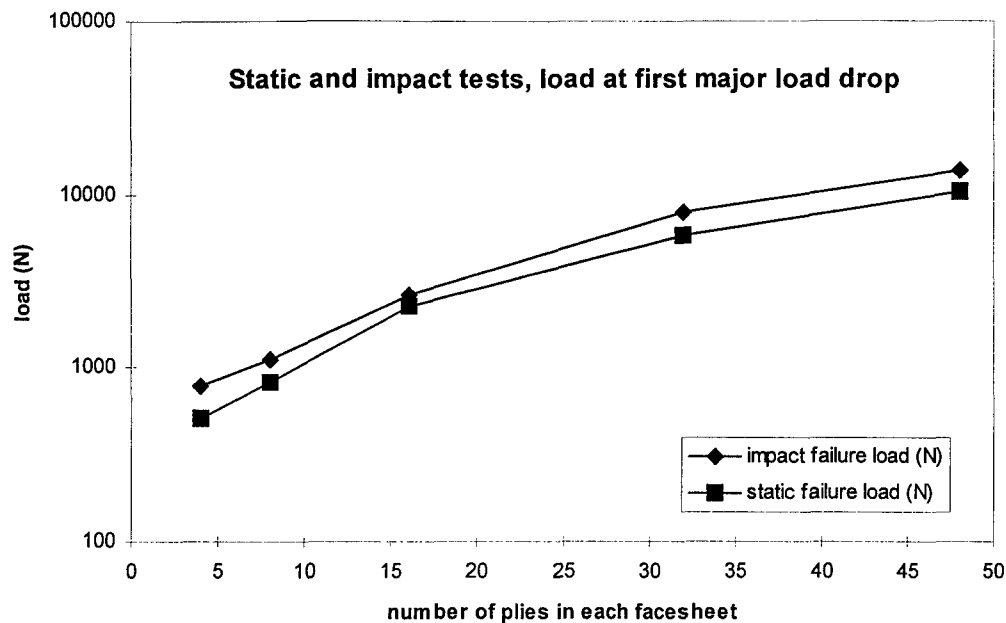


Figure 4-35 Comparison of load at the first major load drop for static and dynamic tests showing that specimens fail at lower load under static than dynamic tests.

Figure 4-35 summarizes the failure load information from figures 4-28 through 4-32. Note that the load is given with a logarithmic scale so that the magnitude of the difference between the static and dynamic failure loads is much greater for the thick facesheets. The tendency for the static tests to show the first major load drop at a lower load than the impact tests indicates that static tests and analyses are likely to be conservative if used to predict the effects of low-velocity impact. This conservatism becomes more pronounced for the thicker facesheet sandwiches.

4.7.1.2 Absorbed energy. Absorbed energy relates directly to strain energy release and is therefore a measure of damage. The area enclosed by the load versus displacement curve (figures 4-28 through 4-32) during loading and unloading is taken to represent the energy absorbed during the event. Integrating the load versus displacement data for both the loading and unloading portions of the test using a simple trapezoidal rule produces the energy which is not returned to the tup during the event. This energy is taken to be the energy absorbed by the specimen. Figure 4-36 shows that the energy absorbed by a composite sandwich plate subjected to static indentation until first major load drop is below that of a specimen loaded dynamically to the same criteria (first major load drop). This again highlights the conservatism of the quasi-static assumption since the absorbed energy is in some sense a measure of the damage. Beyond this, in the opinion of the

author, figure 4-36 indicates the range of validity of the quasi-static assumption may be limited to the thin facesheet regime.

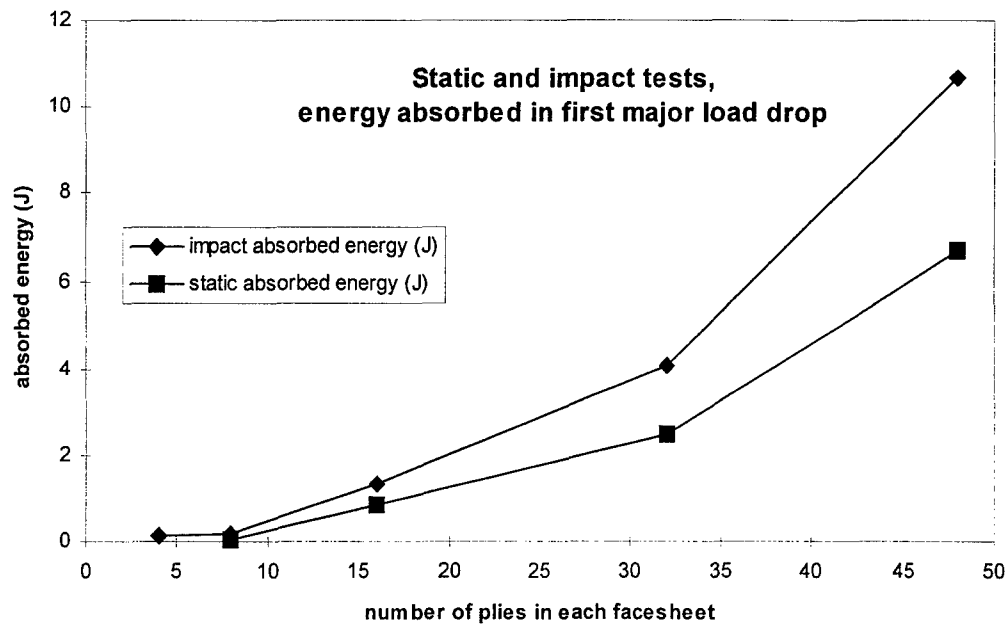


Figure 4-36 Comparison of energy absorbed in the first major load drop for static and dynamic tests showing that specimens absorb less energy with static than dynamic tests.

4.8 Conclusions

4.8.1 *Corrected absorbed energy seems to indicate damage.* Figures 4-6 through 4-10 demonstrate a jump in absorbed energy at the impact energy that initiates damage. It is possible to determine if there is failure within a composite sandwich plate subjected to low-velocity impact by an instrumented impactor without relying on post-impact inspection of the specimen.

4.8.2 *Thick and damaged sandwiches are not quasi-static.* The assumption that low-velocity impact damage within a composite sandwich plate is independent of the loading rate does not appear to be valid in these cases. The static and dynamic events differ significantly in the load at which the first major load drop occurs and the energy that is absorbed in the damage process associated with the first major load drop.

4.8.3 *Important damage information may be obtained from force history.* For the range of parameters in this study, the first major load drop observed in the load history is associated with core failure.

4.8.4 *3-dimensional effects are localized.* The global stiffness of the plate is independent of the damage produced by low-velocity impact. In a global-local model of the event, contact is a local effect which can be removed from the global model.

5. *Elasticity Solution*

Low-velocity impact to composite sandwich plates is a three-dimensional problem. The current work is based upon two-dimensional plane stress finite elements. The basic assumption (plane stress) is that transverse direct stress is zero, but this is violated by the applied load on the top surface. In addition, plane stress theory is applicable when the plate is thin, but composite sandwich structures may not satisfy this criteria either. Three-dimensional equilibrium post-processing partially alleviates this inconsistency, but since failure criteria will be stress based, good three-dimensional stress results are required. To check the stresses, comparison to an exact theoretical solution is invaluable. In what can be called a classical series of papers on the application of elasticity theory to the analysis of composite laminates, Pagano wrote two papers in 1969 which have become de facto standards for benchmarking approximate solutions. In the first [236] he presented a solution for elastic cylindrical bending of bi-directional (cross-ply) laminates and in the second [237] he extended this solution to rectangular bi-directional composites laminates and sandwich plates.

The analytical portion of the current work involves a highly iterative, geometrically and materially nonlinear system for which the experimental work provides a final benchmark. Before proceeding with all of complications from these nonlinearities, linear elastic benchmarks for the finite element portion of the analysis (with three-dimensional equilibrium post-processing) were developed from Pagano's elasticity solutions. The loading in [236] is a half sine wave in the span direction while that of [237] is sinusoidal in both in-plane directions. This loading was found to be quite benign from a three-dimensional point of view when compared to a Hertzian contact load representing an impactor. An algorithm which can accurately reproduce the stresses of an exact solution for a simple sinusoidal load may still fall far short when a Hertzian contact load is applied. Therefore, the elasticity solutions of [236] and [237] were extended to Hertzian contact loading by the principle of superposition and a Fourier sine series approximation for the load. In this way, a more representative benchmark for models of impact loaded plates is provided. Mathcad templates for the solutions presented in [236] and [237] are given in Appendix A and FORTRAN programs which extend these solutions to generalized Fourier series loading and generate the Fourier coefficients for a Hertzian contact loading are given in Appendix B.

5.1 Objectives

The objective of this portion of the current work was to provide an elasticity theory solution for a simply supported, rectangular, bi-directional, composite sandwich plate loaded by a Hertzian contact stress. This solution was then available to meet several objectives of the current work as a whole.

5.1.1 Analytical solution for undamaged plate.

Chapter 4 showed that as long as the load applied to a composite sandwich is below some critical value (which may be different for static and dynamic loading), damage does not initiate and the deflections are small. In such a case, a linear elastic solution may accurately model the structure. Insights gained from this solution play an important role in understanding the errors introduced by some of the approximations needed to solve the more complicated case after damage. These approximations include assumed kinematic relationships, laminated plate theory, interpolation functions, and load distribution.

5.1.2 Failure criteria checkout.

The issue of appropriate criteria for damage initiation and progression in impact loaded composite sandwich plates is by no means resolved. Many failure theories have been used with varying degrees of success. The exact solution provided by the current work coupled with the experimental data of Chapter 4 provides a near-ideal environment for comparing the various failure theories as they apply to the problem of interest. The majority of these failure theories are based on stress. The elasticity solution can potentially provide exact three-dimensional stresses (within the assumptions of elasticity) at the value of load at which the experimental program indicates failure initiates. These stresses produce failure indices (normalized to unity at failure) by application of the various failure criteria. The failure criteria can then be judged by how close they come to producing unit indices for the stress field which elasticity theory says existed just prior to the empirically observed failure.

5.1.3 Benchmark for FEA.

In addition to the role of guiding the interpretation of the computational results, the elasticity solution provides a benchmark for the computational algorithm in a regime close to, but not in, the realm of interest (where exact solution is not currently available). Just as would-be-successful

armies must “train like they intend to fight” so also would-be-successful algorithms must be benchmarked on problems as near to the intended application as possible. The only extrapolations from the elasticity benchmark for this effort (where the quality of the solution is known in detail) to the application of the algorithm (where the quality of the solution is known only to the detail available from empirical measures) are: 1) the contact algorithm including the assumed load profile; and 2) the damage algorithm.

5.2 *Cylindrical Bending Solution*

A first step toward understanding the response of composite sandwich plates to impact loads can be made by solving a simpler problem having many similar features to the problem of interest. It has been pointed out that the impact problem is three-dimensional whereas the proposed finite element based solution is essentially two-dimensional (plane stress) with the transverse effects brought in via equilibrium. Transverse stresses from the finite element solution then, are expected to be less accurate than in-plane stresses. Considering a slice through the thickness at the center of impact, a two-dimensional cylindrical bending analysis of that slice may reveal some of the important transverse effects. An elasticity solution that includes transverse stresses was found in the literature and applied here. Pagano [236] presented an elasticity solution for bidirectional (0° - 90°) layered composite laminates in cylindrical bending. The solution as applied in this research is briefly described here, and an example of how it was used is provided in Appendix A.

In figure 5-1, a laminate composed of m orthotropic layers such that the axes of material symmetry are aligned with the plate axes x , y , z is considered. The body is in a state of plane strain with respect to the xz plane and is simply supported on the ends $x = 0$ and $x = L$. A normal traction $q(x)$ is applied to the upper surface $z = h/2$.

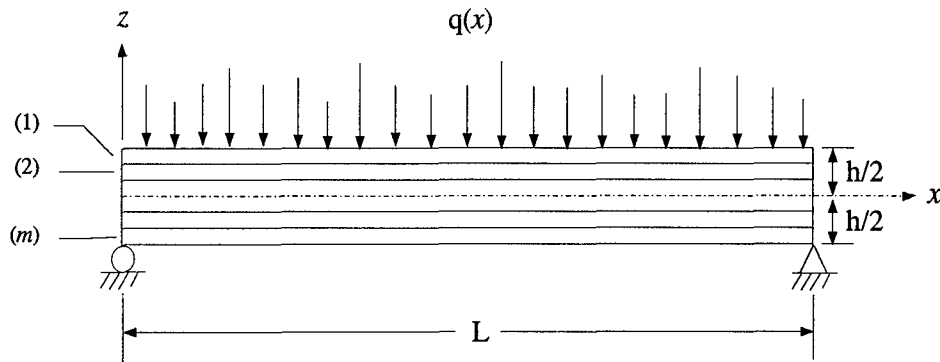


Figure 5-1 Cylindrical bending plate notation.

For each layer, the orthotropic constitutive relations for plane strain are given by [236 reference 4]

$$\begin{aligned}\varepsilon_x &= R_{11}\sigma_x + R_{13}\sigma_z \\ \varepsilon_z &= R_{13}\sigma_x + R_{33}\sigma_z \\ \gamma_{xz} &= R_{55}\tau_{xz}\end{aligned}\quad (5-1)$$

$$R_{ij} = S_{ij} - \frac{S_{i3}S_{j3}}{S_{33}} \quad (i, j = 1, 3, 5)$$

In which the R_{ij} are the reduced compliance coefficients for plane strain, and the S_{ij} are the compliances with respect to the axes of material symmetry. The equations of equilibrium for plane strain in the xz plane are

$$\begin{aligned}\sigma_{x,x} + \tau_{xz,z} &= 0 \\ \sigma_{z,z} + \tau_{xz,x} &= 0\end{aligned}\quad (5-2)$$

and the linear strain-displacement relations are

$$\varepsilon_x = u_{,x} \quad \varepsilon_z = w_{,z} \quad \gamma_{xz} = u_{,z} + w_{,x} \quad (5-3)$$

These complete the governing equations for the problem, and it should be observed that all stress, strain, and displacement components are independent of the y coordinate. The stress boundary conditions on the upper and lower surfaces are given by

$$\begin{aligned}
\sigma_z\left(x, \frac{h}{2}\right) &= -q(x) \\
\sigma_z\left(x, -\frac{h}{2}\right) &= \tau_{xz}\left(x, \pm \frac{h}{2}\right) = 0
\end{aligned}
\tag{5-4}$$

and the simple support conditions are

$$\begin{aligned}
\sigma_x(0, z) &= \sigma_x(L, z) = 0 \\
w(0, z) &= w(L, z) = 0
\end{aligned}
\tag{5-5}$$

Next, we introduce the index i to identify the lamina such that the top lamina corresponds to $i=1$, and define construct a local coordinate system x_i, z_i on the center of the i^{th} lamina at the end $x = 0$. Further, define h_i to be the thickness of the i^{th} lamina. Stress and displacement continuity between lamina can be expressed as

$$\begin{aligned}
\sigma_z^{(i)}\left(x, \frac{-h_i}{2}\right) &= \sigma_z^{(i+1)}\left(x, \frac{h_{i+1}}{2}\right) \\
\tau_{xz}^{(i)}\left(x, \frac{-h_i}{2}\right) &= \tau_{xz}^{(i+1)}\left(x, \frac{-h_{i+1}}{2}\right) \\
u^{(i)}\left(x, \frac{-h_i}{2}\right) &= u^{(i+1)}\left(x, \frac{-h_{i+1}}{2}\right) \\
w^{(i)}\left(x, \frac{-h_i}{2}\right) &= w^{(i+1)}\left(x, \frac{-h_{i+1}}{2}\right)
\end{aligned}
\tag{5-6}$$

$(i = 1, 2, \dots, m-1)$

Taking now a particular form for $q(x)$, namely

$$\begin{aligned}
q(x) &= q_0 \sin(px) \\
q_0 &= \text{constant} \\
p &= \frac{\pi}{L}
\end{aligned}
\tag{5-7}$$

Pagano [236] shows that the solution of the boundary value problem described by equations 5-1 through 5-7 can be found by putting

$$\begin{aligned}
\sigma_x^{(i)} &= f_i'(z) \sin(px) \\
\sigma_z^{(i)} &= -p^2 f_i(z) \sin(px) \\
\tau_{xz}^{(i)} &= -p f_i'(z) \cos(px)
\end{aligned}
\tag{5-8}$$

in which the functions $f_i(z)$ are expressed by

$$\begin{aligned}
 f_i(z) &= \sum_{j=1}^4 A_{ji} e^{m_{ji} z_i} & (i = 1, 2, \dots, m) \\
 A_{ji} &\text{ are constants} \\
 m_{ji} &= -(-1)^j p \sqrt{\frac{a_i - (-1)^j b_i}{c_i}} \\
 a_i &= R_{55}^{(i)} + 2R_{13}^{(i)} \\
 b_i &= \sqrt{a_i^2 - 4R_{11}^{(i)} R_{33}^{(i)}} \\
 c_i &= 2R_{11}^{(i)}
 \end{aligned} \tag{5-9}$$

The stresses then can be expressed as

$$\begin{aligned}
 \sigma_x^{(i)} &= \sin(px) \sum_{j=1}^4 A_{ji} m_{ji}^2 e^{m_{ji} z_i} \\
 \sigma_z^{(i)} &= -p^2 \sin(px) \sum_{j=1}^4 A_{ji} e^{m_{ji} z_i} \\
 \tau_{xz}^{(i)} &= -p \cos(px) \sum_{j=1}^4 A_{ji} m_{ji} e^{m_{ji} z_i}
 \end{aligned} \tag{5-10}$$

and the displacements can then be expressed as

$$\begin{aligned}
 u_i &= \frac{\cos(px)}{p} \sum_{j=1}^4 A_{ji} \left(R_{13}^{(i)} p^2 - R_{11}^{(i)} m_{ji}^2 \right) e^{m_{ji} z_i} \\
 w_i &= \sin(px) \sum_{j=1}^4 A_{ji} \left(R_{13}^{(i)} m_{ji} - \frac{R_{33}^{(i)}}{m_{ji}} p^2 \right) e^{m_{ji} z_i}
 \end{aligned} \tag{5-11}$$

which satisfy the simple support boundary conditions (equations 5-5) identically. Satisfaction of the remaining boundary conditions, equations 5-4 and 5-6 leads to a system of $4m$ equations for the $4m$ unknowns A_{ji} . This system was set up for the present research by placing the A_{ji} in a $(4m \times 1)$ vector, \mathbf{AA}

$$\mathbf{AA}_{j+4(i-1)} = A_{ji} \tag{5-12}$$

and defining a matrix **B** which, premultiplying **AA** produced a vector, **BC**, of the boundary conditions.

$$\begin{aligned}
 \mathbf{BC}_1 &= q_0 \\
 \mathbf{BC}_{j+4(i-1)} &= 0 \quad (j = 1,2,3,4; \ i = 1,2,\dots,m; \ ij \neq 1)
 \end{aligned}
 \tag{5-13}$$

$$\begin{array}{ccc}
 \mathbf{B} & \mathbf{AA} & = \mathbf{BC} \\
 (4m \times 4m) & (4m \times 1) & (4m \times 1)
 \end{array}$$

For example, σ_z on the top and bottom surfaces (the LHS of equations 5-4) was placed into equation 5-13 by setting

$$\begin{aligned}
 \mathbf{B}_{1,j} &= -p^2 e^{\frac{1}{2}m_j h} \\
 \mathbf{B}_{1,j+4(m-1)} &= -p^2 e^{-\frac{1}{2}m_{jm} h}
 \end{aligned}
 \tag{5-14}$$

The contributions to **B** from the other boundary conditions and interface continuity conditions are given in Appendix A. **AA** was then obtained by inverting **B**.

$$\mathbf{AA} = \mathbf{B}^{-1} \mathbf{BC}
 \tag{5-15}$$

The stresses and displacements were then obtained by equations 5-10 through 5-12 with **AA** from equation 5-15.

5.2.1 Material properties.

Material properties for the specimens used for the present research were obtained from the manufacturers test data or chosen to be consistent with that data. The properties used in the elasticity solution calculations are summarized in table 5-1. In table 5-1, the numerical subscripts for the facesheet properties (1,2,3) refer to the longitudinal, lateral, and transverse lamina directions while for the core properties they refer to the ribbon, lateral, and transverse directions. X, Y, and Z are the strengths in the longitudinal, lateral, and transverse lamina directions, and S_{ij} are the shear strengths.

	facesheet (AS4/3501-6)	core (HRH10-1/8-4.0)
E_1	144.8 GPa	80.4 MPa
E_2	9.7 GPa	80.4 MPa
E_3	9.7 GPa	1.005 GPa
G_{23}	3.6 GPa	75.8 GPa
G_{13}	6.0 GPa	120.6 MPa
G_{12}	6.0 GPa	32.2 MPa
ν_{23}	0.34	0.02
ν_{13}	0.3	0.02
ν_{12}	0.3	0.25
X_t	2.17 GPa	N/A
X_c	-1.72 GPa	N/A
Y_t	53.8 MPa	N/A
Y_c	-205.5 MPa	N/A
Z_c	-205.5 MPa	3.83 MPa
S_{23}	89.3 MPa	142.3 MPa
S_{13}	120.7 MPa	177.9 MPa
S_{12}	120.7 MPa	N/A

Table 5-1 Material properties.

5.2.2 Sinusoidal load, same material and geometry as test specimens.

Appendix A is a Mathcad template which was created to apply the solution given in [236] to sandwich structures having the material properties and dimensions of interest in the current research. As noted above, the loading in this solution is transverse pressure distributed as a half sine wave over the top surface of the plate and the supports are simple. The geometry is shown in figure 5-2. The solution of this problem is exact, within the assumptions of elasticity, and thus serves as an appropriate benchmark for the computational algorithm developed in Chapter 6. It is

compared to that obtained from finite element analysis (with equilibrium post-processing) of a plate strip in chapter 7.

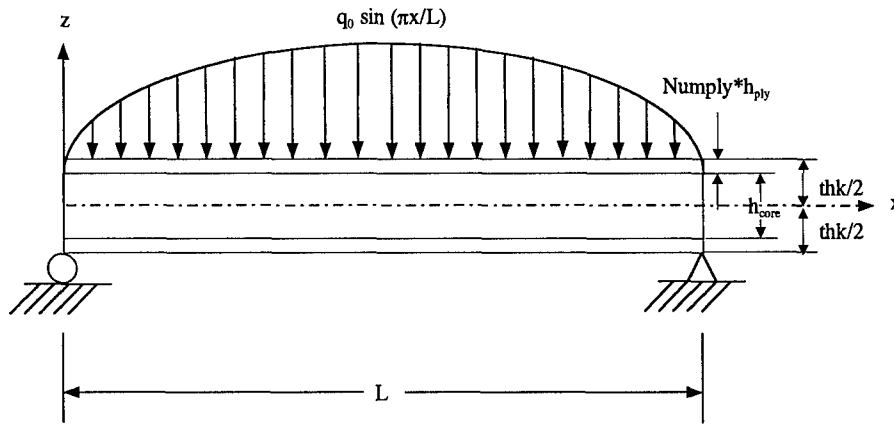


Figure 5-2 Geometry for sinusoidally loaded sandwich plate in cylindrical bending.

5.2.3 Extension for indentation problem.

The sinusoidal load of the previous solution is distributed over the entire plate top surface, whereas the load for the impact problem will be concentrated over the small portion of the top surface which is in contact with the impactor. In order to more accurately model the load profile of an impact problem, a truncated Fourier sine series approximation of a Hertzian contact load distribution was applied to the elasticity solution algorithm of Appendix A. In this case, however, a FORTRAN program was used in place of the Mathcad template because the computational effort required did not lend itself to solution within Mathcad's interactive environment. The increased computational intensity resulted from the fact that the problem had to be solved for each term in the odd (i.e. sine since all cosine terms vanish) Fourier series and the solutions superposed. For small contact radii, the number of Fourier terms required to accurately represent a Hertzian load can be more than one hundred. Figure 5-3 shows a Hertzian load with a small contact radius (1.59 mm) and the equivalent Fourier series truncated to 50, 150, 250, and 350, terms. It should be observed in that figure that to show the differences, only the portion of the load near and to the right of center ($63.5 \text{ mm} < x < 67 \text{ mm}$) is plotted. The 1.59 mm contact radius was chosen for this illustration because it is typical of those measured for 8-, 16- and 32-ply specimens before damage in the static indentation tests discussed in Chapter 4. The small improvement in fidelity obtained by increasing the number of odd Fourier terms above 150 for this contact radius was not judged to be worth the significant additional computational expense.

The FORTRAN program ETPSFL (elasticity theory, cylindrical bending, Fourier load) developed for this solution is included in Appendix A. In that program, a user-supplied subroutine fills an array of the odd Fourier coefficients. A Mathcad template written to calculate the Fourier coefficients for that subroutine is also included in Appendix A. As with the previous sinusoidal load, the solution of this problem is exact, within the assumptions of elasticity and for the approximated load distribution, and thus serves as another appropriate benchmark for the computational algorithm developed in Chapter 6. It is compared to that obtained from finite element analysis of a plate strip loaded with the same truncated Fourier series load in chapter 7.

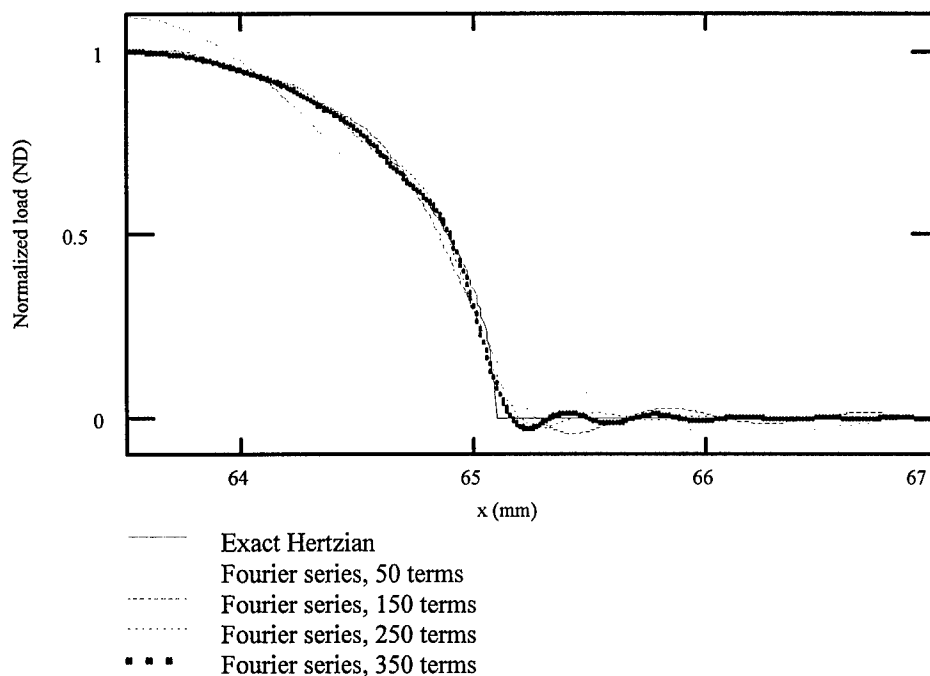


Figure 5-3 Hertzian load approximation by truncated Fourier series for the 1.59 mm contact radius case showing that minimal improvement is obtained by increasing the number of terms above 150.

5.2.4 Cylindrical bending solution to Hertzian loaded sandwich plate.

This cylindrical bending solution to a simply supported, Hertzian loaded, sandwich plate provided both a benchmark for the finite element analysis before damage and a tool to judge the appropriateness of the various failure theories in the context of impact to composite sandwich structures. The cylindrical bending solution required only a one-dimensional Fourier series for the loading and thus hundreds of terms could be used to represent a contact-type load over a very small contact area without encountering solution matrix singularity problems associated with a two-dimensional Fourier series. Cylindrical bending elasticity solution stress data for two cross-

sections of the specimens (the planes defined by the 0° and 90° ply orientation directions) were then studied to develop a general understanding of how a contact load is distributed into a sandwich plate and the role that facesheet thickness plays in the process. This solution was found to be so valuable for this purpose that it suggests an entirely new study beyond the scope of this research in which parameters such as core thickness, core stiffness, impactor radius, and facesheet material properties can all be varied and their influences presented in a usable form for designers of these structures. It is possible that rules-of-thumb to aid the designers in the many tradeoff decisions inherent in any structural application of composite sandwich plates could result from such a study.

Figure 5-4 shows the variation of transverse direct stress σ_z through the thickness predicted by cylindrical bending elasticity theory for the various specimens tested in the experimental portion of the current work. The intuitive idea that the thicker facesheets distribute the load over a greater portion of the core and thus reduce the peak core compressive stress is both verified and quantified by these data. The top surface of the core in the 4-ply specimens apparently was under 56 percent of the peak applied stress. The thicker facesheets lowered the peak stress at the top of the core to such an extent that the top surface of the core in the 48-ply specimens apparently was under only 8 percent of the peak applied stress.

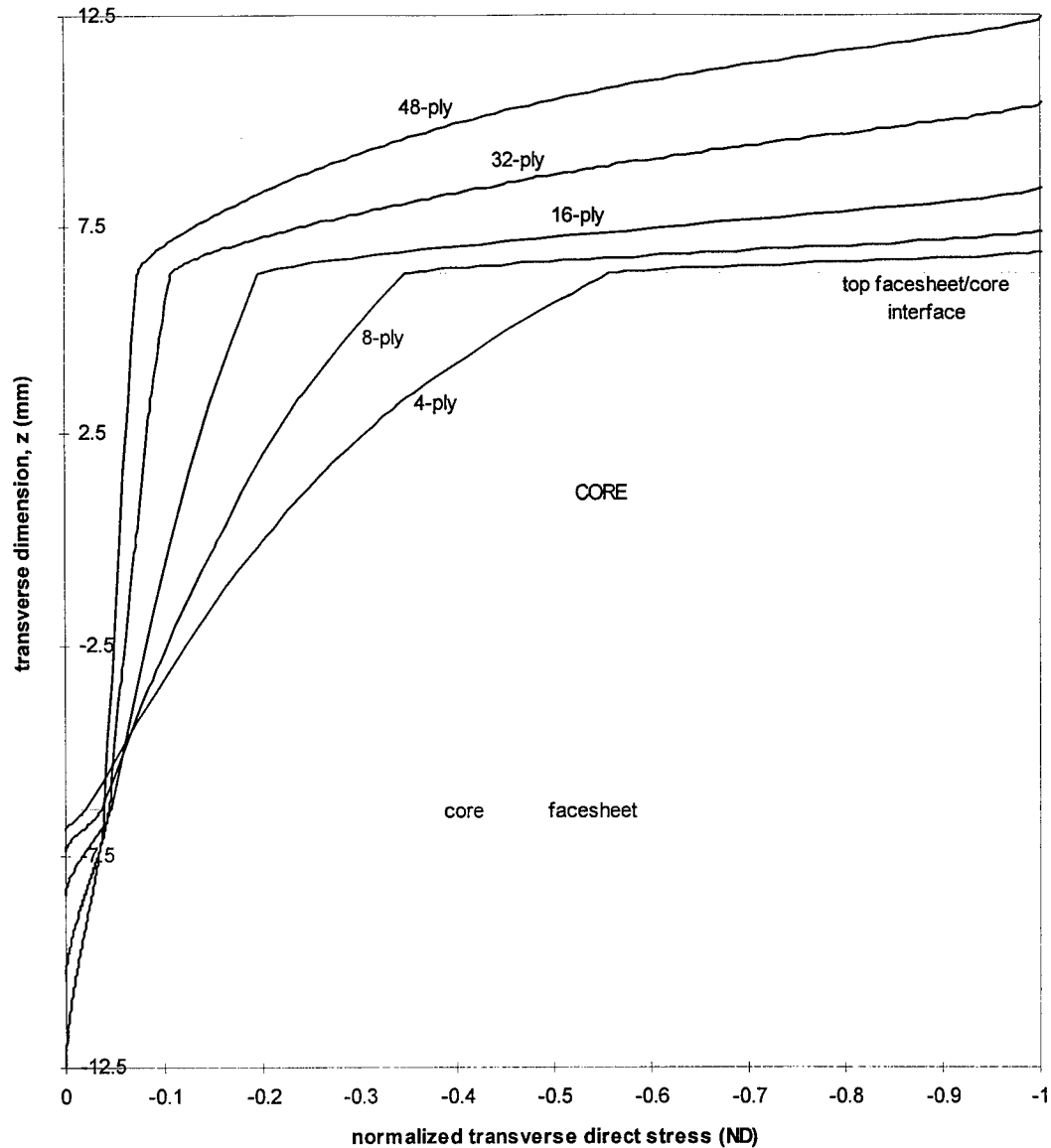


Figure 5-4 Normalized transverse direct stress under the center of a Hertzian load showing how thicker facesheets serve to reduce the compressive stress seen by the core, thus delaying core failure. Contact half-width was 1.59 mm and normalization is by the peak applied stress.

One advantage of sandwiches with the thicker facesheets (which can be seen in figure 5-4) is that they will achieve a higher peak load before core failure will happen. This advantage is, of course, tempered by the fact that for a given impact energy the thicker facesheets, being stiffer, also produce greater loads. To account for this, the stress data in figure 5-4 were scaled by empirical data from Chapter 4. The plane stress elasticity solution was run using the particular contact radius and peak stress at the first major load drop from the experiment for each facesheet

thickness. The transverse stress profile from this solution was used as an estimate of the transverse stress profile through the thickness which was present at the first major load drop. The result is plotted for each facesheet thickness in figure 5-5.

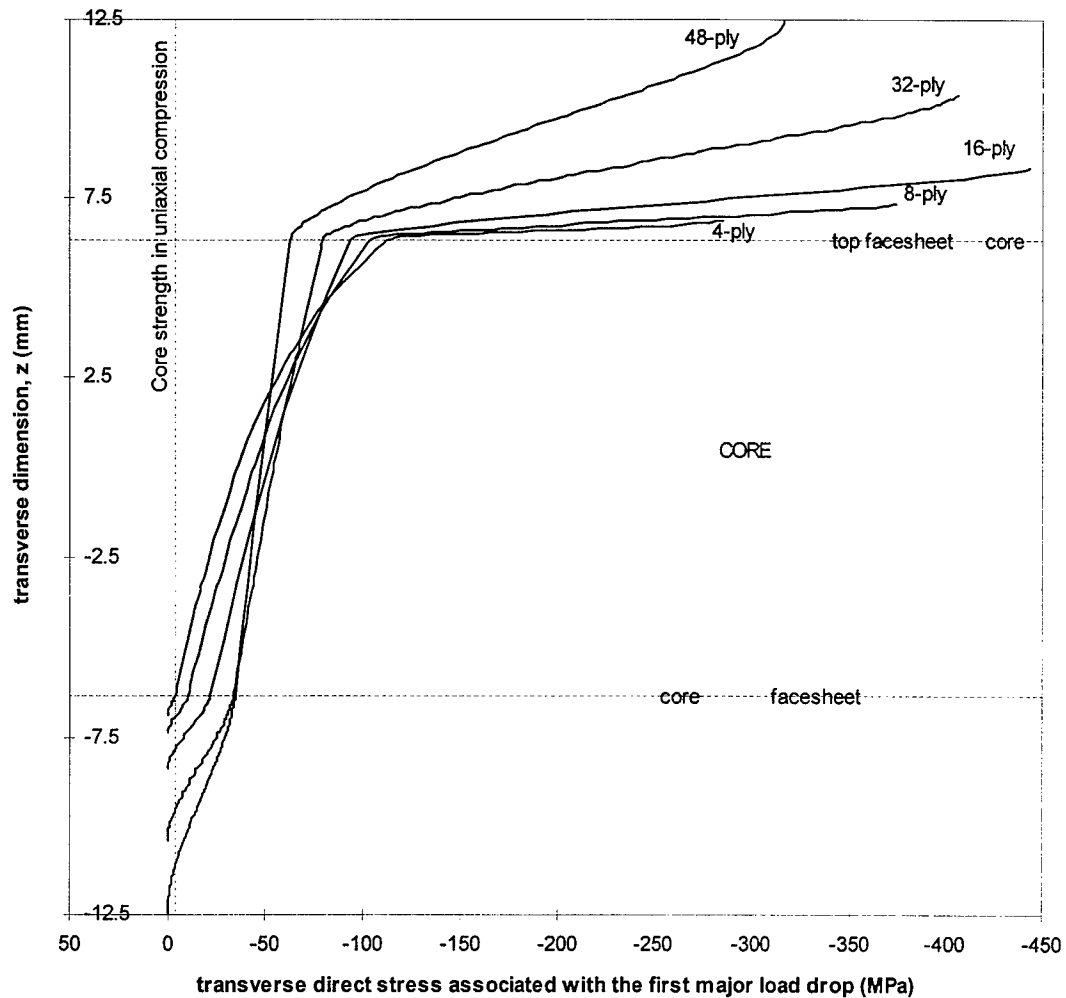


Figure 5-5 Transverse direct stress under the center of a Hertzian load scaled to match the peak stress and contact radius for the first major load drop seen in the experiments. For comparison, uniaxial core strength is also plotted indicating that the core achieves a stress higher than its uniaxial compression strength before failure.

The scaling of figure 5-5 allows another point to be observed. The only compression strength data available for the core is from uniaxial compression and shear tests [128]. Uniaxial compression strength is shown as the vertical line in figure 5-5. In the experiments of Chapter 4, core failure always occurred near the interface between the core and the top facesheet. As facesheet thickness increased, figure 5-5 clearly indicates that the transverse compressive stress

associated with the first major load drop decreased at the interface between the core and the top facesheet. None of the specimens, however, apparently experienced core failure until this stress was well above the uniaxial core strength. Chapter 4 demonstrated that the first major load drop was associated with core failure. This suggests that a maximum stress failure criterion incorporating uniaxial core strength is highly-conservative for predicting core failure. The error decreases with increasing facesheet thickness, but is significant for all facesheet thicknesses tested. Other criteria incorporating shear are not expected to significantly improve upon maximum stress either, since both transverse and in-plane shear are zero at the center. This presents a potentially critical problem to any analysis intending to predict failure based upon stress, particularly Chapter 6 of the current work. A semi-empirical maximum stress failure criterion incorporating a facesheet-thickness-dependent core strength is given in equation (5-16).

$$\text{apparent core strength} = \bar{\sigma}_z \frac{3}{2\pi} \frac{F_{Fail}}{R_{contact}^2}$$

$$\bar{\sigma}_z = \text{normalized transverse direct stress at top of core (from elasticity solution)} \quad (5-16)$$

$$F_{Fail} = \text{load at first major load drop (empirical)}$$

$$R_{contact} = \text{contact radius at first major load drop (empirical)}$$

$$\frac{3}{2\pi R_{contact}^2} = \text{load to peak stress conversion factor for Hertzian contact}$$

The semi-empirical maximum stress failure criterion given in equation (5-16) allows the analysis to predict core failure from the stress at the top surface of the core. By providing the through-the-thickness transverse direct stress profile, the cylindrical bending elasticity solution bridges the gap between the experimental data and the needed core strengths. Figure 5-6 shows the semi-empirical apparent core strength as a function of facesheet thickness.

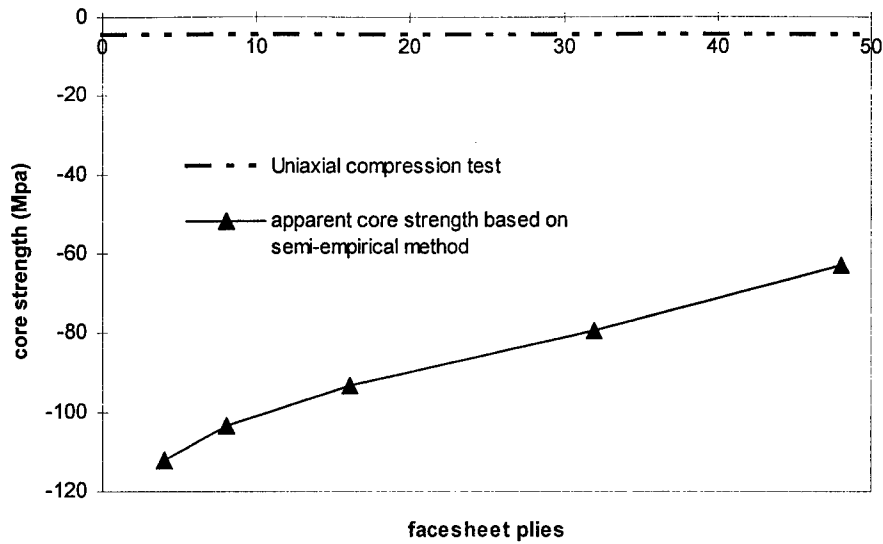


Figure 5-6 Apparent core strength as calculated by equation (5-16).

Figure 5-7 shows the in-plane stress σ_x normalized by the peak applied stress for the cylindrical bending elasticity solution. The first and most obvious bit of information to gain from this scaling is that thicker facesheets lead to lower in-plane loads for static indentation problems. This comes as no surprise since thicker facesheets imply that the same load can be spread out over more plies, reducing the average stress in each ply. More interesting in figure 5-7 is the fact that the facesheet bending stresses which effectively resist the transverse load and distribute that load over a larger portion of the core are clearly visible. Considering first the 4-ply data, one can see that the top facesheet is fully in compression while the bottom facesheet is fully in tension. Thus global plate bending is of at least as great importance to the 4-ply in-plane stress as is local facesheet bending which gives rise to a linearly varying stress through the thickness. If one considers the total stress to be the sum of these global and local components, the fact that σ_x is near zero at the bottom of the top facesheet indicates that local and global bending are canceling each other and are therefore contributing approximately equal (but opposite) stresses at that location. This indicates that roughly half of the peak stress at the top of the top facesheet comes from facesheet bending while half comes from global bending. Increasing facesheet thickness increases the global bending stiffness much faster than it does the local facesheet bending stiffness because of the proportionality shown in equation 5-17. This explains the fact that the data in figure 5-7 show progressively more local bending stress and relatively less global bending stress as the facesheet thickness increases.

$$\Delta_{\text{local}} (\text{facesheet}) \text{ bending stiffness} \propto \left(\frac{\Delta h}{2}\right)^3$$

$$\text{while, } \Delta_{\text{global}} (\text{plate}) \text{ bending stiffness} \propto \left(\frac{h}{2} + \Delta h\right)^3 \quad (5-17)$$

The last observation from figure 5-7 is that the top facesheet does have more local bending than the bottom facesheet for all of the facesheet thicknesses. This is the expected result because the core serves to relax the coupling between the bottom and top facesheet motions so the radius of curvature of the bottom facesheet is greater than that of the top.

Since σ_x is the principal contributor to fiber failure and has little contribution to the other failure mechanisms, the preceding comments apply almost directly to the influence of facesheet thickness on fiber failure. Figure 5-8 scales the data of figure 5-7 to show estimates for the fiber stresses at the applied load that produced the first major load drop. This alarming plot indicates that sandwich plates of all of the facesheet thicknesses should have shown fiber failure prior to the major load drop. This could account for the increased noise in the load histories often observed just prior to the major load drop as individual fibers failed. Perhaps the most alarming thing about this is that fiber failure was not observed in the specimens when they were sectioned, polished, and viewed under magnification. Also, the peak compressive fiber stress occurs at the top surface of the plate and the significant fiber failure indicated by figure 5-8 should be observable on the surface even without sectioning the specimen. No such failure was observed in this or the previous experimental effort [5]. These data indicate that maximum stress may be an overly-conservative criterion for fiber failure, but since no fiber failure has been observed in the experiments, ignoring this potential failure mechanism may be justifiable on that basis.

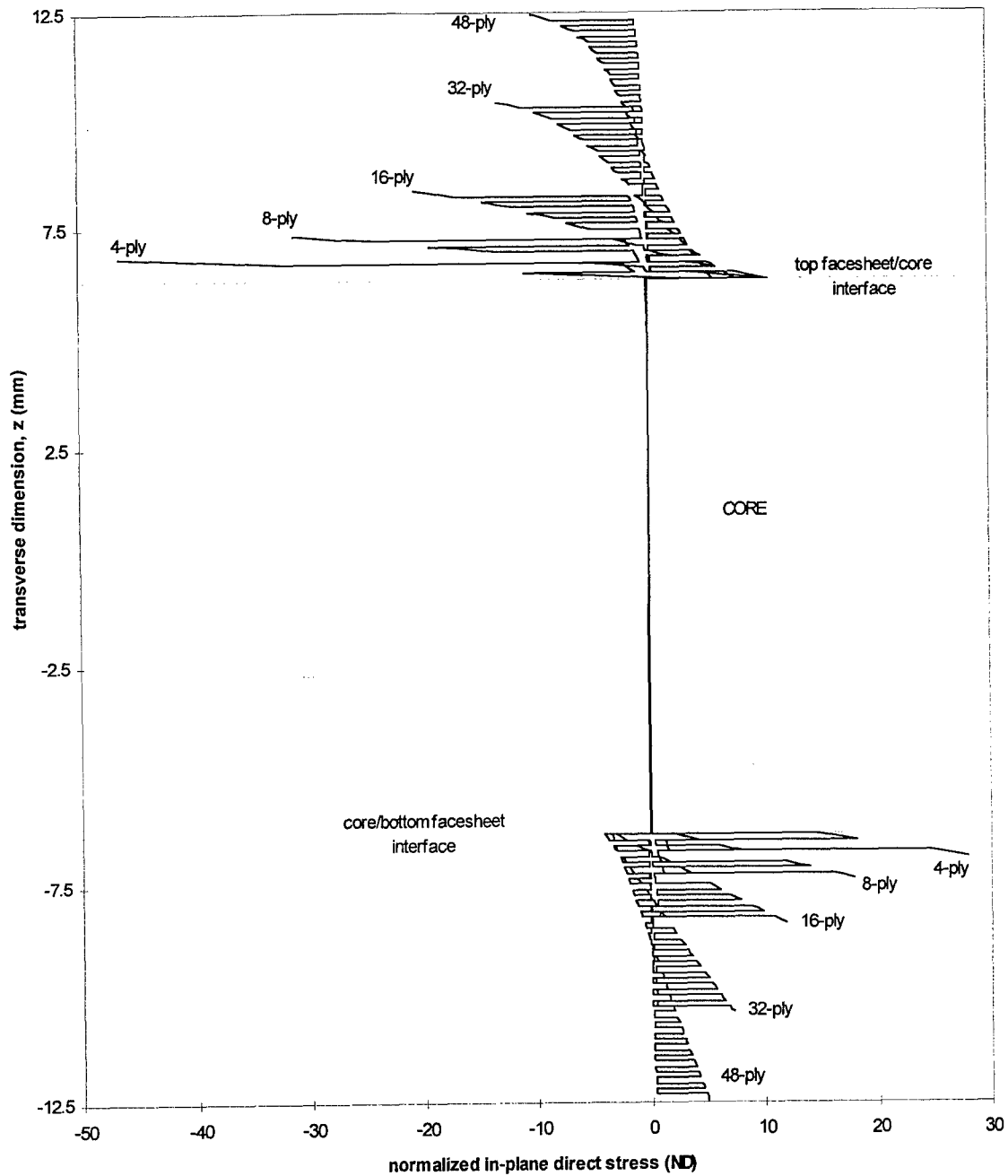


Figure 5-7 In-plane direct stress under the center of a Hertzian load normalized by peak applied (transverse) stress showing the reduction in in-plane stress brought about by thicker facesheets. Contact half-width was 1.59 mm and normalization is by the peak applied stress.

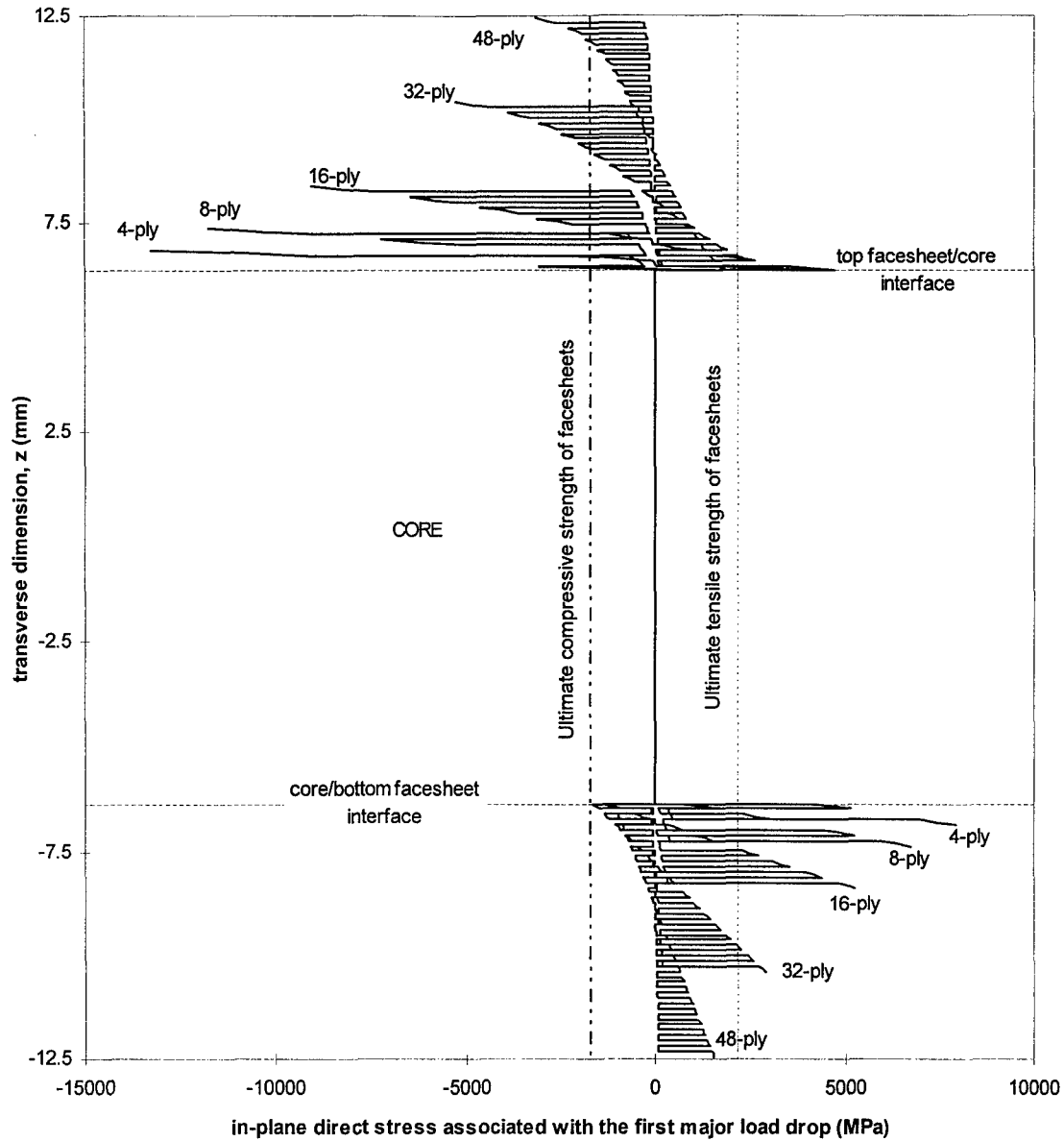


Figure 5-8 Transverse direct stress under the center of a Hertzian load scaled to show values for the first major load drop seen in the experiments. For comparison, ultimate tensile and compressive strengths of the facesheets are also plotted indicating that the facesheets achieve a stress higher than ultimate strength before the first major load drop.

Transverse shear stress is the dominant driver for matrix cracking and delamination. Unlike fiber failure, these damage mechanisms have been observed extensively in all the damaged specimens. Unlike transverse or in-plane direct stress, shear does not have a peak in the center of the plate. To locate the x dimension of the peak of transverse shear, as well as to show the x-

dependence of transverse shear, the shear at the midplane of the top facesheet is plotted against x-dimension in figure 5-9.

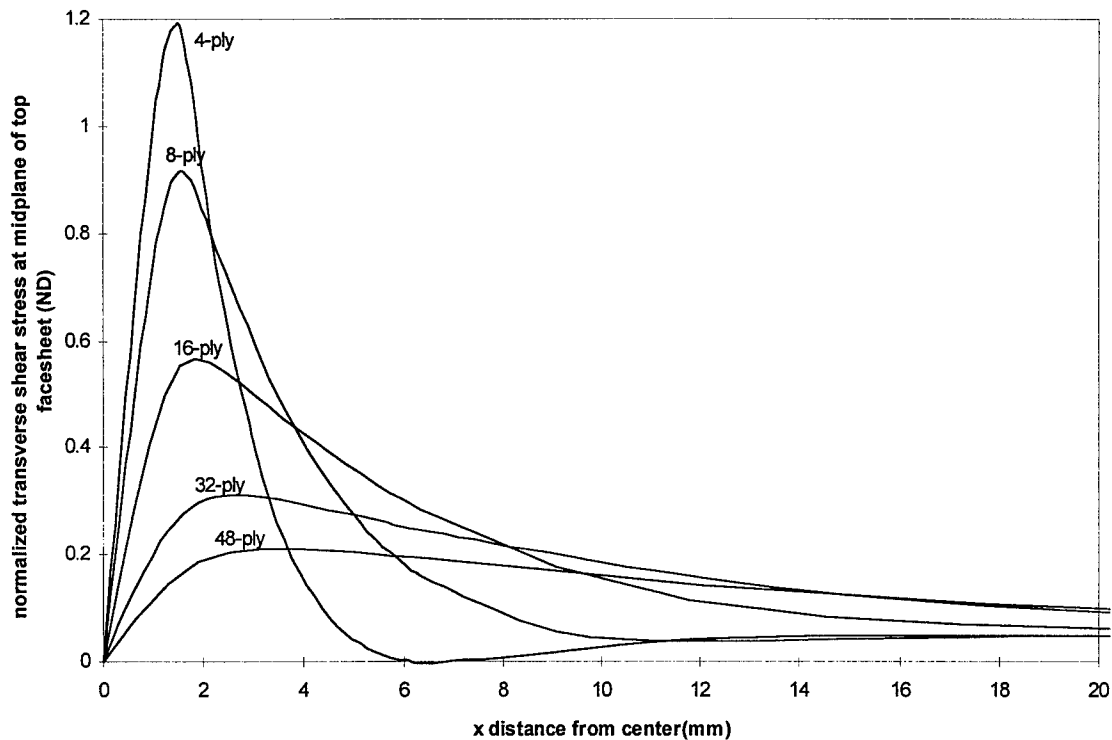


Figure 5-9 Normalized transverse shear stress in the midplane of the top facesheet showing how thicker facesheets serve to reduce the peak transverse shear stress and move its location away from the center of the plate. Contact half-width was 1.59 mm and normalization is by the peak applied stress.

Figure 5-9 shows that increasing the thickness of the facesheets has at least three important affects on transverse shear and therefore both delamination and matrix cracking. The first, and most dramatic is the reduction in the peak value which will serve to delay initiation of damage. The second is that it moves the peak value away from the plate center so that the damages will be initiating from a location further from the point of application of the load. The third is that the peaks are broadened and flattened so that damage will not be as well defined and repeatable. This conjecture is based on the assumptions that shear dominates the initiation of damage and that damage can occur when shear is within a range and not only at a specific value. Thus a broad, flat peak puts a relatively large portion of the facesheet within the critical stress range and matrix cracking and delamination initiation may start from anywhere within that range. Once started, strain energy released in the process of damage, load redistribution, and stress singularities at the

crack tips will bias the progression of the damage in a way that is dependent on the initiation point. Though simplistic, these ideas do explain the fact that C-scans show damage in thin facesheet specimens impacted at the same energies are more consistent than those of thick facesheet specimens. C-scans from thin facesheet specimens also show more bi-directional symmetry which is consistent with these ideas.

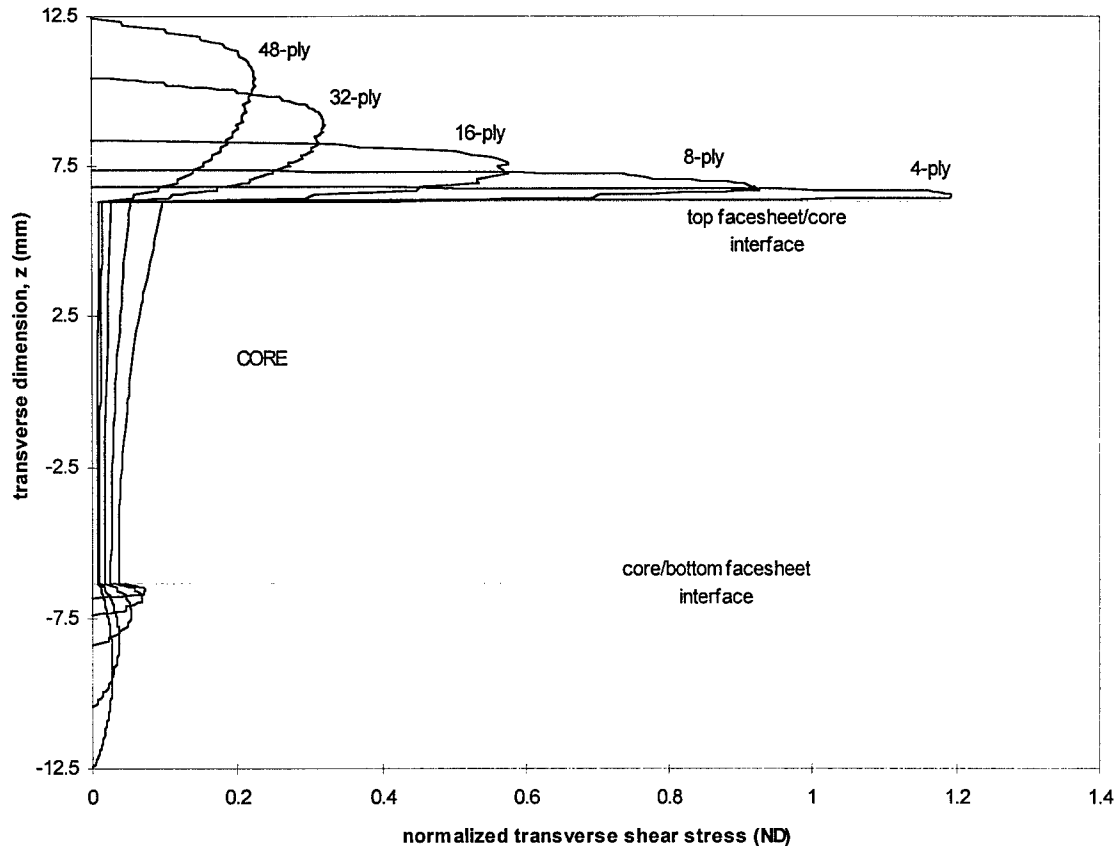


Figure 5-10 Transverse shear stress at the location of the peaks found in figure 5-9, normalized by peak applied (transverse) stress, showing the reduction in transverse shear stress brought about by thicker facesheets. Contact half-width was 1.59 mm and normalization is by the peak applied stress.

Normalized transverse shear stress at the x-locations of the peaks in figure 5-8 is plotted through-the-thickness in figure 5-10. This figure shows very clearly why delaminations and matrix cracks are found in the top facesheets but not in the bottom facesheets. These data are scaled to the first major load drop values in figure 5-11. This figure indicates that for the thin facesheet specimens facesheet damage in the form of matrix cracking and or delaminations should precede core failure if indeed the major load drop is an indicator of core failure as found in Chapter 4.

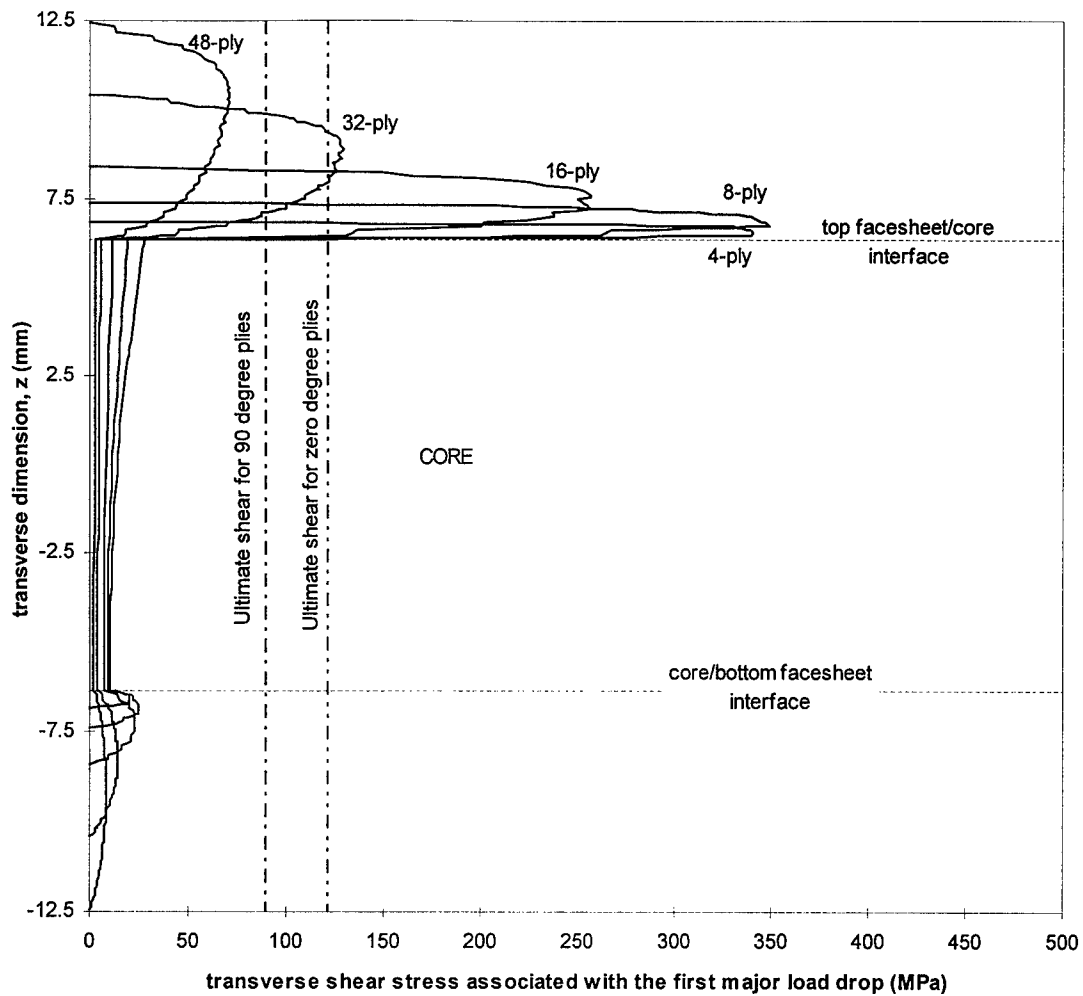


Figure 5-11 Transverse shear stress at the location of the peaks found in figure 5-9, scaled to show values for the first major load drop seen in the experiments. For comparison, ultimate shear strengths of the 0 and 90 degree plies of the facesheets are also plotted indicating that for most facesheet thicknesses a maximum stress criteria would indicate matrix cracking before the first major load drop.

5.2.5 Failure criteria checkout.

The cylindrical bending elasticity solution can be used to qualitatively judge the failure criteria that are available to predict damage in the sandwich structure. One must keep in mind that the empirical data available are for a center loaded square plate while the cylindrical bending solution directly applies to a line loaded strip of infinite depth. The differences of the loads and boundary conditions are illustrated in figure 5-12.

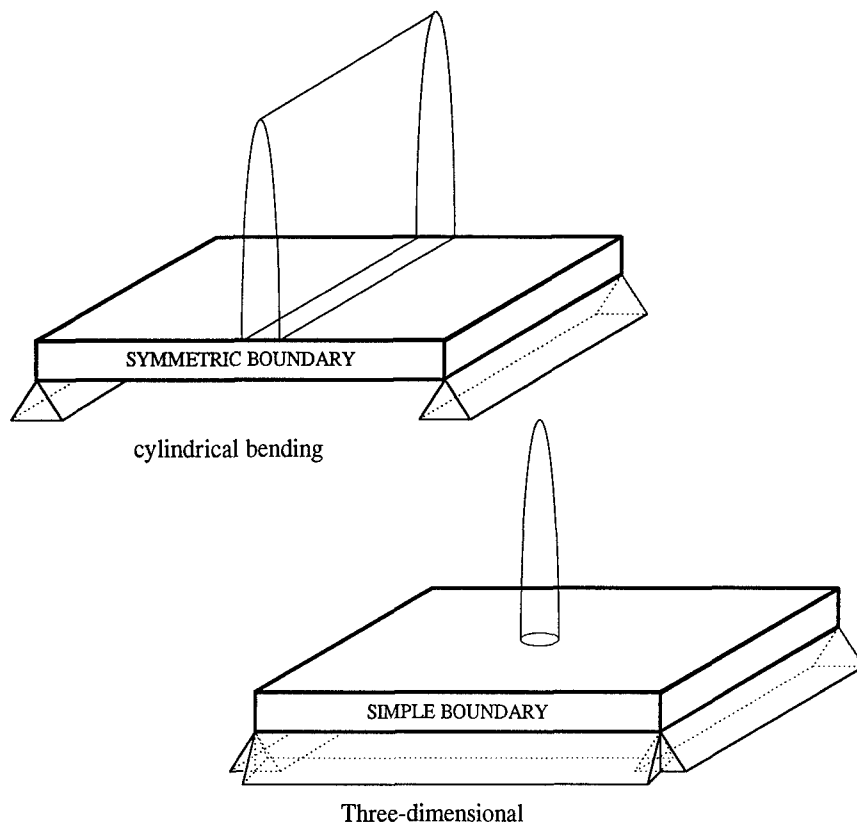


Figure 5-12 Cylindrical bending and three-dimensional plate geometries.

Obviously, for the same load profile and plate depth, the cylindrical bending model experiences a much greater total load and is supported more flexibly, so the deflections and in-plane stresses will be expected to be greater. Nevertheless, in a plane cut through the center of the load in the three-dimensional case, the applied transverse direct stress is the same as the cylindrical bending case and the conditions consistent with a symmetric boundary exist due to the symmetries of the loading and geometry. Thus, one would expect the transverse direct stress within that plane to be similar to that of the cylindrical bending model. At the very least, it must satisfy the same boundary

conditions on the top and bottom surfaces of the plate. Transverse direct stress is the principal driver for core damage. These ideas then, taken together, point toward an analogy between the three-dimensional and the cylindrical bending at least as far as core crushing is concerned.

Transverse shear stress is not so analogous between the two. Letting the transverse dimension of the cutting plane be labeled z , and the other dimension be labeled x , and considering the third differential equation of equilibrium,

$$\sigma_{xz,x} + \sigma_{yz,y} + \sigma_{zz,z} = 0, \quad (5-18)$$

one can see that for the cylindrical bending case,

$$\begin{aligned} \sigma_{yz} &= \sigma_{yz,y} = 0 \\ \text{so that,} \\ \sigma_{xz,x} + \sigma_{zz,z} &= 0 \end{aligned} \quad (5-19)$$

and, for a known σ_{zz} , σ_{xz} can be written as,

$$\sigma_{xz} = - \int_0^x \sigma_{zz,z} d\xi.$$

This differs significantly from the three-dimensional case in which, though

$$\begin{aligned} \sigma_{yz} &= 0, \text{ its gradient, } \sigma_{yz,y} \neq 0, \\ \text{(it is, in fact, a maximum at the center).} \\ \text{so that } \sigma_{xz} &\text{ must now be written as,} \end{aligned} \quad (5-20)$$

$$\sigma_{xz} = - \int_0^x (\sigma_{zz,z} + \underline{\sigma_{yz,y}}) d\xi.$$

The additional (underlined) term in the expression for σ_{xz} is generally not small. All this is to say that the transverse shear stresses from the cylindrical bending model are not expected to model those of the three-dimensional case. This can explain the disparity between figure 5-11 which indicates all but the thickest facesheet specimens should have facesheet shear-type damages well before the first major load drop and the empirical data of Chapter 4 which found no such damages until after the first major load drop. Evidently, the transverse shear through-the-thickness profile provided by the elasticity solution does not represent the profile of the three-dimensional experimental test in those areas where three-dimensional effects are very strong (e.g. under the tup). This is unfortunate, since it would be of the greatest value there.

The first failure criteria to be addressed is for fiber failure. As noted above, the cylindrical bending model experiences a greater total load per unit depth and is supported on only two of its four sides allowing greater deflections so in-plane stresses (and hence tendency toward fiber failure) are expected to be greater than those of the three-dimensional case. Two different criteria have been used to predict fiber failure in the cylindrical bending case. The following are applied only to the plies having fibers running parallel to the cutting plane.

<p>maximum stress:</p> <p>case $\sigma_1 > 0$,</p> $\left(\frac{\sigma_1}{X_t}\right)^2 \geq 1$ <p>case $\sigma_1 < 0$,</p> $\left(\frac{\sigma_1}{X_c}\right)^2 \geq 1$	<p>Hashin [242]:</p> <p>case $\sigma_1 > 0$,</p> $\left(\frac{\sigma_1}{X_t}\right)^2 + \left(\frac{\tau_{13}}{S}\right)^2 \geq 1$ <p>case $\sigma_1 < 0$,</p> $\left(\frac{\sigma_1}{X_c}\right)^2 \geq 1$	<p>(5-21)</p>
--	---	---------------

The left hand side of the appropriate inequality in equation 5-21 served as a damage metric for fiber failure. Since the solution is linear, the relative magnitude of the metrics indicates which of the criteria is more conservative. The fiber failure metric can be compared to the other damage metrics (i.e. matrix cracking, delamination, and core failure) to indicate which damage is predicted to happen at the lowest load.

Elasticity solution

4-ply, $R_{\text{contact}}=0.96$ mm, $q_0=285$ MPa, $F_0 = 550$ N

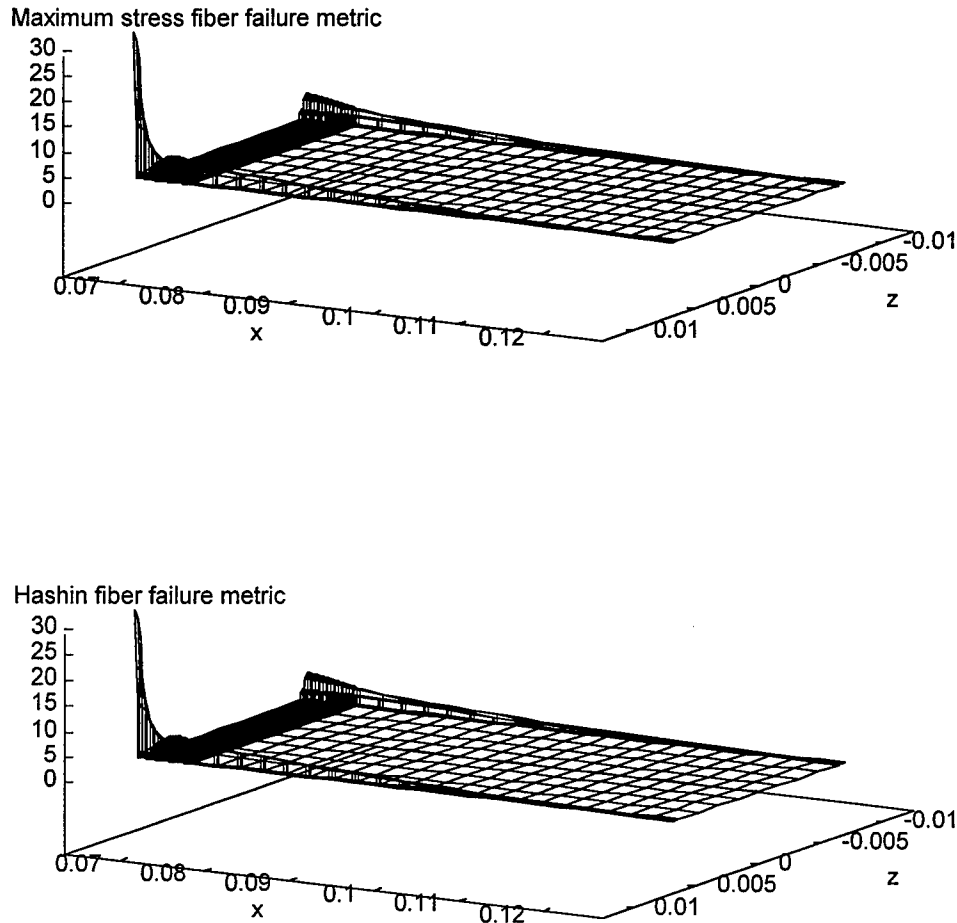


Figure 5-13 Cylindrical bending fiber failure metric for applied load that produced first major load drop in the three-dimensional indentation tests of the 4-ply specimens. This shows that the in-plane stress predicted by the cylindrical bending assumption is very high compared to the actual three-dimensional experiment which saw no fiber failure. Positive z is up and load is applied to the positive z side of the plate in the negative z direction.

For fiber failure in the cylindrical bending case of low-velocity impact, Hashin and maximum stress are nearly identical criteria because the peak in-plane stress is compressive (figure 5-8) and they are identical for compressive stress (equation 5-21). Where the in-plane stress is tensile (as seen in figure 5-8) the shear term that differentiates between Hashin and maximum stress is small as seen in figure 5-11. The three-dimensional plots like figure 5-13 become even more difficult to read when the number of facesheet plies increases, so rather than present them all, a two-dimensional summary showing only the values at the center of the plate is given in figure 5-14. In figure 5-14,

the 0° fiber failure metric at the center of the plate for the load that produced the first major load drop in the experiments is plotted through the thickness for each specimen. A value of one indicates that the fibers fail.

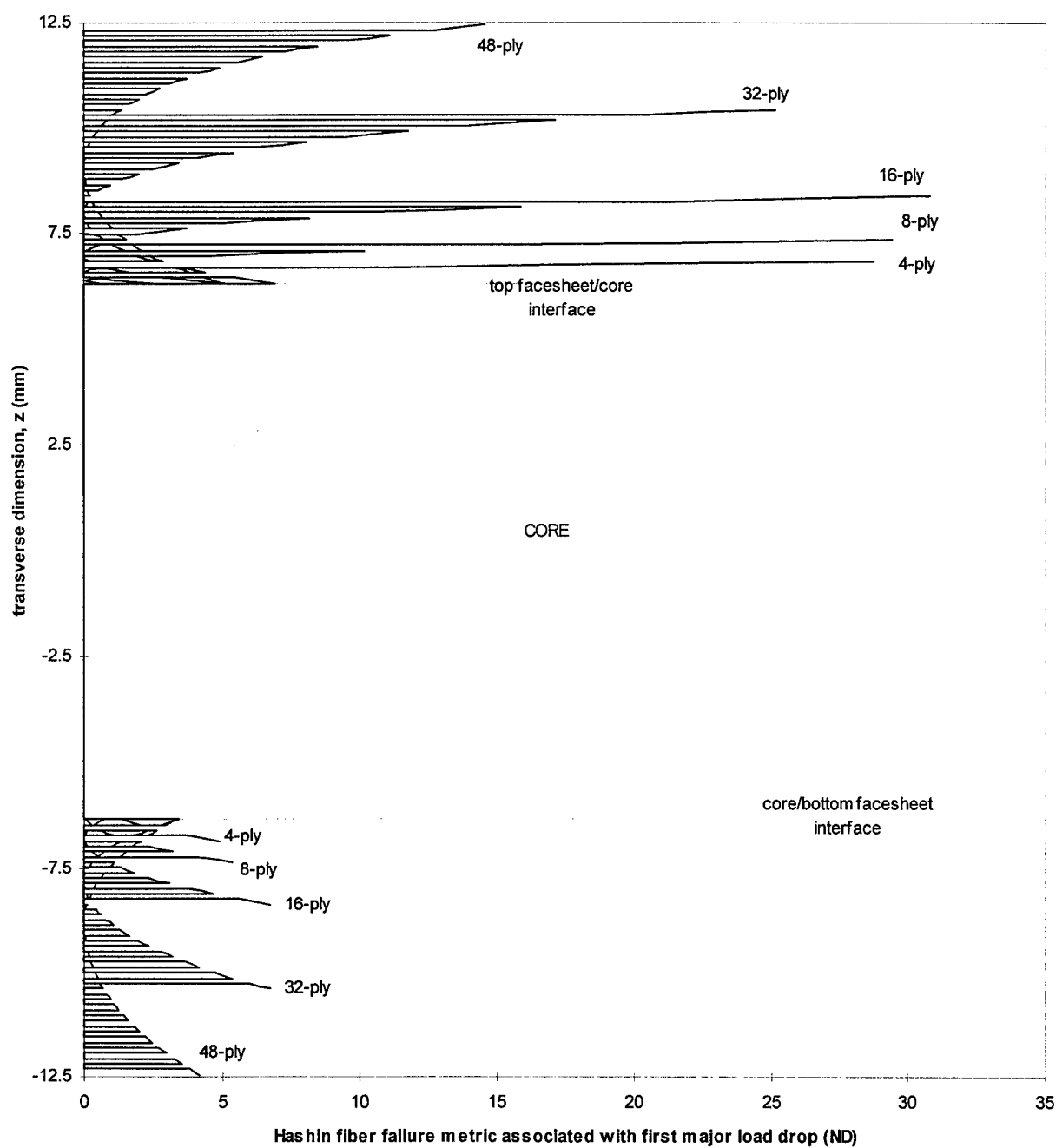


Figure 5-14 Cylindrical bending fiber failure metric at the plate center for applied load that produced first major load drop in the three-dimensional indentation tests. Hashin criterion.

Figure 5-14 should be read to indicate that fiber failures occur at the center of both top and bottom facesheets well below the load associated with the first major load drop for all of the facesheet thicknesses considered. Such fiber damage was not found in the experimental results. This premature fiber failure illustrates the idea previously discussed that the cylindrical bending case could be expected to produce in-plane stresses that were much higher than those of the experiment. That is, for the two-dimensional boundary conditions, the structure is more flexible than the three-dimensional case (figure 5-12) and for two-dimensional loading of a given peak pressure and contact half-width, the force per unit plate depth is much higher than the three-dimensional case with the same peak pressure and a contact radius equal to the contact half-width of the two-dimensional case. Thus, the in-plane stresses from the two cases can not be meaningfully compared. For this reason, the fiber failure criteria applied to the elasticity solution could not be meaningfully compared with the experiment. The only experimental verification of the appropriateness of the fiber failure criteria for this research was that they should not produce widespread fiber failure when applied to the center loaded plate finite element model, since none was observed in the experimental post impact analysis. In this respect, maximum stress and Hashin are identical except for the lower portion of the top facesheet and the upper portion of the bottom facesheet (where $\sigma_1 > 0$) where Hashin is slightly more conservative. Hashin's fiber failure metric was chosen for the balance of this research.

Three different matrix cracking failure criteria were used to predict damage to the facesheets. These are maximum tensile stress, Lee [66], and Hashin [242]. The Lee criteria reduces to what appears to be a maximum shear criteria because in this case in-plane shear is zero. The criteria are given in equations (5-22). As noted above, transverse shear stress in the cylindrical bending model may differ considerably from that in the three-dimensional specimens, so failure criteria based on transverse shear stress (Lee and Hashin) may produce failure metrics which are not consistent with the actual failures observed in the experiments. Also, failure criteria based on in-plane stress (maximum stress and Hashin) may predict early failure because in-plane stresses for the cylindrical bending case are high compared to the three-dimensional actual tests. The following are applied only to the plies having fibers running perpendicular to the cutting plane.

maximum stress:	Lee [66]:	Hashin [242]:
case $\sigma_2 > 0$,		case $(\sigma_2 + \sigma_3) > 0$,
$\left(\frac{\sigma_2}{Y_t}\right)^2 \geq 1$	$\left(\frac{\tau_{23}}{S}\right)^2 \geq 1$	$\left(\frac{\sigma_2 + \sigma_3}{Y_t}\right)^2 + \frac{\tau_{23}^2 - \sigma_2\sigma_3}{S^2} \geq 1$
case $\sigma_2 < 0$,		case $(\sigma_2 + \sigma_3) < 0$,
$\left(\frac{\sigma_2}{Y_c}\right)^2 \geq 1$		$\left(\frac{\sigma_2 + \sigma_3}{Y_c}\right) \left\{ \left(\frac{Y_c}{2S}\right)^2 - 1 \right\}$
		$+ \left(\frac{\sigma_2 + \sigma_3}{2S}\right)^2 + \frac{\tau_{23}^2 - \sigma_2\sigma_3}{S^2} \geq 1$

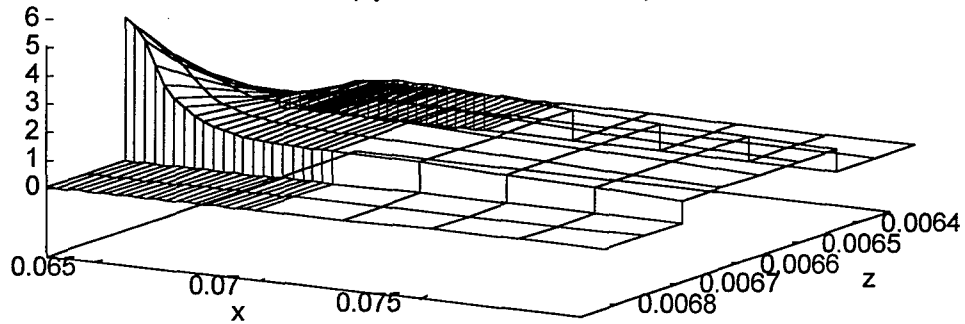
(5-22)

As for fiber failure, the left hand side of the appropriate inequality in equation 5-22 served as a damage metric for matrix cracking. It is this quantity that is plotted in the cutting plane in the following. Matrix cracking found in the experiments was confined to the top facesheet. Tensile in-plane stress was present in the bottom facesheets (figure 5-8). The magnitude of the tensile stress in the plies orthogonal to the cutting plane was greatly reduced compared to those plies with fibers in the plane, but it was non-zero. This positive σ_2 lead both maximum stress and Hashin criteria to predict matrix cracking on the bottom facesheet for the 4-ply case. Since the in-plane stresses are known to be high compared to the experiment and no failure has been found on the bottom facesheet, failure indication on the bottom facesheet was ignored. Therefore the following plots, focus in on what is happening in the top facesheet near the point of application of the load.

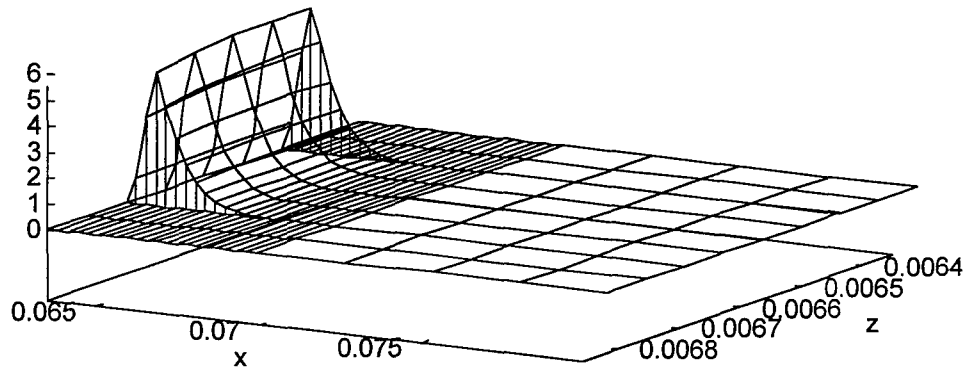
Elasticity solution

Maximum stress matrix failure metric

4-ply, $R_{\text{contact}}=0.96$ mm, $q_0=285$ MPa, $F_0 = 550$ N



Lee matrix failure metric



Hashin matrix failure metric

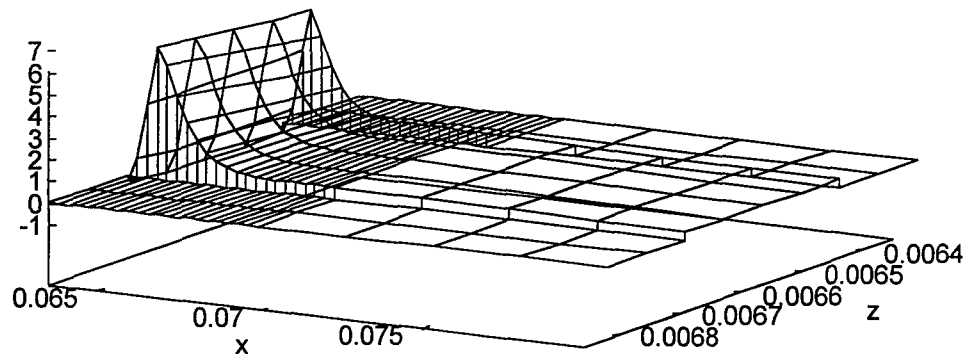
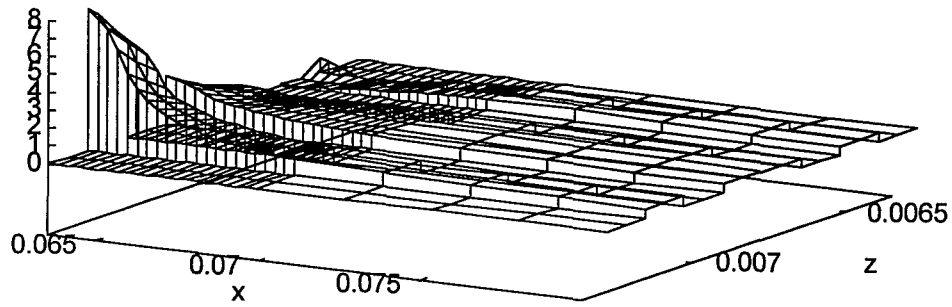


Figure 5-15 4-ply specimen cylindrical bending matrix failure metric in the top facesheet near the plate center for applied load that produced first major load drop in the three-dimensional indentation tests.

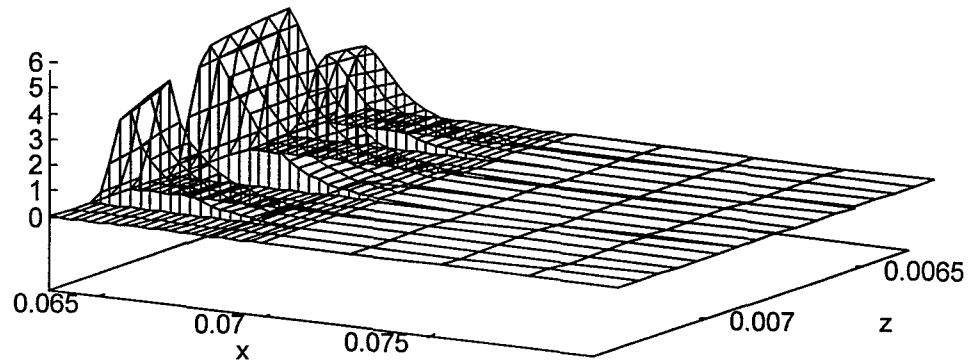
Elasticity solution

Maximum stress matrix failure metric

8-ply, $R_{\text{contact}}=1.18$ mm, $q_0=377$ MPa, $F_0 = 1100$ N



Lee matrix failure metric



Hashin matrix failure metric

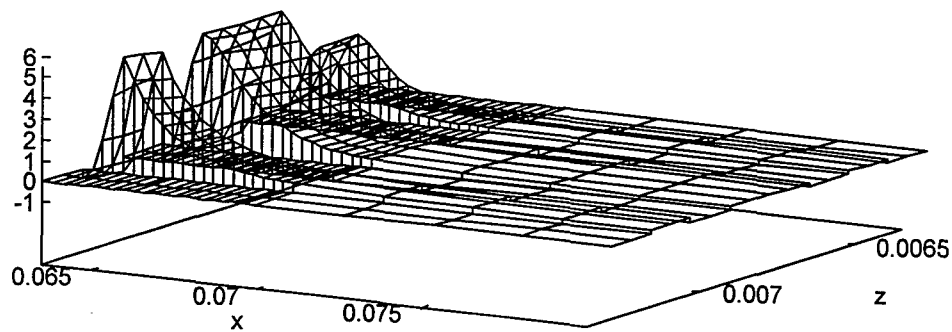
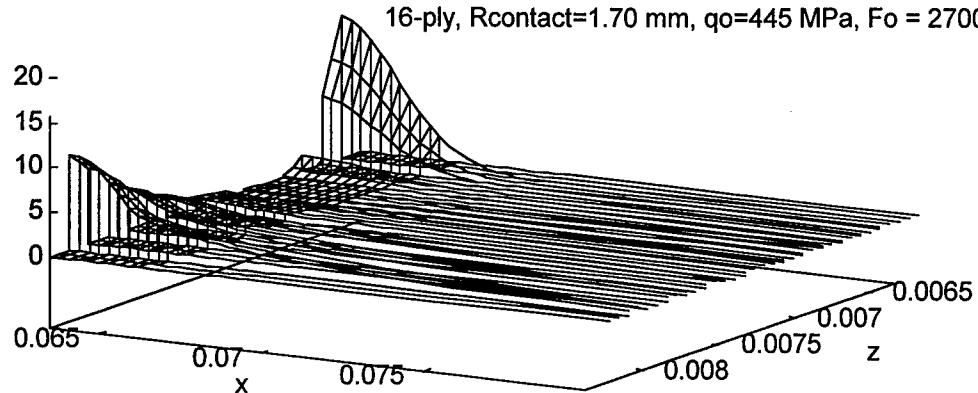
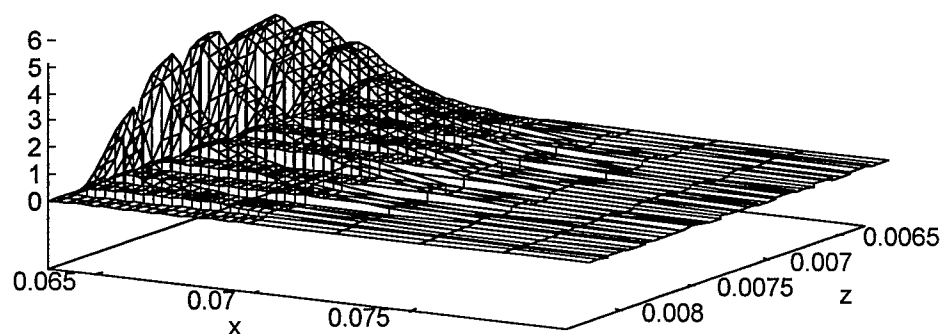


Figure 5-16 8-ply specimen cylindrical bending matrix failure metric in the top facesheet near the plate center for applied load that produced first major load drop in the three-dimensional indentation tests.

Elasticity solution
Maximum stress matrix failure metric
16-ply, $R_{\text{contact}}=1.70$ mm, $q_0=445$ MPa, $F_0 = 2700$ N



Lee matrix failure metric



Hashin matrix failure metric

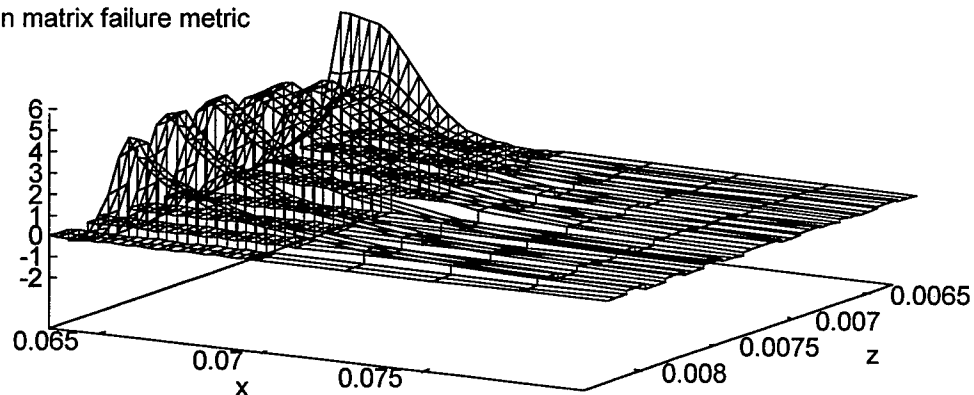
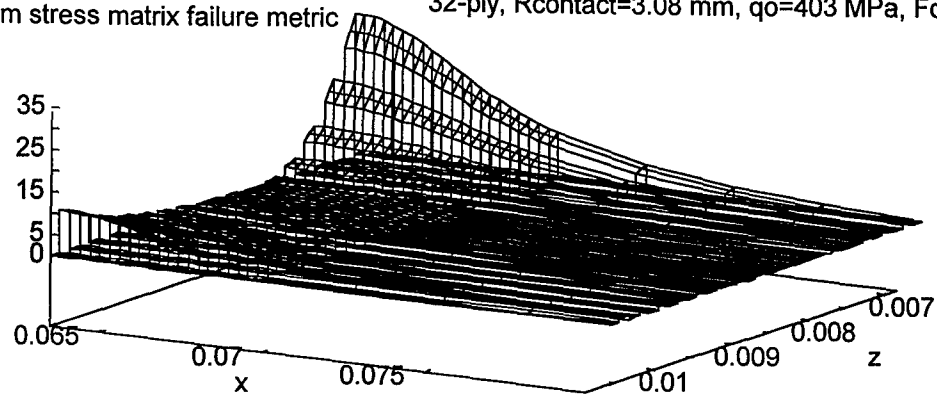
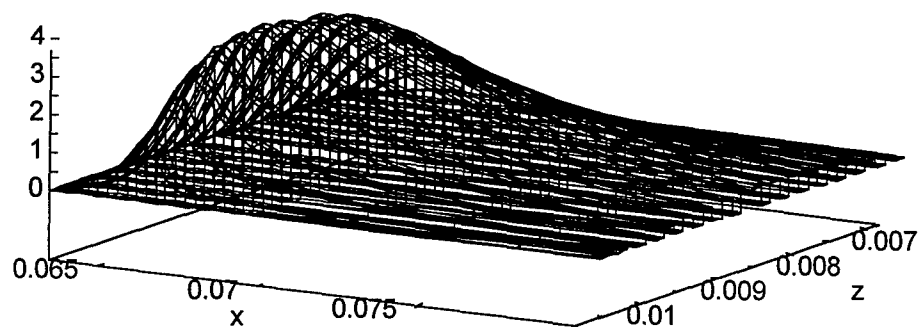


Figure 5-17 16-ply specimen cylindrical bending matrix failure metric in the top facesheet near the plate center for applied load that produced first major load drop in the three-dimensional indentation tests.

Elasticity solution
 Maximum stress matrix failure metric 32-ply, $R_{\text{contact}}=3.08$ mm, $q_0=403$ MPa, $F_0 = 8000$ N



Lee matrix failure metric



Hashin matrix failure metric

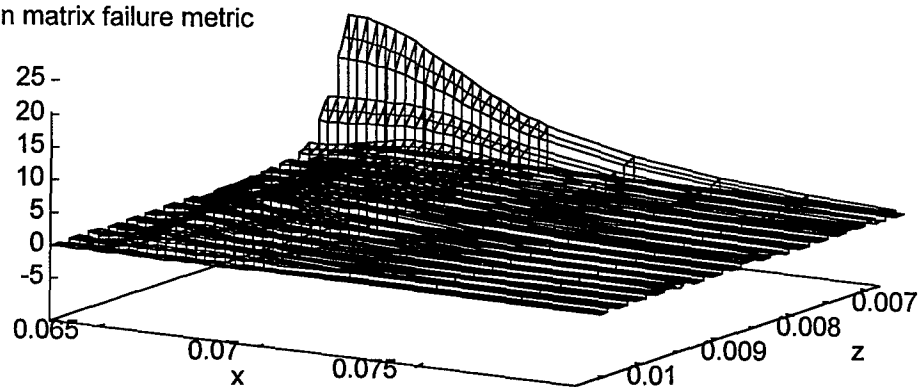
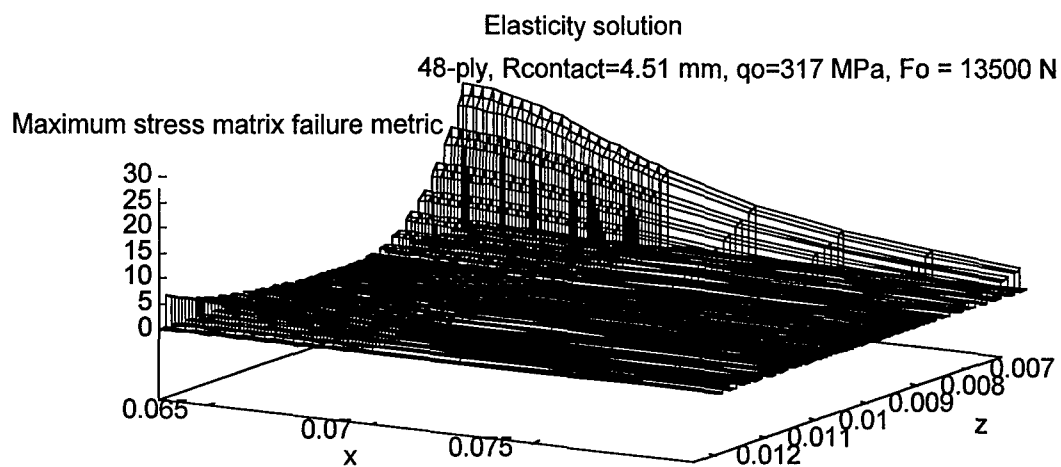
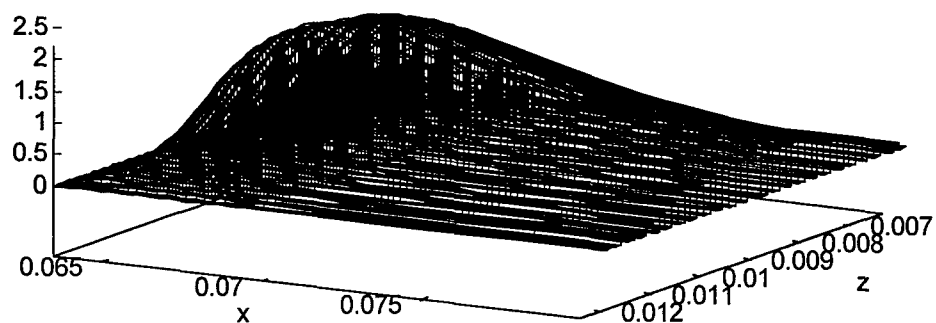


Figure 5-18 32-ply specimen cylindrical bending matrix failure metric in the top facesheet near the plate center for applied load that produced first major load drop in the three-dimensional indentation tests.



Lee matrix failure metric



Hashin matrix failure metric

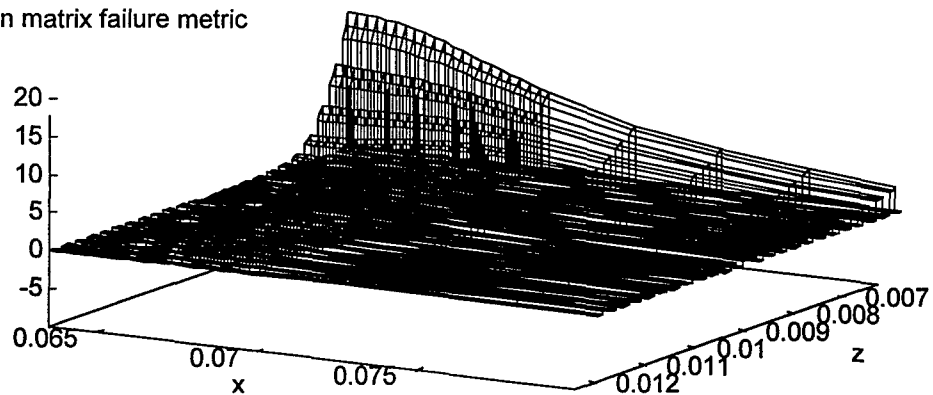


Figure 5-19 48-ply specimen cylindrical bending matrix failure metric in the top facesheet near the plate center for applied load that produced first major load drop in the three-dimensional indentation tests.

Using the photomicrographs from the experimental work by Harrington [5], direct comparison between matrix failure metric and experimentally observed matrix cracking can be made. In particular, the figure numbers for the photomicrographs in Harrington's thesis that correspond to the matrix failure metrics in the present figures 5-15 through 5-19 are given in table 5-1. Harrington's photomicrographs are included here as figures 5-20 through 5-33. The comparison between the experimental cross sections and the matrix failure metrics applied to the elasticity solution reveals several important features of the three failure criteria and was the basis for the choice of matrix failure criterion for the work of Chapter 6.

Specimen	Failure metric figure	Harrington figures	Cross-section figures
4-ply	5-15	3.9, 3.10, 3.11	5-20, 5-21, 5-22
8-ply	5-16	3.47, 3.48	5-23, 5-24, 5-25
16-ply	5-17	3.90, 3.91	5-26, 5-27, 5-28
32-ply	5-18	3.119, 3.120	5-29, 5-30, 5-31
48-ply	5-19	3.161, 3.162	5-32, 5-33

Table 5-2 Cylindrical bending matrix failure metric figures with their experimental counterparts.



Figure 5-20 Part A of 0° cross section of 4-ply specimen after 1.4 J impact (25X). From [5] figure 3.9. Label D identifies a matrix crack and label I identifies a failed core cell wall.

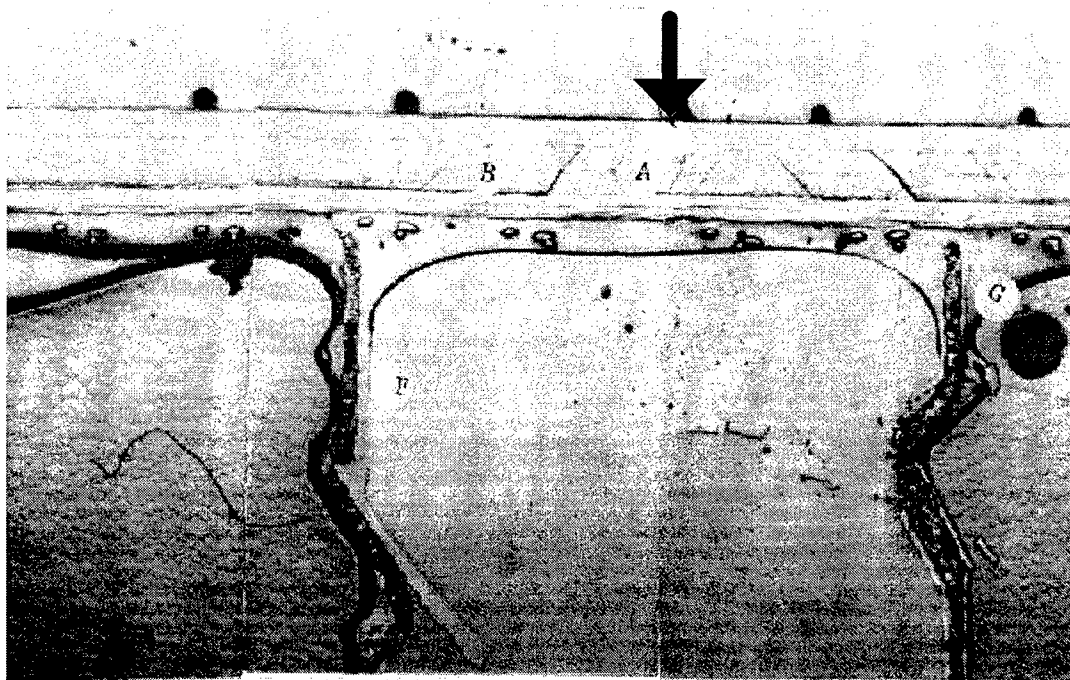


Figure 5-21 Part B of 0° cross section of 4-ply specimen after 1.4 J impact (25X). From [5] figure 3.10. Label B identifies matrix cracks with a delamination. Label A identifies nearly vertical matrix cracks. The arrow shows the approximate x-location of the point of impact and labels F and G identify failed core cell walls adjacent to the point of impact.

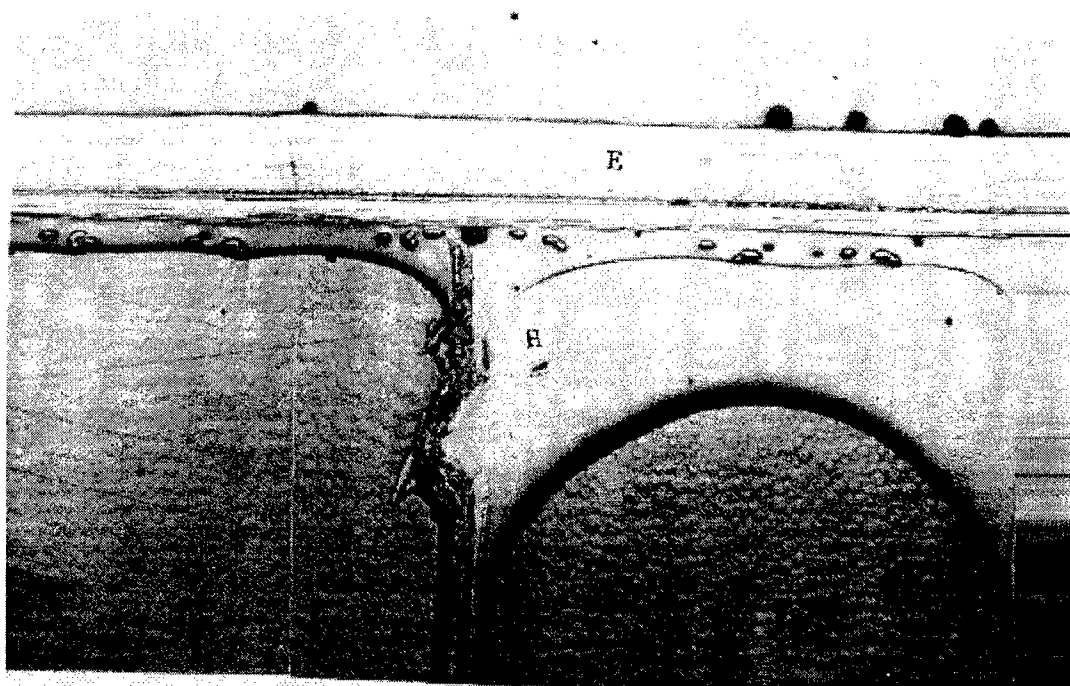


Figure 5-22 Part C of 0° cross section of 4-ply specimen after 1.4 J impact (25X). From [5] figure 3.11. Label E identifies matrix cracks and label H identifies a failed core cell wall.

For the 4-ply case, Harrington's minimum impact energy of 1.4 J was well above the damage initiation impact energy of 0.3 J found in the present work for this facesheet thickness. This was presumably due to the fact that Harrington used the drop weight impact test system exclusively and could therefore not get data at impact energies low enough to resolve initiation of damage in the 4- and 8-ply specimens. The result is that damage is already well developed in the specimen shown in Harrington's micrographs. Harrington observed matrix cracking in the center two plies as all of the failure metrics predict in figure 5-14. Harrington observed extensive matrix cracking from the point of impact out to approximately 5 mm to either side. The peaks of all three failure metrics extend over a similar 5 mm range from the center. The widest of the cracks seen in Harrington's micrographs are located approximately 0.7 mm from the point of impact. This is very near the peaks of the Lee and Hashin failure metrics, while maximum stress finds a peak at the center. By this then, matrix cracking in the 4-ply experiment appears to be dominated by shear and Lee and Hashin do equally well at predicting its location and extent. The 4-ply experimental data thus reduces the field of candidate failure criteria from three to two.

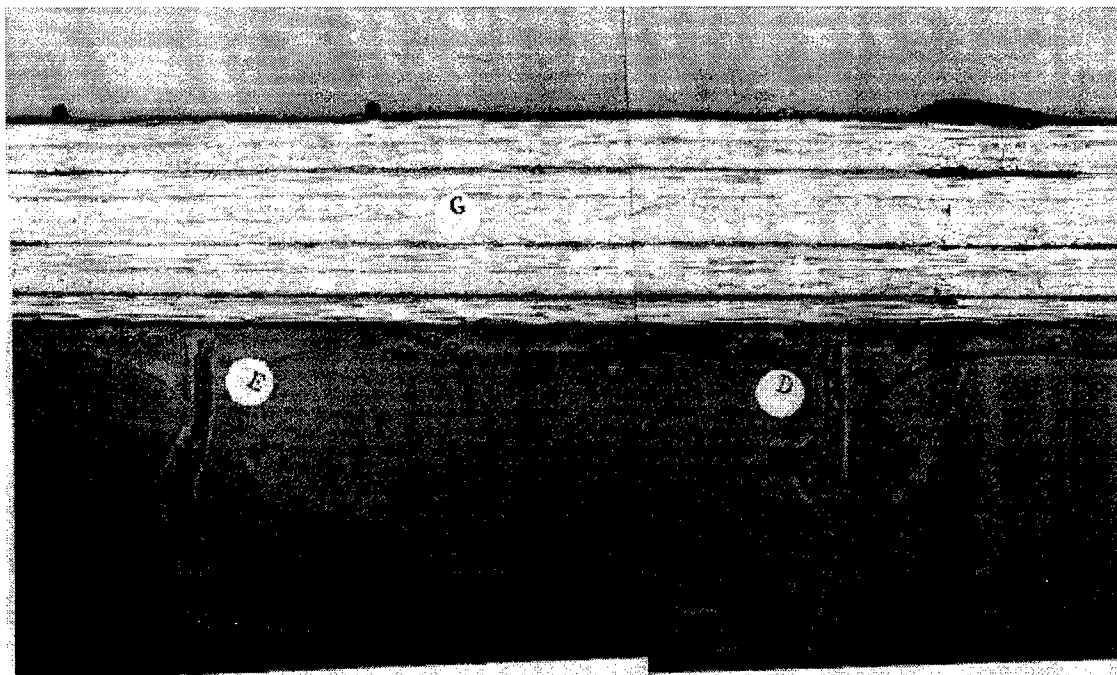


Figure 5-23 Part A of 0° cross section of 8-ply specimen after 2.7 J impact (25X). From [5] figure 3.47. Label G identifies matrix cracks and labels E and D identify failed core cell walls.

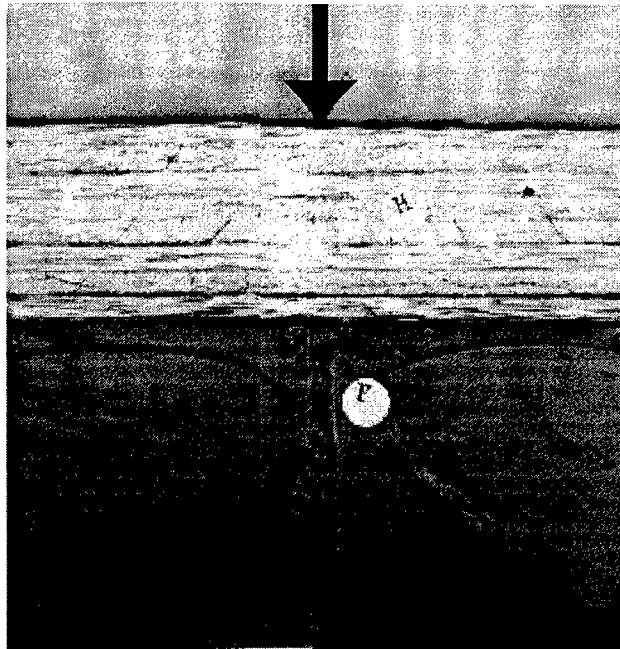


Figure 5-24 Part B of 0° cross section of 8-ply specimen after 2.7 J impact (25X). From [5] figures 3.47 and 3.48. The arrow shows the approximate x-location of the point of impact. Label H identifies matrix cracks and label F identifies a failed core cell wall under the point of impact.

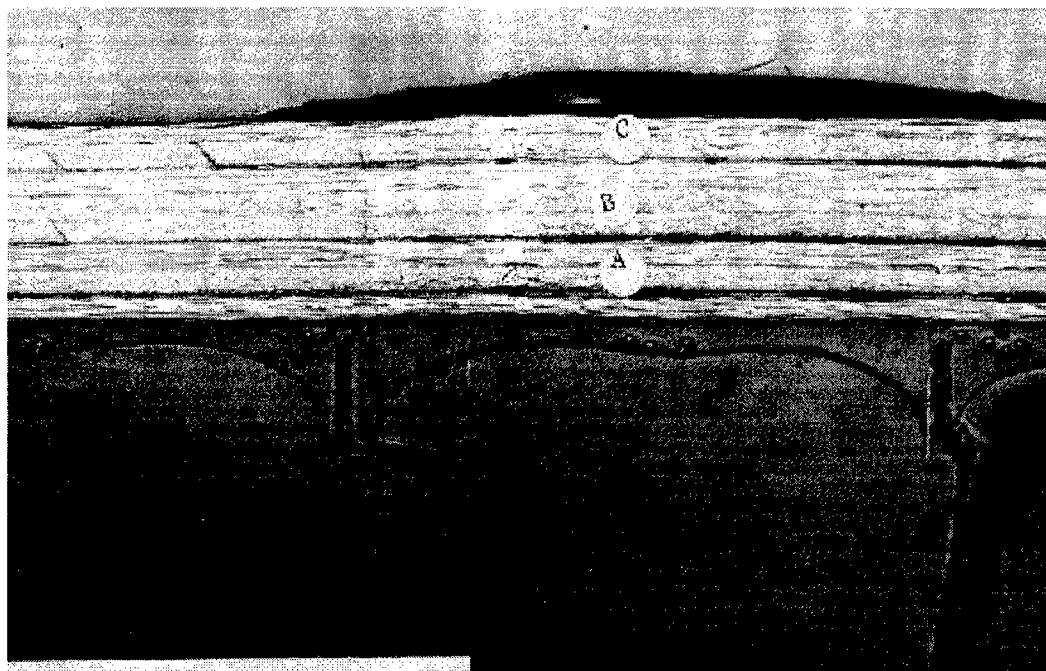


Figure 5-25 Part C of 0° cross section of 8-ply specimen after 2.7 J impact (25X). From [5] figure 3.48. Labels C, B, and A identify major delaminations.

For the 8-ply case (figures 5-23 through 5-25), Harrington's minimum impact energy of 2.7 J was also well above the damage initiation impact energy of 0.5 J found in the present work for this facesheet thickness. Again, the drop weight impact test system's impact energy lower limit is to blame. The result is that damage is already well developed in the specimen shown in Harrington's micrographs. Harrington observed matrix cracking in the four 90° plies as both Lee and Hashin failure metrics predict in figure 5-15. Maximum stress fails to predict matrix cracking in the lower 90° plies. The cracks observed in Harrington's micrographs extend from about 1 mm to about 4 mm from the point of impact on either side. Again the peaks of the Lee and Hashin failure metrics have a very similar range. Maximum stress, with its characteristic center peak, does not compare well in this respect either. It is concluded from this then, that matrix cracking in the 8-ply experiment, as in the 4-ply, appears to be dominated by shear and Lee and Hashin do equally well at predicting its location and extent. The 8-ply experimental data thus confirms the conclusion drawn from the 4-ply data that maximum stress is not an appropriate criterion in this situation, but still does not distinguish between Lee and Hashin, both do equally well.

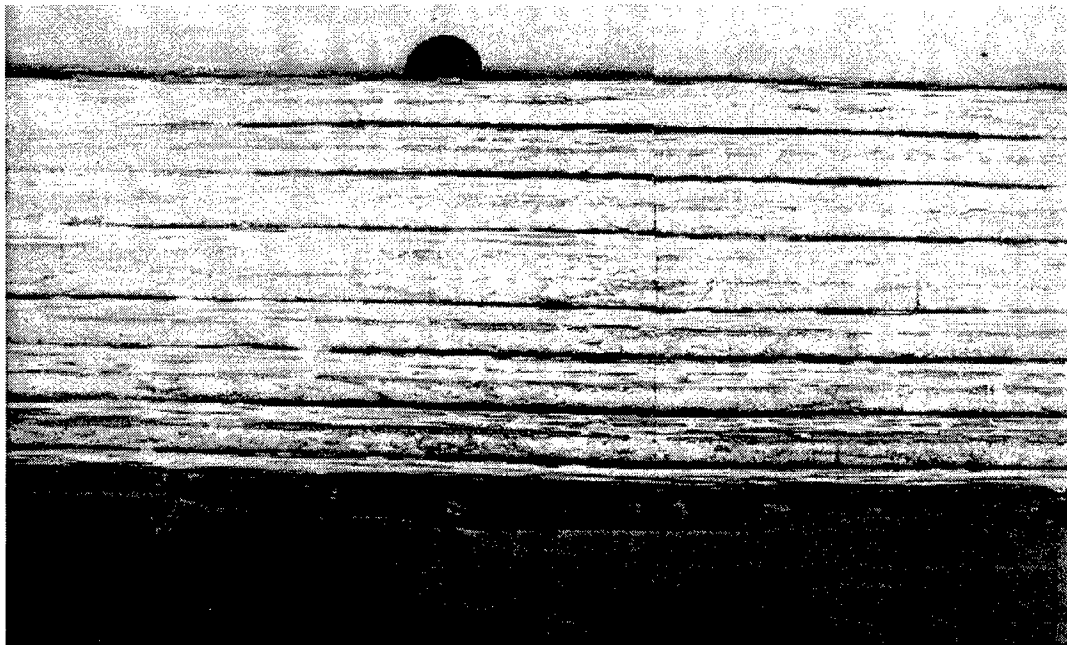


Figure 5-26 Part A of 0° cross section of 16-ply specimen after 4.1 J impact (25X). From [5] figure 3.90.



Figure 5-27 Part B of 0° cross section of 16-ply specimen after 4.1 J impact (25X). From [5] figures 3.90 and 3.91. The arrow identifies the approximate location of the impact point.

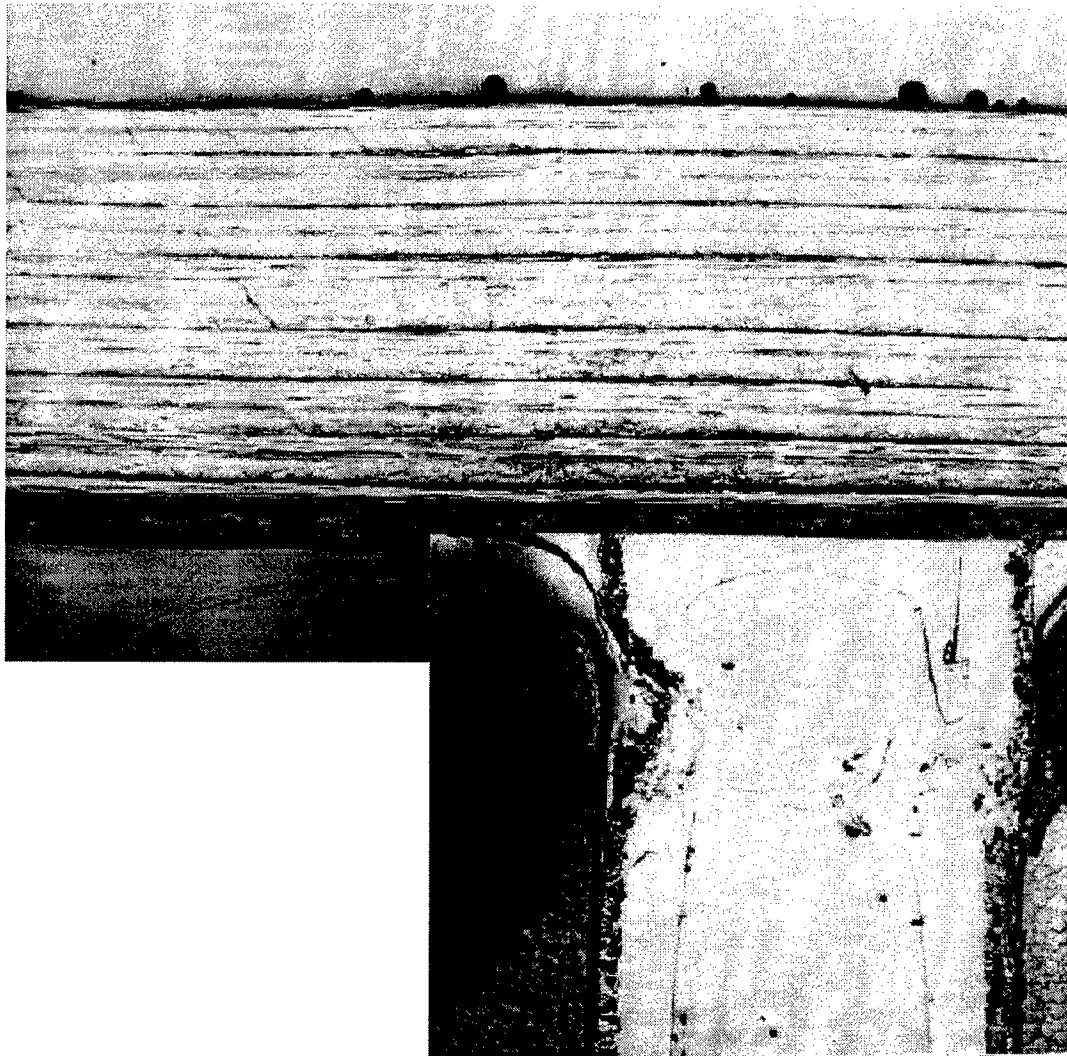


Figure 5-28 Part C of 0° cross section of 16-ply specimen after 4.1 J impact (25X). From [5] figure 3.91.

For the 16-ply case (figures 5-26 through 5-28), Harrington's minimum impact energy of 4.1 J was still well above the damage initiation impact energy of 1.3 J found in the present work for this facesheet thickness. As a result, damage is already well developed in the specimen shown in Harrington's micrographs. Harrington observed matrix cracking in all eight 90° plies as both Lee and Hashin failure metrics predict in figure 5-16. Maximum stress fails to predict matrix cracking in three of the 90° plies near the midplane of the facesheet. The matrix cracks observed in Harrington's micrographs extend from about 1 mm to about 6 mm from the point of impact on either side. Again, the peaks of the Lee and Hashin failure metrics have a very similar range. As before, maximum stress, with its characteristic center peak, does not compare well in this respect either. The 16-ply case is the first case in which the difference between Lee and Hashin becomes significant. Lee, including only shear, is unaffected by the tensile in-plane stress in the lower

portion of the top facesheet. Hashin includes the effect of this tensile stress, but since the magnitude of the in-plane loads are exaggerated by the cylindrical bending assumption, this effect is exaggerated as well. It is concluded from this then, that matrix cracking in the 16-ply experiment, as in the 4- and 8-ply, appears to be dominated by shear and Lee is sufficient to predict its location and extent. The more elaborate Hashin criterion is may, in fact, be just as good or better given the correct stress field, but this can not be confirmed by the experimental data. Hashin suffers, perhaps unjustly, from the cylindrical bending assumption in this analysis, but more important is the fact that for the 16-ply data, the shear-based matrix cracking criterion of Lee has all the complexity required. Evidently, three-dimensional in-plane stresses in the actual test are not sufficient to initiate matrix cracking. The 16-ply experimental data thus confirms the conclusion drawn from the 4- and 8-ply data that maximum stress is not an appropriate criterion in this situation. The 16-ply cylindrical bending case distinguishes between Lee and Hashin for the first time and shows that Lee does well at predicting the location and extent of matrix cracking.

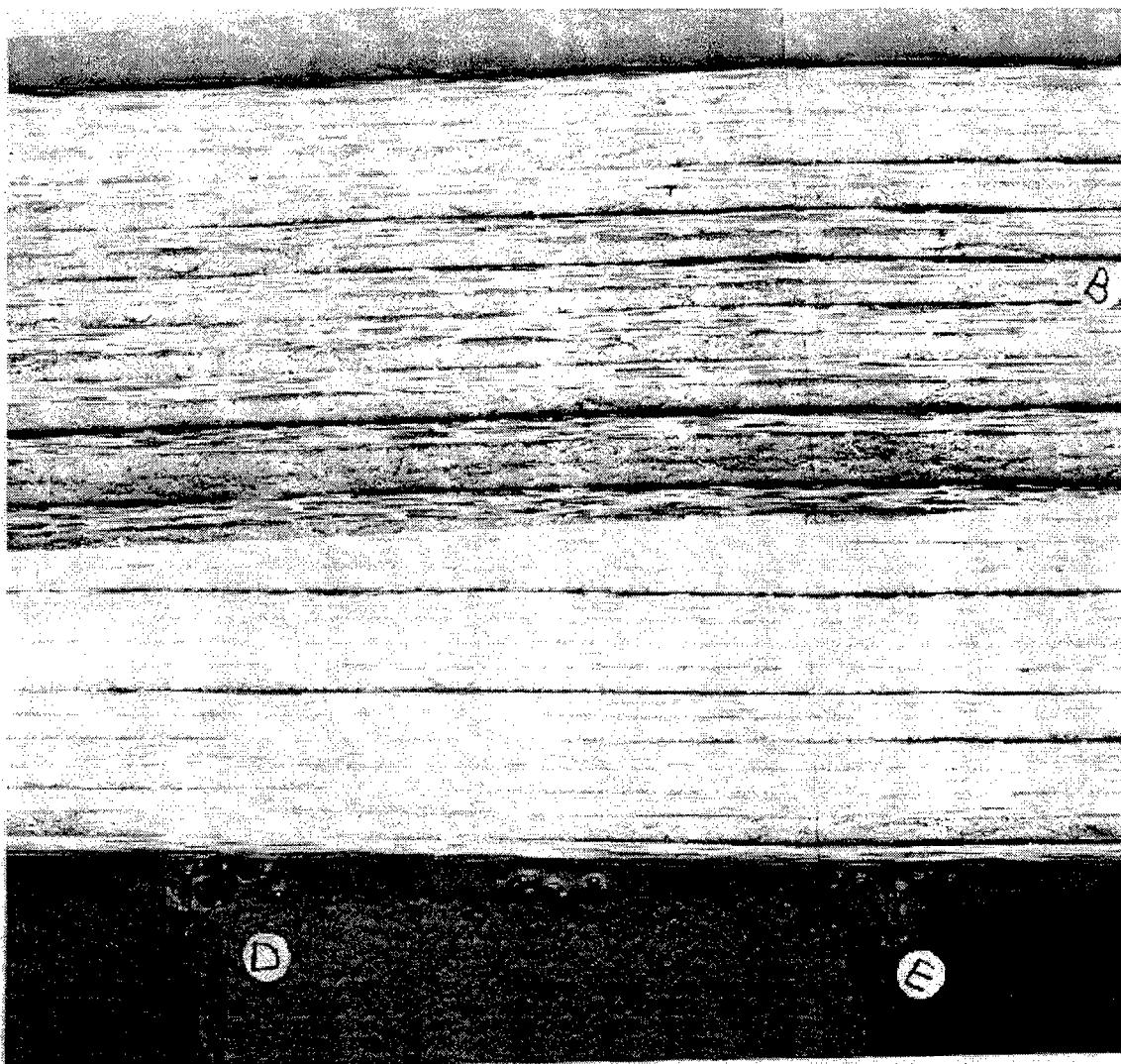


Figure 5-29 Part A of 0° cross section of 32-ply specimen after 5.0 J impact (25X). From [5] figure 3.119. Label B identifies matrix cracks and labels D and E identify failed core cell walls.



Figure 5-30 Part B of 0° cross section of 32-ply specimen after 5.0 J impact (25X). From [5] figure 3.120. The arrow identifies the approximate location of the impact point.

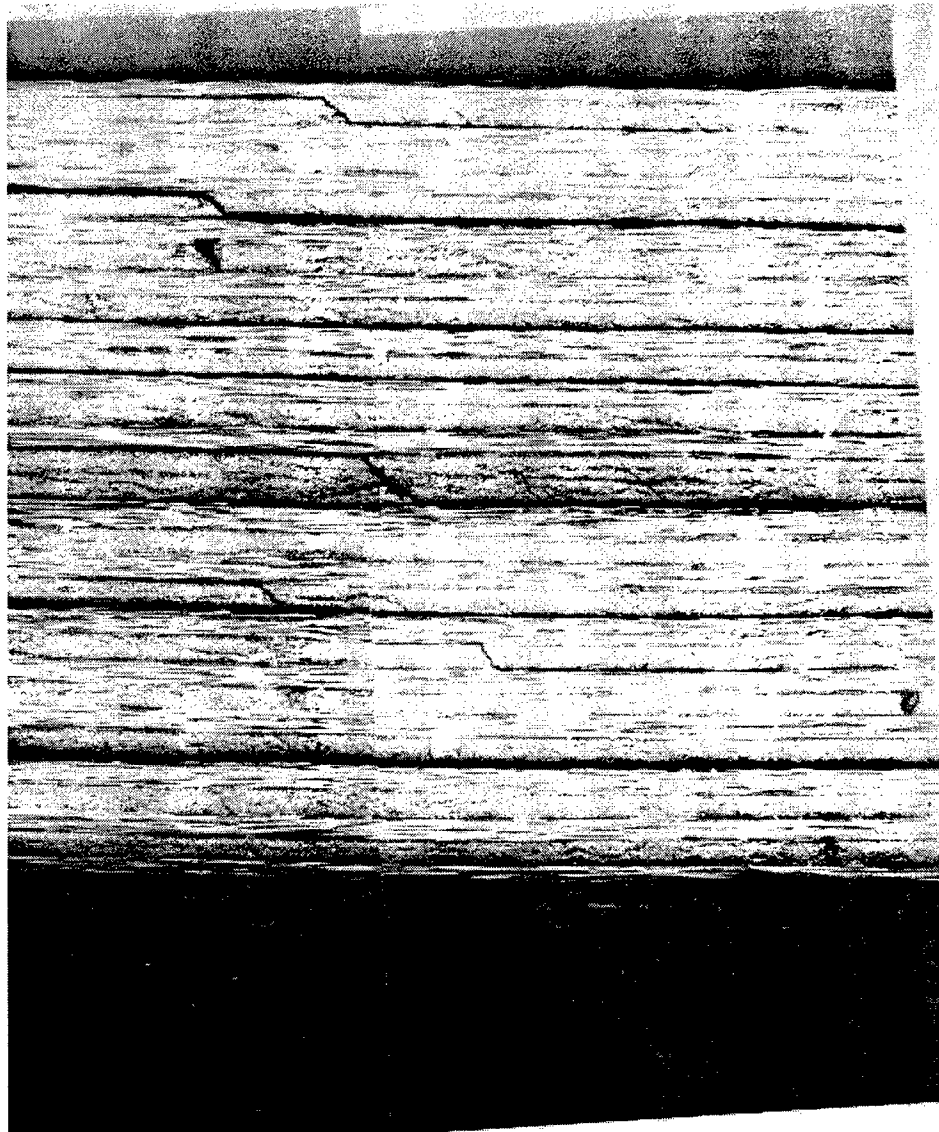


Figure 5-31 Part C of 0° cross section of 32-ply specimen after 5.0 J impact (25X). From [5] figure 3.120.

For the 32-ply case (figures 5-29 through 5-31), Harrington's minimum impact energy of 5 J was the same as the damage initiation impact energy of 5 J found in the present work for this facesheet thickness. As a result, damage in the specimen shown in Harrington's micrographs can be considered the initial damage for the first major load drop. Harrington observed matrix cracking in most of the 90° plies as both Lee and Hashin failure metrics predict in figure 5-17. Maximum stress fails to predict matrix cracking in the 90° plies near the midplane of the facesheet. The matrix cracks observed in Harrington's micrographs extend from about 2.5 mm to about 5 mm from the point of impact on either side. The peaks of the Lee failure metric has a very similar range. As for the thinner facesheets, maximum stress, with its characteristic center peak, does not compare well in

this respect either. For the cylindrical bending solution of the 32-ply case, the in-plane tensile loads in the lower portion of the top facesheet (figure 5-7) have become so significant that even the 90° plies carry enough load to produce matrix cracking as seen in the Hashin metric in figure 5-17. This has no correspondence to the actual three-dimensional experiment. The discussion in the 16-ply case concerning the comparison between Lee and Hashin applies here as well. It is concluded from this then, that matrix cracking in the 32-ply experiment, as in the thinner facesheets, appears to be dominated by shear and Lee is sufficient to predict its location and extent. The 32-ply experimental data thus confirms the conclusion drawn from the thinner facesheet data that maximum stress is not an appropriate criterion in this situation. The 32-ply cylindrical bending case shows that Lee does well at predicting the location and extent of matrix cracking.

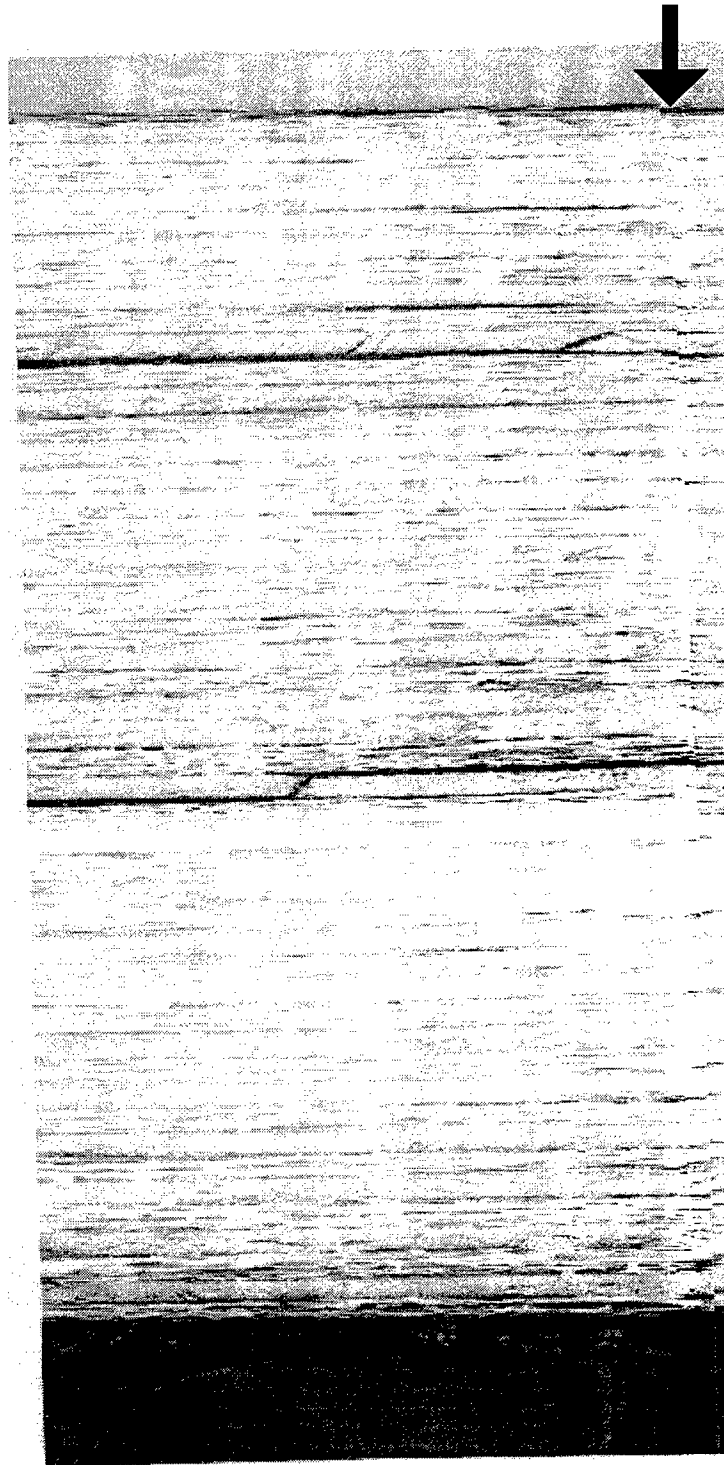


Figure 5-32 Part A of 0° cross section of 48-ply specimen after 9.7 J impact (25X). From [5] figure 3.161. The arrow identifies the approximate location of the impact point.



Figure 5-33 Part B of 0° cross section of 48-ply specimen after 9.7 J impact (25X). From [5] figure 3.162.

For the 48-ply case (figures 5-32 and 5-33), Harrington's maximum impact energy of 9.7 J was just below the impact energy of 10.7 J found to produce the first major load drop in the present work for this facesheet thickness. As a result, the damage in the specimen shown in Harrington's

micrographs is damage that occurs before the first major load drop. It is for this reason even more interesting than the thinner facesheet micrographs because the damage is less developed. This data shows that before the major energy absorbing damage, matrix cracking and delamination are present in the 48-ply specimens while core failure is not. This supports the conclusion of Chapter 4 that core failure precipitates the major energy absorbing processes in low-velocity impact to composite sandwich plates. Harrington observed matrix cracking in and near the center-most 90° plies as the peak of the Lee failure metric predicts in figure 5-18. The matrix cracks observed in Harrington's micrographs are located at about 3 mm from the point of impact on either side. The peaks of the Lee failure metric are at very nearly the same location (see the peak in the shear stress in figure 5-8). The discussion in the 16-ply case concerning the comparison between Lee and Hashin applies here as well. It is concluded from this then, that matrix cracking in the 48-ply experiment, as in the thinner facesheets, appears to be dominated by shear and Lee is sufficient to predict its location.

Three different delamination failure criteria were considered to predict damage to the facesheets. These are: maximum transverse tensile stress, Lee [66], and Hashin [242]. Maximum transverse tensile stress could be immediately eliminated as a candidate because the transverse direct stress in the analysis was consistently compressive. The other two are given for the cylindrical bending case in equation 5-23.

$$\begin{array}{ll}
 \text{Lee [66]:} & \text{Hashin [242]:} \\
 & \text{case } \sigma_3 > 0, \\
 \left(\frac{\tau_{xz}}{S} \right)^2 \geq 1 & \left(\frac{\sigma_3}{Y_t} \right)^2 + \left(\frac{\tau_{xz}}{S} \right)^2 \geq 1 \quad (5-23) \\
 & \text{case } \sigma_3 < 0, \\
 & \left(\frac{\tau_{xz}}{S} \right)^2 \geq 1
 \end{array}$$

For the case in which the transverse direct stress is compressive, all three criteria give the same metric at the interfaces of 0° and 90° plies as the Lee criteria for matrix cracking. Thus the Lee matrix failure metric, the Lee delamination failure metric, and the Hashin delamination failure metric are identical at the interfaces of 0° and 90° plies in the cylindrical bending case. The cylindrical bending results then, can obviously not be used to distinguish between these failure

criteria and judge which is best. A general comment can be made that delaminations and matrix cracking observed in Harrington's data happened together and generally at the same locations, though delaminations extended further from the point of application of the load. Since 1) the Lee matrix cracking criterion appears to correctly predict matrix cracking, and 2) matrix cracking and delaminations happen together, and 3) it is the same as these delamination criteria, it stands to reason that these criteria correctly predict delamination in the cylindrical bending case.

Prediction of core failure could be based upon a maximum stress criterion. The issue to be resolved then, would be the value of strength to be used in that criterion. The criterion is:

$$\left(\frac{\sigma_z}{Z_c} \right)^2 \geq 1 \quad (5-24)$$

Figure 5-5 indicates that using the uniaxial compression strength in the criterion may predict core failure at a load that is an order of magnitude too small. The apparent core strength depends on the facesheet thickness as shown in figure 5-6. This is not a problem, from the point of view of the analyst, as long as empirical data exists for the given core and facesheet thickness. The strengths of figure 5-6, the core failure metric defined as the left hand side of equation (5-24), and the cylindrical bending solution with the applied load that produced the first major load drop in the experiments, were used together to produce an estimate of the core failure metric distribution just prior to core failure. The value of the metric at the center of the specimen is plotted through the thickness in figure 5-34. The value of the metric at the top of the core is plotted as a function of the in-plane coordinate in figure 5-35.

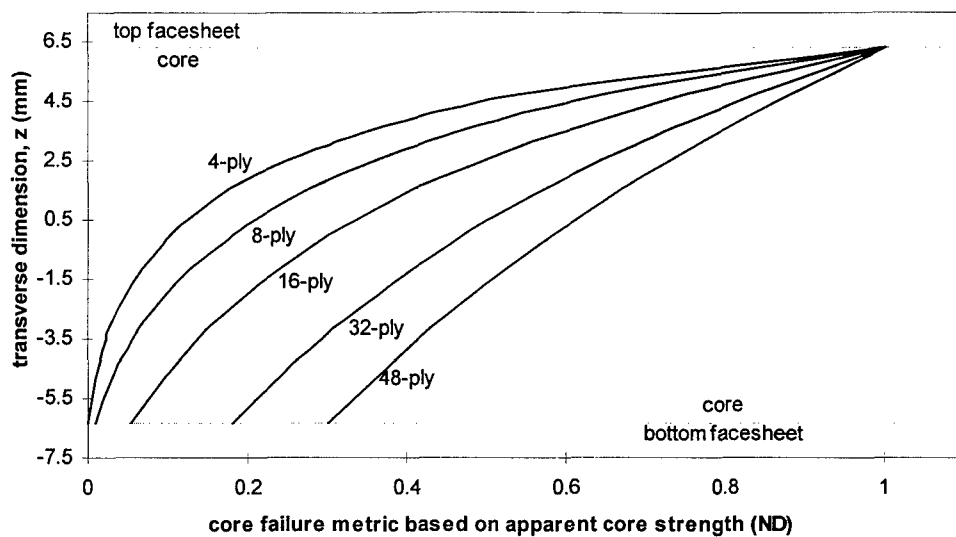


Figure 5-34 Core failure metric at the center of the specimen for the applied load that produced first major load drop. This shows that the strengths of figure 5-5 effectively normalize the metric to unity at the top of the core when the first major load drop occurs.

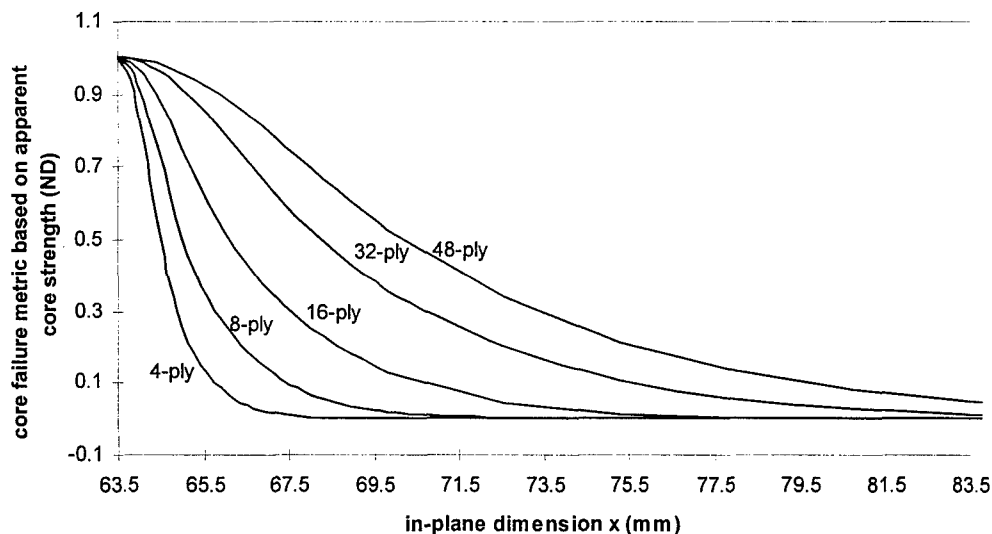


Figure 5-35 Core failure metric at the top of the core for the applied load that produced first major load drop. This shows that the strengths of figure 5-5 effectively normalize the metric to unity at the center of the specimen when the first major load drop occurs.

The cylindrical bending elasticity solution has been shown to be a useful tool for qualitatively judging some of the failure criteria which will be needed to predict damage in composite sandwich plates subjected to low-velocity impact. In addition, the cylindrical bending elasticity solution has proven to be a valuable tool for interpreting experimental data because it relates the internal stresses in a cylindrical bending model to the externally applied load in the experiment. This allows the analyst to relate the load applied to the damage resulting in a meaningful way. The effects of

different material properties, dimensions, and loads can be quickly estimated from an exact cylindrical bending elasticity solution similar to the three-dimensional problem of interest. Of course, if a beam or strip were of interest rather than a center loaded plate, the solution could prove even more valuable.

5.3 Three-Dimensional Solution to Hertzian Loaded Plate

The difficulties found in relating a cylindrical bending solution to a truly three-dimensional problem could have been avoided if a true three-dimensional elasticity solution was available. Such a solution for a rectangular sandwich plate under a sinusoidal loading does indeed exist [237]. This solution is a valuable tool for benchmarking the finite element analysis, and is used for that purpose in Chapter 7. A Mathcad template was written to carry out the very burdensome manipulations and is included in Appendix A. The low-velocity impact problem differs from the sinusoidally loaded plate chiefly in the relative area over which the load is applied. The Fourier series representation of the Hertzian contact load used in the cylindrical bending solution suggests the possibility of applying a double Fourier series to the three-dimensional plate to approximate the contact load. This is nothing more than extending the cylindrical bending solution to a third dimension. In theory, it sounds like a great idea whose time has come. In practice, there are some difficulties. The coding of the solution is an extension of the program ETSPFL written for the cylindrical bending solution. A FORTRAN program called PAG3D was written using, as much as possible, variable names that suggest what they represent in Pagano's paper [237]. PAG3D is included in Appendix B and its output is compared to the finite element solution in Chapter 7. A severe limitation to the usefulness of the three-dimensional solution for low-velocity impact problems is that when the large number of odd Fourier terms needed to accurately represent a Hertzian contact load was used the matrix solver failed due to the fact that the coefficient matrix became numerically singular. The solution procedure outlined in this chapter effectively limited the number of odd Fourier terms that could be used to represent the Hertzian load to eight in each in-plane direction or 64 total terms. It is possible that a modified procedure in which the direct matrix inversion of equation 5-15 was avoided could relieve this limitation, but such a procedure was not attempted for this research. The actual maximum number of odd Fourier terms was larger for thin facesheet sandwiches (11x11) and even larger for thin monolithic laminates (25x25) but was considered inadequate to represent the load which was applied experimentally. The loads are shown in figure 5-36.

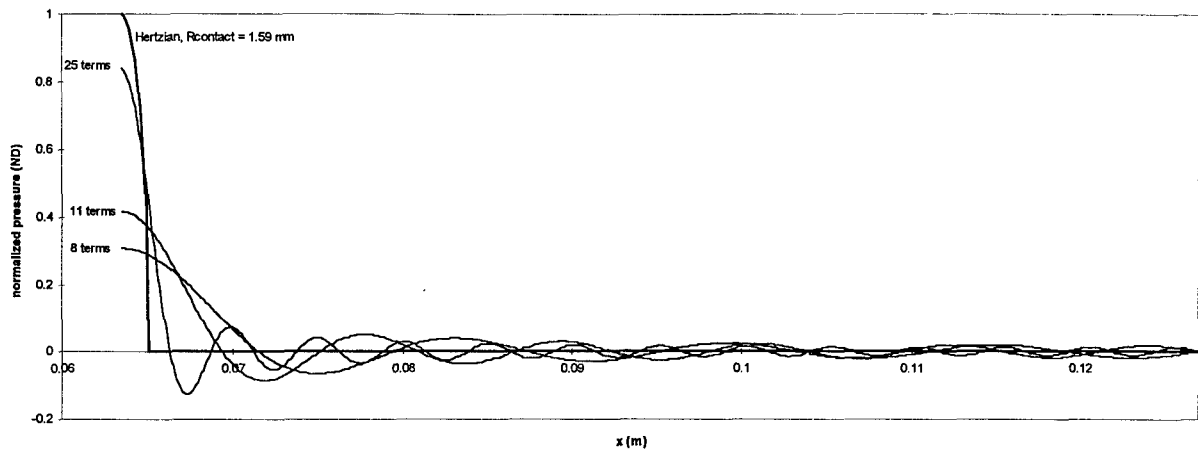


Figure 5-36 Truncated Fourier sine series representations of Hertzian contact with 1.59 mm contact radius showing poor representation of loading with the number of terms for which a three-dimensional solution was available. The maximum number of terms for a sandwich was 11 (4-ply).

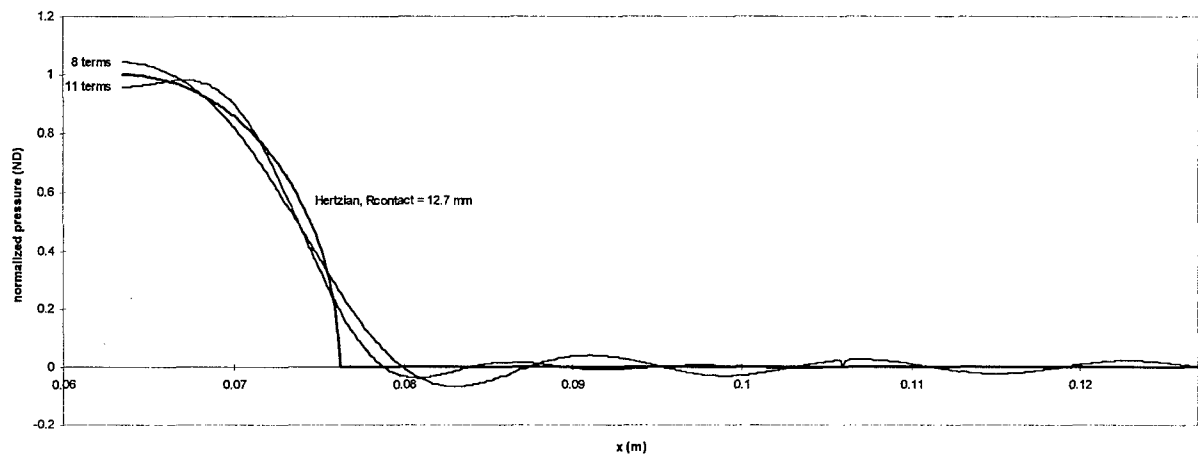


Figure 5-37 Truncated Fourier sine series representations of Hertzian contact with 12.7 mm contact radius showing marginal representation of loading with the number of terms for which a three-dimensional solution was available.

A Hertzian load that could be marginally well represented by a Fourier series truncated to a few terms is shown in figure 5-37. The contact radius of this load is 12.7 mm. This large contact radius implied an unrealistic tup radius (many meters) rather than the 12.7 mm actual tup radius. In short, the three-dimensional elasticity solution could not be used to interpret experimental data as the cylindrical bending elasticity solution was, because the contact radius of the two could not be matched. Without matching contact radii, the applied pressure (and hence σ_z) could not be matched. Thus, any comparison between the experiment and the analysis would be meaningless. Even so, the three-dimensional elasticity solution with this large contact radius did provide a benchmark for the

finite element code because the loading on the finite element model could be matched to the truncated Fourier series for which the three-dimensional elasticity problem could be solved. The two are compared in Chapter 7.

5.4 Conclusions

The elasticity solution is a useful tool for developing a general understanding of the characteristics of the stress field produced in a composite sandwich plate by a contact type load. It has been used to choose an appropriate criteria for matrix cracking and delamination. While the three-dimensional solution can only be used for unrealistically large contact radii, the cylindrical bending solution can be used for realistic contact dimensions.

6. Theory and Approach

As noted in Chapter 1, several elements of the present research involve novel approaches and/or extensions to the current state-of-the-art. The theoretical aspects of these are addressed first and the more practical aspects of including them in the analytical development are addressed afterward.

6.1 Sandwich Plate

While the majority of the literature on impact to composite laminates is focused on monolithic plates and shells, this research focused on sandwich plate constructions. The basic geometry and assumptions involved in sandwich plate analyses are here described.

6.1.1 Geometry and coordinate systems.

Figure 6.1 illustrates the geometry and coordinate systems which were used for modeling sandwich plates. The facesheets are composite laminates of arbitrary stacking sequence. The facesheets are perfectly bonded to an assumed homogeneous core of Nomex honeycomb. Both X-Y-Z (X_1 - X_2 - X_3) and L-T-Z represent orthogonal systems. The longitudinal and lateral directions correspond to the principal material directions of an orthotropic ply. As shown in figure 6-1, a ply's orientation angle θ is the angle from X to L (or from Y to T). All plates analyzed in this research were symmetric about their midplanes ($z=0$), that is, $\theta(z) = \theta(-z)$. This symmetry was chosen for convenience; it is not required by the theory.

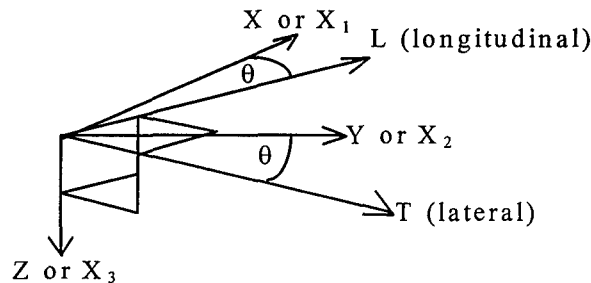
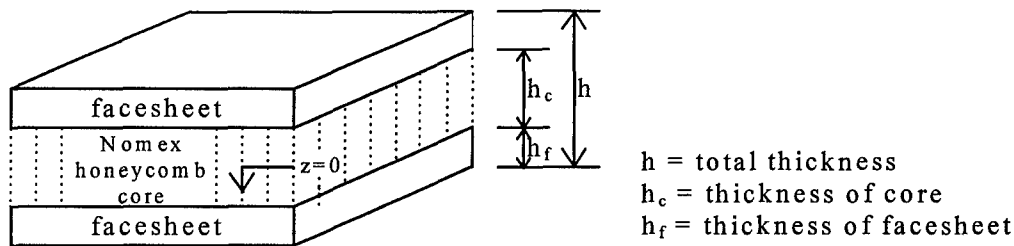


Figure 6-1 Sandwich plate geometry and coordinate systems.

6.1.2 Plate assumptions.

Several assumptions are inherent in most plate analyses and are retained or relaxed in the present research. These are here described. A plate is assumed to be in a state of plane stress at distances from the datum surface. As a result, all transverse normal stresses σ_z are zero, and plate behavior can be described by displacements and rotations at and relative to the midsurface. Transverse normal strains ϵ_z are nonzero in general, but they are consequences (due to Poisson effects) of the other strains and do not affect the stress state. Transverse shear strains ϵ_{xz} and ϵ_{yz} are assumed to have parabolic distributions in the Z -direction. This distribution satisfies the boundary conditions of zero transverse shear on the top and bottom plate surfaces.

6.2 Kinematics

6.2.1 Plate midplane displacements without delamination.

Various plate theories are available to describe the through-the-thickness variation of strains. Displacements of the midplane of the plate are used to characterize displacements throughout the plate. Polynomial functions of z are most often employed with the order of the theory based on the highest order polynomial present in the kinematics. The order of the transverse shear is typically one less than the order of the displacement function, so for example, a parabolic shear deformation theory will require cubic terms in the in-plane displacements. Parabolic shear deformation theory was used for this research due to its presumed ability to capture the most

important features of the transverse shear with relatively few degrees of freedom. Displacement functions for a few of the classical theories are described below leading to that used in this research.

6.2.1.1 Kirchhoff kinematics.

The Kirchhoff assumption is that straight lines originally normal to the undeformed middle surface remain straight and normal to that surface after deformation. In this case, a simple rotation of the plate normal takes place and the angle of rotation of the normal is the same as the slope of the midplane. Displacement functions through-the-thickness are linear functions of the through-the-thickness coordinate z :

$$\begin{aligned} u_1(x, y, z) &= u(x, y) + zw(x, y)_{,1} \\ u_2(x, y, z) &= v(x, y) + zw(x, y)_{,2} \\ u_3(x, y, z) &= w(x, y) \end{aligned} \tag{6-1}$$

where u , v , and w are the displacements of the midplane and $w_{,1}$ and $w_{,2}$ represent the first derivatives of w in the x - and y -directions respectively.

6.2.1.2 Reissner kinematics.

The Reissner assumption is that straight lines normal to undeformed middle surface remain straight (no warping) but not necessarily normal to that surface after deformation. In this case, a simple rotation of the plate normal takes place but the angle is generally different from the slope of the midplane $w_{,a}$. Displacement functions through-the-thickness are linear functions of the through-the-thickness coordinate z :

$$\begin{aligned} u_1(x, y, z) &= u(x, y) + z\psi_1(x, y) \\ u_2(x, y, z) &= v(x, y) + z\psi_2(x, y) \\ u_3(x, y, z) &= w(x, y) \end{aligned} \tag{6-2}$$

where u , v , and w are the displacements of the midplane, and ψ_1 and ψ_2 represent the bending rotations of a line element originally normal to undeformed middle surface about the y - and x -axes respectively. Of interest in these theories is their representation of transverse shear. The linearity of the displacement leads to a constant transverse shear (i.e. independent of z). With these kinematics, the only way to satisfy the boundary conditions of zero transverse shear on the top

and bottom surface is for transverse shear to be zero everywhere. Linear transverse shear has the same problem. This limitation leads to interest in cubic kinematics to represent parabolic transverse shear.

6.2.1.3 Parabolic Transverse Shear.

With this theory straight lines normal to undeformed middle surface remain neither straight nor normal to that surface after deformation.

$$\begin{aligned}u_1(x, y, z) &= u(x, y) + z\psi_1(x, y) + z^2\phi_1(x, y) + z^3\theta_1(x, y) \\u_2(x, y, z) &= v(x, y) + z\psi_2(x, y) + z^2\phi_2(x, y) + z^3\theta_2(x, y) \\u_3(x, y, z) &= w(x, y)\end{aligned}\tag{6-3}$$

in equation 6-3, ϕ_1 , θ_1 , ϕ_2 , and θ_2 are determined from the boundary conditions of zero transverse shear on the top and bottom surfaces of the plate. Using linear strain displacements for these, the transverse shear engineering strains are:

$$\begin{aligned}2\gamma_{13} &= u_{1,3} + u_{3,1} = \psi_1 + 2z\phi_1 + 3z^2\theta_1 + w_{,1} \\2\gamma_{23} &= u_{2,3} + u_{3,2} = \psi_2 + 2z\phi_2 + 3z^2\theta_2 + w_{,2}\end{aligned}\tag{6-4}$$

Setting these to zero on the top and bottom surface yields:

$$\begin{aligned}0 &= \psi_1 + h\phi_1 + \frac{3}{4}h^2\theta_1 + w_{,1} \\0 &= \psi_1 - h\phi_1 + \frac{3}{4}h^2\theta_1 + w_{,1} \\0 &= \psi_2 + h\phi_2 + \frac{3}{4}h^2\theta_2 + w_{,2} \\0 &= \psi_2 - h\phi_2 + \frac{3}{4}h^2\theta_2 + w_{,2}\end{aligned}\tag{6-5}$$

Solving for the four constants:

$$\begin{aligned}\phi_1 &= \phi_2 = 0 \\\theta_1 &= -\frac{4}{3h^2}(\psi_1 + w_{,1}) \\\theta_2 &= -\frac{4}{3h^2}(\psi_2 + w_{,2})\end{aligned}\tag{6-6}$$

Leading to the familiar flat plate, parabolic shear deformation theory displacement field:

$$\begin{aligned}
u_1(x,y,z) &= u + z\psi_1 + z^3k(\psi_1 + w_{,1}) \\
u_2(x,y,z) &= v + z\psi_2 + z^3k(\psi_2 + w_{,2}) \\
u_3(x,y,z) &= w \\
k &= -4 / (3h^2)
\end{aligned}
\tag{6-7}$$

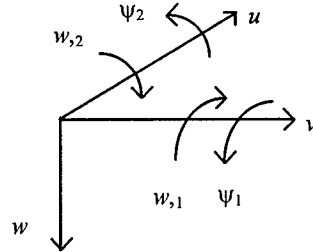


Figure 6-2 Plate displacement vector components.

Each point within the plate's midsurface has seven displacement components as shown in figure 6-2. Displacements u , v and w are translations in the X, Y and Z directions. The terms $w_{,1}$ and $w_{,2}$ are physical slopes of the midsurface in the X-Z and Y-Z planes, while ψ_1 and ψ_2 are rotations due to bending alone in those respective planes. Transverse shearing in a single plane is described by the algebraic sum of the two rotations. Translational displacements away from the midsurface are evaluated through the previous plate kinematics.

6.2.2 Plate midplane displacements with delamination.

In order to include delamination between plies within the element, there must be some means to independently describe the motion of the sublaminates above and below the delamination. New degrees of freedom could be included to allow the sublaminates to move independently. This independence could be accomplished by including Heaviside step functions in the kinematic expressions. Chattopadhyay and Gu [6] used this type of kinematic representation in their work. Additional displacement functions must be defined. The new degrees of freedom represent the displacement jumps across the delamination. Applying these ideas to the cubic kinematic equations (6-3) (before they are reduced) it is convenient to re-label the z coefficients in the displacements.

$$\begin{Bmatrix} U_{00} \\ V_{00} \\ W_0 \\ U_{01} \\ V_{01} \\ U_{02} \\ V_{02} \\ U_{03} \\ V_{03} \end{Bmatrix} \equiv \begin{Bmatrix} u \\ v \\ w \\ \psi_1 \\ \psi_2 \\ \phi_1 \\ \phi_2 \\ \theta_1 \\ \theta_2 \end{Bmatrix} \quad (6-8)$$

Where the U , V , and W are indicative of the directions X , Y , and Z while the subscript zero refers to the midplane and the second subscript of U and V identify the exponent of z in the kinematic expressions. That is, (U_{00}, V_{00}, W_0) are the displacements of a point (x,y) on the midplane and $(U_{0i}, V_{0i}; i=1,2,3)$ are the i^{th} order transverse shear correction terms. Let a delamination exist at a ply interface at $z = h_1$, and a point within the delamination be designated (x,y,h_1) . There will be a discontinuity of displacements (a jump) at the z location h_1 . The values of

the displacement jumps are labeled (U_{j0}, V_{j0}, W_j) where $j = \begin{cases} 1, h_1 < 0 \\ 2, h_1 > 0 \end{cases}$. As an example, for the

X -direction displacement, the value of the jump is U_{10} when the delamination is above the midplane and U_{20} when the delamination is below the midplane. These jumps are illustrated for X -direction displacement in figure 6-3.

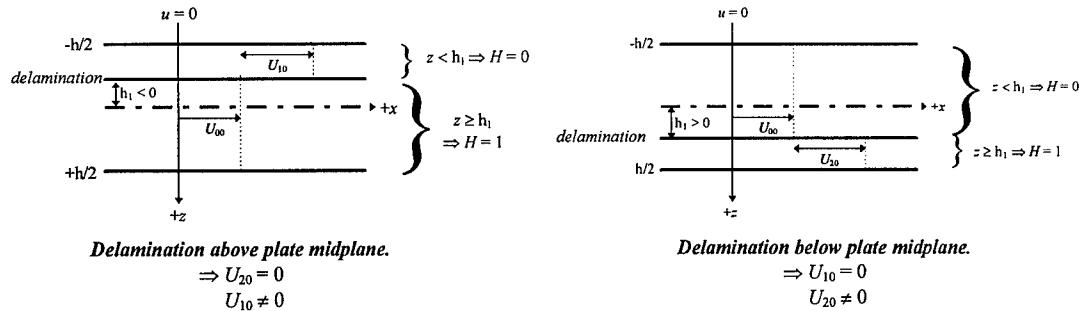


Figure 6-3 X-direction displacement jump across a delamination.

The correspondence between midplane displacements (U_{00}, V_{00}, W_0) and delamination displacement jumps (U_{j0}, V_{j0}, W_j) is direct. Similarly, define jumps for the i^{th} order transverse

shear correction terms as $(U_{ji}, V_{ji}; i=1,2,3; j=1,2)$. Displacements can be described as a function of z with the use of the Heaviside step function defined as

$$H = H(z - h_1) = \begin{cases} 1, z \geq h_1 \\ 0, z < h_1 \end{cases} \quad (6-9)$$

With these step functions multiplying the jump magnitudes, and providing for the delamination to be arbitrarily located ($h/2 > h_1 > -h/2$) either above or below the midplane, equations 6-3 are re-written for delamination as,

$$\begin{aligned} u_1 &= U_{00} + (1-H)U_{10} + HU_{20} + z(U_{01} + (1-H)U_{11} + HU_{21}) \\ &\quad + z^2(U_{02} + (1-H)U_{12} + HU_{22}) + z^3(U_{03} + (1-H)U_{13} + HU_{23}) \\ u_2 &= V_{00} + (1-H)V_{10} + HV_{20} + z(V_{01} + (1-H)V_{11} + HV_{21}) \\ &\quad + z^2(V_{02} + (1-H)V_{12} + HV_{22}) + z^3(V_{03} + (1-H)V_{13} + HV_{23}) \\ u_3 &= W_0 + (1-H)W_1 + HW_2 \end{aligned} \quad (6-10)$$

The values of these displacement jumps at the nodes will become degrees of freedom in the finite element model. Whereas equation 6-3 had nine coefficients (not all independent after boundary conditions are examined) equation 6-10 has 27. It is apparent that we have now tripled the degrees of freedom in the model. Actually, when a delamination is defined, it will have a specific z location (specified ply interface). The sublaminates containing the geometric midplane will have no jumps, hence only half of the new degrees of freedom will be active. Thus we have doubled, and not tripled the degrees of freedom in the delaminated region. One might ask what we have gained over simply modeling the delamination with two separate elements as Sankar and Rao [219]. The multiple element approach is certainly valid, but one must then know a priori where (between which plies and over what area) the delamination will take place. The new formulation can proceed without knowing the location of the delamination until the failure criterion indicates a particular location and interface, and it can simply activate degrees of freedom as they are required to model the progression of the delamination. Thus a more integrated, automated solution sequence is possible. In addition, the multiple element approach requires some method (such as a gap element) to ensure that the sublaminates do not pass through one another, while that problem is addressed more directly in the new formulation by specifying that certain degrees of freedom take on only non-negative values. For the present discussion, only one delamination was considered. Extension of the theory for multiple delaminations will prove

more cumbersome, but not more complicated. A single delamination is sufficient to demonstrate the merits (or lack thereof) of the method.

With the well-known modified von Karman plate (PSDT) kinematics it was possible to reduce the 9 displacement components to 7 by enforcing zero transverse shear on the plate surfaces. A similar approach is taken here, except that zero transverse shear is enforced on the top, bottom and both interior (above and below the delamination) surfaces. With the von Karman-type nonlinearity and the MACSYMA program [220, Appendix B], the transverse shear strains can be expressed in terms of the displacement components as:

$$\begin{aligned}\gamma_{13} &= (z^3(U_{23}\delta(z-h_1)-U_{13}\delta(z-h_1))+z^2(U_{22}\delta(z-h_1)-U_{12}\delta(z-h_1))+z(U_{21}\delta(z-h_1)-U_{11}\delta(z-h_1))+U_{20}\delta(z-h_1)-U_{10}\delta(z-h_1)+3z^2(U_{23}H(z-h_1)+U_{13}(1-H(z-h_1))+U_{03})+2z(U_{22}H(z-h_1)+U_{12}(1-H(z-h_1))+U_{02})+W_{2,1}H(z-h_1)+U_{21}H(z-h_1)+W_{1,1}(1-H(z-h_1))+U_{11}(1-H(z-h_1))+W_{0,1}+U_{01})/2 \\ \gamma_{23} &= (z^3(V_{23}\delta(z-h_1)-V_{13}\delta(z-h_1))+z^2(V_{22}\delta(z-h_1)-V_{12}\delta(z-h_1))+z(V_{21}\delta(z-h_1)-V_{11}\delta(z-h_1))+V_{20}\delta(z-h_1)-V_{10}\delta(z-h_1)+3z^2(V_{23}H(z-h_1)+V_{13}(1-H(z-h_1))+V_{03})+2z(V_{22}H(z-h_1)+V_{12}(1-H(z-h_1))+V_{02})+W_{2,2}H(z-h_1)+V_{21}H(z-h_1)+W_{1,2}(1-H(z-h_1))+V_{11}(1-H(z-h_1))+W_{0,2}+V_{01})/2\end{aligned}\quad (6-11)$$

In equation 6-11, 27 displacement components are included, U_{ij} , V_{ij} , and W_i ($i=0,1,3$; $j=0,1,2,3$). As mentioned above, locating the delamination (i.e. specifying the ply interface) will reduce these to 18. To illustrate this reduction, consider the delamination occurring in the lower facesheet of the plate (or anywhere below the midplane). Then,

$$U_{ij} = V_{ij} = W_i = 0 \quad (j=0,1,2,3) \quad (6-12)$$

which reduces the shear expressions to:

$$\begin{aligned}\gamma_{13} &= (z^3(U_{23}\delta(z-h_1))+z^2(U_{22}\delta(z-h_1))+z(U_{21}\delta(z-h_1))+U_{20}\delta(z-h_1)+3z^2(U_{23}H(z-h_1)+U_{03})+2z(U_{22}H(z-h_1)+U_{02})+W_{2,1}H(z-h_1)+U_{21}H(z-h_1)+W_{0,1}+U_{01})/2 \\ \gamma_{23} &= (z^3(V_{23}\delta(z-h_1))+z^2(V_{22}\delta(z-h_1))+z(V_{21}\delta(z-h_1))+V_{20}\delta(z-h_1)+3z^2(V_{23}H(z-h_1)+V_{03})+2z(V_{22}H(z-h_1)+V_{02})+W_{2,2}H(z-h_1)+V_{21}H(z-h_1)+W_{0,2}+V_{01})/2\end{aligned}\quad (6-13)$$

It is important to show that these reduce to equation 6-4 when delamination is not present, i.e. when $U_{2j} = V_{2j} = W_2 = 0$ for $(j=0,1,2,3)$. With these substitutions,

$$\begin{aligned}\gamma_{13} &= (3z^2(U_{03}) + 2z(U_{02}) + W_{0,1} + U_{01})/2 \\ \gamma_{23} &= (3z^2(V_{03}) + 2z(V_{02}) + W_{0,2} + V_{01})/2\end{aligned}\tag{6-14}$$

which is the same as equation 6-4 with the re-labeling defined by equation 6-8.

Evaluating equation 6-13 at $z=h/2$, $-h/2$, and h_1^+ , and h_1^- (the surfaces, including those of the delamination as well as the top and bottom of the plate) produces eight algebraic equations which are used to determine U_{02} , V_{02} , U_{22} , V_{22} , U_{03} , V_{03} , U_{23} , and V_{23} in terms of the other displacement components. In this way only 14 displacement components including $W_{0,1}$, $W_{2,1}$, $W_{0,2}$, and $W_{2,2}$ are required. Specifically, the dirac delta function has a value of zero throughout the laminate (its singularity is "in" the delamination) hence it can be ignored at all boundaries, and H has the following values at the boundaries:

$z=$	$-h/2$	h_1^-	h_1^+	$h/2$
$H=$	0	0	1	1

(6-15)

The transverse shears evaluated at the four boundaries are:

$$\begin{aligned}0 &= 3(-h/2)^2(U_{03}) + 2(-h/2)(U_{02}) + W_{0,1} + U_{01} \\ 0 &= 3(-h/2)^2(V_{03}) + 2(-h/2)(V_{02}) + W_{0,2} + V_{01} \\ 0 &= 3(h_1)^2(U_{03}) + 2(h_1)(U_{02}) + W_{0,1} + U_{01} \\ 0 &= 3(h_1)^2(V_{03}) + 2(h_1)(V_{02}) + W_{0,2} + V_{01} \\ 0 &= 3(h_1)^2(U_{23} + U_{03}) + 2(h_1)(U_{22} + U_{02}) + W_{2,1} + U_{21} + W_{0,1} + U_{01} \\ 0 &= 3(h_1)^2(V_{23} + V_{03}) + 2(h_1)(V_{22} + V_{02}) + W_{2,2} + V_{21} + W_{0,2} + V_{01} \\ 0 &= 3(h/2)^2(U_{23} + U_{03}) + 2(h/2)(U_{22} + U_{02}) + W_{2,1} + U_{21} + W_{0,1} + U_{01} \\ 0 &= 3(h/2)^2(V_{23} + V_{03}) + 2(h/2)(V_{22} + V_{02}) + W_{2,2} + V_{21} + W_{0,2} + V_{01}\end{aligned}\tag{6-16}$$

Writing these equations as a matrix equation in the displacement components to be eliminated,

$$\begin{bmatrix}
 h & k & & & & & & \\
 & & h & k & & & & \\
 -2h_1 & -3h_1^2 & & & & & & \\
 & & -2h_1 & -3h_1^2 & & & & \\
 -2h_1 & -2h_1 & -3h_1^2 & -3h_1^2 & & & & \\
 & & -2h_1 & -2h_1 & -3h_1^2 & -3h_1^2 & & \\
 -h & -h & k & k & & & & \\
 & & -h & -h & k & k & &
 \end{bmatrix}
 \begin{Bmatrix}
 U_{02} \\
 U_{22} \\
 U_{03} \\
 U_{23} \\
 V_{02} \\
 V_{22} \\
 V_{03} \\
 V_{23}
 \end{Bmatrix}
 =
 \begin{bmatrix}
 1 & & & & & & & \\
 & 1 & & & & & & \\
 & & 1 & & & & & \\
 & & & 1 & & & & \\
 1 & 1 & & & 1 & 1 & & \\
 & & 1 & 1 & & & 1 & 1 \\
 1 & 1 & & & 1 & 1 & & \\
 & & 1 & 1 & & & 1 & 1
 \end{bmatrix}
 \begin{Bmatrix}
 U_{01} \\
 U_{21} \\
 V_{01} \\
 V_{21} \\
 W_{0,1} \\
 W_{2,1} \\
 W_{0,2} \\
 W_{2,2}
 \end{Bmatrix}$$

$$k = -\frac{3h^2}{4}$$

(6-17)

In equation 6-17, the matrix on the left-hand-side is nonsingular, so that each of the eight displacement components on the left-hand-side can be expressed in terms of the eight displacement components on the right-hand-side. These substitutions (equation 6-17 solved for the vector on the left-hand-side) as well as those of equations 6-15 and 6-12 are made in equation 6-10 so that only 14 displacement components remain in the kinematics. The kinematic expressions are no longer polynomials in z due to the step functions (H). The new kinematic expressions as well as the 14 component displacement vector (q_H) are given in equation 6-18.

$$\begin{array}{ccc}
\begin{array}{c} \left\{ \begin{array}{c} u_1 \\ u_2 \\ u_3 \end{array} \right\} \\ 3 \times 1 \end{array} & = & \begin{array}{ccc} \begin{array}{c} 1 \\ 0 \\ 0 \\ z^2(k_1 + Hk_4) + z^3k_3(1-2H) \\ 0 \\ z + z^2(k_1 + Hk_4) + z^3k_3(1-2H) \\ 0 \\ H \\ 0 \\ 0 \\ z^2Hk_2 - z^3Hk_3 \\ 0 \\ zH + z^2Hk_2 - z^3Hk_3 \\ 0 \end{array} & \begin{array}{c} 0 \\ 1 \\ 0 \\ 0 \\ z^2(k_1 + Hk_4) + z^3k_3(1-2H) \\ 0 \\ z + z^2(k_1 + Hk_4) + z^3k_3(1-2H) \\ 0 \\ H \\ 0 \\ 0 \\ z^2Hk_2 - z^3Hk_3 \\ 0 \\ zH + z^2Hk_2 - z^3Hk_3 \end{array} & \begin{array}{c} 0 \\ 0 \\ 1 \\ 0 \\ 0 \\ 0 \\ 0 \\ 0 \\ H \\ 0 \\ 0 \\ 0 \\ 0 \end{array} \end{array} \begin{array}{c} \begin{array}{c} U_{00} \\ V_{00} \\ W_0 \\ W_{0,1} \\ W_{0,2} \\ U_{01} \\ V_{01} \\ U_{20} \\ V_{20} \\ W_2 \\ W_{2,1} \\ W_{2,2} \\ U_{21} \\ V_{21} \end{array} \\ 14 \times 1 \end{array} \begin{array}{c} \left. \begin{array}{c} \begin{array}{c} U_{00} \\ V_{00} \\ W_0 \\ W_{0,1} \\ W_{0,2} \\ U_{01} \\ V_{01} \end{array} \\ \begin{array}{c} U_{20} \\ V_{20} \\ W_2 \\ W_{2,1} \\ W_{2,2} \\ U_{21} \\ V_{21} \end{array} \end{array} \right\} \begin{array}{c} \text{midplane} \\ \text{displacements} \\ \\ \text{delamination} \\ \text{interface} \\ \text{displacement} \\ \text{jumps} \end{array} \end{array}
\end{array}
\quad (6-18)$$

q_H

$$k_1 = \frac{2h_1 - h}{2h_1h} \quad k_2 = -\frac{2h_1 + h}{2h_1h} \quad k_3 = \frac{2}{3h_1h} \quad k_4 = -\frac{2}{h}$$

in which the midplane and interface displacement vector q_H has been defined.

Equation 6-18 shows how the assumed kinematics relate the displacements everywhere within the delaminated plate to seven midplane displacement components and seven delamination displacement components. Importantly, all z dependence is included in the 3×14 matrix and all x and y dependence is included in the midplane and interface displacement vector on the right-hand-side. This decoupling should be exploited in the finite element stiffness matrix integration.

6.3 Strain-Displacement Relations

6.3.1 Full nonlinear strain displacement relations.

Full nonlinear Green strain displacement relations were not used in this analysis. It is required to consider what effects were neglected by the assumption of von Karman-type relations. The full nonlinear Green strain displacement relations in Cartesian coordinates are given in Saada [221, equations 6-3.3]. When the assumed kinematic relations (PSDT without delamination capability) are applied to them (using MACSYMA [220]) the following in-plane strains are the result (underlined terms are not included in the von Karman plate equations):

$$\begin{aligned}
\varepsilon_1 \equiv \varepsilon_{xx} &= \frac{(k(w_{,21} + \psi_{2,1})z^3 + \psi_{2,1}z + v_{,1})^2}{2} + \frac{(k(w_{,11} + \psi_{1,1})z^3 + \psi_{1,1}z + u_{,1})^2}{2} \\
&\quad + k(w_{,11} + \psi_{1,1})z^3 + \psi_{1,1}z + (w_{,1})^2/2 + u_{,1} \\
\varepsilon_2 \equiv \varepsilon_{yy} &= \frac{(k(w_{,22} + \psi_{2,2})z^3 + \psi_{2,2}z + v_{,2})^2}{2} + \frac{(k(w_{,12} + \psi_{1,2})z^3 + \psi_{1,2}z + u_{,2})^2}{2} \\
&\quad + k(w_{,22} + \psi_{2,2})z^3 + \psi_{2,2}z + (w_{,2})^2/2 + v_{,2} \\
\varepsilon_6 \equiv \gamma_{xy} &= 2((k(w_{,21} + \psi_{2,1})z^3 + \psi_{2,1}z + v_{,1})(k(w_{,22} + \psi_{2,2})z^3 + \psi_{2,2}z + v_{,2})/2 \\
&\quad + (k(w_{,21} + \psi_{2,1})z^3 + k(w_{,12} + \psi_{1,2})z^3 + \psi_{2,1}z + \psi_{1,2}z + v_{,1} + u_{,2})/2 + (k(w_{,11} + \psi_{1,1})z^3 \\
&\quad + \psi_{1,1}z + u_{,1})(k(w_{,12} + \psi_{1,2})z^3 + \psi_{1,2}z + u_{,2})/2 + w_{,1}w_{,2}/2)
\end{aligned} \tag{6-19}$$

6.3.2 Von Karman-type nonlinear strain displacement relations.

For this research, von Karman strain-displacement relations and parabolic shear deformation theory kinematics (equation 6-7) were used. Though the plate displacements are expected to be small, the deflections of the top surface of the plate in the contact region are not. In particular, the solution is expected to be improved by inclusion of the slopes of the midplane in the strain-displacement relations. The von Karman-type strain displacement relations are [172]:

$$\begin{aligned}
\varepsilon_1 &= u_{,1} + \frac{1}{2} w_{,1}^2 \\
\varepsilon_2 &= u_{,2} + \frac{1}{2} w_{,2}^2 \\
\varepsilon_6 &= u_{,1,2} + u_{,2,1} + w_{,1} w_{,2} \\
\varepsilon_4 \equiv \gamma_{yz} &= (1 + 3z^2 k)(w_{,2} + \psi_{2,2}) \\
\varepsilon_5 \equiv \gamma_{xz} &= (1 + 3z^2 k)(w_{,1} + \psi_{1,1})
\end{aligned} \tag{6-20}$$

Taking in-plane derivatives of equations 6-7,

$$\begin{aligned}
u_{1,1} &= u_{,1} + z\psi_{1,1} + z^3 k(\psi_{1,1} + w_{,11}) \\
u_{1,2} &= u_{,2} + z\psi_{1,2} + z^3 k(\psi_{1,2} + w_{,12}) \\
u_{2,1} &= v_{,1} + z\psi_{2,1} + z^3 k(\psi_{2,1} + w_{,12}) \\
u_{2,2} &= v_{,2} + z\psi_{2,2} + z^3 k(\psi_{2,2} + w_{,22}) \\
u_{3,1} &= w_{,1} \\
u_{3,2} &= w_{,2}
\end{aligned} \tag{6-21}$$

Substituting the assumed kinematic expressions into the von Karman strain displacement relations, the strains used in this analysis are expressed in terms of the displacement components as:

$$\begin{aligned}
\varepsilon_1 &= u_{,1} + z\psi_{1,1} + z^3 k(\psi_{1,1} + w_{,11}) + \frac{1}{2} w_{,1}^2 \\
\varepsilon_2 &= v_{,2} + z\psi_{2,2} + z^3 k(\psi_{2,2} + w_{,22}) + \frac{1}{2} w_{,2}^2 \\
\varepsilon_6 &= u_{,2} + v_{,1} + z(\psi_{1,2} + \psi_{2,1}) + z^3 k(\psi_{1,2} + \psi_{2,1} + 2w_{,12}) + w_{,1} w_{,2}
\end{aligned} \tag{6-22}$$

The differences between equations 6-19 and 6-22 are the underlined terms in equations 6-19. Neglecting these terms removes the higher order membrane effects. The nonlinear terms included are only the last term in each equation. The assumed nonlinearity allows that $w_{,1}$ and $w_{,2}$ are not so small that their squares and product are negligible while any other displacement derivatives are so small.

Before considering the strains resulting from delamination-capable kinematics, it is convenient at this point to rewrite equation 6-22 as an operator on the displacements. This notation will simplify the development of the equilibrium equations later on.

$$\begin{Bmatrix} \varepsilon_1 \\ \varepsilon_2 \\ \varepsilon_6 \end{Bmatrix} = \begin{bmatrix} \partial_1 & \frac{cu_{3,1}}{2} \partial_1 \\ & \partial_2 & \frac{cu_{3,2}}{2} \partial_2 \\ \partial_2 & \partial_1 & cu_{3,1} \partial_2 \end{bmatrix} \begin{Bmatrix} u_1 \\ u_2 \\ u_3 \end{Bmatrix} \tag{6-23}$$

where $\partial_\alpha = \partial/\partial x_\alpha$, $c = 1$ for von Karman strain displacement relations or $c = 0$ for linear strain displacement relations, and recognize from equation 6-18 that,

$$u_3 = W_0 + HW_2, \text{ so that } u_{3,1} = W_{0,1} + HW_{2,1} \text{ and } u_{3,2} = W_{0,2} + HW_{2,2} \tag{6-24}$$

equation 6-23 can then be rewritten for delamination-capable kinematics as,

$$\begin{Bmatrix} \varepsilon_1 \\ \varepsilon_2 \\ \varepsilon_6 \end{Bmatrix} = \begin{bmatrix} \partial_1 & 0 & 0 \\ 0 & \partial_2 & 0 \\ \partial_2 & \partial_1 & 0 \end{bmatrix} \begin{Bmatrix} u_1 \\ u_2 \\ u_3 \end{Bmatrix} + \frac{c}{2} \begin{bmatrix} 0 & 0 & 0 & W_{0,1} + 2HW_{2,1} & 0 & 0 & 0 & 0 & 0 & H^2 W_{2,1} & 0 & 0 & 0 \\ 0 & 0 & 0 & 0 & W_{0,2} + 2HW_{2,2} & 0 & 0 & 0 & 0 & 0 & H^2 W_{2,2} & 0 & 0 \\ 0 & 0 & 0 & 2W_{0,2} + 2HW_{2,2} & 2HW_{2,1} & 0 & 0 & 0 & 0 & 0 & 2H^2 W_{2,1} & 0 & 0 \end{bmatrix} \mathbf{q}_H \tag{6-25}$$

Substituting equation 6-18 into equation 6-25, the strain displacement relations are expressed in terms of the midplane and interface displacement vector \mathbf{q}_H as

$$\begin{aligned}
\begin{Bmatrix} \varepsilon_1 \\ \varepsilon_2 \\ \varepsilon_6 \end{Bmatrix} &= \begin{bmatrix} \partial_1 & 0 & \partial_2 \\ 0 & \partial_2 & \partial_1 \\ 0 & 0 & 0 \\ (z^2(k_1 + Hk_4) + z^3k_3(1-2H))\partial_1 & 0 & (z^2(k_1 + Hk_4) + z^3k_3(1-2H))\partial_2 \\ 0 & (z^2(k_1 + Hk_4) + z^3k_3(1-2H))\partial_2 & (z^2(k_1 + Hk_4) + z^3k_3(1-2H))\partial_1 \\ (z + z^2(k_1 + Hk_4) + z^3k_3(1-2H))\partial_1 & 0 & (z + z^2(k_1 + Hk_4) + z^3k_3(1-2H))\partial_2 \\ 0 & (z + z^2(k_1 + Hk_4) + z^3k_3(1-2H))\partial_2 & (z + z^2(k_1 + Hk_4) + z^3k_3(1-2H))\partial_1 \\ H\partial_1 & 0 & H\partial_2 \\ 0 & H\partial_2 & H\partial_1 \\ 0 & 0 & 0 \\ (z^2Hk_2 - z^3Hk_3)\partial_1 & 0 & (z^2Hk_2 - z^3Hk_3)\partial_2 \\ 0 & (z^2Hk_2 - z^3Hk_3)\partial_2 & (z^2Hk_2 - z^3Hk_3)\partial_1 \\ (zH + z^2Hk_2 - z^3Hk_3)\partial_1 & 0 & (zH + z^2Hk_2 - z^3Hk_3)\partial_2 \\ 0 & (zH + z^2Hk_2 - z^3Hk_3)\partial_2 & (zH + z^2Hk_2 - z^3Hk_3)\partial_1 \end{bmatrix} \mathbf{q}_H \\
&+ \frac{c}{2} \begin{bmatrix} 0 & 0 & 0 & W_{0,1} + 2HW_{2,1} & 0 & 0 & 0 & 0 & 0 & H^2W_{2,1} & 0 & 0 & 0 \\ 0 & 0 & 0 & 0 & W_{0,2} + 2HW_{2,2} & 0 & 0 & 0 & 0 & 0 & H^2W_{2,2} & 0 & 0 \\ 0 & 0 & 0 & 2W_{0,2} + 2HW_{2,2} & 2HW_{2,1} & 0 & 0 & 0 & 0 & 0 & 2H^2W_{2,1} & 0 & 0 \end{bmatrix}
\end{aligned} \tag{6-26}$$

6.4 Constitutive Relations

6.4.1 Before damage.

Before damage, all ply materials are assumed linearly elastic and orthotropic. The three-dimensional k^{th} ply constitutive relations for stress and strain are:

$$\begin{Bmatrix} \sigma_1 \\ \sigma_2 \\ \sigma_3 \\ \sigma_4 \\ \sigma_5 \\ \sigma_6 \end{Bmatrix}^k = \begin{bmatrix} \overline{Q}_{11} & \overline{Q}_{12} & \overline{Q}_{13} & & & \overline{Q}_{16} \\ \overline{Q}_{12} & \overline{Q}_{22} & \overline{Q}_{23} & & & \overline{Q}_{26} \\ \overline{Q}_{13} & \overline{Q}_{23} & \overline{Q}_{33} & & & \overline{Q}_{36} \\ & & & \overline{Q}_{44} & \overline{Q}_{45} & \\ & & & \overline{Q}_{45} & \overline{Q}_{55} & \\ \overline{Q}_{16} & \overline{Q}_{26} & \overline{Q}_{36} & & & \overline{Q}_{66} \end{bmatrix}^k \begin{Bmatrix} \varepsilon_1 \\ \varepsilon_2 \\ \varepsilon_3 \\ \varepsilon_4 \\ \varepsilon_5 \\ \varepsilon_6 \end{Bmatrix}^k \tag{6-27}$$

where the numerical subscripts on the stress and strain represent the following indexing of the stress and strain tensor components:

$$\begin{aligned}
[\sigma] &= \begin{bmatrix} \sigma_1 & \sigma_6 & \sigma_5 \\ \sigma_6 & \sigma_2 & \sigma_4 \\ \sigma_5 & \sigma_4 & \sigma_3 \end{bmatrix} = \begin{bmatrix} \sigma_{xx} & \sigma_{xy} & \sigma_{zx} \\ \sigma_{xy} & \sigma_{yy} & \sigma_{yz} \\ \sigma_{zx} & \sigma_{yz} & \sigma_{zz} \end{bmatrix} \\
[\varepsilon] &= \begin{bmatrix} \varepsilon_1 & \frac{1}{2}\varepsilon_6 & \frac{1}{2}\varepsilon_5 \\ \frac{1}{2}\varepsilon_6 & \varepsilon_2 & \frac{1}{2}\varepsilon_4 \\ \frac{1}{2}\varepsilon_5 & \frac{1}{2}\varepsilon_4 & \varepsilon_3 \end{bmatrix} \equiv \begin{bmatrix} \varepsilon_{xx} & \frac{1}{2}\gamma_{xy} & \frac{1}{2}\gamma_{xz} \\ \frac{1}{2}\gamma_{xy} & \varepsilon_{yy} & \frac{1}{2}\gamma_{yz} \\ \frac{1}{2}\gamma_{xz} & \frac{1}{2}\gamma_{yz} & \varepsilon_{zz} \end{bmatrix} = \begin{bmatrix} \varepsilon_{xx} & \varepsilon_{xy} & \varepsilon_{zx} \\ \varepsilon_{xy} & \varepsilon_{yy} & \varepsilon_{yz} \\ \varepsilon_{zx} & \varepsilon_{yz} & \varepsilon_{zz} \end{bmatrix}
\end{aligned} \tag{6-28}$$

and the k^{th} ply constitutive matrix $[Q]_k$ is transformed to the laminate axis system by the modified direction cosine matrix for the k^{th} ply, $[T]_k$.

$$[\bar{Q}]^k = [T]_k [Q]_k [T]_k^T \tag{6-29}$$

The in-plane k^{th} ply constitutive relations for stress and strain for the originally assumed transverse direct stress ($\sigma_3 = 0$) are a simple contraction of the three-dimensional constitutive relations:

$$\begin{Bmatrix} \sigma_1 \\ \sigma_2 \\ \sigma_6 \end{Bmatrix}^k = \begin{bmatrix} \bar{Q}_{11} & \bar{Q}_{12} & \bar{Q}_{16} \\ \bar{Q}_{12} & \bar{Q}_{22} & \bar{Q}_{26} \\ \bar{Q}_{16} & \bar{Q}_{26} & \bar{Q}_{66} \end{bmatrix}^k \begin{Bmatrix} \varepsilon_1 \\ \varepsilon_2 \\ \varepsilon_6 \end{Bmatrix}^k \tag{6-30}$$

6.4.2 Matrix damage.

Matrix cracking softens the material properties. For matrix cracking, this softening was represented by a modified constitutive relation for the damaged ply. On the micromechanic scale, matrix crack propagation through the ply thickness and along the fiber direction takes time and is also load dependent. On the macromechanic scale, matrix cracks accumulate so that matrix crack density changes with time and loading. For this research, the time scale of the micromechanic processes were assumed to be very short, so that for the purposes of this analysis they happen instantaneously. To include the growth of the matrix crack density would require either a very highly detailed secondary FEM or an empirical relationship between ply strain and matrix crack density [75]. Neither were included in this research. Matrix failure was assumed to be complete when it was present. For cross-ply and angle-ply laminates in which, for example, the k^{th} ply is constrained by the $(k-1)^{\text{th}}$ and $(k+1)^{\text{th}}$ plies which are oriented so as to provide some fiber stiffness to resist the lateral strain of the k^{th} ply (i.e. any lay-up in which there are not multiple lamina with the same orientation found sequentially in the stack) Talreja [75] found that the “ply discount method” over predicted the stiffness reduction. Such are the facesheets of interest in this study.

Conservatively then, the matrix damage for any given ply within any given element were assumed to be either nonexistent or fully developed. Analyses based on this assumption have shown good agreement with experimental results for both angle-ply and cross-ply tension specimens [21]. For fully developed matrix damage within a ply, the constitutive coefficients Q_{12} , Q_{22} , Q_{23} , Q_{44} , and Q_{66} should be set to zero. For the purposes of this research, they were reduced by three orders of magnitude from their undamaged values in order to avoid the numerical difficulties of zeros.

6.4.3 Fiber failure.

Fiber failure is not a principal damage mode for the low energy portion of low-velocity impact of composite sandwich plates [5]. Before a composite sandwich absorbs enough energy for fiber failure to occur on an important scale, delamination has degraded the residual strength to the point that it can no longer resist its design load. This research focuses on the low-energy portion of the impact test envelope. Nevertheless, fiber failure is considered here for completeness. To a greater degree than matrix cracking, fiber damage will soften the material properties. As with matrix cracking, this softening can be represented by a modified constitutive relation for the damaged ply. Similar to the handling of matrix cracking, failure of an entire ply (within an element) can be assumed when the failure criteria indicate this mode of damage. Analyses based on this assumption have shown good agreement with experimental results for both angle-ply and cross-ply tension specimens [21]. For fully developed fiber damage within a ply, the constitutive coefficients Q_{11} , Q_{12} , Q_{13} , Q_{55} , and Q_{66} were reduced by three orders of magnitude from their undamaged values. When both matrix and fiber damage are present, the entire ply stiffness was be effectively removed.

6.4.4 Core properties/damage.

The principal functions of the core in a sandwich construction are to resist transverse compression (supporting the facesheets) and transfer shear loads. Nomex honeycomb core is known to exhibit nonlinear load deflection relations in both compression and shear before any damage [128]. In order to model the core as a linear elastic material up to the point of failure, certain assumptions are required. The reasoning leading to the model to be used in this research is as follows. The deformation of a sandwich plate under low-velocity impact can be considered as having two components, overall plate bending, and localized response to the impactor. The increased bending stiffness of a sandwich plate over a monolithic plate having the same mass

decreases impact damage resistance because it increases the impact force. In pure bending, the primary load taken by the core is shear. In pure bending, a core shear failure mode should be considered. On the other hand, for impact problems, in the local area surrounding the impact point, the primary load taken by the core is transverse compression. The core's principal contribution to impact damage resistance then, is in supporting the impacted facesheet by resisting transverse compression [95, 129, 130, 131]. Since local effects such as facesheet bending give rise to the principal failure modes of matrix damage, fiber fracture, and delamination within the facesheets [133], core shear resistance is of secondary importance as long as the contact area is small compared to the overall plate geometry. The other principal failure mode, core crushing, is also a localized effect [5, 126, 127] dependent on transverse compression. It is therefore believed that a core constitutive model that includes a linear secant modulus for the ratio of transverse direct stress to transverse direct strain before core damage is appropriate. In particular taking the core to be in-plane isotropic before damage,

$$\begin{Bmatrix} \sigma_1 \\ \sigma_2 \\ \sigma_3 \\ \sigma_4 \\ \sigma_5 \\ \sigma_6 \end{Bmatrix}^{\text{core}} = \begin{bmatrix} & & & & & \\ & & & & & \\ & \bar{Q}_{33} & & & & \\ & & \bar{Q}_{44} & \bar{Q}_{45} & & \\ & & \bar{Q}_{45} & \bar{Q}_{55} & & \\ & & & & & \bar{Q}_{66} \end{bmatrix} \begin{Bmatrix} \varepsilon_1 \\ \varepsilon_2 \\ \varepsilon_3 \\ \varepsilon_4 \\ \varepsilon_5 \\ \varepsilon_6 \end{Bmatrix}^{\text{core}} \quad (6-31)$$

where

$$\bar{Q}_{33} = \frac{\sigma_{zz_{crush}}}{\varepsilon_{zz_{crush}}} \quad (6-32)$$

After damage, entire core stiffness was effectively removed. Core failure was considered to be a localized event and was not considered in the global model. The local model represented the core as an elastic foundation supporting a monolithic facesheet. In a sandwich structure under a contact load, the effect of damaged core is that the core no longer supports the facesheet, this effect was modeled by removing the stiffness provided by the elastic foundation in the local finite element model. The condition $\sigma_3 = \sigma_4 = \sigma_5 = 0$ was enforced in the core locally at the interface between the core and the facesheet [69] by zeroing the limits of integration on the equilibrium equations (this integration will be discussed later) from which the transverse stresses were obtained.

6.4.5 Core/facesheet adhesive bondline damage.

Failure of the adhesive bondline between the core and the facesheets is a possible damage mode for sandwich structures. Were this bondline to fail, it could not transfer transverse shear loads or tensile transverse direct loads from the facesheet to the core. Compressive transverse loads ($\sigma_3 > 0$) would be transferred. Thus, a nonlinear constitutive law would be required. Fortunately, damage to this bondline was never observed in references [5, 95, 126, 127, 129] and no mention of such damage is made in the other low-velocity impact to composite facesheet sandwich plate references [e.g. 130, 131]. To the author's knowledge, adhesive bondline failure has not been observed in low-velocity impact tests of composite facesheet honeycomb sandwich panels. This bondline was assumed not to fail for the purposes of this research. Nevertheless, a situation closely related to this bondline failure occurs when core crushing is manifest just below the top facesheet [5]. The difference is that in core crushing all loads were assumed to vanish, i.e. even compressive transverse loads as described above.

6.4.6 Interface (delamination) damage.

The approach for delamination used in this research was different from what would have been used were the delamination-capable kinematics incorporated into the finite element code. With the delamination-capable kinematics, when the interface is damaged, the ply constitutive relations can be assumed unaffected. The k^{th} ply constitutive relations would be the same as equation 6-30 modified as necessary for matrix cracking (section 6.4.2) or core damage (section 6.4.4) that may be present. For complete delamination of a given element, the "stiffness" reduction implied by the delamination would manifest itself in strain discontinuities between plies, not stiffness changes in the plies themselves. For the present work, damage to the interface was simulated by reduction of the ply constitutive relations for the plies adjacent to the delamination. The reduction was the same as described above for matrix cracking, i.e. for fully developed delamination damage at an interface, the constitutive coefficients Q_{12} , Q_{22} , Q_{23} , Q_{44} , and Q_{66} for the plies adjacent to that interface were reduced by three orders of magnitude from their undamaged values. It should be pointed out that this model does not include the reduced in-plane compressive stiffness which delaminations produce by allowing individual sublaminates to buckle independent of one another.

6.5 Impact Dynamics

Low-velocity implies that strain rate dependencies of the material properties can be neglected. This assumption is made for the current research.

Low-velocity has been taken to imply that contact times are large compared to the time it takes a stress wave to traverse the plate thickness. This assumption is less valid for thicker plates and particularly for sandwich structures which have high bending stiffness (hence shorter contact times) and more compliant cores (hence longer transit times for stress waves) than it is for thin monolithic plates. This line of thinking leads the writer to question some of the quasi-static assumptions often made in this business when they are extended to sandwich structures. It is suspected that a static analysis may neglect some important contributions to the load and damage progression mechanisms of the problem. Nevertheless, as a first step, a static analysis is conducted for this research and impact dynamics are considered by the three-degree of freedom model of Chapter 3.

6.6 Three-Dimensional Equilibrium Equations

6.6.1 Transverse stresses.

The displacement-based parabolic shear deformation theory FEM in which stresses are obtained from strains (via constitutive relations) and strains are calculated from displacement derivatives, produces good results for in-plane stresses, but neglects transverse direct stress σ_z and produces poor estimates of transverse shear stresses σ_{zx} and σ_{yz} . In particular, the transverse shear strains are continuous, so at an interface between plies where the constitutive relations change the transverse shear stresses are discontinuous. This fact is illustrated in figure 6-4, in which the transverse shear stress obtained by this method is labeled "FEM Constitutive." In order to improve the prediction of the transverse stress components this research will abandon the constitutive relations for calculating σ_{zx} and σ_{yz} in favor of satisfying the three-dimensional equilibrium equations with the FEA in-plane stresses as a means of estimating both transverse direct stress σ_z and transverse shear stresses σ_{zx} and σ_{yz} . The stresses thus obtained are an improvement over those obtained from the constitutive equations alone [172]. This is also

illustrated in figure 6-4, in which the transverse shear stress obtained by this method is labeled “FEM Equilibrium.”

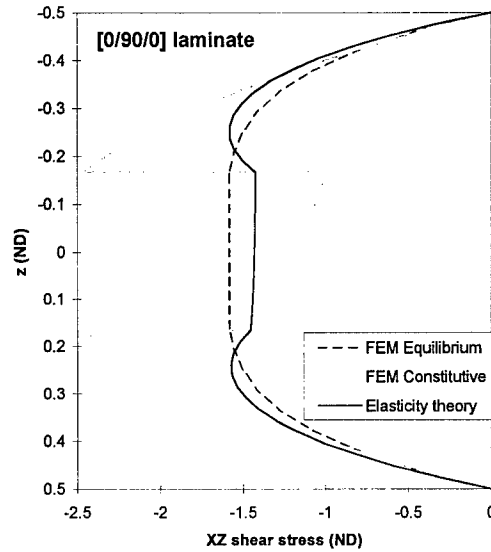


Figure 6-4 Transverse shear as calculated by elasticity theory, constitutive relations, and equilibrium equations for sinusoidally loaded plate in cylindrical bending. Dimensions, material properties, and scaling from Pagano [236].

From elasticity, the three-dimensional differential equilibrium equations of a continuous body expressed in terms of 2nd Piola-Kirchhoff stresses are (Washizu, [238, equation 3.27]):

$$\left[(\delta_{ij} + u_{i,j}) \sigma_{kj} \right]_{,k} + P_i = 0 \quad (i = 1, 2, 3) \quad (6-33)$$

where P_1, P_2, P_3 are the components of the body force vector. Neglecting body forces and expanding the first two of these equations we obtain:

$$\begin{aligned} & \left[(1 + u_{1,1}) \sigma_{11} \right]_{,1} + \left[(u_{1,2}) \sigma_{12} \right]_{,1} + \left[(u_{1,3}) \sigma_{13} \right]_{,1} \\ & + \left[(1 + u_{1,1}) \sigma_{21} \right]_{,2} + \left[(u_{1,2}) \sigma_{22} \right]_{,2} + \left[(u_{1,3}) \sigma_{23} \right]_{,2} \\ & + \left[(1 + u_{1,1}) \sigma_{31} \right]_{,3} + \left[(u_{1,2}) \sigma_{32} \right]_{,3} + \left[(u_{1,3}) \sigma_{33} \right]_{,3} = 0 \end{aligned} \quad (6-34a)$$

$$\begin{aligned} & \left[(u_{2,1}) \sigma_{11} \right]_{,1} + \left[(1 + u_{2,2}) \sigma_{12} \right]_{,1} + \left[(u_{2,3}) \sigma_{13} \right]_{,1} \\ & + \left[(u_{2,1}) \sigma_{21} \right]_{,2} + \left[(1 + u_{2,2}) \sigma_{22} \right]_{,2} + \left[(u_{2,3}) \sigma_{23} \right]_{,2} \\ & + \left[(u_{2,1}) \sigma_{31} \right]_{,3} + \left[(1 + u_{2,2}) \sigma_{32} \right]_{,3} + \left[(u_{2,3}) \sigma_{33} \right]_{,3} = 0 \end{aligned} \quad (6-34b)$$

Conjugate to the 2nd Piola-Kirchhoff stresses in equation 6-33 are Green strains. For the reasons discussed in section 6.3.2, full nonlinear Green strain-displacement relations were not used for this research, instead, von Karman plate strain-displacement relations were used (equation 6-22). Consistent with the assumption of von Karman-type nonlinearity, namely,

$$u_{\alpha,\beta} \ll 1 \quad (\alpha, \beta = 1, 2) \quad (6-35)$$

equations 6-34a and 6-34b are reduced to,

$$\sigma_{11,1} + \sigma_{12,2} + \sigma_{13,3} = 0 \quad (6-36a)$$

$$\sigma_{12,1} + \sigma_{22,2} + \sigma_{23,3} = 0 \quad (6-36b)$$

and can be expressed in the x-y-z coordinate system as,

$$\sigma_{xx,x} + \sigma_{xy,y} + \sigma_{xz,z} = 0 \quad (6-37a)$$

$$\sigma_{xy,x} + \sigma_{yy,y} + \sigma_{yz,z} = 0 \quad (6-37b)$$

The third of equations 6-33 is expanded as,

$$\begin{aligned} & [(u_{3,1})\sigma_{11}]_{,1} + [(u_{3,2})\sigma_{12}]_{,1} + [(1 + u_{3,3})\sigma_{13}]_{,1} \\ & + [(u_{3,1})\sigma_{21}]_{,2} + [(u_{3,2})\sigma_{22}]_{,2} + [(1 + u_{3,3})\sigma_{23}]_{,2} \\ & + [(u_{3,1})\sigma_{31}]_{,3} + [(u_{3,2})\sigma_{32}]_{,3} + [(1 + u_{3,3})\sigma_{33}]_{,3} = 0 \end{aligned} \quad (6-38)$$

Further, expansion of the derivatives via the product rule produces,

$$\begin{aligned} & (u_{3,11})\sigma_{11} + (u_{3,1})\sigma_{11,1} + (u_{3,12})\sigma_{12} + (u_{3,2})\sigma_{12,1} + \sigma_{13,1} + (u_{3,13})\sigma_{13} + (u_{3,3})\sigma_{13,1} \\ & + (u_{3,12})\sigma_{21} + (u_{3,1})\sigma_{12,2} + (u_{3,22})\sigma_{22} + (u_{3,2})\sigma_{22,2} + \sigma_{23,2} + (u_{3,23})\sigma_{23} + (u_{3,3})\sigma_{23,2} \\ & + (u_{3,13})\sigma_{31} + (u_{3,1})\sigma_{13,3} + (u_{3,23})\sigma_{32} + (u_{3,2})\sigma_{23,3} + \sigma_{33,3} + (u_{3,33})\sigma_{33} + (u_{3,3})\sigma_{33,3} = 0 \end{aligned} \quad (6-39)$$

Recognizing appropriate combinations of terms that add to factors multiplying the LHS of the first two equilibrium equations (each of which is zero),

$$\begin{aligned}
& (u_{3,1})(\text{equation 6-36a}) + (u_{3,2})(\text{equation 6-36b}) \\
& + (u_{3,11})\sigma_{11} + (u_{3,12})\sigma_{12} + \sigma_{13,1} + (u_{3,13})\sigma_{13} + (u_{3,3})\sigma_{13,1} \\
& + (u_{3,12})\sigma_{21} + (u_{3,22})\sigma_{22} + \sigma_{23,2} + (u_{3,23})\sigma_{23} + (u_{3,3})\sigma_{23,2} \\
& + (u_{3,13})\sigma_{31} + (u_{3,23})\sigma_{32} + \sigma_{33,3} + (u_{3,33})\sigma_{33} + (u_{3,3})\sigma_{33,3} = 0
\end{aligned} \tag{6-40}$$

Recognizing that $u_{3,3}$ is the linear part of transverse direct strain, and hence $u_{3,3} \ll 1$, so that,

$$\begin{aligned}
& (u_{3,11})\sigma_{11} + (u_{3,12})\sigma_{12} + \sigma_{13,1} \\
& + (u_{3,12})\sigma_{21} + (u_{3,22})\sigma_{22} + \sigma_{23,2} \\
& + (u_{3,13})\sigma_{31} + (u_{3,23})\sigma_{32} + \sigma_{33,3} + (u_{3,33})\sigma_{33} = 0
\end{aligned} \tag{6-41}$$

Eliminating the cross derivatives of the transverse displacement ($u_{3,13}$, $u_{3,13}$, and $u_{3,12}$) as higher order, produces,

$$(u_{3,11})\sigma_{11} + (u_{3,22})\sigma_{22} + (u_{3,33})\sigma_{33} + \sigma_{13,1} + \sigma_{23,2} + \sigma_{33,3} = 0 \tag{6-42}$$

The first three terms in 6-42 are stress times curvature which for the present research are taken to be higher order, though for post buckling considerations the first two can be the driving terms, i.e.

$$u_{3,ii} \sigma_{ii} \approx \text{H.O.T.} \quad (i = 1,2,3), \text{ (no sum)} \tag{6-43}$$

Leaving the third equilibrium equation to be,

$$\sigma_{13,1} + \sigma_{23,2} + \sigma_{33,3} = 0 \tag{6-44}$$

which can be expressed in the x - y - z coordinate system as,

$$\sigma_{xz,z} + \sigma_{yz,y} + \sigma_{zz,z} = 0 \tag{6-45}$$

The first two equilibrium equations, (6-37a) and (6-37b), each contain a single unknown and can be readily integrated through the thickness with traction free boundaries on the surface of the plate and (potentially) on any delaminated ply interface to obtain σ_x and σ_y through the thickness (h) of the plate. That is, for any given in-plane coordinate (x, y),

$$\begin{aligned}\sigma_{zx}(z) &= \int_{-\frac{h}{2}}^z (-\sigma_{xx,x}(\zeta) - \sigma_{xy,y}(\zeta)) d\zeta \\ \sigma_{yz}(z) &= \int_{-\frac{h}{2}}^z (-\sigma_{xy,x}(\zeta) - \sigma_{yy,y}(\zeta)) d\zeta\end{aligned}\tag{6-46}$$

In equation 6-46, the integration must be done on a ply-by-ply basis. It is evident that the boundary condition of zero transverse shear on the bottom surface of the plate is met identically by this integration process, but in general the boundary condition of zero transverse shear on the top surface is not. A least squares technique similar to that of [141] by which the bottom and top boundary conditions, and the interface continuity conditions could be simultaneously approximated in the least squares sense was developed and remains in the code, but was not needed in practice. The difference between the transverse shear stresses at the top surface resulting from the straight forward integration of equation 6-46 and zero was less than 1 percent of the peak transverse shear stress and was neglected. With these quantities known, in-plane (and with the von Karman terms, transverse) derivatives can be taken and the third equilibrium equation can be integrated with a traction free boundary on the lower surface to obtain the transverse direct stress, σ_{zz} . The integration involved is:

$$\sigma_{zz}(z) = \int_{-\frac{h}{2}}^z (-\sigma_{xz,x}(\zeta) - \sigma_{yz,y}(\zeta)) d\zeta\tag{6-47}$$

The integration given in equation 6-47 assumes continuity of transverse direct stress across ply interfaces. The integration is carried out ply-by-ply from the bottom surface (zero stress) to the top. A comment on the top surface transverse direct stress is in order. If carried out strictly as shown in equation 6-47, the σ_{zz} at the top of the plate would not be constrained to meet the boundary condition that it must equal the applied pressure profile. Here, a significant weakness associated with using two-dimensional (plane stress) stresses and assuming them to be in three-dimensional equilibrium became evident. The transverse direct stress resulting from that assumption suffers much more than the transverse shear stresses. This is expected because the plane stress assumption completely eliminates σ_{zz} from the analysis while it allows transverse shear stresses to result from transverse shear strains and be recovered by constitutive relationships. Thus, the plane stress assumption in the finite element model is expected to produce a stress field which is not in three-dimensional equilibrium and it is not surprising that the σ_{zz} stresses from equation 6-47 are poorer than the transverse shear stresses from equation 6-46. To

recover some useful information with regard to σ_{zz} from the two-dimensional finite element/three-dimensional equilibrium solution, the fact that the surface pressure profile (σ_{zz} on the top of the plate) was known a priori was used. This pressure is the applied pressure from an assumed Hertzian distribution from the contact with the tip. A constant, C_{Hertz} , was added to the integrand of equation 6-47. This constant was chosen to enforce the known boundary condition on the top surface, $\sigma_{zz}(h/2)$ by the relation,

$$C_{Hertz} = \frac{1}{h} \left[\sigma_{zz} \left(\frac{h}{2} \right) + \int_{-\frac{h}{2}}^{\frac{h}{2}} (\sigma_{xz,x}(\zeta) + \sigma_{yz,y}(\zeta)) d\zeta \right] \quad (6-48)$$

This effectively added a linear function to the transverse direct stress resulting in a situation in which equilibrium was not formally satisfied, but the known boundary conditions were. Thus the transverse shear stress gradients in equation 6-47 provided the “shape” of the transverse direct stress through-the-thickness profile (much the same as figure 5-4) while C_{Hertz} scaled this to meet the boundary conditions.

Integration of the three-dimensional equilibrium equations (6-46 and 6-47) is complicated by the von Karman type strain displacement nonlinearity. The following details the complication and the developments needed to handle it. The in-plane stresses are obtained from the FEM displacement solution by applying the constitutive relations and strain displacement relations to the displacement vector, \mathbf{q} . The assumed displacement field for parabolic transverse shear deformation theory (based on assumed linear strain displacement relations for the transverse shear engineering strain at the top and bottom surface of the plate) are equations 6-7 (repeated here for the convenience of the reader):

$$\begin{aligned} u(x, y, z) &= u + \psi_1 z + k(w_{,1} + \psi_1) z^3 \\ v(x, y, z) &= v + \psi_2 z + k(w_{,2} + \psi_2) z^3 \\ w(x, y, z) &= w \end{aligned} \quad (6-7)$$

where $k = -4/3h^2$, and the italic quantities u , v , and w are the midplane displacements which are independent of z so that, for example, $u = u(x, y)$. It will prove convenient to express this assumed displacement field in terms of the midplane displacement component vector, \mathbf{q} :

$$\begin{Bmatrix} u \\ v \\ w \end{Bmatrix} = \begin{bmatrix} 1 & & z^3 k & z + z^3 k \\ & 1 & & z + z^3 k \\ & & 1 & \\ & & & z + z^3 k \end{bmatrix} \begin{Bmatrix} u \\ v \\ w \\ w_{,1} \\ w_{,2} \\ \psi_1 \\ \psi_2 \end{Bmatrix}, \quad (6-49)$$

$$\equiv \begin{bmatrix} 1 & & z^3 k & z + z^3 k \\ & 1 & & z + z^3 k \\ & & 1 & \\ & & & z + z^3 k \end{bmatrix} \mathbf{q}$$

which is a degeneration of the delamination-capable kinematic relation found in equation 6-18 obtained by putting $H=0$ and $h_1=-h/2$ in equation 6-18.

The in-plane components of the von Karman strain-displacement relations (equations 6-20) are [153]:

$$\begin{aligned} \varepsilon_1 &= u(x,y,z)_{,1} + \frac{1}{2} [w(x,y,z)_{,1}]^2 \\ \varepsilon_2 &= v(x,y,z)_{,2} + \frac{1}{2} [w(x,y,z)_{,2}]^2 \\ \varepsilon_6 &= u(x,y,z)_{,2} + v(x,y,z)_{,1} + w(x,y,z)_{,1} w(x,y,z)_{,2} \end{aligned} \quad (6-50)$$

With the assumed kinematics these become,

$$\begin{aligned} \varepsilon_1 &= u_{,1} + \frac{c}{2} (w_{,1})^2 + \psi_{1,1} z + k (w_{,11} + \psi_{1,1}) z^3 \\ \varepsilon_2 &= v_{,2} + \frac{c}{2} (w_{,2})^2 + \psi_{2,2} z + k (w_{,22} + \psi_{2,2}) z^3 \\ \varepsilon_6 &= u_{,2} + v_{,1} + c w_{,1} w_{,2} + (\psi_{1,2} + \psi_{2,1}) z + k (2 w_{,12} + \psi_{1,2} + \psi_{2,1}) z^3 \end{aligned} \quad (6-51)$$

in which the parameter "c" is included to trace the terms brought about by using von Karman-type strain-displacement relations; i.e. $c = 0$ for linear strains and $c = 1$ for von Karman.

In order to calculate the transverse stresses, equilibrium is enforced with the in-plane stresses. The following strain and stress gradients based on the von Karman plate equations were needed in the first two equilibrium equations:

$$\begin{aligned}
\varepsilon_{1,1} &= u_{,11} + z\psi_{1,11} + z^3 k(\psi_{1,11} + w_{,111}) + cw_{,1} w_{,11} \\
\varepsilon_{1,2} &= u_{,12} + z\psi_{1,12} + z^3 k(\psi_{1,12} + w_{,112}) + cw_{,1} w_{,12} \\
\varepsilon_{2,1} &= v_{,21} + z\psi_{2,21} + z^3 k(\psi_{2,21} + w_{,122}) + cw_{,2} w_{,12} \\
\varepsilon_{2,2} &= v_{,22} + z\psi_{2,22} + z^3 k(\psi_{2,22} + w_{,222}) + cw_{,2} w_{,22} \\
\varepsilon_{6,1} &= u_{,21} + v_{,11} + z(\psi_{1,12} + \psi_{2,11}) + z^3 k(\psi_{1,12} + \psi_{2,11} + 2w_{,112}) + cw_{,11} w_{,2} + cw_{,1} w_{,12} \\
\varepsilon_{6,2} &= u_{,22} + v_{,12} + z(\psi_{1,22} + \psi_{2,12}) + z^3 k(\psi_{1,22} + \psi_{2,12} + 2w_{,122}) + cw_{,1} w_{,22} + cw_{,2} w_{,12}
\end{aligned}$$

$$\begin{Bmatrix} \sigma_{1,1} \\ \sigma_{2,2} \\ \sigma_{6,1} \\ \sigma_{6,2} \end{Bmatrix}^k = \begin{bmatrix} \bar{Q}_{11} & & & \\ & \bar{Q}_{12} & & \\ & & \bar{Q}_{22} & \\ \bar{Q}_{16} & & & \bar{Q}_{66} \\ & \bar{Q}_{16} & & \\ & & \bar{Q}_{26} & \\ & & & \bar{Q}_{66} \end{bmatrix}^k \begin{Bmatrix} \varepsilon_{1,1} \\ \varepsilon_{1,2} \\ \varepsilon_{2,1} \\ \varepsilon_{2,2} \\ \varepsilon_{6,1} \\ \varepsilon_{6,2} \end{Bmatrix} \quad (6-52)$$

The strains can be expressed in operator/matrix form as:

$$\begin{Bmatrix} \varepsilon_1 \\ \varepsilon_2 \\ \varepsilon_6 \end{Bmatrix} = \begin{bmatrix} \partial_1 & 0 & 0 & z^3 k \partial_1 & 0 & (z + z^3 k) \partial_1 & 0 \\ 0 & \partial_2 & 0 & 0 & z^3 k \partial_2 & 0 & (z + z^3 k) \partial_2 \\ \partial_2 & \partial_1 & 0 & 2z^3 k \partial_2 & 0 & (z + z^3 k) \partial_2 & (z + z^3 k) \partial_1 \end{bmatrix} + \begin{bmatrix} 0 & 0 & 0 & \frac{c}{2} w_{,1} & 0 & 0 & 0 \\ 0 & 0 & 0 & 0 & \frac{c}{2} w_{,2} & 0 & 0 \\ 0 & 0 & 0 & cw_{,2} & 0 & 0 & 0 \end{bmatrix} \begin{Bmatrix} u \\ v \\ w \\ w_{,1} \\ w_{,2} \\ \psi_1 \\ \psi_2 \end{Bmatrix} \quad (6-53)$$

where $\partial_\alpha = \partial/\partial x_\alpha$. Again, this is a degenerated form of the relation found for the delamination-capable kinematics, equation 6-26. As in equation 6-26, the nonlinear terms have been isolated into a separate matrix in order to provide insight into their role in the development. The in-plane strain derivatives can be written (there is some liberty as to how to write this due to the cross-derivative terms):

$$\begin{aligned}
\begin{Bmatrix} \varepsilon_{1,1} \\ \varepsilon_{1,2} \\ \varepsilon_{2,1} \\ \varepsilon_{2,2} \\ \varepsilon_{6,1} \\ \varepsilon_{6,2} \end{Bmatrix} &= \begin{bmatrix} \partial_{11} & 0 & 0 & z^3 k \partial_{11} & 0 & (z+z^3 k) \partial_{11} & 0 \\ \partial_{12} & 0 & 0 & z^3 k \partial_{12} & 0 & (z+z^3 k) \partial_{12} & 0 \\ 0 & \partial_{12} & 0 & 0 & z^3 k \partial_{12} & 0 & (z+z^3 k) \partial_{12} \\ 0 & \partial_{22} & 0 & 0 & z^3 k \partial_{22} & 0 & (z+z^3 k) \partial_{22} \\ \partial_{12} & \partial_{11} & 0 & 2z^3 k \partial_{12} & 0 & (z+z^3 k) \partial_{12} & (z+z^3 k) \partial_{11} \\ \partial_{22} & \partial_{12} & 0 & 0 & 2z^3 k \partial_{12} & (z+z^3 k) \partial_{22} & (z+z^3 k) \partial_{12} \end{bmatrix} + C \begin{bmatrix} 0 & 0 & 0 & w_1 \partial_1 & 0 & 0 & 0 \\ 0 & 0 & 0 & 0 & w_1 \partial_1 & 0 & 0 \\ 0 & 0 & 0 & w_2 \partial_2 & 0 & 0 & 0 \\ 0 & 0 & 0 & 0 & w_2 \partial_2 & 0 & 0 \\ 0 & 0 & 0 & w_2 \partial_1 & w_1 \partial_1 & 0 & 0 \\ 0 & 0 & 0 & w_2 \partial_2 & w_1 \partial_2 & 0 & 0 \end{bmatrix} \begin{Bmatrix} u \\ v \\ w \\ w_{,1} \\ w_{,2} \\ \psi_1 \\ \psi_2 \end{Bmatrix} \\
&\equiv [\partial \partial] q \\
&\quad 6 \times 7 \quad 7 \times 1
\end{aligned}$$

(6-54)

in which the 6x7 operator matrix (including linear and nonlinear portions) has been defined as $[\partial \partial]$. There are no surprises in applying the same process to equation 6-26 to produce a 6x14 version of $[\partial \partial]$ which premultiplies q_H to produce the strain derivatives (other than the fact that it can no longer be printed legibly on a single page). For the present research the delamination capable kinematics involved in equation 6-26 were not used. Writing the midplane displacement vector as q , and considering the equilibrium equations and the stress-gradient/strain-gradient constitutive relation given in equations 6-52, the transverse shear stress gradients can be written:

$$\begin{aligned}
\begin{Bmatrix} \sigma_{4,3} \\ \sigma_{5,3} \end{Bmatrix}^k &= - \begin{bmatrix} 1 & 1 \\ 1 & 1 \end{bmatrix} \begin{Bmatrix} \sigma_{1,1} \\ \sigma_{2,2} \\ \sigma_{6,1} \\ \sigma_{6,2} \end{Bmatrix}^k \\
&= - \begin{bmatrix} 1 & 1 \\ 1 & 1 \end{bmatrix} \begin{bmatrix} \bar{Q}_{11} & \bar{Q}_{12} & \bar{Q}_{16} \\ \bar{Q}_{16} & \bar{Q}_{12} & \bar{Q}_{26} \\ \bar{Q}_{16} & \bar{Q}_{26} & \bar{Q}_{66} \end{bmatrix}^k \begin{Bmatrix} \varepsilon_{1,1} \\ \varepsilon_{1,2} \\ \varepsilon_{2,1} \\ \varepsilon_{2,2} \\ \varepsilon_{6,1} \\ \varepsilon_{6,2} \end{Bmatrix}^k \quad (6-55)
\end{aligned}$$

which can be written in a more compact form as:

$$\begin{matrix} \left\{ \begin{matrix} \sigma_{4,3} \\ \sigma_{5,3} \end{matrix} \right\}^k & = & - \left[\begin{matrix} \bar{Q}_{16} & \bar{Q}_{12} & \bar{Q}_{26} & \bar{Q}_{22} & \bar{Q}_{66} & \bar{Q}_{26} \\ \bar{Q}_{11} & \bar{Q}_{16} & \bar{Q}_{12} & \bar{Q}_{26} & \bar{Q}_{16} & \bar{Q}_{66} \end{matrix} \right]^k [\partial\partial] \mathbf{q} \\ 2 \times 1 & & 2 \times 6 & & 6 \times 7 & 7 \times 1 \end{matrix} \quad (6-56)$$

In equation 6-56 it can be seen that the whole of the z dependence (for any given ply) is contained in the $[\partial\partial]$ operator. The integration through the thickness for the nonlinear operator $[\partial\partial]$ portion is carried out as follows.

$$\int [\partial\partial]^k dz = z \left[\begin{matrix} \partial_{11} & 0 & 0 & z^3 \frac{k}{4} \partial_{11} & 0 & \left(\frac{1}{2}z + z^3 \frac{k}{4} \right) \partial_{11} & 0 \\ \partial_{12} & 0 & 0 & z^3 \frac{k}{4} \partial_{12} & 0 & \left(\frac{1}{2}z + z^3 \frac{k}{4} \right) \partial_{12} & 0 \\ 0 & \partial_{12} & 0 & 0 & z^3 \frac{k}{4} \partial_{12} & 0 & \left(\frac{1}{2}z + z^3 \frac{k}{4} \right) \partial_{12} \\ 0 & \partial_{22} & 0 & 0 & z^3 \frac{k}{4} \partial_{22} & 0 & \left(\frac{1}{2}z + z^3 \frac{k}{4} \right) \partial_{22} \\ \partial_{12} & \partial_{11} & 0 & z^3 \frac{k}{2} \partial_{12} & 0 & \left(\frac{1}{2}z + z^3 \frac{k}{4} \right) \partial_{12} & \left(\frac{1}{2}z + z^3 \frac{k}{4} \right) \partial_{11} \\ \partial_{22} & \partial_{12} & 0 & 0 & z^3 \frac{k}{2} \partial_{12} & \left(\frac{1}{2}z + z^3 \frac{k}{4} \right) \partial_{22} & \left(\frac{1}{2}z + z^3 \frac{k}{4} \right) \partial_{12} \end{matrix} \right] + C \left[\begin{matrix} 0 & 0 & 0 & w_1 \partial_1 & 0 & 0 & 0 \\ 0 & 0 & 0 & 0 & w_1 \partial_1 & 0 & 0 \\ 0 & 0 & 0 & w_2 \partial_2 & 0 & 0 & 0 \\ 0 & 0 & 0 & 0 & w_2 \partial_2 & 0 & 0 \\ 0 & 0 & 0 & w_2 \partial_1 & w_1 \partial_1 & 0 & 0 \\ 0 & 0 & 0 & w_2 \partial_2 & w_1 \partial_2 & 0 & 0 \end{matrix} \right] + [C_1]^k \quad (6-57)$$

in which the matrix of integration constants $[C_1]^k$ is chosen to match the stress boundary condition on the bottom of the k^{th} ply. It should be noted that the condition of zero transverse stress on the bottom (positive z) surface of the plate is used here to obtain the integration constants for the first ply. For other plies, the condition of transverse stress continuity across the interface provides the constants. In this way, zero transverse shear stress at the top surface is not, in general, satisfied. This implies that there was a residual stress on the top surface, representing an error in the analysis. This error was less than one percent of the maximum transverse shear stress and was ignored.

Recognizing that this integration is ply-by-ply (it is not required to integrate over the delamination) the step functions in the nonlinear operator for the delamination-capable case do not pose a problem.

The three-dimensional equilibrium equations have provided an alternative means to obtain the transverse shear stresses without the standard use of the constitutive relations, i.e.,

$$\begin{Bmatrix} \sigma_4 \\ \sigma_5 \end{Bmatrix}^k = - \begin{bmatrix} \bar{Q}_{16} & \bar{Q}_{12} & \bar{Q}_{26} & \bar{Q}_{22} & \bar{Q}_{66} & \bar{Q}_{26} \\ \bar{Q}_{11} & \bar{Q}_{16} & \bar{Q}_{12} & \bar{Q}_{26} & \bar{Q}_{16} & \bar{Q}_{66} \end{bmatrix}^k \int [\partial\partial] dz q \quad (6-58)$$

as opposed to [172],

$$\begin{Bmatrix} \sigma_4 \\ \sigma_5 \end{Bmatrix}^k = \begin{bmatrix} \bar{Q}_{44} & \bar{Q}_{45} \\ \bar{Q}_{45} & \bar{Q}_{55} \end{bmatrix}^k \begin{bmatrix} 0 & 0 & 0 & 0 & 1 & 0 & 1 \\ 0 & 0 & 0 & 1 & 0 & 1 & 0 \end{bmatrix} 2(1 + 3kz^2)q \quad (6-59)$$

The third equilibrium equation (6-44) requires in-plane derivatives of these stresses. Here the nonlinear portion of the $[\partial\partial]$ operator complicates the situation. Taking derivatives of the integrated $[\partial\partial]$ times q expressions of equation 6-58 (in which both the operator and the vector have in-plane coordinate dependencies):

$$\begin{aligned} \frac{\partial(\int [\partial\partial] dz q)}{\partial x_1} = & z \begin{bmatrix} \partial_{111} & 0 & 0 & z^3 \frac{k}{4} \partial_{111} & 0 & \left(\frac{1}{2}z + z^3 \frac{k}{4}\right) \partial_{111} & 0 \\ \partial_{112} & 0 & 0 & z^3 \frac{k}{4} \partial_{112} & 0 & \left(\frac{1}{2}z + z^3 \frac{k}{4}\right) \partial_{112} & 0 \\ 0 & \partial_{112} & 0 & 0 & z^3 \frac{k}{4} \partial_{112} & \left(\frac{1}{2}z + z^3 \frac{k}{4}\right) \partial_{112} & 0 \\ 0 & \partial_{122} & 0 & 0 & z^3 \frac{k}{4} \partial_{122} & \left(\frac{1}{2}z + z^3 \frac{k}{4}\right) \partial_{122} & 0 \\ \partial_{112} & \partial_{111} & 0 & z^3 \frac{k}{2} \partial_{112} & 0 & \left(\frac{1}{2}z + z^3 \frac{k}{4}\right) \partial_{112} & \left(\frac{1}{2}z + z^3 \frac{k}{4}\right) \partial_{111} \\ \partial_{122} & \partial_{112} & 0 & 0 & z^3 \frac{k}{2} \partial_{112} & \left(\frac{1}{2}z + z^3 \frac{k}{4}\right) \partial_{122} & \left(\frac{1}{2}z + z^3 \frac{k}{4}\right) \partial_{112} \end{bmatrix} + c \begin{bmatrix} 0 & 0 & 0 & w_{,1} \partial_{11} & 0 & 0 & 0 \\ 0 & 0 & 0 & 0 & w_{,1} \partial_{11} & 0 & 0 \\ 0 & 0 & 0 & w_{,2} \partial_{12} & 0 & 0 & 0 \\ 0 & 0 & 0 & 0 & w_{,2} \partial_{12} & 0 & 0 \\ 0 & 0 & 0 & w_{,2} \partial_{11} & w_{,1} \partial_{11} & 0 & 0 \\ 0 & 0 & 0 & w_{,2} \partial_{12} & w_{,1} \partial_{12} & 0 & 0 \end{bmatrix} \begin{Bmatrix} u \\ v \\ w \\ w_{,1} \\ w_{,2} \\ \psi_1 \\ \psi_2 \end{Bmatrix} \\ & + cz \begin{bmatrix} 0 & 0 & 0 & w_{,11}^2 & 0 & 0 & 0 \\ 0 & 0 & 0 & 0 & w_{,11} w_{,12} & 0 & 0 \\ 0 & 0 & 0 & w_{,12}^2 & 0 & 0 & 0 \\ 0 & 0 & 0 & 0 & w_{,12} w_{,22} & 0 & 0 \\ 0 & 0 & 0 & w_{,11} w_{,12} & w_{,11} w_{,12} & 0 & 0 \\ 0 & 0 & 0 & w_{,12}^2 & w_{,11} w_{,22} & 0 & 0 \end{bmatrix} + [C_2]^k \end{aligned}$$

(6-60a)

$$\begin{aligned}
& \frac{\partial(\int[\partial\partial]dzq)}{\partial x_2} = \\
& z \begin{bmatrix} \partial_{112} & 0 & 0 & z^3 \frac{k}{4} \partial_{112} & 0 & \left(\frac{1}{2}z + z^3 \frac{k}{4}\right) \partial_{112} & 0 \\ \partial_{122} & 0 & 0 & z^3 \frac{k}{4} \partial_{122} & 0 & \left(\frac{1}{2}z + z^3 \frac{k}{4}\right) \partial_{122} & 0 \\ 0 & \partial_{122} & 0 & 0 & z^3 \frac{k}{4} \partial_{122} & 0 & \left(\frac{1}{2}z + z^3 \frac{k}{4}\right) \partial_{122} \\ 0 & \partial_{222} & 0 & 0 & z^3 \frac{k}{4} \partial_{222} & 0 & \left(\frac{1}{2}z + z^3 \frac{k}{4}\right) \partial_{222} \\ \partial_{122} & \partial_{112} & 0 & z^3 \frac{k}{2} \partial_{122} & 0 & \left(\frac{1}{2}z + z^3 \frac{k}{4}\right) \partial_{122} & \left(\frac{1}{2}z + z^3 \frac{k}{4}\right) \partial_{112} \\ \partial_{222} & \partial_{122} & 0 & 0 & z^3 \frac{k}{2} \partial_{122} & \left(\frac{1}{2}z + z^3 \frac{k}{4}\right) \partial_{222} & \left(\frac{1}{2}z + z^3 \frac{k}{4}\right) \partial_{122} \end{bmatrix} + c \begin{bmatrix} 0 & 0 & 0 & w_1 \partial_{12} & 0 & 0 & 0 \\ 0 & 0 & 0 & 0 & w_1 \partial_{12} & 0 & 0 \\ 0 & 0 & 0 & w_2 \partial_{22} & 0 & 0 & 0 \\ 0 & 0 & 0 & 0 & w_2 \partial_{22} & 0 & 0 \\ 0 & 0 & 0 & w_2 \partial_{12} & w_1 \partial_{12} & 0 & 0 \\ 0 & 0 & 0 & w_2 \partial_{22} & w_1 \partial_{22} & 0 & 0 \end{bmatrix} \begin{Bmatrix} u \\ v \\ w \\ w_{,1} \\ w_{,2} \\ \psi_1 \\ \psi_2 \end{Bmatrix} \\
& + cz \begin{bmatrix} 0 & 0 & 0 & w_{,11} w_{,12} & 0 & 0 & 0 \\ 0 & 0 & 0 & 0 & w_{,12}^2 & 0 & 0 \\ 0 & 0 & 0 & w_{,12} w_{,22} & 0 & 0 & 0 \\ 0 & 0 & 0 & 0 & w_{,22}^2 & 0 & 0 \\ 0 & 0 & 0 & w_{,11} w_{,22} & w_{,12}^2 & 0 & 0 \\ 0 & 0 & 0 & w_{,12} w_{,22} & w_{,12} w_{,22} & 0 & 0 \end{bmatrix} + [C_3]^k
\end{aligned}$$

(6-60b)

In equations 6-60a and 6-60b, a second nonlinear matrix has been separated from the operator matrix - displacement vector multiplication in each of these derivatives in order to better display the higher-order nonlinearities present. As an example, the first row on the RHS of equation 6-60b (without the constant) is,

$$zu_{,112} + \left(czw_{,1} + \frac{z^4}{4} k \right) w_{,112} + \left(\frac{z^2}{2} + \frac{z^4}{4} k \right) \psi_{1,112} + czw_{,11} w_{,12} \quad (6-61)$$

It should be observed that the transverse shear stress obtained in this way is forth-order in z as compared to parabolic for the standard constitutive solution.

The third equilibrium equation solved for the transverse direct stress gradient becomes:

$$\sigma_{3,3}^k = \begin{bmatrix} \bar{Q}_{16} & \bar{Q}_{12} & \bar{Q}_{26} & \bar{Q}_{22} & \bar{Q}_{66} & \bar{Q}_{26} \\ \bar{Q}_{11} & \bar{Q}_{16} & \bar{Q}_{12} & \bar{Q}_{26} & \bar{Q}_{16} & \bar{Q}_{66} \end{bmatrix}^k \left\{ \frac{\frac{\partial(\int[\partial\partial]dzq)}{\partial x_2}}{\frac{\partial(\int[\partial\partial]dzq)}{\partial x_1}} \right\}^k \quad (6-62)$$

and integrating through the thickness once more,

$$\sigma_3^k = \begin{bmatrix} \bar{Q}_{16} & \bar{Q}_{12} & \bar{Q}_{26} & \bar{Q}_{22} & \bar{Q}_{66} & \bar{Q}_{26} \\ \bar{Q}_{11} & \bar{Q}_{16} & \bar{Q}_{12} & \bar{Q}_{26} & \bar{Q}_{16} & \bar{Q}_{66} \end{bmatrix}^k \left\{ \frac{\partial \left(\int \int [\partial \partial] d\zeta dz q \right)}{\partial x_2} \right. \\ \left. \frac{\partial \left(\int \int [\partial \partial] d\zeta dz q \right)}{\partial x_1} \right\} \quad (6-63a)$$

where,

$$\frac{\partial \left(\int \int [\partial \partial] d\zeta dz q \right)}{\partial x_2} = \frac{1}{2} z^2 \begin{bmatrix} \partial_{112} & 0 & 0 & z^3 \frac{k}{10} \partial_{112} & 0 & \left(\frac{1}{3} z + z^3 \frac{k}{10} \right) \partial_{112} & 0 \\ \partial_{122} & 0 & 0 & z^3 \frac{k}{10} \partial_{122} & 0 & \left(\frac{1}{3} z + z^3 \frac{k}{10} \right) \partial_{122} & 0 \\ 0 & \partial_{122} & 0 & 0 & z^3 \frac{k}{10} \partial_{122} & 0 & \left(\frac{1}{3} z + z^3 \frac{k}{10} \right) \partial_{122} \\ 0 & \partial_{222} & 0 & 0 & z^3 \frac{k}{10} \partial_{222} & 0 & \left(\frac{1}{3} z + z^3 \frac{k}{10} \right) \partial_{222} \\ \partial_{122} & \partial_{112} & 0 & z^3 \frac{k}{5} \partial_{122} & 0 & \left(\frac{1}{3} z + z^3 \frac{k}{10} \right) \partial_{122} & \left(\frac{1}{3} z + z^3 \frac{k}{10} \right) \partial_{112} \\ \partial_{222} & \partial_{122} & 0 & 0 & z^3 \frac{k}{5} \partial_{122} & \left(\frac{1}{3} z + z^3 \frac{k}{10} \right) \partial_{222} & \left(\frac{1}{3} z + z^3 \frac{k}{10} \right) \partial_{122} \end{bmatrix} + c \begin{bmatrix} 0 & 0 & 0 & w_1 \partial_{12} & 0 & 0 & 0 \\ 0 & 0 & 0 & 0 & w_1 \partial_{12} & 0 & 0 \\ 0 & 0 & 0 & w_2 \partial_{22} & 0 & 0 & 0 \\ 0 & 0 & 0 & 0 & w_2 \partial_{22} & 0 & 0 \\ 0 & 0 & 0 & w_2 \partial_{12} & w_1 \partial_{12} & 0 & 0 \\ 0 & 0 & 0 & w_2 \partial_{22} & w_1 \partial_{22} & 0 & 0 \end{bmatrix} \begin{Bmatrix} u \\ v \\ w \\ w_1 \\ w_2 \\ \psi_1 \\ \psi_2 \end{Bmatrix} \\ + \frac{c}{2} z^2 \begin{bmatrix} 0 & 0 & 0 & w_{,11} w_{,12} & 0 & 0 & 0 \\ 0 & 0 & 0 & 0 & w_{,12}^2 & 0 & 0 \\ 0 & 0 & 0 & w_{,12} w_{,22} & 0 & 0 & 0 \\ 0 & 0 & 0 & 0 & w_{,22}^2 & 0 & 0 \\ 0 & 0 & 0 & w_{,11} w_{,22} & w_{,12}^2 & 0 & 0 \\ 0 & 0 & 0 & w_{,12} w_{,22} & w_{,12} w_{,22} & 0 & 0 \end{bmatrix} + [C_4]^k \quad (6-63b)$$

$$\begin{aligned}
& \frac{\partial \left(\iint [\partial \partial] d\zeta dz q \right)}{\partial x_1} = \\
& \frac{1}{2} z^2 \begin{bmatrix} \partial_{111} & 0 & 0 & z^3 \frac{k}{10} \partial_{111} & 0 & \left(\frac{1}{3} z + z^3 \frac{k}{10} \right) \partial_{111} & 0 \\ \partial_{112} & 0 & 0 & z^3 \frac{k}{10} \partial_{112} & 0 & \left(\frac{1}{3} z + z^3 \frac{k}{10} \right) \partial_{112} & 0 \\ 0 & \partial_{112} & 0 & 0 & z^3 \frac{k}{10} \partial_{112} & 0 & \left(\frac{1}{3} z + z^3 \frac{k}{10} \right) \partial_{112} \\ 0 & \partial_{122} & 0 & 0 & z^3 \frac{k}{10} \partial_{122} & 0 & \left(\frac{1}{3} z + z^3 \frac{k}{10} \right) \partial_{122} \\ \partial_{112} & \partial_{111} & 0 & z^3 \frac{k}{5} \partial_{112} & 0 & \left(\frac{1}{3} z + z^3 \frac{k}{10} \right) \partial_{112} & \left(\frac{1}{3} z + z^3 \frac{k}{10} \right) \partial_{111} \\ \partial_{122} & \partial_{112} & 0 & 0 & z^3 \frac{k}{5} \partial_{112} & \left(\frac{1}{3} z + z^3 \frac{k}{10} \right) \partial_{122} & \left(\frac{1}{3} z + z^3 \frac{k}{10} \right) \partial_{112} \end{bmatrix} + c \begin{bmatrix} 0 & 0 & 0 & w_{11} \partial_{11} & 0 & 0 & 0 \\ 0 & 0 & 0 & 0 & w_{11} \partial_{11} & 0 & 0 \\ 0 & 0 & 0 & w_{21} \partial_{12} & 0 & 0 & 0 \\ 0 & 0 & 0 & 0 & w_{21} \partial_{12} & 0 & 0 \\ 0 & 0 & 0 & w_{21} \partial_{11} & w_{11} \partial_{11} & 0 & 0 \\ 0 & 0 & 0 & w_{21} \partial_{12} & w_{11} \partial_{12} & 0 & 0 \end{bmatrix} \begin{Bmatrix} u \\ v \\ w \\ w_{,1} \\ w_{,2} \\ \psi_1 \\ \psi_2 \end{Bmatrix} \\
& + \frac{c}{2} z^2 \begin{bmatrix} 0 & 0 & 0 & w_{,11}^2 & 0 & 0 & 0 \\ 0 & 0 & 0 & 0 & w_{,11} w_{,12} & 0 & 0 \\ 0 & 0 & 0 & w_{,12}^2 & 0 & 0 & 0 \\ 0 & 0 & 0 & 0 & w_{,12} w_{,22} & 0 & 0 \\ 0 & 0 & 0 & w_{,11} w_{,12} & w_{,11} w_{,12} & 0 & 0 \\ 0 & 0 & 0 & w_{,12}^2 & w_{,11} w_{,22} & 0 & 0 \end{bmatrix} + [C_5]^k
\end{aligned}
\tag{6-63c}$$

in which, as before, the matrices of integration constants $[C_4]^k$ and $[C_5]^k$ are chosen to match the stress boundary condition on the bottom of the k^{th} ply. It should be noted that the condition of zero transverse direct stress on the bottom (positive z) surface of the plate is used here to obtain the integration constants for the first ply. For other plies, the condition of transverse stress continuity across the interface provides the constants. In this way, zero transverse direct stress at the top surface where no load is applied is not, in general, satisfied. This implies that there was a non-zero stress on the top surface. The correction given by adding C_{hertz} from equation 6-47 to the integrand in 6-46 repaired this. As an example, the first row on the RHS of equation 6-63b (without the constant) is,

$$\frac{z^2}{2} u_{,111} + \left(c \frac{z^2}{2} w_{,1} + \frac{z^5}{20} k \right) w_{,111} + \left(\frac{z^3}{6} + \frac{z^5}{20} k \right) \psi_{1,111} + c \frac{z^2}{2} w_{,11}^2 \tag{6-64}$$

It should be observed that the transverse direct stress obtained in this way is fifth-order in z as compared to zero for the standard constitutive solution.

6.6.2 Inconsistency of in-plane stresses.

There is an inherent inconsistency in the method described above which is here addressed. In formulating the equilibrium equations for the finite element method, the transverse stresses included in the potential energy were those based on the assumed kinematics and constitutive relationship with the assumption of zero transverse direct stress. The new transverse stresses imply a different potential energy, hence the transverse stresses are inconsistent with the finite element formulation. In order to approximately alleviate the inconsistency, the change in strain energy between the finite element transverse stresses and the equilibrium transverse stresses can be accounted for within the Newton-Raphson iterative scheme as follows.

The transverse direct stress calculated above is in general nonzero and implies a nonzero transverse direct strain. The inverse stress-strain relation is then employed to obtain ε_3 .

$$\varepsilon_3^k = (\bar{S}_{13}\sigma_1 + \bar{S}_{23}\sigma_2 + \bar{S}_{33}\sigma_3)^k \quad (6-65)$$

This non-zero ε_3 can be used to update the in-plane stresses via the stress-strain relation.

$$\begin{Bmatrix} \sigma_1 \\ \sigma_2 \\ \sigma_6 \end{Bmatrix}^k = \begin{bmatrix} \bar{Q}_{11} & \bar{Q}_{12} & \bar{Q}_{13} & \bar{Q}_{16} \\ \bar{Q}_{12} & \bar{Q}_{22} & \bar{Q}_{23} & \bar{Q}_{26} \\ \bar{Q}_{16} & \bar{Q}_{26} & \bar{Q}_{36} & \bar{Q}_{66} \end{bmatrix}^k \begin{Bmatrix} \varepsilon_1 \\ \varepsilon_2 \\ \varepsilon_3 \\ \varepsilon_6 \end{Bmatrix}^k \quad (6-66)$$

These updated stresses differ from the original FEM stresses equation 6-30 repeated here for the reader's convenience).

$$\begin{Bmatrix} \sigma_1 \\ \sigma_2 \\ \sigma_6 \end{Bmatrix}^k = \begin{bmatrix} \bar{Q}_{11} & \bar{Q}_{12} & \bar{Q}_{16} \\ \bar{Q}_{12} & \bar{Q}_{22} & \bar{Q}_{26} \\ \bar{Q}_{16} & \bar{Q}_{26} & \bar{Q}_{66} \end{bmatrix}^k \begin{Bmatrix} \varepsilon_1 \\ \varepsilon_2 \\ \varepsilon_6 \end{Bmatrix}^k \quad (6-30)$$

In terms of stress, the differences are the residual stresses

$$\begin{Bmatrix} \Delta\sigma_1 \\ \Delta\sigma_2 \\ \Delta\sigma_6 \end{Bmatrix}^k = \begin{Bmatrix} \bar{Q}_{13} \\ \bar{Q}_{23} \\ \bar{Q}_{36} \end{Bmatrix}^k (\bar{S}_{13}\sigma_1 + \bar{S}_{23}\sigma_2 + \bar{S}_{33}\sigma_3)^k \quad (6-67)$$

For any element (subscript "e") the strain energies associated with each of these residual stresses are:

$$\Delta U_{ei} = \iiint_{V_e} \frac{1}{2} \Delta \sigma_i \varepsilon_i dV \quad (i = 1, 2, 6 \text{ no sum}) \quad (6-68)$$

which is integrated ply-by-ply as,

$$\begin{aligned} \begin{Bmatrix} \Delta U_1 \\ \Delta U_2 \\ \Delta U_6 \end{Bmatrix}_e &= \frac{\text{Area}_e}{2} \sum_{k=1}^n \left\{ \int_{h_{k-1}}^{h_k} \begin{Bmatrix} \Delta \sigma_1 \varepsilon_1 \\ \Delta \sigma_2 \varepsilon_2 \\ \Delta \sigma_6 \varepsilon_6 \end{Bmatrix}_e^k dz \right\} \\ &= \frac{\text{Area}_e}{2} \sum_{k=1}^n \left\{ \int_{h_{k-1}}^{h_k} \begin{Bmatrix} \bar{Q}_{13} \varepsilon_1 \\ \bar{Q}_{23} \varepsilon_2 \\ \bar{Q}_{36} \varepsilon_6 \end{Bmatrix}_e^k (\bar{S}_{13} \sigma_1 + \bar{S}_{23} \sigma_2 + \bar{S}_{33} \sigma_3)_e^k dz \right\} \end{aligned} \quad (6-69)$$

Or, following the initial stress development initial stresses in Cook et al [173] section 4.1-6, in terms of nodal forces the residuals are:

$$\mathbf{r}_e = \iiint_{V_e} \mathbf{B}^T \Delta \boldsymbol{\sigma} dV \quad (6-70)$$

where $\mathbf{B} = [\partial][N]$, $[\partial]$ is the nonlinear operator in equation 6-53 or equation 6-26, and $[N]$ is the matrix of shape functions. This contributes directly to the right-hand-side of the Newton-Raphson solution in the form

$$\mathbf{K}_T \Delta \mathbf{q} = (\mathbf{r}_g) \quad (6-71)$$

where \mathbf{r}_g is the vector of element residual nodal forces expanded to the global degrees of freedom, \mathbf{K}_T is the tangent stiffness matrix, \mathbf{q} is the generalized displacement vector, and $\Delta \mathbf{q}$ is the unknown increment to the displacements. This correction, though attractive from a theoretical perspective because it allows a three-dimensional correction to the two-dimensional finite element solution, was not found to improve the transverse stresses obtained in this effort. Apparently, correcting the three-dimensional effects by means of the forces as provided by equation 6-70, does not make up for the fact that the kinematics inherent in the two-dimensional solution stiffness matrix in equation 6-71 are not correct. This suggests that iterative improvement might be obtained with more general (e.g. zig-zag kinematics). Confirming this idea was considered to be beyond the scope of the current research.

6.7 *Finite Element Solution*

Previous researchers have left the legacy of a working dynamic finite element code which can handle undamaged monolithic shells [56, 174, 223]. Siler [153] made modifications to a static monolithic finite element code to allow it to handle undamaged sandwich plates. The ideas, and, wherever possible, the code, which previously existed were used as building blocks for this research. Still, many and significant advances and whole new formulations were required. The more important and new portions of the stratagem include: equilibrium integration of the finite element in-plane stresses to approximate the transverse stresses (section 6.6), a new higher-order element using 5th order Hermitian interpolation functions (section 6.72), a contact algorithm to simulate contact with a spherical indenter (section 6.9), an adaptive mesh algorithm (section 6.10), a progressive damage algorithm (sections 6.8, 6.11, and 6.12), a local model including an elastic-plastic foundation (section 6.13), and a local-global approach for the top surface displacement (section 6.14). Most of the new code is exterior to the finite element algorithm itself. In this section, those changes which effected the finite element algorithm are discussed.

6.7.1 *General ideas.*

Without the delamination kinematics of section 6.2.2, the only essential active degrees of freedom are those related to the midplane displacements, slopes, and rotations of equation 6-7. The analysis reduces to that of parabolic shear deformation theory, and rectangular plate elements with four nodes and 28 degrees of freedom (seven per node as in figure 6-2) could be used. The geometry of an individual element and the representation of its global, local and natural coordinates are shown in figure 6-5.

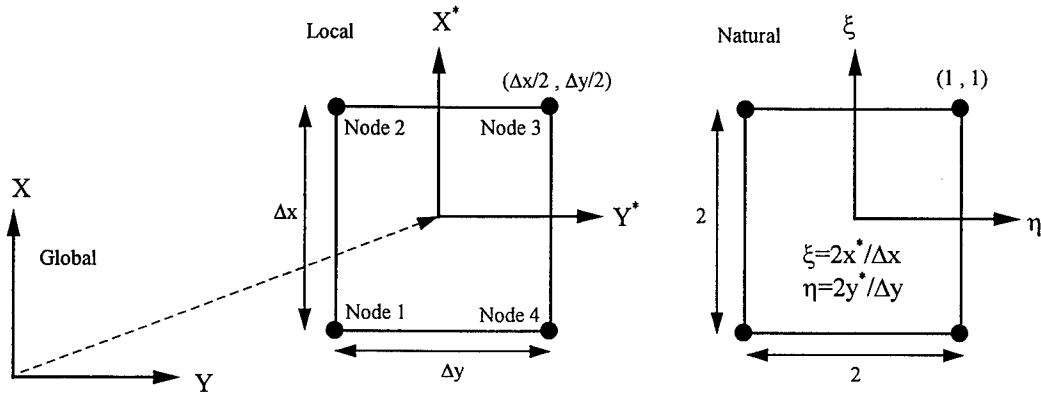


Figure 6-5 Four-node plate element geometry and coordinate systems.

Displacements within the given element are interpolated from the nodal displacements through appropriate shape functions. The displacement field for w requires C^1 continuity (as defined in the textbook by Cook et al. [173]), therefore cubic Hermitian shape functions have been used in previous research for nodal displacements w , $w_{,1}$ and $w_{,2}$ or, for the delamination-capable element W_i , $W_{i,1}$, and $W_{i,2}$, ($i = 0,1$ or $i = 0,2$ depending on delamination location). The interpolation can be represented as,

$$w(\xi, \eta) = \begin{bmatrix} H_1 & H_2 & H_3 & H_4 \end{bmatrix} \begin{Bmatrix} q_1 \\ q_2 \\ q_3 \\ q_4 \end{Bmatrix} \quad (6-72a)$$

$$H_K = \begin{Bmatrix} \frac{1}{8}(1+\xi_K\xi)(1+\eta_K\eta)(2+\xi_K\xi+\eta_K\eta-\xi^2-\eta^2) \\ \frac{1}{8}\Delta x \xi_K(1+\xi_K\xi)^2(\xi_K\xi-1)(1+\eta_K\eta) \\ \frac{1}{8}\Delta y \eta_K(1+\xi_K\xi)(\eta_K\eta-1)(1+\eta_K\eta)^2 \end{Bmatrix}^T \quad (6-72b)$$

$$q_K = \{w \quad w_{,1} \quad w_{,2}\}_K^T \quad (6-72c)$$

where $K=1$ through 4 represent the local node numbers for an element found at global position (x,y) . ξ_K and η_K are the values of the natural coordinates at node K . Thus equation 6-72b represents 12 cubic polynomial interpolation functions. These are determined as follows. Defining a function for each degree of freedom, m ($m=1,2,\dots,12$),

$$H^m(\xi, \eta) = a_1^m + a_2^m \xi + a_3^m \eta + a_4^m \xi^2 + a_5^m \xi \eta + a_6^m \eta^2 + a_7^m \xi^3 + a_8^m \xi^2 \eta + a_9^m \xi \eta^2 + a_{10}^m \eta^3 + a_{11}^m \xi^3 \eta + a_{12}^m \xi \eta^3 \quad (6-73)$$

in which the coefficients are different for each degree of freedom, its in-plane derivatives are readily evaluated as,

$$\begin{aligned} H^m_{,\xi}(\xi, \eta) &= a_2^m + 2a_4^m \xi + a_5^m \eta + 3a_7^m \xi^2 + 2a_8^m \xi \eta + a_9^m \eta^2 + 3a_{11}^m \xi^2 \eta + a_{12}^m \eta^3 \\ H^m_{,\eta}(\xi, \eta) &= a_3^m + a_5^m \xi + 2a_6^m \eta + a_8^m \xi^2 + 2a_9^m \xi \eta + 3a_{10}^m \eta^2 + a_{11}^m \xi^3 + 3a_{12}^m \xi \eta^2 \end{aligned} \quad (6-74)$$

We define a vector of the coordinates for each degree of freedom, m ,

$$AA^m = \{a_1, a_2, a_3, \dots, a_{12}\}^m \quad (6-75)$$

And define an 12-dimensional vector function of the coordinates for each degree of freedom, m , containing the interpolation functions and their derivatives evaluated at the nodes,

$$HH_n(AA^m) = \begin{Bmatrix} H^m(\xi_1, \eta_1), H^m_{,\xi}(\xi_1, \eta_1), H^m_{,\eta}(\xi_1, \eta_1), \dots, \\ H^m(\xi_4, \eta_4), H^m_{,\xi}(\xi_4, \eta_4), H^m_{,\eta}(\xi_4, \eta_4) \end{Bmatrix} \quad (6-76)$$

We now let that vector function take on values of a unit basis vector for each degree of freedom, m , i.e.,

$$HH_n(AA^m) = \delta_n^m. \quad (6-77)$$

Which we solve for the coefficients AA^m for each degree of freedom, m . With these then H^m is fully defined and can be placed in the relationship given in equation 6-72b by separating them out by nodes.

The other displacement fields only need C^0 continuity and employ Lagrangian shape functions:

$$\begin{Bmatrix} u(x, y) \\ v(x, y) \\ \psi_1(x, y) \\ \psi_2(x, y) \end{Bmatrix} = \begin{bmatrix} N_1 & 0 & 0 & 0 & \dots & N_4 & 0 & 0 & 0 \\ 0 & N_1 & 0 & 0 & \dots & 0 & N_4 & 0 & 0 \\ 0 & 0 & N_1 & 0 & \dots & 0 & 0 & N_4 & 0 \\ 0 & 0 & 0 & N_1 & \dots & 0 & 0 & 0 & N_4 \end{bmatrix} \begin{Bmatrix} q_1 \\ q_2 \\ q_3 \\ q_4 \end{Bmatrix} \quad (6-78a)$$

$$N_K = \frac{1}{4}(1 + \xi_K \xi)(1 + \eta_K \eta) \quad (6-78b)$$

$$q_K = \{u \quad v \quad \psi_1 \quad \psi_2\}_K^T \quad (6-78c)$$

The formulation of such an element and the solution of the resulting finite element problem for static analysis is fully described in the textbook by Palazotto and Dennis [172].

6.7.2 *Higher order element development.*

The 4-noded, 28 degree-of-freedom element of Palazotto and Dennis [172], used as the starting point for this research, employs shape functions that are at most cubic polynomials in the in-plane coordinates. In the displacement based, plane stress, finite element formulation, the transverse direct stress is assumed zero and the transverse shear stress is assumed to be related to the transverse shear strains via constitutive relationships. This is to say, the element is two-dimensional, and the assumed kinematics limit the accuracy of the available transverse stresses. To provide better transverse stresses, the current research solved the finite element problem to obtain displacements (and strains), and then used constitutive relationships to obtain in-plane stresses, and finally used three-dimensional equilibrium equations to obtain transverse stresses. Since the three-dimensional equilibrium satisfaction did not affect the finite element solution, it can be considered a post-processing algorithm. The equilibrium post-processing in the present research required third derivatives of the in-plane and shear displacements and fourth derivatives of the transverse displacement. This can be observed in equations 6-63a by noting the derivative operators in 6-63b and 6-63c and the displacement vector components they operate on. Here the interpolation used for the displacement vector becomes important. Clearly, if the displacement vector contains at most cubic polynomials (as it does in the 28 degree of freedom element of [172]) and third and fourth derivatives are taken of it, little will survive and the transverse stresses of equations 6-58 and 6-63a have little hope of accurately representing the three-dimensional effects. The approach taken for this research to get higher-order midplane displacement functions for equations 6-58 and 6-63a was to increase the order of the polynomial shape functions representing the displacements inside the element. This required a new element with more degrees of freedom at the nodes. The capability to use the 28 degree of freedom element was retained by writing the code to allow the user to select the order of the interpolation polynomials for the w , ψ_1 , and ψ_2 displacement functions. In particular, 3rd or 5th order polynomials could be chosen for w , while linear or 3rd order polynomials could be chosen for ψ_1 and ψ_2 . Linear interpolation was by Lagrangian functions as described in [172] providing C^0 continuity while Hermitian functions

provided C^1 and C^2 for the 3rd and 5th order interpolations respectively. The terms included in the Hermitian interpolation polynomials are illustrated in figure 6-6.

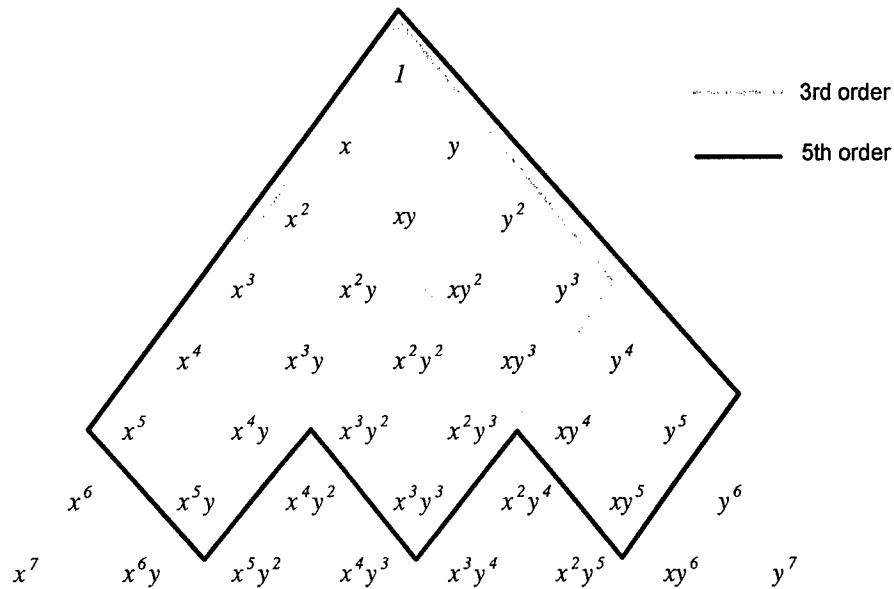


Figure 6-6 Pascal's triangle showing interpolation polynomials for 3rd and 5th order shape functions. Note, polynomials are complete to 3rd and 5th order, respectively.

The 3rd order Hermitian functions are precisely the same as those defined above for w , but for the higher order elements they can be applied to ψ_1 and ψ_2 as well as w . Interpolation using the 5th order Hermitian interpolation functions can be represented as,

$$w(x, y) = \begin{bmatrix} H_1 & H_2 & H_3 & H_4 \end{bmatrix} \begin{Bmatrix} q_1 \\ q_2 \\ q_3 \\ q_4 \end{Bmatrix}, \quad (6-79)$$

in which each H_K is now a 1x6 row vector rather than the 1x3 vector shown in equation 6-72b and,

$$q_K = \{w \quad w_{,1} \quad w_{,2} \quad w_{,11} \quad w_{,12} \quad w_{,22}\}_K^T \quad (6-80)$$

Thus equation 6-79 represents 24 5th order polynomial interpolation functions. These are determined as follows. Defining a function for each degree of freedom, m ($m=1,2,\dots,24$),

$$\begin{aligned} H^m(\xi, \eta) = & a_1^m + a_2^m \xi + a_3^m \eta + a_4^m \xi^2 + a_5^m \xi \eta + a_6^m \eta^2 + \\ & a_7^m \xi^3 + a_8^m \xi^2 \eta + a_9^m \xi \eta^2 + a_{10}^m \eta^3 + \\ & a_{11}^m \xi^4 + a_{12}^m \xi^3 \eta + a_{13}^m \xi^2 \eta^2 + a_{14}^m \xi \eta^3 + a_{15}^m \eta^4 + \\ & a_{16}^m \xi^5 + a_{17}^m \xi^4 \eta + a_{18}^m \xi^3 \eta^2 + a_{19}^m \xi^2 \eta^3 + a_{20}^m \xi \eta^4 + a_{21}^m \eta^5 + \\ & a_{22}^m \xi^5 \eta + a_{23}^m \xi^3 \eta^3 + a_{24}^m \xi \eta^5 \end{aligned} \quad (6-81)$$

in which, as before, the coefficients are different for each degree of freedom, its in-plane derivatives of concern are now,

$$\begin{aligned} & H^m_{,\xi} \\ & H^m_{,\eta} \\ & H^m_{,\xi\xi} \\ & H^m_{,\xi\eta} \\ & H^m_{,\eta\eta} \end{aligned} \quad (6-82)$$

We again define a vector of the coordinates for each degree of freedom, m ,

$$AA^m = \{a_1, a_2, a_3, \dots, a_{24}\}^m \quad (6-83)$$

and define an 24-dimensional vector function of the coordinates for each degree of freedom, m , containing the interpolation functions and their derivatives evaluated at the 4 nodes,

$$HH_n(AA^m) = \left\{ \begin{aligned} & H^m(\xi_1, \eta_1), H^m_{,\xi}(\xi_1, \eta_1), H^m_{,\eta}(\xi_1, \eta_1), \\ & H^m_{,\xi\xi}(\xi_1, \eta_1), H^m_{,\xi\eta}(\xi_1, \eta_1), H^m_{,\eta\eta}(\xi_1, \eta_1), \\ & \dots, \\ & H^m(\xi_4, \eta_4), H^m_{,\xi}(\xi_4, \eta_4), H^m_{,\eta}(\xi_4, \eta_4), \\ & H^m_{,\xi\xi}(\xi_4, \eta_4), H^m_{,\xi\eta}(\xi_4, \eta_4), H^m_{,\eta\eta}(\xi_4, \eta_4) \end{aligned} \right\} \quad (6-84)$$

We now let that vector function take on values of a unit basis vector for each degree of freedom, m , i.e.,

$$HH_n(AA^m) = \delta_n^m \quad (6-85)$$

Which we again solve for the coefficients AA^m for each degree of freedom, m . With these then, H^m is fully defined and can be placed in the relationship given in equation 6-79 by separating them out by nodes. The 5th order Hermitian shape functions thus derived are,

$$H_1 = \left\{ \begin{array}{l} \frac{1}{32}(-1+\xi)(-1+\eta)(8-7\eta-7\eta^2+3\eta^3+3\eta^4-7\xi+2\eta\xi-7\xi^2+2\eta^2\xi+2\eta\xi^2+2\eta^2\xi^2+3\xi^3+3\xi^4) \\ \frac{1}{32}(-1+\xi)^2(-1+\eta)(1+\xi)(-5+2\eta+2\eta^2+2\xi+3\xi^2) \\ \frac{1}{32}(-1+\eta)^2(-1+\xi)(1+\eta)(-5+2\eta+3\eta^2+2\xi+2\xi^2) \\ \frac{1}{32}(-1+\eta)(-1+\xi)^3(1+\xi)^2 \\ \frac{1}{16}(-1+\eta)^2(1+\eta)(-1+\xi)^2(1+\xi) \\ \frac{1}{32}(-1+\eta)^3(-1+\xi)(1+\eta)^2 \end{array} \right\}^T$$

(6-86a)

$$H_2 = \left\{ \begin{array}{l} \frac{1}{32}(-1+\eta)(1+\xi)(-8+7\eta+7\eta^2+2\eta\xi+2\eta^2\xi-3\eta^3-3\eta^4-7\xi+7\xi^2-2\eta\xi^2-2\eta^2\xi^2+3\xi^3-3\xi^4) \\ \frac{1}{32}(1+\xi)^2(-1+\eta)(-1+\xi)(-5+2\eta+2\eta^2-2\xi+3\xi^2) \\ \frac{1}{32}(-1+\eta)^2(1+\xi)(1+\eta)(5-2\eta-3\eta^2+2\xi-2\xi^2) \\ \frac{1}{32}(1-\eta)(-1+\xi)^2(1+\xi)^3 \\ \frac{1}{16}(-1+\eta)^2(1+\eta)(-1+\xi)(1+\xi)^2 \\ \frac{1}{32}(1-\eta)^3(1+\xi)(1+\eta)^2 \end{array} \right\}^T$$

(6-87b)

$$H_3 = \left\{ \begin{array}{l} \frac{1}{32}(1+\eta)(1+\xi)(8+7\eta-7\eta^2+2\eta\xi-2\eta^2\xi-3\eta^3+3\eta^4+7\xi-7\xi^2-2\eta\xi^2+2\eta^2\xi^2-3\xi^3+3\xi^4) \\ \frac{1}{32}(1+\xi)^2(1+\eta)(-1+\xi)(5+2\eta-2\eta^2+2\xi-3\xi^2) \\ \frac{1}{32}(1+\eta)^2(1+\xi)(-1+\eta)(5+2\eta-3\eta^2+2\xi-2\xi^2) \\ \frac{1}{32}(1+\eta)(-1+\xi)^2(1+\xi)^3 \\ \frac{1}{16}(-1+\eta)(1+\eta)^2(-1+\xi)(1+\xi)^2 \\ \frac{1}{32}(-1+\eta)^2(1+\xi)(1+\eta)^3 \end{array} \right\}^T$$

(6-88c)

$$H_4 = \begin{Bmatrix} \frac{1}{32}(1+\eta)(-1+\xi)(-8-7\eta+7\eta^2+2\eta\xi-2\eta^2\xi+3\eta^3-3\eta^4+7\xi+7\xi^2+2\eta\xi^2-2\eta^2\xi^2-3\xi^3+3\xi^4) \\ \frac{1}{32}(-1+\xi)^2(1+\eta)(1+\xi)(5+2\eta-2\eta^2-2\xi-3\xi^2) \\ \frac{1}{32}(1+\eta)^2(-1+\xi)(-1+\eta)(-5-2\eta+3\eta^2+2\xi+2\xi^2) \\ \frac{1}{32}(1+\eta)(1+\xi)^2(1-\xi)^3 \\ \frac{1}{16}(-1+\eta)(1+\eta)^2(-1+\xi)^2(1+\xi) \\ \frac{1}{32}(-1+\eta)^2(1-\xi)(1+\eta)^3 \end{Bmatrix}^T$$

(6-89d)

Nodal degrees of freedom for the linear case consisted of the values of displacement functions at the nodes. Nodal degrees of freedom for the 3rd order Hermitian interpolation polynomials consisted of the values of displacement functions as well as the slopes of those functions at the nodes. Nodal degrees of freedom for the 5th order Hermitian interpolation polynomials consisted of the values of displacement function, the slopes of that function, and the second and cross derivatives of the function at the nodes. Allowing the user to select the order of the interpolation polynomials for the w , ψ_1 , and ψ_2 independently provided the possibility of using elements having 7, 9, 10, 11, 12, or 14 degrees-of-freedom per node. Though the code is capable of all of these elements, it was only exercised for this research using 7, 11, and 14 degrees-of-freedom per node. After checking out the transverse stress results (via equilibrium) using these, the 14 degrees-of-freedom per node element was settled on for the remainder of the work. The element with 7 degrees-of-freedom per node has nodal degrees-of-freedom u , v , w , $w_{,x}$, $w_{,y}$, ψ_1 , and ψ_2 . The element with 11 degrees-of-freedom per node has nodal degrees-of-freedom u , v , w , $w_{,x}$, $w_{,y}$, ψ_1 , $\psi_{1,x}$, $\psi_{1,y}$, ψ_2 , $\psi_{2,x}$, and $\psi_{2,y}$. The element with 14 degrees-of-freedom per node has nodal degrees-of-freedom u , v , w , $w_{,x}$, $w_{,y}$, $w_{,xx}$, $w_{,xy}$, $w_{,yy}$, ψ_1 , $\psi_{1,x}$, $\psi_{1,y}$, ψ_2 , $\psi_{2,x}$, and $\psi_{2,y}$. All elements used 5x5 point Gauss quadrature. These three elements and their nodal degrees-of-freedom are illustrated in figure 6-7.

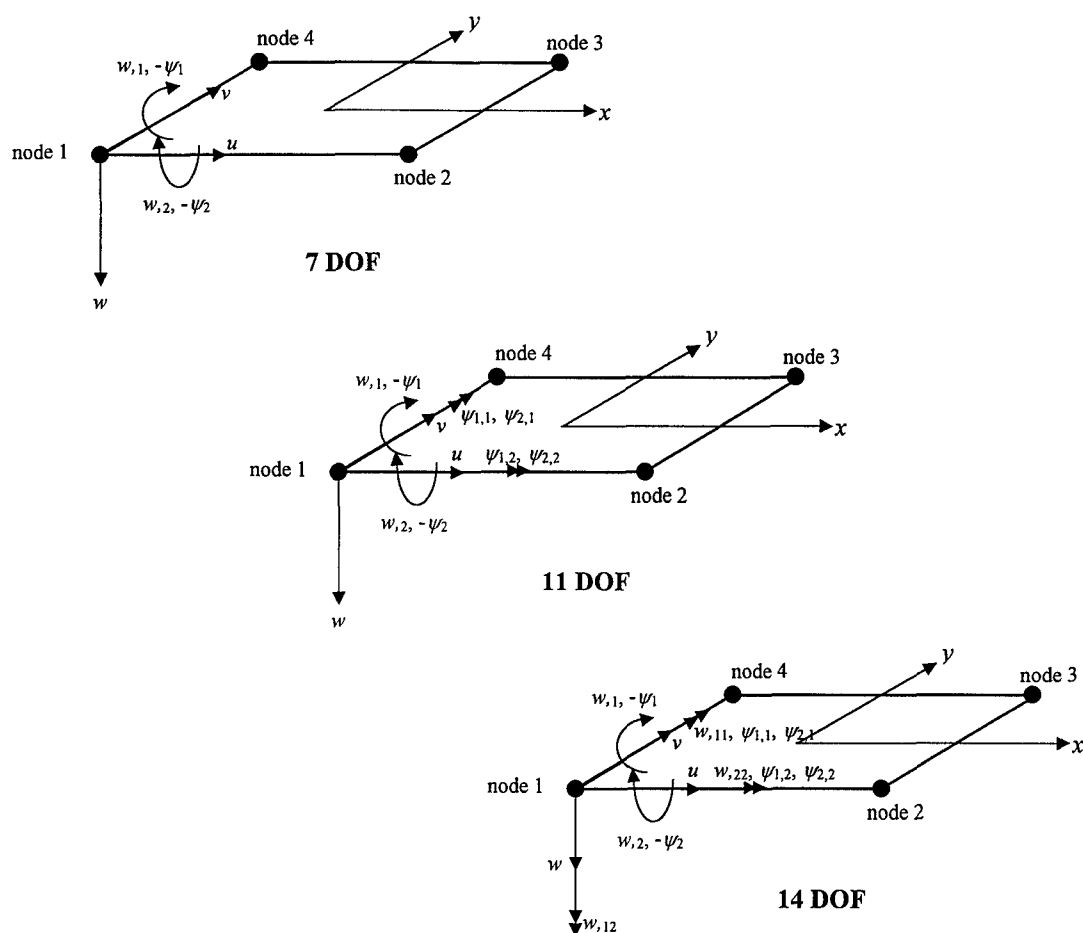


Figure 6-7 Four-node plate elements with 7, 11, and 14 degrees of freedom per node.

6.7.3 Higher order element testing.

A comparison of the elements using 7, 11, and 14 degrees-of-freedom per node is provided here to justify the selection of the element used for the remainder of the research. As mentioned previously, the need for the higher order elements becomes apparent when considering the derivatives that must be taken of the displacement functions in order to evaluate the stress gradients which are involved in integration of the equilibrium equations (6-58 and 6-60). To compare these elements in a scenario similar to the intended application, plate strip composed of 21 rectangular elements with a simply-supported boundary on one end and a symmetric boundary on the other end was employed. The plate was loaded with a one-dimensional Hertzian contact load on the symmetric end. The contact half-width was 1.27 cm while the plate length was 6.35 cm (simulating a 12.7 cm full plate width). The boundary conditions were chosen such that plate

was in cylindrical bending. The zero moment condition at the simple support was enforced by setting the curvature (here, $w_{,yy}$) to zero.

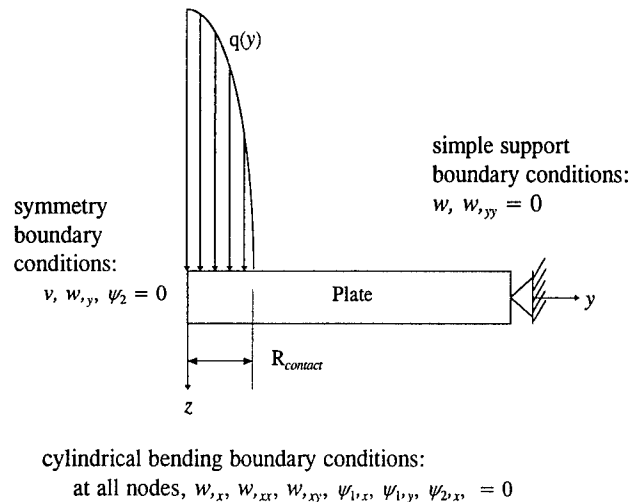


Figure 6-8 Geometry and boundary conditions for 7, 11, and 14 DOF per node element tests.

Both monolithic laminates and sandwich plates were compared based on transverse shear stress and transverse direct stress. The elasticity solution of Chapter 5 provided an exact solution by which each element could be judged. The sandwich plate elements chosen for this study were the same as those tested experimentally for Chapter 4 (4-, 8-, 16-, 32-, and 48-ply). In addition to the sandwich plates, monolithic (same material throughout, i.e. no core) plates representing just the top facesheet were also compared to the elasticity solution. This was done because the local finite element model described later in this chapter was based modeling just one facesheet on a spring-type foundation. The monolithic elements chosen matched the individual facesheets of the sandwiches. The choice of elements to compare with the elasticity solution then, was based on the fact that the global model used in Chapters 7 and 8 used a sandwich element while the local model used a monolithic plate (the facesheet) on an elastic foundation. For this reason, the accuracy of the elements at predicting transverse stresses (via equilibrium) was of interest for both sandwich and monolithic laminates with Hertzian contact loads. Because the accuracy will also depend on facesheet thickness, each facesheet thickness was modeled. Insights into the strengths and limitations of these elements for Hertzian contact problems were obtained and are expounded in what follows. As described in Chapter 5, Hertzian contact is a much more severe loading than uniform or sinusoidal loading. In particular, the in-plane stress gradients are much larger. An element that can produce accurate transverse stresses for a slowly-varying load may still do poorly

for a Hertzian contact loading. Testing with Hertzian contact while not sacrificing the exact solution was possible because of the developments of Chapter 5. This provided a testing parameter space for these elements which was similar to the intended application and was therefore a good yardstick by which to determine the appropriate number of degrees of freedom to be used in the low-velocity impact simulations of Chapters 7 and 8. In figures 6-7 through 6-16, the applied load is,

$$q(y) = \begin{cases} 0, & y > R_{contact} \\ q_0 \sqrt{1 - \frac{y^2}{R_{contact}^2}}, & y \leq R_{contact} \end{cases} \quad (6-90)$$

$$R_{contact} = 1.27 \text{ cm}$$

$R_{contact}$ is the contact half-width and is shown in figure 6-8. In figures 6-9 through 6-18 and the discussion following them, the different element solutions are indicated by the number of degrees of freedom per node, so that for example 7 DOF stands for the element which has 7 degrees of freedom per node. In those figures the normalized quantities here defined are plotted,

$$\tau_{mid} = \frac{\tau_{yz}(y, z \text{ of facesheet midplane})}{q_0} \quad \begin{array}{l} \text{Normalized transverse shear stress} \\ \text{at the midplane of the top facesheet} \end{array}$$

$$\tau_{peak} = \frac{\tau_{yz}(y \text{ of peak found in } \tau_{mid}, z)}{q_0} \quad \begin{array}{l} \text{Normalized transverse shear stress} \\ \text{at the peak found in } \tau_{mid} \end{array} \quad (6-91)$$

$$\sigma_{ctr} = \frac{\sigma_z(0, z)}{q_0} \quad \begin{array}{l} \text{Normalized transverse direct stress} \\ \text{at the center of the plate} \end{array}$$

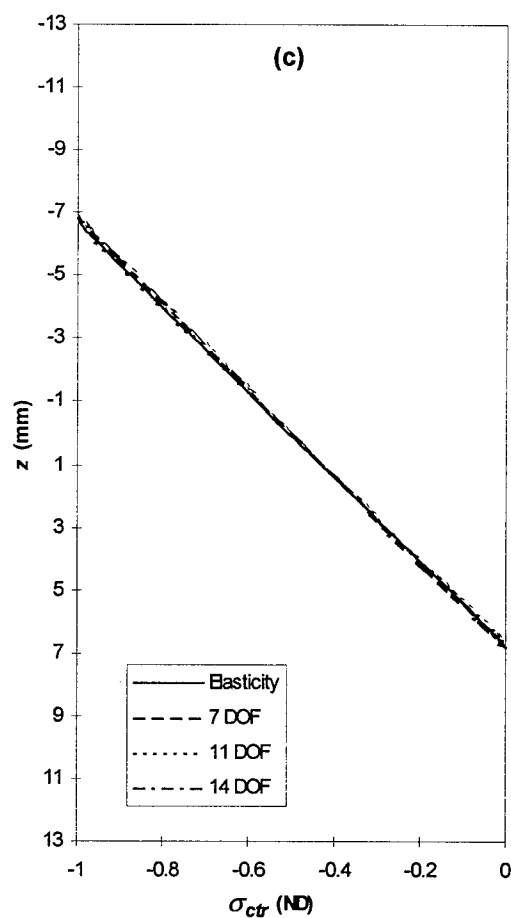
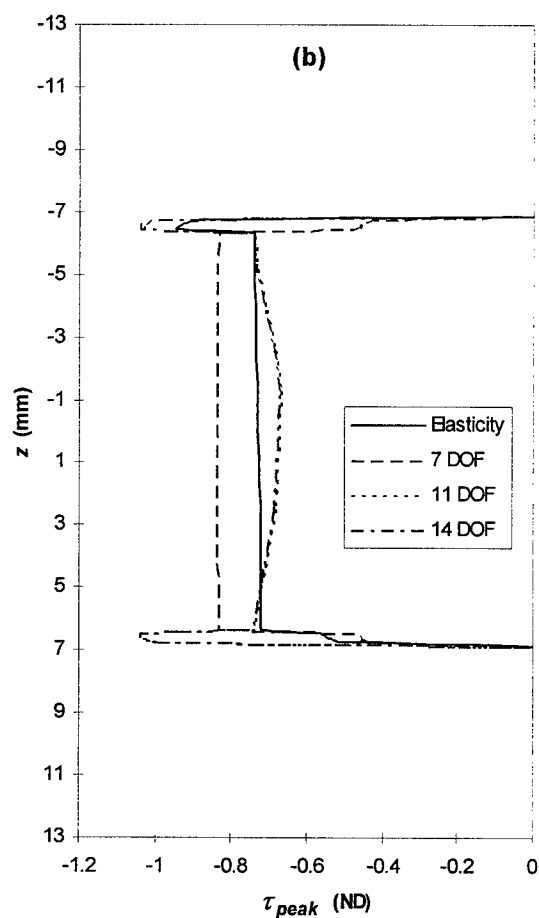
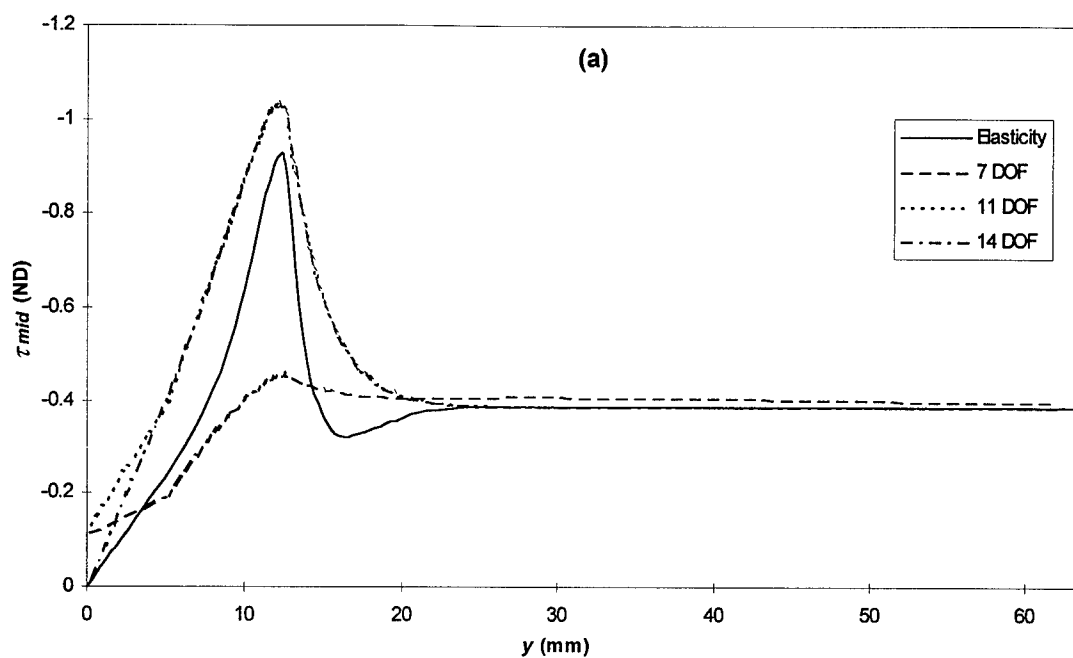


Figure 6-9 Comparison of current and elasticity solutions for 4-ply sandwich plate.

6.7.3.1 4-ply sandwich.

In figure 6-9a, it can be observed that the element with only 7 degrees of freedom per node fails to pick up the high peak in transverse shear at the edge of the contact region ($y=12.7$ mm). This error is non-conservative. The 11 DOF and 14 DOF elements are very close, they both over-predict the peak transverse shear stress (conservative), predict the correct y- and z-location of the peak, and are significantly closer to the elasticity solution than the 7 DOF element. Figure 6-8b indicates that all of the plate finite element solutions show transverse symmetry in the transverse shear stress. This transverse symmetry is due to the fact that the finite element displacements through the thickness are functions of the midplane displacements and assumed kinematic relationships which do not show the true three-dimensional nature of the problem. The lower facesheet peak is ignored in all of the current work since it is known to be fictitious and no experimental failures of the bottom facesheet were observed. The difference between the various elements in terms of transverse direct stress is not clear in figure 6-9c. The closeness of the transverse direct stresses may be due to the fact that the facesheets are so thin that the transverse stress does not change much within the facesheet. The linear variation through the core overwhelms the small change in the facesheet, so all of the elements have similar transverse direct stress profiles.

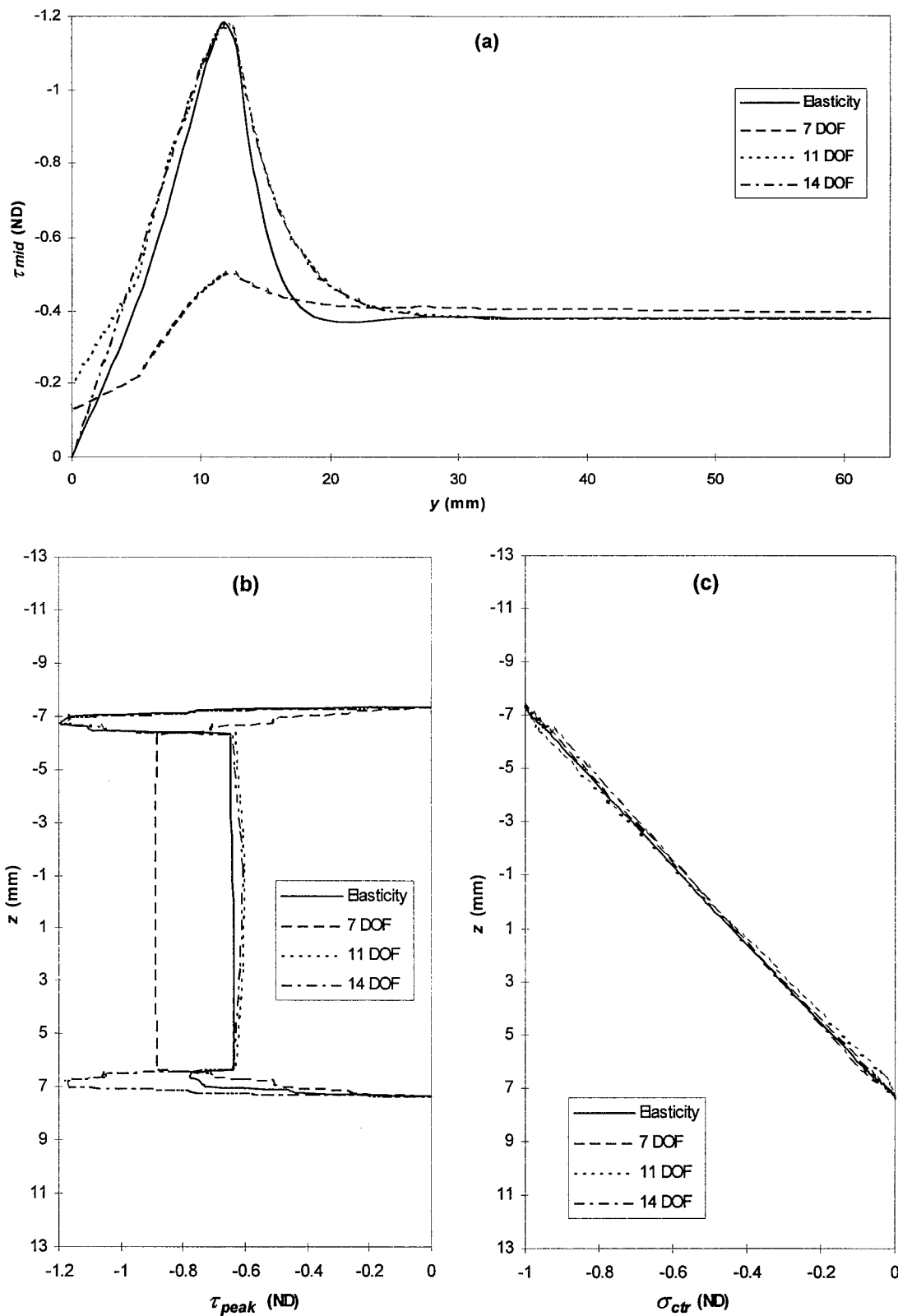


Figure 6-10 Comparison of current and elasticity solutions for 8-ply sandwich plate.

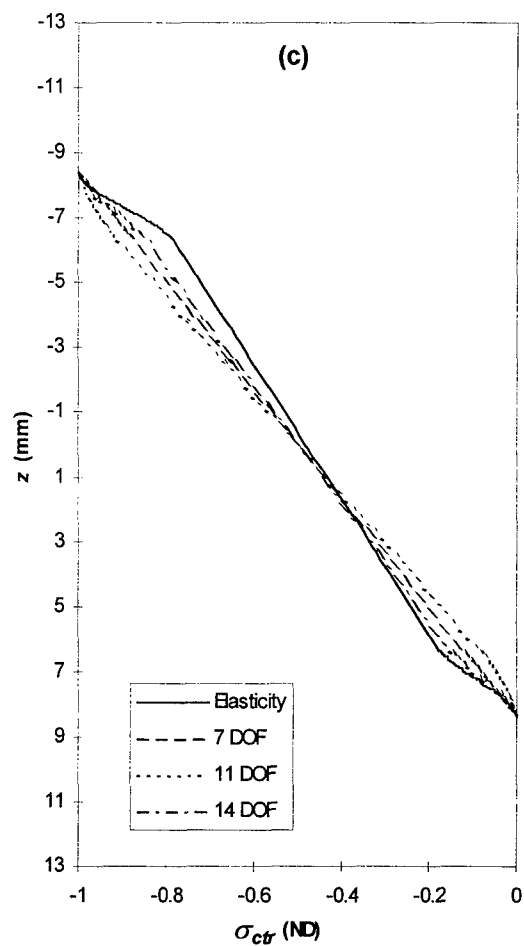
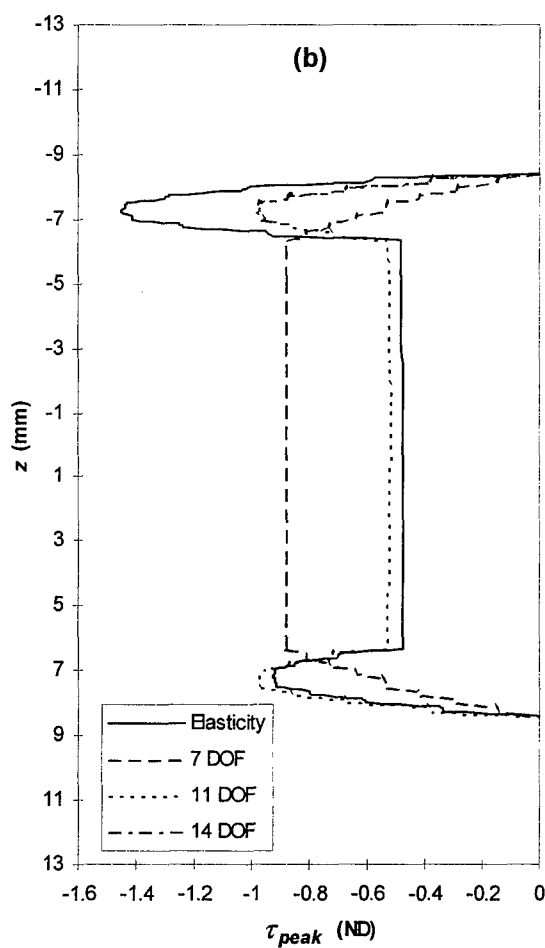
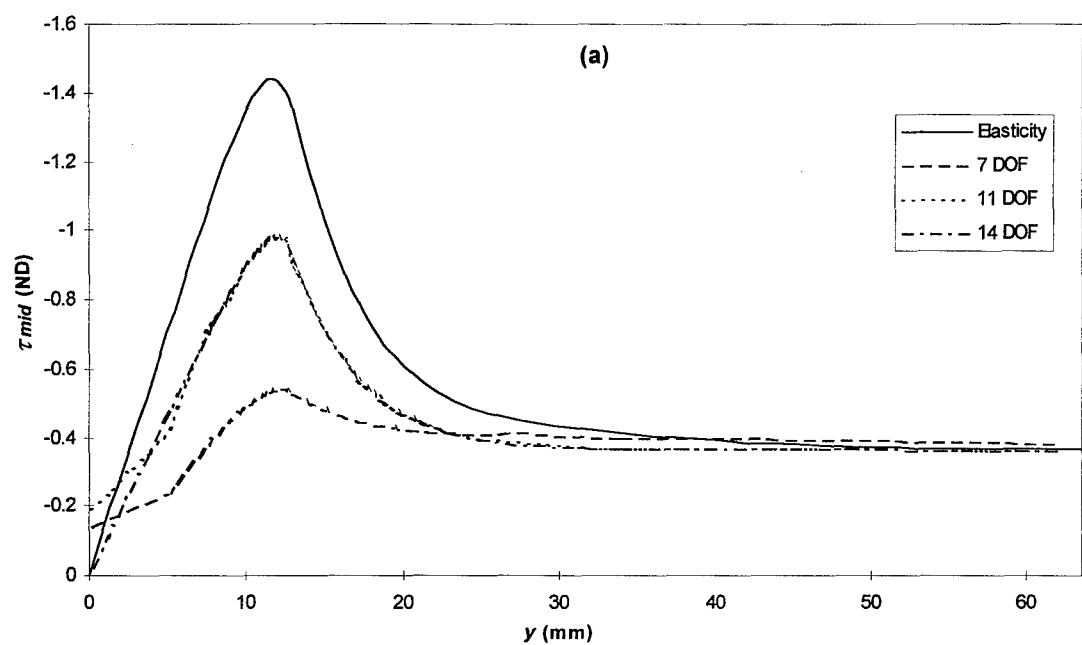


Figure 6-11 Comparison of current and elasticity solutions for 16-ply sandwich plate.

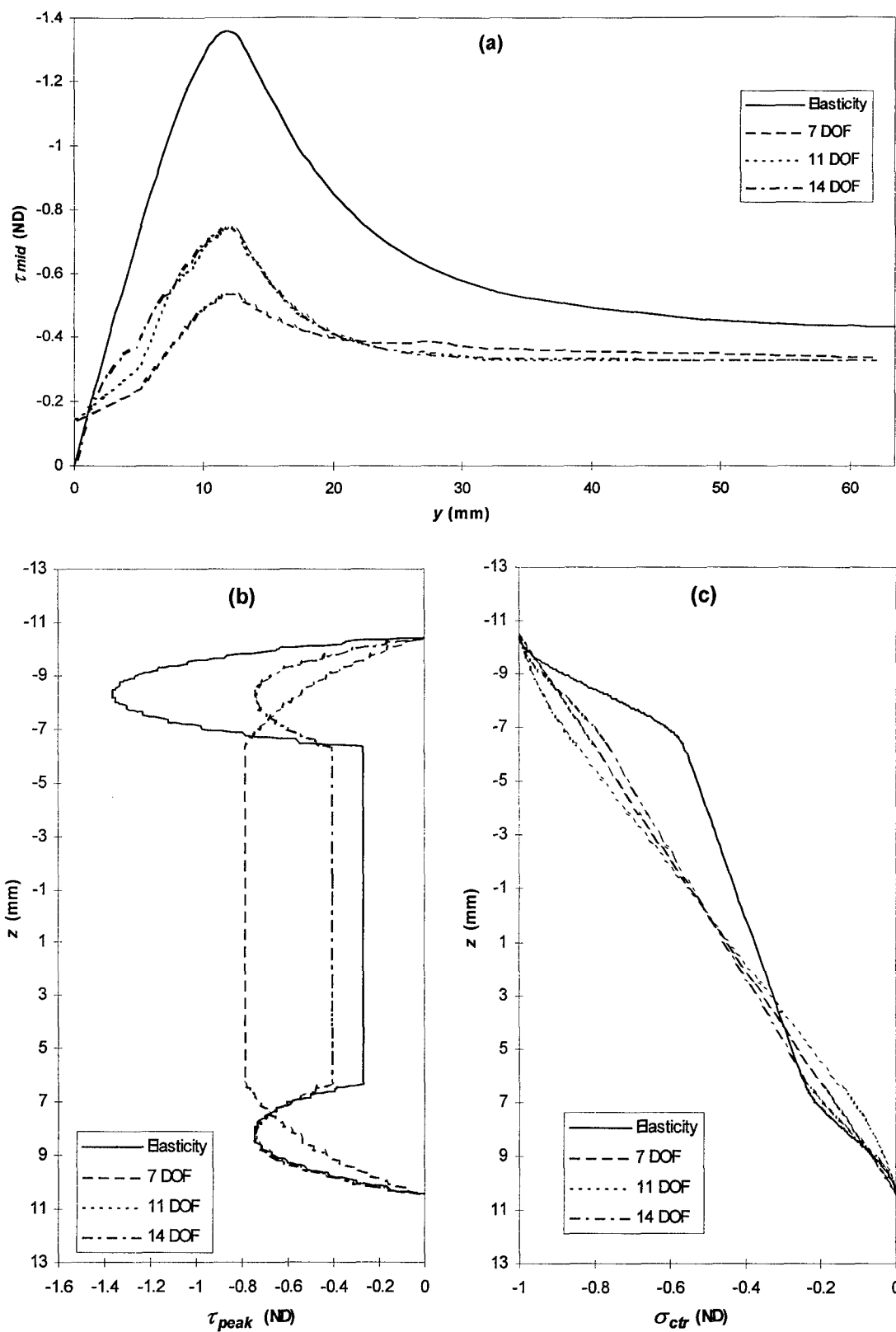


Figure 6-12 Comparison of current and elasticity solutions for 32-ply sandwich plate.

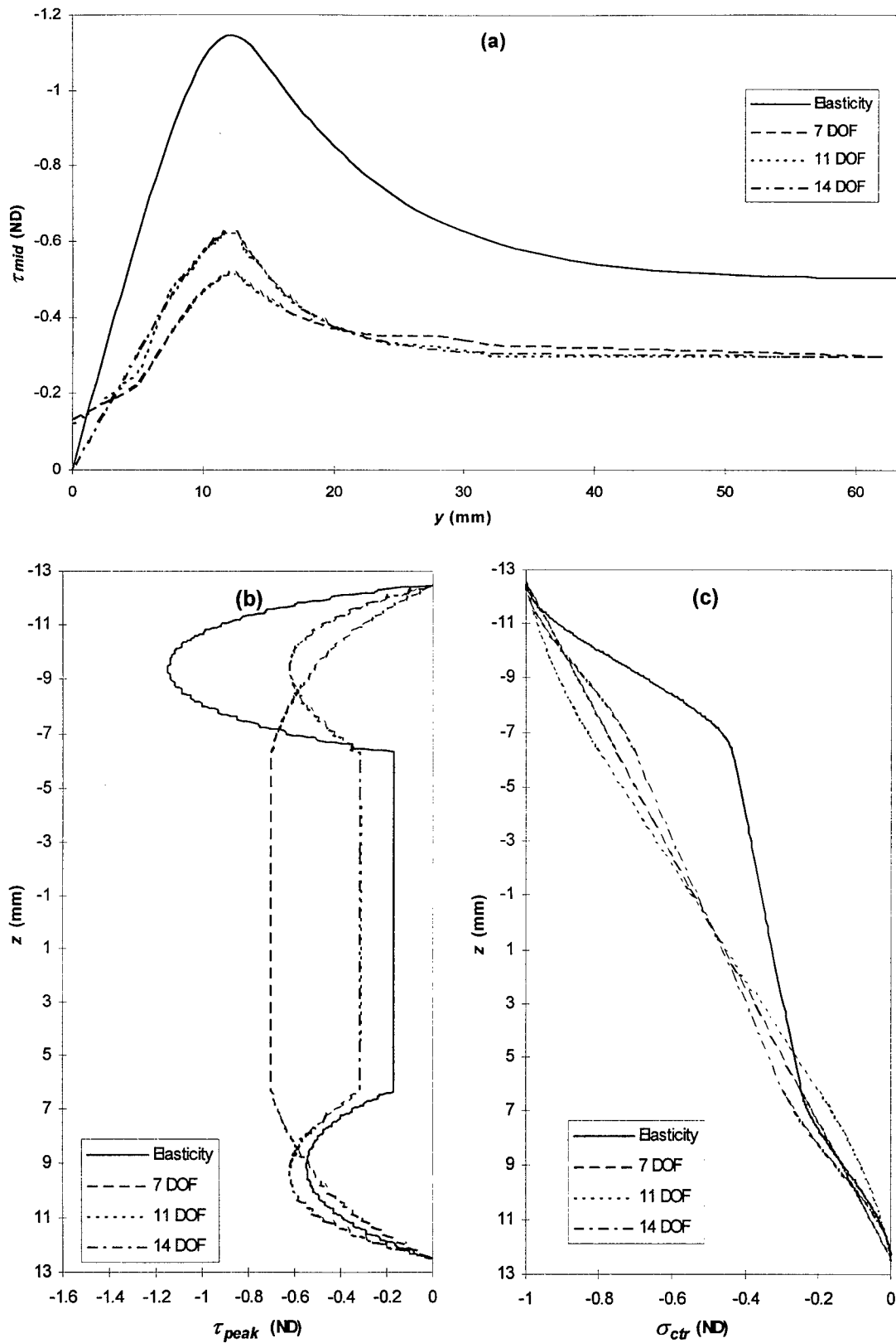


Figure 6-13 Comparison of current and elasticity solutions for 48-ply sandwich plate.

6.7.3.2 8-ply sandwich.

In figure 6-10a, it can be observed that the 11 DOF and 14 DOF elements are very close to the elasticity solution in predicting transverse shear stress at the midplane of the top facesheet in the 8-ply sandwich case. The 14 DOF elements are able to meet the symmetric boundary condition of zero transverse shear stress center of the plate while the 11 DOF elements do not. The 11 DOF and 14 DOF elements both correctly predict the correct y- and z-locations of the peak, and are significantly closer to the elasticity solution than the 7 DOF element (figures 6-10a and 6-10b). The difference between the various elements in terms of transverse direct stress is not considered significant (figure 6-10c). This may be due to the fact that the facesheets are so thin that the transverse stress does not change much within the facesheet. The linear variation through the core overwhelms the small change in the facesheet, so all of the elements have similar transverse direct stress profiles.

6.7.3.3 16-ply sandwich.

In figure 6-11a, it can be observed that the 11 DOF and 14 DOF elements are well below the elasticity solution in predicting transverse shear stress at the midplane of the top facesheet in the 16-ply sandwich case. Again, the 14 DOF elements are able to meet the symmetric boundary condition of zero transverse shear stress center of the plate while the 11 DOF elements do not. The 11 DOF and 14 DOF elements both correctly predict the correct y- and z-locations of the peak, and are significantly closer to the elasticity solution than the 7 DOF element (figures 6-11a and 6-11b). The difference between the various elements in terms of transverse direct stress begins to show in the 16-ply case (figure 6-11c). In terms of transverse direct stress prediction, the stress at the top of the core ($z = -6.35$ mm) is a good metric for judging the accuracy of the elements. With this metric, the 14 DOF element is best (6% error), followed by the 7 DOF element (6% error), while the 11 DOF element is poorest (14% error).

6.7.3.4 32-ply sandwich.

In figure 6-12a, it can be observed that the 11 DOF and 14 DOF elements are again well below the elasticity solution in predicting transverse shear stress at the midplane of the top facesheet in the 32-ply sandwich case. Again, the 14 DOF elements are able to meet the symmetric boundary condition of zero transverse shear stress center of the plate while the 11 DOF elements do not. The 11 DOF and 14 DOF elements both correctly predict the correct y-

and z-locations of the peak, and are significantly closer to the elasticity solution than the 7 DOF element (figures 6-12a and 6-12b). The difference between the various elements in terms of transverse direct stress begins to wane in the 32-ply case (figure 6-12c) as the errors of all of the elements become large. In terms of transverse direct stress at the top of the core, the 14 DOF element is still best (20% error), followed by the 7 DOF element (24% error), while the 11 DOF element is poorest (28% error). Figure 6-12c shows the weakness of the sandwich plate solution with regard to predicting the core transverse direct stress. Particularly, when the contact radius becomes small compared to the facesheet thickness, the three-dimensionality of the actual stress field is not well represented by a two-dimensional sandwich finite element even with the three-dimensional equilibrium post processing. This problem was addressed by abandoning the sandwich finite element model for stress (using it to obtain displacements only) and using a local finite element model in which the top facesheet was modeled as a monolithic element on an elastic-plastic foundation. In this way the element kinematics need only represent the facesheet displacements (not the core and two facesheets) and the result is that the motion away from the midplane is much better represented.

6.7.3.5 48-ply sandwich.

All of the general comments made for the 32-ply case are applicable to the 48-ply case as well. In terms of transverse direct stress at the top of the core, the 14 DOF element is still best (25% error), followed by the 7 DOF element (30% error), while the 11 DOF element is poorest (35% error).

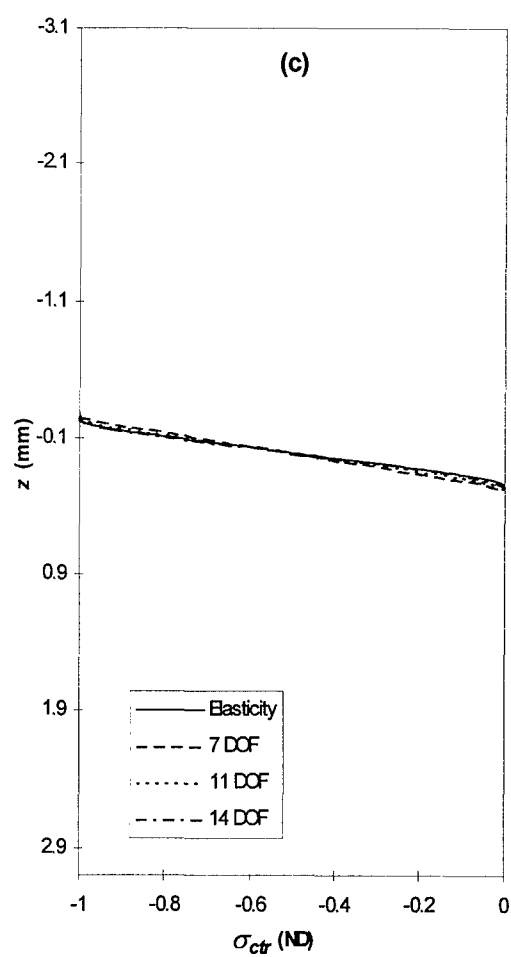
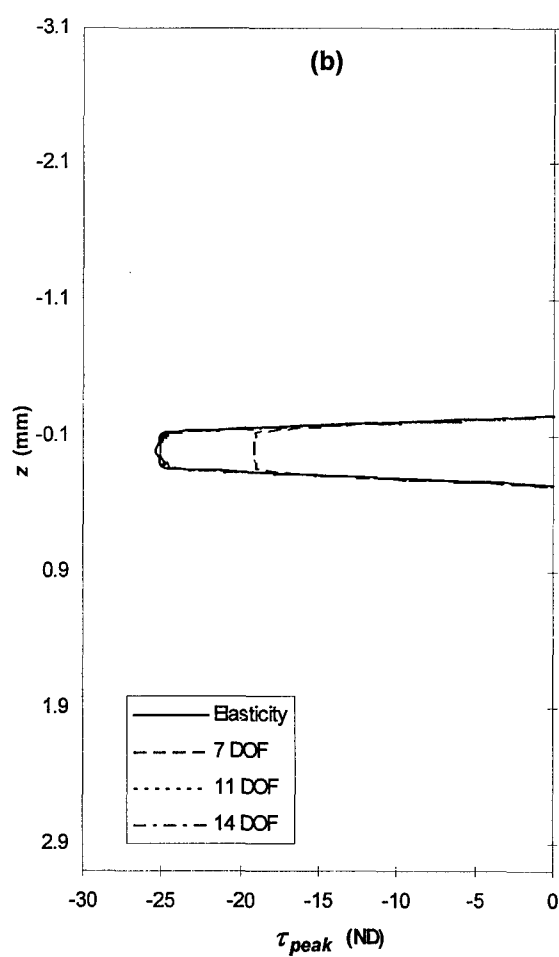
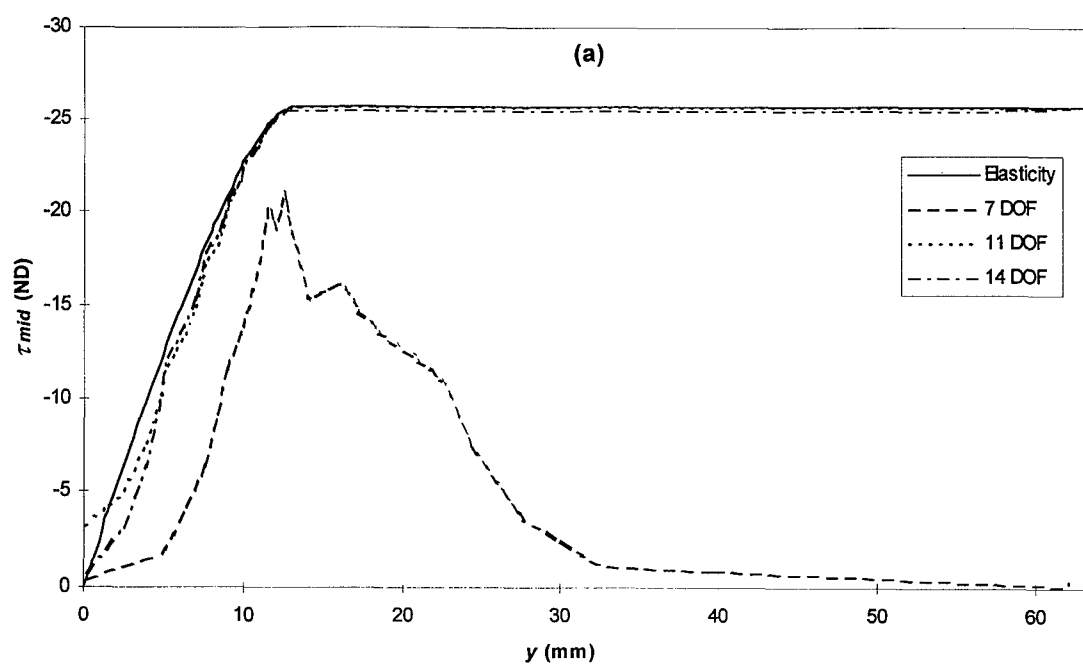


Figure 6-14 Comparison of current and elasticity solutions for 4-ply monolithic plate.

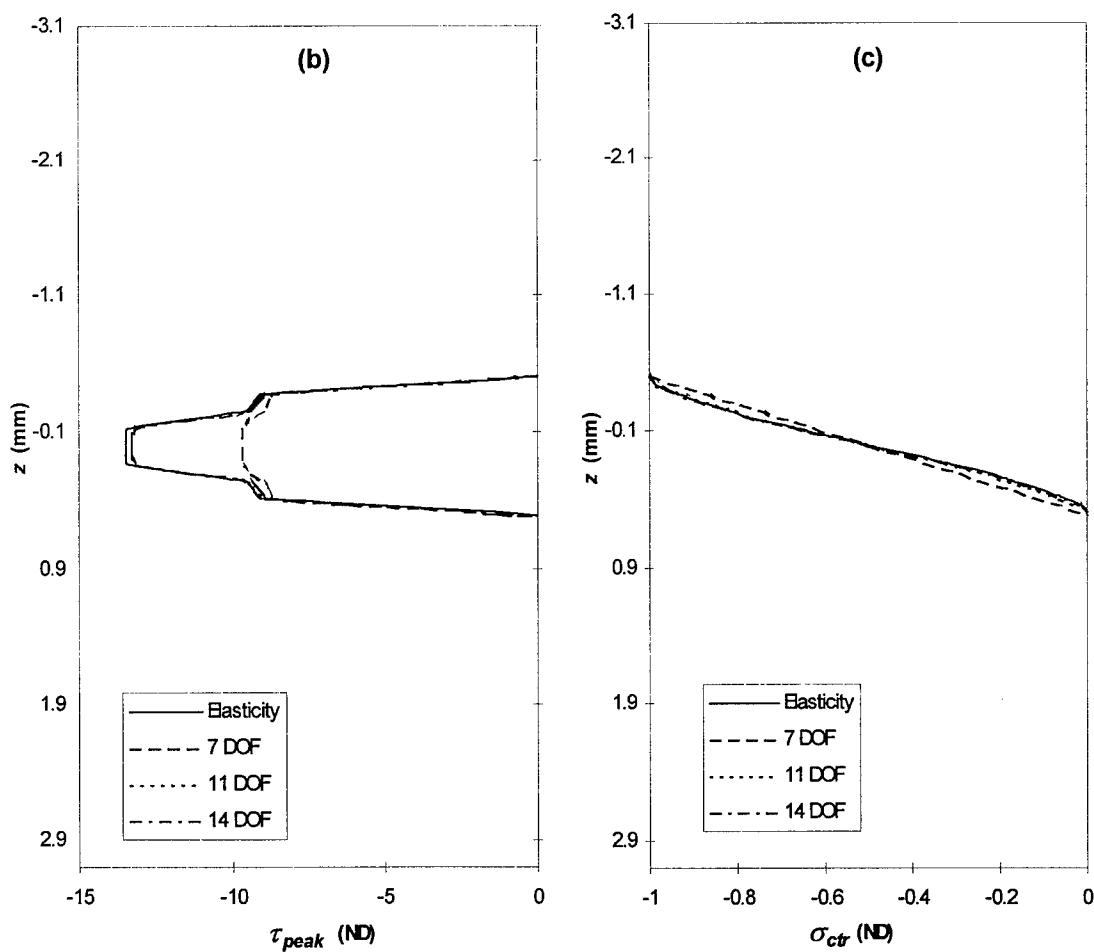
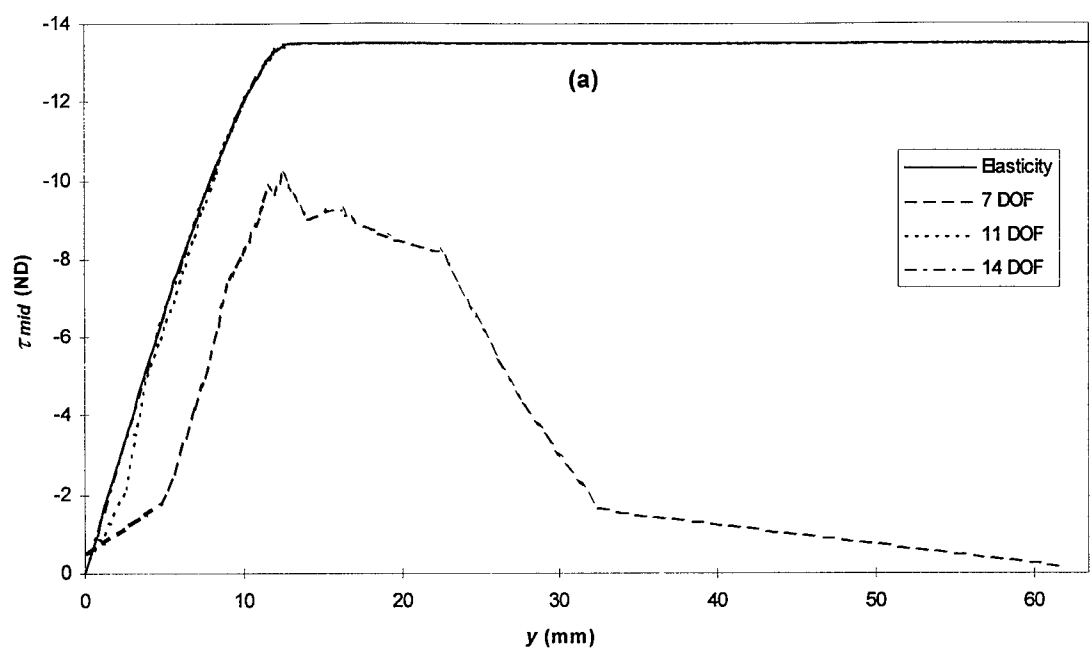


Figure 6-15 Comparison of current and elasticity solutions for 8-ply monolithic plate.

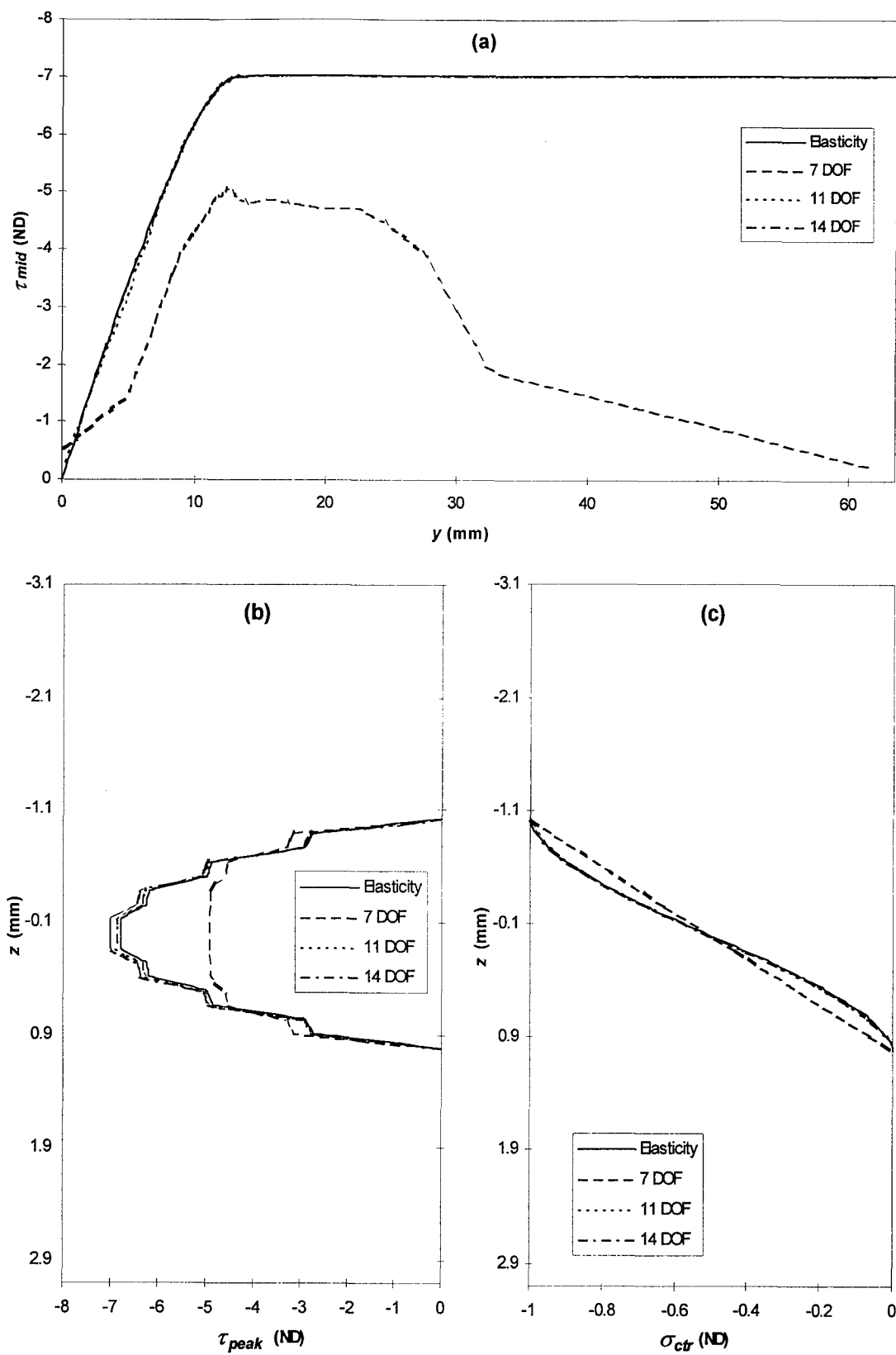


Figure 6-16 Comparison of current and elasticity solutions for 16-ply monolithic plate.

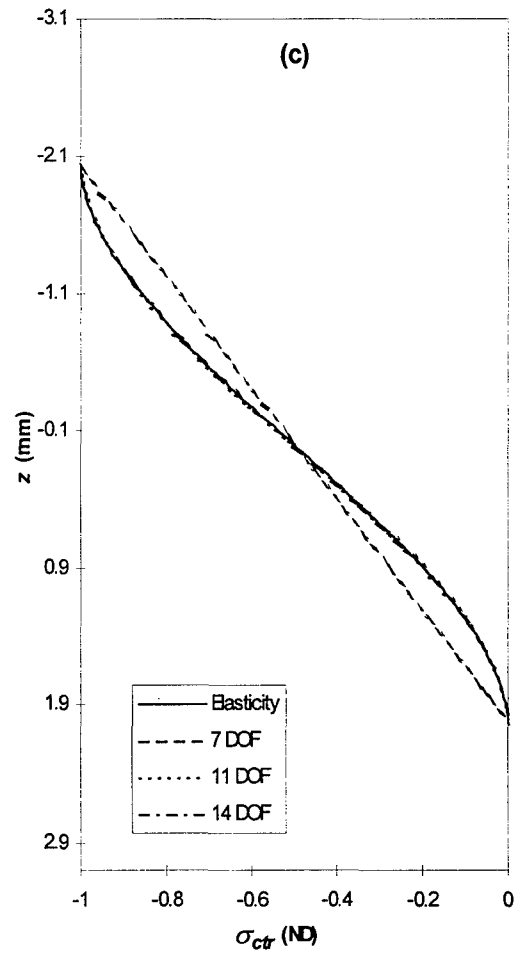
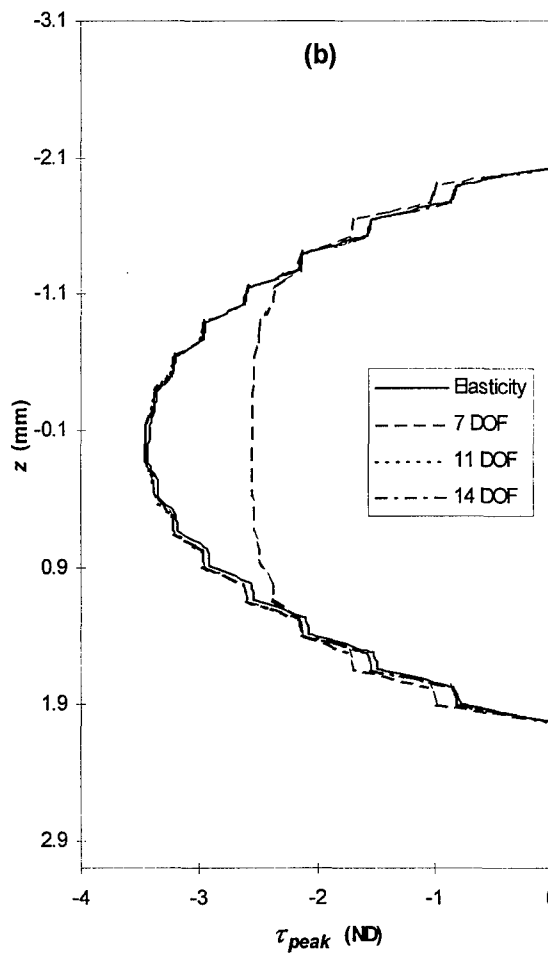
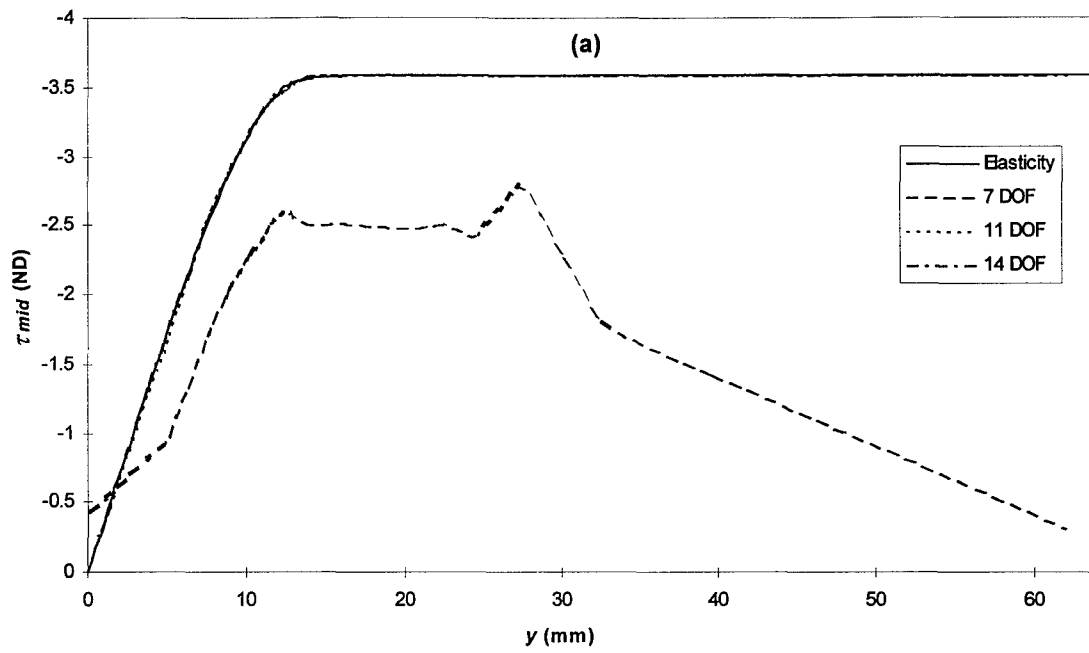


Figure 6-17 Comparison of current and elasticity solutions for 32-ply monolithic plate.

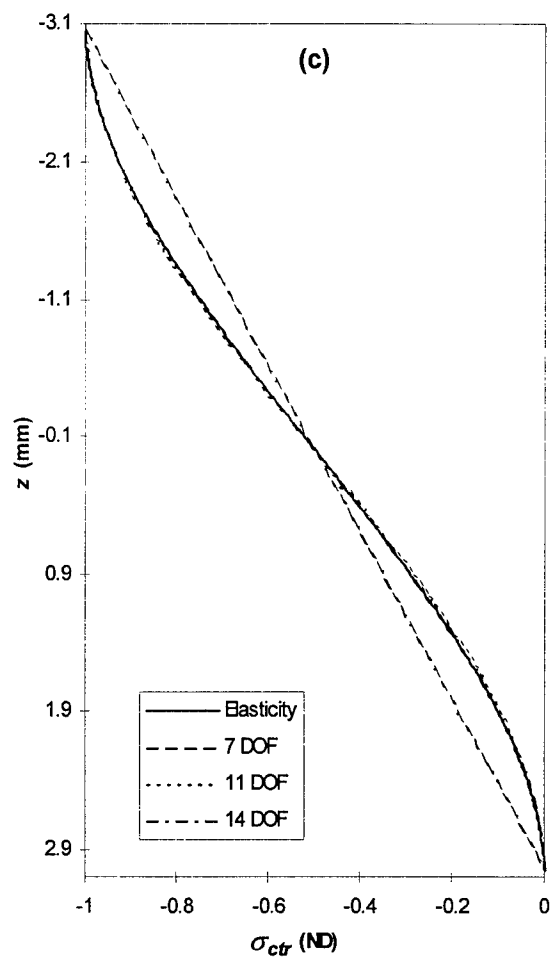
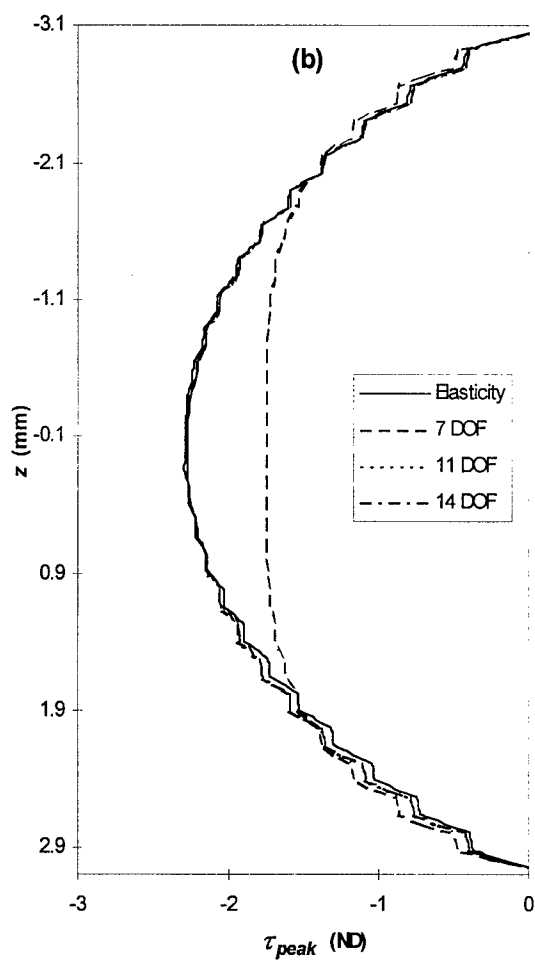
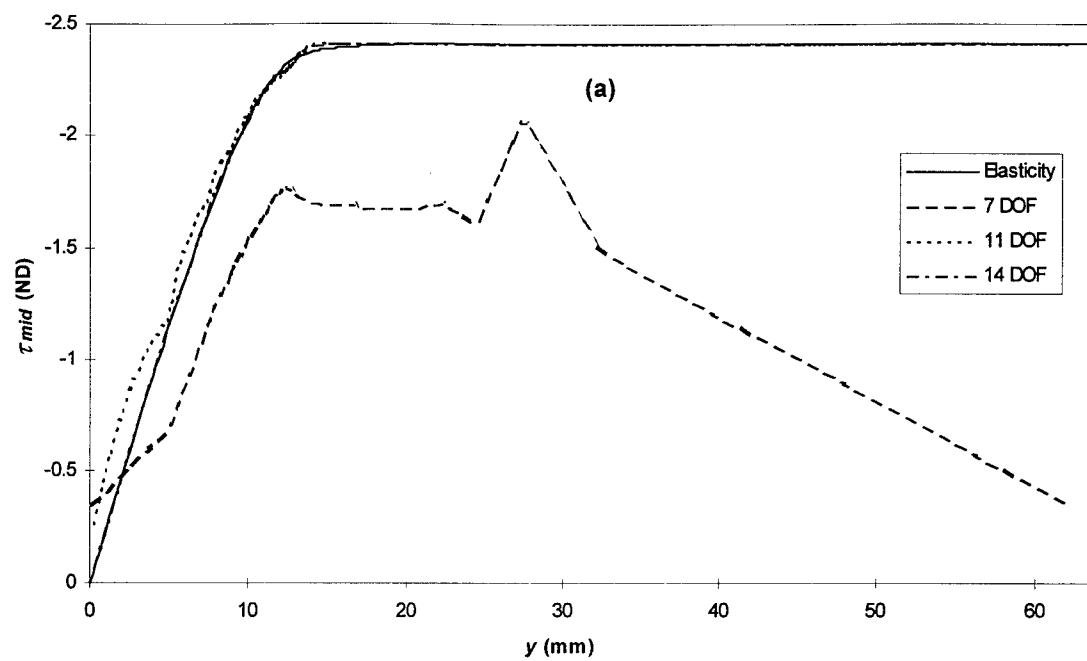


Figure 6-18 Comparison of current and elasticity solutions for 48-ply monolithic plate.

6.7.3.6 4-, 8-, 16-, 32-, and 48-ply monolith.

The 7 DOF element has a very significant error in transverse shear stress for the 4-ply monolithic plate test shown in figure 6-14a. This error is non-conservative and is carried through to all the facesheet thicknesses modeled (figures 6-15a, 6-16a, 6-17a, and 6-18a). The 11 DOF and 14 DOF elements both are significantly closer to the elasticity solution than the 7 DOF element for all facesheet thicknesses modeled. Figure 6-14b indicates that the transverse symmetry of the transverse shear stress predicted by the plate finite elements is actually present in this case. Since the core was not modeled for these tests, three-dimensional effects were not prominent (the plates are relatively thin) in this case and therefore the two-dimensional plate elements produce in-plane stresses that are very nearly in three-dimensional equilibrium. The value of the higher order shape functions is not as evident in figure 6-14c as it is in figures 6-15c, 6-16c, 6-17c, and 6-18c. This is due to the vertical scaling of the figures chosen to facilitate direct comparison between the different facesheet thicknesses. The higher order elements do significantly better than the lower order elements in predicting transverse direct stress. Though the difference between the transverse direct stresses predicted by the higher order elements and the 7 DOF element is significant for all facesheet thicknesses in the monolithic cases, the difference between the 11 DOF element, the 14 DOF element, and the elasticity solution is not significant (less than 1% over the entire range).

6.7.4 Generalized Newton-Raphson method.

For this research, geometric nonlinearity of the response of a sandwich structure to load was allowed by a generalization of the Newton-Raphson method. Letting the displacement be represented by the vector \mathbf{q} , the nonlinear stiffness of the structure be represented by the matrix $\mathbf{K}(\mathbf{q})$, and the applied load be represented by the vector \mathbf{R} , equilibrium of the structure with the applied load can be represented by the matrix-vector equation,

$$\mathbf{K}(\mathbf{q})\mathbf{q} = \mathbf{R}. \quad (6-92)$$

When material nonlinearities are also present (as in the case of damage in the current research), analysis must proceed in an incremental manner because the solution at any given displacement may depend not only on the current displacement but also on the previous loading history [239]. The problem is linearized over any increment of load by considering two stiffness matrices $\mathbf{K}_T(\mathbf{q})$, and $\mathbf{K}_S(\mathbf{q})$, which represent the tangent and secant stiffnesses. An iterative procedure is employed

for each load increment, i , to solve for \mathbf{q}_i . Let \mathbf{q}_i^0 be the converged displacement vector for the $(i-1)^{\text{th}}$ load increment \mathbf{R}_{i-1} . That is,

$$\mathbf{R}_{i-1} - \mathbf{K}_S(\mathbf{q}_i^0)\mathbf{q}_i^0 \approx 0 \quad (6-93)$$

Then when the load is incremented, the solution is no longer in equilibrium,

$$\mathbf{R}_i - \mathbf{K}_S(\mathbf{q}_i^0)\mathbf{q}_i^0 \equiv \text{residual force} \neq 0 \quad (6-94)$$

We desire to modify the displacement vector in order to get the structure in equilibrium with the new load. This update is done by solving,

$$\mathbf{K}_T(\mathbf{q}_i^0)\Delta\mathbf{q} = \mathbf{R}_i - \mathbf{K}_S(\mathbf{q}_i^0)\mathbf{q}_i^0, \quad (6-95)$$

for $\Delta\mathbf{q}$ and updating \mathbf{q}_i .

$$\mathbf{q}_i^1 = \mathbf{q}_i^0 + \Delta\mathbf{q}. \quad (6-96)$$

For iteration step j we solve,

$$\mathbf{K}_T(\mathbf{q}^{j-1}_i)\Delta\mathbf{q} = \mathbf{R}_i - \mathbf{K}_S(\mathbf{q}^{j-1}_i)\mathbf{q}^{j-1}_i, \quad (6-97)$$

and update \mathbf{q}_i ,

$$\mathbf{q}^j_i = \mathbf{q}^{j-1}_i + \Delta\mathbf{q}. \quad (6-98)$$

We continue this process until,

$$\frac{\sqrt{\sum_n (\mathbf{q}_n^j)^2} - \sqrt{\sum_n (\mathbf{q}_n^{j-1})^2}}{\sqrt{\sum_n (\mathbf{q}_n^1)^2}} \leq \text{convergence tolerance}, \quad (6-99)$$

in which the summations over n represent summations over each degree-of-freedom in the vector \mathbf{q} . So that,

$$\mathbf{R}_i - \mathbf{K}_S(\mathbf{q}^j_i)\mathbf{q}^j_i \approx 0, \quad (6-100)$$

and then set,

$$\mathbf{q}_{i+1}^0 = \mathbf{q}_i^j, \quad (6-101)$$

and proceed with the next load increment, $i+1$. Terminate when load increment \mathbf{R}_i is at least equal to the maximum load required for the given analysis.

Every quasi-three-dimensional case study in this research considered a square plate with simply supported edges (u and v translations are free). Since all ply orientations were either 0 or 90 degrees, it was only necessary to generate finite element meshes for a single quadrant of each plate by prescribing bi-axial symmetry. Figure 6-19 shows the displacement boundary conditions which were applied to each square quarter-plate. In addition to the boundary conditions shown in figure 6-19, the models using cubic Hermitian shape functions for ψ_1 and ψ_2 (11 DOF and 14 DOF) had $\psi_{1,1}$ and $\psi_{2,2}$ set to zero on the simple support boundaries and $\psi_{1,2}$ and $\psi_{2,1}$ set to zero on the symmetric boundaries. The 14 DOF model used 5th order Hermitian interpolation for w and had the additional boundary conditions of $w_{,11}$ and $w_{,22}$ set to zero on the simple support boundaries and $w_{,12}$ set to zero on the symmetric boundaries.

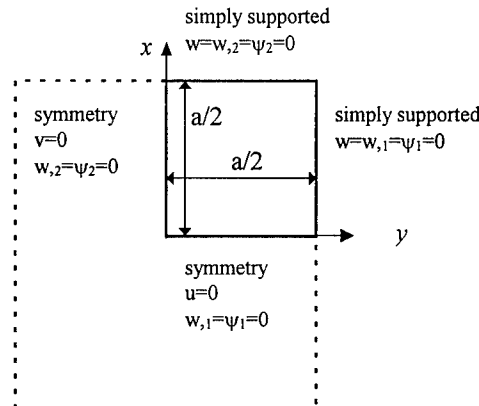


Figure 6-19 Boundary conditions common to each square quarter plate.

6.8 Failure Criteria

As discussed in Chapter 2, progressive failure analysis of composite structures with arbitrary lay-ups and loading requires both a laminate stress analysis model and a failure model that can account for general states of stress and modes of damage. After pointwise stresses in each layer of the composite are known from laminate analysis, failure of the composite is predicted either by employing a phenomenological failure criterion at the macromechanical (lamina) level or by relating the lamina stresses to the stresses in each constituent of the composite and employing a

failure criterion at the micromechanical level. Micromechanical criteria were not be considered in this research. Failure criteria discussed in Chapter 2 were used for determining the extent of matrix cracking and core damage as well as predicting the onset and progress of delamination. These were compared with one another and with the experimental results in an attempt to determine which are best for the particular mode in question.

6.8.1 Matrix cracking and core damage.

With the improved stress values anticipated from the three-dimensional equilibrium integration, stress-based failure criteria looked particularly promising for this research. The progression of matrix cracking and core damage was assumed to be governed by load transfer associated with previous failures, so that the failure criteria combined with a reduced stiffness routine was used to follow the progression of damage

6.8.2 Delamination.

Two classifications of analyses into which the published work can be separated are damage mechanics and fracture mechanics. Damage mechanics, or progressive degradation modeling, describes the damage with damage state variables, cracks are not directly modeled. Stress-based damage evolution laws are typically used to model the progression of damage. The analysis can begin without any damage. Fracture mechanics, on the other hand, follows the growth of a particular crack. No crack initiation is predicted, instead an initial crack is assumed and its progression is sought. A Griffith type energy release rate-based criterion is typically used to predict the growth of the crack. The scales of these two classifications of analyses are typically very different. Fracture mechanics often requires a smaller scale since a particular crack, rather than a multiply cracked lamina for example, must be modeled. The delamination damage progression tool used in this research was of the damage mechanics classification. A stress-based failure criterion indicated delamination and a stiffness reduction was in the lamina adjacent to the indicated delamination was used to model the effect of the delamination on the response of the structure.

6.9 Contact Problem

The interaction between the flexible plate and the near-rigid hemispherical tup is a very important facet of the low-velocity impact problem for composite sandwich panels. The force that the tup applies to the plate must be distributed over some area (contact area) so that finite stress is induced in the plate. The induced stresses produce local deformations in the plate that tend to conform the plate surface to the tup surface, changing the contact area. Since the contact area influences the stress and the stress influences the contact area, the contact problem is evidently non-conservative. As discussed in section 2.7, the non-conservative nature of the contact problem was neglected.

The quasi-static assumption made here simplifies the approach by making the tup force a program input rather than an unknown. The problem is reduced to that of an indenter in static equilibrium (at any given load) with a deformed (and perhaps damaged) plate. In order to load the finite element model simulating this event, a Hertzian contact law was employed to distribute the tup force over the contact area. This contact law is axisymmetric (elliptical or proportional to distance from the axis of symmetry to the $3/2$ power). This contact law idea has its roots in isotropic analyses where it has proved valuable. The validity of the assumed axisymmetric pressure response of anisotropic plates to a hemispherical indenter or tup is certainly questionable, since the plate properties are directional. For tup radii that are small compared to the global curvature of the plate under load, the contact radii will be small and the particular form of the contact pressure profile may be less important than the total load and the area over which it acts. These two parameters, load and contact area, can be experimentally correlated to verify that the analysis is distributing the load in a way that simulates the true load distribution of the experiment. It should be kept in mind that the spherical indenter is itself a simulation of the generally-shaped impactor (e.g. stone, dropped wrench, or other hard object) that these structures will encounter in service. Hence the Hertzian contact law given in equation 6-90 (but with a variable $R_{contact}$) was used for the current work.

The following describes the impact event which is of interest, and the static contact algorithm employed for this research.

A moving rigid mass (the tup) makes contact with a simply-supported, stationary, laminated composite plate at time $t = 0$. The progress of the tup is impeded by the presence of the plate. For the tup to continue its motion, it must move the plate or deform it. Rigid body motion of the plate is prevented by the supports. The deformation of the plate stores elastic (and possibly, plastic and damage) energy until the kinetic energy of the tup is reduced to zero (the tup does work on the plate). The stored elastic energy then does work on the tup, accelerating it back up. In both cases, the work is done by the force between the two bodies moving through a distance. Force then can be considered the actual load applied to the plate, while the distribution of that force (pressure profile or "footprint") is determined by the radius of the indenter and the local stiffness of the plate. The quasi-static assumption has removed time from the picture.

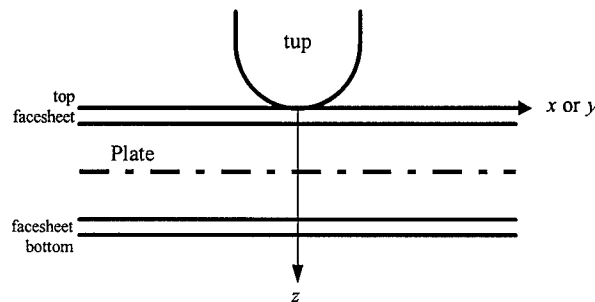


Figure 6-20 Contact problem geometry and coordinate system.

Let the x -, y -, and z -direction displacements of the plate for a given tup force, F , be $u_1(x,y,z,F)$, $u_2(x,y,z,F)$, and $u_3(x,y,z,F)$ to distinguish them from the midplane displacements $u(x,y,F)$, $v(x,y,F)$, and $w(x,y,F)$. Let the vertical displacement of the center of the contact area (the point $(0,0)$, where the tup and the plate first touch) be,

$$w_{top}(0,0,F) = u_3(0,0,-\frac{h}{2},F) \quad (6-102)$$

Assume that when F is zero the configuration is that of figure 6-20 and the plate has just made contact with the tup. The plate deflection is zero when F is zero. Choose some small interval of load, ΔF such that no damage occurs below $F = \Delta F$. The portion of the event between $F = 0$ and $F = \Delta F$ is then of no concern to this analysis. Choose also some small radius of contact, $R_{contact}$, and assume that the load, ΔF , is distributed over the contact area as,

$$q(r) = \begin{cases} 0, & r > R_{\text{contact}} \\ q_0 \sqrt{1 - \frac{r^2}{R_{\text{contact}}^2}}, & r \leq R_{\text{contact}} \end{cases} \quad (6-103)$$

$$q_0 = \frac{3F}{2\pi R_{\text{contact}}^2}$$

Apply the first ΔF , so that at load $F = \Delta F$ the tup has moved a distance:

$$w_{\text{top}}(0,0,\Delta F) = u_3(0,0,-\frac{h}{2},\Delta F) = K_{\text{Eff}}^{-1}(\Delta F)\Delta F \quad (6-104)$$

in which $K_{\text{eff}}(F)$ is the nonlinear effective plate stiffness including both the plate bending stiffness and the contact stiffness as described in Chapter 3. Neglecting the transverse strain, of the plate, the two-dimensional finite element solution without the equilibrium integration produces the situation illustrated in figure 6-21.

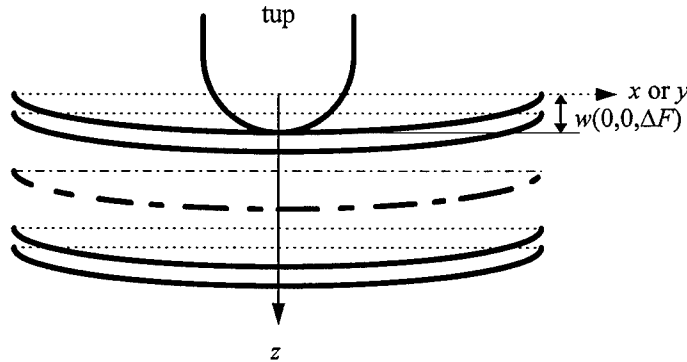


Figure 6-21 Finite element displacements for initial small load.

Notice that this implies that the top surface and midplane of the plate move together with the tup. This effectively equates the motion of the top of the plate with that of the midplane. Though this assumption is common for plate problems, it is clearly wrong for transverse impact. Equilibrium integration is used to improve on these assumptions.

When the load is applied to the finite element model, the resulting plate displacement produces a response force from the stiffness of the plate (via FEM) as well as a transverse direct strain profile through the thickness under the point of impact (via constitutive relationships and transverse stresses found from the equilibrium equations and the in-plane stresses from the FEA).

Call this first iteration value of the force F_1 and strain ε_3 . With the appropriate terms from the stiffness conceptually,

$$F_1 = K(K_{Eff}^{-1}(\Delta F)\Delta F) \quad (6-105)$$

$$\frac{\partial}{\partial F} w_{top}(0,0,\Delta F) = \frac{\partial}{\partial F} u_3(0,0,-\frac{h}{2},\Delta F) = K_{Eff}^{-1}(\Delta F) . \quad (6-106)$$

This ties the FEM solution to the three degree of freedom model of Chapter 3. And suggests a check of K_{Eff} with that derived empirically from the dynamic experimental data may be another way to quantify the importance of dynamic effects. If K_{eff} from equation 6-104 agrees with that from equation 3-42, the dynamic effects may be negligible.

The transverse strain $\varepsilon_3(q)$ comes from equations 6-63a, 6-65 etc. and leads to relative motion between the midplane and the top surface of the plate. That is, for a compressive strain, the top surface moves toward the midplane (see figure 6-22). For any given load F , call this relative motion Δh .

$$\Delta h(x,y) = \int_0^{-h/2} \varepsilon_3(x,y,z)dz \quad (6-107)$$

This integration is carried out for all Gauss points (where stresses are calculated) within the contact area prescribed by the assumed contact radius, $R_{contact}$, and added to the midplane displacements at those points to produce a top surface deflection profile under the tup.

$$w_{top}(x,y) = \Delta h(x,y) + w(x,y) \quad (6-108)$$

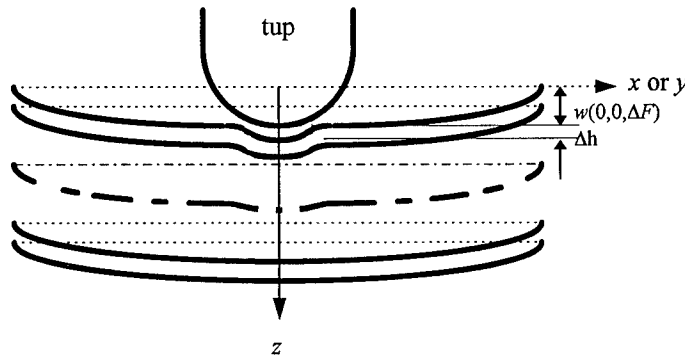


Figure 6-22 After first step of FEM/3D-equations of motion.

The total displacement of the top surface illustrated in figure 6-22 does not, in general enforce the condition that the tup is rigid and the plate can not occupy the space occupied by the tup. Assuming the top surface of the center of the plate is in contact with the surface of the tup, this constraint is simply that the top surface must displace at least as much as the surface of the tup. The surface of the tup is illustrated in figure 6-23.

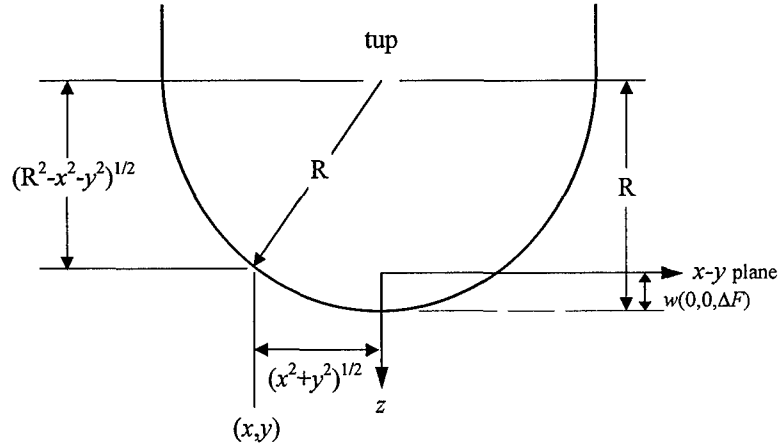


Figure 6-23 Tup surface as a constraint on the plate top surface displacement.

The constraint can be expressed as,

$$w_{top}(x, y, F) \geq w_{top}(0, 0, F) - R + \sqrt{R^2 - x^2 - y^2} \quad (6-109)$$

where R is the tup radius and the inequality in equation 6-109 implies an iterative approach and enforces the condition that the surface can not move into the space occupied by the tup (rigid spherical contact surface).

Having shown how the top surface displacements are found (equation 6-108) and the constraint that must be imposed upon them through the an iterative approach (equation 6-109), the specific algorithm developed for the present research to enforce the constraint will now be described. For an elastic spherical tup in contact with an elastic half-plane Timoshenko and Goodier [243] give the relationship between contact radius $R_{contact}$, applied load F , tup radius R , and elastic modulus E , as,

$$R_{contact} = 1.109 \sqrt[3]{\frac{FR}{E}} \quad (6-110)$$

This suggests that for a given load and material, a proportionality should exist between the contact radius and the tup radius, i.e.

$$R_{contact} \propto \sqrt[3]{R} \quad (6-111)$$

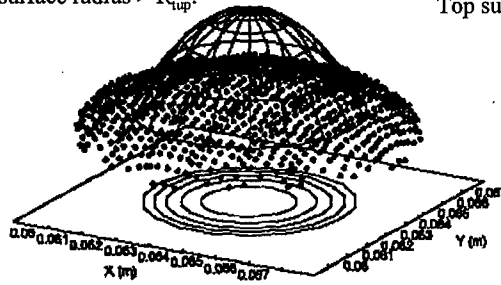
This idea was used to iterate the finite element solution for any given load (and damage condition) to obtain the contact radius. In particular, the radius of the top surface under the load was made to be the same (within a specified tolerance) as the tup radius by changing the estimated contact radius. The top surface displacement of all Gauss points within the assumed contact radius were fitted to a sphere of arbitrary radius by a least squares method resulting in a calculated tup radius, R_{top} , (the radius that best fits the top surface displacements) which was in general different from the tup radius, R , which the simulation was intended to model. The contact radius is updated to reflect the fact that it produced the wrong tup radius and another iteration of the solution is performed with this new $R_{contact}$. For iteration i , the estimate of the contact radius was given by,

$$R_{contact_i} = R_{contact_{i-1}} \sqrt[3]{\frac{R}{R_{top}}} \quad (6-112)$$

and the finite element solution was repeated with the new contact radius (and resulting Hertzian contact pressure profile). This process continued until the calculated tup radius was the same as the required tup radius within some small tolerance. In practice, this convergence took only 3 to 5 iterations. Both top surface radius, R_{top} , and contact radius, $R_{contact}$ are shown as a function of contact iteration number in figure 6-24.

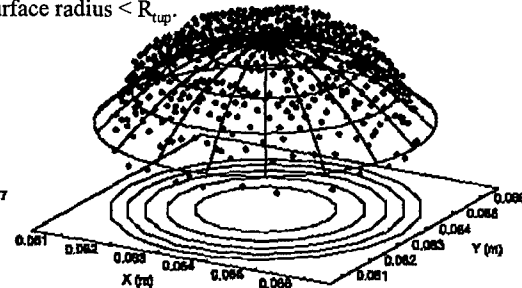
Iteration 1, R_{contact} too large.

Top surface radius $> R_{\text{tup}}$.

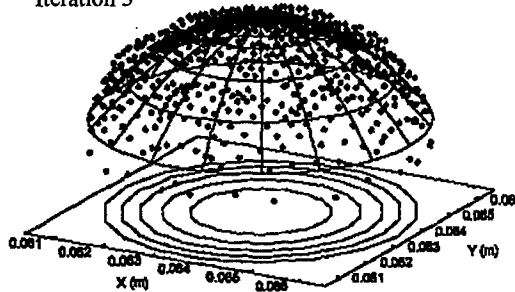


Iteration 2, R_{contact} too small.

Top surface radius $< R_{\text{tup}}$.



Iteration 3



Iteration 4

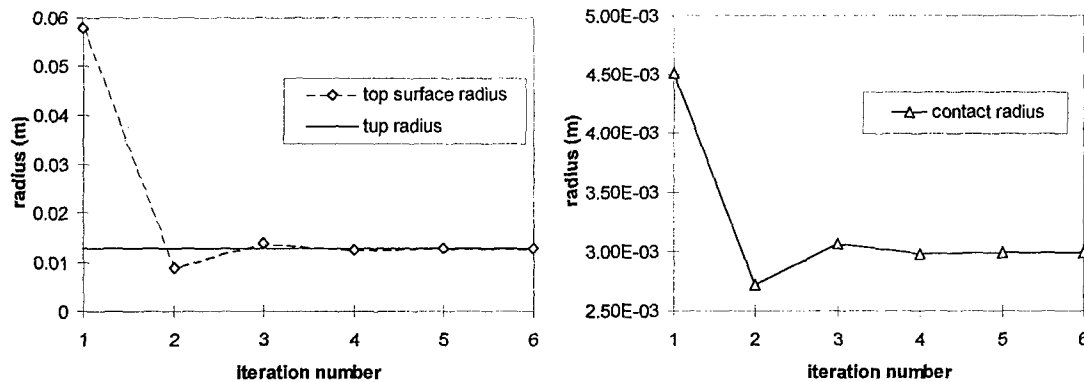
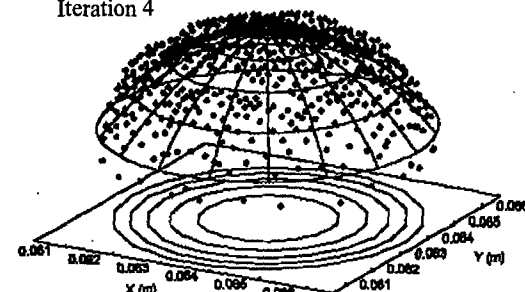


Figure 6-24 Typical convergence of top surface radius and contact radius with contact iteration.

When the contact solution had converged, the damage algorithm was invoked. At some point, the damage criteria identified a damage. When that happened, the stiffness was modified and the iteration continued with the contact algorithm again. The contact algorithm was iterated within the local model and the resulting contact radius was used in the global model. Further discussion will be subsequently presented to show how the contact algorithm was incorporated into the local and global finite element models.

6.10 Adaptive Mesh

As the contact algorithm is invoked, the contact radius changes, so that with a fixed grid, the number of elements over which the contact load is applied may change. In particular, as the load increases, the contact radius does as well. A mesh that is refined enough for one contact radius may not be refined well enough for a different contact radius. To overcome this problem, one could make a single grid which is refined tightly enough in the center for the smallest contact radius anticipated and refined far enough away from the center for the largest contact radius anticipated, but the number of degrees of freedom for such a model would be large compared to that of a mesh refined for a single contact radius. The highly iterative nature of the solution algorithm used in this analysis demanded the number of degrees of freedom be as small as practical. To accomplish this, an adaptive mesh algorithm in which the plate dimensions, initial contact radius, and number of elements was chosen by the user, but the adaptive mesh algorithm set the grid spacing within the computational domain based on the current contact radius. The equation defining the grid spacing was designed to place the majority of the elements within 2.5 contact radii of the center of the plate and provide near unit element aspect ratios in that region. The equation defining the element x-dimension length was,

$$\Delta x_i = a \left\{ \left[\left(\frac{si}{n} \right) + \left(\frac{i}{n} - 1 + (1-s)^{1/power} \right)^{power} \right] - \left[\left(\frac{s(i-1)}{n} \right) + \left(\frac{i-1}{n} - 1 + (1-s)^{1/power} \right)^{power} \right] \right\}$$

where,

a = plate half width (63.5 mm)

$power = 16$

(6-113)

$$s = \frac{4R_{contact}}{a}$$

n = number of elements in the x - direction

$i = 1, 2, \dots, n$

in which the choices of s and $power$ were made after a parameter study in which the resulting grids were compared graphically and subjectively judged by the author with respect to the degree of refinement near the contact region and the smoothness of the transition. With this choice of parameters,

$$\Delta x_1 \approx \frac{4}{n} R_{contact}$$

and,

$$\sum_{i=1}^n \Delta x_i = a$$
(6-114)

Each time the contact algorithm modified the contact radius, the adaptive mesh algorithm redefined the grid spacing, so that the new grid was tailored to the new contact radius. The change in the position of the nodes required the finite element stiffness to be recalculated. It should be observed that moving the nodes implied that the degrees of freedom from one contact iteration to the other were not the same. An implication of the modified degrees of freedom was that the displacements from one load increment to the next load increment may not be based on the same nodal coordinates. The nodal coordinates were made consistent between load increments by starting each load increment with the contact radius (hence nodal coordinates) found from the previous load increment. Nodal displacements could not be compared directly between load increments except at the corners of the model (one of which was at the center of the applied load), because only there were the nodal coordinates fixed. In practice, the contact radius change between load increments was small, and the change in the location of the nodes between load increments was small. Particular results of the adaptive mesh algorithm, including grids generated, are shown in the mesh refinement study given in Chapter 8.

6.11 Core Properties

As noted in section 6.4.4, the primary functions of the core in a sandwich construction are to resist transverse compression (supporting the facesheets) and transfer shear loads. Although Nomex honeycomb core is known to exhibit nonlinear load deflection relations in both compression and shear before any damage [128], linear material properties were used in this research up to the point of core damage. A core constitutive model that includes a linear secant modulus for the ratio of transverse direct stress to transverse direct strain before core damage was used. Similarly, the ratio of maximum transverse shear stress to transverse shear strain in each of the in-plane directions will form the constitutive components for the 4 and 5 components. Having no data from which to deduce Q_{45} or Q_{66} , Q_{45} was assumed to be zero and Q_{66} was assumed to have a value of 10% of the average of Q_{44} and Q_{55} . The later was done to avoid problems

associated with a zero stiffness in in-plane shear. In particular, the terms in equation 6-27 before translation are:

$$Q_{33} = \frac{\sigma_{zz_{crush}}}{\epsilon_{3_{crush}}}, Q_{44} = \frac{\sigma_{yz_{max}}}{\epsilon_{4@ \sigma_{yz_{max}}}}, Q_{55} = \frac{\sigma_{zx_{max}}}{\epsilon_{5@ \sigma_{zx_{max}}}}, Q_{66} = \frac{Q_{44} + Q_{55}}{20}, Q_{45} = 0 \quad (6-115)$$

6.12 Damage progression

6.12.1 Matrix cracking.

Matrix cracking was assumed to be present in a particular lamina when one of the stress-based failure criteria was violated. As noted in section 6.4.2, matrix cracking was handled as a constitutive change in which the coefficients Q_{12} , Q_{22} , Q_{23} , Q_{44} , and Q_{66} were reduced by three orders of magnitude. The progression of matrix cracking was based on load transfer within the finite element model. It is assumed that all forms of damage are coupled, so that matrix cracking will affect and be affected by core damage and delamination. Both core damage and delamination were modeled in the local FEM as was matrix cracking. Matrix cracking progression was not included in the global FEM. That is, the stiffness reduction associated with matrix cracking and as well as the load transfer leading to the continuation of matrix cracking was included in the local but not the global finite element model. The approach then, was not complicated. Within the local model, after each FEA step, in-plane stress was calculated. Three-dimensional equilibrium was approximately satisfied (section 6.6), producing transverse stresses and modified in-plane stresses. These stresses are used in the failure criteria (section 6.8) to determine if matrix cracking was present in any particular ply at any particular Gaussian point (all integration was done at these points rather than the nodes). If matrix cracking was determined to exist, the constitutive relation for that ply in that element was modified in proportion to the number of Gaussian points that failed. That is, if one fifth of the Gauss points within a given element showed matrix cracking at ply k , the constitutive terms for that ply were reduced by one fifth. The finite element solution was repeated without changing the load. Within the damage algorithm, iteration continued until no additional changes to the constitutive relation ensued.

6.12.2 Core damage.

In the global model, core damage was handled in much the same way as matrix cracking. Comments in 6.11.1 apply directly to core damage as well as matrix cracking. After damage, the

entire core stiffness was effectively removed (it was necessary to leave it nonzero to avoid conditioning problems). In the local model, core damage was modeled by removing the elastic foundation stiffness for elements found to have core damage. In addition to this stiffness change, equilibrium integration for the local model was accomplished with zero stress at the bottom surface of the facesheet (since the core stiffness is zero). This was done by integrating equations 6-56 and 6-63a through the facesheet and taking the lower boundary condition as zero. In this way, the condition $\sigma_3 = \sigma_4 = \sigma_5 = 0$ is enforced for the facesheet locally at the interface between the core and the facesheet. This equilibrium change partially accounts for the fact that when the core is damaged it does not support the facesheet. That is, the motion of the facesheet into the space formerly occupied by the core will not induce any transverse direct or shear stress at the lower surface of the facesheet. The effect was a much higher bending-type load within the top facesheet as the transverse direct stress formerly taken by the core must be transferred by transverse shear within the facesheet to the surrounding supported facesheet. The intact core immediately surrounding the damaged core saw an increased transverse load since it acts as a fulcrum for the bending top facesheet. The interaction between the tup, the top facesheet, and the core is illustrated schematically in figure 6-25. In the figure, the core is represented by springs to emphasize its role in providing vertical support for the top facesheet. The leftmost undamaged spring in figure 6-25 is seeing a greatly increased transverse load as described above.

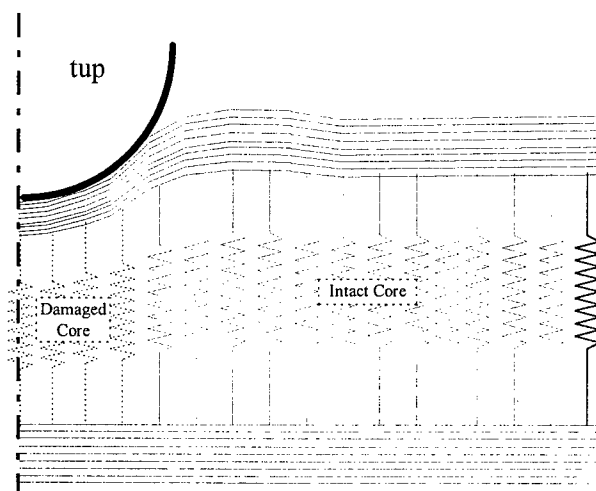


Figure 6-25 Schematic of core failure

6.12.3 Delamination.

The effect of delamination on the plate response was considered in the local model through a procedure very similar to that described above for matrix cracking. The only significant differences were that the failure criterion was based on the interface stresses and constitutive terms for both plies adjacent to the failed interface were reduced. In this way, the constitutive terms contributing to transverse shear stiffness were reduced, but the in-plane stiffness of the facesheet was unaffected by the simulated delamination.

6.13 Local Model Solution Algorithm

The algorithm developed for this research is local-global in that it incorporates a local model which is solved first and a global model which depends on the local model solution. The local model simulates the sandwich structure by modeling the top facesheet as a plate and the core as a foundation supporting the facesheet. The core stiffness is constant (elastic) until the core stress reaches the yield stress, taken to be the maximum stress attained in uniaxial compression [128]. The strain at which the core first attains the yield stress is the yield strain. Between yield strain and failure strain, the core (secant) stiffness varies to maintain the core yield stress at the lower surface of the top facesheet. Thus the foundation must be called elastic-plastic, even though the finite element does not include plasticity. The principal feature not included in the local model (hence the need for a global model) is midplane displacement of the sandwich. The motion of the top facesheet relative to the sandwich midplane is modeled in the local model and the motion of the sandwich midplane is modeled in the global model (a full sandwich plate). Facesheet damage modes (fiber failure, matrix cracking, and delamination) are assumed to develop in such a way that they can be approximated by a progressive reduction in plate stiffness through the constitutive relations. Core crushing is also treated as a stiffness reduction of sorts, but is included as a reduction in the foundation stiffness rather than a constitutive adjustment. In the global model, facesheet damage made such a small difference to the global stiffness in the early runs, that it was neglected for the later runs. The main features of the local model algorithm are presented in flowchart form in figure 6-26. The applicable sections of this dissertation (where more details can be found) are shown beside the steps.

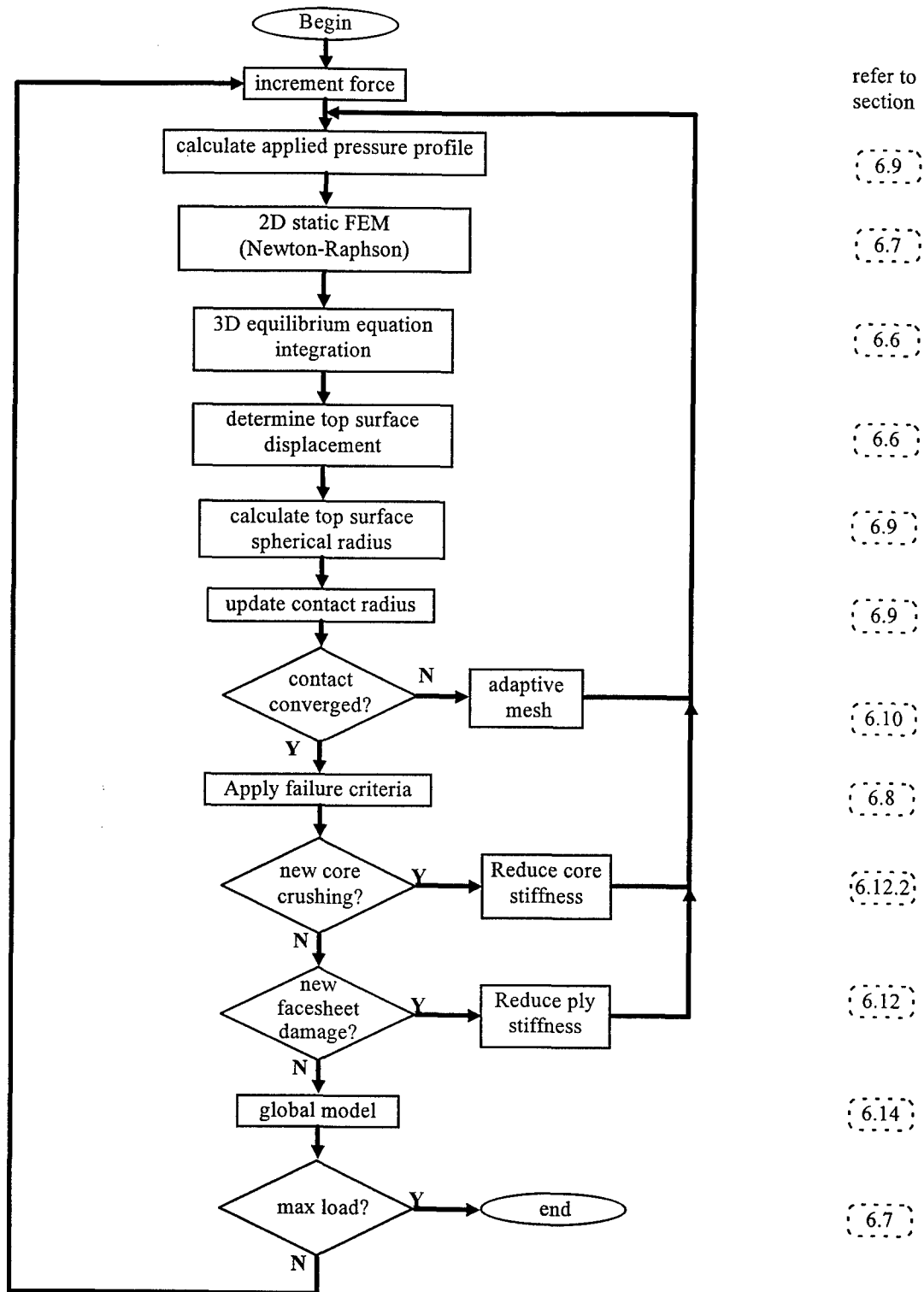


Figure 6-26 Local-global solution algorithm flowchart.

For a given load increment, the solution proceeds as follows. An estimated contact radius (that of the previous load increment, or the user-supplied starting value for the first load

increment) determines the mesh and applied pressure profile. The finite element model for these boundary conditions is solved using a modified Newton-Raphson iterative procedure. The displacements from the finite element solution are used to calculate in-plane stresses and the in-plane stresses are used in the three-dimensional equilibrium equations to determine the transverse stresses and the transverse direct strain. The transverse direct strain is integrated through the thickness and added to the midplane displacements to estimate the top surface displacement profile. The top surface displacements within the contact region are fit to a sphere using a least squares technique and the contact radius is updated based on the resulting surface radius. This is iterated until the top radius and the top surface radius are in agreement. When the contact radius has thus converged, the core failure algorithm is invoked. The failure criteria are checked to determine if any new core failures are found. If so, the foundation stiffness is modified for the affected elements and contact algorithm is repeated. This iteration of the core failure continues until no additional core failures ensue. At that point, facesheet damage is checked. If new facesheet damage is found, the appropriate ply stiffnesses are reduced and the core failure algorithm is repeated. The facesheet damage algorithm is iterated until no additional facesheet damages are found. At that point, the contact, core, and facesheet algorithms have converged and the global model is run using the present load and contact radius to determine the sandwich plate midplane displacements. The load is then incremented and the process is begun anew.

6.14 Global Model Solution Algorithm

As mentioned above, the principal feature not included in the local model is displacement of the sandwich midplane. It is desired to compare load versus displacement curves between the analysis and the experiment. The displacements available from the local model are with respect to the sandwich midplane and thus do not include the overall bending of the sandwich under the applied load. This motivates the need for a global model in order to obtain the displacement of the sandwich midplane. The displacements predicted by the local/global analysis are the sum of the midplane displacement of the global model and the displacement from the local model. The global model uses the same grid, boundary conditions (except it does not include a foundation), contact radius, and load as the local model. Damage is not included in the global model, and contact is not iterated so the global model solution algorithm is much simpler than the local model. The global model solution algorithm is illustrated by a flowchart in figure 6-27.

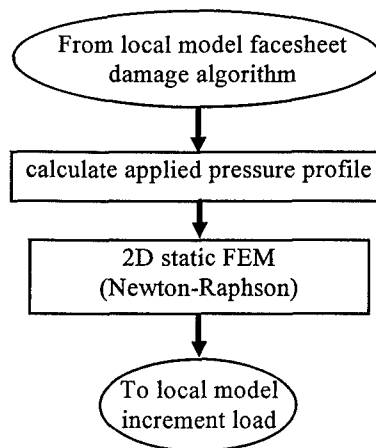


Figure 6-27 Global solution algorithm flowchart.

6.15 Local/Global Interaction

The local model determines the contact radius based on the deformations in the vicinity of the tup. Localized stiffness changes due to core and facesheet damage are included. The only interaction then, between the local model and the global model is the contact radius. For any given load step, the local model is satisfied first. The contact radius determined by the local model is used with the given load (and the assumption of Hertzian distribution) to produce the applied pressure profile for the global model. The global model midplane displacement is added to the local model displacement to obtain the predicted total displacement.

6.16 Summary

A solution algorithm has been developed which is believed to have the capability of modeling the most important features of the problem of low-velocity impact to composite sandwich plates. Though originally it was intended to use just the global model described here, the transverse stresses available from that model for very small contact radii were found to be unacceptable. Contact radius depends strongly on the transverse stresses. Since the finite element solution for a monolithic plate with the dimensions of interest was found to produce significantly better transverse stresses, a local-global solution algorithm was embraced. In the local model the sandwich plate is modeled as a plate (the top facesheet) on an elastic-plastic foundation (the core). The displacements from the local model are added to the midplane displacements of the global (sandwich) model to correct the fact that the local model foundation was flat while the sandwich

plate core displaced due to plate bending. The local model was solved first and the contact radius from the local model was used to load the global model.

7. Comparison to Elasticity Theory

The purpose of this chapter is to compare the results of the finite element analysis described in Chapter 6 to the elasticity theory results obtained from the modified Pagano solution described in Chapter 5. In particular, the stresses available from the local (facesheet on an elastic foundation) and global (sandwich) models are compared to the elasticity solution. Though the local model was actually a plate on an elastic-plastic foundation, for this chapter fixed contact radii and unit loads were used so that core strains were in the elastic range. Thus, in this chapter the local model is referred to as the elastic foundation model, rather than elastic-plastic foundation model. There is no difference between the two except the magnitude of the load. Two test cases were chosen for presentation here. The test cases were chosen in order to display both the strengths and the weaknesses of the analysis. Since the major goal of this research was to analytically model the response of composite sandwich plates to low-velocity impact, toward that goal, this chapter provides a measure of the success of the finite element analysis at predicting stress under contact-type loading. One facesheet thickness (16-ply) is chosen for comparison here.

7.1 General Ideas

As seen in figures 6-7 through 6-11, even for the 14 DOF element, the global (sandwich) model stresses leave something to be desired as compared to the elasticity solution. The comparisons in this chapter show how much better the stresses obtained by the local model are and motivate the use of the local model to predict failure in the specimen and to follow the progression of damage. In the current algorithm, contact, facesheet damage, and core damage are all iterated in the local model. The global model provides the gross deformations (midplane displacements) so that comparison of load verses displacement curves with the experiment can be made.

Two distinct types of elasticity test cases were used to judge the finite element solution. The two types are two-dimensional cylindrical bending of a plate strip and three-dimensional bending of a square plate. Both cases were loaded in the center by a Hertzian load distribution (as approximated by a Fourier sine series). In the two-dimensional case the stress was distributed over the entire plate depth, while in the three-dimensional case the stress was symmetric about the z

axis (figure 5-11). As discussed in Chapter 5, the three-dimensional elasticity solution was only available for relatively few Fourier terms. For this reason, the Hertzian contact radii which could be modeled by the three-dimensional elasticity solution were much larger than the contact radii observed in the experiment. Thus, it was not possible to use the three-dimensional elasticity solution to benchmark the finite element analysis for contact radii of the dimensions found in the experiment. Instead, the three-dimensional elasticity solution was used to benchmark the finite element analysis for large contact radii and the two-dimensional elasticity solution was used to benchmark the finite element analysis for small contact radii. In the elasticity solution test cases conducted for this research, sandwich plate structures were loaded by a Hertzian load distribution (figures 5-2, and 5-36) simulating contact with a spherical indenter located at the center of the plate and moved transverse to the plane of the plate. In the finite element based analysis methodology developed for this research (Chapter 6), a sandwich plate was modeled using plane stress elements and loaded with a Hertzian contact load. Two different models were actually studied, a local model and a global model. In the local model, the top facesheet was modeled with monolithic plate elements on an elastic-plastic foundation (simulating the core). In the global model both facesheets and the core were modeled by a sandwich element having stiffness contributions from each.

7.2 Three-Dimensional Solution

To benchmark the finite element analysis with a three-dimensional elasticity test case, the 8x8-term double Fourier sine series representation of a 12.7 mm radius Hertzian contact load illustrated in figure 5-36 was used. To be sure the problem remained in the elastic regime, the total force applied was 1.0 N. The finite element model was loaded with a Hertzian contact load having a 12.7 mm radius and the same total force. In figure 7-1 through 7-3, the 16-ply results are shown for both the global (sandwich) and the local (plate on elastic foundation) models. It should be pointed out that the displacements for the global and local finite element models are not comparable because of the very different nature of the restraints (simple supports verses simple supports plus elastic foundation). Nevertheless, both models were designed to simulate the same event, so the top facesheet stresses are comparable. It is these stresses that are shown in figures 7-1 through 7-3.

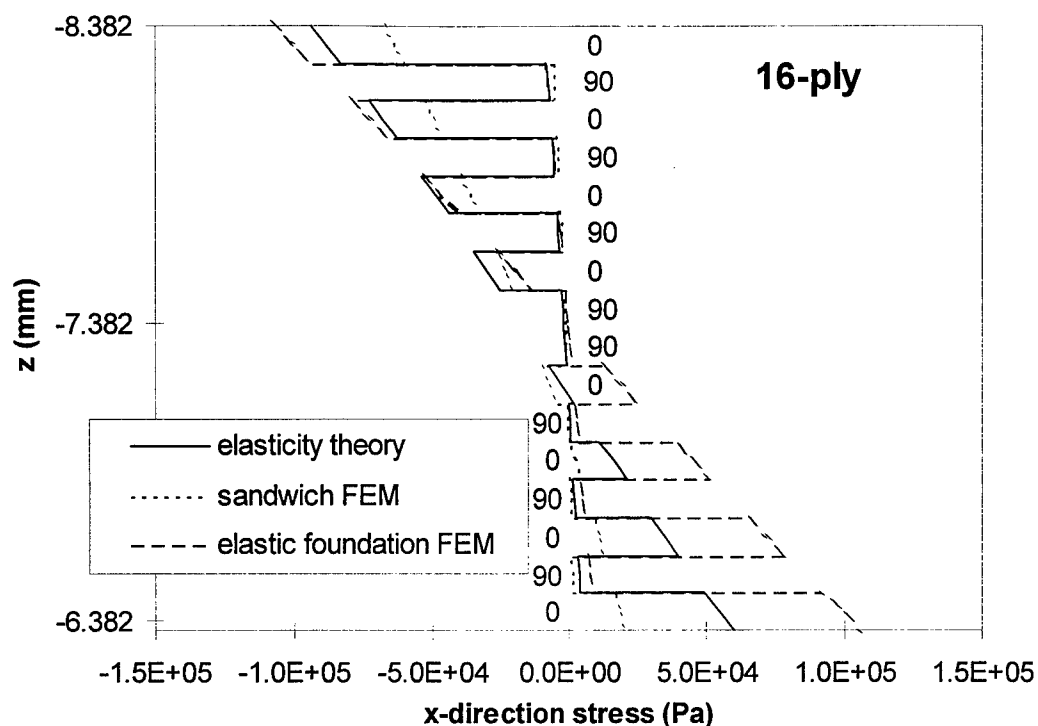


Figure 7-1 Comparison of top facesheet in-plane direct stress, σ_x , at the center of the plate for the large contact radius, three-dimensional case (12.7 cm square sandwich plate, 16-ply facesheets, 1.0 N load, 12.7 mm contact radius).

Figure 7-1 shows how the in-plane stresses compare between the finite element models and the three-dimensional elasticity solution. As expected, the 0° plies, having much greater x-direction stiffness than the 90° plies, are shown to take the majority of the load (observe the abrupt changes in stress occur at the interfaces and the 0° plies are the . It should be noted that the though the primary damage mechanism driven by in-plane stress is fiber failure (in compression near the top surface), depending on the damage criteria chosen, matrix cracking could also be affected. Taking the elasticity solution to be the correct one (within the approximation of the Hertzian load and the assumption that the material behaves elastically) it can be seen that the elastic foundation (local) solution is significantly better than the sandwich (global) solution, particularly near the top surface where fiber failure will begin. An interesting observation that can be made from figure 7-1 is that the elasticity solution shows the stress in the 0° plies to be almost linearly related to z in the top facesheet. The elastic foundation finite element solution is able to model this feature because the cubic kinematics can represent a linear function and only the top facesheet is in the model. The sandwich finite element model is not able to represent a linear function through the thickness of the top facesheet, because the core and bottom facesheet

represent significant property variation through the thickness, and thus require the familiar “zig-zag” kinematic relationship which is not well represented by the cubic kinematics in the model. It is true that the properties vary through the thickness within the facesheets, but since the lamina are thin and many, the error associated with averaging their properties through the facesheet thickness is small. Thus, in a gross sense, the sandwich behaves as a three-ply laminate in which the two facesheets are considered to be represented by two stiff plies and the core is a single flexible ply between them. The in-plane displacement of such a laminate is known to take on a Z shape [236,237] which is not well approximated by a cubic. For this reason, it is thought that including zig-zag kinematics could improve the in-plane stresses of the sandwich model, but that the elastic foundation model would be less drastically improved. It further suggests what the author believes to be a new idea for the kinematics of sandwich plate elements. Rather than include full zig-zag kinematics in which each lamina has its own linear (or higher) function of z (with the attending complications and computational overhead), one could give the facesheets independent kinematic relationships from the core while maintaining a polynomial kinematic relationship within each facesheet and within the core. Continuity of displacement (but not of the slope) would be maintained at the interfaces between the core and the facesheets. The resulting kinematics would not increase the number of degrees of freedom in the model when the number of plies in the facesheet increased. It would provide what may be the most important benefit of zig-zag kinematics for sandwich structures (the ability to model the “kink” in the displacement curve at the core-facesheet interfaces) while avoiding the most important liability of zig-zag kinematics (model size grows with the number of distinctly oriented plies). Such an approach is similar to the “warping functions” recently applied by Greer [244] to composite shells.

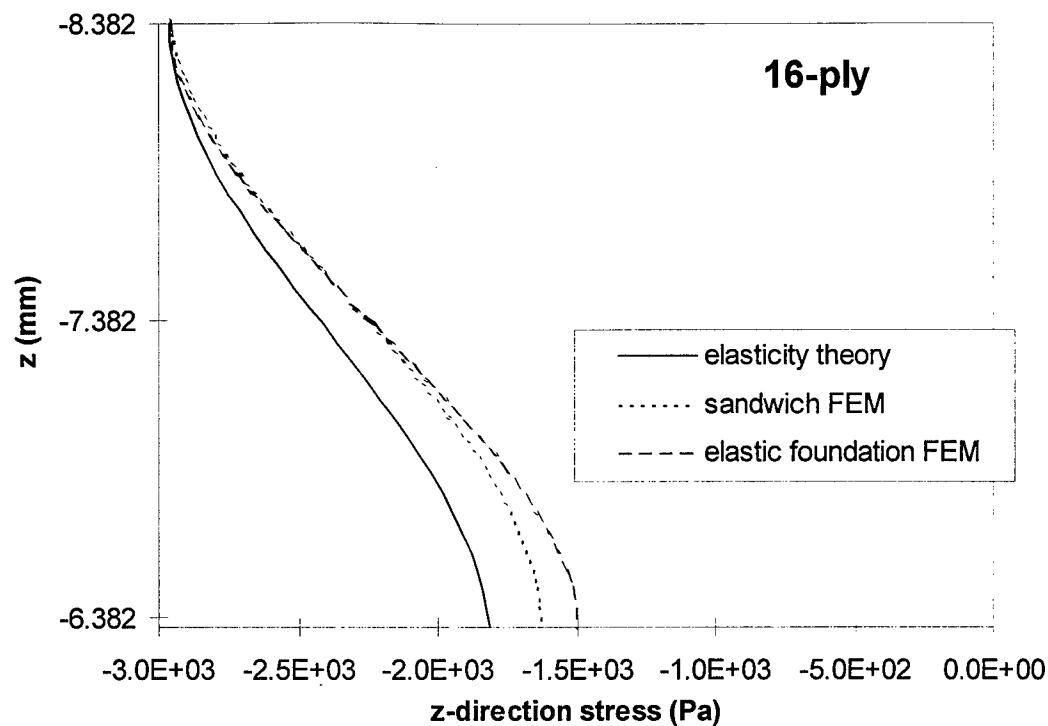


Figure 7-2 Comparison of top facesheet transverse direct stress, σ_z , at the center of the plate for the large contact radius, three-dimensional case (12.7 cm square sandwich plate, 16-ply facesheets, 1.0 N load, 12.7 mm contact radius).

Figure 7-2 shows that σ_z for the large contact radius case is marginally well predicted by either the sandwich or the elastic foundation model. It can be observed that the sandwich model does somewhat better than the elastic foundation, but either one will be non-conservative for a stress based core failure prediction since the σ_z at the bottom of the top facesheet ($z = -6.35$ mm) is identically the same as the stress at the top of the core. Thus, the low prediction of core stress will presumably result in a high prediction of core crushing load if a stress based criteria for core failure is employed. This result was not found for the elastic foundation model when the contact radius was significantly reduced (section 7.3).

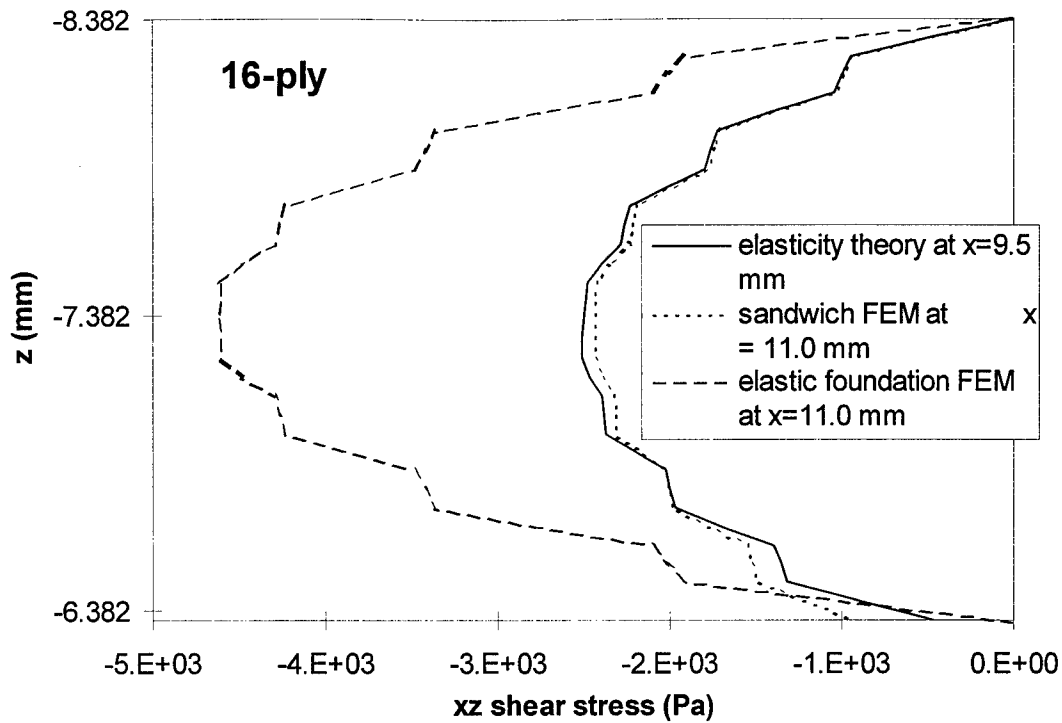


Figure 7-3 Comparison of top facesheet transverse shear stress, τ_{xz} , at the location of the peak for the large contact radius, three-dimensional case (12.7 cm square sandwich plate, 16-ply facesheets, 1.0 N load, 12.7 mm contact radius).

For the 16-ply large contact radius case, figure 7-3 shows the transverse shear stress, τ_{xz} , through the thickness at the x-location of the peak transverse shear stress (and $y = 0$). This location is between 9.5 and 11.0 mm away from the plate centerline. As shown in figure 5-8, the transverse shear stress is zero at the plate centerline but grows quickly in the x-direction, attaining a peak near the edge of the applied load (12.7 mm in this case). While the sandwich finite element model prediction is slightly low, the elastic foundation model prediction is very high. This result, combined with that of figure 7-2 indicates that for the large contact radius case, the sandwich model produces a better three-dimensional stress result than the elastic foundation model, albeit non-conservative for shear. Both models correctly predict the peak shear in the middle two 90° plies.

The fact that the transverse shear is nearly symmetric with respect to the facesheet midplane, as seen for the elasticity case in figure 7-3, has implications with respect to the three-dimensional nature of the large contact radius case. Considering the first equilibrium equation, (6-37a), repeated here for the readers convenience,

$$\sigma_{xx,x} + \sigma_{xy,y} + \sigma_{xz,z} = 0 \quad (6-37a)$$

and recognizing that on the symmetric boundary $y=0$, the in-plane shear gradient $\sigma_{xy,y}$ is zero, we find that, on the $y=0$ boundary,

$$\sigma_{xx,x} = -\sigma_{xz,z} \quad (7-1)$$

Clearly, if the transverse shear stress is symmetric with respect to the top facesheet midplane, its transverse gradient is anti-symmetric with respect to the top facesheet midplane. Equation 7-1 indicates that the in plane stress gradient is then anti-symmetric with respect to the top facesheet midplane. All this is to say that the bending effect of the applied load is felt by the bottom surface of the top facesheet to the same degree that it is felt by the top surface of the top facesheet. Thus, to the top facesheet, the loading is not fundamentally three-dimensional, but can be thought of as the sum of a pure bending and a membrane load. The precise z -location of the application of the transverse load is not important. In contrast to this, the small contact radius problem is truly three-dimensional and the shear near-symmetry observed in the large contact radius case in figure 7-3 is not present there (see figure 7-6 below).

7.3 Two-Dimensional (Cylindrical Bending) Solution

The contact radius used in the three-dimensional solution above was effectively limited to the 12.7 mm value for which the 16-ply cases are shown above due to the numerical singularity in Pagano's formulation of the elasticity equations when a large number of double Fourier series terms are used. To benchmark the finite element analysis with a contact radius more representative of those anticipated in actual test cases of Chapter 8, the two-dimensional elasticity solution was used. A 250-term (single) Fourier sine series representation of a 1.0 mm radius Hertzian contact load was used. This load is similar to that shown in figure 5-2 which shows a series representation of a 1.59 mm radius Hertzian contact load. To be sure the problem remained in the elastic regime, the total force applied was 1.0 N. The finite element model was loaded with a Hertzian contact load having a 1.0 mm radius and the same total force. In figure 7-4 through 7-6, the 16-ply results are shown for both the global (sandwich) and the local (plate on elastic foundation) models. The top facesheet stresses are shown in figures 7-4 through 7-6.

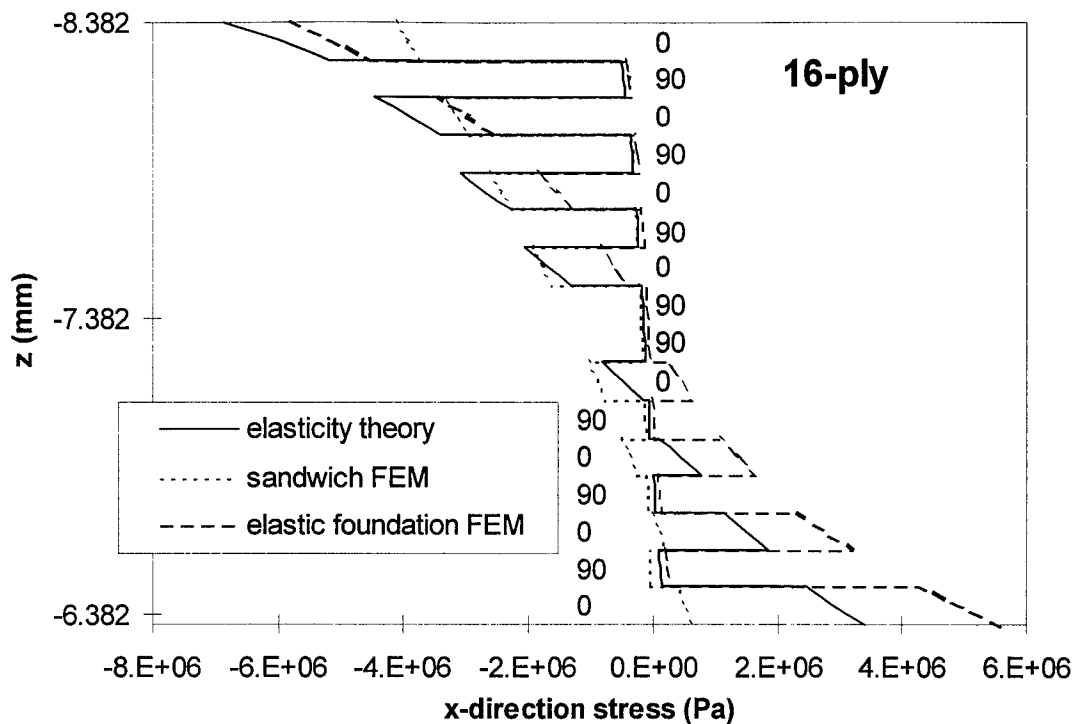


Figure 7-4 Comparison of top facesheet in-plane direct stress, σ_x , at the center of the plate for the small contact radius, two-dimensional case (cylindrical bending, 12.7 cm wide sandwich plate strip, 16-ply facesheets, 4.65 N/m load, 1.0 mm contact radius).

Figure 7-4 shows how the in-plane stresses compare between the finite element models and the two-dimensional elasticity solution when the contact radius is small (1.0 mm). As with the three-dimensional solution, the 0° plies, having much greater x-direction stiffness than the 90° plies, are shown to take the majority of the load. As for the three-dimensional case, it can be seen that the elastic foundation (local) solution is significantly better than the sandwich (global) solution, particularly near the top surface where fiber failure will begin. An interesting observation that can be made from figure 7-4 is that the backward "S" curvature seen in the elasticity solution shows up in the elastic foundation solution as well. The elastic foundation finite element solution is able to model this feature because the cubic kinematics can represent a backward "S" function and only the top facesheet is in the model. The sandwich finite element model is not able to represent a backward "S" function through the thickness of the top facesheet for the same reason that it could not represent a linear function in the three-dimensional case, i.e. the need for a zig-zag kinematic relationship. In fact, the elastic foundation solution stress in the 0° plies appears to follow the elasticity solution, but is off by a constant. One can think of the constant as the membrane stress in the facesheet due to the gross bending of the sandwich. The

elastic foundation solution does not have the sandwich plate bending, hence the compressive facesheet membrane stress that would result from sandwich bending is missing.

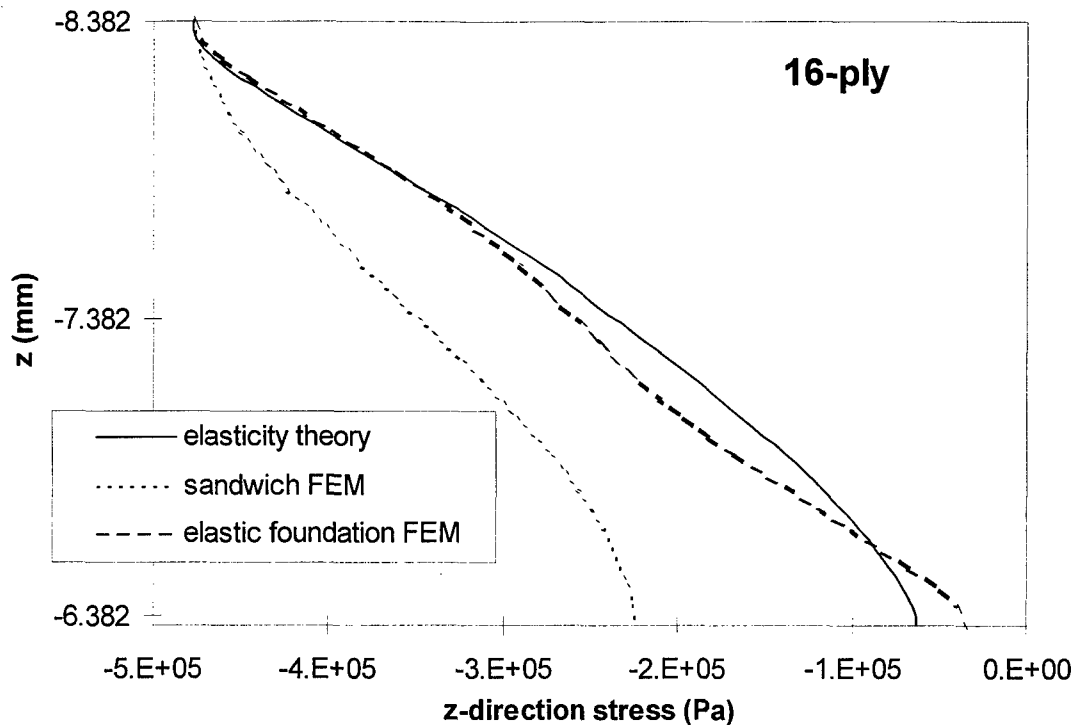


Figure 7-5 Comparison of top facesheet transverse direct stress, σ_z , at the center of the plate for the small contact radius, two-dimensional case (cylindrical bending, 12.7 cm wide sandwich plate strip, 16-ply facesheets, 4.65 N/m load, 1.0 mm contact radius).

Figure 7-5 shows that transverse direct stress, σ_z , for the small contact radius case is significantly better predicted by the elastic foundation model than it is by the sandwich model. Since all the cases in Chapter 8 (comparison to experiment) have relatively small contact radii, this motivates the use of the elastic foundation model, rather than the sandwich model, to predict core failure. Depending on the choice of failure theories, matrix cracking and delamination may also be influenced by σ_z . For the purposes of the present research, all damage predictions, including those in the facesheets, were based on stresses from the elastic foundation model.

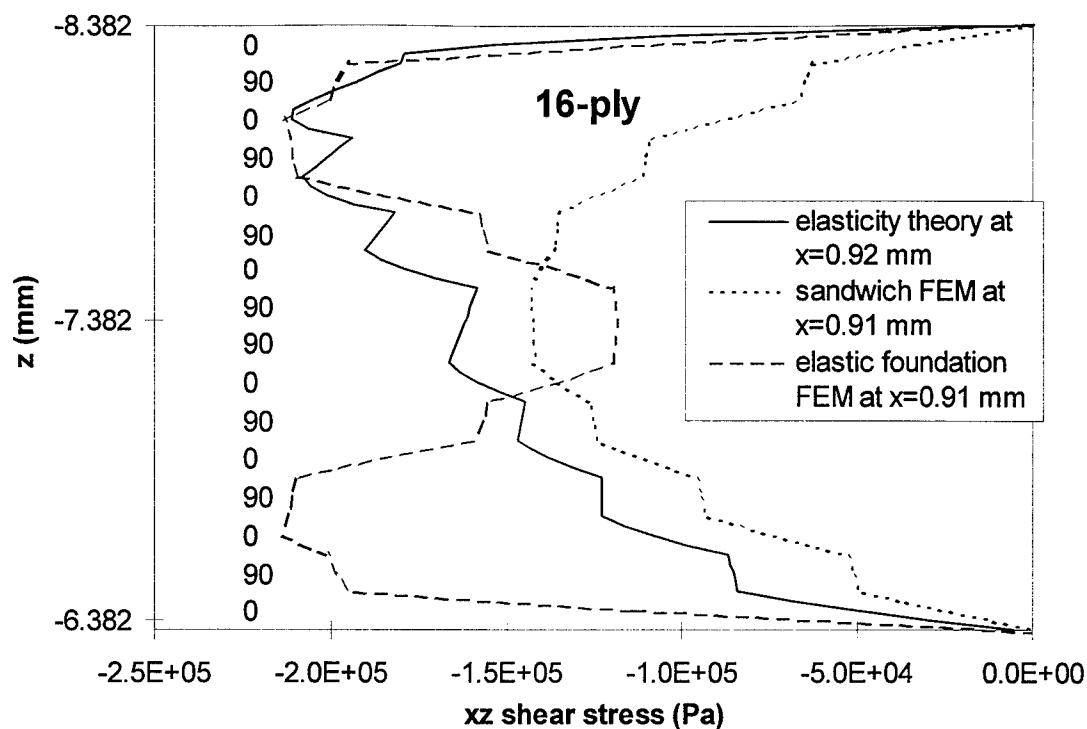


Figure 7-6 Comparison of top facesheet transverse shear stress, τ_{xz} , at the location of the peak for the small contact radius, two-dimensional case (cylindrical bending, 12.7 cm wide sandwich plate strip, 16-ply facesheets, 4.65 N/m load, 1.0 mm contact radius).

For the 16-ply small contact radius case, figure 7-6 shows the transverse shear stress, τ_{xz} , through the thickness at the x-location of the peak transverse shear stress (and $y = 0$). This location is just less than 1.0 mm away from the plate centerline. The elasticity solution in this figure shows that the small contact radius problem is truly three-dimensional because the shear near-symmetry observed in the large contact radius case in figure 7-3 is not present here. This implies that the loading in the top facesheet can not be considered to be the sum of pure bending and membrane loads. The z-location of the application of the load (the top surface) is important. In the finite element models, the load was always applied as nodal forces (i.e. at the midplane). The resulting transverse shear stresses were typically characterized by symmetry with respect to the midplane. In the case of the sandwich model, symmetry was with respect to the midplane of the entire sandwich (see figures 6-7 through 6-11), while in the case of the elastic foundation model, symmetry was with respect to the facesheet midplane (compare figures 6-12 through 6-16). In figure 7-6, the elastic foundation model solution is arguably better than the sandwich model solution. The elastic foundation model correctly predicts both the magnitude and the z-location (second 0° ply from the top) of the peak shear stress for this case. The second peak near

the lower surface of the top facesheet is thought to be a consequence of the two-dimensional nature of the finite element solution. This lower peak shows up in the top facesheet of the elastic foundation solution (see elastic foundation FEM plot in figure 7-6), and in the bottom facesheet of the sandwich solution (see, for example the 11 and 14 DOF plots in figure 6-9b). Figure 7-6 indicates that for this case, with a shear stress failure criterion, the sandwich solution will predict delamination and matrix cracking to first occur at the midplane of the top facesheet and the load at which it first occurs will be 30 percent too high (as compared to the elasticity solution). This can be seen by observing in figure 7-6 that the peak shear stress in the elasticity solution is approximately 1.3 times the peak shear stress in the sandwich solution. In contrast to this, the elastic foundation solution will predict delamination and matrix cracking to occur at the correct load but simultaneously near the top and bottom of the top facesheet, while the elasticity solution indicates only near the top. The author judges the elastic foundation solution to be better than the sandwich solution because it gives both the correct failure load and the correct failure location, even though it gives an extra failure location which is erroneous.

7.4 Conclusions

The three-dimensional stresses obtained from the equilibrium equations and the in-plane finite element stresses compare favorably with the elasticity solution. The sandwich (global) model does reasonably well for the case in which the load is distributed over a large portion of the top surface, but for the small contact radius case, the elastic foundation (local) model does better. In the balance of this research, the global (sandwich) model will be used to predict the plate midplane displacements, but the state of stress will be predicted by the local (elastic-plastic foundation) model. Due to the symmetry of the transverse shear stress predicted by the local model with respect to the top facesheet midplane, delaminations and matrix cracks near the bottom surface of the top facesheet may be erroneously indicated. The major goal of this research was to analytically model the response of composite sandwich plates to low-velocity impact. The data presented in this chapter indicates that the two-dimensional (plane stress) finite element analysis, when combined with the three-dimensional equations of stress equilibrium can reasonably well predict the three-dimensional state of stress in a composite sandwich under contact-type (Hertzian) loading.

8. Comparison to Experiment

The purpose of this chapter is to compare the results of the finite element analysis described in Chapter 6 to the experimental results related to the static indentation tests of the experimental program described in Chapter 4. Several test cases were chosen for presentation here. The test cases were chosen in order to display both the strengths and the weaknesses of the analysis. A major goal of this research was to analytically model the response of composite sandwich plates to low-velocity impact. Thus, this chapter must provide some measure of the success of the finite element analysis. Toward this end, several metrics are developed by which the ability of the analysis to predict the experimental results can be judged. One facesheet thickness (16-ply) is chosen for detailed comparison and more general comparisons are made of the other facesheet thicknesses.

8.1 General Ideas

In the tests conducted for this research, sandwich plate structures were loaded both statically and dynamically through contact with a 12.7 mm radius spherical indenter located at the center of the plate which moved transverse to the plane of the plate (figures 4-2, 4-4, and 4-5). In the finite element based analysis methodology developed for this research (Chapter 6), a sandwich plate was modeled using plane stress elements and loaded with a Hertzian contact load. Two different models were actually used, a local model and a global model. In the local model, the top facesheet was modeled with plane stress elements while the balance of the plate was modeled by an elastic-plastic foundation supporting the top facesheet. This local model was adopted because the sandwich model transverse direct stresses in the core were in error, particularly when the contact radius was small. The elastic stiffness of the foundation was the same as the core, so that local deformations of the top facesheet relative to the bottom facesheet were obtained while the global deformations of the entire sandwich were not. The finite element in-plane stresses were used with the three-dimensional equilibrium equations to evaluate the transverse stresses, strains, and displacements to obtain the displaced surface under the load. This surface was made to conform to the top surface through an iterative procedure described in section 6.9. In a second model (the global model) the entire sandwich structure (both facesheets and the core) was modeled using plane stress elements to obtain the gross deformations of the plate. The grids, loads, and edge

boundary conditions for the two models were the same. The sum of the displacement of the midplane of the global model and the displacement of the top surface in the local model was taken to be the predicted displacement of the top surface of the sandwich plate. In this way, the global model provides the solution for the sandwich plate bending while the local facesheet bending and the contact between the indenter and the specimen were modeled by the plate on an elastic-plastic foundation in the local model. Stress and failure were evaluated from the results of the local model. Damage was modeled in the local model by constitutive (facesheet) and foundation (core) stiffness reductions in the elements in which damage was indicated by stress and strain based criteria.

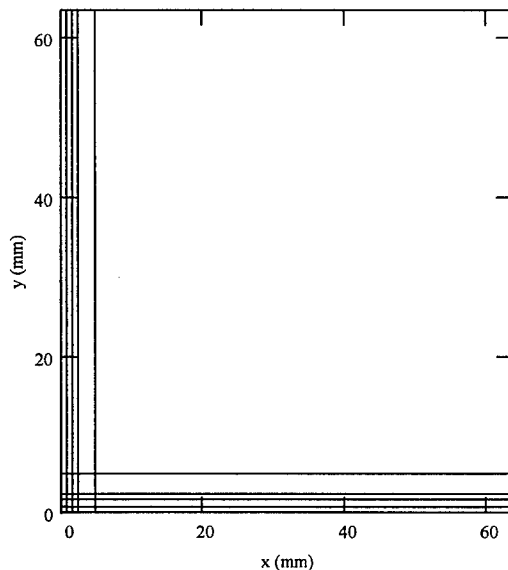
A significant difference between the analysis and the experiment must be kept in mind when interpreting these results, namely, the fact that the experiment was conducted using displacement “control” while the analysis used load control. That is, in the experiment, indenter (or impactor) displacement was the controlled parameter (input) while the load developed by the plate was a result (output). In the analysis, the load applied by the indenter was the controlled parameter, and the displacement was a result. Load control in the analysis was needed in order to maintain a Hertzian contact pressure under the indenter, but it led to the inability of the analysis to directly resolve load drops associated with damage.

8.2 Mesh Refinement

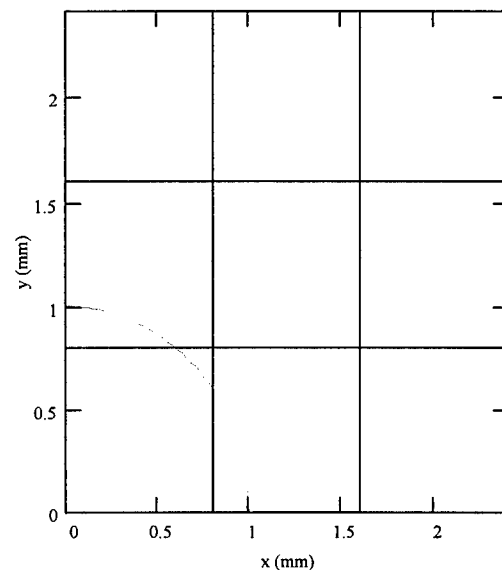
The adaptive mesh algorithm described in section 6.9 was employed to set the geometric spacing of the nodes in the grid for both the local and global models. By that algorithm, the mesh in the vicinity of the applied load was refined as the contact radius decreased, but since this was accomplished by moving the nodes, without increasing the total number of elements in the model, it was at the expense of the refinement of the mesh away from the applied load and was limited by the total number of elements in the model. In this way a given mesh was modified based on the contact radius, but it was not globally refined by increasing the number of elements in the mesh to improve the solution. In order to determine the number of elements required for the mesh, refinement of the whole mesh was performed by increasing the number of elements in the model (allowing the adaptive mesh algorithm to define their spacing) until additional elements ceased to significantly change the solution. In order to keep number of elements (mesh size) the same for each run, a single mesh size was sought. The mesh had to be refined enough that the most severe

runs (those with the highest strain gradients) would not require further refinement. Two test cases were identified which were thought to be more severe, from a strain gradient point of view, than the experimental cases for which a model was required. The two cases involved the thinnest and thickest facesheets (4-ply and 48-ply) and were sandwich plates. Sandwich plate analysis (i.e. the global model) was chosen for this study because it was found to be more sensitive to mesh size. Thus, a mesh that is refined enough for the sandwich (global) analysis was believed to be refined enough for the foundation-supported facesheet (local) analysis.

For each case, a Hertzian load with the smallest empirically observed contact radius, 1.0 mm, was applied to meshes of elements with from 5 to thirteen elements in each direction (grids 5x5 through 13x13). Grids for the 5x5, 9x9, and 13x13 meshes with a 1.0 mm contact radius are shown in figures 8-1 through 8-3.

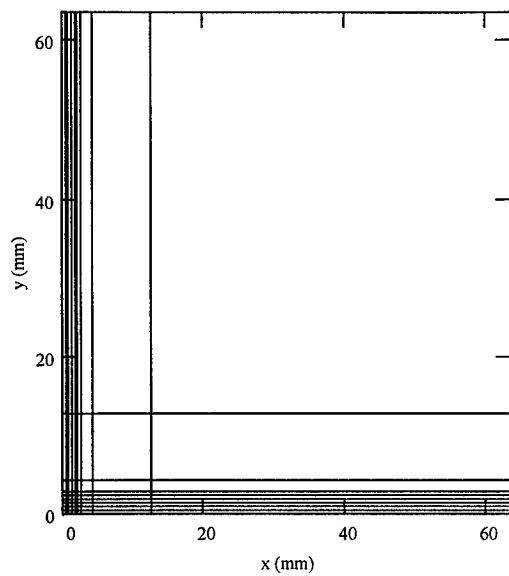


(see detail a)

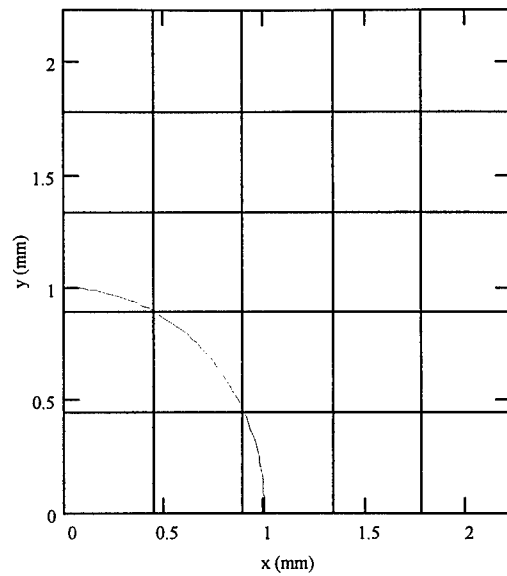


(detail a)

Figure 8-1 5x5 grid for contact radius = 1.0 mm. Maximum aspect ratio = 73.

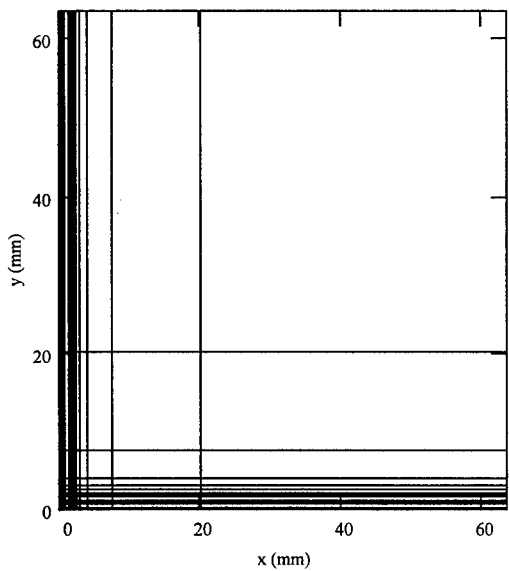


(see detail a)

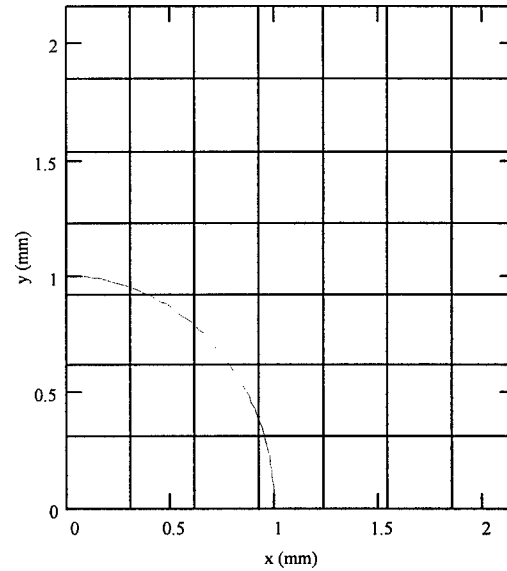


(detail a)

Figure 8-2 9x9 grid for contact radius = 1.0 mm. Maximum aspect ratio = 115.



(see detail a)



(detail a)

Figure 8-3 13x13 grid for contact radius = 1.0 mm. Maximum aspect ratio = 141.

It should be emphasized that the grids shown in figures 8-1 through 8-3 are for the smallest contact radius observed in the experiment, so that the grid distortion shown in those figures (the distortion of the elements from a square shape) is the maximum expected from the simulations of the test data. That is, no actual test runs are expected to have poorer shaped elements, so if a given mesh refinement is sufficient for these test cases, it should be sufficient for all of the actual

test runs as well. As can be seen in figures 8-1 through 8-3, the adaptive mesh algorithm placed the majority of the elements within 2.5 contact radii of the center of the plate, and bilateral symmetry was exploited. Though the adaptive mesh algorithm did maintain square elements in the vicinity of the applied load (where strain gradients are high), the aspect ratio of the elements far from the applied load is seen to be very high. Thus, even the 13x13 mesh must still be considered coarse away from the applied load. The problems associated with high aspect ratio elements were not observed in these tests. This may be due to the fact that the stress in the poorly shaped elements was nearly aligned with the long axis of the elements, and the strain gradients within those elements were relatively small. Results from the 4- and 48-ply test cases with a 1.0 mm contact radius and a unit (1.0 N) load are shown for the various grid sizes in figures 8-4, 8-5, and 8-6. Figure 8-4 shows that the center displacement of the plate increased with grid refinement, but appears to asymptotically approach a limit. This figure indicates that the finite element model was too stiff, as expected, but that the stiffness error is virtually eliminated by refining the mesh to a 9x9 grid. Increasing the grid size above 9x9 did not, in the opinion of the writer, significantly improve of the stiffness of the finite element solution.

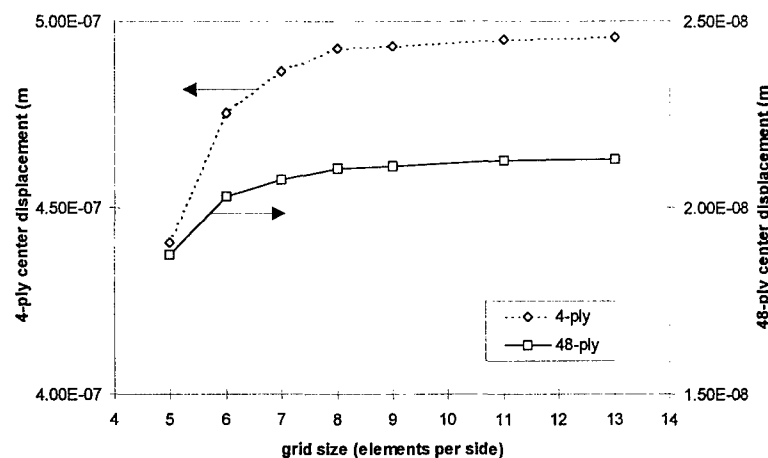


Figure 8-4 Plate center displacement versus grid size (4- and 48-ply sandwich plate, 1.0 N load, contact radius = 1.0 mm), showing that above 9 elements per side, the solution does not significantly change.

As discussed in Chapter 6, the failure criteria employed for the facesheets in the analysis were based on stress. It is therefore relevant to consider how mesh refinement effects the state of stress predicted by the model. In-plane stresses are calculated from in-plane strains directly via the constitutive relations while transverse stresses require in-plane gradients of the in-plane strains to be integrated through the thickness. It is therefore expected that the in-plane stresses are less

sensitive to grid refinement than are transverse stresses, since the latter require correct strain gradients and not only correct strains. Facesheet midplane transverse shear stress in the y-z plane is plotted against y in figures 8-5 and 8-6 for the 4- and 48-ply sandwich models with a 1.0 mm assumed contact radius. Those figures illustrate how mesh refinement effected stress and indicate that refining the grid more than the 9x9 grid does not significantly change the solution. For all of the subsequent work, the 9x9 grid was employed, but the adaptive grid algorithm effectively sized the elements to keep the same number of elements (indeed, the very same Gauss points) within the quarter-circular contact region shown in figure 8-2.

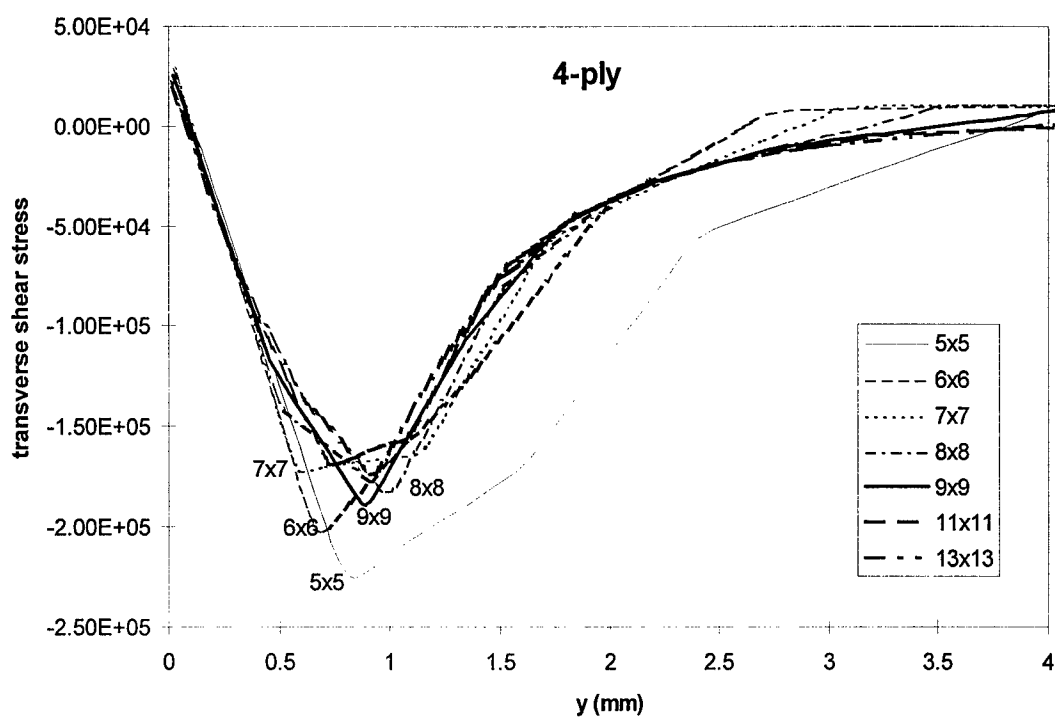


Figure 8-5 Top facesheet midplane transverse shear along the y axis (4-ply sandwich plate, 1.0 N load, contact radius = 1.0 mm).

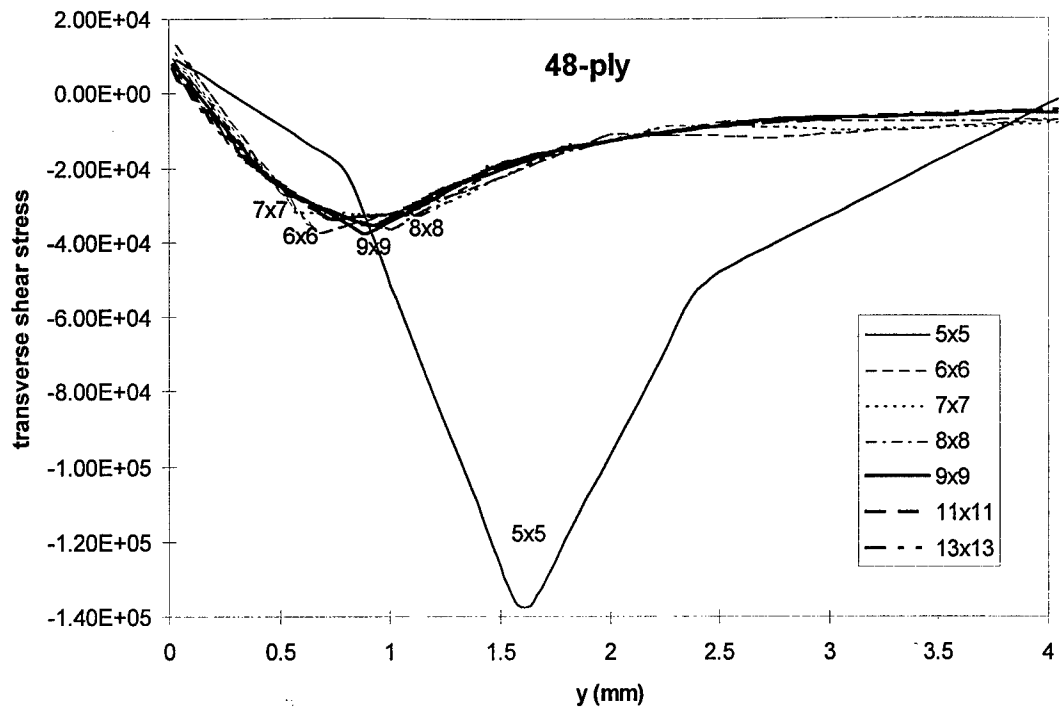


Figure 8-6 Top facesheet midplane transverse shear along the y axis (48-ply sandwich plate, 1.0 N load, contact radius = 1.0 mm).

8.3 Core Stress versus Strain

The elastic-plastic foundation was based on uniaxial stress-strain data obtained from the manufacturer of the Nomex honeycomb core. The uniaxial core stress-strain data and the elastic-plastic foundation stress-strain curve used in the studies which follow are shown in figure 8-7. The uniaxial data in reference [128] did not continue past a strain value of 0.0284, so it was not known what the actual failure strain was. For the current research failure strain was taken to be 0.035.

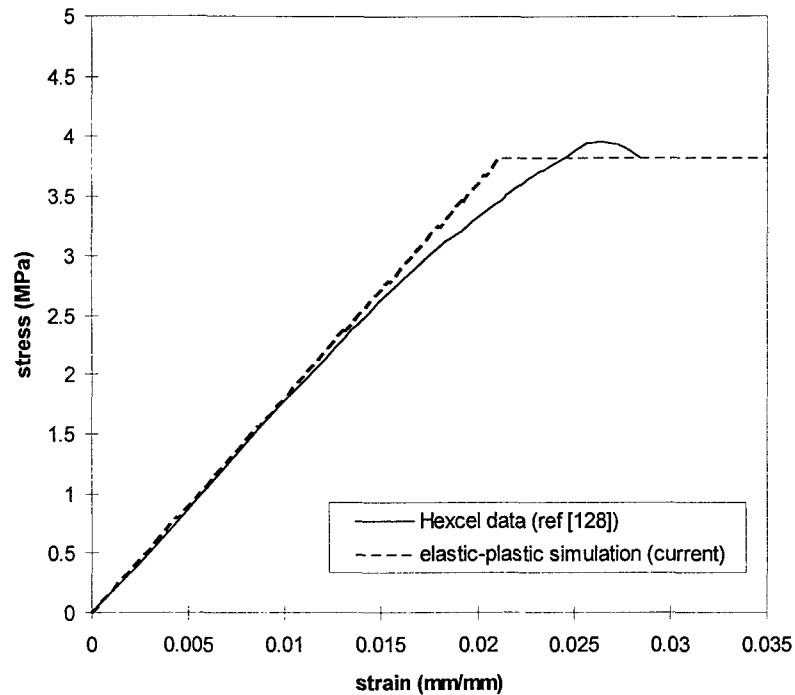


Figure 8-7 Core stress verses strain curves.

8.4 Test Cases

For the 16-ply specimens, three test cases were run in order to highlight the roles of the different damage mechanisms. For each case, the tup radius was 12.7 mm and the load varied in 16 equal increments from 409.1 N to 3477.2 N. The symmetric boundary conditions were those shown in figure 6-17 in which $a/2$ took on the value of 63.5 mm so that the entire plate modeled was 127 mm square as was the fixture in which the specimens were tested in the experimental portion of this research as described in Chapter 4. The element employed had 14 degrees of freedom per node and is described in Chapter 6. Each case employed a local model in which the facesheet was modeled as a monolithic laminate on an elastic foundation, and a global model on which both facesheets and the core were modeled by a sandwich element. Details peculiar to each test case are described below.

8.4.1 Case 1, no damage.

In the first case, no damage was modeled. For each step in load, the contact problem was solved iteratively with the local model. The core and facesheet material properties in the local model were constant for all loads. The contact radius (as a function of load) obtained from the

local model was used in the global model so that the applied load distribution on the global model, for any given load, was determined by the local facesheet bending and core compression effects as modeled in the local model. This case provided a baseline to show the effects of the damage in the other two cases which included damage.

8.4.2 Case 2, core damage only.

In the second case, core damage was modeled, but facesheet damage was not. That is, in the local model, the elastic-plastic foundation stiffness was reduced under each element that showed core failure. This was done via the damage algorithm described in section 6.11.2. The reduction of the stiffness was constant for the entire element and proportional to the number of Gauss points within the element that failed due to core crushing. Within the local model, and for a given load increment, if the core failed, the contact algorithm was reiterated until a new converged contact radius was obtained. The damage algorithm was then re-invoked to determine if additional damages were brought about by load shedding due to the core stiffness reduction or by load redistribution due to the changed contact radius. This process was repeated for any given load step until the damage did not change further and the contact algorithm indicated that the portion of the top surface of the plate over which the load was applied was conformed to the known spherical top radius. Contact and damage algorithms were thus nested so that for any given load increment the local model provided a converged damage profile and contact radius. The resulting contact radius (as a function of load) was the same as that of case 1 until the load at which core damage began (core damage initiation load) was reached. Beyond this core damage initiation load, the contact radius for case 2 was generally different from that of case 1. The contact radius output from the local model was used to load the global model with Hertzian contact loads. While the core failure algorithm was employed for this case, the facesheet failure algorithm was not. The material properties of the facesheets were constant for all loads. This case provided a means to understand the role of core damage without facesheet damage.

8.4.3 Case 3, facesheet and core damage.

In the third case, core and facesheet damages (fiber failure, delamination, matrix cracking, and core crushing) were all modeled together. Within the local model, facesheet damages were allowed in the top facesheet only. This restriction was considered due to the fact that damage was not found in the bottom facesheet in the experimental effort. No damages were modeled in the

global model. The third case shows the ability of the algorithms developed for this research to model the damage of a composite sandwich structure by transverse Hertzian contact-type loads simulating low-velocity impact.

8.5 Metrics for Success of the Analysis

The analysis and the experimental data must be compared in some meaningful way to determine how well the analysis did at predicting the experimental results. The particular measures chosen as the basis for comparison between experimental and analytical results are, contact radius as a function of load, the load verses displacement curves, and delamination patterns. The metrics are here described.

8.5.1 Contact radius.

The first metric is contact radius as a function of load. This metric should indicate how well the contact algorithm in the analysis models the actual event. The experimental data available for contact radius were not measured directly. As described in Chapter 4, separate tests were conducted in which a pressure sensitive paper was placed between the indenter and the specimen. After loading to the prescribed load, the pattern left on the paper was an impression of the "footprint" of the indenter for that load. The widest portion of the footprint was measured with a ruler and taken to be twice the contact radius for that load. The edges of the footprint were not well defined, so the measurements were rather subjective. For this reason, the experimental contact radii should be considered rough estimates. The experimental error was not determined.

8.5.2 Load verses displacement curve.

The static indentation load verses displacement curves provide a stiffness check of the finite element algorithm as well as a check of the load at which core failure begins. The load drops seen in the experiment were not observed in the analysis because the analysis, being load controlled, did not permit load reduction.

8.5.3 Delamination pattern.

The C-scans from the experimental portion of this research (some of which are shown in figure 4-26) can be compared to the delamination patterns predicted by the analysis. Though the analysis determined the delamination pattern at each interface, the C-scans provide only a single

pattern for the whole facesheet. The through the thickness variation of the delamination pattern was provided by Harrington's photomicrographs [5].

8.6 Test Results

8.6.1 Case 1, no damage.

8.6.1.1 Contact radius.

Figure 8-8 shows the undamaged plate contact radius verses the applied load. The experimental result, (which included damage) is also plotted on the same figure for comparison. The apparently linear experimental result below the first major load drop (which occurred at 2250 N) is curious since the curve must go through the origin. It is well known that the initial contact is a highly nonlinear process. It appears that in the experiment the nonlinearity of the initial contact was not seen above 500 N. That is, above 500 N the contact radius was a linear function of load until damage. This compares to the analytical result in which the nonlinearity continues to at least 1500 N. From this data, one might argue that the analytical result is in gross error. In particular, the analysis under-predicts the contact radius. This error, if it is real, is serious because the contact radius determines the peak load and the hence the failure initiation in the plate. The plate should fail very early if the contact radius is this poorly represented.

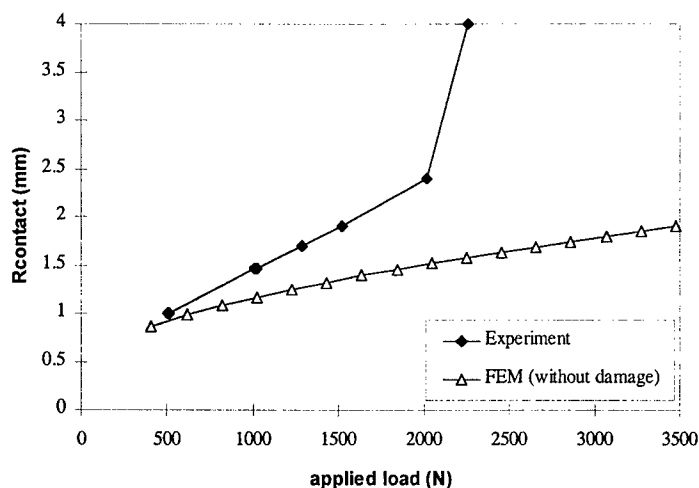


Figure 8-8 Contact radius predicted by local finite element model without considering damage (16-ply).

Core failure, being dominated by transverse direct stress, is most sensitive to contact radius, especially for thin facesheets where the applied pressure load is felt almost directly by the core. A

back-of-the-envelope calculation will illustrate the error in core failure load expected from an error in contact radius. Assuming Hertzian distribution of the contact load, the core failure load $F_{core\ failure}$, is related to the contact radius $R_{contact}(F)$ by the relationship,

$$F_{core\ failure} = \alpha q_0 \frac{2\pi [R_{contact}(F_{core\ failure})]^2}{3} \quad (8-1)$$

in which q_0 is the peak pressure in the center of the plate and α is the normalized transverse stress at the top of the core (see figure 5-4). As an illustration, α for 4-, 8-, 16-, 32-, and 48-ply sandwich plates in cylindrical bending with a 1.59 mm contact radius are found from figure 5-4 to be, 0.56, 0.34, 0.19, 0.10, 0.07 respectively. Equation 8-1 is nothing more than the relationship between force and peak Hertzian contact stress with the appropriate substitutions for core failure load. It can be seen from equation 8-1 that an in contact radius will be squared when it contributes to core failure. That is, for example, if the contact radius were low by a factor of two, the predicted core failure will be low by a factor of four.

Bearing in mind that the accuracy of the experimental contact radius was not determined and the measurement was rather subjective, the core failure load will be used to confirm or deny the implication from figure 8-8 that the analysis does a poor job of modeling the contact between the indenter and the plate. If the core failure load is significantly low, this will support the indication from figure 8-8 that the analysis poorly models the contact radius. If not, the unknown experimental error in the contact radius measurements can be blamed for the disparity in figure 8-8.

8.6.1.2 Load verses displacement curve.

The second metric used to judge the analysis is the load verses displacement curve. For the undamaged case, this is basically a stiffness comparison between the experiment and the analysis. In the experiment, top and bottom surface displacement were measured. These were used to represent the local and global stiffnesses of the specimens in Chapter 4. In the finite element model, these stiffnesses were available directly since the problem was broken up into local and global parts. Figure 8-9 compares the local and global load verses displacement curves of the analysis with the top and bottom surface load verses displacement curves from the experiment.

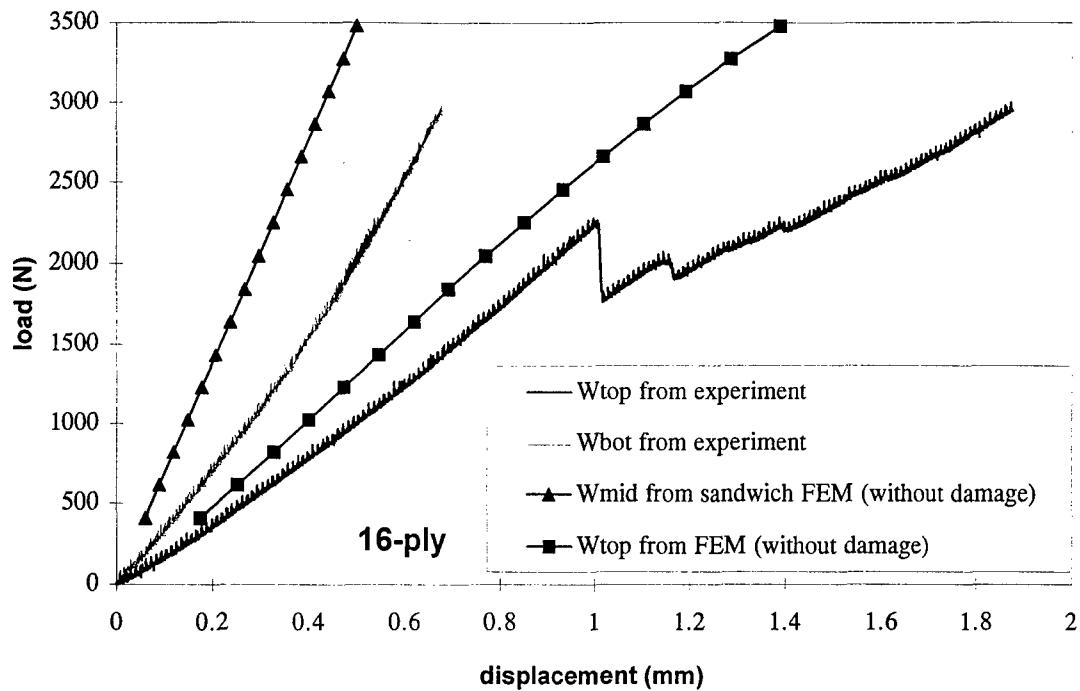


Figure 8-9 Load versus displacement predicted by local finite element model without damage (16-ply).

The initial nonlinear concave-up portions of the experimental loading curves shown in figure 8-9 are not fully captured by the analysis, but the slopes (stiffnesses) are very close. In figure 8-9, Wtop is the sum of the midplane displacement of the global (sandwich) model and the top surface displacement of the local (facesheet on an elastic foundation) model. This figure supports the idea used in this analysis that the global and local displacements can be superposed to represent the total displacement of the specimen.

8.6.2 Case 2, core damage only.

8.6.2.1 Contact radius.

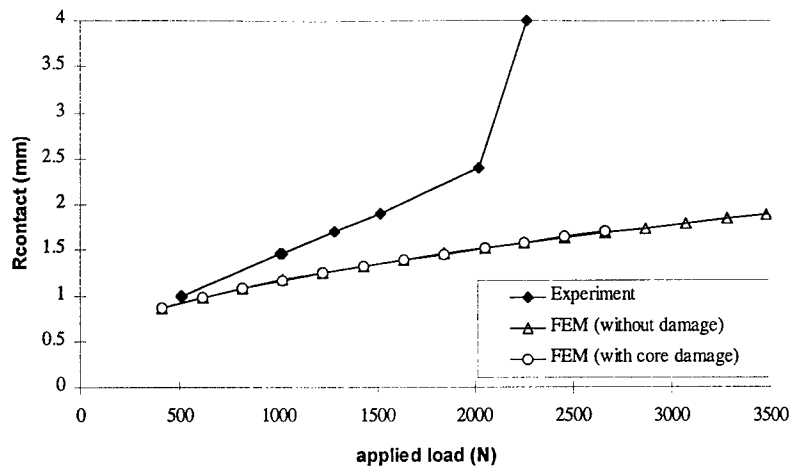


Figure 8-10 Contact radius predicted by local finite element model with only core damage considered (16-ply).

Figure 8-10 indicates that the failure of the core has very little effect on the contact radius in the analysis. This is contrary to the experimental result that the core failure was always accompanied by large increase in contact radius.

8.6.2.2 Load versus displacement curve.

Figure 8-11 shows the same data as figure 8-9, but with the addition of the data from the analysis including core damage. Most significant in figure 8-11 is the fact that the core begins to fail at very nearly the same load as seen in the experiment. While the experiment shows a load drop when the core fails, this was not observed in the analysis due to the fact that the load control was used. It should also be observed in figure 8-11 that core failure in the analysis does not present a radical bifurcation, it appears to be a gradual process. This contrasts with the very radical event in the experiment (the load drop). Failure of discrete core honeycomb cells could account for some steps in the experimental load displacement curve. The finite element analysis core (a continuous elastic-plastic foundation) could not resolve such discrete cell failure events. Nevertheless, lack of the analytical ability to resolve individual cell failures can not fully explain the difference between the failures seen in figure 8-11 because the load increments in the finite element analysis were great enough that each time the core failed, a core area encompassing (what is in the experiment) multiple cells failed.

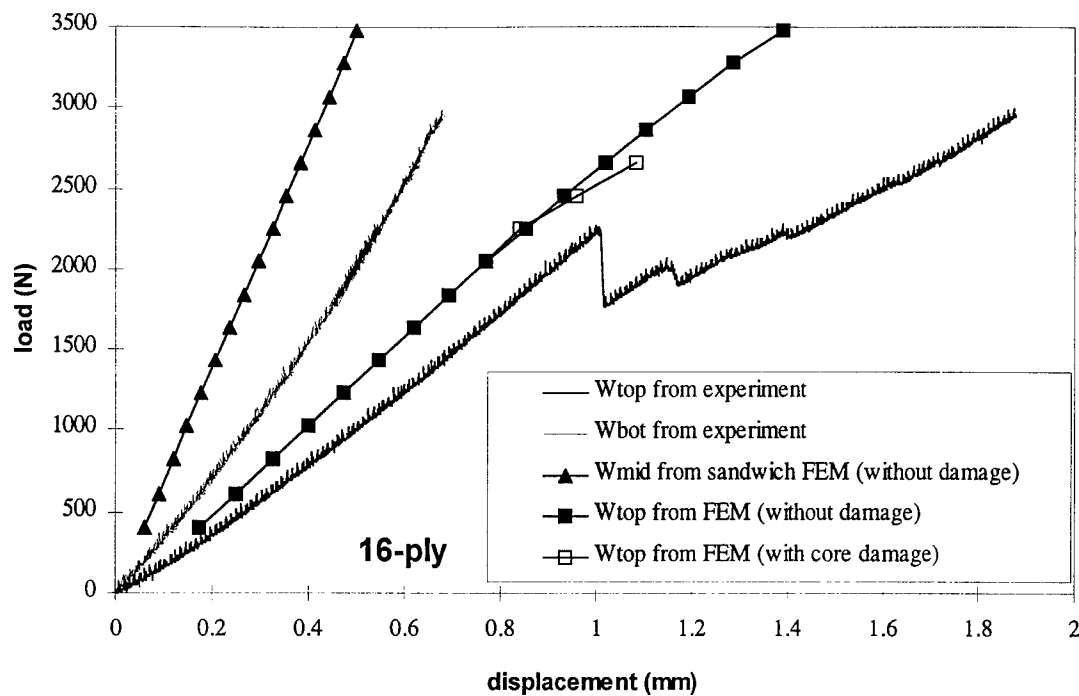


Figure 8-11 Load versus displacement predicted by local finite element model with and without considering core damage (16-ply).

The large difference between the experimental top surface displacement the first time the load reaches 2250 N and the top surface displacement the second time load reaches 2250 N can better be explained by a discrete multiple cell failure in which failure of the highest loaded cells precipitates failure of less highly loaded neighboring cells. That is, the core fails not in a continuous process, but suddenly. In figure 8-11, at a top surface displacement of 1.0 mm the failure of the cells immediately under the indenter results in transfer of the load to the cells surrounding the failed cells. The additional load now taken by the cells surrounding the failed cells causes them to fail as well. The failed core does not support the facesheet, so the facesheet indentation increases, relaxing the sandwich midplane displacement (while keeping the top surface displacement constant). This allows the strain energy in the sandwich to be released as the sandwich midplane displacement is relieved. In this way the core failure propagates under constant top surface displacement until the strain seen by the intact core is below the failure strain. At this point, the load is well below the load that first caused failure of the core. Increasing the top surface displacement following the load drop increases the load again, but the top surface displacement has to be considerably greater (approximately 1.5 mm in figure 8-11) before the load reaches 2250 N again.

8.6.3 Case 3, facesheet and core damage.

8.6.3.1 Contact radius.

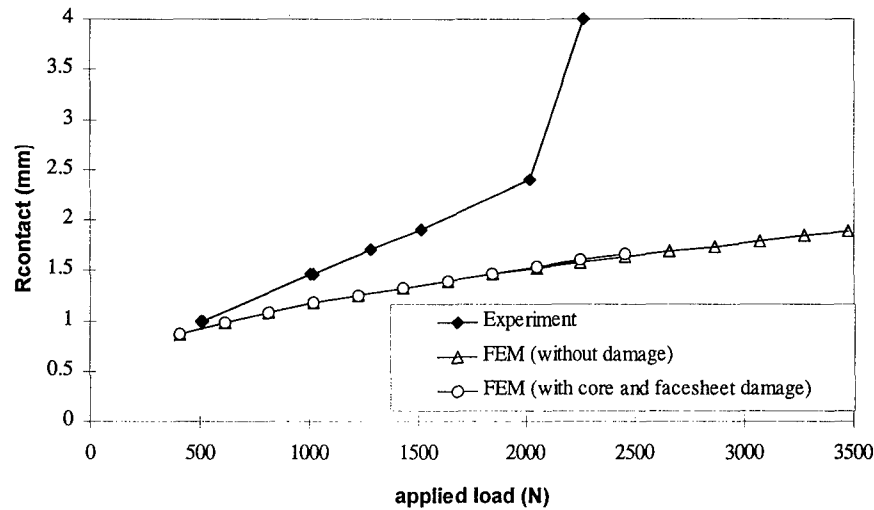


Figure 8-12 Contact radius predicted by local finite element model with facesheet and core damage considered (16-ply).

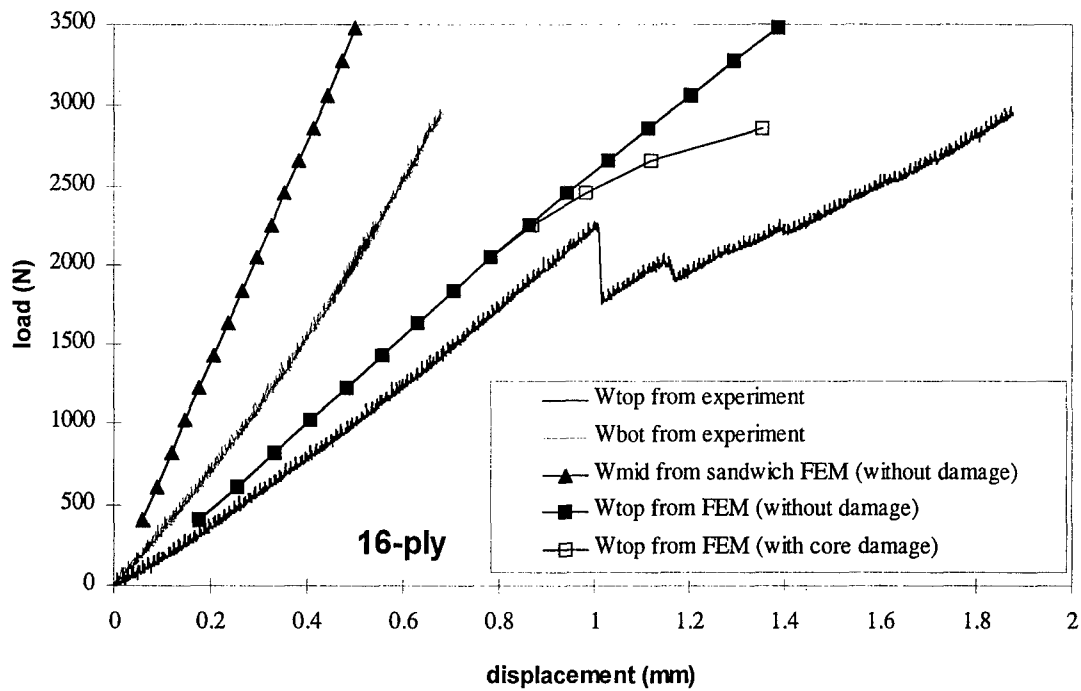


Figure 8-13 Load verses displacement predicted by local finite element model with and without considering facesheet and core damage (16-ply).

8.6.3 Case 3, facesheet and core damage.

The third case of interest includes the effects of facesheet damage in the forms of fiber breakage, inter-ply delamination, and intra-ply matrix cracking in addition to the core damage from case 2 and the contact algorithm from cases 1 and 2.

8.6.3.1 Contact radius.

In the analysis, the inclusion of facesheet damage in the form of reduced constitutive terms in the damaged elements has very little effect on the contact radius. This can be seen in figure 8-11, in which facesheet damage was present for all loads above 1300 N.

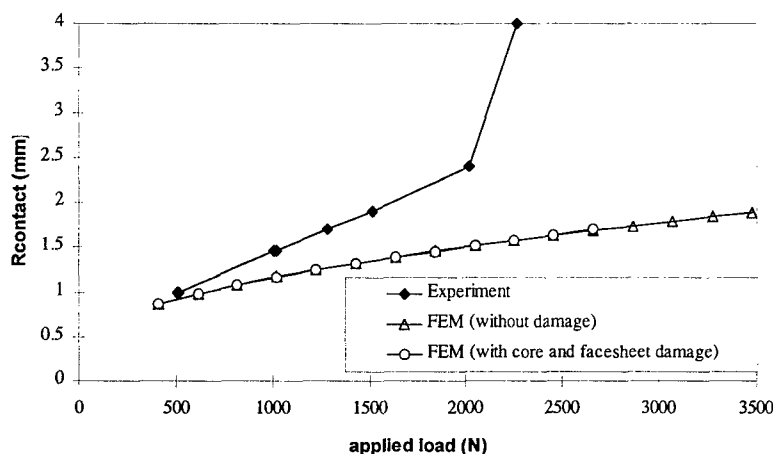


Figure 8-12 Contact radius predicted by local finite element model with facesheet and core damage considered (16-ply).

As seen in the experimental data in figure 8-12, the contact radius in the experiment is very profoundly effected by the presence of localized damage which occurred at 2250 N. The load of 2250 N is the load associated with the first major load drop in the static testing of the 16-ply specimens (see the top surface load curve in figure 4-22). The localized damage associated with this load in the experiment was to both the core and the facesheet. Even with the inclusion of both of these damage types, the analysis does not show the experimentally observed jump in the contact radius. The failure of the analysis to predict the jump in contact radius indicates a limitation of the this research. The three-dimensional effects of the damage as they "soften" the contact between the tup and the specimen are evidently not well modeled by the algorithm. This is believed to be due to the fact that the algorithm reduces the stiffness of the facesheet in the area of

damage, but still models the damaged facesheet as a single element through the thickness. A single element with continuous kinematic relations through the thickness is not able to model the reduction in local bending stiffness which must be present when delaminations exist. Locally, delaminations change a single, relatively thick laminate into multiple, kinematically independent, comparatively thin, sublaminae. The local bending stiffness provided by the sum of all of the sublaminae contributions is much less than the local bending stiffness of the single laminate. The facesheet damage algorithm used in this research reduced the shear stiffnesses of the plies adjacent to the delamination, but did not allow the sublaminae to move independently. A thick laminate with reduced shear stiffnesses is still stiffer in bending than would be the sum of the component sublaminae. The effect of maintaining the single-plate kinematics in the presence of delaminations is that the stiffness reduction in the damage algorithm does not adequately reduce the local bending stiffness of the facesheet. Since the local bending stiffness of the facesheet is too high, the midplane curvature under the load is too low. The top surface displacement is calculated from the sum of the midplane displacement and the through the thickness integral of the transverse direct strain. The low curvature of the midplane thus produces a low curvature of the top surface. The contact algorithm uses the curvature of the top surface to determine what the next estimate of the contact radius should be. In effect, the contact algorithm forces the top surface curvature to conform to the curvature of the top. If the midplane curvature is low, the contact radius will be artificially small. Thus, the facesheet damage algorithm is believed to be responsible for the inability of the analytical algorithm to model the contact radius jump observed in the experiments. Modeling the delaminated facesheet with multiple independent elements stacked through the thickness as in [9,11,56,61] may sufficiently model the local bending stiffness loss associated with delamination to allow the contact radius jump to be predicted, but was considered to be beyond the scope of this research. Another approach that may be able to improve the modeling would be to include delamination capable kinematics as discussed in Chapter 6. It should be observed, however, that the developments in Chapter 6 allow only a single delamination, whereas the experiments, elasticity solution, and finite element solution all show multiple delaminations. Extension of the delamination capable kinematics of Chapter 6 to multiple delaminations was also considered beyond the scope of this research.

Another simplification in the analysis contributing to the contact radius error is the fact that the contact algorithm is only used in the local model. Thus, sandwich midplane curvature can not

effect the contact radius. The author believes this error to be small, but nothing was done to quantify it.

8.6.3.2 Load verses displacement.

As for the contact radius, the inclusion of facesheet damage as modeled with reduced constitutive terms in the damaged elements has very little effect on the local stiffness as shown in the load verses displacement curves in figure 8-12. In that figure, the curves representing load verses displacement including only core damage and that including both core and facesheet damage are so close as to be indistinguishable. It should be noted that facesheet damage was present for all loads above 1300 N.

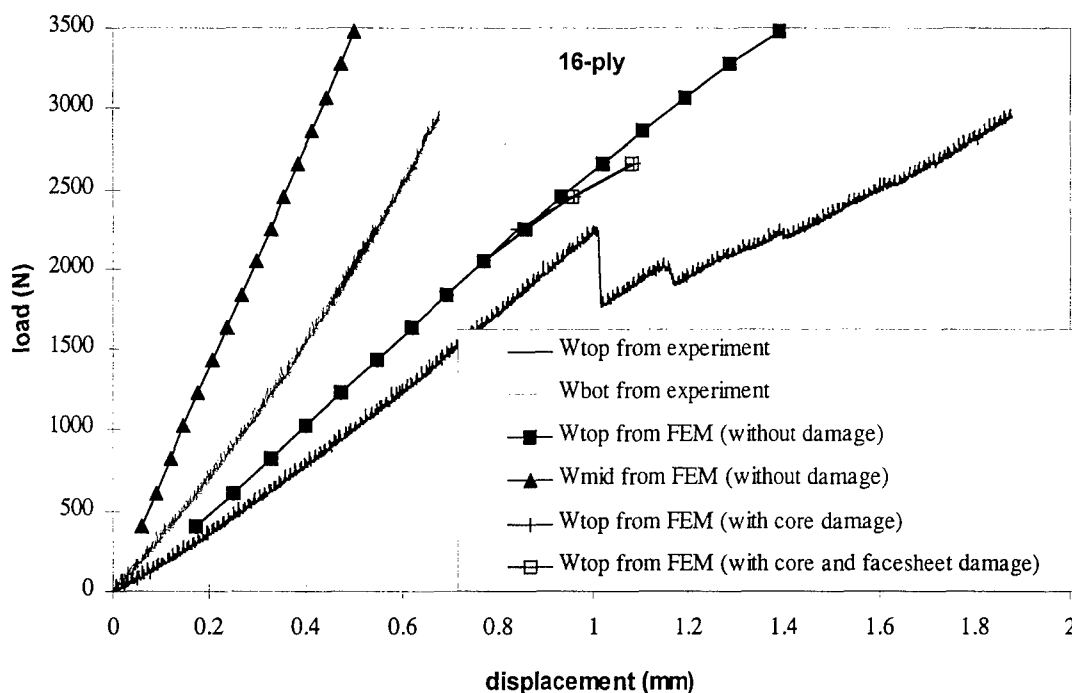


Figure 8-13 Load verses displacement predicted by local finite element model with and without considering facesheet and core damage (16-ply).

As seen in the experimental data in figure 8-13 as discussed in Chapter 4, load verses displacement curve is very profoundly effected by the occurrence of localized damage which occurred at 2250 N. The load of 2250 N is the load associated with the first major load drop in

the static testing of the 16-ply specimens. The localized damage associated with this load in the experiment was to both the core and the facesheet. Since load control was used in the analysis, it was not possible to predict the load drop associated with damage. Instead, it was expected that an abrupt increase in displacement for a given small increase in load would be found. That is, if the model were behaving as the experiment would under load control, at 2250 N the displacement should jump from 1 mm to just over 1.4 mm (horizontally from the first peak in the W_{top} from experiment curve at 1 mm displacement and 2250 N to where the next 2250 N equilibrium point at 1.43 mm displacement). Even with the inclusion of both facesheet and core damages, the analysis does not show the experimentally expected jump in the displacement. An apparently smooth and continuous digression from the undamaged load verses displacement curve can be observed beginning between 2000 N and 2250 N in figure 8-13. The load associated with the beginning of this new equilibrium curve is the load at which core damage begins. Though the beginning of core damage is apparently well predicted by the analysis, the effect of the damage is suppressed by the fact that the facesheet local bending stiffness has not been properly reduced to account for the delaminations present there. The progress of core damage under a given (constant) load is illustrated in figure 8-14.

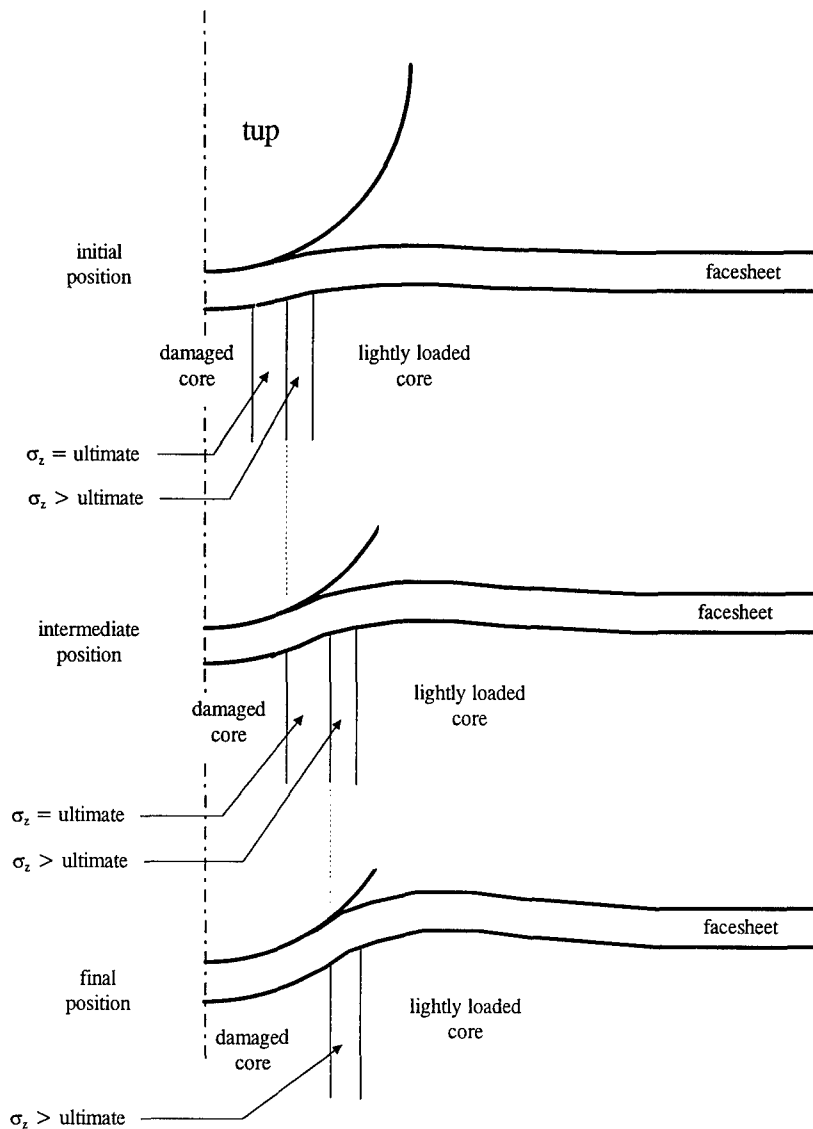


Figure 8-14 *Illustration of the progress of core damage under a constant applied force.*

When core damage is present in some localized area of the sandwich, the only resistance to motion of the top surface toward the midplane (or vice versa in the static experiment) within the damaged area is the local bending stiffness of the top facesheet. In the experiment core damage leads to large movement of midplane of the specimen toward the top surface due to the flexibility of the delaminated facesheet. This flexibility also is thought to lead to rotation of the facesheet at the edge of the core damage region, so that the entire transverse load is reacted by a relatively thin ring of the core surrounding the damaged core. This situation is illustrated as the "initial position" in figure 8-14. The innermost portion of this thin ring of core experiences high stresses (ultimate) and core failure continues, expanding the ring. The expanded ring, having more area

due to a greater radius, reacts to the transverse load with a lower average stress. This situation is illustrated as the "intermediate position" in figure 8-13. When the stress in the undamaged core at the edge of the damage is above (less negative than) the compressive ultimate stress of the core, the core failure is halted ("final position" in figure 8-14).

As discussed above, the delaminated facesheet in the analysis is relatively inflexible in bending, so that the rotation that gives rise to the high stresses in the core at the edge of the core damage region is under predicted. The core stress at the edge of the damaged region is therefore too low. Thus, the tendency of the core damage to progress under a constant load as illustrated in figure 8-14 is greatly reduced. In this way, it is thought that the facesheet damage model, as of the current research, limits the ability of the analysis to model the progression of damage. Damage initiation is correctly predicted, but damage progression is under predicted. A more accurate local bending stiffness in the delaminated region should produce better damage progression results.

8.6.3.3 *Delamination patterns.*

Delamination can significantly reduce the residual compressive strength of a composite. It is therefore important to determine the delaminations produced by a given impact event. For this reason, delamination patterns were chosen as a metric to judge the analysis. The delaminations predicted by the finite element analysis can be compared with the C-scans shown in figure 4-27. The physical dimensions are not given in figure 4-27, but the scans are magnified by 150% so that the maximum width of the 16-ply static case is 12 mm. Figure 8-15 shows the delamination patterns produced by the analysis for the same load. The shapes of the delaminations predicted by the analysis appear to be very good, while the size of the delaminations are too small by a factor of 2.0. This is to be expected, because the contact in the analysis is overly stiff after facesheet damage due to the facesheet damage algorithm as described above. The patterns shown in figure 8-15 are surprisingly close to those seen in the C-scan in figure 4-27 when one considers that the analysis based delamination on stress alone and did not include a singularity (crack tip) or even a physical discontinuity as was present in the experiment.

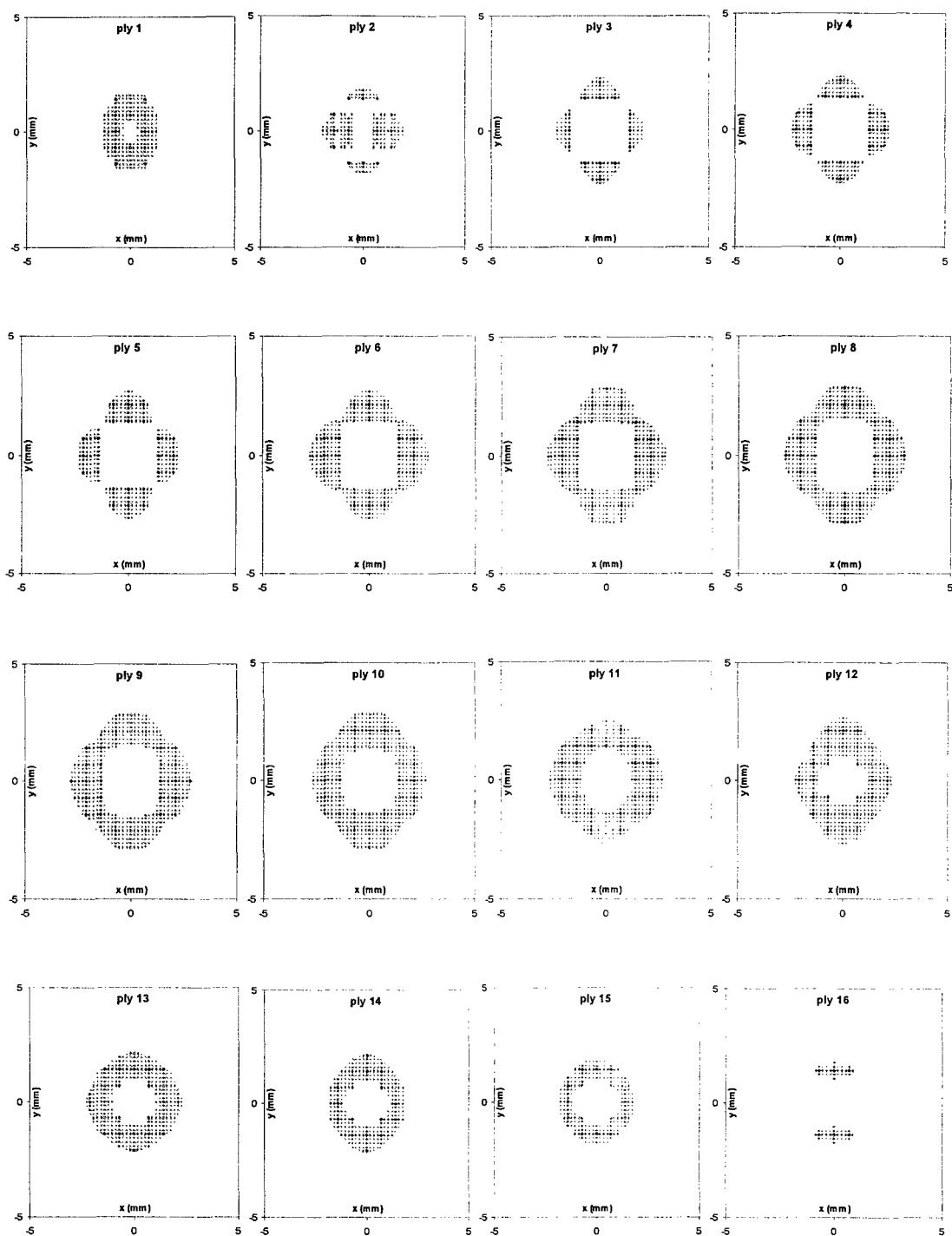


Figure 8-15 Delamination patterns predicted by local finite element model for 2250 N load (16 ply)

8.7 *Summary*

The analysis shows the ability to model some of the important features of static indentation of composite sandwich structures. In particular, the slope of the load displacement curve (stiffness), including contact, before damage is well represented. Perhaps the most important feature, core failure load, is predicted by the analysis within ten percent of the experimental value. Damage progression is under predicted by the analysis. This is believed to be attributable to the facesheet damage algorithm which evidently does not adequately reduce the local bending stiffness of the top facesheet when delamination occurs. Delamination patterns predicted by the analysis bear a striking resemblance to the C-scans from the experiments, but are smaller in size. A more accurate model for the local bending stiffness in the delaminated region should produce better damage progression results. Possible ways to do this without resorting to a full three-dimensional finite element model are by modeling the delaminated facesheet as a stack of independent sublaminates, or, including delamination capable kinematics as described in Chapter 6.

9. Summary and Conclusions

The susceptibility of composite sandwich structures to low-velocity impact damage such as that brought about by dropped tools and runway/taxiway debris has been addressed through an experimental and analytical study of low-velocity impact on sandwich plates with graphite/epoxy facesheets and Nomex honeycomb cores. In particular, simply supported, 12.7 cm square flat panels were impacted at their center by an instrumented impactor with a 12.7 mm spherical radius. Static indentation tests were also performed and comparisons of equilibrium paths (load verses displacement curves) and resulting damage provided insight into the range of validity of the quasi-static assumption commonly made in testing and analyzing low-velocity impact specimens. Elasticity solutions available in the literature for simply supported laminated plates in cylindrical bending and three-dimensional bending were extended to simulate contact loading by representing the assumed Hertzian contact load by a Fourier sine series. The resulting solution provided a benchmark for a finite element based model of the impact event. A higher-order shear deformation theory, plane stress, finite element code was extended to provide quasi-three-dimensional stresses via integration of the three-dimensional equations of stress equilibrium. Contact between the plate and the impactor was simulated by an algorithm which enforced the condition that contact area of the plate must have the same curvature as the assumed rigid impactor.

Several advances were made in the characterization of instrumented impactor test systems which provide a better understanding of the system dynamics and improve the data available from these systems. A three-degree of freedom dynamic model was able to resolve several important features of the impact force history of an instrumented impactor test and show the difference between measured and actual contact force. A simple empirically-derived force correction can significantly improve the energy histories obtained from instrumented impactor tests. Without this correction, absorbed energy values can have significant error which masks the damage initiation energy. With the correction, as impact energy is increased, a sharp jump in absorbed energy was indicative of damage in these specimens. A simple predictor of the temporal fidelity of instrumented impact test systems called the tup mass ratio was identified. Minimizing the tup mass ratio is shown to significantly improve the temporal fidelity of the load

data produced by an instrumented impactor test system. In particular, load cell dynamics are effectively removed from force oscillations following a major load drop. This allows insight into the actual dynamics of the impact event which was not previously possible. The first major load drop excited the plate vibration modes and the force oscillations appear to have been the result of plate vibrations. The frequency of the plate vibrations was not significantly effected by the damage, indicating that the damage had little effect on the bending stiffness of the plate. This correlated with the post impact inspections which indicated that the damage was localized in the area of the impact.

Low-velocity impact tests on composite sandwich plates of several different facesheet thicknesses were conducted. Load histories were recorded by the use of an instrumented impactor. The equation of motion of the impactor was time integrated using the measured force histories and impactor mass to obtain the velocity history (and hence kinetic energy history) of the impactor. The difference between the kinetic energy of the impactor at the instant of initial contact and the kinetic energy of the impactor at a given time during the impact event was taken to be the "absorbed energy" of the specimen. The absorbed energy includes both the kinetic and strain energies of the specimen. Absorbed energy at the end of the impact event seems to indicate strain energy release occurred in some of the impact events. Post impact inspections found the specimens showing this strain energy release to be damaged while those not showing the strain energy release were not found to be damaged. Therefore these results indicate that it is possible to determine if there is failure within a composite sandwich plate subjected to low-velocity impact by an instrumented impactor without relying on post-impact inspection of the specimen. The absorbed energy at the end of the impact event can be used as an indicator for damage.

Low-velocity impact of sandwich structures with thick facesheets or damage does not appear to be a quasi-static process. That is, for such structures, the "static" (actually slowly time variant) and dynamic impact events differed significantly in the load at which the first major load drop occurred and the energy that was absorbed in the damage process associated with the first major load drop. Further, the equilibrium paths after the first major load drop (i.e. damaged specimens) differed significantly as the static event showed that the load increased

nearly monotonically with displacement while the dynamic event showed a much higher degree of load fluctuation.

For the range of parameters in this study, the first major load drop observed in the load history is associated with core failure. This was confirmed by static tests in which the displacements of both the top and bottom surfaces were measured and the average transverse strain under the impactor was found to jump when the first significant load drop occurred. The measured bottom surface displacements were also used to show that the global stiffness of the plate is independent of the damage produced by low-velocity impact. This fact was used to argue that in a global-local model of the event, contact is a local effect which can be removed from the global model.

The elasticity solution of Pagano was modified for a composite sandwich subjected to a Hertzian contact load in either cylindrical bending or square plate configurations. It proved to be a useful tool for developing a general understanding of the characteristics of the stress field produced in a composite sandwich plate by a contact type load. While the three-dimensional solution can only be used for unrealistically large contact radii, the cylindrical bending solution can be used for realistic contact dimensions. Damage is not included in either of the solutions, but failure criteria are used to indicate the load at which damage is anticipated.

The principal analytical tool developed for this research was a displacement-based finite element code for low-velocity impact of composite sandwich structures. The major goal of this research was to analytically model the response of composite sandwich plates to low-velocity impact. The data presented in this dissertation indicate that the two-dimensional (plane stress) finite element analysis, when combined with the three-dimensional equations of stress equilibrium can reasonably well predict the three-dimensional state of stress in an undamaged composite sandwich under contact-type loading. The three-dimensional stresses obtained from the equilibrium equations and the in-plane finite element stresses compare favorably with the elasticity solution. The sandwich (global) model does reasonably well for the case in which the load is distributed over a large portion of the top surface, but for the small contact radius case, the elastic foundation (local) model does better.

The contact between the impactor and the sandwich plate is modeled by an algorithm that forces the top surface under the load to conform to the shape of the impactor. The contact radius is allowed to vary to match the top surface shape to that of the impactor. The contact radius thus predicted is smaller than the radii measured experimentally. This error also caused the predicted damages (delaminations) to be physically smaller than those observed experimentally.

When compared to the experimental data of Chapter 4, the finite element analysis shows the ability to model some of the important features of static indentation of composite sandwich structures. In particular, the slope of the load displacement curve (stiffness), including contact, before damage is well represented. Perhaps the most important feature, core failure load, is predicted by the analysis within ten percent of the experimental value. Damage progression is under predicted by the analysis. That is, whereas the effect of damage observed experimentally is a radical departure from the undamaged equilibrium curve, the effect of damage observed analytically is a gradual departure from the undamaged equilibrium curve. This is believed to be attributable to the facesheet damage algorithm which evidently does not adequately reduce the local bending stiffness of the top facesheet when delamination occurs. The phenomenon of facesheet delamination is a three-dimensional phenomenon which was not well modeled by a two-dimensional element. Delamination patterns predicted by the analysis are similar in shape to the delaminations observed by C-scans from the experiments, but are smaller for the same load.

Appendix A

Mathcad Elasticity Solutions

Part 1, 2D (Cylindrical Bending) Solution

This algorithm is taken from the following reference:

Exact Solutions for Composite Laminates in Cylindrical Bending
N.J. Pagano
Journal of Composite Materials, Vol 3, pg. 398-411, 1969

It has been extended here to handle sandwich structures as well as the original monolithic laminates. The particular example shown is for a 3-ply monolithic laminate with a length to thickness ratio, $S=4$, for comparison to the referenced solution. Changes needed for sandwich plate are shown.

Some Mathcad constants defined.

```

ORIGIN:=1
O:=0
psi:=10^6
ii:=1..6
jj:=1..6
MPa:=10^6
GPa:=10^9
TPa:=10^12

```

Material properties (change these for the particular problem of interest):

For facesheet materials in Pagano's example:	For facesheet materials in Herup's dissertation:	For core material in Herup's dissertation:
$E_1 = 25 \cdot 10^6 \text{ psi}$	$E_1 = 144.8 \text{ GPa}$	$E_1 = 80.4 \text{ MPa}$
$E_2 = 1 \cdot 10^6 \text{ psi}$	$E_2 = 9.7 \text{ GPa}$	$E_2 = 80.4 \text{ MPa}$
$E_3 = 1 \cdot 10^6 \text{ psi}$	$E_3 = 9.7 \text{ GPa}$	$E_3 = 1.005 \text{ GPa}$
$G_{12} = 5 \cdot 10^5 \text{ psi}$	$G_{12} = 6 \text{ GPa}$	$G_{12} = 32.16 \text{ MPa}$
$G_{13} = 5 \cdot 10^5 \text{ psi}$	$G_{13} = 6 \text{ GPa}$	$G_{13} = 120.6 \text{ MPa}$
$G_{23} = 2 \cdot 10^5 \text{ psi}$	$G_{23} = 3.6 \text{ GPa}$	$G_{23} = 75.84 \text{ MPa}$
$\nu_{12} = 0.25$	$\nu_{12} = 0.3$	$\nu_{12} = 0.25$
$\nu_{23} = 0.25$	$\nu_{23} = 0.34$	$\nu_{32} = 0.25$
$\nu_{13} = 0.25$	$\nu_{13} = 0.3$	$\nu_{31} = 0.25$

Other Poisson ratios:

$$\begin{aligned} \nu_{32} &= \frac{E_3}{E_2} \nu_{23} & \nu_{31} &= \frac{E_3}{E_1} \nu_{13} & \nu_{21} &= \frac{E_2}{E_1} \nu_{12} & \nu_{23} &= \frac{E_2}{E_3} \nu_{32} & \nu_{31} &= \frac{E_3}{E_1} \nu_{13} & \nu_{21} &= \frac{E_2}{E_1} \nu_{12} \\ \nu_{c32} &= \frac{E_{c3}}{E_2} \nu_{23} & \nu_{c31} &= \frac{E_{c3}}{E_1} \nu_{13} & \nu_{c21} &= \frac{E_{c2}}{E_1} \nu_{12} & \nu_{c23} &= \frac{E_{c2}}{E_3} \nu_{32} & \nu_{c31} &= \frac{E_{c3}}{E_1} \nu_{13} & \nu_{c21} &= \frac{E_{c2}}{E_1} \nu_{12} \end{aligned}$$

Compliance matrices (from Jones textbook eqn 2.23)
for the 0 degree plies

$$S_0 = \begin{bmatrix} \frac{1}{E_1} & 0 & -\left(\frac{\nu_{13}}{E_1}\right) & 0 & -\left(\frac{\nu_{12}}{E_1}\right) & 0 & 0 & 0 \\ 0 & -\left(\frac{\nu_{13}}{E_1}\right) & \frac{1}{E_3} & 0 & -\left(\frac{\nu_{32}}{E_3}\right) & 0 & 0 & 0 \\ 0 & -\left(\frac{\nu_{12}}{E_1}\right) & 0 & -\left(\frac{\nu_{32}}{E_3}\right) & \frac{1}{E_2} & 0 & 0 & 0 \\ 0 & 0 & 0 & \frac{1}{G_{23}} & 0 & 0 & 0 & 0 \\ 0 & 0 & 0 & 0 & 0 & \frac{1}{G_{12}} & 0 & 0 \\ 0 & 0 & 0 & 0 & 0 & 0 & \frac{1}{G_{13}} & 0 \end{bmatrix}$$

note: in S to the left, directions
2 and 3 are swapped due to
coordinates in the first half of
Pagano's May 69 paper.

Reduced compliance for plane strain:

$$R_{\text{units},0_{ii,jj}} = S_{0_{ii,jj}} - S_{0_{ii,3}} S_{0_{jj,3}} / S_{0_{3,3}}$$

$$R_{\text{units},0} = \begin{bmatrix} 0.005787 & -0.001813 & 0 & 0 & 0 & 0 \\ -0.001813 & 0.1359728 & 0 & 0 & 0 & 0 \\ 0 & 0 & 0 & 0 & 0 & 0 \\ 0 & 0 & 0 & 0.7251885 & 0 & 0 \\ 0 & 0 & 0 & 0 & 0.2900754 & 0 \\ 0 & 0 & 0 & 0 & 0 & 0.2900754 \end{bmatrix} \cdot \frac{1}{\text{GPa}}$$

Compliance matrices (from Jones textbook eqn 2.23)
for the 90 degree plies

$$S_{90} = \begin{bmatrix} \frac{1}{E_2} & 0 - \left(\frac{\nu_{23}}{E_2} \right) & 0 - \frac{\nu_{21}}{E_2} & 0 & 0 & 0 \\ 0 - \left(\frac{\nu_{23}}{E_2} \right) & \frac{1}{E_3} & 0 - \left(\frac{\nu_{31}}{E_3} \right) & 0 & 0 & 0 \\ 0 - \frac{\nu_{21}}{E_2} & 0 - \left(\frac{\nu_{31}}{E_3} \right) & \frac{1}{E_1} & 0 & 0 & 0 \\ 0 & 0 & 0 & \frac{1}{G_{13}} & 0 & 0 \\ 0 & 0 & 0 & 0 & \frac{1}{G_{12}} & 0 \\ 0 & 0 & 0 & 0 & 0 & \frac{1}{G_{23}} \end{bmatrix}$$

reduced compliance for plane strain:

$$R_{\text{units } 90_{ij}, ij} = S_{90_{ij}, ij} - \frac{S_{90_{ii}, 3} S_{90_{jj}, 3}}{S_{90_{3, 3}}}$$

$$R_{\text{units } 90} = \begin{bmatrix} 0.1446751 & -0.036622 & 0 & 0 & 0 & 0 \\ -0.036622 & 0.1446751 & 0 & 0 & 0 & 0 \\ 0 & 0 & 0 & 0 & 0 & 0 \\ 0 & 0 & 0 & 0.2900754 & 0 & 0 \\ 0 & 0 & 0 & 0 & 0.2900754 & 0 \\ 0 & 0 & 0 & 0 & 0 & 0.7251885 \end{bmatrix} \cdot \frac{1}{\text{GPa}}$$

Compliance matrices (from Jones textbook eqn 2.23)
for the core

$$S_c = \begin{bmatrix} \frac{1}{E_c 1} & 0 & \left(\frac{v_c 13}{E_c 1} \right) & 0 & 0 & 0 \\ 0 & \left(\frac{v_c 13}{E_c 1} \right) & \frac{1}{E_c 3} & 0 & 0 & 0 \\ 0 & \left(\frac{v_c 12}{E_c 1} \right) & 0 & \left(\frac{v_c 32}{E_c 3} \right) & \frac{1}{E_c 2} & 0 \\ 0 & 0 & 0 & 0 & \frac{1}{G_c 23} & 0 \\ 0 & 0 & 0 & 0 & 0 & \frac{1}{G_c 12} \\ 0 & 0 & 0 & 0 & 0 & \frac{1}{G_c 13} \end{bmatrix}$$

reduced compliance for plane strain:

$$R_{\text{units}, c_{ii}, ij} := S_{c_{ii}, ij} - \frac{S_{c_{ii}, 3} S_{c_{jj}, 3}}{S_{c_{3}, 3}}$$

$$R_{\text{units}, c} = \begin{bmatrix} 11.6604478 & -0.3109453 & 0 & 0 & 0 & 0 \\ -0.3109453 & 0.9900498 & 0 & 0 & 0 & 0 \\ 0 & 0 & 0 & 0 & 0 & 0 \\ 0 & 0 & 0 & 13.185654 & 0 & 0 \\ 0 & 0 & 0 & 0 & 31.0945274 & 0 \\ 0 & 0 & 0 & 0 & 0 & 8.291874 \end{bmatrix} \cdot \frac{1}{\text{GPa}}$$

For the remainder of the work, dimensionless quantities are defined

$$R_0 := \begin{bmatrix} R_{\text{units}, 0_1, 1} & R_{\text{units}, 0_1, 2} & 0 \\ R_{\text{units}, 0_2, 1} & R_{\text{units}, 0_2, 2} & 0 \\ 0 & 0 & R_{\text{units}, 0_6, 6} \end{bmatrix} \cdot \text{Pa}$$

$$R_0 = \begin{bmatrix} 5.787 \cdot 10^{-12} & -1.813 \cdot 10^{-12} & 0 \\ -1.813 \cdot 10^{-12} & 1.36 \cdot 10^{-10} & 0 \\ 0 & 0 & 2.901 \cdot 10^{-10} \end{bmatrix}$$

$$R_{90} := \begin{bmatrix} R_{\text{units}, 90_1, 1} & R_{\text{units}, 90_1, 2} & 0 \\ R_{\text{units}, 90_2, 1} & R_{\text{units}, 90_2, 2} & 0 \\ 0 & 0 & R_{\text{units}, 90_6, 6} \end{bmatrix} \cdot \text{Pa}$$

$$R_{90} = \begin{bmatrix} 1.447 \cdot 10^{-10} & -3.662 \cdot 10^{-11} & 0 \\ 3.662 \cdot 10^{-11} & 1.447 \cdot 10^{-10} & 0 \\ 0 & 0 & 7.252 \cdot 10^{-10} \end{bmatrix}$$

$$R_c := \begin{bmatrix} R_{\text{units}, c_1, 1} & R_{\text{units}, c_1, 2} & 0 \\ R_{\text{units}, c_2, 1} & R_{\text{units}, c_2, 2} & 0 \\ 0 & 0 & R_{\text{units}, c_6, 6} \end{bmatrix} \cdot \text{Pa}$$

$$R_c = \begin{bmatrix} 1.166 \cdot 10^{-8} & -3.109 \cdot 10^{-10} & 0 \\ -3.109 \cdot 10^{-10} & 9.9 \cdot 10^{-10} & 0 \\ 0 & 0 & 8.292 \cdot 10^{-9} \end{bmatrix}$$

Change these parameters for the particular problem:

$$\text{Numply} \equiv 3$$

$$\text{Mat} \equiv \begin{pmatrix} 0 \\ 0 \\ 0 \end{pmatrix} \quad \text{Mat} \equiv \begin{pmatrix} 0 \\ 1 \\ 0 \end{pmatrix}$$

$$\text{Mat} \equiv 2$$

$$\begin{pmatrix} 0 \\ 1 \\ 1 \\ 0 \\ 0 \\ 1 \\ 1 \\ 0 \end{pmatrix}$$

Book keeping

$$i \equiv 1 \dots \text{Numply}$$

$$ii \equiv 1 \dots 2$$

$$jj \equiv 1 \dots 2$$

$$ia \equiv 1 \dots \text{Numply} - 1$$

$$j \equiv 1 \dots 4$$

$$k \equiv 1 \dots 4$$

$$\text{Paper1} \equiv 1$$

$$\text{Paper2} \equiv 1 - \text{Paper1}$$

For Pagano's example:

$$S \equiv 4$$

$$h_{\text{plate}} \equiv \text{Numply} \cdot 0.005 \cdot \frac{\text{in}}{\text{m}}$$

$$L \equiv S \cdot h_{\text{plate}}$$

For Herup's dissertation:

$$\text{plythick} \equiv 0.005 \cdot \frac{\text{in}}{\text{m}}$$

$$L \equiv 5 \cdot \frac{\text{in}}{\text{m}}$$

$$\text{corethick} \equiv 0.5 \cdot \frac{\text{in}}{\text{m}}$$

$$h_i \equiv \text{if}(\text{Mat}_i \equiv 2, \text{corethick}, \text{plythick})$$

$$\text{thk} \equiv \sum_i h_i$$

$$S \equiv \frac{L}{\text{thk}}$$

$$S = 4$$

$$\text{thk} = 0.015 \cdot \frac{\text{in}}{\text{m}}$$

$$h = \begin{pmatrix} 0.005 \\ 0.005 \\ 0.005 \end{pmatrix} \cdot \frac{\text{in}}{\text{m}}$$

A-6

Strength quantities (change these parameters for the particular problem):

$$Xt \equiv 0.2 \cdot 10^6 \frac{\text{psi}}{\text{Pa}} \quad Xc \equiv -0.2 \cdot 10^6 \frac{\text{psi}}{\text{Pa}} \quad Yt \equiv 5 \cdot 10^3 \frac{\text{psi}}{\text{Pa}} \quad Yc \equiv -30 \cdot 10^3 \frac{\text{psi}}{\text{Pa}} \quad Sg \equiv 10 \cdot 10^3 \frac{\text{psi}}{\text{Pa}} \quad Ze \equiv -5150 \frac{\text{psi}}{\text{Pa}} \quad Sc \equiv 3270 \frac{\text{psi}}{\text{Pa}}$$

load parameters

$$q_0 \equiv -1.0 \cdot 10^4 \quad p \equiv \frac{\pi}{L} \quad p1 \equiv 1 \quad p2 \equiv 1$$

Pagano's eqns 15 are

$$a_i \equiv \text{if}(\text{Mat}_i \equiv 0, R_{03,3} + 2 \cdot R_{01,2}, \text{if}(\text{Mat}_i \equiv 1, R_{903,3} + 2 \cdot R_{901,2}, R_{c3,3} + 2 \cdot R_{c1,2}))$$

$$b_i \equiv \text{if}(\text{Mat}_i \equiv 0, \sqrt{(a_i)^2 - 4 \cdot R_{01,1} \cdot R_{02,2}}, \text{if}(\text{Mat}_i \equiv 1, \sqrt{(a_i)^2 - 4 \cdot R_{901,1} \cdot R_{902,2}}, \sqrt{(a_i)^2 - 4 \cdot R_{c1,1} \cdot R_{c2,2}})$$

$$c_i \equiv \text{if}(\text{Mat}_i \equiv 0, 2 \cdot R_{01,1}, \text{if}(\text{Mat}_i \equiv 1, 2 \cdot R_{901,1}, 2 \cdot R_{c1,1}))$$

a _i	b _i	c _i
<div>2.864 · 10¹⁰</div>	<div>2.809 · 10¹⁰</div>	<div>1.157 · 10¹¹</div>
<div>6.519 · 10¹⁰</div>	<div>5.842 · 10¹⁰</div>	<div>2.894 · 10¹⁰</div>
<div>2.864 · 10¹⁰</div>	<div>2.809 · 10¹⁰</div>	<div>1.157 · 10¹¹</div>

Pagano's eqns 14 are

$$m1_{1,i} = p \cdot \sqrt{\frac{a_i + b_i}{c_i}} \quad m1_{2,i} = p \cdot \sqrt{\frac{a_i + b_i}{c_i}}$$

$$m1_{3,i} = p \cdot \sqrt{\frac{a_i - b_i}{c_i}} \quad m1_{4,i} = p \cdot \sqrt{\frac{a_i - b_i}{c_i}}$$

$$m1 = \begin{bmatrix} 1.443 \cdot 10^4 & 4.261 \cdot 10^3 & 1.443 \cdot 10^4 \\ -1.443 \cdot 10^4 & -4.261 \cdot 10^3 & -1.443 \cdot 10^4 \\ 1.427 \cdot 10^3 & 997.331 & 1.427 \cdot 10^3 \\ -1.427 \cdot 10^3 & -997.331 & -1.427 \cdot 10^3 \end{bmatrix}$$

Create a matrix B (4m X 4m) which, premultiplying a vector AA (Aji) produces a vector of the BC's.

Satisfying the BC's on sig z at the top and bottom surface (Pagano eqns 6).

sig z top	$B_{1,j} = \frac{m1_{j,1} \cdot \frac{thk}{2}}{p \cdot e}$		
sig z bottom	$B_{2,j+4} = \frac{m1_{j,Numpy} \cdot \frac{thk}{2}}{p \cdot e}$	interface z values:	$z_{ia} = \frac{thk}{2} \sum_{k=1}^{ia} h_k$
tau xz top	$B_{3,j} = \frac{m1_{j,1} \cdot \frac{thk}{2}}{p \cdot m1_{j,1} \cdot e}$		
tau xz bottom	$B_{4,j+4} = \frac{m1_{j,Numpy} \cdot \frac{thk}{2}}{p \cdot m1_{j,Numpy} \cdot e}$		

Satisfying the interface continuity conditions (Pagano eqns 8):

sigz

$$B_4 + ia,j + 4 \cdot (ia - 1) = p \cdot e^{2 \cdot \frac{ml_{j,ia} \cdot z_{ia}}{p}}$$

$$B_4 + ia,j + 4 \cdot ia = p \cdot e^{2 \cdot \frac{ml_{j,ia+1} \cdot z_{ia}}{p}}$$

tauxz

$$B_3 + \text{Numply} + ia,j + 4 \cdot (ia - 1) = p \cdot \left(\frac{ml_{j,ia} \cdot z_{ia}}{p} \cdot e^{2 \cdot \frac{ml_{j,ia} \cdot z_{ia}}{p}} \right)$$

$$B_3 + \text{Numply} + ia,j + 4 \cdot ia = p \cdot \left(\frac{ml_{j,ia+1} \cdot z_{ia}}{p} \cdot e^{2 \cdot \frac{ml_{j,ia+1} \cdot z_{ia}}{p}} \right)$$

u

$$B_2 + 2 \cdot \text{Numply} + ia,j + 4 \cdot (ia - 1) = \frac{1}{p} \cdot e^{2 \cdot \frac{ml_{j,ia} \cdot z_{ia}}{p}} \cdot \left[\text{Mat}_{ia} = 0, \left[R_{01,2} \cdot p^2 - R_{01,1} \cdot (ml_{j,ia})^2 \right], \text{if Mat}_{ia} = 1, \left[R_{901,2} \cdot p^2 - R_{901,1} \cdot (ml_{j,ia})^2 \right], R_{c1,2} \cdot p^2 - R_{c1,1} \cdot (ml_{j,ia})^2 \right]$$

$$B_2 + 2 \cdot \text{Numply} + ia,j + 4 \cdot ia = \frac{1}{p} \cdot e^{2 \cdot \frac{ml_{j,ia+1} \cdot z_{ia}}{p}} \cdot \left[\text{Mat}_{ia+1} = 0, \left[R_{01,2} \cdot p^2 - R_{01,1} \cdot (ml_{j,ia+1})^2 \right], \text{if Mat}_{ia+1} = 1, \left[R_{901,2} \cdot p^2 - R_{901,1} \cdot (ml_{j,ia+1})^2 \right], R_{c1,2} \cdot p^2 - R_{c1,1} \cdot (ml_{j,ia+1})^2 \right]$$

W

$$B_1 + 3 \cdot \text{Numply} + ia_j + 4 \cdot (ia - 1) = e^{ml_{j,ia} \cdot z_{ia}} \cdot \left[\text{if Mat}_{ia} = 0, \left(R_{01,2} \cdot ml_{j,ia} - \frac{R_{02,2,2}}{ml_{j,ia}} \cdot p \right), \text{if Mat}_{ia} = 1, \left(R_{901,2} \cdot ml_{j,ia} - \frac{R_{902,2,2}}{ml_{j,ia}} \cdot p \right), \left(R_{c1,2} \cdot ml_{j,ia} - \frac{R_{c2,2,2}}{ml_{j,ia}} \cdot p \right) \right]$$

$$B_1 + 3 \cdot \text{Numply} + ia_j + 4 \cdot ia = \left(e^{ml_{j,ia+1} \cdot z_{ia}} \cdot \left[\text{if Mat}_{ia+1} = 0, \left(R_{01,2} \cdot ml_{j,ia+1} - \frac{R_{02,2,2}}{ml_{j,ia+1}} \cdot p \right), \text{if Mat}_{ia+1} = 1, \left(R_{901,2} \cdot ml_{j,ia+1} - \frac{R_{902,2,2}}{ml_{j,ia+1}} \cdot p \right), \left(R_{c1,2} \cdot ml_{j,ia+1} - \frac{R_{c2,2,2}}{ml_{j,ia+1}} \cdot p \right) \right] \right)$$

$$BC_{i4} = Op$$

$$BC_1 = q_0$$

$$i4 = 1 \dots 4 \text{ Numply}$$

$$Op = 0$$

$$n = 1 \dots \text{Num}$$

$$\text{Num} = 25$$

The solution (Aji in Pagano eqn 13):

$$AA = B^{-1} \cdot BC$$

$$A_{1,i} = AA_1 + 4 \cdot (i - 1)$$

$$A_{2,i} = AA_2 + 4 \cdot (i - 1)$$

$$A_{3,i} = AA_3 + 4 \cdot (i - 1)$$

$$A_{4,i} = AA_4 + 4 \cdot (i - 1)$$

$$A = \begin{bmatrix} -6.364 \cdot 10^{-5} & 3.04 \cdot 10^{-5} & -8.836 \cdot 10^{-4} \\ 9.354 \cdot 10^{-4} & -1.553 \cdot 10^{-4} & 5.976 \cdot 10^{-5} \\ 0.005 & 0.004 & 0.006 \\ 0.005 & 0.002 & 0.004 \end{bmatrix}$$

A-10

internal z values:

$$zz_{n,i} = \frac{thk}{2} \sum_{k=1}^i h_k \frac{n-1}{Num-1} \cdot h_i + h_i$$

$$Z_{(i-1) \cdot Num + n} = zz_{n,i}$$

$$iz = 1 \dots Numply \cdot Num$$

$$Z_{bar(i-1) \cdot Num + n} = \frac{zz_{n,i}}{2 \cdot zz_{1,1}}$$

The solution (Pagano eqns 16 and 17):

$$u(x,z,i) = \frac{\cos(p \cdot x)}{p} \cdot \sum_{j=1}^4 A_{j,i} \cdot e^{m1_{j,i} \cdot z} \cdot \text{if} \left[\text{Mat}_1 = 0, \left[R_{0,2} \cdot p^2 - R_{0,1} \cdot (m1_{j,i})^2 \right], \text{if} \left[\text{Mat}_1 = 1, \left[R_{90,2} \cdot p^2 - R_{90,1} \cdot (m1_{j,i})^2 \right], \left[R_{c1,2} \cdot p^2 - R_{c1,1} \cdot (m1_{j,i})^2 \right] \right] \right]$$

$$\text{Pagano (28)} \quad U_{(i-1) \cdot Num + n} = \frac{E_2 \cdot u(0, zz_{n,i}, i)}{thk \cdot q_0 \cdot (S^3 \cdot Paper2 + Paper1)}$$

$$w(x,z,i) = \sin(p \cdot x) \cdot \sum_{j=1}^4 A_{j,i} \cdot e^{m1_{j,i} \cdot z} \cdot \text{if} \left[\text{Mat}_1 = 0, \left(R_{0,2} \cdot m1_{j,i} \cdot \frac{R_{0,2,2}}{m1_{j,i}} \cdot p^2 \right), \text{if} \left[\text{Mat}_1 = 1, \left(R_{90,2} \cdot m1_{j,i} \cdot \frac{R_{90,2,2}}{m1_{j,i}} \cdot p^2 \right), \left(R_{c1,2} \cdot m1_{j,i} \cdot \frac{R_{c2,2,2}}{m1_{j,i}} \cdot p^2 \right) \right] \right]$$

$$\text{Pagano (28)} \quad W_{(i-1) \cdot Num + n} = \frac{100 \cdot E_2 \cdot w\left(\frac{L}{2}, zz_{n,i}, i\right)}{thk \cdot S^4 \cdot q_0}$$

$$\text{Or in dimensional form: } W_{(i-1) \cdot Num + n} = w\left(\frac{L}{2}, zz_{n,i}, i\right)$$

$$\sigma_x(x, z, i) = \sin(p \cdot x) \cdot \sum_{j=1}^4 A_{j,i} \left[(m1_{j,i})^2 \cdot e^{m1_{j,i} \cdot z} \right]$$

$$\text{Pagano (28)} \quad \frac{\sum x_{(i-1) \cdot \text{Num} + n} \cdot \sigma_x \left(\frac{L}{2}, zz_{n,i}, i \right)}{q_0 \cdot (S^2 \cdot \text{Paper2} + \text{Paper1})}$$

$$\text{Or in dimensional form:} \quad \sum x_{(i-1) \cdot \text{Num} + n} \cdot \sigma_x \left(\frac{L}{2}, zz_{n,i}, i \right)$$

Failure metric:

$$X_{\text{fail}}(x, z, i) = \text{if} \left(\text{Mat}_1 < 2, \text{if} \left(\text{Mat}_1 = 0, \left| \frac{\sigma_x(x, z, i)}{X_t} \right|, \text{if} \left(\text{Re}(\sigma_x(x, z, i)) > 0, \frac{\sigma_x(x, z, i)}{Y_t}, \frac{\sigma_x(x, z, i)}{Y_c} \right) \right), 0 \right)$$

$$X_{\text{failure}}_{(i-1) \cdot \text{Num} + n} = X_{\text{fail}} \left(\frac{L}{2}, zz_{n,i}, i \right)$$

$$\sigma_z(x, z, i) = -p^2 \cdot \sin(p \cdot x) \cdot \sum_{j=1}^4 A_{j,i} \cdot e^{m1_{j,i} \cdot z}$$

$$\text{Pagano (28)} \quad \frac{\sum z_{(i-1) \cdot \text{Num} + n} \cdot \sigma_z \left(\frac{L}{2}, zz_{n,i}, i \right)}{q_0 \cdot (S^2 \cdot \text{Paper2} + \text{Paper1})}$$

Or in dimensional form:

$$\Sigma z_{(i-1) \cdot \text{Num} + n} \sigma_z \left(\frac{L}{2}, z z_{n,i} \right)$$

Failure metric:

$$Z_{\text{fail}}(x, z, i) := \text{if} \left(\text{Mat}_1 < 2, \text{if} \left(\text{Mat}_1 = 0, \frac{\sigma_z(x, z, i)}{X_c}, \frac{\sigma_z(x, z, i)}{Y_c} \right), \frac{\sigma_z(x, z, i)}{Z_c} \right)$$

$$Z_{\text{failure}_{(i-1) \cdot \text{Num} + n}} = Z_{\text{fail}} \left(\frac{L}{2}, z z_{n,i} \right)$$

$$\tau_{xz}(x, z, i) = -p \cos(p \cdot x) \cdot \sum_{j=1}^4 A_{j,i} \left(m l_{j,i} e^{\left(\frac{m l_{j,i} z}{j, i} \right)} \right)$$

Pagano (28)

$$\tau_{xz(i-1) \cdot \text{Num} + n} = \frac{\tau_{xz}(0 \cdot L, z z_{n,i})}{q_0(S \cdot \text{Paper2} + \text{Paper1})}$$

Or in dimensional form:

$$\tau_{xz(i-1) \cdot \text{Num} + n} = \tau_{xz}(0 \cdot L, z z_{n,i})$$

Failure metric:

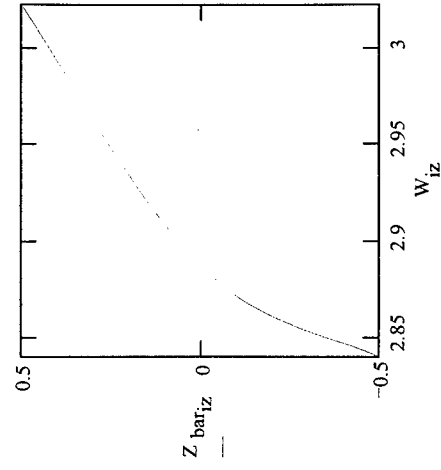
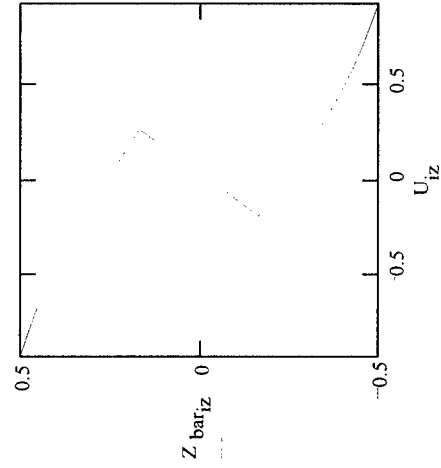
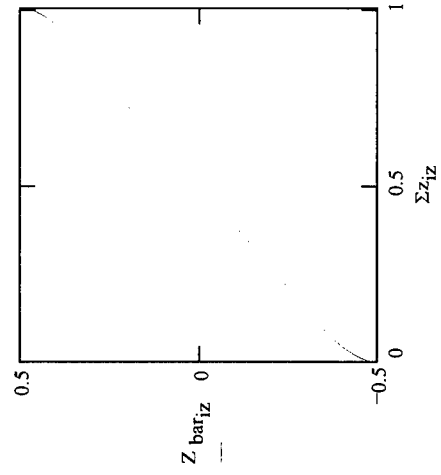
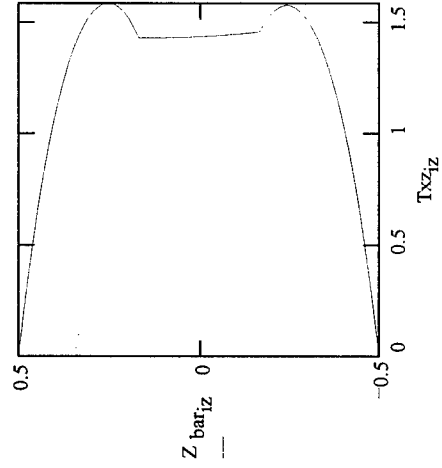
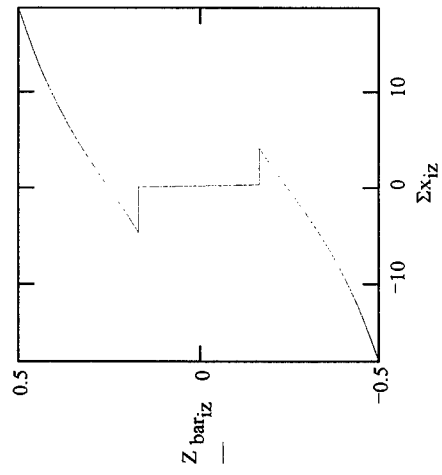
$$S_{\text{fail}}(x, z, i) := \text{if} \left(\text{Mat}_1 < 2, \left| \frac{\tau_{xz}(x, z, i)}{S_g} \right|, \left| \frac{\tau_{xz}(x, z, i)}{S_c} \right| \right)$$

$$S_{\text{failure}_{(i-1) \cdot \text{Num} + n}} = S_{\text{fail}}(0 \cdot L, z z_{n,i})$$

Cylindrical Bending Solution

Numpy = 3

S = 4



Part 2, 3D Solution

This algorithm taken from the following reference:
 Exact Solutions for Rectangular Bidirectional Composites and Sandwich Plates
 N.J. Pagano
Journal of Composite Materials, Vol 4, pg. 20-34. 1970

Plate dimensions

$$S=4 \quad L=254 \quad h_{plate} = \frac{L}{S} \quad h_k = \frac{h_{plate}}{N_{ply}} \quad thk = \sum_k h_k$$

$$q_0 = 1$$

$$h = \begin{pmatrix} 0.833 \\ 0.833 \\ 0.833 \end{pmatrix} \cdot \frac{\text{in}}{\text{m}} \quad thk = 2.5 \cdot \frac{\text{in}}{\text{m}}$$

strengths

$$X_t = 0.2 \cdot 10^6 \frac{\text{psi}}{\text{Pa}} \quad Y_t = 5 \cdot 10^3 \frac{\text{psi}}{\text{Pa}} \quad S_g = 10 \cdot 10^3 \frac{\text{psi}}{\text{Pa}}$$

$$X_c = 0.2 \cdot 10^6 \frac{\text{psi}}{\text{Pa}} \quad Y_c = 30 \cdot 10^3 \frac{\text{psi}}{\text{Pa}} \quad Z_c = 5150 \frac{\text{psi}}{\text{Pa}}$$

$$S_c = 3270 \frac{\text{psi}}{\text{Pa}}$$

$$ORIGIN = 1$$

$$N_{ply} = 3$$

$$k = 1..N_{ply}$$

$$kk = 1..2$$

$$jj = 1..2$$

$$Paper1 = 0$$

$$Paper2 = 1 - Paper1$$

$$ka = 1..N_{ply} - 1$$

$$j = 1..3$$

$$i = 1..3$$

$$p(n) = n \cdot \frac{\pi}{L}$$

$$q(m) = m \cdot \frac{\pi}{L}$$

$$Mat = \begin{pmatrix} 0 \\ 1 \\ 0 \\ 1 \\ 1 \\ 0 \\ 1 \\ 0 \end{pmatrix}$$

used for scaling

$$E_2 = 10^6 \frac{\text{psi}}{\text{Pa}}$$

$$h_k = \text{if}(Mat_k = 2, 0.5 \cdot \frac{\text{in}}{\text{m}}, 0.005 \cdot \frac{\text{in}}{\text{m}})$$

$$h_k = \text{if}(Mat_k < 2, \frac{h_{plate}}{10}, \frac{4 \cdot h_{plate}}{5})$$

ply constitutive matrices

$$C_0 = \begin{bmatrix} 1.735 \cdot 10^{11} & 2.314 \cdot 10^9 & 2.314 \cdot 10^9 & 0 & 0 & 0 \\ 2.314 \cdot 10^9 & 7.385 \cdot 10^9 & 1.869 \cdot 10^9 & 0 & 0 & 0 \\ 2.314 \cdot 10^9 & 1.869 \cdot 10^9 & 7.385 \cdot 10^9 & 0 & 0 & 0 \\ 0 & 0 & 0 & 1.379 \cdot 10^9 & 0 & 0 \\ 0 & 0 & 0 & 0 & 3.447 \cdot 10^9 & 0 \\ 0 & 0 & 0 & 0 & 0 & 3.447 \cdot 10^9 \end{bmatrix}$$

$$C_{90} = \begin{bmatrix} 7.385 \cdot 10^9 & 2.314 \cdot 10^9 & 1.869 \cdot 10^9 & 0 & 0 & 0 \\ 2.314 \cdot 10^9 & 1.735 \cdot 10^{11} & 2.314 \cdot 10^9 & 0 & 0 & 0 \\ 1.869 \cdot 10^9 & 2.314 \cdot 10^9 & 7.385 \cdot 10^9 & 0 & 0 & 0 \\ 0 & 0 & 0 & 3.447 \cdot 10^9 & 0 & 0 \\ 0 & 0 & 0 & 0 & 1.379 \cdot 10^9 & 0 \\ 0 & 0 & 0 & 0 & 0 & 3.447 \cdot 10^9 \end{bmatrix}$$

$$C_c = \begin{bmatrix} 3.073 \cdot 10^8 & 8.668 \cdot 10^7 & 9.85 \cdot 10^7 & 0 & 0 & 0 \\ 8.668 \cdot 10^7 & 3.073 \cdot 10^8 & 9.85 \cdot 10^7 & 0 & 0 & 0 \\ 9.85 \cdot 10^7 & 9.85 \cdot 10^7 & 7.387 \cdot 10^8 & 0 & 0 & 0 \\ 0 & 0 & 0 & 4.137 \cdot 10^8 & 0 & 0 \\ 0 & 0 & 0 & 0 & 4.137 \cdot 10^8 & 0 \\ 0 & 0 & 0 & 0 & 0 & 1.103 \cdot 10^8 \end{bmatrix}$$

$$C44_k = \text{if}(\text{Mat}_k = 0, C_{04,4}, \text{if}(\text{Mat}_k = 1, C_{904,4}, C_{c4,4}))$$

$$C55_k = \text{if}(\text{Mat}_k = 0, C_{05,5}, \text{if}(\text{Mat}_k = 1, C_{905,5}, C_{c5,5}))$$

$$C66_k = \text{if}(\text{Mat}_k = 0, C_{06,6}, \text{if}(\text{Mat}_k = 1, C_{906,6}, C_{c6,6}))$$

eqns 11:

$$A_k := \text{if}(\text{Mat}_k=0, C_{0,3,3} \cdot C_{0,4,4} \cdot C_{0,5,5}, \text{if}(\text{Mat}_k=1, C_{90,3,3} \cdot C_{90,4,4} \cdot C_{90,5,5}, C_{e_{3,3}} \cdot C_{e_{4,4}} \cdot C_{e_{5,5}}))$$

$$B_k := \text{if}(\text{Mat}_k=0, p(1)^2 \cdot \left[\begin{array}{l} C_{0,4,4} \cdot C_{0,1,1} \cdot C_{0,3,3} - (C_{0,1,3})^2 \dots \\ + C_{0,5,5} \cdot (C_{0,6,6} \cdot C_{0,3,3} - 2 \cdot C_{0,1,3} \cdot C_{0,4,4}) \dots \\ + q(1)^2 \cdot \left[\begin{array}{l} C_{0,5,5} \cdot C_{0,2,2} \cdot C_{0,3,3} - (C_{0,2,3})^2 \dots \\ + C_{0,4,4} \cdot (C_{0,6,6} \cdot C_{0,3,3} - 2 \cdot C_{0,2,3} \cdot C_{0,5,5}) \dots \end{array} \right] \dots \\ \dots, \text{if}(\text{Mat}_k=1, p(1)^2 \cdot \left[\begin{array}{l} C_{90,4,4} \cdot C_{90,1,1} \cdot C_{90,3,3} - (C_{90,1,3})^2 \dots \\ + C_{90,5,5} \cdot (C_{90,6,6} \cdot C_{90,3,3} - 2 \cdot C_{90,1,3} \cdot C_{90,4,4}) \dots \\ + q(1)^2 \cdot \left[\begin{array}{l} C_{90,5,5} \cdot C_{90,2,2} \cdot C_{90,3,3} - (C_{90,2,3})^2 \dots \\ + C_{90,4,4} \cdot (C_{90,6,6} \cdot C_{90,3,3} - 2 \cdot C_{90,2,3} \cdot C_{90,5,5}) \dots \end{array} \right] \dots \\ \dots, p(1)^2 \cdot \left[\begin{array}{l} C_{e_{4,4}} \cdot C_{e_{1,1}} \cdot C_{e_{3,3}} - (C_{e_{1,1}} \cdot C_{e_{3,3}} - (C_{e_{6,6}} \cdot C_{e_{3,3}} - \\ + C_{e_{5,5}} \cdot (C_{e_{6,6}} \cdot C_{e_{3,3}} - \\ + q(1)^2 \cdot \left[\begin{array}{l} C_{e_{5,5}} \cdot C_{e_{2,2}} \cdot C_{e_{3,3}} - \\ + C_{e_{4,4}} \cdot (C_{e_{6,6}} \cdot C_{e_{3,3}} - \end{array} \right] \dots \end{array} \right] \dots \end{array} \right]$$

$$C_k := \text{if}(\text{Mat}_k=0, \left[\begin{array}{l} p(1)^4 \cdot \left[\begin{array}{l} C_{0,6,6} \cdot C_{0,1,1} \cdot C_{0,3,3} - (C_{0,1,3})^2 \dots \\ + C_{0,5,5} \cdot (C_{0,1,1} \cdot C_{0,4,4} - 2 \cdot C_{0,1,3} \cdot C_{0,6,6}) \dots \\ + p(1)^2 \cdot q(1)^2 \cdot \left[\begin{array}{l} C_{0,1,1} \cdot C_{0,2,2} \cdot C_{0,3,3} - (C_{0,2,3})^2 \dots \\ + 2 \cdot (C_{0,1,2} + C_{0,6,6} \cdot C_{0,1,3} + C_{0,5,5}) \cdot (C_{0,2,3} + C_{0,4,4}) \dots \\ + 2 \cdot C_{0,4,4} \cdot C_{0,5,5} \cdot C_{0,6,6} \dots \\ + 2 \cdot C_{0,4,4} \cdot C_{0,1,1} \cdot C_{0,2,3} \dots \\ + C_{0,1,2} \cdot C_{0,3,3} \cdot (C_{0,1,2} + 2 \cdot C_{0,6,6}) \dots \\ + C_{0,1,3} \cdot C_{0,2,2} \cdot (C_{0,1,3} + 2 \cdot C_{0,5,5}) \dots \end{array} \right] \dots \\ + q(1)^4 \cdot \left[\begin{array}{l} C_{0,6,6} \cdot C_{0,2,2} \cdot C_{0,3,3} - (C_{0,2,3})^2 \dots \\ + C_{0,4,4} \cdot (C_{0,2,2} \cdot C_{0,5,5} - 2 \cdot C_{0,2,3} \cdot C_{0,6,6}) \dots \end{array} \right] \dots \end{array} \right] \dots, \text{if}(\text{Mat}_k=1, \left[\begin{array}{l} p(1)^4 \cdot \left[\begin{array}{l} C_{90,6,6} \cdot C_{90,1,1} \cdot C_{90,3,3} - (C_{90,1,3})^2 \dots \\ + C_{90,5,5} \cdot (C_{90,1,1} \cdot C_{90,4,4} - 2 \cdot C_{90,1,3} \cdot C_{90,6,6}) \dots \\ + p(1)^2 \cdot q(1)^2 \cdot \left[\begin{array}{l} C_{90,1,1} \cdot C_{90,2,2} \cdot C_{90,3,3} - (C_{90,2,3})^2 \dots \\ + 2 \cdot (C_{90,1,2} + C_{90,6,6} \cdot (C_{90,1,3} + C_{90,5,5})) \cdot (C_{90,2,3} + C_{90,4,4}) \dots \\ + 2 \cdot C_{90,4,4} \cdot C_{90,5,5} \cdot C_{90,6,6} \dots \\ + 2 \cdot C_{90,4,4} \cdot C_{90,1,1} \cdot C_{90,2,3} \dots \\ + C_{90,1,2} \cdot C_{90,3,3} \cdot (C_{90,1,2} + 2 \cdot C_{90,6,6}) \dots \\ + C_{90,1,3} \cdot C_{90,2,2} \cdot (C_{90,1,3} + 2 \cdot C_{90,5,5}) \dots \end{array} \right] \dots \\ + q(1)^4 \cdot \left[\begin{array}{l} C_{90,6,6} \cdot C_{90,2,2} \cdot C_{90,3,3} - (C_{90,2,3})^2 \dots \\ + C_{90,4,4} \cdot (C_{90,2,2} \cdot C_{90,5,5} - 2 \cdot C_{90,2,3} \cdot C_{90,6,6}) \dots \end{array} \right] \dots \end{array} \right] \dots \end{array} \right]$$

$$D_k = \text{if } \text{Mat}_k = 0, C_{0,1,1} \cdot p(1)^6 \cdot C_{06,6} \cdot C_{05,5} \dots, \text{if } \text{Mat}_k = 1, C_{90,1,1} \cdot p(1)^6 \cdot C_{906,6} \cdot C_{905,5} \dots$$

$$+ \left[\begin{aligned} & (C_{0,1,1} \cdot C_{04,4} - 2 \cdot C_{01,2} \cdot C_{05,5}) \cdot C_{06,6} \dots \cdot q(1)^2 \cdot p(1)^4 \dots \\ & + \left[\begin{aligned} & (C_{01,2})^2 + C_{01,1} \cdot C_{02,2} \end{aligned} \right] \cdot C_{05,5} \\ & + \left[\begin{aligned} & (-2 \cdot C_{01,2} \cdot C_{04,4} + C_{02,2} \cdot C_{05,5}) \cdot C_{06,6} \dots \cdot q(1)^4 \cdot p(1)^2 \dots \\ & + \left[\begin{aligned} & (C_{01,2})^2 + C_{01,1} \cdot C_{02,2} \end{aligned} \right] \cdot C_{04,4} \end{aligned} \right] \cdot C_{06,6} \dots \cdot q(1)^6 \end{aligned}$$

$$+ C_{02,2} \cdot C_{04,4} \cdot C_{06,6} \cdot q(1)^6$$

$$+ \left[\begin{aligned} & (C_{90,1,1} \cdot C_{904,4} - 2 \cdot C_{901,2} \cdot C_{905,5}) \cdot C_{906,6} \dots \cdot q(1)^2 \cdot p(1)^4 \dots \\ & + \left[\begin{aligned} & (C_{901,2})^2 + C_{901,1} \cdot C_{902,2} \end{aligned} \right] \cdot C_{905,5} \\ & + \left[\begin{aligned} & (-2 \cdot C_{901,2} \cdot C_{904,4} + C_{902,2} \cdot C_{905,5}) \cdot C_{906,6} \dots \cdot q(1)^4 \cdot p(1)^2 \dots \\ & + \left[\begin{aligned} & (C_{901,2})^2 + C_{901,1} \cdot C_{902,2} \end{aligned} \right] \cdot C_{904,4} \end{aligned} \right] \cdot C_{906,6} \dots \cdot q(1)^6 \end{aligned}$$

$$+ C_{902,2} \cdot C_{904,4} \cdot C_{906,6} \cdot q(1)^6$$

$$+ C_{c1,1} \cdot p(1)^6 \cdot C_{c6,6}$$

$$+ \left[\begin{aligned} & (C_{c1,1} \cdot C_{c4,4} - 2 \cdot C_{c1,2} \cdot C_{c5,5}) \cdot C_{c6,6} \dots \cdot q(1)^2 \cdot p(1)^4 \dots \\ & + \left[\begin{aligned} & (C_{c1,2})^2 + C_{c1,1} \cdot C_{c2,2} \end{aligned} \right] \cdot C_{c5,5} \\ & + \left[\begin{aligned} & (-2 \cdot C_{c1,2} \cdot C_{c4,4} + C_{c2,2} \cdot C_{c5,5}) \cdot C_{c6,6} \dots \cdot q(1)^4 \cdot p(1)^2 \dots \\ & + \left[\begin{aligned} & (C_{c1,2})^2 + C_{c1,1} \cdot C_{c2,2} \end{aligned} \right] \cdot C_{c4,4} \end{aligned} \right] \cdot C_{c6,6} \dots \cdot q(1)^6 \end{aligned}$$

$$+ C_{c2,2} \cdot C_{c4,4} \cdot C_{c6,6}$$

values of eqns 11:

A_k
$3.51 \cdot 10^{28}$
$3.51 \cdot 10^{28}$
$3.51 \cdot 10^{28}$

B_k
$3.088 \cdot 10^{32}$
$3.088 \cdot 10^{32}$
$3.088 \cdot 10^{32}$

C_k
$-3.102 \cdot 10^{35}$
$-3.102 \cdot 10^{35}$
$-3.102 \cdot 10^{35}$

D_k
$3.254 \cdot 10^{37}$
$3.254 \cdot 10^{37}$
$3.254 \cdot 10^{37}$

eqns 14:

$$-3 \cdot d_k^2 \cdot A = 3 \cdot C \cdot A + B^2$$

$$-27 \cdot f_k \cdot A^3 = 2 \cdot B^3 + 9 \cdot A \cdot B \cdot C + 27 \cdot D \cdot A^2$$

$$d_k = \frac{1}{3} \left[\frac{-3 \cdot C_k \cdot A_k - (B_k)^2}{(A_k)^2} \right]$$

$$f_k = \frac{1}{27} \left[\frac{-2 \cdot (B_k)^3 - 9 \cdot A_k \cdot B_k \cdot C_k - 27 \cdot D_k \cdot (A_k)^2}{(A_k)^3} \right]$$

eqn 15:

$$H_k = \frac{(f_k)^2}{4} + \frac{(d_k)^3}{27}$$

$$H = \begin{bmatrix} 1.882 \cdot 10^{19} \\ 1.882 \cdot 10^{19} \\ -1.882 \cdot 10^{19} \end{bmatrix}$$

eqns 16 & 17:

$$\gamma_{j,k} = 2 \cdot \left(\frac{d_k}{3} \right)^{\frac{1}{2}} \cdot \cos \left[\frac{1}{3} \cdot \arccos \left(\frac{-f_k \cdot \sqrt{27}}{3} + 2 \cdot (j-1) \cdot \pi \right) \right]$$

$$\gamma = \begin{bmatrix} 4.726 \cdot 10^3 & 4.726 \cdot 10^3 & 4.726 \cdot 10^3 \\ -2.813 \cdot 10^3 & -2.813 \cdot 10^3 & -2.813 \cdot 10^3 \\ -1.913 \cdot 10^3 & -1.913 \cdot 10^3 & 1.913 \cdot 10^3 \end{bmatrix}$$

eqn 21:

$$m_{j,k} = \left(\frac{\gamma_{j,k} + \frac{B_k}{3 \cdot A_k}}{2} \right)^{\frac{1}{2}} \alpha_{j,k} \quad \text{if } \operatorname{Re} \left(\gamma_{j,k} + \frac{B_k}{3 \cdot A_k} \right) > 0, 1, 1$$

$$\alpha = \begin{pmatrix} 1 & 1 & 1 \\ 1 & 1 & 1 \\ 1 & 1 & 1 \end{pmatrix}$$

eqns 20:

$$C_{(j,k,z)} = \left(\frac{B_k}{3 \cdot A_k} \right)^{\frac{1}{2}} \cdot \left(\frac{\gamma_{j,k} + \frac{B_k}{3 \cdot A_k}}{2} \right)^{\frac{1}{2}} \cdot \cos(m_{j,k} \cdot z) \quad \text{if } \operatorname{Re} \left(\gamma_{j,k} + \frac{B_k}{3 \cdot A_k} \right) > 0, \cosh(m_{j,k} \cdot z), \cos(m_{j,k} \cdot z)$$

$$S_{(j,k,z)} = \left(\frac{B_k}{3 \cdot A_k} \right)^{\frac{1}{2}} \cdot \left(\frac{\gamma_{j,k} + \frac{B_k}{3 \cdot A_k}}{2} \right)^{\frac{1}{2}} \cdot \sin(m_{j,k} \cdot z) \quad \text{if } \operatorname{Re} \left(\gamma_{j,k} + \frac{B_k}{3 \cdot A_k} \right) > 0, \sinh(m_{j,k} \cdot z), \sin(m_{j,k} \cdot z)$$

$\gamma_{j,k} + \frac{B_k}{3 \cdot A_k}$	B_k
7.658·10 ³	7.658·10 ³
7.658·10 ³	7.658·10 ³
7.658·10 ³	7.658·10 ³
118.736	118.736
118.736	118.736
118.736	118.736
1.019·10 ³	1.019·10 ³
1.019·10 ³	1.019·10 ³
1.019·10 ³	1.019·10 ³

eqns 22:

$$J_{j,k} = \text{if } Mat_K=0, C_{03,3} \cdot C_{04,4} \cdot (m_{j,k})^4 \dots$$

$$+ \alpha_{j,k} \cdot (m_{j,k})^2 \cdot \left[\begin{array}{l} -p(1)^2 \cdot (C_{05,5} \cdot C_{04,4} + C_{03,3} \cdot C_{06,6}) \dots \\ + q(1)^2 \cdot (C_{02,3}^2 - C_{02,2} \cdot C_{03,3} + 2 \cdot C_{02,3} \cdot C_{04,4}) \\ + (C_{06,6} \cdot p(1)^2 + C_{02,2} \cdot q(1)^2) \cdot (C_{05,5} \cdot p(1)^2 + C_{04,4} \cdot q(1)^2) \end{array} \right] \dots$$

$$+ \alpha_{j,k} \cdot (m_{j,k})^2 \cdot \left[\begin{array}{l} -p(1)^2 \cdot (C_{905,5} \cdot C_{904,4} + C_{903,3} \cdot C_{906,6}) \dots \\ + q(1)^2 \cdot (C_{902,3}^2 - C_{902,2} \cdot C_{903,3} + 2 \cdot C_{902,3} \cdot C_{904,4}) \\ + (C_{906,6} \cdot p(1)^2 + C_{902,2} \cdot q(1)^2) \cdot (C_{905,5} \cdot p(1)^2 + C_{904,4} \cdot q(1)^2) \end{array} \right] \dots$$

$$+ \alpha_{j,k} \cdot (m_{j,k})^2 \cdot \left[\begin{array}{l} -p(1)^2 \cdot (C_{905,5} \cdot C_{904,4} + C_{903,3} \cdot C_{906,6}) \dots \\ + q(1)^2 \cdot (C_{902,3}^2 - C_{902,2} \cdot C_{903,3} + 2 \cdot C_{902,3} \cdot C_{904,4}) \\ + (C_{906,6} \cdot p(1)^2 + C_{902,2} \cdot q(1)^2) \cdot (C_{905,5} \cdot p(1)^2 + C_{904,4} \cdot q(1)^2) \end{array} \right] \dots$$

$$L_{j,k} = \text{if } Mat_K=0, \frac{p(1) \cdot q(1)}{J_{j,k}} \cdot \left[\begin{array}{l} \alpha_{j,k} \cdot (m_{j,k})^2 \cdot (C_{03,3} \cdot C_{01,2} + C_{06,6}) \dots \\ + (C_{02,3} + C_{04,4}) \cdot (C_{01,3} + C_{05,5}) \\ + (C_{01,2} + C_{06,6}) \cdot (C_{05,5} \cdot p(1)^2 + C_{04,4} \cdot q(1)^2) \end{array} \right] \dots$$

$$+ \alpha_{j,k} \cdot (m_{j,k})^2 \cdot \left[\begin{array}{l} \alpha_{j,k} \cdot (m_{j,k})^2 \cdot (C_{903,3} \cdot C_{901,2} + C_{906,6}) \dots \\ + (C_{902,3} + C_{904,4}) \cdot (C_{901,3} + C_{905,5}) \\ + (C_{901,2} + C_{906,6}) \cdot (C_{905,5} \cdot p(1)^2 + C_{904,4} \cdot q(1)^2) \end{array} \right] \dots$$

$$R_{j,k} = \text{if } Mat_K=0, \frac{p(1) \cdot m_{j,k}}{J_{j,k}} \cdot \left[\begin{array}{l} \alpha_{j,k} \cdot (m_{j,k})^2 \cdot C_{04,4} \cdot (C_{01,3} + C_{05,5}) \dots \\ + (C_{01,3} + C_{05,5}) \cdot C_{06,6} \cdot p(1)^2 + C_{02,2} \cdot q(1)^2 \dots \\ + q(1)^2 \cdot (C_{02,3} + C_{04,4}) \cdot (C_{01,2} + C_{06,6}) \end{array} \right] \dots$$

$$+ \alpha_{j,k} \cdot (m_{j,k})^2 \cdot \left[\begin{array}{l} \alpha_{j,k} \cdot (m_{j,k})^2 \cdot C_{904,4} \cdot (C_{901,3} + C_{905,5}) \dots \\ + (C_{901,3} + C_{905,5}) \cdot (C_{906,6} \cdot p(1)^2 + C_{902,2} \cdot q(1)^2) \dots \\ + q(1)^2 \cdot (C_{902,3} + C_{904,4}) \cdot (C_{901,2} + C_{906,6}) \end{array} \right] \dots$$

eqn 24:

$$M(i,j,k) = \text{if } Mat_K=0, -p(1) \cdot C_{01,i} \cdot C_{02,i} \cdot L_{j,k} \dots, \text{if } Mat_K=1, -p(1) \cdot C_{901,i} \cdot C_{902,i} \cdot L_{j,k} \dots, \text{if } Mat_K=1, -p(1) \cdot C_{e1,i} \cdot C_{e2,i} \cdot L_{j,k} \dots$$

$$+ \alpha_{j,k} \cdot m_{j,k} \cdot R_{j,k} \cdot C_{03,i} \quad + \alpha_{j,k} \cdot m_{j,k} \cdot R_{j,k} \cdot C_{903,i} \quad + \alpha_{j,k} \cdot m_{j,k} \cdot R_{j,k} \cdot C_{e3,i}$$

Create a matrix \mathbf{A} (6m X 6m) which, premultiplying a vector \mathbf{FG} (containing F_{jk} and G_{jk}) produces a vector \mathbf{bC} of the BC's.

Satisfying the BC's on sig z at the top and bottom surface (6).

$$\mathbf{A}_{1,j} = \mathbf{M}(3,j,1) \cdot \mathbf{C}_{\left(j,1, \frac{thk}{2}\right)}$$

sig z top

$$\mathbf{A}_{1,j+3} = \mathbf{M}(3,j,1) \cdot \mathbf{S}_{\left(j,1, \frac{thk}{2}\right)}$$

$$\mathbf{A}_{2,j+6(Numpy-1)} = \mathbf{M}(3,j,Numpy) \cdot \mathbf{C}_{\left(j,Numpy, \frac{thk}{2}\right)}$$

sig z bottom

$$\mathbf{A}_{2,j+6(Numpy-1)+3} = \mathbf{M}(3,j,Numpy) \cdot \mathbf{S}_{\left(j,Numpy, \frac{thk}{2}\right)}$$

$$\mathbf{A}_{3,j} = (\mathbf{m}_{j,1} \cdot \mathbf{L}_{j,1} + q(1) \cdot \mathbf{R}_{j,1}) \cdot \alpha_{j,1} \cdot \mathbf{S}_{\left(j,1, \frac{thk}{2}\right)}$$

tau yz top

$$\mathbf{A}_{3,j+3} = (\mathbf{m}_{j,1} \cdot \mathbf{L}_{j,1} + q(1) \cdot \mathbf{R}_{j,1}) \cdot \mathbf{C}_{\left(j,1, \frac{thk}{2}\right)}$$

$$\mathbf{A}_{4,j+6(Numpy-1)} = (\mathbf{m}_{j,Numpy} \cdot \mathbf{L}_{j,Numpy} + q(1) \cdot \mathbf{R}_{j,Numpy}) \cdot \alpha_{j,Numpy} \cdot \mathbf{S}_{\left(j,Numpy, \frac{thk}{2}\right)}$$

tau yz bottom

$$\mathbf{A}_{4,j+6(Numpy-1)+3} = (\mathbf{m}_{j,Numpy} \cdot \mathbf{L}_{j,Numpy} + q(1) \cdot \mathbf{R}_{j,Numpy}) \cdot \mathbf{C}_{\left(j,Numpy, \frac{thk}{2}\right)}$$

$$\mathbf{A}_{5,j} = (\mathbf{m}_{j,1} + p(1) \cdot \mathbf{R}_{j,1}) \cdot \alpha_{j,1} \cdot \mathbf{S}_{\left(j,1, \frac{thk}{2}\right)}$$

tau xz top

$$\mathbf{A}_{5,j+3} = (\mathbf{m}_{j,1} + p(1) \cdot \mathbf{R}_{j,1}) \cdot \mathbf{C}_{\left(j,1, \frac{thk}{2}\right)}$$

$$\begin{aligned} \bar{A}_{6,j+6 \cdot (\text{Numpy} - 1)} &= (\mathbf{m}_{j, \text{Numpy} + p(1)} \cdot \mathbf{R}_{j, \text{Numpy} + \alpha_j, \text{Numpy}})^{\frac{\text{thk}}{2}} \cdot \mathbf{S}_{(j, \text{Numpy}, \frac{\text{thk}}{2})} \\ \bar{A}_{6,j+6 \cdot (\text{Numpy} - 1) + 3} &= (\mathbf{m}_{j, \text{Numpy} + p(1)} \cdot \mathbf{R}_{j, \text{Numpy}})^{\frac{-\text{thk}}{2}} \cdot \mathbf{G}_{(j, \text{Numpy}, \frac{-\text{thk}}{2})} \end{aligned}$$

tau xz bottom

Interfaces

interface z values:

$$z_{ka} = \frac{\text{thk}}{2} \sum_{k=1}^{ka} h_k$$

$$\bar{A}_{6+ka,j+6 \cdot (ka-1)} = \mathbf{M}(3, j, ka) \cdot \mathbf{G}_{(j, ka, z_{ka})}$$

$$\bar{A}_{6+ka,j+6 \cdot (ka-1) + 3} = \mathbf{M}(3, j, ka) \cdot \mathbf{S}_{(j, ka, z_{ka})}$$

sigz

$$\bar{A}_{6+ka,j+6 \cdot ka} = \mathbf{M}(3, j, ka+1) \cdot \mathbf{G}_{(j, ka+1, z_{ka})}$$

$$\bar{A}_{6+ka,j+6 \cdot ka+3} = \mathbf{M}(3, j, ka+1) \cdot \mathbf{S}_{(j, ka+1, z_{ka})}$$

$$\bar{A}_{5+\text{Numpy}+ka,j+6 \cdot (ka-1)} = C44_{ka} (\mathbf{m}_{j, ka} \cdot \mathbf{L}_{j, ka+q(1)} \cdot \mathbf{R}_{j, ka})^{\alpha_j, ka} \cdot \mathbf{S}_{(j, ka, z_{ka})}$$

$$\bar{A}_{5+\text{Numpy}+ka,j+6 \cdot (ka-1) + 3} = C44_{ka} (\mathbf{m}_{j, ka} \cdot \mathbf{L}_{j, ka+q(1)} \cdot \mathbf{R}_{j, ka})^{\alpha_j, ka} \cdot \mathbf{G}_{(j, ka, z_{ka})}$$

tau yz

$$\bar{A}_{5+\text{Numpy}+ka,j+6 \cdot ka} = C44_{ka+1} (\mathbf{m}_{j, ka+1} \cdot \mathbf{L}_{j, ka+1+q(1)} \cdot \mathbf{R}_{j, ka+1})^{\alpha_j, ka+1} \cdot \mathbf{S}_{(j, ka+1, z_{ka})}$$

$$\bar{A}_{5+\text{Numpy}+ka,j+6 \cdot ka+3} = C44_{ka+1} (\mathbf{m}_{j, ka+1} \cdot \mathbf{L}_{j, ka+1+q(1)} \cdot \mathbf{R}_{j, ka+1})^{\alpha_j, ka+1} \cdot \mathbf{G}_{(j, ka+1, z_{ka})}$$

$$\bar{A}_{4+2 \cdot \text{Numply} + ka, j+6 \cdot (ka-1)} := \text{C55}_{ka} \cdot (m_{j, ka+1} \cdot p(1) \cdot R_{j, ka})^{\alpha_{j, ka}} \cdot S_{(j, ka, z_{ka})}$$

$$\bar{A}_{4+2 \cdot \text{Numply} + ka, j+6 \cdot (ka-1) + 3} := \text{C55}_{ka} \cdot (m_{j, ka+1} \cdot p(1) \cdot R_{j, ka}) \cdot G_{(j, ka, z_{ka})}$$

$$\bar{A}_{4+2 \cdot \text{Numply} + ka, j+6 \cdot ka} := \text{C55}_{ka+1} \cdot (m_{j, ka+1} \cdot p(1) \cdot R_{j, ka+1})^{\alpha_{j, ka+1}} \cdot S_{(j, ka+1, z_{ka})}$$

$$\bar{A}_{4+2 \cdot \text{Numply} + ka, j+6 \cdot ka + 3} := \text{C55}_{ka+1} \cdot (m_{j, ka+1} \cdot p(1) \cdot R_{j, ka+1}) \cdot G_{(j, ka+1, z_{ka})}$$

$$\sum_{j=1}^3 (m_{j, k+1} \cdot R_{j, k})^{\alpha_{j, k}} \cdot FG_{j+(k-1) \cdot 6} \cdot S_{(j, k, z)} \cdot FG_{j+(k-1) \cdot 6 + 3} \cdot G_{(j, k, z)}$$

$$\bar{A}_{3+3 \cdot \text{Numply} + ka, j+6 \cdot (ka-1)} = G_{(j, ka, z_{ka})}$$

$$\bar{A}_{3+3 \cdot \text{Numply} + ka, j+6 \cdot (ka-1) + 3} = S_{(j, ka, z_{ka})}$$

$$\bar{A}_{3+3 \cdot \text{Numply} + ka, j+6 \cdot ka} = G_{(j, ka+1, z_{ka})}$$

$$\bar{A}_{3+3 \cdot \text{Numply} + ka, j+6 \cdot ka + 3} = S_{(j, ka+1, z_{ka})}$$

tauxz

u

$$\mathbf{A}_{2+4\cdot\text{Numpy}+ka,j+6\cdot(ka-1)} \mathbf{L}_{j,ka} \mathbf{U}_{(j,ka,z_{ka})}$$

$$\mathbf{A}_{2+4\cdot\text{Numpy}+ka,j+6\cdot(ka-1)+3} \mathbf{L}_{j,ka} \mathbf{S}_{(j,ka,z_{ka})}$$

v

$$\mathbf{A}_{2+4\cdot\text{Numpy}+ka,j+6\cdot ka} \mathbf{L}_{j,ka+1} \mathbf{G}_{(j,ka+1,z_{ka})}$$

$$\mathbf{A}_{2+4\cdot\text{Numpy}+ka,j+6\cdot ka+3} \mathbf{L}_{j,ka+1} \mathbf{S}_{(j,ka+1,z_{ka})}$$

$$\mathbf{A}_{1+5\cdot\text{Numpy}+ka,j+6\cdot(ka-1)} \mathbf{R}_{j,ka} \alpha_{j,ka} \mathbf{S}_{(j,ka,z_{ka})}$$

$$\mathbf{A}_{1+5\cdot\text{Numpy}+ka,j+6\cdot(ka-1)+3} \mathbf{R}_{j,ka} \mathbf{G}_{j,ka,z_{ka}}$$

w

$$\mathbf{A}_{1+5\cdot\text{Numpy}+ka,j+6\cdot ka} \mathbf{R}_{j,ka+1} \alpha_{j,ka+1} \mathbf{S}_{(j,ka+1,z_{ka})}$$

$$\mathbf{A}_{1+5\cdot\text{Numpy}+ka,j+6\cdot ka+3} \mathbf{R}_{j,ka+1} \mathbf{G}_{(j,ka+1,z_{ka})}$$

$$\mathbf{b} \mathbf{C}_{k4} \mathbf{Op}$$

$$\mathbf{b} \mathbf{C}_1 \mathbf{q}_o$$

The solution:

$$\mathbf{FG} \mathbf{A} \mathbf{b} \mathbf{C}$$

$$\text{length}(\mathbf{FG}) = 18$$

$$k4 = 1..6 \cdot \text{Numpy}$$

$$\text{Op} \neq 0$$

$$n = 1.. \text{Num}$$

[illegible]

$$\sum_{k=1}^k h_k - \frac{h_k + h_{k+1}}{2} \frac{n-1}{\text{Num} \dots 1}$$

$$\overline{b}c =$$

$$u\left(\frac{L}{\gamma}, \frac{L}{\gamma}, zz, p, k, k\right)$$

$$j + (k - 1) \cdot 6 + 3$$

$$E_{2^v}^{L L}(z, z, {}^{zz}\pi_k, k)$$

$$j \rightarrow j + (k - 1) \cdot 6 + 3$$

$$100 \cdot E_{2 \cdot w} \left(\frac{L}{2}, \frac{L}{2}, \dots, \frac{L}{2}, z z_{n_k}, k \right)$$

$$\sigma_x(x,y,z,k) := \sin(p(1) \cdot x) \cdot \sin(q(1) \cdot y) \cdot \sum_{j=1}^3 \mathbf{M}(1,j,k) \cdot \left[\mathbf{FG}_{j+(k-1) \cdot 6} \cdot \mathbf{C}_{(j,k,z)} \dots \right. \\ \left. + \mathbf{FG}_{j+(k-1) \cdot 6+3} \cdot \mathbf{S}_{(j,k,z)} \right]$$

$$\Sigma x_{(k-1) \cdot \text{Num} + n} = \frac{\sigma_x\left(\frac{L}{2}, \frac{L}{2}, zz_{n,k}, k\right)}{q_o \cdot (S^2 \cdot \text{Paper2} + \text{Paper1})}$$

$$\sigma_y(x,y,z,k) := \sin(p(1) \cdot x) \cdot \sin(q(1) \cdot y) \cdot \sum_{j=1}^3 \mathbf{M}(2,j,k) \cdot \left[\mathbf{FG}_{j+(k-1) \cdot 6} \cdot \mathbf{C}_{(j,k,z)} \dots \right. \\ \left. + \mathbf{FG}_{j+(k-1) \cdot 6+3} \cdot \mathbf{S}_{(j,k,z)} \right] \\ \Sigma y_{(k-1) \cdot \text{Num} + n} = \frac{\sigma_y\left(\frac{L}{2}, \frac{L}{2}, zz_{n,k}, k\right)}{q_o \cdot (S^2 \cdot \text{Paper2} + \text{Paper1})}$$

$$\text{Fib}_{\text{fail}}(x,y,z,k) := \begin{cases} \text{Mat}_k < 2, & \text{if } \left(\text{Re} \left(\sigma_x(x,y,z,k) \right) > 0, -\frac{\sigma_x(x,y,z,k)}{X_t}, \frac{\sigma_x(x,y,z,k)}{X_c} \right) \\ \text{Mat}_k = 0, & \text{if } \left(\text{Re} \left(\sigma_y(x,y,z,k) \right) > 0, \frac{\sigma_y(x,y,z,k)}{X_t}, \frac{\sigma_y(x,y,z,k)}{X_c} \right) \\ 0, & \text{otherwise} \end{cases}$$

$$\text{Fib}_{\text{failure}}(k-1) \cdot \text{Num} + n = \text{Fib}_{\text{fail}}\left(\frac{L}{2}, \frac{L}{2}, zz_{n,k}, k\right)$$

$$\sigma_z(x,y,z,k) := \sin(p(1) \cdot x) \cdot \sin(q(1) \cdot y) \cdot \sum_{j=1}^3 \mathbf{M}(3,j,k) \cdot \left[\mathbf{FG}_{j+(k-1) \cdot 6} \cdot \mathbf{C}_{(j,k,z)} \dots \right. \\ \left. + \mathbf{FG}_{j+(k-1) \cdot 6+3} \cdot \mathbf{S}_{(j,k,z)} \right]$$

$$\Sigma Z(k-1) \cdot \text{Num} + n \cdot \frac{\sigma_z \left(\frac{L}{2}, \frac{L}{2}, \frac{ZZ_n}{2}, k \right)}{q_0}$$

$$Z_{\text{fail}}(x, y, z, k) := \text{if} \left(\text{Mat}_k < 2, \text{if} \left(\text{Re}(\sigma_z(x, y, z, k)) > 0, \frac{\sigma_z(x, y, z, k)}{Y_t}, \frac{\sigma_z(x, y, z, k)}{Y_c} \right), \frac{\sigma_z(x, y, z, k)}{Z_c} \right)$$

$$Z_{\text{failure}}(k-1) \cdot \text{Num} + n \cdot \frac{\sigma_z \left(\frac{L}{2}, \frac{L}{2}, \frac{ZZ_n}{2}, k \right)}{q_0}$$

$$\tau_{yz}(x, y, z, k) = C44_k \cdot \sin(p(1) \cdot x) \cdot \cos(q(1) \cdot y) \cdot \sum_{j=1}^3 (m_j \cdot k \cdot L_{j,k} + q(1) \cdot R_{j,k}) \cdot \left[\alpha_{j,k} \cdot \text{FG}_{j+(k-1) \cdot 6} \cdot \mathbf{S}_{(j,k,z)} \dots \right. \\ \left. + \text{FG}_{j+(k-1) \cdot 6+3} \cdot \mathbf{C}_{(j,k,z)} \right]$$

$$\tau_{xz}(x, y, z, k) = C55_k \cdot \cos(p(1) \cdot x) \cdot \sin(q(1) \cdot y) \cdot \sum_{j=1}^3 (m_j \cdot k + p(1) \cdot R_{j,k}) \cdot \left[\alpha_{j,k} \cdot \text{FG}_{j+(k-1) \cdot 6} \cdot \mathbf{S}_{(j,k,z)} \dots \right. \\ \left. + \text{FG}_{j+(k-1) \cdot 6+3} \cdot \mathbf{C}_{(j,k,z)} \right]$$

$$\tau_{xy}(x, y, z, k) = C66_k \cdot \cos(p(1) \cdot x) \cdot \cos(q(1) \cdot y) \cdot \sum_{j=1}^3 (q(1) + p(1) \cdot L_{j,k}) \cdot \left[\text{FG}_{j+(k-1) \cdot 6} \cdot \mathbf{C}_{(j,k,z)} \dots \right. \\ \left. + \text{FG}_{j+(k-1) \cdot 6+3} \cdot \mathbf{S}_{(j,k,z)} \right]$$

$$S_{fail}(x,z,k) := \text{if} \left(\text{Mat}_k < 2, \left[\frac{\tau_{xz}\left(x, \frac{L}{2}, z, k\right)}{S_g}, \frac{\tau_{xz}\left(x, \frac{L}{2}, z, k\right)}{S_c} \right] \right)$$

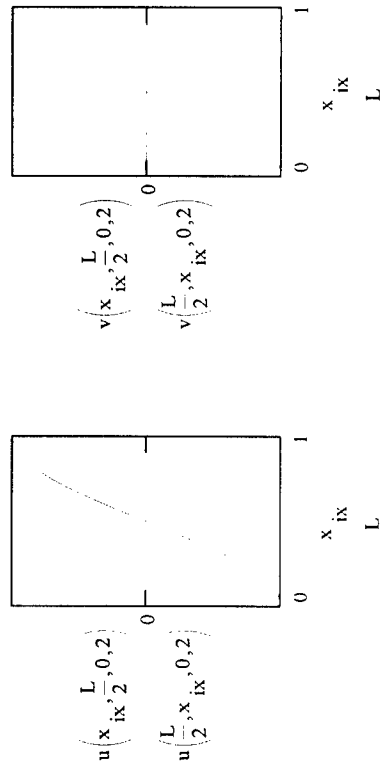
$$S_{failure}(k-1) \cdot \text{Num} + n := S_{fail}(0 \cdot L, zz_n, k, k)$$

$$Ty_z(k-1) \cdot \text{Num} + n := \frac{\tau_{yz}\left(\frac{L}{2}, 0 \cdot L, zz_n, k, k\right)}{q_o(S \cdot \text{Paper2} + \text{Paper1})}$$

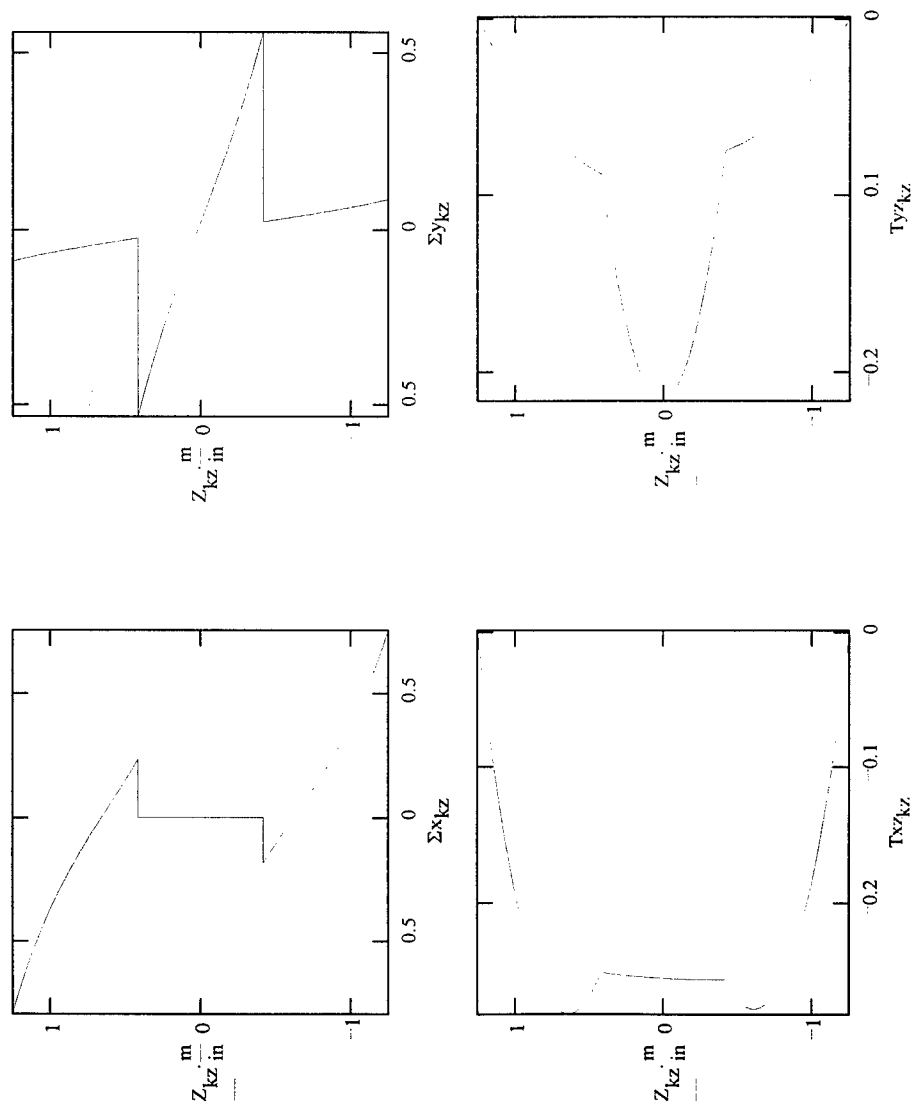
$$Tx_z(k-1) \cdot \text{Num} + n := \frac{\tau_{xz}\left(0 \cdot L, \frac{L}{2}, zz_n, k, k\right)}{q_o(S \cdot \text{Paper2} + \text{Paper1})}$$

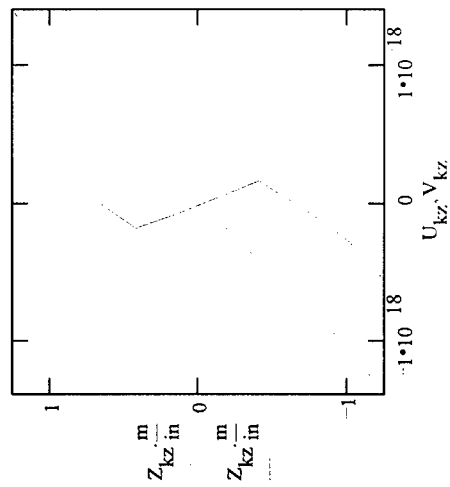
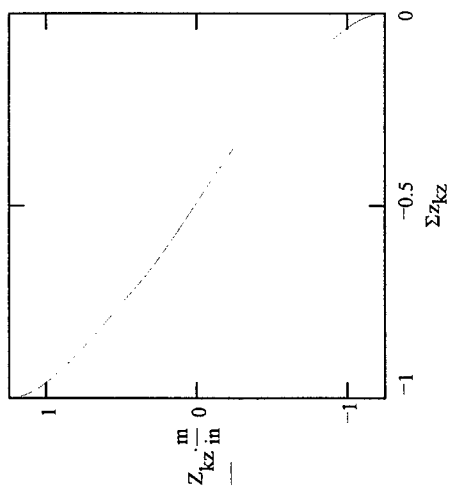
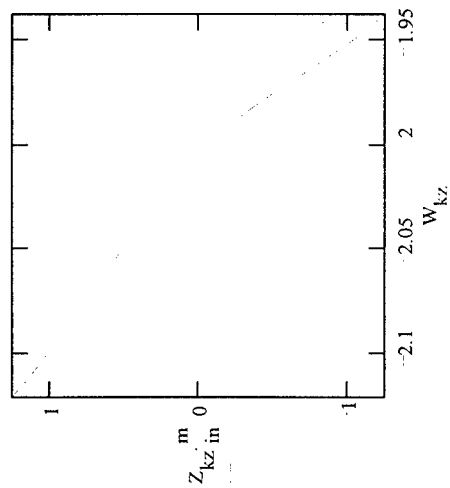
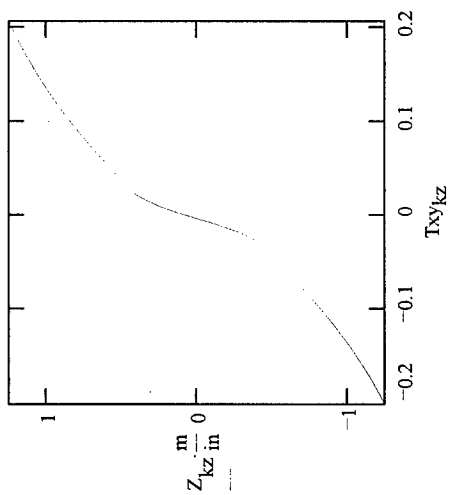
$$Txy(k-1) \cdot \text{Num} + n := \frac{\tau_{xy}(0 \cdot L, 0 \cdot L, zz_n, k, k)}{q_o(S \cdot \text{Paper2} + \text{Paper1})}$$

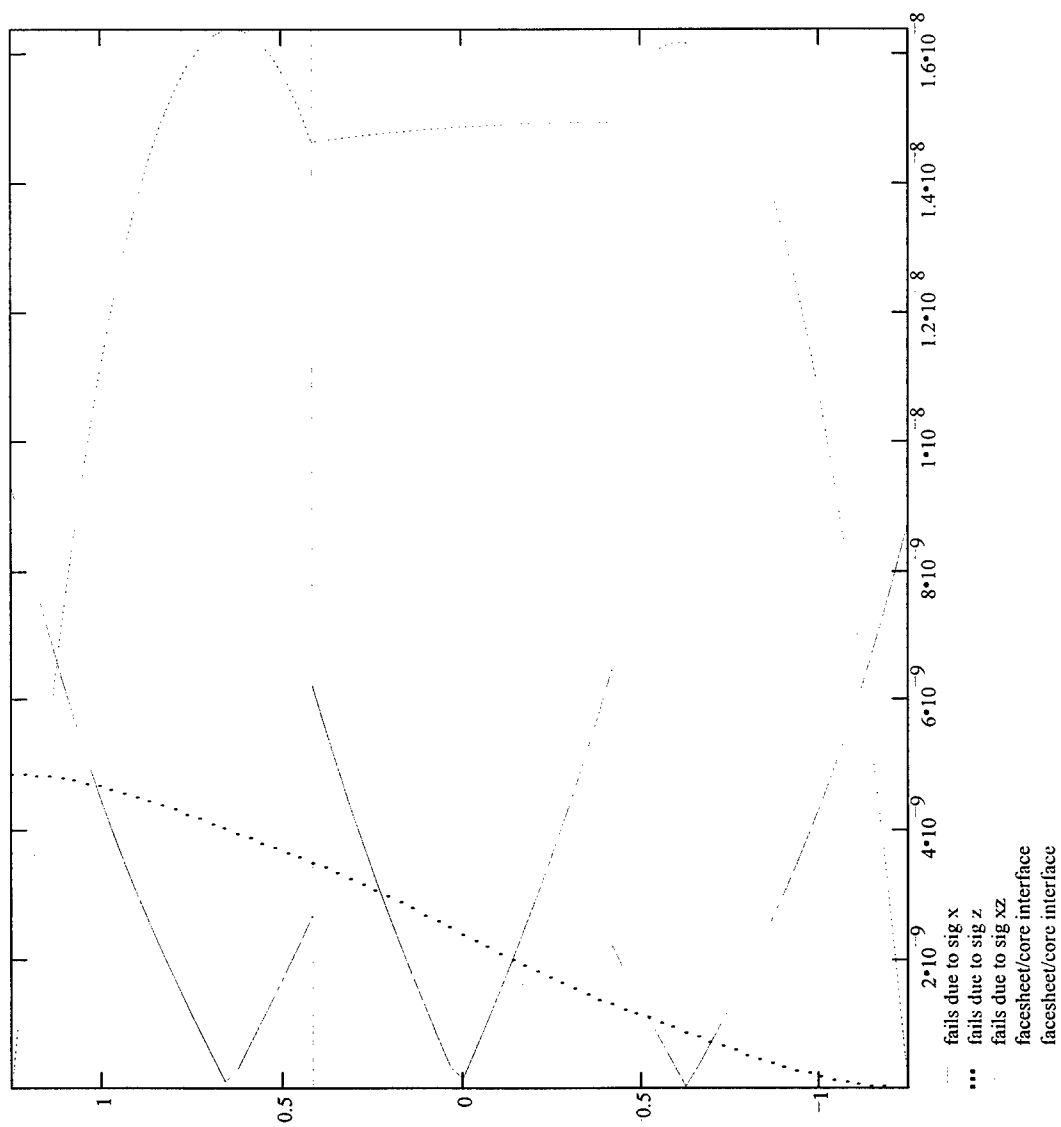
Now look at the solution:



3D Solution, [0/90/0], sine loading







Appendix B

FORTRAN Elasticity Solutions with Hertzian Contact

```

c
c dimension aa(nply),bb(nply),cc(nply),bc(4*mply),bc(4*mply,nfourier)
c , ,ans(4*mply),brix(4*mply,4*mply)
c dimension ipvt(4*mply)
c dimension h(nply)
c , ,coeff(nfourier)
c , ,z(nply-1),zz(nzpts,nply),xx(nxpts)
c
c Here the user supplies the reduced compliance coefficients
c for plane strain as in Pagano's equation (1). Three sets are
c required for the 0 degree, 90 degree and core properties,
c respectively.
c
c The Mathcad template for the sinusoidal load case also included
c in Appendix A of Herup's dissertation calculates these for a given
c set of material properties.
c data R/
c 60520 values for Pagano's paper (to check) .
c 0 degree
c . 5.7986d-12,-1.813d-12, 0.0d0,
c . -1.813d-12, 9.97134d-11, 0.0d0,
c . 0.0d0, 0.0d0, 2.900754d-10,
c 90 degree
c . 7.248259d-10,-1.816597d-10, 0.0d0,
c . -1.816597d-10, 1.446751d-10, 0.0d0,
c . 0.0d0, 0.0d0, 7.251885d-10,
c
c 60520 values for material tested in dissertation
cc 0 degree
c . 6.864441d-12,-2.776243d-12, 0.0d0,
c . -2.776243d-12, 9.1175258d-11, 0.0d0,
c . 0.0d0, 0.0d0, 1.66666667d-10,
cc 90 degree
c . 1.024712365d-10,-3.567309335d-11, 0.0d0,
c . -3.567309335d-11, 1.024712365d-10, 0.0d0,
c . 0.0d0, 0.0d0, 2.77777778d-10,
cc
cc core
c . 1.166044776d-8, -3.109452736d-10, 0.0d0,
c . -3.109452736d-10, 9.900497512d-10, 0.0d0,
c . 0.0d0, 0.0d0, 8.291873964d-9/
c conversions to si units
c
c inch = 2.54d-2
c psi = 6894.758813202d0
c
c Here the user supplies the Et modulus value for the facesheets
c which is only used in the scaling.
c
c 60520 values for material tested in dissertation
c Et = 9.7d9
c 60520 values for Pagano's paper (to check) .
c if (nfourier.eq.1) Et = 6.8947588d9
c
c Here the user supplies the ultimate strength values.
c
c Xt = 2.172d9
c Xc = -1.724d9
c Yt = 5.38d7
c Yc = -2.055d8

```



```

szscale = 1.0d0
txzscale = 1.0d0

c internal zz values
c
do 330 i = 1,numpy
do 330 m = 1,nzpts
zz(m,i) = thk/2.0d0 - (m - nzpts)*h(i)/(nzpts - 1)
do 340 ib = 1,1
zz(m,i) = zz(m,i) - h(ib)
340 continue
330 continue
c
c write(*,*)'in inches zz(1,1)',zz(1,1)/inch
c write(*,*)'in inches zz(BOT)',zz(nzpts,numpy)/inch
c
c satisfy BC's
c
do 400 j = 1,4
do 410 n = 1,nfourier
B(1,j,n) = -p(n)**2*exp(cm(j,1,n)*thk/2.0d0)
B(2,j + 4*(numpy - 1),n) = -p(n)**2*
. exp(-1*cm(j,numpy,n)*thk/2.0d0)
B(3,j,n) = -p(n)*cm(j,1,n)*exp(cm(j,1,n)*thk/2.0d0)
B(4,j + 4*(numpy - 1),n) = -p(n)*cm(j,numpy,n)*
. exp(-1*cm(j,numpy,n)*thk/2.0d0)
c interfaces
do 420 ia = 1,numpy-1
c sigz
B(4 + ia,j + 4*(ia - 1),n) = -p(n)**2*exp(cm(j,ia,n)*z(ia))
B(4 + ia,j + 4*ia,n) = p(n)**2*exp(cm(j,ia + 1,n)*z(ia))
c tauzz
B(3 + ia + numpy,j + 4*(ia - 1),n) = -p(n)*cm(j,ia,n)*
. exp(cm(j,ia,n)*z(ia))
B(3 + ia + numpy,j + 4*ia,n) = p(n)*cm(j,ia + 1,n)*
. exp(cm(j,ia + 1,n)*z(ia))
c
B(2 + ia + 2*numpy,j + 4*(ia - 1),n) = (1/p(n))*
. exp(cm(j,ia,n)*z(ia))*
. (R(1,2,Mat(ia))*p(n)**2 - R(1,1,Mat(ia))*cm(j,ia,n)**2)
B(2 + ia + 2*numpy,j + 4*ia,n) = (-1/p(n))*
. exp(cm(j,ia + 1,n)*z(ia))*
. (R(1,2,Mat(ia + 1))*p(n)**2 -
. R(1,1,Mat(ia + 1))*cm(j,ia + 1,n)**2)
c
B(1 + ia + 3*numpy,j + 4*(ia - 1),n) =
. exp(cm(j,ia,n)*z(ia))*
. (R(1,2,Mat(ia))*cm(j,ia,n) - (R(2,2,Mat(ia))/cm(j,ia,n))*p(n)**2)
c
write(10,*)'B second part of w, ia,j,n=',ia,j,n
write(10,*)'cm(j,ia + 1,n) =',cm(j,ia + 1,n)
write(10,*)'z(ia) =',z(ia)
write(10,*)'-exp(cm(j,ia + 1,n)*z(ia)) =',
. -exp(cm(j,ia + 1,n)*z(ia))
write(10,*)'p(n) =',p(n)
write(10,*)'Mat(ia) =',Mat(ia)
write(10,*)'R(1,2,Mat(ia)) =',R(1,2,Mat(ia))
write(10,*)'R(2,2,Mat(ia)) =',R(2,2,Mat(ia))
write(10,*)'Rstuff =',
. (R(1,2,Mat(ia))*cm(j,ia + 1,n) -
. (R(2,2,Mat(ia))/cm(j,ia + 1,n))*p(n)**2)
c
B(1 + ia + 3*numpy,j + 4*ia,n) =
. -exp(cm(j,ia + 1,n)*z(ia))*
. (R(1,2,Mat(ia + 1))*cm(j,ia + 1,n) -
. (R(2,2,Mat(ia + 1))/cm(j,ia + 1,n))*p(n)**2)
c

```

```

420 continue
c
c initialize arrays
c
do 430 i = 1, ndim
  bc(i,n) = 0.0d0
430 continue
  bc(1,n) = -coeff(n)*q0
c1023 if (mod(n,2) .ne. 0) bc(1,n) = -coeff((n+1)/2)*q0
440 continue
c
c write(10,*)'B='
c do 440 jx=1, ndim
c write(10,*)'row 'jx, ','
c 440 write(10,*) (B(jx,ix,1), ix=1, ndim)
c
c the solution
c
do 500 n = 1, nfourier
  do 510 i = 1, ndim
    ans(i) = bc(i,n)
    do 510 j = 1, ndim
      btrix(i,j) = B(i,j,n)
510 continue
c write(10,*)'before decomp ans(i)=', (ans(i), i=1, ndim)
c write(10,*)'Btrix='
c do 540 jx=1, ndim
c write(10,*)'row 'jx, ','
c 540 write(10,*) (B(jx,ix,1), ix=1, ndim)
c call decomp (ndim, ndim, btrix, ipvt, det)
c call xsolve (ndim, ndim, btrix, ipvt, ans)
c write(10,*)'after det =', det
c write(10,*) (Ans(i), i=1, numply)
c do 520 i = 1, numply
  do 520 j = 1, 4
    A(j,i,n) = ans(j + 4*(i-1))
520 continue
530 continue
c
c open for output
c
open(11, file='sigeth2d.u', status='unknown')
open(12, file='sigeth2d.w', status='unknown')
open(13, file='sigeth2d.sx', status='unknown')
open(14, file='sigeth2d.sz', status='unknown')
open(15, file='sigeth2d.txz', status='unknown')
open(16, file='sigeth2d.x', status='unknown')
open(17, file='sigeth2d.z', status='unknown')
open(18, file='sigeth2d lod', status='unknown')
open(19, file='fdata1d.f', status='unknown')
open(20, file='sigeth2d.wbr', status='unknown')
open(21, file='sigeth2d.fbr', status='unknown')
open(22, file='sigeth2d.mtx', status='unknown')
open(23, file='sigeth2d.dlm', status='unknown')
open(24, file='sigeth2d.crz', status='unknown')
open(25, file='sigeth2d.crt', status='unknown')
open(26, file='sigeth2d.gen', status='unknown')
c
c
c Superpose all nfourier solutions:
c
do 620 i = 1, nply*nzpts

```



```

c      write(15,999)xm,zz(m,i),txzscale*dreal(tauxz(k,l))
c 60521 for comparison with FEM symmetric solution
c      write(11,999)xm,-zz(m,i),uscale*dreal(u(k,l))
c      write(12,999)xm,-zz(m,i),-wscale*dreal(w(k,l))
c      write(13,999)xm,-zz(m,i),sxscale*dreal(sigz(k,l))
c      write(14,999)xm,-zz(m,i),szscale*dreal(sigz(k,l))
c      write(15,999)xm,-zz(m,i),-txzscale*dreal(tauxz(k,l))
c      write(*,*)'in main, k,i,l=',k,i,l
c      f1=fiberMS(k,i,l)
c      f2=fiberL(k,i,l)
c      f3=fiberH(k,i,l)
c      f4=matrixMS(k,i,l)
c      f5=matrixL(k,i,l)
c      f6=matrixH(k,i,l)
c      f7=0.0d0
c      if (m.eq.1)f7=delamL(k,i,l)
c      f8=0.0d0
c      if (m.eq.1)f8=delamO(k,i,l)
c      f9=0.0d0
c      if (m.eq.1)f9=delamH(k,i,l)
c      f10=corez(k,i,l)
c      f11=coret(k,i,l)

c      write(21,999)xm,zz(m,i),f1,f2,f3
c      write(22,999)xm,zz(m,i),f4,f5,f6
c      write(23,999)xm,zz(m,i),f7,f8,f9
c      write(24,999)xm,zz(m,i),f10
c      write(25,999)xm,zz(m,i),f11
c      write(26,999)xm,zz(m,i),dmax1(f1,f2,f3,f4,f5,f6,f7,f8,f9)
c 710 continue
c      write(11,998)
c      write(12,998)
c      write(13,998)
c      write(14,998)
c      write(15,998)
c      write(21,998)
c      write(22,998)
c      write(23,998)
c      write(24,998)
c      write(25,998)
c      write(26,998)
c 700 continue
c      do 800 i = 1,numpy
c      do 800 m = 1,nzpts
c      write(17,999)zz(m,i)
c 800 continue
c      c print out surface (applied) pressure profile
c
c      do 900 k = 1,2*nzpts
c      do 900 k = nzpts+1,2*nzpts
c      if (k.le. nzpts) then
c      xm = xx(nzpts + 1 - k)
c      else
c      xm = xlength - xx(k - nzpts)
c      endif
c      write(18,999)xm,dreal(sigz(k,l))
c 900 continue
c 999 format(1x,120e20,10)
c      write(*,*)' s,whar =',s,dreal(w(1, (nply*nzpts + 1)/2))
c      write(*,*)' sz =',dreal(sigz(1, 1))
c      write(20, '(12d20.13)')s,dreal(w(1, (nply*nzpts + 1)/2))

```

```

1000 continue
c
c 998 format(1x)
c
c      write(*,*)'Pagano finished without error.'
c      write(*,*)((Char(7)),ik=1,40)
c      stop
c      end
c
c      double complex function ufunc(x,z,i,n)
c      implicit double complex (a-h,o-z)
c
c      double precision p,r,z,x
c
c      parameter (nply=36,nFourier=250,nMat=3,nzpts=5,nxpts=125)
c
c      common/stuff1/cm(4,nply,nfourier),A(4,nply,nfourier)
c      common/stuff2/R(3,3,nMat),p(nfourier)
c      common/stuff3/Mat(nply)
c
c      double complex cm,A
c
c      u = 0.0d0
c      do 100 j = 1,4
c      u = u + A(j,i,n)*cdexp(cm(j,i,n)*z)*(R(1,2,Mat(i))*p(n)**2 -
c      . R(1,1,Mat(i))*cm(j,i,n)**2)
c 100 continue
c      ufunc = (dcos(p(n)*x)/p(n))*u
c      return
c      end
c
c      double complex function wfunc(x,z,i,n)
c      implicit double complex (a-h,o-z)
c
c      double precision p,r,z,x
c
c      parameter (nply=36,nFourier=250,nMat=3,nzpts=5,nxpts=125)
c
c      common/stuff1/cm(4,nply,nfourier),A(4,nply,nfourier)
c      common/stuff2/R(3,3,nMat),p(nfourier)
c      common/stuff3/Mat(nply)
c
c      double complex cm,A
c
c      w = 0.0d0
c      do 100 j = 1,4
c      w = w + A(j,i,n)*cdexp(cm(j,i,n)*z)*(R(1,2,Mat(i))*cm(j,i,n) -
c      . R(2,2,Mat(i))*p(n)**2)/cm(j,i,n)
c 100 continue
c      wfunc = (dsin(p(n)*x))*w
c      return
c      end
c
c      double complex function sxfunc(x,z,i,n)
c      implicit double complex (a-h,o-z)

```

```

c
double precision p,r,z,x
parameter (nply=36,nfourier=250,nMat=3,nzpts=5,nxpts=125)
c
common/stuff1/cm(4,nply,nfourier),A(4,nply,nfourier)
common/stuff2/R(3,3,nMat),p(nfourier)
common/stuff3/Mat(nply)
c
double complex cm,A
c
sx = 0.0d0
do 100 j = 1,4
  sx = sx + A(j,i,n)*cm(j,i,n)**2*exp(cm(j,i,n)*z)
100 continue
c
write(*,*) 'sx,p(n)*x,dsin(p(n)*x)',x,p(n)*x,dsin(p(n)*x)
sxfunc = (dsin(p(n)*x))*sx
return
end

double complex function szfunc(x,z,i,n)
implicit double complex (a-h,o-z)
double precision p,r,z,x
parameter (nply=36,nfourier=250,nMat=3,nzpts=5,nxpts=125)
c
common/stuff1/cm(4,nply,nfourier),A(4,nply,nfourier)
common/stuff2/R(3,3,nMat),p(nfourier)
common/stuff3/Mat(nply)
c
double complex cm,A
c
sz = 0.0d0
do 100 j = 1,4
  sz = sz + A(j,i,n)*exp(cm(j,i,n)*z)
100 continue
szfunc = -p(n)**2*(dsin(p(n)*x))*sz
return
end

double complex function txzfunc(x,z,i,n)
implicit double complex (a-h,o-z)
double precision p,r,z,x
parameter (nply=36,nfourier=250,nMat=3,nzpts=5,nxpts=125)
c
common/stuff1/cm(4,nply,nfourier),A(4,nply,nfourier)
common/stuff2/R(3,3,nMat),p(nfourier)
common/stuff3/Mat(nply)
c
double complex cm,A
c
txz = 0.0d0
do 100 j = 1,4
  txz = txz + A(j,i,n)*cm(j,i,n)*exp(cm(j,i,n)*z)
100 continue
txzfunc = -p(n)*(dcos(p(n)*x))*txz

return
end

double precision function fiberl(k,i,l)
implicit double precision (a-h,o-z)
double complex u,w,sigx,sigz,tauxz
parameter (nply=36,nfourier=250,nMat=3,nzpts=5,nxpts=125)
c
common/stuff3/Mat(nply)
common/stuff4/Xt,Xc,Yt,Yc,Sg,Sc,Zc
common/stuff5/u(2*nxpts,nzpts*nply),w(2*nxpts,nzpts*nply)
, sigx(2*nxpts,nzpts*nply),sigz(2*nxpts,nzpts*nply)
, tauxz(2*nxpts,nzpts*nply)
c
fiberl = 0.0d0
write(*,*) 'in fiberl, k,i,l = ',k,i,l
if (Mat(i).eq.1) then
  fiberl = (dreal(tauxz(k,l))/Sg)**2
endif
return
end

double precision function fiberH(k,i,l)
implicit double precision (a-h,o-z)
double complex u,w,sigx,sigz,tauxz
parameter (nply=36,nfourier=250,nMat=3,nzpts=5,nxpts=125)
c
common/stuff3/Mat(nply)
common/stuff4/Xt,Xc,Yt,Yc,Sg,Sc,Zc
common/stuff5/u(2*nxpts,nzpts*nply),w(2*nxpts,nzpts*nply)
, sigx(2*nxpts,nzpts*nply),sigz(2*nxpts,nzpts*nply)
, tauxz(2*nxpts,nzpts*nply)
c
fiberH = 0.0d0
write(*,*) 'in fiberH, k,i,l = ',k,i,l
if ((Mat(i).eq.1).and.
  (dreal(sigx(k,l)).lt.0.0d0)) then
  fiberH = (dreal(sigx(k,l))/Xc)**2
else if ((Mat(i).eq.1).and.
  (dreal(sigx(k,l)).gt.0.0d0)) then
  fiberH = (dreal(sigx(k,l))/Xt)**2 + (dreal(tauxz(k,l))/Sg)**2
endif
return
end

double precision function fiberMS(k,i,l)
implicit double precision (a-h,o-z)
double complex u,w,sigx,sigz,tauxz
parameter (nply=36,nfourier=250,nMat=3,nzpts=5,nxpts=125)
c
common/stuff3/Mat(nply)
common/stuff4/Xt,Xc,Yt,Yc,Sg,Sc,Zc
common/stuff5/u(2*nxpts,nzpts*nply),w(2*nxpts,nzpts*nply)
, sigx(2*nxpts,nzpts*nply),sigz(2*nxpts,nzpts*nply)
, tauxz(2*nxpts,nzpts*nply)
c

```

```

c      fiberWS = 0.0d0
c      write(*,')in fiberWS, k,i,l = ',k,i,l
c      if ((Mat(i).eq. 1) .and.
c      . (dreal(sigx(k,l)) .lt. 0.0d0)) then
c          fiberMS = dreal(sigx(k,l))/Xc)**2
c      else if ((Mat(i).eq. 1) .and.
c      . (dreal(sigx(k,l)) .gt. 0.0d0)) then
c          fiberMS = (dreal(sigx(k,l))/Yt)**2
c      endif
c      return
c      end

c
c      double precision function matrixL(k,i,l)
c      implicit double precision (a-h,o-z)
c      double complex u,w,sigx,sigz,tauxz
c
c      parameter (nPly=36,nFourier=250,nMat=3,nzpts=5,nxpts=125)
c
c      common/stuff3/Mat(nply)
c      common/stuff4/Xt,Xc,Yt,Yc,Sg,Sc,Zc
c      common/stuff5/u(2*nxpts,nzpts*npLy), w(2*nxpts,nzpts*npLy)
c      , sigx(2*nxpts,nzpts*npLy), sigz(2*nxpts,nzpts*npLy)
c      , tauxz(2*nxpts,nzpts*npLy)
c
c      matrixL = 0.0d0
c      if ((Mat(i).eq. 2) .and.
c      . ((dreal(sigx(k,l)) + dreal(sigz(k,l))) .gt. 0.0d0)) then
c          matrixH = ((dreal(sigx(k,l)) + dreal(sigz(k,l)))/Yt)**2 +
c      . (dreal(tauxz(k,l))**2 - dreal(sigx(k,l))*dreal(sigz(k,l)))/Sg**2 +
c      . (dreal(Mat(i).eq. 2) then
c      elseif (Mat(i).eq. 2) then
c          matrixH = ((dreal(sigx(k,l)) + dreal(sigz(k,l)))/Yc)*
c      . ((Yc/(2.0d0*Sg))**2 - 1) +
c      . (dreal(sigx(k,l)) + dreal(sigz(k,l))**2*(0.5d0/Sg)**2 +
c      . (dreal(tauxz(k,l))**2 - dreal(sigx(k,l))*dreal(sigz(k,l)))/Sg**2
c      endif
c      return
c      end

c
c      double precision function delamL(k,i,l)
c      implicit double precision (a-h,o-z)
c      double complex u,w,sigx,sigz,tauxz
c
c      parameter (nPly=36,nFourier=250,nMat=3,nzpts=5,nxpts=125)
c
c      common/stuff3/Mat(nply)
c      common/stuff4/Xt,Xc,Yt,Yc,Sg,Sc,Zc
c      common/stuff5/u(2*nxpts,nzpts*npLy), w(2*nxpts,nzpts*npLy)
c      , sigx(2*nxpts,nzpts*npLy), sigz(2*nxpts,nzpts*npLy)
c      , tauxz(2*nxpts,nzpts*npLy)
c
c      delamL = dreal(tauxz(k,l))**2/Sg**2
c      return
c      end

c
c      double precision function delamo(k,i,l)
c      implicit double precision (a-h,o-z)
c      double complex u,w,sigx,sigz,tauxz
c
c      parameter (nPly=36,nFourier=250,nMat=3,nzpts=5,nxpts=125)
c
c      common/stuff3/Mat(nply)
c      common/stuff4/Xt,Xc,Yt,Yc,Sg,Sc,Zc
c      common/stuff5/u(2*nxpts,nzpts*npLy), w(2*nxpts,nzpts*npLy)
c      , sigx(2*nxpts,nzpts*npLy), sigz(2*nxpts,nzpts*npLy)
c      , tauxz(2*nxpts,nzpts*npLy)
c
c      delamo = (dreal(sigz(k,l))/Yt)**2 + dreal(tauxz(k,l))**2/Sg**2
c      return
c      end

c
c      double precision function delamH(k,i,l)
c      implicit double precision (a-h,o-z)
c      double complex u,w,sigx,sigz,tauxz
c
c      parameter (nPly=36,nFourier=250,nMat=3,nzpts=5,nxpts=125)

```



```

C
C      dimension A (NDIM,N), B (N)
C
C      NDIM IS UPPER BOUND ON THE ORDER N
C      A CONTAINS FACTORS OBTAINED BY DECOMP
C      B IS RIGHT HAND SIDE VECTOR
C      IPVT IS PIVOT VECTOR OBTAINED BY DECOMP
C      ON OUTPUT B CONTAINS SOLUTION X
C
C      INTEGER NM1,K,KB,KP1,KM1,M,I
C      double complex S
C
C      FORWARD ELIMINATION
C
C      IF (N.EQ.1) GO TO 30
C      NM1 = N-1
C      DO 10 K = 1,NM1
C      KP1 = K+1
C      M = IPVT(K)
C      S = B(M)
C      B(M) = B(K)
C      B(K) = S
C      DO 10 I = KP1,N
C      10 B(I) = B(I)+A(I,K)*S
C
C      BACK SUBSTITUTION
C
C      DO 20 KB = 1,NM1
C      KM1 = N-KB
C      K = KM1+1
C      B(K) = B(K)/A(K,K)
C      S = -B(K)
C      DO 20 I = 1,KM1
C      20 B(I) = B(I)+A(I,K)*S
C
C      30 B(1) = B(1)/A(1,1)
C      RETURN
C      END

```

```

C
C      program et3dl609
C
C      This program evaluates the stresses by Pagano's solution
C      for a rectangular plate (25 Oct 1969 paper) with modified
C      load (Hertzian contact load) as represented by a double
C      Fourier sine series.
C      .....
C      implicit double precision (a-h,o-z)
C
C      double precision u,v,w,sigx,sigy,sigz,tauxz,tauyz,tau23c,tau13c
C      double precision nu12,nu23,nu13,nu12c,nu23c,nu13c
C      double precision pi
C      . xlength,xhalf,xtight,xhalfinv,xx,xm
C      . ylength,yhalf,ytight,yhalfinv,yy,ym
C      . ,ABCD,alpha
C      . ,zero
C      . ,f1,f2,f3,f4,f5
C      . ,fiber,matrix,delam,corez,coret,corecomb
C      . ,Xt,Xc,Yt,Yc,S12,S13,S23,X1,S1,Sc,Zc
C      . ,e1,e2,e3,g12,g13,g23
C      . ,e1c,e2c,e3c,g12c,g13c,g23c
C      . ,inch,psi
C      . ,Con,qnot,S
C      . ,uscale,vscale,wscale
C      . ,sxscale,syscale,syscale
C      . ,tzyscale,txyscale,txyscale
C      . ,C11,C12,C13,C22,C23,C33,C44,C55,C66
C      . ,P,q
C      . ,oJ,oL,oR,oM
C      double precision z,zz,Cz,Sz
C      . ,zm,thk
C      . ,amax,aa
C
C      double precision gamma,cm
C      double precision d,f,H
C      . ,A,FG,bc,Btrix
C      character*20 inname,dbgname,yzname,xzname,xynname,sumname
C
C      nply is the total number of plies including the core and any
C      additional plies used to get better resolution of data.
C
C      nzpts and nxpts must be odd
C
C      parameter (nply=35,nFourier=9,nMat=3,nxpts=21,nypts=21,nzpts=3)
C      parameter (nply=11,nFourier=11,nMat=3,nxpts=11,nypts=11,nzpts=3)
C
C      common/stuff1/cm(3,nply),ABCD(4,nply)
C      . ,gamma(3,nply),alpha(3,nply)
C      common/stuff2/Con(6,6,0,nMat-1),p(nFourier),q(nFourier)
C      common/stuff3/Mat(nply),n,m
C      common/stuff4/
C      . ,Xt,Xc,Yt,Yc,S12,S13,S23,X1,S1,Sc,Zc
C      . ,e1,e2,e3,g12,g13,g23,nu12,nu23,nu13
C      . ,e1c,e2c,e3c,g12c,g13c,g23c,nu12c,nu23c,nu13c
C      common/stuff5/ u(nxpts,nypts,nzpts*nply)
C      . ,v(nxpts,nypts,nzpts*nply)
C      . ,w(nxpts,nypts,nzpts*nply)
C      . ,sigx(nxpts,nypts,nzpts*nply)
C      . ,sigy(nxpts,nypts,nzpts*nply)
C      . ,sigz(nxpts,nypts,nzpts*nply)
C      . ,tauxz(nxpts,nypts,nzpts*nply)
C      . ,tauyz(nxpts,nypts,nzpts*nply)
C      . ,tauxz(nxpts,nypts,nzpts*nply)
C      . ,tauyz(nxpts,nypts,nzpts*nply)
C      common/stuff6/

```



```

thk = 0.0d0
c
c fill array p and print out coeff
c
  write(10,*)'coeff(n,m):'
  do 12 n = 1,8
    write(10, '(100(1e13.4))') (coeff(n,m),m=1,8)
  12 continue
  do 110 n = 1,nfourier
    p(n) = dfloat(2*n - 1)*pi/xlength
    q(n) = dfloat(2*n - 1)*pi/ylength
  110 continue
c
c fill array of lamina thicknesses
c
  ncorechk = 0
  do 100 kp = 1,numpy
    c
    c ** change for Pagano vs sandwich
    c
    c most plys 0.005 inch = 1.27d-4 meter
    c
    h(kp) = 5.0d-3 * inch
  100 continue
c
c for Pagano's solution:
c
c   h(kp) = xlength/(s*numpy)
c
c1023 allow several layers within core to get better resolution
c
  if (Mat(kp).gt. 1) then
    c
    c core .5 inch
    c
    h(kp) = .5d0 * inch
    ncorechk = ncorechk + 1
    if (ncoreply.ne. 1) h(kp) = h(kp)/(2.0d0*dfloat(ncoreply))
    if (ncorechk.gt. 2*ncoreply/3) h(kp) = 4.0d0*h(kp)
  endif
  thk = thk + h(kp)
100 continue
c
c calculate S when it is not an input parameter
c
  S = xlength/thk
  write(*,*)'in inches thk=',thk/inch,' S =',S
c
c scale as in Pagano's 3-d paper Oct 69
c
  vscale = -e2/(thk*qs0*S**3)
  vscale = -e2/(thk*qs0*S**3)
  wscale = -100.0d0*e2/(thk*qs0*S**4)
  xscale = 1.0d0/(qs0*S*S)
  syscale = 1.0d0/(qs0*S*S)
  szscale = 1.0d0/qs0
  tyzscale = 1.0d0/(qs0*S)
  txzscale = 1.0d0/(qs0*S)
  txyscale = 1.0d0/(qs0*S*S)
c
c don't scale as in Pagano's 3-d paper Oct 69
c
  uscale = 1.0d0

```

```

vscale = 1.0d0
wscale = -1.0d0
xscale = 1.0d0
syscale = 1.0d0
szscale = 1.0d0
tyzscale = 1.0d0
txzscale = 1.0d0
txyscale = 1.0d0
c
c
do 210 k = 1,numpy
c11(k) = Con(1,1,Mat(k))
c22(k) = Con(2,2,Mat(k))
c33(k) = Con(3,3,Mat(k))
c44(k) = Con(4,4,Mat(k))
c55(k) = Con(5,5,Mat(k))
c66(k) = Con(6,6,Mat(k))
c12(k) = Con(1,2,Mat(k))
c13(k) = Con(1,3,Mat(k))
c23(k) = Con(2,3,Mat(k))
ABCD(1,k) = c33(k)*c44(k)*c55(k)
210 continue
c
c initialize arrays
c
do 620 i = 1,nxpts
do 620 j = 1,nypts
do 620 k = 1,nply*nzpts
  u(i,j,k) = 0.0d0
  v(i,j,k) = 0.0d0
  w(i,j,k) = 0.0d0
  sigx(i,j,k) = 0.0d0
  sigy(i,j,k) = 0.0d0
  sigz(i,j,k) = 0.0d0
  tauyz(i,j,k) = 0.0d0
  tauxz(i,j,k) = 0.0d0
  tauxy(i,j,k) = 0.0d0
620 continue
c
c interface z values
c
do 310 ia = 1,numpy-1
  z(ia) = thk/2.0d0
do 320 ib = 1,ia
  z(ia) = z(ia) - h(ib)
320 continue
310 continue
c
  write(*,*)'in inches z(1)=',z(1)/39.3700787
c
  write(*,*)'in inches z(BOT)=',z(numpy-1)/39.3700787
c
c xx values
c
  xtight = xhalf/4.0d0
  xx(1) = xhalf
do 325 i = 2,(nxpts + 1)/2
  xx(i) = xhalf - (2*i - 2)*xtight/(nxpts - 1)
  xx(i + nxpts - 1)/2) = xhalf - xtight -
    . (2*i - 2)*(xhalf - xtight)/(nxpts - 1)
325 continue
c
c yy values
c
  ytight = yhalf/4.0d0

```

```

YY(1) = yhalf
do 327 j = 2, (nypts + 1)/2
  yy(j) = yhalf - (2*j - 2)*yright/(nypts - 1)
  yy(j + (nypts - 1)/2) = yhalf - yright -
    . (2*j - 2)*(yhalf - yright)/(nypts - 1)
327 continue
c
c internal zz values
c
do 330 kp = 1, numply
do 330 kz = 1, nzpts
  zz(kz, kp) = thk/2.0d0 - (kz - nzpts)*h(kp)/(nzpts - 1)
do 340 kpb = 1, kp
  zz(kz, kpb) = zz(kz, kp) - h(kpb)
340 continue
330 continue
c
c write(*,*) 'in inches zz(1,1)=' , zz(1,1)*39.3700787
c
c write(*,*) 'in inches zz(BOT)=' , zz(nzpts, numply)*39.3700787
c
c
c loop over all nFourier*2 loads.
c
do 900 m = 1, nFourier
do 900 n = 1, nFourier
c
c loop over all numply phys.
c
do 200 k = 1, numply
c
c fill array ABCD
c
ABCD(2, k) =
. p(n)**2*
. (
. c44(k)*(c11(k)*c33(k) - c13(k)**2)
. + c55(k)*(c66(k)*c33(k) - 2.0d0*c13(k)*c44(k))
. ) +
. q(m)**2*
. (
. c55(k)*(c22(k)*c33(k) - c23(k)**2)
. + c44(k)*(c66(k)*c33(k) - 2.0d0*c13(k)*c55(k))
. )
ABCD(3, k) =
. -p(n)**4*
. (
. c66(k)*(c11(k)*c33(k) - c13(k)**2)
. + c55(k)*(c11(k)*c44(k) - 2.0d0*c13(k)*c66(k))
. + p(n)**2*q(m)**2*
. (
. -c11(k)*(c22(k)*c33(k) - c23(k)**2)
. - 2.0d0*(c12(k) + c66(k))*(c13(k) + c55(k))*(c23(k) + c44(k))
. - 2.0d0*c44(k)*c55(k)*c66(k)
. + 2.0d0*c44(k)*c11(k)*c23(k)
. + c12(k)*c33(k)*(c12(k) + 2.0d0*c66(k))
. )
. )
gamma(j, k) = 2.0d0*dsqrt(-d(k)/3.0d0)
. *dcos(
. (1.0d0/3.0d0)*
. dacos(
. (-f(k)*dsqrt(27.0d0))
. / (2.0d0*(-d(k))**(1.5d0))
. )
. + 2.0d0*dfloat(j - 1)*pi
. )
cm(j, k) = dsqrt(dabs(gamma(j, k) + ABCD(2, k)/(3.0d0*ABCD(1, k))))
alpha(j, k) = 1.0d0
if (dreal(gamma(j, k) + ABCD(2, k)/(3.0d0*ABCD(1, k)))) .lt. 0.0d0)
. then
  alpha(j, k) = -1.0d0
. else
  endif
  out(j, k) = c33(k)*c44(k)*cm(j, k)**4
. + alpha(j, k)*cm(j, k)**2
. (
. - p(n)**2*(c44(k)*c55(k) + c33(k)*c66(k))
. + q(m)**2*(c23(k)**2
. - c22(k)*c33(k)
. + 2.0d0*c23(k)*c44(k))
. )

```



```

      + (
      .   p(n)**2*c66(k)
      .   + q(m)**2*c22(k)
      .   )*(
      .   p(n)**2*c55(k)
      .   + q(m)**2*c44(k)
      .   )
      .   oL(j,k) = (p(n)*q(m)/oJ(j,k))*
      .   (
      .   .   alpha(j,k)*cm(j,k)**2*
      .   .   (
      .   .   .   c33(k)*(c12(k) + c66(k))
      .   .   .   - (c23(k) + c44(k))*(c13(k) + c55(k))
      .   .   .   )
      .   .   - (c12(k) + c66(k))*(p(n)**2*c55(k)
      .   .   + q(m)**2*c44(k))
      .   .   )
      .   oR(j,k) = (p(n)*cm(j,k)/oJ(j,k))*
      .   (
      .   .   alpha(j,k)*cm(j,k)**2*c44(k)*(c13(k) + c55(k))
      .   .   - (c13(k)
      .   .   + c55(k))*(p(n)**2*c66(k)
      .   .   + q(m)**2*c22(k))
      .   .   + q(m)**2*(c23(k) + c44(k))*(c12(k) + c66(k))
      .   .   )
      .   oM(1,j,k) =
      .   .   - p(n)*c11(k)
      .   .   - q(m)*c12(k)*oL(j,k)
      .   .   + alpha(j,k)*cm(j,k)*oR(j,k)*c13(k)
      .   .   oM(2,j,k) =
      .   .   - p(n)*c12(k)
      .   .   - q(m)*c22(k)*oL(j,k)
      .   .   + alpha(j,k)*cm(j,k)*oR(j,k)*c23(k)
      .   .   oM(3,j,k) =
      .   .   - p(n)*c13(k)
      .   .   - q(m)*c23(k)*oL(j,k)
      .   .   + alpha(j,k)*cm(j,k)*oR(j,k)*c33(k)
      .   .   )
      .   220 continue
c
c
c   write(10,'(a12,20e15.6)') 'c1j:',c11(k),c12(k),c13(k)
c   write(10,'(a12,20e15.6)') 'c2j:',c22(k),c23(k)
c   write(10,'(a12,20e15.6)') 'c3j:',c33(k)
c   write(10,'(a12,20e15.6)') 'c4j:',c44(k),c55(k),c66(k)
c   write(10,'(a12,20e15.6)') 'n,m,p,q:',n,m,p,q, 'p(n),q(m)
c   write(10,'(a10,i2,20e15.6)') 'k,ABCD:',k,ABCD(1,k),ABCD(2,k)
c   .,ABCD(3,k),ABCD(4,k)
c   write(10,'(a12,20e15.6)') 'd,e,h:',d(k),e(k),h(k)
c   write(10,'(a12,20e15.6)') 'gamma:',(gamma(j,k),j=1,3)
c   write(10,'(a12,20e15.6)') 'alpha:',(alpha(j,k),j=1,3)
c   write(10,'(a12,20e15.6)') 'cm:',(cm(j,k),j=1,3)
c   write(10,'(a12,20e15.6)') 'oJ:',(oJ(j,k),j=1,3)
c   write(10,'(a12,20e15.6)') 'oL:',(oL(j,k),j=1,3)
c   write(10,'(a12,20e15.6)') 'oR:',(oR(j,k),j=1,3)
c   write(10,'(a12,20e15.6)') 'oM(1,j,k):',(oM(1,j,k),j=1,3)
c   write(10,'(a12,20e15.6)') 'oM(2,j,k):',(oM(2,j,k),j=1,3)
c   write(10,'(a12,20e15.6)') 'oM(3,j,k):',(oM(3,j,k),j=1,3)
c
c   200 continue
c
c   265 continue
c

```



```

c
kp = 1
kz = 1
k = 1
do 850 i = 1, 2*nxpts
  if (i .le. nxpts) then
    im = i
    xm = xx(nxpts + 1 - i)
  else
    im = 2*nxpts - i + 1
    xm = xlength - xx(i - nxpts)
  endif
  do 860 j = 1, 2*nypts
    if (j .le. nypts) then
      jm = j
      ym = yy(nypts + 1 - j)
    else
      jm = 2*nypts - j + 1
      ym = ylength - yy(j - nypts)
    endif
    c
    write(15, '(120e20,10)') xm, ym, zz(kz, kp), dreal(w(im, jm, k))
    c
    write(22, '(120e20,10)') xm, ym, zz(kz, kp), dreal(sizg(im, jm, k))
    c
    write(13, '(120e20,10)') xm, ym, -zz(kz, kp)
    c
    , dreal(u(im, jm, k))
    c
    , dreal(v(im, jm, k))
    c
    , dreal(w(im, jm, k))
    c
    , dreal(sizg(im, jm, k))
    c
    , dreal(sizy(im, jm, k))
    c
    , dreal(sizg(im, jm, k))
    c
    , dreal(tauyz(im, jm, k))
    c
    , dreal(tauzx(im, jm, k))
    c
    860 continue
    write(13, 60)
    write(22, 60)
    c
    850 continue
    write(*,*) 'ET run ', inname, ' finished without error.'
    write(*,*) 'The center displacement Wc = ', dreal(w(nxpts, nypts, 1))
    60 format (1x)
    stop
  end
  subroutine fcoeff(quot)
  double precision coeff
  common/coeffd/coeff(25, 25)
  c
  data coeff/
    . 0.0821381d0, -0.0757974d0, 0.0641617d0, -0.0491206d0, 0.032956d0,
    . -0.0178156d0, 0.00566946d0, 0.00250516d0, -0.00654407d0,
    . 0.00706533d0, -0.00519273d0, 0.0022576d0, 0.000545978d0,
    . -0.0065953d0, 0.00299842d0, -0.00242686d0, 0.00117937d0,
    . 0.000237025d0, -0.00122122d0, 0.00162573d0, -0.00139507d0,
    . 0.000724178d0, 0.000908427d0, -0.000739395d0, 0.00102836d0,
    . -0.0757974d0, 0.0698079d0, -0.0588143d0, 0.046443d0, -0.0294725d0,
    . 0.0153819d0, -0.00415646d0, -0.00326923d0, 0.00676858d0,
    . -0.00696527d0, 0.00494229d0, -0.00199473d0, -0.000734616d0,
    . 0.00696527d0, 0.00494229d0, -0.00199473d0, -0.000734616d0,
    . 0.00249003d0, -0.00298734d0, 0.00236065d0, -0.00109329d0,
    . -0.000272023d0, 0.00126218d0, -0.0016367d0, 0.0013709d0,
    . -0.000686617d0, -0.000125464d0, 0.000760139d0, -0.00103157d0,
    . 0.0641617d0, -0.0588143d0, 0.0490582d0, -0.0365609d0, 0.0232284d0,
    . -0.0110123d0, 0.00150202d0, 0.00455679d0, -0.0070753d0,
    . 0.00668795d0, -0.00443524d0, 0.00148355d0, 0.00108936d0,
    . -0.00263737d0, 0.00282342d0, -0.00221928d0, 0.000921031d0,
    . 0.000414223d0, -0.0013411d0, 0.00164083d0, -0.00135003d0,
    . 0.000611166d0, 0.00019274d0, -0.000801347d0, 0.00103489d0,
    . -0.0491206d0, 0.046443d0, -0.0365609d0, 0.0262367d0, -0.0152567d0,
    . 0.0056736d0, 0.0016477d0, -0.00593382d0, 0.00722886d0,
    . -0.0061247d0, 0.00362573d0, -0.000778617d0, -0.00156805d0,
    . 0.00281203d0, -0.00287007d0, 0.00200114d0, -0.00069251d0,
    . 0.000608114d0, 0.00143645d0, -0.00163081d0, 0.00124607d0,
    . -0.000543446d0, -0.000275805d0, 0.000835334d0, -0.00103404d0,
    . 0.032956d0, -0.0294725d0, 0.0232284d0, -0.0152567d0, 0.0073123d0,
    . -0.000333266d0, -0.0045503d0, 0.00694493d0, -0.00696363d0,
    . 0.00519055d0, -0.00252705d0, -0.000124794d0, 0.00207488d0,
    . -0.00288408d0, 0.0026834d0, -0.00169322d0, 0.000340738d0,
    . 0.000843738d0, -0.00153037d0, 0.00159426d0, -0.00111935d0,
    . 0.00039323d0, 0.000402402d0, -0.000884856d0, 0.000990256d0,
    . -0.0178156d0, 0.0153819d0, -0.0110123d0, 0.00567636d0,
    . -0.000333266d0, -0.00393771d0, 0.00653713d0, -0.00720038d0,
    . 0.00612299d0, -0.00386473d0, 0.00129471d0, 0.00108604d0,
    . -0.00255189d0, 0.00280324d0, -0.00234648d0, 0.00126364d0,
    . 0.000425889d0, -0.00109829d0, 0.00160719d0, -0.00151885d0,
    . 0.000940208d0, -0.000154596d0, -0.000555277d0, 0.000972565d0,
    . -0.00100068d0,
    . 0.00566946d0, -0.00415646d0, 0.00150202d0, 0.0016477d0,
    . -0.0045503d0, 0.00653713d0, -0.00702108d0, 0.00649744d0,
    . -0.0046736d0, 0.00226901d0, 0.000106581d0, -0.00196166d0,
    . 0.00288195d0, -0.00281522d0, 0.00196196d0, -0.000771612d0,
    . -0.000455426d0, 0.00130411d0, -0.00163923d0, 0.0013734d0,
    . -0.000723121d0, -0.0000579881d0, 0.000702232d0, -0.001015d0,
    . 0.000950424d0,
    . 0.00250516d0, -0.00326923d0, 0.00455679d0, -0.00593382d0,
    . 0.00694493d0, -0.00720038d0, 0.00649744d0, -0.00493313d0,
    . 0.00278855d0, -0.000503097d0, -0.00141749d0, 0.00263152d0,
    . -0.00297536d0, 0.00249954d0, -0.0014484d0, 0.000203525d0,
    . 0.000895538d0, -0.00165436d0, 0.00160024d0, -0.00117684d0,
    . 0.00045912d0, 0.000291455d0, -0.000842453d0, 0.00103679d0,
    . -0.000872872d0,
    . -0.00654407d0, 0.00676858d0, -0.0070753d0, 0.00722886d0,
    . -0.00696363d0, 0.00612299d0, -0.0046736d0, 0.00278855d0,
    . -0.000745971d0, -0.0010914d0, 0.00239856d0, -0.00296291d0,
    . 0.00273501d0, -0.00194847d0, 0.000766672d0, 0.000408847d0,
    . -0.00126481d0, 0.00162698d0, -0.0014692d0, 0.00090621d0,
    . -0.000160064d0, -0.000523256d0, 0.000953169d0, -0.00102173d0,
    . 0.00076614d0,
    . 0.00706533d0, -0.00696527d0, 0.00668795d0, -0.0061247d0,
    . 0.00519055d0, -0.00386473d0, 0.00226901d0, -0.000503097d0,
    . -0.0010914d0, 0.0023026d0, -0.00291913d0, 0.00286577d0,
    . -0.00102165d0, 0.00117498d0, -0.0000253519d0, -0.000951772d0,
    . 0.00152859d0, -0.00160266d0, 0.00122626d0, -0.00059052d0,
    . 0.000114313d0, 0.000762913d0, -0.00102468d0, 0.000961002d0,
    . -0.000613531d0,
    . -0.00519273d0, 0.00494229d0, -0.00443524d0, 0.00362573d0,

```

. -0.0025270540,0.00129471d0,0.000106581d0,-0.00141749d0,
. 0.00239856d0,-0.002391313d0,0.00289963d0,-0.00233364d0,
. 0.00143066d0,-0.000321575d0,-0.000669774d0,0.00137353d0,
. 0.00498957d0,-0.00145226d0,-0.000905905d0,0.000193224d0,
. 0.000472073d0,-0.000912541d0,0.00103402d0,-0.0008402d0,
. 0.000406361d0,
. 0.0022576d0,-0.00199473d0,0.00148355d0,-0.000778617d0,
. 0.000124794d0,0.00108604d0,-0.00196166d0,0.00283152d0,
. 0.00296291d0,-0.00286577d0,-0.00233564d0,0.00149969d0,
. 0.000498957d0,-0.000492977d0,0.00122958d0,-0.00160923d0,
. 0.0015646d0,-0.00114281d0,0.000497576d0,0.000200347d0,
. 0.000743454d0,0.00103717d0,-0.000971976d0,0.00065538d0,
. 0.000185912d0,
. 0.000545978d0,-0.000734616d0,0.00108936d0,-0.00156805d0,
. 0.00207488d0,-0.00255188d0,0.00288195d0,-0.00297536d0,
. 0.00273501d0,-0.00222165d0,0.00142306d0,-0.000498957d0,
. 0.000412538d0,0.00114269d0,-0.00156486d0,0.00161122d0,
. 0.00129219d0,0.000722401d0,-0.000509691d0,-0.000523982d0,
. 0.000940171d0,-0.00103096d0,0.000828721d0,-0.000430402d0,
. 0.0000495959d0,
. 0.00254993d0,0.00249003d0,-0.00263737d0,0.00281203d0,
. 0.00288408d0,0.00280324d0,-0.00281522d0,0.00249554d0,
. 0.00194847d0,0.00117498d0,-0.000321575d0,-0.000492977d0,
. 0.00114269d0,-0.00154391d0,0.00162299d0,-0.00139348d0,
. 0.000867846d0,-0.00027489d0,-0.000386153d0,0.000831504d0,
. 0.00102379d0,-0.00094324d0,-0.000617997d0,0.000160488d0,
. 0.000277344d0,
. 0.00298842d0,-0.00298734d0,0.00282342d0,-0.00287007d0,
. 0.002634d0,-0.00234648d0,0.00196196d0,-0.0014484d0,
. 0.000766672d0,-0.0000253519d0,-0.000669774d0,0.00122958d0,
. 0.00156486d0,0.00162299d0,-0.00142017d0,0.00092906d0,
. 0.000339324d0,-0.000256783d0,0.000737655d0,-0.000992961d0,
. 0.0010135d0,-0.000757864d0,0.000349398d0,0.000112694d0,
. 0.000483808d0,
. 0.0024686d0,0.00236065d0,-0.00222192d0,0.00200114d0,
. 0.00169322d0,0.00126364d0,-0.000771612d0,0.00020325d0,
. 0.000408847d0,-0.000951772d0,0.00137353d0,-0.00160923d0,
. 0.00161122d0,-0.00139348d0,0.00092906d0,-0.000365648d0,
. 0.00021229d0,0.000683763d0,-0.000973763d0,0.00106074d0,
. 0.000846754d0,0.000474536d0,-0.0000466196d0,-0.000358835d0,
. 0.000633964d0,
. 0.00117937d0,-0.00109328d0,0.000921031d0,-0.000669251d0,
. 0.000340738d0,0.0000425889d0,-0.00045426d0,0.000895538d0,
. 0.00126481d0,0.00152859d0,-0.00163379d0,0.0015646d0,
. 0.00129219d0,0.000867846d0,-0.000339324d0,-0.00021229d0,
. 0.000633659d0,-0.000951793d0,0.00109201d0,-0.000900852d0,
. 0.000577671d0,-0.000172056d0,-0.000249254d0,0.000560962d0,
. 0.000071379d0,
. 0.000237025d0,-0.000272023d0,0.000414223d0,-0.000608114d0,
. 0.000843738d0,-0.00109829d0,0.00130411d0,-0.00165436d0,
. 0.00162698d0,-0.00160266d0,0.00145226d0,-0.00114281d0,
. 0.000722401d0,-0.000227489d0,-0.000256783d0,0.00083763d0,
. 0.000951793d0,0.00103768d0,-0.000919468d0,0.000642686d0,
. 0.000245485d0,-0.000160409d0,0.000502354d0,-0.000690434d0,
. 0.000699232d0,

. -0.00122122d0,0.00126218d0,-0.0013411d0,0.00143645d0,
. 0.00153037d0,0.00160719d0,-0.00163923d0,0.00160024d0,
. 0.0014692d0,0.00122626d0,-0.000905905d0,0.000497576d0,
. 0.0000509691d0,-0.000386153d0,0.000737655d0,-0.000973763d0,
. 0.00109201d0,-0.000919468d0,0.000651097d0,-0.000283688d0,
. 0.000109326d0,0.000447531d0,-0.000663608d0,0.000712949d0,
. 0.00059679d0,
. 0.00162573d0,-0.00163676d0,0.00164083d0,-0.00163081d0,
. 0.00159426d0,-0.001518885d0,0.00137734d0,-0.0017684d0,
. 0.00096211d0,-0.000559052d0,0.000193224d0,0.000200347d0,
. 0.000523982d0,0.000831504d0,-0.000992961d0,0.00106074d0,
. 0.000900852d0,0.000642686d0,-0.000283688d0,-0.000924677d0,
. 0.000421184d0,-0.0006643214d0,0.000718035d0,-0.000633428d0,
. 0.000414026d0,
. 0.00139507d0,0.0013709d0,-0.00135003d0,0.00124607d0,
. 0.00111935d0,0.000940208d0,-0.000723121d0,0.00045912d0,
. 0.000160064d0,0.000114313d0,0.000472073d0,-0.000743454d0,
. 0.000940717d0,-0.00102379d0,0.00101335d0,-0.000846754d0,
. 0.000577671d0,-0.000245485d0,-0.000109326d0,0.000421184d0,
. 0.000638291d0,0.000716827d0,-0.000653344d0,0.000385605d0,
. 0.000186055d0,
. 0.000724178d0,-0.000686617d0,0.000611166d0,-0.000543446d0,
. 0.000339323d0,-0.000154596d0,-0.0000579881d0,0.000291455d0,
. 0.000523256d0,0.000762913d0,-0.000912541d0,0.00101717d0,
. 0.00103096d0,0.00094324d0,-0.000757864d0,0.000474536d0,
. 0.000172056d0,-0.000160409d0,0.000447531d0,-0.000643214d0,
. 0.000716827d0,-0.000660605d0,0.000408873d0,-0.00022638d0,
. 0.0000616743d0,
. 0.0000908427d0,-0.000125464d0,0.00019274d0,-0.000275805d0,
. 0.000402402d0,-0.000555277d0,0.000702328d0,-0.000842453d0,
. 0.000953169d0,-0.000102468d0,0.00103402d0,-0.000971976d0,
. 0.000828721d0,-0.000617997d0,0.000349398d0,-0.0000466196d0,
. 0.000249254d0,0.000502354d0,-0.000663608d0,0.000718035d0,
. 0.000653344d0,0.000408873d0,-0.000236325d0,-0.000528149d0,
. 0.000279154d0,
. 0.000739395d0,0.000760139d0,-0.000801347d0,0.000835334d0,
. 0.000884856d0,0.000972565d0,-0.001015d0,0.00103679d0,
. 0.00102173d0,0.000961002d0,-0.0008402d0,0.000655328d0,
. 0.000430402d0,0.000160488d0,0.000112694d0,-0.000358835d0,
. 0.000560962d0,-0.000690434d0,0.000712949d0,-0.000633428d0,
. 0.000385605d0,-0.00022638d0,-0.000528149d0,0.000276832d0,
. 0.000446911d0,
. 0.00102836d0,-0.00103157d0,0.00103489d0,-0.00103404d0,
. 0.000990256d0,-0.00100068d0,0.000950424d0,-0.000872872d0,
. 0.00075614d0,-0.000613531d0,0.000406361d0,-0.000185912d0,
. 0.0000495959d0,0.000277344d0,-0.000483808d0,0.000633964d0,
. 0.00071379d0,0.000699232d0,-0.00059679d0,0.000414026d0,
. 0.000186055d0,-0.0000616743d0,0.000279154d0,-0.000446911d0,
. 0.000522764d0/
return
end

This Mathcad template calculates the Fourier coefficients for a one-dimensional Hertzian contact pressure distribution. The user supplies the length (L), the peak value (q_0 , usually unity), number of Fourier terms to calculate (N), and the contact half-width (R_{contact})

User supplied parameters:

length: $L = 5 \cdot \frac{\text{in}}{\text{m}}$

peak load: $q_0 = 1$

contact half-width: $R_{\text{contact}} = 0.0625 \cdot \frac{\text{in}}{\text{m}}$

number of Fourier terms: $N = 1000$

ORIGIN $\equiv 1$

Numx $\equiv 2000$

$i \equiv 1 \dots \text{Numx}$

$x_i \equiv \frac{i-1}{\text{Numx}-1} \cdot L$

PRNPRECISION $\equiv 16$

PRNCOLWIDTH $\equiv 24$

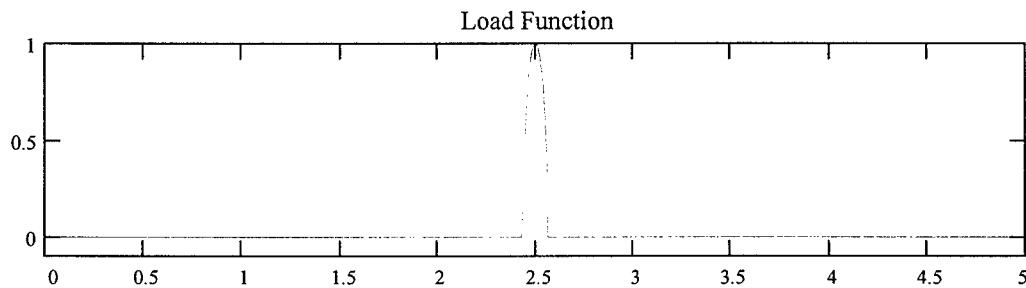
$n \equiv 1 \dots N$

$p(n) \equiv \frac{n \cdot \pi}{L}$

$\text{odd}_n \equiv 2 \cdot n - 1$

Calculations begin here:

distance from center $r(x) \equiv \left| \frac{L}{2} - x \right|$ Hertzian function $f(x, R) = q_0 \cdot \left(1 - \frac{r(x)^2}{R^2} \right)^{\frac{1}{2}}$



The odd Fourier coefficients (CRC pg 403) Mathcad uses Romberg method:

$$b_n = \frac{2}{L} \int_{\frac{L}{2} - R_{\text{contact}}}^{\frac{L}{2} + R_{\text{contact}}} f(x, R_{\text{contact}}) \cdot \sin(p(\text{odd}_n) \cdot x) dx$$

Generate a file for the FORTRAN subroutine $\text{WRITEPRN}(\text{four1000 dat}) = \text{Re}(b)$

read in the file (used when plotting profiles
and not regenerating b each time)

$b = \text{READPRN}(\text{four1000 dat})$

$\text{Numx} = 400$

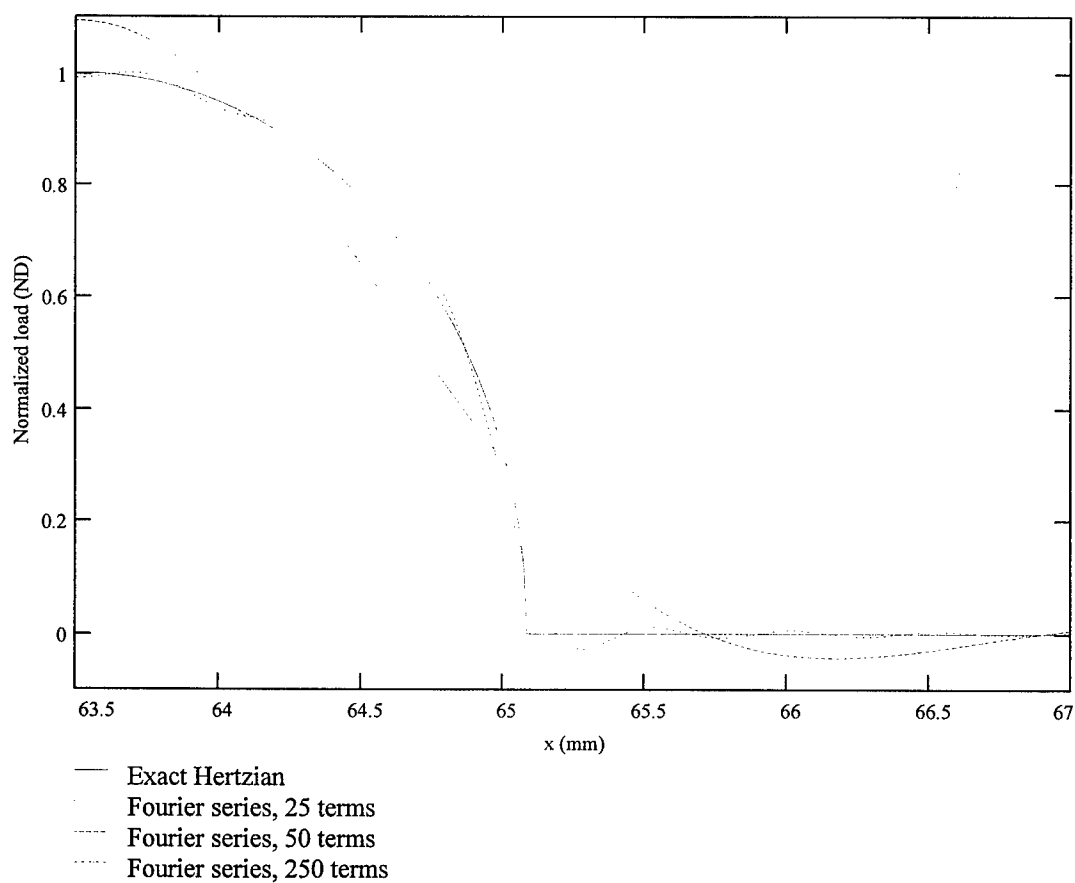
$i = 1 \dots \text{Numx}$

The truncated series
approximation of the function f

$$ff(x, M) = \sum_{n=1}^M (b_n \cdot \sin(p(\text{odd}_n) \cdot x))$$

x values to plot

$$x_i = \frac{i-1}{\text{Numx}-1} \cdot 0.0035 + 0.0635$$



Bibliography

- 1) Hackman, L.E. "Sandwich construction and design," in *Analysis and design of flight vehicle structures*. Ed. E.F. Bruhn. c12.1-c12.52. Tri-State Offset Company, 1965.
- 2) Rhodes, M.D. "Impact fracture of composite sandwich structures," *16th Structure, Structural Dynamics, and Materials Conference, AIAA paper, No. 75-748*, 1-9. 1975.
- 3) Rhodes, M.D. "Impact tests on fibrous composite sandwich structures," *National Aeronautics and Space Administration, Scientific and Technical Information Office SERIES: NASA technical memorandum ; 78719*, 1978.
- 4) Schoeppner, G.A. "Low velocity impact response of tension preload composite laminates," *Proceedings of the 10th DOD/NASA/FAA Conference on Fibrous Composites in Structural Design*. VIII-47-VIII-61. 1994.
- 5) Harrington, T.M. *An Experimental Investigation of Sandwich Panels Under Low Velocity Impact*, MS thesis, AFIT/GAE/ENY/94D-22. School of Engineering, Air Force Institute of Technology (AU), Wright-Patterson AFB OH, December 1994.
- 6) Chattopadhyay, A., and Gu, H. "New Higher Order Plate Theory in Modeling Delamination Buckling of Composite Laminates," *ALAA Journal*, Vol. 32, No. 8: 1709-1716 (1994).
- 7) Corigliano, A. "Formulation, identification and use of interface models in the numerical analysis of composite delamination," *International Journal of Solids and Structures*, Vol. 30, No. 20, 2779-2811 (1993).
- 8) Ladeveze, P. "A damage computational method for composite structures," *Computers & Structures*, Vol. 44, No. 1: 79-87 (1992).
- 9) Allix, O., and Daudeville, L., and Ladeveze, P. "Delamination and damage mechanics," *Mechanics and Mechanisms of Damage in Composites and Multi-materials: (1991)*.
- 10) Bottega, W.J. "A growth law for propagation of arbitrary shaped delaminations in layered plates," *International Journal of Solids and Structures*, Vol. 19, No. 11: 1009-1017 (1983).
- 11) Allix, O., and Ladeveze, P. "Interlaminar interface modeling for the prediction of delamination," *International Journal of Composite Structures*, Vol. 22, No. 4: 235-242 (1992).
- 12) Sela, N., and Ishai, O. "Interlaminar fracture toughness and toughening of laminated composite materials: a review," *Composites*, Vol. 20, No. 5: 423-435 (1989).
- 13) Abrate, S. "Impact on laminated composite materials," *Applied Mechanics Reviews*, Vol. 44, No. 4: 155-190 (1991).

- 14) Zhong, Z.-H., and Mackerle, J. "Contact-impact problems: A review with bibliography," *Applied Mechanics Reviews*, Vol. 47, No. 2: 55-76 (1994).
- 15) Tsang, P.H.W. *Impact resistance and damage tolerance of composite sandwich panels*, PhD dissertation, MIT. 1994.
- 16) Cantwell, W.J., and Morton, J. "The impact resistance of composite materials - A review," *Composites*, Vol. 22: 347-362 (1991).
- 17) Nahas, M.N. "Survey of failure and post-failure theories of laminated fiber-reinforced composites," *Journal of Composites Technology & Research*, Vol. 8, No. 4: 138-153 (1986).
- 18) Sandhu, R.S. *A survey of failure theories of isotropic and anisotropic materials*, AFFDL-TR-72-71. 1972 (AD756889).
- 19) Reddy, Y.S.N., and Reddy, J.N. "Linear and nonlinear failure analysis of composite laminates with transverse shear," *Composites Science and Technology*, Vol. 44: 227-255 (1991).
- 20) Rowlands, R.E., "Strength (failure) theories and their experimental correlation," *Handbook of Composites - Vol 3 - Failure Mechanics of Composites*, Ed. Sih, G.C. and Skurda, A.M., Elsevier, Amsterdam. 1985.
- 21) Hwang, W.C., and Sun, C.T. "Failure analysis of laminated composites by using iterative three-dimensional finite element method," *Computers & Structures*, Vol. 33: 41-47 (1989).
- 22) Sandhu, R.S. *Ultimate strength analysis of symmetric laminates*, AFFDL-TR-73-137. 1974 (AD779927).
- 23) Abu-Farsakh, G.A., and Abdel-Jawad, Y.A. "A new failure criterion for nonlinear composite materials," *Journal of Composites Technology & Research*, Vol. 16, No. 2: 138-145 (1994).
- 24) Bachrach, W.E., and Hansen, R.S. "Mixed finite element method for composite cylinder subjected to impact," *AIAA Journal*, Vol. 27, No. 5: 632-638 (1989).
- 25) Chang, F.K., and Choi, H.Y., and Jeng, S.T. "Study on impact damage in laminated composites," *Mechanics of materials : an international journal*, Vol. 10, No. 1: 83-95 (1990).
- 26) Cron, S.M., Palazotto, A.N., and Sandhu, R.S. "A failure criterion evaluation for composite materials," *Composite Materials: Testing and Design (Ninth Volume)*, ASTM STP 1059. 494-507 ASTM, 1990.
- 27) Finn, S.R. *Delaminations in composite plates under transverse static or impact loads*. PhD dissertation. Stanford University, 1991.

- 28) Ghaffari, S. *Impact damage in graphite/epoxy laminates: Damage characterization, acoustic emission, and finite element simulation (volumes I and II)*. PhD dissertation, Drexel University, 1989.
- 29) Hart-Smith, L.J. "The role of biaxial stresses in discriminating between meaningful and illusory composite failure theories," *Composite Structures*, Vol. 25: 3-20 (1993).
- 30) Hashemi, S., and Kinloch, A.J., and Williams, G. "Mixed-mode fracture in fiber-polymer composite laminates," in *Composite Materials: Fatigue and Fracture (3rd vol) ASTM STP 1110, No. 3*. 143-168. ASTM, 1991.
- 31) Jih, C.-J. *Analysis of delamination in composite laminates under low velocity impact*. PhD dissertation, Purdue University, 1991.
- 32) Jung, H.S. *Finite element modeling of static indentation damage in laminated composites*, PhD dissertation, University of Florida, 1991.
- 34) Liu, S., and Chang, F.K. "Matrix cracking effect on delamination growth in composite laminates induced by a spherical indenter," *Journal of Composite Materials*, Vol. 28, No. 10: 940-977 (1994).
- 35) Montemurro, M.P., and Hansen, J.S., and Houde, M.J.L. *Finite element analysis of the response of composite plates and shells under impact*. 1-17. unpublished source. 1992.
- 36) Nahas, M.N. "Survey of failure and post-failure theories of laminated fiber-reinforced composites," *Journal of Composites Technology & Research*, Vol. 8, No. 4: 138-153 (1986).
- 37) Razi, H. *An experimental and numerical study of delamination propagation and arrest in composite beams and plates when subjected to low velocity impact*. PhD dissertation. University of Washington, 1991.
- 38) Sandhu, R.S. "Nonlinear behavior of unidirectional and angle ply laminates," *Journal of Aircraft*, Vol. 13, No. 2: 104-111 (1976).
- 39) Sandhu, R.S., and Gallo, R.L., and Sendekyj, G.P. "Initiation and accumulation of damage in composite laminates," *Composite Materials: Testing and Design (Sixth Conference)*, ASTM STP 787, ASTM, 1982.
- 40) Shivakumar, K.N., and Elber, W., and Illg, W. "Prediction of low-velocity impact damage in thin circular laminates," *AIAA Journal*, Vol. 23, No. 5: 442-449 (1984).
- 41) Tolson, S., and Zabaras, N. "Finite element analysis of progressive failure in laminated composite plates," *Computers & Structures*, Vol. 38, No. 3: 361-376 (1991).
- 42) Tsai, S.W., and Wu, E.M. "A general theory of strength for anisotropic materials," *Journal of Composite Materials*, Vol. 5: 58-80 (1971).

- 43) Wang, C.-Y. *A study of impact damage in composite laminates*, PhD thesis. University of Texas at Austin, 1989.
- 44) Wu, C.-L. *Low-velocity impact of composite sandwich plate*, PhD dissertation. Purdue University, C.T. Sun 1992.
- 45) Wu, H.-Y.T. *Impact damage of composites (delamination)*, PhD dissertation. Drexel University, 1987.
- 46) Wu, H.T., and Springer, G.S. "Impact damage of composites," *1st Technical Conference of the American Society of Composites*. Dayton OH: American Society of Composites, 1986.
- 47) Cairns, D.S., and Lagace, P.A. "A consistent engineering methodology for the treatment of impact in composite materials," *Journal of Reinforced Plastics and Composites*, Vol. 11, No. 4: 395-412 (1992).
- 48) Choi, H.Y., and Wu, H.Y.T., and Chang, F.K. "A new approach toward understanding damage mechanisms and mechanics of laminated composites due to low-velocity impact, Part II - Analysis," *Journal of Composite Materials*, Vol. 25, No. 8: 1012-1038 (1991).
- 49) Davila, C.G., and Johnson, E.R. "Analysis of delamination initiation in postbuckled dropped-ply laminates," *AIAA Journal*, Vol. 31, No. 4: 721-727 (1993).
- 50) Grady, J.E. *Dynamic delamination crack propagation in a graphite/epoxy laminate*, PhD dissertation. Purdue University, 1985.
- 51) Liu, S. *Damage mechanics of cross-ply laminates resulting from transverse concentrated loads*. PhD Thesis. Stanford University, 1992.
- 52) Liu, S., and Kutlu, Z., and Chang, F.-W. "Matrix cracking and delamination in laminated composite beams subjected to a transverse concentrated line load," *Journal of Composite Materials*, Vol. 27, No. 5: 436-470 (1993).
- 53) Martin, R.J., and Sandhu, R.S., and Palazotto, A.N. "Experimental and analytical comparisons of failure in thermoplastic composite laminates," *Experimental Mechanics*, Vol. 34, No. 1: 53-65 (1994).
- 54) Wang, H. *Low velocity impact damage in carbon fiber/peek composite laminates*. PhD dissertation. Ecole Polytechnique, Montreal, Canada, 1993.
- 55) Daniels, J.A., Palazotto, A.N., and Sandhu, R.S. "Failure characteristics in thermoplastic composite laminates due to an eccentric circular discontinuity," *AIAA Journal*, Vol. 29, No. 5: 830-837 (1991).
- 56) Daudeville, L., and Ladeveze, P. "A damage mechanics tool for laminate delamination," *Composite Structures*, Vol. 25: 547-555 (1993).

- 57) Atluri, S.N., and Nishioka, T. "Energy-release rates in dynamic fracture: path-invariant integrals, and some computational studies," in *Proceedings of the International Conference on Fracture Mechanics Applied to Materials Evaluation and Structure Design*, 635-655, Boston, MA: Martinus Nijhoff, 1982.
- 58) Averill, R.C. *Nonlinear analysis of laminated composite shells using a micromechanics-based progressive damage model*. PhD dissertation. Virginia Polytechnic Institute and State University, 1992.
- 59) Garg, A.C. "Delamination - A Damage Mode in Composite Structures," *Engineering Fracture Mechanics*, Vol. 29, No. 5: 557-584 (1988).
- 60) Hu, S. *Dynamic delamination propagation in composite beams under impact*, PhD dissertation. University of Florida, B.V. Sankar, Gainesville, FL, 1990.
- 61) Allix, O., and Ladeveze, P. "A damage prediction method for composite structures," *International Journal for Numerical Methods in Engineering*, Vol. 27: 271-283 (1989).
- 62) Kwon, Y.W. "Calculation of effective moduli of fibrous composites with micro-mechanical damage," *Composite Structures*, Vol. 25: 187-192 (1993).
- 63) Kwon, Y.W., and Berner, J. "Analysis of matrix damage evolution in laminated composite plates," *Engineering Fracture Mechanics*, Vol. 48, No. 6: 811-817 (1994).
- 64) Larsson, P.-L. "On multiple delamination buckling and growth in composite plates," *International Journal of Solids and Structures*, Vol. 27, No. 13: 1623-1637 (1991).
- 65) Lee, J-W., Allen, D.H., and Harris, C.E. "The upper bounds of reduced axial and shear moduli in cross-ply laminates with matrix cracks," in *Composite Materials: Fatigue and Fracture (3rd vol) ASTM STP 1110*, No. 3. 56-69. ASTM 1991.
- 66) Lee, J.D. "Three dimensional finite element analysis of damage accumulation in composite laminate," *Computers & Structures*, Vol. 15, No. 3: 335-350 (1982).
- 67) Liu, S. "Quasi-Impact Damage Initiation and Growth of Thick-Section and Toughened Composite Materials," *International Journal of Solids and Structures*, Vol. 31, No. 22: 3079-3098 (1994).
- 68) Mahishi, J.M., and Adams, D.F. "Energy release rate during delamination crack growth in notched composite laminates," in *Delamination and Debonding of Materials, ASTM STP 876*. 95-111. ASTM, 1985.
- 69) Minguet, P.J. "A Model for Predicting the Behavior of Impact-Damaged Minimum Gage Sandwich Panels Under Compression," *AIAA/ASME/ASCE/AHS/ASC 32nd Structures-Structural Dynamics- & Materials Conference- Baltimore- MD*. 1112-1122. 1991.

- 70) Norman, T.L., and Sun, C.T. "Delamination growth in [90_5/0_5/90_5] laminates with adhesive strips subjected to static and dynamic impact loading," *Proceedings of the American Society for Composites 5th Technical Conference*. 633-643. 1990.
- 71) Salpekar, S.A. "Analysis of delamination in cross-ply laminates initiating from impact induced matrix cracking," *Journal of Composites Technology & Research*, Vol. 15, No. 2: 88-94 (1993).
- 72) Sankar, B.V. "A finite element for modeling delaminations in composite beams," *Computers & Structures*, Vol. 38, No. 2: 239-246 (1991).
- 73) Sankar, B.V., and Hu, S. "Dynamic delamination propagation in composite beams," *Journal of Composite Materials*, Vol. 25, No. 11: 1414-1426 (1993).
- 74) Sankar, B.V., and Pinheiro, M.A. "An offset beam finite element for fracture analysis of delaminations," *AIAA/ASME/ASCE/AHS/ASC 31st Structures, Structural Dynamics, and Materials Conference [April 2-4, 1990, Long Beach, CA]*. 1227-1233. 1990.
- 75) Talreja, R. "Transverse cracking and stiffness reduction in composite laminates," *Journal of Composite Materials*, Vol. 19: 355-375 (1985).
- 76) Talreja, R. "Stiffness properties of composite laminates with matrix cracking and interior delamination," *Engineering Fracture Mechanics*, Vol. 25, No. 5: 751-762 (1986).
- 77) Tay, T.E., and Lim, E.H. "Analysis of stiffness loss in cross-ply composite laminates," *Composite Structures*, Vol. 25: 419-425 (1993).
- 78) Wang, J.T.S., and Huang, J.T. "Skin/stiffener interface delamination using continuous analysis," *Composite Structures*, Vol. 30: 319-328 (1995).
- 79) Xu, Y., and Keer, L.M. "Analysis of crack moving and curving in anisotropic solids," *International Journal of Solids and Structures*, Vol. 31, No. 24: 3475-3491 (1994).
- 80) Aboudi, J. "Stiffness reduction of cracked solids," *Engineering Fracture Mechanics*, Vol. 25, No. 5: 637-650 (1987).
- 81) Chan, W.S., and Chou, C.J. "Effects of delamination and ply fiber waviness on effective axial and bending stiffnesses in composite laminates," *Composite Structures*, Vol. 30: 299-306 (1995).
- 82) Chen, H.P., and Leib, D. "Dynamic delamination growth in laminated composite structures," *Composites Science and Technology*, Vol. 46, No. 4: 325-333 (1993).
- 83) Choi, S.R., and Lee, K.S., and Earmme, Y.Y. "Analysis of a kinked interfacial crack under out-of-plane shear," *Journal of Applied Mechanics*, Vol. 61: 38-44 (1994).
- 84) Dandy, L.T., and Kelkar, A.D., and Sandhu, R.S. "Analysis of Progressive Damage in Thin and Thick Composite Laminates Subjected to Low-Velocity Impact Loadings,"

Presentation at the 9th International Conference on Mathematical and Computer Modelling, July 26-29, 1993, to appear in the *Journal of Mathematical and Computer Modelling*.

- 85) Doxsee, L.E., Rubbrecht, P., Li, L., Verpoest, I., and Scholle M. "Delamination Growth in Composite Plates Subjected to Transverse Loads," *Journal of Composite Materials*, Vol. 27, No. 8: 764-781 (1993).
- 86) Gibson, R.F. "Analysis of fracture," in *Principles of Composite Material Mechanics*. 338-373. New York: McGraw-Hill, 1993.
- 87) Grady, J.E., and Sun, C.T. "Dynamic delamination propagation in a graphite/epoxy laminate," in *Composite Materials: Fatigue and Fracture, ASTM STP 907*. 5-31. ASTM, 1986.
- 88) Highsmith, A.L., and Reifsnider, K.L. "Stiffness-reduction mechanisms in composite laminates," in *Damage in Composite Materials, ASTM STP 775*. 103-117. ASTM, 1982.
- 89) Hitchen, S.A., and Ogin, S.L. "Matrix cracking and modulus reduction during the fatigue of an injection-moulded glass/nylon composite," *Composites Science and Technology*, Vol. 46: 239-244 (1993).
- 90) Jones, S., and Paul, J., and Tay, T.E., Williams J.F. "Assessment of the Effect of Impact Damage in Composites: Some Problems and Answers," *Composite Structures*, Vol. 10: 51-73 (1988).
- 91) Kanninen, M.F. "A dynamic analysis of unstable crack propagation and arrest in the DCB test specimen," *International Journal of Fracture*, Vol. 10, No. 3: 415-430 (1974).
- 92) Kardomateas, G.A. "The initial post-buckling and growth behavior of internal delaminations in composite plates," *Journal of Applied Mechanics*, Vol. 60: 903-910 (1993).
- 93) Kardomateas, G.A., and Pelegri, A.A. "The stability of delamination growth in compressively loaded composite plates," *International Journal of Fracture*, Vol. 65, No. 3: 261-276 (1994).
- 94) Kassapoglou, C., and Jonas, P.J., and Abbott, R. "Compressive Strength of Composite Sandwich Panels After Impact Damage: An Experimental and Analytical Study," *Journal of Composites Technology & Research*, Vol. 10: 65-73 (1988).
- 95) Lagace, P.A., and Williamson, J.E. "Contribution of the core and facesheet to the impact damage resistance of composite sandwich panels," *Proceedings of the tenth DOD/NASA/FAA conference on fibrous composites in structural design (volume I), Report, No. NAWCADWAR-94096-60*. II-53-II-73. 1994.
- 96) Lakshminarayana, H.V., and Boukhili, R., and Gauvin, R. "Finite element simulation of impact tests of laminated composite plates," *Composite Structures*, Vol. 28: 47-59 (1994).

- 97) Lammerant, L., and Verpoest, I. "The Interaction Between Matrix Cracks and Delaminations During Quasi-Static Impact of Composites," *Composites Science and Technology*, Vol. 51: 505-516 (1994).
- 98) Larsson, P.-L., and Leckie, F.A. "Plane strain delamination growth in composite panels," *Composite Structures*, Vol. 20, No. 3: 175-184 (1992).
- 99) Armanios, E.A. "Delamination analysis for laminated composites. I: Fundamentals" *Journal of Aerospace Engineering*, Vol. 4, No. 2: 194-215 (1991).
- 100) Lee, J.-W., and Allen, D.H. "Internal state variable approach for predicting stiffness reductions in fibrous laminated composites with matrix cracks," *Journal of Composite Materials*, Vol. 23: 1273-1291 (1989).
- 101) Lee, S.M., and Zahuta, P. "Instrumented Impact and Static Indentation of Composites," *Journal of Composite Materials*, Vol. 25: 204-222 (1991).
- 102) Lu, X., and Liu, D. "Finite element analysis of strain energy release rate at delamination front," *Journal of Reinforced Plastics and Composites*, Vol. 10: 279-292 (1992).
- 103) Minnetyan, L., and Murthy, P.L.N., and Chamis, C.C. "Progressive damage and fracture of stiffened composite pressure vessels (94-1404)," *AIAA/ASME/ASCE/AHS/ASC 35th Structures, Structural Dynamics, & Materials Conference, Hilton Head Island SC*. 1994.
- 104) Naganarayana, B.P., and Atluri, S.N. "Energy-release-rate evaluation for delamination growth prediction in a multi-plate model of a laminate composite," *FAA Center of Excellence for Computational Modeling of Aircraft Structures*. 1994.
- 105) Norman, T.L., and Sun, C.T. "Delamination growth in composite laminates with adhesive strips subjected to static and impact loading," *Composites Science and Technology*, Vol. 46, No. 3: 203-211 (1993).
- 106) O'Brien, T.K. "Characterization of delamination onset and growth in a composite laminate," in *Damage in Composite Materials, ASTM STP 775*. 140-167. ASTM, 1982.
- 107) Takeda, N., and Ogihara, S. "Initiation and growth of delamination from the tips of transverse cracks in CFRP cross-ply laminates," *Composites Science and Technology*, Vol. 52: 309-318 (1994).
- 108) Tandon, G.P., and Pagano, N.J. "On the effective transverse shear modulus of debonding composites," *Proceedings of the American Society for Composites 5th Technical Conference*. 319-325. 1990.
- 109) Varna, J., and Berglund, L.A. "Thermo-elastic properties of composite laminates with transverse cracks," *Journal of Composites Technology & Research*, Vol. 16, No. 1: 77-87 (1994).

- 110) Vizzini, A.J., and Lagace, P.A. "An elastic foundation model to predict the growth of delaminations," *AIAA/ASME/ASCE/AHS 28th Structures, Structural Dynamics and Materials Conference*. 776-782. 1987.
- 111) Whitcomb, J.D. "Strain-energy release rate analysis of cyclic delamination growth in compressively loaded laminates," in *Effects of Defects in Composite Materials*, ASTM STP 836. 175-193. ASTM, 1984.
- 112) Zhang, J., Soutis, C., and Fan, J. "Strain energy release rate associated with local delamination in cracked composite laminates," *Composites*, Vol. 25, No. 9: 851-862 (1994).
- 113) Pandey, A.K., and Reddy, J.N. "A post first-ply failure analysis of composite laminates," *AIAA/ASME/ASCE/AHS 28th Structures, Structural Dynamics and Materials Conference*. 788-797. 1987.
- 114) Bakuckas, J.G. Jr., Lau, A.C.W., Tan, T.-M. and Awerbuch, J. "A Numerical Model for Predicting Crack Path and Modes of Damage in Unidirectional Composites," *Proceedings of the American Society for Composites, 6th Technical Conference, Albany, NY*. 502-512. ASC, 1991.
- 115) Joshi, S.P., and Goode, R.J. "Laminated plate finite element with damage evolution constitutive laws," *Proceedings of the American Society for Composites 5th Technical Conference*. 296-305. ASC, 1990.
- 116) Wang, S.S. "Fracture mechanics for delamination problems in composite materials," in *Mechanics of Delamination*. 114-127. 1983.
- 117) Comninou, M. "The interface crack in a shear field," *Journal of Applied Mechanics*, Vol. 45: 287-290 (1978).
- 118) Comninou, M., and Schmueser, D. "The interface crack in a combined tension-compression and shear field," *Journal of Applied Mechanics*, Vol. 46: 345-358 (1979).
- 119) Comninou, M., and Dundurs, J. "On the behavior of interface cracks," *Res Mechanica*, Vol. 1: 249-264 (1980).
- 120) Gutesen, A.K., and Dundurs, J. "Interface crack under combined loading," *Journal of Applied Mechanics*, Vol. 55, No. 3: 580-586 (1988).
- 121) Gutesen, A.K., and Dundurs, J. "On the solution to a Cauchy principle value integral equation which arises in fracture mechanics," *Journal of Applied Mathematics*, Vol. 47: 109-116 (1987).
- 122) Gutesen, A.K., and Dundurs, J. "The interface crack in a tension field," *Journal of Applied Mechanics*, Vol. 54: 93-98 (1987).

- 123) England, A.H. "A crack between dissimilar media," *Journal of Applied Mechanics*, Vol. 32: 400-402 (1965).
- 124) Malyshev, B.M., and Salganik, R.L. "The strength of adhesive joints using the theory of fracture," *International Journal of Fracture Mechanics*, Vol. 1: 114-128 (1965).
- 125) Chang, F.-K., and Kutlu, Z. "Delamination effects on composite shells," *Journal of Engineering Materials and Technology*, Vol. 112, No. 3: 336-340 (1990).
- 126) Bernard, M.L. *Impact Resistance and Damage Tolerance of Composite Sandwich Plates*, MS thesis. TELAC Report 87-11. MIT, 1987.
- 127) Llorente, S., and Weems, D., and Fay, R. "Evaluation of Advanced Sandwich Structure Designed for Improved Durability and Damage Tolerance," *46th Annual Forum of the American Helicopter Society - Washington - DC*. 825-831. AHS, 1990.
- 128) Bitzer, T.N. *Honeycomb toughness and proportional limits*, Hexcel Corporation Report LSR 932277. 1983.
- 129) Tsang, P. H. W., and Lagace, P.A. "Failure mechanisms of impact-damaged sandwich panels under uniaxial compression," *AIAA-94-1396-CP*. 745-754. AIAA, 1994.
- 130) Oplinger, D.W., and Slepetz, J.M. "Impact Damage Tolerance of Graphite-Epoxy Sandwich Panels," *Foreign object impact damage to composites : a symposium, Philadelphia, Pa., 20 Sept. 1973/ sponsored by ASTM, special technical publication 568*. 30-48. 1975.
- 131) Tsang, P.H.W. *Impact resistance and damage tolerance of composite sandwich panels*. MS thesis. TELAC Report 94-3. MIT. 1994.
- 132) Doyle, J.F. "Determining the contact force during the transverse impact of plates," *Experimental Mechanics*, Vol. 27: 68-72 (March 1987).
- 133) Hussein, R., and Fazio, P., and Morsi, M. "Analytical evaluations of damage of sandwich panels," *AIAA/ASME/ASCE/AHS 26th Structures, Structural Dynamics and Materials Conference*. 25-33, 1985.
- 134) Pryor, C.W., and Barker, R.M. "A finite element analysis including transverse shear effects for applications to laminated plates," *AIAA Journal*, Vol. 9, No. 5: 912-917 (1971).
- 135) Bencharif, N., and Ng, S.F. "Linear and non-linear deflection analysis of thick rectangular plates - I. Theoretical derivation - II. Numerical applications," *Computers & Structures*, Vol. 50: 757-776 (1994).
- 136) Whitney, J.M. "A modified shear deformation theory for laminated anisotropic plates," *Proceedings of the American Society for Composites 5th Technical Conference*. 469-478. ASC, 1990.

- 137) Byun, C., and Kapania, R.K. "Prediction of interlaminar stresses in laminated plates using global orthogonal interpolation polynomials," *AIAA Journal*, Vol. 30, No. 11: 2740-2749 (1992).
- 138) Chaudhuri, R.A. "An equilibrium method for prediction of transverse shear stresses in a thick laminated plate," *Computers & Structures*, Vol. 23, No. 2: 139-146 (1986).
- 139) Chaudhuri, R.A., and Seide, P. "An approximate semi-analytical method for prediction of interlaminar shear stresses in an arbitrarily laminated thick plate," *Computers & Structures*, Vol. 25, No. 4: 627-636 (1987).
- 140) Engblom, J.J., and Ochoa, O.O. "Through-the-Thickness Stress Predictions for Laminated Plates of Advanced Composite Materials," *International Journal for Numerical Methods in Engineering*, Vol. 21: 1759-1776 (1985).
- 141) Engblom, J.J., and Ochoa, O.O. "Finite Element Formulation Including Interlaminar Stress Calculations," *Computers & Structures*, Vol. 23, No. 2: 241-249 (1986).
- 142) Iarve, E.V., and Haq, I.U., and Soni, S.R. "The effect of material inhomogeneity in composite laminates under impact loading," *Proceedings of the American Society for Composites, 6th Technical Conference*. 513-522. Albany, NY: ASC, 1991.
- 143) Lu, X., and Liu, D. "An Interlaminar stress continuity theory for composite laminates," *Proceedings of the American Society for Composites 5th Technical Conference*. 479-488. 1990.
- 144) Ng, S.F., and Bencharif, N. "On the design and analysis of simply supported and clamped thick rectangular plates," *Computers & Structures*, Vol. 38, No. 5: 589-596 (1991).
- 145) Noor, A.K., and Burton, W.S. "Stress and free vibration analyses of multilayered composite plates," *Composite Structures*, Vol. 11: 183-204 (1989).
- 146) Noor, A.K., and Burton, W.S., and Peters, J.M. "Predictor-corrector procedures for stress and free vibration analyses of multilayered composite plates and shells," *Computer Methods in Applied Mechanics and Engineering*, Vol. 82: 341-363 (1993).
- 147) Noor, A.K., and Burton, W.S. "Assessment of computational models for multilayered anisotropic plates," *Composite Structures*, Vol. 14: 233-265 (1990).
- 148) Noor, A.K., and Kim, Y.H., and Peters, J.M. "Transverse shear stresses and their sensitivity coefficients in multilayered composite panels," *AIAA Journal*, Vol. 32, No. 6: 1259-1269 (1994).
- 149) Ochoa, C.M., and Kozik, T.J. "Transverse shear and normal stresses in laminated plates," *AIAA/ASME/ASCE/AHS 25th Structures, Structural Dynamics and Materials Conference*. 389-398. 1984.

- 150) Qian, Y. *Impact response of carbon/epoxy laminated plates*. PhD dissertation. The University of Utah, 1990.
- 151) Reddy, J.N. "An evaluation of equivalent-single-layer and layerwise theories of composite laminates," *Composite Structures*, Vol. 25: 21-35 (1993).
- 152) Schoeppner, G.A., Wolfe, W.E., and Sandhu, R.S. "Stress-based elastodynamic discrete laminated plate theory," *AIAA Journal*, Vol. 32, No. 3: 616-626 (1994).
- 153) Siler, D.J. *Finite element methods for nonlinear static analysis of sandwich plates*. MS thesis. AFIT/GAE/ENY/94D-18. School of Engineering, Air Force Institute of Technology (AU), Wright-Patterson AFB OH, 1994.
- 154) Whitney, J.M. "Stress analysis of thick laminated composites and sandwich plates," *Journal of Composite Materials*, Vol. 6: 426-440 (1984).
- 155) Banerjee, R. "Recovery of transverse shear and normal stress in anisotropic laminate under static bending," *AIAA/ASME/ASCE/AHS/ASC 35th Structures, Structural Dynamics, and Materials Conference [April 18-21, 1994]*. 1994.
- 156) Banerjee, R., and Whitney, J.M. *Analysis of a simply supported rectangular anisotropic laminate under lateral loading*. 1994.
- 157) Bonanni, D.L., Johnson, E.R., and Starnes, J.H. Jr. "Local buckling and crippling of composite stiffener sections," *Center for Composite Materials and Structures, CCMS-88-08*, 126-158. Virginia Polytechnic and State University, 1988.
- 158) Hong, S.-J., Sandhu, R.S., and Chohan, H.S. "Consistent shear constitutive relations for a laminated plate," *Journal of Composites Technology & Research*, Vol. 14, No. 1: 20-30 (1992).
- 159) Ng, S.F., and Bencharif, N. "A finite difference computer program for the modelling of thick rectangular plates," *Computers & Structures*, Vol. 33, No. 4: 1011-1016 (1989).
- 160) Noor, A.K., and Burton, W.S., and Peters, J.M. "Heirarchical adaptive modeling of structural sandwiches and multilayered composite panels," *Applied Numerical Mathematics*, Vol. 14: 69-90 (1994).
- 161) Reissner, E. "The effect of transverse shear deformation on the bending of elastic plates," *Journal of Applied Mechanics*, Vol. 55: 69-77 (June 1945).
- 162) Shames, I.H., and Dym, C.D. *Energy and finite element methods in structural mechanics*, New York: McGraw-Hill, 1985.
- 163) Wang, H., and Vu-Khanh, T. "Impact-Induced Delamination in [0_{sub 5}, 90_{sub 5}, 0_{sub 5}] Carbon Fiber/Polyetheretherketone Composite Laminates," *Polymer Engineering and Science*, Vol. 31, No. 18: 1301-1309 (1991).

- 164) Wijeyewickrema, A.C., and Keer, L.M. "Axial decay of stresses in a layered composite with slipping interfaces," *Composites Engineering*, Vol. 4, No. 9: 895-899 (1994).
- 165) Xiaoyu, J. "Linear and non-linear 3-D analysis of hybrid composite laminates," *Composites Science and Technology*, Vol. 52: 377-385 (1994).
- 166) Aoki, T., and Kondo, K. "Delamination energy release rates under thermal loading in fiber-reinforced composite laminates," *Composite Structures*, Vol. 14, No. 3: 213-231 (1990).
- 167) Babuska, I., and Miller, A. "The post-processing approach in the finite element method (Pt 1 and Pt 2)," *International Journal for Numerical Methods in Engineering*, Vol. 20, No. 6: 1055-1129 (1984).
- 168) Bogdanovich, A.E., and Yarve, E.V. "Numerical analysis of laminated composite plates subjected to impact loading," *Proceedings of the American Society for Composites, 4th Technical Conference*. 399-405. Lancaster PA: ASC, 1989.
- 169) Corradi, L. "On stress computation in displacement finite element models," *Computer Methods in Applied Mechanics and Engineering*, Vol. 54: 325-339 (1986).
- 170) Gamby, D., and Rebiere, J.L. "A two-dimensional analysis of multiple matrix cracking in a laminated composite close to its characteristic damage state," *Composite Structures*, Vol. 25: 325-337 (1993).
- 171) Wu, C-P. and Hsu, C.-S. "A new local high-order laminate theory," *Composite Structures*, Vol. 25: 439-448 (1993).
- 172) Palazotto, A.N., and Dennis, S.T. *Nonlinear analysis of shell structures*, AIAA Education Series. Washington DC: AIAA, 1992.
- 173) Cook, R.D., Malkus, D.S., and Plesha, M.E. *Concepts and applications of the finite element method*, third edition, John Wiley & Sons, 1989.
- 174) Dennis, S.T. *Large displacement and rotational formulation for laminated cylindrical shells including parabolic transverse shear*. PhD dissertation. Air Force Institute of Technology (AU), Wright-Patterson AFB OH, May 1988 (AD-A194871).
- 175) Tsai, C.T., and Palazotto, A.N. "On the finite element analysis of non-linear vibration for cylindrical shells with high-order shear deformation theory," *International Journal of Non-Linear Mechanics*, Vol. 26: 379-388 (1991).
- 176) Banerjee, R. "Numerical simulation of impact damage in composite laminates," *Proceedings of the 7th technical conf. of ASC*. 1992.
- 177) Keer, L.M., and Kim, S.H., and Eberhardt, A.W.; Vithoontien, V. "Compliance of coated elastic bodies in contact," *International Journal of Solids and Structures*, Vol. 27, No. 6: 681-698 (1991).

- 178) Christoforou, A.P. "On the contact of a spherical indenter and a thin composite laminate," *Composite Structures*, Vol. 26: 77-82 (1993).
- 179) Karaoglan, L., and Springer, G.S. "Axial impact of composites," *Computers & Structures*, Vol. 49, No. 5: 807-823 (1993).
- 180) Kuo, C.H., and Keer, L.M. "Contact stress analysis of a layered transversely isotropic half-space," *Journal of Tribology*, Vol. 114: 253-262 (1992).
- 181) Lin, W., Kuo, C.H., and Keer, L.M. "Analysis of a Transversely Isotropic Half Space Under Normal and Tangential Loadings," *Journal of Tribology*, Vol. 113: 335-338 (1991).
- 182) Liu, S. "Delamination and matrix cracking of cross-ply laminates due to a spherical indenter," *Composite Structures*, Vol. 25: 257-265 (1993).
- 183) Malone, J.G., and Johnson, N.L. "A Parallel Finite Element Contact/Impact Algorithm for Non-linear Explicit Transient Analysis: Part I--The Search Algorithm and Contact Mechanics," *International journal for numerical methods in engineering*, Vol. 37, No. 4: 559-590 (1994).
- 184) Malone, J.G., and Johnson, N.L. "A Parallel Finite Element Contact/Impact Algorithm for Non-linear Explicit Transient Analysis: Part II--Parallel Implementation," *International journal for numerical methods in engineering*, Vol. 37, No. 4: 591- (1994).
- 185) Okrouhlik, M. "Mechanics of contact impact," *Applied Mechanics Reviews*, Vol. 47, No. 2: 33-99 (1994).
- 186) Sun, C.T., and Chen, J.K. "On the impact of initially stressed composite laminates," *Journal of Composite Materials*, Vol. 19: 490-504 (1985).
- 187) Tan, T.M., and Sun, C.T. "Use of Statical Indentation Laws in the Impact Analysis of Laminated Composite Plates," *Journal of Applied Mechanics*, Vol. 52: 6-11 (March 1985).
- 188) Thomsen, O.T. "Analysis of local bending effects in sandwich plates with orthotropic face layers subjected to localized loads," *Composite Structures*, Vol. 25: 511-520 (1993).
- 189) Wu, E., and Yen, C.-S. "The contact behavior between laminated composite plates and rigid spheres," *Journal of Applied Mechanics*, Vol. 61: 60-66 (1994).
- 190) Zhou, M., and Schonberg, W.P. "Comment on global/local method for low-velocity impact problems," *Journal of Engineering Mechanics*, Vol. 120, No. 5: 1042-1056 (1994).
- 191) Ahmadi, N., and Keer, L.M. "Non-Hertzian stress analysis - normal and sliding contact," *International Journal of Solids and Structures*, Vol. 19, No. 4: 357-373 (1983).

- 192) Dobyns, A.L. "Analysis of Simply Supported Plates Subjected to Static and Dynamic Loads," *AIAA Journal*, Vol. 19, No. 5: 642-650 (1981).
- 193) Christoforou, A.P. "Normalized impact response and damage in a thin composite laminate supported by a rigid substrate," *Journal of Composite Materials*, Vol. 28, No. 16: 1553-1573 (1994).
- 194) Keer, L.M., and Lee, J.C. "Dynamic impact of an elastically supported beam - large area contact," *International Journal of Engineering Science*, Vol. 23, No. 10: 987-997 (1985).
- 195) Lie, S.C. *Damage Resistance and Damage Tolerance of Thin Composite Facesheet Honeycomb Panels*, MS thesis. TELAC Report 89-3. MIT, 1989.
- 196) Kan, H.P., and Graves, M.J., et al. *Damage Tolerance of Composites - Vol III Analysis, Methods, Development, and Test Verification*, AFWAL-TR-87-3030, Wright-Patterson AFB, OH, Vol. 3, 1988.
- 197) Ramkumar, R.L., and Chen, P.C. "Low-Velocity Impact Response of Laminated Plates," *AIAA Journal*, Vol. 21, No. 10: 1448-1452 (1983).
- 198) Takeda, N., and Sierakowski, R.L. "Localized Impact Problems of Composite Laminates," *Shock and Vibration Digest*, Vol. 12: 3-10 (1980).
- 199) Thangjitham, S., and Librescu, L., and Cederbaum, G. "Low Velocity Impact Response of Orthotropic Plates using a Higher Order Theory," *AIAA/ASME/ASCE/AHS 28th Structures, Structural Dynamics and Materials Conference*. 448-457. 1987.
- 200) Yang, S.H., and Sun, C.T. "Indentation Law for Composite Laminates," *Composite Materials: Testing and Design (Sixth Conference)*, ASTM STP 787. 425-449. ASTM, 1982.
- 201) Jackson, W.C., and Poe, C.C. Jr. "The Use of Impact Force as a Scale Parameter For the Impact Response of Composite Laminates," *Journal of Composites Technology & Research*, Vol. 15, No. 4: 282-289 (1993).
- 202) Koller, M.G. "Elastic impact on sandwich plates," *Journal of Applied Mathematics and Physics*, Vol. 37, No. 2: 256-269 (1986).
- 203) Koller, M.G., and Busenhardt, M. "Elastic impact of spheres on thin shallow spherical shells," *International Journal of Impact Engineering*, Vol. 4, No. 1: 11-21 (1986).
- 204) Wu, H.T., and Springer, G.S. "Impact Induced Stresses, Strains, and Delaminations in Composite Plates," *Journal of Composite Materials*, Vol. 22: 533-560 (1988).
- 205) Choi, H.Y., and Chang, F.K. "A Model for Predicting Damage in Graphite/Epoxy Laminated Composites Resulting from Low-Velocity Point Impact," *Journal of Composite Materials*, Vol. 26, No. 14: 2134-2169 (1992).

- 206) Sun, C.T. *An analytical method for evaluation of impact damage energy of laminated composites*, ASTM STP 617. ASTM, 1977.
- 207) Greszczuk, L.B. "Damage in composite materials due to low velocity impact," in *Impact Dynamics*. 55-93. 1982.
- 208) Bucinell, R.B., Nuismer, R.J., and Koury, J.L. "Response of composite plates to quasi-static impact events," in *Composite Materials: Fatigue and Fracture (3rd vol) ASTM STP 1110, No. 3*. 528-549. 1991.
- 209) Sankar, B.V., and Sun, C.T. "Indentation of a beam by a rigid indenter," *International Journal of Solids and Structures*, Vol. 19, No. 4: 293-303 (1983).
- 210) Whitcomb, J.D. "Analysis of a Laminate with a Postbuckled Embedded Delamination, Including Contact Effects," *Journal of Composite Materials*, Vol. 26, No. 10: 1523-1535 (1992).
- 211) Caprino, G., and Teti, R. "Impact and post-impact behavior of foam core sandwich structures," *Composite Structures*, Vol. 29: 47-55 (1994).
- 212) Rotem, A. "Residual flexural strength of FRP composite specimens subjected to transverse impact loading," *SAMPE Journal*, Vol. 24, No. 2: 19-25 (1988).
- 213) Chou, P.C., and Flis, W.J. "Design curve for beams under impact loading," *AIAA Journal*, Vol. 15, No. 4: 455-456 (1977).
- 214) Sjoblom, P.O., Hartness, J.Y., and Cordell, T.M. "On Low-Velocity Impact Testing of Composite Materials," *Journal of Composite Materials*, Vol. 22: 30-52 (1988).
- 215) Lal, K.M. "Residual strength assessment of low velocity impact damage of graphite-epoxy laminates," *Journal of Reinforced Plastics and Composites*, Vol. 2: 226-238 (1983).
- 216) Lal, K.M. "Low velocity transverse impact behavior of 8-ply, graphite-epoxy laminates," *Journal of Reinforced Plastics and Composites*, Vol. 2: 216-225 (1983).
- 217) Choi, I.H., and Hong, C.S. "New Approach for Simple Prediction of Impact Force History on Composite Laminates," *AIAA Journal*, Vol. 32, No. 10: 2067-2072 (1994).
- 218) Schoeppner, G.A. *Damage in Graphite/Epoxy Plates Subjected to Low Velocity Impact*, 1988 USAF-UES Summer Faculty Research Program / Graduate Student Summer Support Program - Final Report. 1988.
- 219) Sankar, B.V., and Rao, V.S. "A Plate Finite Element for Modeling Delaminations," *Journal of Reinforced Plastics and Composites*, Vol. 12, No. 2: 227-236 (1993).
- 220) Symbolics Inc. *Vax UNIX MACSYMA reference manual*, Symbolics Inc., document, No. SMI0501030.011, 1985.

- 221) Saada, A.S. *Elasticity theory and applications*. Malabar FL: Robert E. Krieger, 1987.
- 222) Katona, M.G., and Zienkiewicz, O.C. "A unified set of single step algorithms Part 3: The beta-m method, a generalization of the Newmark scheme," *International Journal for Numerical Methods in Engineering*, Vol. 21: 1345-1359 (1985).
- 223) Monteverde, J.L. *Effects of thickness and curvature on the natural frequencies of cylindrical composite shells*. MS thesis. AFIT/GAE/ENY/94J-2. School of Engineering, Air Force Institute of Technology (AU), Wright-Patterson AFB OH, June 1994 (AD-A280689).
- 224) Palazotto, A.N., and Linnemann, P.E. "Vibration and Buckling Characteristics of Composite Cylindrical Panels Incorporating the Effects of a Higher Order Shear Theory," *International Journal of Solids and Structures*, Vol. 28, No. 3: 341-361 (1991).
- 225) Liu, D. "Impact-Induced Delamination - A View of Bending Stiffness Mismatching," *Journal of Composite Materials*, Vol. 22: 674-692 (1988).
- 226) Cantwell, W.J., and Morton, J. "Geometrical effects in the low velocity impact response of CFRP," *Composite Structures*, Vol. 12: 39-59 (1989).
- 227) Rhodes, M.D., and Williams, J.G., and Starnes, J.H. "Low Velocity Impact Damage in Graphite-fiber Reinforced Epoxy Laminates," *Polymer Composites*, Vol. 2, No. 1: 36-44 (1981).
- 228) Jones, R.L. *Impact analysis of composite sandwich panels as a function of skin, core, and resin materials*, MS thesis. Florida Institute of Technology, 1989.
- 229) Finn, S.R. *Composite plates impact damage : an atlas*. Technomic Pub. Co., 1991.
- 230) Wu, C-P. and Lin, C.-C. "Analysis of sandwich plates using a mixed finite element," *Composite Structures*, Vol. 25: 397-405 (1993).
- 231) Lu, X., and Liu, D. "Interlayer shear slip theory for cross-ply laminates with nonrigid interfaces," *ALAA Journal*, Vol. 30, No. 4: 1063-1073 (1992).
- 232) American Cyanamid Company. *FM 300-2 Film adhesive - Modified epoxy resin film, Product Description*, American Cyanamid Company, Engineered Materials Department, 1990.
- 233) Abrate, S. "Impact on laminated composites: Recent advances," *Applied Mechanics Reviews*, Vol. 47, No. 11: 517-544 (1994).
- 234) Rao, K.P., and Sridhar, C. "Estimation of low-velocity impact damage in laminated composite circular plates using nonlinear finite element analysis," *Computers & Structures*, Vol. 54, No. 6: 1183- (1995).
- 235) Bazenhov, S.L. "Interlaminar and intralaminar fracture modes in 0/90 cross-ply glass/epoxy laminate," *Composites*, Vol. 26, No. 2: 125- (1995).

- 236) Pagano, N.J.. "Exact solutions for composite laminates in cylindrical bending," *Journal of Composite Materials*, Vol. 3: 398-411 (1969).
- 237) Pagano, N.J.. "Exact solutions for rectangular bidirectional composites and sandwich plates," *Journal of Composite Materials*, Vol. 4: 20-34 (1970).
- 238) Washizu, K. *Varitaional methods in elasticity and plasticity*, 3rd Edition, Oxford: Pergamon Press, 1982.
- 239) Owen, D.R., and Hinton, E. *Finite elements in plasticity*, Swansea, U.K.: Pineridge Press, 1980.
- 240) Noor, A.K. Burton, W.S. "Computational models for sandwich panels and shells," *Applied Mechanics Reviews*, Vol 49, No 3: 155-199 (1996).
- 241) Jaeger J. "Analytical solutions of contact impact problems," *Applied Mechanics Reviews*, Vol 47, No 2: 35-54 (1994).
- 242) Hashin, Z.-H. Failure criteria for unidirectional fiber composites," *Journal of Applied Mechanics*, Vol 47: 329-334 (1980).
- 243) Timoshenko, S. and Goodier, J.N. *Theory of Elasticity*, New York: McGraw-Hill, 1951.
- 244) Greer, James M. PhD dissertation. Air Force Institute of Technology (AU), Wright-Patterson AFB OH, January 1996.

Vlua

Eric J. Herup [REDACTED]. He attended Irvington High School through the 11th grade and, after obtaining a High School equivalency certificate in 1978, he enlisted in the Air Force. Eric entered the Air Force Academy in 1980 and, in 1984 he was commissioned and graduated with a Bachelor of Science degree in Aeronautical Engineering. His first assignment after commissioning was as a project officer at Kirtland AFB performing research in support of ground and space based laser initiatives. In 1989 he graduated from the Air Force Institute of Technology with a Master of Science degree in Aeronautical Engineering. His next assignment was as lead C-130 damage tolerance engineer at the C-130 depot at Robins AFB. In 1993 Eric returned to the Air Force Institute of Technology to begin his studies toward the degree Doctor of Philosophy in Aeronautical Engineering. Upon completion of the AFIT program, Eric will be assigned as chief of the Applied Composites Branch, Structures and Controls Division, Space and Missiles Technology Directorate, of Phillips Laboratory at Kirtland AFB.

Eric is married to the former Naomi Hathaway of Colorado Springs, Colorado. They have four children, Rachel [REDACTED], Paul [REDACTED], Joshua [REDACTED] and Caleb [REDACTED]. Eric is the son of William and Jacklyn Herup of [REDACTED].

[REDACTED]
[REDACTED]

REPORT DOCUMENTATION PAGE			Form Approved OMB No. 0704-0188	
Public reporting burden for this collection of information is estimated to average 1 hour per response, including the time for reviewing instructions, searching existing data sources, gathering and maintaining the data needed, and completing and reviewing the collection of information. Send comments regarding this burden estimate or any other aspect of this collection of information, including suggestions for reducing this burden, to Washington Headquarters Services, Directorate for Information Operations and Reports, 1215 Jefferson Davis Highway, Suite 1204, Arlington, VA 22202-4302, and to the Office of Management and Budget, Paperwork Reduction Project (0704-0188), Washington, DC 20503.				
1. AGENCY USE ONLY (Leave blank)		2. REPORT DATE July 1996		3. REPORT TYPE AND DATES COVERED Doctoral Dissertation
4. TITLE AND SUBTITLE LOW-VELOCITY IMPACT ON COMPOSITE SANDWICH PLATES			5. FUNDING NUMBERS	
6. AUTHOR(S) Eric J. Herup, Major, USAF				
7. PERFORMING ORGANIZATION NAME(S) AND ADDRESS(ES) Air Force Institute of Technology 2750 P Street Wright-Patterson AFB, OH 45433-7765			8. PERFORMING ORGANIZATION REPORT NUMBER AFIT/DS/ENY/96-11	
9. SPONSORING/MONITORING AGENCY NAME(S) AND ADDRESS(ES) Mr. William Baron WL/FIBA, Bldg 45 2130 Eighth St, Ste 1 Wright-Patterson AFB, OH 45433-7524			10. SPONSORING/MONITORING AGENCY REPORT NUMBER	
11. SUPPLEMENTARY NOTES				
12a. DISTRIBUTION / AVAILABILITY STATEMENT Approved for public release; distribution unlimited			12b. DISTRIBUTION CODE	
13. ABSTRACT (Maximum 200 words) The purpose of this research is to analytically model the response of composite sandwich plates to low-velocity impact. A displacement based, plane stress, finite element code is modified. New algorithms include 5 th order Hermitian interpolation, three-dimensional equilibrium integration for transverse stress calculations, sandwich core modeling as an elastic foundation, loading by simulated contact with a spherical indenter, adaptive mesh, damage prediction, damage progression via stiffness reduction, and local-global analysis for displacement. An experimental effort is also included. Composite sandwich plates with graphite-epoxy facesheets and Nomex honeycomb core are subjected to low-velocity impact and static indentation. Classical elasticity solutions are modified for Hertzian contact, providing an exact solution. The finite element analysis predicts the three-dimensional state of stress in an undamaged composite sandwich under contact-type loading, comparing favorably with the elasticity solution. When compared to the experimental data, the analysis shows the ability to model the slope of the load displacement curve (stiffness), including contact, before damage. Core failure load is predicted by the analysis within ten percent of the experimental value. Delamination patterns predicted by the analysis are similar in shape to the delaminations observed by C-scans from the experiments, but are smaller for the same load.				
14. SUBJECT TERMS Composite sandwich, Honeycomb, low-velocity impact, Hertzian contact, Hermitian interpolation, instrumented impactor, impactor dynamics			15. NUMBER OF PAGES 362	
			16. PRICE CODE	
17. SECURITY CLASSIFICATION OF REPORT Unclassified	18. SECURITY CLASSIFICATION OF THIS PAGE Unclassified	19. SECURITY CLASSIFICATION OF ABSTRACT Unclassified	20. LIMITATION OF ABSTRACT UL	

GENERAL INSTRUCTIONS FOR COMPLETING SF 298

The Report Documentation Page (RDP) is used in announcing and cataloging reports. It is important that this information be consistent with the rest of the report, particularly the cover and title page. Instructions for filling in each block of the form follow. It is important to *stay within the lines* to meet optical scanning requirements.

Block 1. Agency Use Only (Leave blank).

Block 2. Report Date. Full publication date including day, month, and year, if available (e.g. 1 Jan 88). Must cite at least the year.

Block 3. Type of Report and Dates Covered. State whether report is interim, final, etc. If applicable, enter inclusive report dates (e.g. 10 Jun 87 - 30 Jun 88).

Block 4. Title and Subtitle. A title is taken from the part of the report that provides the most meaningful and complete information. When a report is prepared in more than one volume, repeat the primary title, add volume number, and include subtitle for the specific volume. On classified documents enter the title classification in parentheses.

Block 5. Funding Numbers. To include contract and grant numbers; may include program element number(s), project number(s), task number(s), and work unit number(s). Use the following labels:

C - Contract	PR - Project
G - Grant	TA - Task
PE - Program Element	WU - Work Unit Accession No.

Block 6. Author(s). Name(s) of person(s) responsible for writing the report, performing the research, or credited with the content of the report. If editor or compiler, this should follow the name(s).

Block 7. Performing Organization Name(s) and Address(es). Self-explanatory.

Block 8. Performing Organization Report Number. Enter the unique alphanumeric report number(s) assigned by the organization performing the report.

Block 9. Sponsoring/Monitoring Agency Name(s) and Address(es). Self-explanatory.

Block 10. Sponsoring/Monitoring Agency Report Number. (If known)

Block 11. Supplementary Notes. Enter information not included elsewhere such as: Prepared in cooperation with...; Trans. of...; To be published in.... When a report is revised, include a statement whether the new report supersedes or supplements the older report.

Block 12a. Distribution/Availability Statement. Denotes public availability or limitations. Cite any availability to the public. Enter additional limitations or special markings in all capitals (e.g. NOFORN, REL, ITAR).

DOD - See DoDD 5230.24, "Distribution Statements on Technical Documents."

DOE - See authorities.

NASA - See Handbook NHB 2200.2.

NTIS - Leave blank.

Block 12b. Distribution Code.

DOD - Leave blank.

DOE - Enter DOE distribution categories from the Standard Distribution for Unclassified Scientific and Technical Reports.

NASA - Leave blank.

NTIS - Leave blank.

Block 13. Abstract. Include a brief (*Maximum 200 words*) factual summary of the most significant information contained in the report.

Block 14. Subject Terms. Keywords or phrases identifying major subjects in the report.

Block 15. Number of Pages. Enter the total number of pages.

Block 16. Price Code. Enter appropriate price code (*NTIS only*).

Blocks 17. - 19. Security Classifications. Self-explanatory. Enter U.S. Security Classification in accordance with U.S. Security Regulations (i.e., UNCLASSIFIED). If form contains classified information, stamp classification on the top and bottom of the page.

Block 20. Limitation of Abstract. This block must be completed to assign a limitation to the abstract. Enter either UL (unlimited) or SAR (same as report). An entry in this block is necessary if the abstract is to be limited. If blank, the abstract is assumed to be unlimited.